Transactions of the ASME®

Journal of Turbomachinery

Technical Editor, **T. H. OKIISHI (1998)**
Associate Technical Editors
Aeromechanical Interaction
R. E. KIELB (1996)
Gas Turbine
C. J. RUSSO (1995)
Heat Transfer
M. G. DUNN (1996)
Nuclear Engineering
H. H. CHUNG (1996)
Power
P. H. GILSON (1996)
Turbomachinery
N. A. CUMPSTY (1995)

BOARD ON COMMUNICATIONS
Chairman and Vice-President
R. MATES

Members-at-Large
T. BARLOW, N. H. CHAO, A. ERDMAN,
G. JOHNSON, L. KEER, E. M. PATTON,
S. PATULSKI, S. ROHDE, R. SHAH,
F. WHITE, J. WHITEHEAD, K. T. YANG

OFFICERS OF THE ASME
President, **D. T. KOENIG**
Executive Director
D. L. BELDEN
Treasurer
R. A. BENNETT

PUBLISHING STAFF
Managing Director, Engineering
CHARLES W. BEARDSLEY
Director, Technical Publishing
JANET M. WEINRIB
Managing Editor, Technical Publishing
CYNTHIA B. CLARK
Managing Editor, Transactions
CORNELIA MONAHAN
Senior Production Editor,
VALERIE WINTERS
Production Assistant,
MARISOL ANDINO

Transactions of the ASME, Journal of Turbomachinery (ISSN 0889-504X) is published quarterly (Jan., Apr., July, Oct.) for $150.00 per year by The American Society of Mechanical Engineers, 345 East 47th Street, New York, NY 10017. Second class postage paid at New York, NY and additional mailing offices. POSTMASTER: Send address changes to Transactions of the ASME, Journal of Turbomachinery, c/o THE AMERICAN SOCIETY OF MECHANICAL ENGINEERS, 22 Law Drive, Box 2300. Fairfield, NJ 07007-2300.
CHANGES OF ADDRESS must be received at Society headquarters seven weeks before they are to be effective. Please send old label and new address.
PRICES: To members, $40.00, annually; to nonmembers, $150.00.
Add $24.00 for postage to countries outside the United States and Canada.

STATEMENT from By-Laws. The Society shall not be responsible for statements or opinions advanced in papers or . . . printed in its publications (B7.1, Par. 3).
COPYRIGHT © 1995 by The American Society of Mechanical Engineers. Authorization to photocopy material for internal or personal use under circumstances not falling within the fair use provisions of the Copyright Act is granted by ASME to libraries and other users registered with the Copyright Clearance Center (CCC) Transactional Reporting Service provided that the base fee of $3.00 per article is paid directly to CCC, 222 Rosewood Dr., Danvers, MA 01923. Request for special permission or bulk copying should be addressed to Reprints/Permission Department.

INDEXED by Applied Mechanics Reviews and Engineering Information, Inc.
Canadian Goods & Services
Tax Registration #126148048

Published Quarterly by The American Society of Mechanical Engineers

VOLUME 117 • NUMBER 3 • JULY 1995

TECHNICAL PAPERS

TECHNICAL BRIEFS

ANNOUNCEMENTS

Downloaded 01 Jun 2010 to 171.66.16.52. Redistribution subject to ASME license or copyright; see http://www.asme.org/terms/Terms_Use.cfm

Turbomachinery Committee Best 1994 Paper Award

Dynamic Control of Rotating Stall in Axial Flow Compressors Using Aeromechanical Feedback

D. L. Gysling
United Technologies Research Center,
East Hartford, CT 06108

E. M. Greitzer
Gas Turbine Laboratory,
Massachusetts Institute of Technology,
Cambridge, MA 02139

Dynamic control of rotating stall in an axial flow compressor has been implemented using aeromechanical feedback. The control strategy developed used an array of wall jets, upstream of a single-stage compressor, which were regulated by locally reacting reed valves. These reed valves responded to the small-amplitude flow-field pressure perturbations that precede rotating stall. The valve design was such that the combined system, compressor plus reed valve controller, was stable under operating conditions that had been unstable without feedback. A 10 percent decrease in the stalling flow coefficient was obtained using the control strategy, and the extension of stable flow range was achieved with no measurable change in the steady-state performance of the compression system. The experiments demonstrate the first use of aeromechanical feedback to extend the stable operating range of an axial flow compressor, and the first use of local feedback and dynamic compensation techniques to suppress rotating stall. The design of the experiment was based on a two-dimensional stall inception model, which incorporated the effect of the aeromechanical feedback. The physical mechanism for rotating stall in axial flow compressors was examined with focus on the role of dynamic feedback in stabilizing compression system instability. As predicted and experimentally demonstrated, the effectiveness of the aeromechanical control strategy depends on a set of nondimensional control parameters that determine the interaction of the control strategy and the rotating stall dynamics.

1.0 Introduction and Background

The operating range of turbomachinery compression systems is generally limited at low mass flow rates by the onset of fluid dynamic instability. The disturbances that result from such instabilities are generally categorized in one of two broad classes of instabilities: surge or rotating stall. Surge is an essentially one-dimensional instability characterized by oscillations in compressor annulus-averaged mass flow and pressure rise extending through the entire compression system. Rotating stall is a two- or three-dimensional disturbance in which regions of low, or reversed, mass flow (termed stall cells) rotate about the annulus of the compressor. Both forms of instability degrade compression system performance and durability (Greitzer, 1981) and are thus to be avoided; the conventional approach for accomplishing this is to operate the system a safe margin from the instability onset point, thereby sacrificing pressure rise capability and possibly efficiency.

Recently, a new approach to alleviate the constraints imposed by compression system instabilities was proposed by Epstein et al. (1989). In this, the stable flow range of the compression system is extended by suppressing instabilities such as rotating stall and surge using dynamic feedback. The view taken is that fully developed rotating stall and surge are large-amplitude, limit cycle oscillations of initially small amplitude instabilities (Moore and Greitzer, 1986). Using feedback to modify the small-amplitude system dynamics and ensure stability, the flow rate at which rotating stall or surge occurs can be reduced, extending the machine's useful operating range. Further, since control of the instabilities is enacted while disturbances are small, the power required to stabilize the compression system is also small, typically more than two orders of magnitude below the steady-state power level.

Since this concept was first presented, several researchers (Ffowcs Williams and Huang, 1989; Gysling et al., 1991; Simon et al., 1993) have used feedback control to stabilize the one-dimensional surge instability and validate the basic idea, but there has been much less work on stabilizing rotating stall. The first successful attempt to extend the stable flow range of an axial flow compressor using feedback was carried out by Day (1993) on a low-speed, multistage compressor. The method used was based on sensing small-amplitude perturbations in axial velocity. When the perturbations reached a predetermined amplitude, an array of injection valves were opened to inject a small amount (1 percent of the mean flow or less) of high-pressure fluid into the tip region of the rotor.

Paduano et al. (1993), working with a single-stage, axial flow compressor, used feedback control to directly modify the small amplitude rotating stall dynamics of the compression system and hence extend the stable flow range. The control strategy employed a description of the perturbation velocity field as a summation of spatial Fourier modes. A spatial array of twelve movable inlet guide vanes, located around the annulus at the face of the compressor, was used to actuate individual spatial modes, with actuation based on the magnitude and spatial phase of the harmonics of the axial velocity perturbation sensed by a spatial array of hot wires. To implement the feedback, a high-speed digital computer was used to perform real-time, spatial Fourier decomposition of the flow field. Paduano's results, followed by similar results of Haynes (1994) on a multistage compressor, gave clear demonstration that control strategies designed to alter the small amplitude dynamic compressor response could extend the stable flow range, closely in line with the concepts presented by Epstein et al. (1989).

Contributed by the International Gas Turbine Institute and presented at the 39th International Gas Turbine and Aeroengine Congress and Exposition, The Hague, The Netherlands, June 13–16, 1994. Manuscript received by the International Gas Turbine Institute March 15, 1994. Paper No. 94-GT-292. Associate Technical Editor: E. M. Greitzer.

2.0 Objectives and Scope of the Present Study

The experiments of Day (1993), Paduano et al. (1993), and Haynes (1994) were successful proof-of-concept demonstrations of active stabilization of rotating stall in axial flow compressors. However, a number of issues remain unresolved, not only in development and implementation of control strategies, but also of a basic fluid dynamic nature.

The primary objective of the present research was to develop and experimentally demonstrate a strategy to stabilize rotating stall in axial flow compressors using *aeromechanical feedback.* This is differentiated from the previous control strategies which have been based on electromechanical implementation of feedback and which have required external real time computation and high bandwidth sensors and actuators. Aeromechanical control has several potential advantages, including stabilization without external input, and the elimination of the need for sensors and actuators.

An additional important difference with previous control schemes is that the present strategy is based on locally reacting feedback. Sensors and actuators are colocated, so that the local unsteady pressure rise versus mass flow performance of the compression system is modified. The approach can thus be contrasted with previous efforts based on control of the different spatial modes (Paduano et al., 1993; Haynes et al., 1994).

In the next section, an outline of the analysis for stability of the compressor flow field is presented. From the results, the physical mechanism responsible for rotating stall is interpreted, and the role of dynamic feedback in stabilizing the flow field is discussed as motivation for the present aeromechanical control strategy. Modeling of the effect of the aeromechanical control strategy on the rotating stall dynamics is also described. The design of a facility based on this analysis is then addressed, followed by discussion of the results of experiments carried out to evaluate the performance of the aeromechanical control strategy as well as to examine the key physical mechanisms associated with the enhanced stability. Finally, conclusions are offered that relate this work to the general goal of stabilizing rotating stall in axial flow compressors.

3.0 Overall Features of Compression System Instability and the Role of Dynamic Feedback

The basic description of the behavior of small-amplitude perturbations about a steady, uniform flow field was first developed by Moore (1984) with additional contributions to the model presented by Moore and Greitzer (1986). The model predicts that there is a critical condition at which small disturbances will grow (initially exponentially) into large-amplitude rotating stall. Stability of the flow field is thus governed by the linearized compression system dynamics.

3.1 Stability of the Basic Compression System. The modeling of the basic compression system is more or less standard and can be found elsewhere (e.g., Moore, 1984; Moore and Greitzer, 1986; Gysling, 1993). We summarize only the relevant results needed for the subsequent discussion. For the problem as posed, the stability of the individual spatial Fourier harmonics is uncoupled and stability can be assessed on a harmonic by harmonic basis. The solutions are expressed in traveling wave form, $e^{in(\theta-\sigma\tau)}$, where the time dependence is given by the eigenvalues, σ. The values of σ are found to be (Moore, 1984)

$$\sigma = \frac{i\dfrac{\partial\Psi}{\partial\Phi} + n\lambda}{4 + n\mu} \tag{1}$$

where $\partial\Psi/\partial\Phi$ is the slope of the (inlet total-to-exit static pres-

Nomenclature

A = area
B = compression system stability parameter $\equiv U_R/2\omega_H L_c$
b = reed valve damping constant
c = chord
C = velocity
C_x = axial velocity
H = annulus height
i = imaginary number $= \sqrt{-1}$
$\tilde{L}$ = length of reed valve normalized by annulus height
L_c = length of inlet duct to compressor
M = complex compressor pressure rise versus mass flow transfer function; modal mass of reed valves
m = mass flow
n = spatial Fourier harmonic number
P = pressure
p = nondimensional pressure $\equiv P/\frac{1}{2}\rho U_R^2$
q = nondimensional reed valve opening $\equiv \Delta/H$
Q = natural frequency of reed valves normalized by rotor frequency $\equiv \omega_n/(U_R/R)$
R = midspan radius of compressor
rms = root mean square
s = complex frequency
SFC = spatial Fourier coefficient
U = velocity
U_R = velocity of rotor at midspan
W = reed mass parameter $\equiv \rho\tilde{L}R^2/M$
z = nondimensional time rate of change of reed valve opening $\equiv \partial q/\partial\tau$
α = ratio of spring constants in visco-elastic dashpot to that in reed valve
δE = rate of nondimensional perturbation energy production across compressor
$\partial\Psi/\partial\Phi$ = slope of compressor characteristic: inlet-total-to-exit-static pressure rise coefficient (Ψ) versus mass flow coefficient (Φ)
Δ = reed valve opening
ζ = reed damping parameter $\equiv b/2M\omega_n$
θ = circumferential position, rad
λ = inertial parameter for rotating blade rows
μ = inertial parameter for blade rows
ν = perturbation circumferential flow coefficient
ρ = ambient density
σ = temporal complex eigenvalue
τ = non-dimensional time $= tU_R/R$
ϕ = axial flow coefficient $= \Phi + \delta\phi$
$\tilde{\phi}_n$ = nth spatial Fourier component of $\delta\phi$
Φ = mean axial flow coefficient $\equiv \dot{m}/\rho A U_R = C_x/U_R$
Φ_i = injection parameter $\equiv C_{x_i}/U_R$
χ = visco-elastic influence parameter $\equiv 2\zeta/Q\alpha$
Ψ = pressure coefficient $\equiv (P_{\text{exit}} - P_{\text{inlet}})/\frac{1}{2}\rho U_R^2$
ω = frequency
ω_n = natural frequency of reed valves

Subscripts

a = axial station of injection
b = axial station downstream of injection region, upstream of compressor
c = compressor
d = downstream flow field
i = injection
n = harmonic number
R = rotor
s = static pressure
t = total pressure
u = upstream flow field

Operators

δ = perturbation quantity
Real = real part of complex quantity
Imag = imaginary part of complex quantity derivative with respect to time

sure) compressor characteristic and λ and μ are parameters representing the inertia of the fluid in the compressor.

The imaginary part of the eigenvalue determines the growth rate of the traveling disturbances and the real part of the eigenvalue determines the rotation rate. The growth rate is given by:

$$\text{growth rate} = \frac{n \dfrac{\partial \Psi}{\partial \Phi}}{4 + n\mu} \tag{2}$$

In this simple description, the stability boundary of each spatial harmonic occurs at the peak of the total to static pressure rise characteristic, $\partial\Psi/\partial\Phi = 0$. At neutral stability, the disturbances are traveling waves with nondimensional rotational speed equal to $n\lambda/(4 + n\mu)$.

The individual compression system parameters thus play the following roles in the predicted disturbance behavior:

1. The slope of the compressor characteristic, $\partial\Psi/\partial\Phi$, determines the stability of the compression system.
2. The inertial parameters (λ and μ) affect the growth (or decay) rate and the rotational speed of the perturbations, but have no direct influence on system stability.

3.2 Mechanism for Instability. Transition of the axisymmetric flow field into large-amplitude rotating stall is a self-excited oscillation, and it is useful to discuss rotating stall dynamics in terms of the energy balances needed to maintain this oscillation. For a given oscillatory disturbance, if the system generates net averaged mechanical energy, compared to the value in a uniform steady flow, the disturbance will grow, whereas if the system dissipates energy, the disturbance will decay (Den Hartog, 1956).

A quantity related to the rate of net energy input by the compressor for a perturbation in flow is the product of the pressure rise perturbation, $\delta\Psi$, and the axial velocity perturbation, $\delta\phi$, integrated over the annulus:

$$\delta E \equiv \int_{\text{annulus}} \delta\Psi \delta\phi dA \tag{3}$$

Justification and detailed discussion of this is given in Gysling (1993). The relation between the perturbations in pressure rise across ($\delta\Psi$), and flow oscillations through ($\delta\phi$), the compressor can be expressed in terms of a compressor transfer function, $M(s)$, defined as

$$M(s) \equiv \frac{\delta\Psi(s)}{\delta\phi(s)} = \text{Real}(M(s)) + i\,\text{Imag}(M(s)) \tag{4}$$

Examination of Eq. (3) shows that only the component of pressure rise in phase with the axial velocity perturbation, i.e., only the real part of the compressor transfer function, affects the unsteady energy production, and hence, the stability of the system. The sign of the real part of the compressor pressure rise versus mass flow transfer function thus determines whether the compressor produces or dissipates perturbations in mechanical energy.

For examining the stability of a variety of compression systems, a useful approximation is that the real part of the compressor transfer function is independent of frequency and is given solely by the slope of the steady-state compressor characteristic, although it is emphasized that the specific model adopted does not affect the general conclusion. For positive slopes, the compressor produces a net flux of energy leading to growing disturbances; for negative slopes, perturbations in mechanical energy are dissipated in the compressor and disturbances decay.

3.3 Role of Dynamic Feedback. From either an energy balance or a linear stability analysis (Gysling, 1993), it is seen that the component of compressor pressure rise perturbation in phase with the mass flow perturbation, i.e., the *real part of the compressor pressure rise versus mass flow transfer function,* plays a dominant role in determining compression system stability. Use of feedback allows modification of the real part of the transfer function so it is no longer determined solely by the steady-state compressor characteristic slope. The stability of the system can thus be enhanced while the steady (mean) performance remains unaltered. From this point of view, the role of an effective feedback control strategy for suppressing rotating stall (or indeed any compressor instability) is modification of the real part of the pressure rise versus mass flow transfer function.

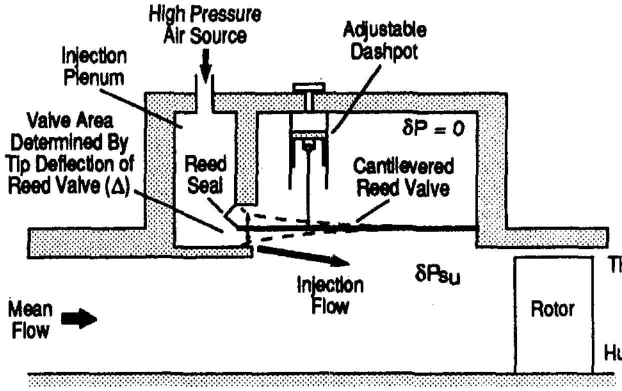

Fig. 1 Schematic of dynamic mass/momentum injection

3.4 Aeromechanical Feedback Strategy. To illustrate the concept and to motivate the present aeromechanical control strategy, consider the configuration shown in Fig. 1. In this strategy, termed dynamic mass/momentum injection, an auxiliary injection plenum is fed by a high-pressure air source so that high-momentum fluid is injected upstream of the compressor. The amount of fluid injected at a given circumferential position is governed by a circumferential array of reed valves, which react locally to perturbations in the static pressure upstream (δPs_u) of the compressor. The cantilevered reed valves are designed such that deflection upward allows an increase of flow to be injected, whereas downward deflection decreases the amount of the injection.

The stabilizing mechanism introduced by the proposed aeromechanical control strategy can be *qualitatively* understood as follows. Consider a disturbance to an initially steady, axisymmetric flow, which causes a small decrease in axial velocity in one region of the compressor annulus. In this region, the static pressure in the potential flow field upstream of the compressor will increase.[1] The increase in static pressure deflects the reed valves in that region, increasing the amount of high-momentum fluid injected and, hence, the local mass flow and pressure rise across the compressor. The net result is an increase in pressure rise across the compressor in the region of decreased axial velocity. The feedback thus serves to add a negative component to the real part of the compressor pressure rise versus mass flow transfer function.

The effect of the aeromechanical feedback on unsteady compressor pressure rise versus mass flow performance is shown schematically in Fig. 2. With feedback, the effective slope of the compression system no longer follows the quasi-steady compressor characteristic, but is determined by the combined influence of compressor performance and feedback, so the region of stable flow is increased.

---

[1] This statement neglects the effect of unsteadiness in the upstream flow field but, as shown in detail in the analysis, this is not of primary importance.

4.0 Fluid and Structural Model for Assessment of Aeromechanical Control

4.1 Fluid Dynamics. To assess whether the qualitative concepts given above can be translated into a useful strategy, a quantitative analysis is necessary. We sketch out here the steps leading to the eigenvalue analysis for the conditions at which instability can occur. Details of the derivation are given by Gysling (1993).

Modeling the injection of high-momentum fluid into the upstream flow field and deducing the effect on compressor performance is a complex problem but fortunately we need only a basic description for the problem of interest. In the approach presented, the jets are assumed to mix radially before entering the compressor. The conceptual model for the injection process is shown in Fig. 3; further comments on the approach are given subsequently.

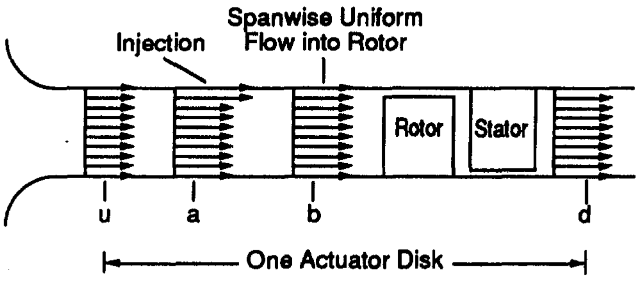

Fig. 3 Conceptual model for dynamic mass/momentum injection

The jets create a change in the spanwise-averaged static pressure, total pressure, and mass flow in the injection region, which is a function of the local reed valve area. To assess such changes, the injection region can be modeled as a two-dimensional actuator disk. Pressure rise and mass flow boundary conditions across the injection region are derived by conserving mass and momentum across the injection region. If the total pressure at which the fluid is injected is constant and the amount of fluid injected is small compared to the mass flow through the compressor, the following linearized relations for the spanwise total pressure and axial velocity perturbations on upstream and downstream sides of the injection region can be derived:

$$\delta p_{t_b} - \delta p_{t_u} = 2\Phi_i(\Phi_i - \Phi_u)\delta q \tag{5}$$

$$\delta\phi_b = \delta\phi_u - \Phi_i\delta q \tag{6}$$

If we assume that the reed valves are only a short distance upstream of the compressor compared to the length scale of the disturbances, the description of the effect of injection (on the compression system dynamics) can be further simplified by combining the actuator disks for the compressor and for the injection region. Doing this leads to the matching conditions, which relate perturbation variables upstream of the injection region and downstream of the compressor. These can be written as:

Conservation of Mass Across the Region:

$$\delta\phi_u + \Phi_i\delta q = \delta\phi_d \tag{7}$$

Pressure Rise Across the Region:

$$\delta\Psi = \delta p_{s_d} - \delta p_{t_u} = \left(\frac{\partial\Psi}{\partial\phi}\right)\delta\phi_d - \lambda\frac{\partial\delta\phi_d}{\partial\theta} - \mu\frac{\partial\delta\phi_d}{\partial t} + 2\Phi_i(\Phi_i - \Phi_u)\delta q \tag{8}$$

Constant Flow Angle at Compressor Exit:

$$\delta\nu_d = 0 \tag{9}$$

All perturbation variables are of the form $e^{in(\theta-\sigma\tau)}$.

4.2 Structural Feedback. It is the response of the reed valves to the local static pressure perturbations in the upstream flow field that provides the feedback. The reed valves are modeled in a first cantilevered bending mode as single-degree-of-freedom, mass-spring-damper systems. The nondimensional, second-order equation that describes the reed valve dynamics is given by:

$$\frac{\partial^2\delta q}{\partial\tau^2} + 2Q\zeta\frac{\partial\delta q}{\partial\tau} + Q^2\delta q = \frac{1}{6}W\delta p_{s_u} \tag{10}$$

where Q is the reed natural frequency normalized by rotor frequency, ζ is the critical damping ratio of the reed valves, and W is the nondimensional reed mass parameter. The static pressure acting on the reed valves is taken to be the static pressure in the flow field upstream of the injection region, i.e., the reed valves are modeled as short axially compared to the length scale of the disturbances, so the pressure perturbation at the compressor face acts over the entire reed.

4.3 Stability Analysis With Aeromechanical Feedback. Matching the flow fields across the actuator disk (Gysling, 1993) leads to the following eigenvalue problem, which determines the stability of the flow field for each spatial harmonic:

$$[\mathbf{A} - \sigma\mathbf{B}]\begin{Bmatrix} A_n \\ \delta q_n \\ \delta z_n \end{Bmatrix} = 0 \tag{11}$$

The **A** and **B** matrices are given by:

$$\mathbf{A} = \begin{bmatrix} \frac{\partial\Psi}{\partial\Phi} - in\lambda & A_{12} & 0 \\ -\frac{1}{3}Wn^2\Phi_u & in\mathrm{Q}^2 & in2Q\zeta \\ 0 & 0 & 1 \end{bmatrix}.$$

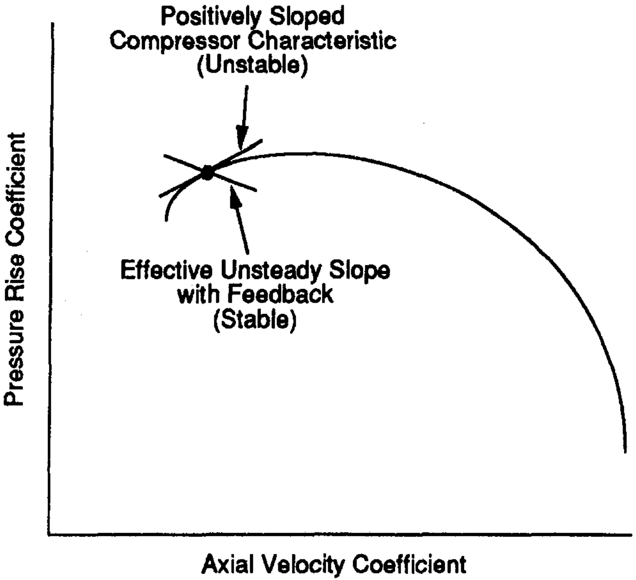

Fig. 2 Effect of dynamic feedback on unsteady compressor performance

$$A_{12} \equiv -\lambda\Phi_i - i\frac{\Phi_i}{n}\left(\frac{\partial\Psi}{\partial\Phi} + 2(\Phi_i - \Phi_u)\right)$$

and

$$\mathbf{B} = \begin{bmatrix} -i(4 + n\mu) & -\left(\frac{2}{n} + \mu\right)\Phi_i & 0 \\ -i\frac{1}{3}Wn^2 & 0 & -n^2 \\ 0 & -in & 0 \end{bmatrix}$$

The stability matrices retain terms associated with the individual fluid dynamic and structural dynamic systems, but there are also terms representing the aeromechanical coupling of the two systems. With the aeromechanical feedback, there are three modes per spatial harmonic instead of only one, as would be the situation for the fluid system alone; the two additional modes are due to the reed dynamics. All modes for any harmonic are independent and stability can still be assessed on a harmonic by harmonic basis.

4.4 Aeromechanical Feedback Control Parameters. Stability is now a function not only of the original system parameters but also of an additional set of (nondimensional) control parameters, which determine the interaction between the reed valves and the flow field:

$$Q \equiv \omega_n \frac{R}{U_R} \quad \text{frequency parameter} \tag{12}$$

$$\zeta \equiv \frac{b}{2M\omega_n} \quad \text{critical damping ratio} \tag{13}$$

$$W \equiv \frac{\rho R^2 \tilde{L}}{M} \quad \text{mass parameter} \tag{14}$$

$$\Phi_i \equiv \frac{C_{x_i}}{U_R} \quad \text{injection parameter} \tag{15}$$

$$\Phi_u \equiv \frac{C_{x_u}}{U_R} \quad \text{mass flow coefficient} \tag{16}$$

As modeled, the amount of steady-state mass flow injected does not enter the stability analysis explicitly, although it exerts influence through the change in the overall pressure rise characteristic. The axial velocity of the injection fluid (equivalently the injection total pressure) is an explicit stability parameter, as is the steady-state mass flow coefficient. The latter appears because it influences the relation between axial velocity and static pressure perturbations in the upstream flow field and, thus, the effect that the feedback can have.

5.0 Parameter Optimization

To determine the effects of the control parameters on stability, as well as to guide in the design of an experimental facility, a parameter optimization study was performed based on the linearized stability analysis. Compressor parameters representative of a low-speed, single-stage, research compressor were selected.

Initial results from the parameter study indicated that, for properly tuned reed dynamics, high values of injection parameter, Φ_i, and mass parameter, W, were desired. To design a physically realizable experimental apparatus, however, several constraints were imposed on the values of the control parameters. For gas turbine engine compression systems, one idea was that the high-pressure injection source could be taken from behind the compressor. Injection pressure was thus restricted to realistic levels, specifically of the order of the dynamic pressure based on mean wheel speed. The mass and frequency parameters of the reed valves used in the parameter study were restricted to reed valves sized to fit the MIT low-speed compressor and constructed from readily obtainable materials. These constraints restricted the injection parameter to $\Phi_i \approx 1$, and the mass parameter to $W \approx 3.5$.

5.1 Design Configuration. Parameter optimization was performed to determine a set of control parameters that optimized the stability of the two lowest spatial harmonics. Dynamics associated with higher spatial harmonics were neglected for the following reasons:

1 Experimental and analytical results indicate that higher harmonic perturbations are more stable than lower spatial harmonics due to unsteady aerodynamic effects within the compressor (Haynes et al., 1993).
2 The rate at which the disturbances decay exponentially (in the axial direction upstream of the compressor) scales with the length scale of the disturbances, and hence with the spatial harmonic number. The assumption that the reed valves act as if the pressure field acts uniformly over their length thus becomes increasingly unrealistic for higher harmonics.

The design parameters resulting from the optimization study were: $\Phi_i = 1.0$; $W = 3.5$; $Q = 0.9$; $\zeta = 0.7$.

Figures 4(*a*) and 4(*b*) show the predicted behavior of the eigenvalues of the basic compression system (without feedback) and of the design configuration for the first two spatial harmonics. The position of the eigenvalues is plotted for different values of compressor mass flow coefficient. For the basic system, the first two harmonics become unstable at a mass flow of $\Phi = 0.528$, corresponding to the peak of the compressor characteristic. For the design configuration, the first and second harmonics were predicted to become unstable at flow coefficients that are considerably lower. The first mode to become unstable is associated with the second spatial harmonic of the compression system; this becomes unstable when the flow coefficient through the compression system is reduced to $\Phi = 0.43$. A mode associated with the first spatial harmonic was found to become unstable at a slightly lower flow coefficient, $\Phi = 0.40$.

Assuming that the neutral stability point of the least stable mode determines the stability of the compression system, the optimized aeromechanical feedback was predicted to reduce the stalling mass flow coefficient of the compression system by 19 percent, compared to the stalling flow coefficient predicted for the basic compression system. The slope of the compressor characteristic at which instability occurs was predicted to be $\partial\Psi/\partial\Phi = 1.2$, compared to zero with the baseline configuration.

The most unstable mode associated with the first spatial harmonic was predicted to rotate at 9 percent of the rotor speed, and that for the second spatial harmonic at 38 percent of the rotor speed. For the basic compression system, the corresponding rates are 17 percent and 25 percent of rotor speed for the first and second harmonics. Aeromechanical feedback thus changes the disturbance rotation rates in addition to the stalling flow coefficient.

5.2 Robustness of Aeromechanical Feedback. The model is a simple description of a complex problem and there are uncertainties in the conclusions that one draws. It is thus important to assess the sensitivity of the performance of the control strategy to variations in control parameters. To do this, the stability boundary was determined by fixing all but one of the control parameters of the design configuration and varying the remaining control parameter. Figure 5 shows the mass flow coefficient at which the least stable mode associated with the first and second spatial harmonics is calculated to become unstable, as a function of the individual control parameters Φ_i, W, Q, and ζ for the design optimized configuration. A maximum

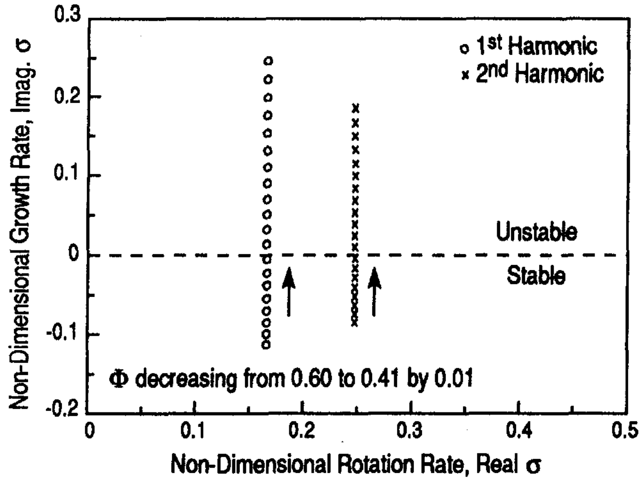

Fig. 4(*a*) Eigenvalues of basic compression system for first and second spatial harmonics ($\lambda = 1.0$, $\mu = 2.0$). Arrows show direction of decreasing flow coefficient.

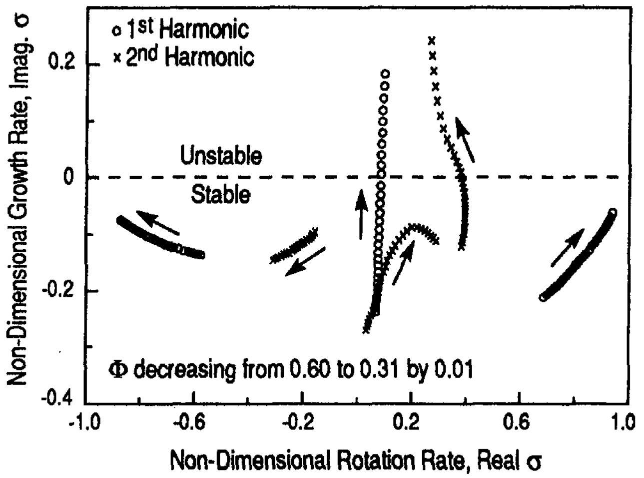

Fig. 4(*b*) Eigenvalues for compression system with design aeromechanical feedback for first and second spatial harmonics ($\lambda = 1.0$, $\mu = 2.0$, $W = 3.5$, $\Phi_i = 1.0$, $Q = 0.9$, $\zeta = 0.7$). Arrows show direction of decreasing flow coefficient.

degree of stabilization exists for variations of each of the control parameters. (The discontinuities in slope of the curves occur because each spatial harmonic contains three eigenmodes, any one of which can become unstable.)

Figure 5 represents the behavior for a specific set of control parameters. In general, a significant increase in injection parameter and/or mass parameter would increase the stabilizing effect of the aeromechanical feedback. However, increasing Φ_i and W will result in increased stability enhancement only when the other control parameters, i.e., ζ and Q, are optimized for the system with the higher values of Φ_i and W.

6.0 Experimental Facility

The experimental phase of this research was conducted on a low-speed, single-stage compressor facility. The facility is shown schematically but approximately to scale, in Fig. 6. The tip diameter is 0.59 m. All data were obtained at 2250 rpm, corresponding to a tip speed of 70 m/s. The compression system has a low B-parameter ($B < 0.1$), allowing the rotating stall dynamics to be studied in isolation from surge. The compressor consisted of a rotor and stator, with no inlet guide vanes. The geometry, given in Table 1, was selected to be similar to a compressor build that had exhibited full-span stall inception (Paduano, 1992).

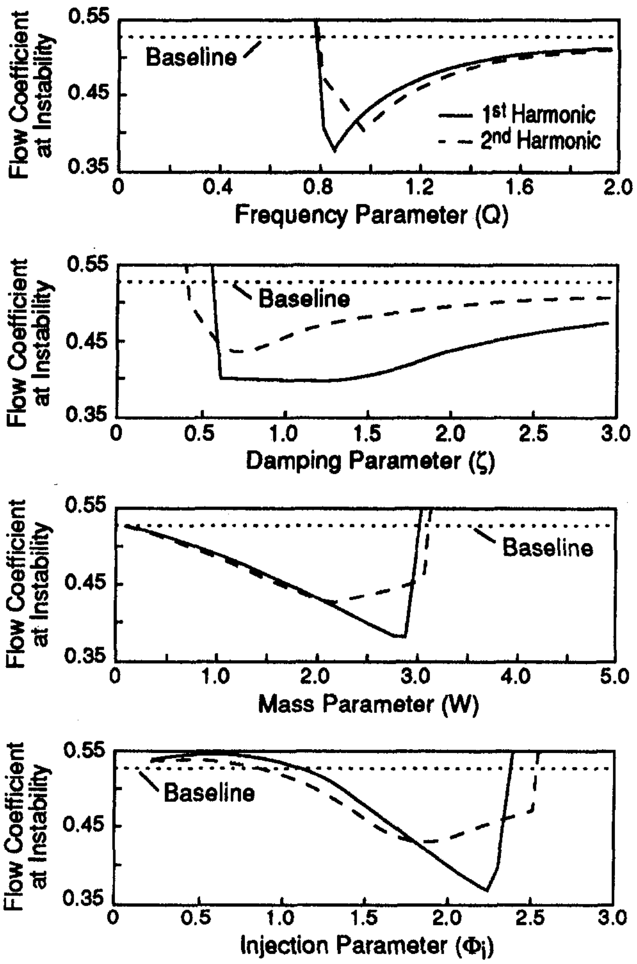

Fig. 5 Flow coefficient at instability for first and second harmonics as a function of individual control parameters; variation around optimized case ($W = 3.5$, $\Phi_i = 1.0$, $Q = 0.9$, $\zeta = 0.7$)

6.1 Dynamic Mass/Momentum Injection System.

The mechanical design of the dynamic mass/momentum injection system represents the first attempt to demonstrate rotating stall stabilization using aeromechanical feedback. For this reason, the design was intended to be as simple as possible. As described above, the design was also constrained to control parameters that could be readily implemented in the facility, so that the configuration was not a globally optimized one.

The annular structure designed and constructed to house the reed valves is also shown in Fig. 6. The housing contained 24

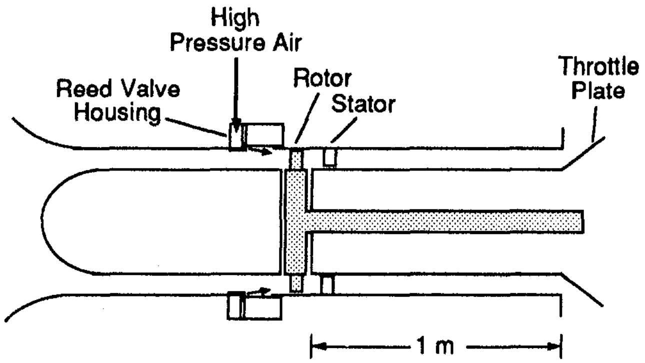

Fig. 6 Schematic of MIT single-stage compressor with dynamic mass/momentum injection

Table 1 Compressor geometry

Number of Stages	1
Tip Diameter	0.591 m
Hub Diameter	0.445 m
Hub/Tip Radius Ratio	0.75
Mean Radius	0.259 m
Rotor/Stator Gap	48 mm

	Rotor	Stator
No. of Blades	44	45
Chord (midspan)	38 mm	38 mm
Camber (midspan)	25 deg	30 deg
Stagger (midspan)	35 deg	22.5 deg
Twist (deg)	30	-5
Solidity (midspan)	1.03	1.08

discrete, cantilevered, graphite-epoxy reed valves; the amount of high-pressure air injected axially into the face of the compressor was determined by the local reed valve area opening. The analysis assumes a continuous array of reed valves, but 24 reeds was considered a good compromise between complexity and spatial resolution. To provide the necessary damping, low-friction, low-mass, adjustable, pneumatic dashpots were installed on each reed valve.

The reed valves formed the outer casing wall of the upstream duct in a region between 33 and 127 mm upstream of the compressor (i.e., the valves formed a 24-sided polygon, approximating the original circular outer casing wall). The axial position selected corresponds to an injection location 1.5 annulus heights, or approximately 0.5 compressor mean radii, upstream of the rotor.

The reed valve housing also contains a continuous, annular injection plenum designed to maintain a constant total pressure air supply to the valve array. In principle, high-pressure air injected in front of the compressor could be bled from the compressor exit, but in the present experiments, an external air source was used. This allowed greater flexibility in the injection parameters and also reduced complexity. To minimize leakage from the injection plenum into the back pressure cavity, the reed valves required sealing to isolate the high-pressure air in the injection plenum from the back pressure cavity behind the reeds. The seals were required to withstand a steady-state pressure loading (on the order of 10^4 N/m^2), as well as to remain flexible in the transverse direction to minimize the effect on reed valve dynamics.

6.2 Reed Valve Dynamics. The reed valve dynamics were characterized by displacing and impulsively releasing a single reed valve over the range of dashpot settings. To capture the transient response of the reed valves over the range of dashpot settings, a visco-elastic model of the pneumatic dashpots was required (Gysling, 1993). The reed valve dynamic parameters were identified as $W = 3.5$, $Q = 1.5$, and $\alpha = 5.0$. The damping ratios ranged from $\zeta = 0.3$ to $\zeta = 3.0$, corresponding to pneumatic dashpots fully opened and fully closed, respectively.

7.0 Steady-State Data

As implemented here, dynamic mass/momentum injection results in nonzero time mean and annulus-averaged mass and momentum injection into the flow path. The steady-state performance and the stability boundary of the compression system are dependent on the injection. It is emphasized, however, that the scope of the research is not to examine the effect of steady-state injection but rather the effect of carrying out the injection in an unsteady manner, linked to the aeromechanical behavior. Therefore, to assess directly the change in stall flow coefficient due to changes in reed dynamics, or in other words, due to aeromechanical feedback, the change in stall flow coefficient was determined as a function of damping ratio for *fixed levels of steady-state injection.* The stall flow coefficient of the compression system was determined by slowly closing the throttle until the compressor exhibited large amplitude rotating stall.

As a benchmark for assessing the effect of the aeromechanical feedback, one would ideally have the reeds perfectly rigid so that no feedback path existed and the only effect was due to steady-state injection. Although the reed valves are not completely rigid with the dashpots closed, the reed dynamic response in this configuration is substantially less than at the optimum dashpot setting. (As an example, the magnitude of the deflection versus pressure transfer function at the frequency corresponding to the first harmonic of rotating stall waves differs by roughly a factor of two for the two cases.) The figure of merit used to evaluate the effectiveness of different configurations was therefore the decrease in stall mass flow coefficient as a percentage of the stall mass flow coefficient for the closed dashpot configuration at the same injection level; the latter will be referred to henceforth as the "rigid reed" configuration.

$$\Delta\Phi \text{ percent} \equiv \left(\frac{\Phi_{\text{rigid}} - \Phi_{\text{w/feedback}}}{\Phi_{\text{rigid}}}\right)_c \quad (17)$$

In the experiments, two nondimensional control parameters were systematically varied, the reed dashpot setting (or damping ratio) ζ, and the injection pressure (or injection parameter) Φ_i. The injection parameter was varied from $\Phi_i = 0.8$ to $\Phi_i = 1.2$, corresponding to injecting between 2 and 7 percent of the compressor mass flow and between 4 and 21 percent of the axial momentum of the flow entering the compressor, at conditions near the stall flow coefficient. The damping parameter was varied between $\zeta = 0.3$ and $\zeta = 3.0$. The reed mass parameter (W), frequency parameter (Q), and spring stiffness ratio (α) were not adjusted.

For each injection level tested, the rigid reed valve configuration stalled at the highest mass flow coefficient over the range of dashpot settings, i.e., *opening the dashpots from the closed position was never destabilizing.* A 10 percent decrease in stalling flow coefficient due to aeromechanical feedback was demonstrated at $\Phi_i = 1.0$ with the dashpots fully opened ($\zeta = 0.3$). At these conditions, 4 percent of the compressor mass flow and 6 percent of the axial momentum entering the compressor was injected.[2]

Figure 7 shows compressor characteristics for operation with: (1) optimized aeromechanical feedback, (2) the compressor with rigid reeds at the same injection level, and (3) the baseline compression system (no injection). The stall flow points are E, B, and F, respectively. The mass flow coefficient is based on the mass flow through the compressor, which is the sum of the mass flow measured far upstream of the injection region and the injected mass flow. The pressure rise coefficient is inlet total to exit static pressure, based on the difference in pressures measured upstream of the injection region and downstream of the compressor.

In the regions of the compressor characteristic which are stable without feedback, aeromechanical feedback has no apparent effect on steady-state compressor performance. At flow coefficients below the rigid reed valve stall flow, the aeromechanical feedback smoothly extends the stable operating region of the compressor. The effect of steady-state injection is a 6 percent decrease in stall flow.

---

[2] Tabulation of the stalling flow coefficients for the various compression system configurations and the percentage decrease in stalling flow coefficient obtained for various injection levels and dashpot settings are given in Gysling (1993).

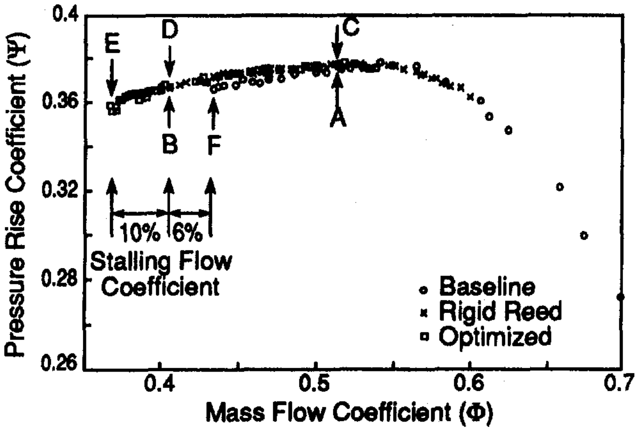

Fig. 7 Compressor characteristics for: (1) basic compression system; (2) rigid reed valve configuration with injection; and (3) experimentally optimized configuration with injection

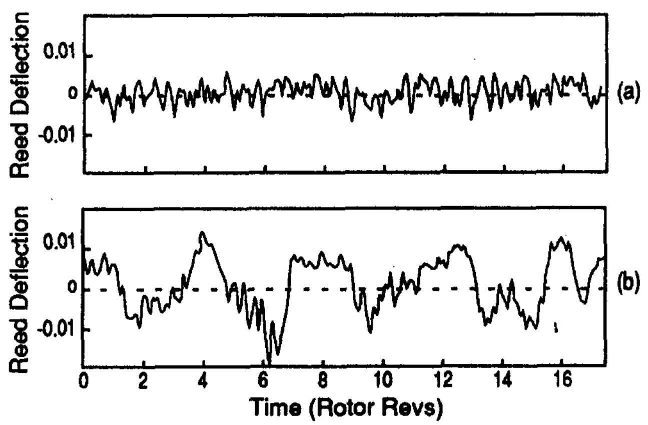

Fig. 9 Time-resolved, nondimensional reed valve deflections ($\delta\Delta/H$) for rigid reed configuration operating at: (a) $\Phi = 0.52$ (point A), (b) $\Phi = 0.41$ (point B)

8.0 Time-Resolved Behavior

Time-resolved data are presented for the rigid reed configuration and the configuration that demonstrated the largest stabilization. Both are at the same injection level. The data are presented in some detail for the first configuration to show the overall behavior, and then only selectively after that when there are points of difference to be brought up.

8.1 Rigid Reed Configuration. Figure 8 shows the time-resolved normalized pressure and axial velocity coefficient perturbations at $\theta = 75$ and 90 deg, respectively, for the rigid reed configuration, with optimal injection parameter ($\Phi_i = 1.0$). The data were recorded at a location $\frac{1}{3}$ chord upstream of the rotor. Data are shown for two mass flow coefficients: one well away from stall ($\Phi = 0.52$) and the second near stall ($\Phi = 0.41$). The operating points corresponding to the two time-resolved data sets are shown on Fig. 7 as points *A* and *B*. As shown, the magnitude of the flow perturbations increases as the flow coefficient is reduced.

Figure 9 shows the normalized reed valve deflections ($\delta q = \Delta/H$) that correspond to the data of Fig. 8. The reed deflection measurements indicate that the reeds are not completely rigid, and that they respond to the static pressure perturbations and thus introduce some degree of aeromechanical feedback.

Spatial Fourier decompositions of the axial velocity perturbations (magnitude and phase of the spatial harmonics), measured $\frac{1}{3}$ chord upstream of the rotor at midspan, are given in Figs. 10 and 11 for the same two operating points. Figure 10 shows that the magnitudes of the first three spatial harmonics grow and decay in a random manner when the compression system operates well away from stall ($\Phi = 0.52$). Further, no coherent traveling waves can be seen in the plot of the unwrapped phase versus time.

For the compression system operating at $\Phi = 0.41$, near stall, the disturbance flow field is much different, as seen in Fig. 11. There is an increase in the magnitude of the first and second spatial harmonics by roughly a factor of five or more compared to those at $\Phi = 0.52$. The unwrapped phase exhibits substantial periods (tens of rotor revolutions) of coherent traveling wave structure for both the first and second spatial harmonics. The third harmonic also exhibits periods of coherent traveling wave structure, but these are more intermittent than the first two spatial harmonics. The phase speeds of the first, second and third traveling spatial harmonics are 26, 30, and 37 percent of the rotor frequency.

8.2 Configuration with Optimized Aeromechanical Feedback. Figure 12 shows time-resolved, normalized pressure and axial velocity perturbations for the compressor with the experimentally optimized control parameters. Data corresponding to three mass flow coefficients are shown: $\Phi = 0.52$, 0.41, and 0.37. The steady-state operating points corresponding

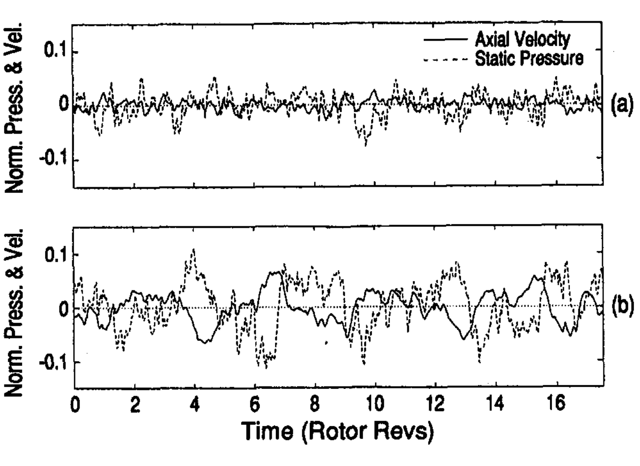

Fig. 8 Time-resolved, nondimensional static pressure ($\delta p/\frac{1}{2}\rho U_R^2$) and axial velocity perturbations ($\delta C_x/U_R$) for rigid reed valve configuration with experimentally optimized injection level ($\Phi_i = 1.0$); (a) $\Phi = 0.52$ (point A), (b) $\Phi = 0.41$ (point B)

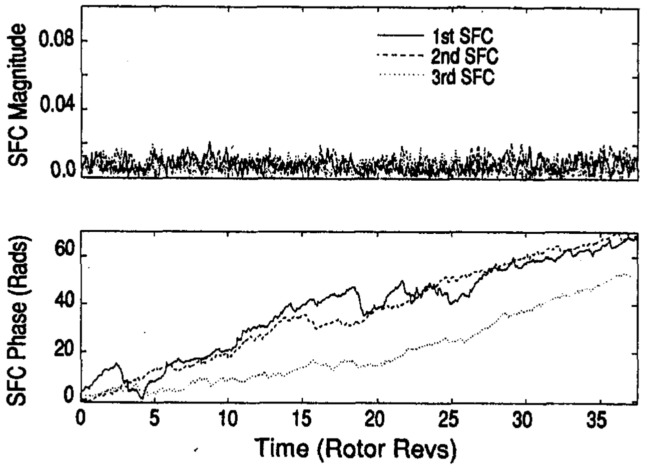

Fig. 10 Spatial Fourier decomposition of nondimensional axial velocity perturbations for rigid reed valve configuration; operation away from stall, $\Phi = 0.52$ (point A)

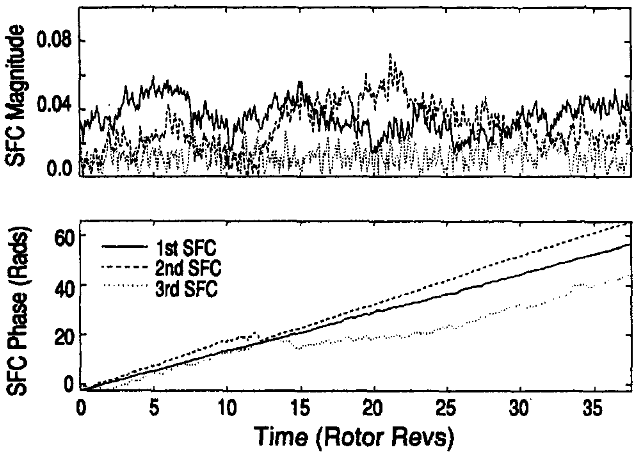

Fig. 11 Spatial Fourier decomposition of nondimensional axial velocity perturbations for rigid reed valve configuration; operation away from stall, $\Phi = 0.41$ (point B)

to the time-resolved data are indicated by points C, D, and E in Fig. 7. The data were recorded at the same axial and circumferential locations as those of Fig. 8.

Comparison of Fig. 12 with Fig. 8 shows that the pressure and axial velocity perturbations for the two systems away from stall (Points D and A) are similar. Examination of data from Points D and B show that the amplitude of the oscillations are reduced in the optimized configuration compared to the rigid valve configuration at the stall mass flow coefficient of the latter. The similarity of data from Points D and E indicates that the aeromechanically stabilized configuration exhibits no qualitative change in behavior in the stabilized region at flows below the stall point for the rigid wall flow.

Figure 13 shows the time-resolved reed valve deflections at conditions corresponding to those of Fig. 12. In the stabilized region, Point E, the reed valves are modulating ±1 percent of the height of the annulus.

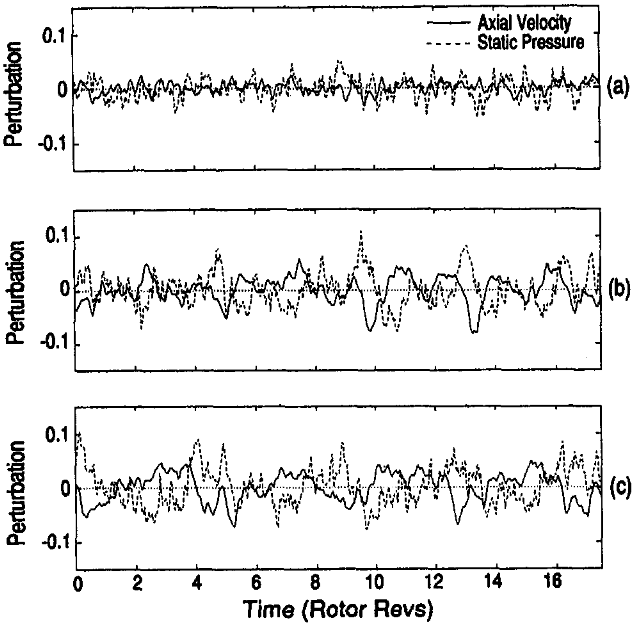

Fig. 12 Time-resolved, nondimensional static pressure ($\delta p/{}^1\!/_2\rho U_R^2$) and axial velocity perturbations ($\delta C_x/U_R$) for optimized configuration at three flow coefficients: (*a*) $\Phi = 0.52$ (point C), (*b*) $\Phi = 0.41$ (point D), (*c*) $\Phi = 0.37$ (point E)

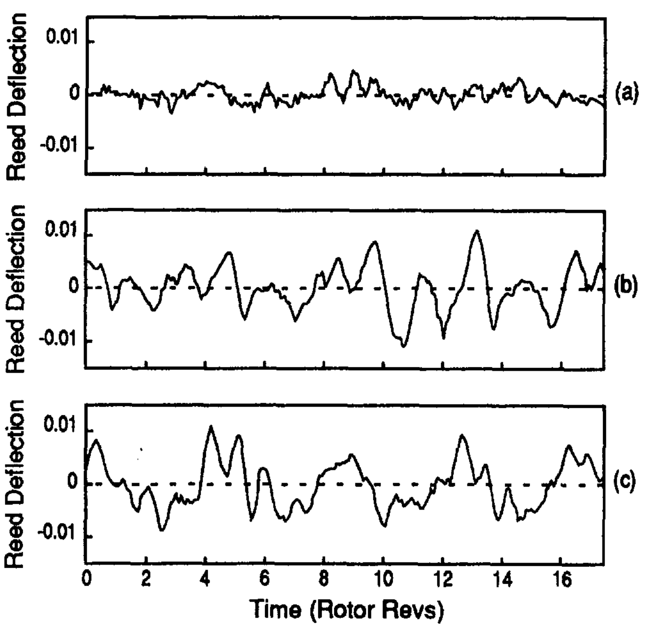

Fig. 13 Time-resolved, nondimensional reed valve deflections ($\delta\Delta/H$) for optimized configuration operating at three flow coefficients: (*a*) $\Phi = 0.52$ (point C), (*b*) $\Phi = 0.41$ (point D), (*c*) $\Phi = 0.37$ (point E)

The spatial Fourier components of the compressor face axial velocity perturbations for the optimized configuration were also examined. At $\Phi = 0.52$ away from stall, the behavior is similar to that with the rigid reeds seen in Fig. 10. The magnitude of the components of the velocity perturbations appears to grow and decay randomly with time, and the phase shows no coherent traveling waves. In Fig. 14, at $\Phi = 0.37$ close to stall, the magnitudes of the spatial harmonic components are more than a factor of three larger than away from stall, also similar to the situation with the rigid reeds. The plot of the perturbation phase now shows that the first, second, and third spatial harmonics exhibit coherent traveling waves. The angular phase speed of the traveling waves associated with the three lowest spatial harmonics is 25, 29, and 33 percent of the rotor frequency, respectively.

A summarized view of the alteration in the unsteady behavior as a function of mass flow is given in Fig. 15, which shows the rms amplitude of the normalized axial velocity perturbations recorded at a station $\frac{1}{3}$ chord upstream of the rotor. Data from

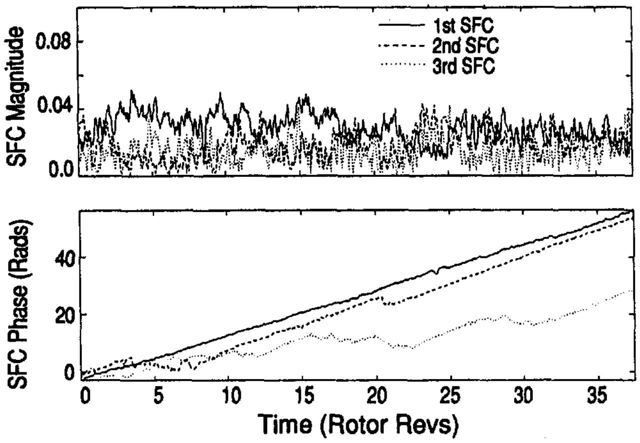

Fig. 14 Spatial Fourier decomposition of nondimensional axial velocity perturbations for optimized configuration; operation near stall, $\Phi = 0.37$ (point E)

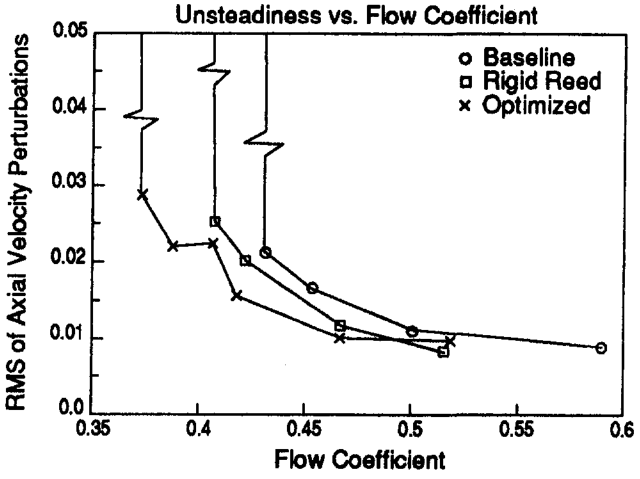

Fig. 15 The rms of nondimensional axial velocity perturbations $(\delta C_x/U_R)$ as a function of mean flow coefficient (Φ) for the baseline, rigid valve, and optimized configurations

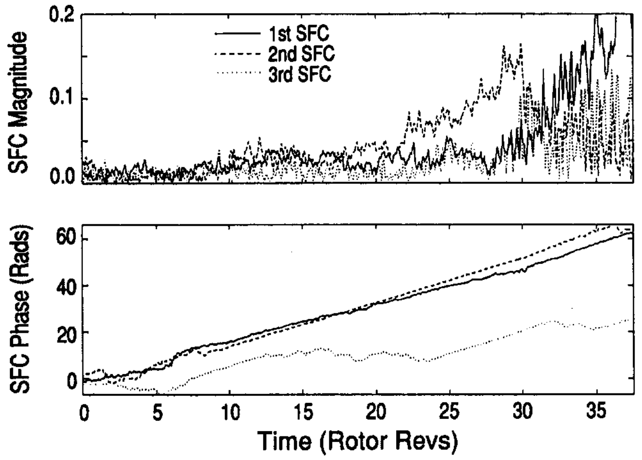

Fig. 17 Spatial Fourier decomposition of nondimensional axial velocity perturbations during stall inception process: rigid reed valve configuration, optimized injection level

the three configurations: (1) baseline compressor, (2) rigid reed valve configuration and, (3) experimentally optimized configuration, are included. The level of unsteadiness increases as the configurations approach their respective stalling flow coefficients. The functional dependence of the level of unsteadiness on flow coefficient in the three systems roughly scales with the difference between the flow coefficient and the stalling flow coefficient. Away from stall (say, $\Phi > 0.50$), the unsteadiness in the three configurations is similar (the rms level of normalized axial velocity perturbations is roughly 0.01), indicating that the magnitude of the unsteadiness at these conditions is not greatly influenced by aeromechanical feedback or steady-state injection.

8.3 Stall Inception. Initial experiments verified that the baseline compressor (without injection) exhibited stall inception in a full-span, long circumferential wavelength manner consistent with the modeling approach. Figure 16 shows axial velocity perturbations recorded during stall inception for the rigid wall. An array of eight equally spaced hot wires, placed $\frac{1}{3}$ chord upstream of the rotor at midspan, was used. The spatial Fourier decomposition of the velocity perturbations during the stall inception event is shown in Fig. 17. Figures 18 and 19 show similar data for the configuration with optimized aeromechanical feedback. With both configurations, a smooth transition

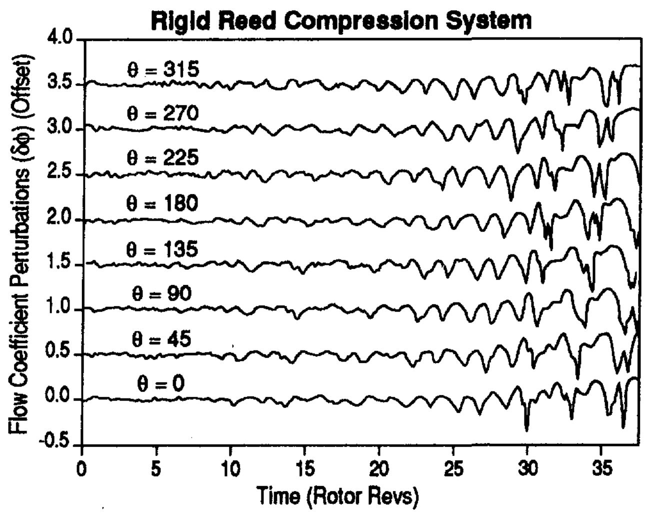

Fig. 16 Nondimensional axial velocity perturbations $(\delta C_x/U_R)$ during stall inception process of rigid reed valve configuration with optimized injection level

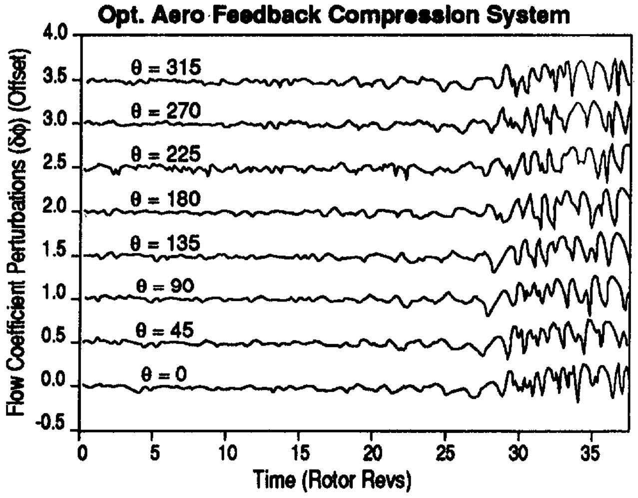

Fig. 18 Nondimensional axial velocity perturbations $(\delta C_x/U_R)$ during stall inception process: optimized configuration

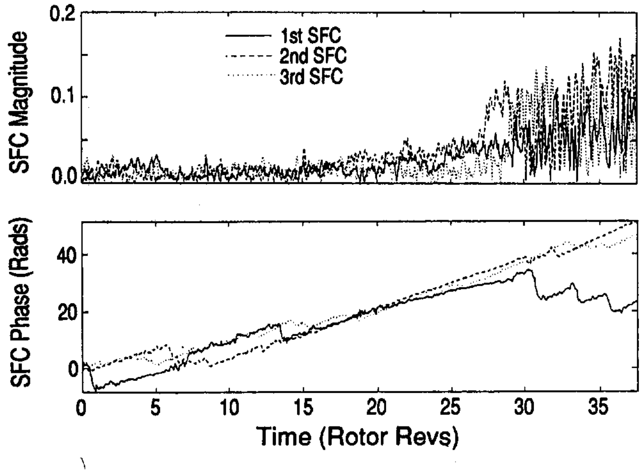

Fig. 19 Spatial Fourier decomposition of nondimensional axial velocity perturbations during stall inception process: optimized configuration

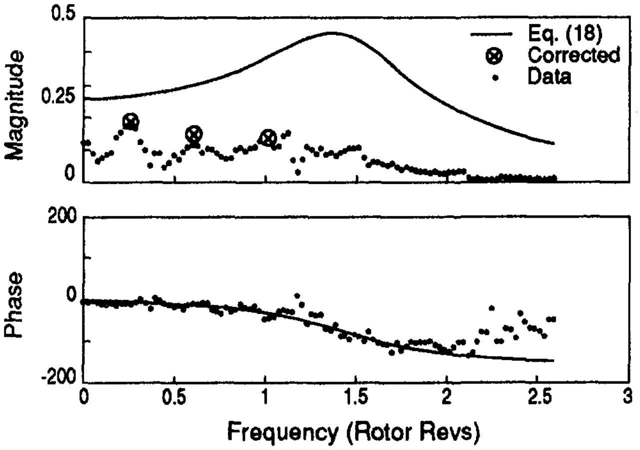

Fig. 20 Magnitude and phase of nondimensional reed valve deflection/static pressure transfer function ($\delta q/\delta p$); optimized configuration, operation near stall

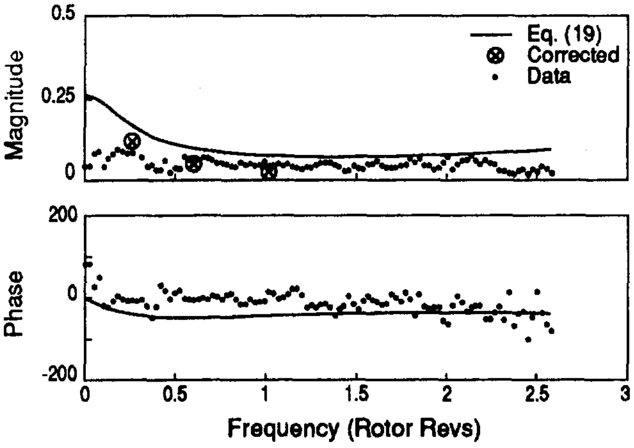

Fig. 21 Magnitude and phase of nondimensional reed valve deflection/static pressure transfer function ($\delta q/\delta p$); rigid reed configuration with optimized injection level, operation near stall

from axisymmetric flow to fully developed rotating stall is exhibited, indicating a stall inception process consistent with the two-dimensional theory. Although not shown, axial velocity measurements at different spanwise positions indicated that the stall inception process was predominantly a full-span event for all configurations tested.

8.4 Reed Deflection/Static Pressure Transfer Function. Examination of the transfer functions between the different parts of the feedback loop is useful in understanding not only the role of the aeromechanical feedback but also the relation to different active control strategies that are currently being explored.

Time-resolved data recorded from the compression system were therefore used to estimate the transfer functions ($\delta q/\delta p$) between reed displacement and static pressure perturbations in the upstream flow field. The conditions were those of naturally occurring unsteadiness within the compression system; no external excitation was used. The transfer functions were estimated using the ratio of the cross power spectrum between the input and output signals and the power spectrum of the input signal (Wellstead, 1981). For high coherence levels (close to unity), this ratio measures the transfer function. The cutoff frequency of the time-resolved measurements was set at 100 Hz, or 2.67 times the rotor frequency.

Figure 20 thus shows the magnitude and phase of the measured transfer function between reed deflections and static pressure perturbations for the experimentally optimized configuration operating near stall. The transfer function is presented as a function of frequency, nondimensionalized by rotor rotational frequency. The reed deflection is nondimensionalized by annulus height and the static pressure perturbation by dynamic head based on compressor wheel speed. The pressure was recorded $\frac{1}{3}$ chord upstream of the rotor and both the pressure and reed deflection signals were recorded at the same circumferential position, $\theta = 75$ deg. The measured coherence between the two signals approaches unity at the frequencies associated with the first (25 percent), second (60 percent) and third harmonics (105 percent), indicating that the measurements give a good estimate of the transfer function at these frequencies (Gysling, 1993).

For low damping rates, the pneumatic dashpot behavior approaches that of a viscous dashpot. An expression for the transfer function between the reed deflection and the static pressure is thus given by:

$$\frac{\delta q(\omega)}{\delta p(\omega)} = \frac{\frac{1}{6}W}{(Q^2 - \omega^2) + 2Q\zeta(i\omega)} \tag{18}$$

where ω is the temporal frequency normalized by rotor frequency. The solid lines in Fig. 20 indicate the transfer function given by Eq. (18) with $W = 3.5$, $Q = 1.5$, and $\zeta = 0.3$. However, because the static pressure field decays exponentially (as e^{-nx}, where n is the spatial harmonic number and x is the axial distance upstream) with distance from the compressor, and the finite axial distance between the pressure transducer and the center of pressure of the reed (approximately 0.35 compressor radii) must be accounted for. The symbols (x) on the plot of the magnitude of the transfer function indicate the calculated transfer function, corrected to account for this effect, at the frequencies associated with traveling wave disturbances of the three lowest spatial harmonics. The good agreement between the calculated and the experimentally determined transfer functions indicates that modeling the reed valves as a second-order system responding to pressure perturbations in the upstream flow field gives a good description of the optimized configuration.

Figure 21 shows the nondimensional reed displacement/pressure transfer function for the rigid reed configuration, with optimized injection level, operating near stall. The model for the visco-elastic reed valve dynamics gives the reed displacement/pressure transfer function as:

$$\frac{\delta q(\omega)}{\delta p_u(\omega)} = \frac{\frac{1}{6}W}{(Q^2 - \omega^2) + \dfrac{2Q\zeta\omega(i + \chi\omega)}{1 + (\chi\omega)^2}} \tag{19}$$

where $\chi \equiv 2\zeta/\alpha Q$.

The transfer function corresponding to Eq. (19) with $W = 3.5$, $Q = 1.5$, $\zeta = 3.0$ and $\alpha = 5.0$, is shown on Fig. 21 as a solid line. The symbols (x) on the plot of the magnitude of the transfer function represent the model corrected for the axial attenuation of the static pressure perturbations, as developed above. There is a reasonable representation of the reed dynamics with the pneumatic dashpots closed.

As indicated by Fig. 21, and by time-resolved data in Fig. 9, the reeds are not completely rigid with the pneumatic dashpots closed, and the reeds respond to the pressure fluctuations. Comparing Figs. 20 and 21 shows that the magnitude of the reed deflection/pressure transfer function for the "rigid" reeds is roughly half that of the optimized configuration at the frequencies associated with the first three harmonics. This implies that the quoted value of 10 percent drop in stall mass flow is probably an underestimation of the actual effect of the feedback.

9.0 Discussion

The primary objective of the research was to obtain increased compressor stabilization by using aeromechanical feedback

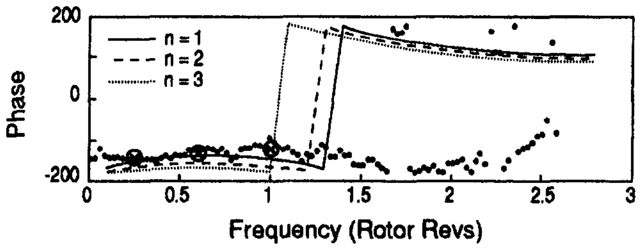

Fig. 22 Phase of nondimensional reed valve deflection/axial velocity transfer function ($\delta q/\delta\phi$): optimized configuration, operation near stall

control and this objective has been achieved. However, several additional issues regarding interpretation and applicability of the results to the more general objective of increasing compression system stable operating range using feedback control warrant further discussion.

The first is a general comment on the use of locally reacting feedback processes, such as employed in these experiments. The aeromechanical control strategy utilized appears to be the first scheme to employ local feedback to suppress rotating stall. This scheme differs from the modal-based control schemes, which have been used by previous researchers to stabilize rotating stall. The latter require arrays of sensors and actuators, as well as extensive real time computations, whereas locally reacting control strategies offer an alternative approach.

The role of the structural dynamics in the control strategy can also be linked to other nonaeromechanical control strategies to stabilize rotating stall. For example, a number of potential sensing and actuating schemes for control of rotating stall in axial flow compressors have been investigated by Hendricks and Gysling (1992). The results indicated that the most effective proportional control strategies included axial velocity sensors and actuators that modified the pressure rise across the compression system. A further conclusion was that actuators with bandwidths at least three times the rotational frequency of the disturbance were required for effective control.

Those results should be contrasted with the results from the aeromechanical feedback scheme investigated in the present work. In this, static pressure was sensed and low bandwidth (roughly equivalent to the rotational frequency of the compressor) actuators were used to modify the pressure rise across the compressor via mass/momentum injection. (The bandwidth of the aeromechanical actuators is defined as the natural frequency of the structural dynamic system.) This apparent contradiction can be explained by considering the role of the reed dynamics in the feedback process. The reeds *respond to* (or sense) static pressure perturbations in the upstream flow field. The reeds *actuate* the flow field by modifying the local pressure rise across the compression system as a function of reed displacement. The relationship between reed displacement and pressure perturbations is determined by the reed valve structural dynamics, which constitute a second order (rather than proportional) control law between sensed variable and actuation. At any one location, there is thus a temporal phase difference between the sensed variable and the actuation.

There is also a phase difference between static pressure and axial velocity perturbations in the upstream flow field, which is a necessary consequence of flow unsteadiness. Properly tuned reed dynamics serve to compensate for this phase difference so that reed deflection remains approximately 180 deg out of phase with the velocity perturbations in the upstream flow field for frequencies up to approximately two times the rotor frequency. To the compressor, therefore, the reeds' behavior appears as if they are being driven by high-bandwidth actuators, commanded by a signal proportional to the velocity perturbations in the upstream flow field. This can be seen from Fig. 22, which shows the phase of the transfer function between the nondimensional reed valve deflection and the axial velocity perturbation. The x's mark the frequencies corresponding to the first, second, and third harmonics. The dashed curves show the analytical results for these three harmonics. Over the frequency range of interest, the data and the analytical results indicate that the reed valve deflection is almost exactly out of phase with the axial velocity perturbations. Assuming that the primary effect of the reed displacement is to increase local pressure rise across the compressor, the feedback introduced by the optimized aeromechanical control scheme in the present study is thus essentially the "best case" in the Hendricks and Gysling study (1992). Interpreting the role of the structural dynamics as providing this *dynamic compensation* suggests that other types of (electromechanical) feedback control strategies can also use dynamic compensation to reduce sensing and actuation constraints.

Another point concerns the modeling approach adopted. It was assumed that the high total pressure jet was injected into a spanwise uniform flow field and mixed out in the spanwise direction before entering the compressor. This is not very realistic and the experiments, in fact, demonstrated that the high total pressure fluid basically filled in the axial momentum deficit in the casing boundary layer, changing the velocity profile entering the compressor. In addition, it seems more relevant to view the effect of the jet as a local influence on the endwall/clearance region, because the nature of the flow in this location is well known to have a major impact on stability. The overall conclusions, however, are not very sensitive to the precise nature of the approximations made much beyond the central idea that injection increases the pressure rise across the compressor. This is the key point, rather than the detailed mechanism by which it occurs.

Using this idea about the relation of injection rate and compressor rise, the stabilizing mechanism of the dynamic control can be interpreted physically. Suppose that injection does serve to increase the local pressure rise across the compressor and that the reed valves respond proportionally, and opposite, to the local mass flow perturbations. The change in pressure rise coefficient will be in phase with the axial flow coefficient upstream of the compressor and is given by:

$$\delta\Psi(\phi, q) = \frac{\partial\Psi}{\partial\Phi}\,\delta\phi_u + \frac{\partial\Psi}{\partial q}\,\delta q = \left(\frac{\partial\Psi}{\partial\Phi} + \frac{\partial\Psi}{\partial \mathrm{q}}\,\frac{\partial \mathrm{q}}{\partial\phi}\right)\delta\phi_u$$

$$= \left\{\frac{\partial\Psi}{\partial\Phi} - \frac{\partial\Psi}{\partial q}\,K\right\}\delta\phi_u \qquad (20)$$

In Eq. (20), δq represents the actuation, $\partial\Psi/\partial q$ is a positive constant representing the effect of actuation on the local pressure rise across the compressor, and $(\partial q/\partial\phi) = -K$ plays the part of a proportional control law between the perturbation in axial velocity and the actuation.

From Eq. (20), we see that the effective slope with feedback (which is the real part of the compressor transfer function) can be expressed in terms of the slope of the steady state compressor characteristic and the effect of the feedback:

$$\text{effective slope} = \left\{\frac{\partial\Psi}{\partial\Phi} - \frac{\partial\Psi}{\partial q}\,K\right\} \qquad (21)$$

The arguments concerning unsteady energy production given earlier thus imply that the flow becomes unstable when the effective slope becomes positive. For the compression system with feedback, Eq. (21) shows that this occurs at a lower flow coefficient than the original compression system.

Finally, the control system design was based on a simplified model of the compression system, which included the effect of aeromechanical feedback and allowed assessment of the role of several control parameters in addition to the compression system parameters. The model was successful in predicting the overall features of the compression system dynamics under the influence of aeromechanical feedback. We emphasize, however, that the control parameters achieved in the proof-of-concept experiment were by no means globally optimized, and the model predicts that additional stabilization could be achieved for a more optimized set of control parameters.

10.0 Summary and Conclusions

The onset of rotating stall in a low-speed, single-stage, axial flow compressor has been suppressed using aeromechanical feedback. The aeromechanical feedback was provided by an array of locally reacting reed valves that responded to static pressure perturbations in the upstream flow field. The reeds, which were modeled as mass-spring-dampers, regulated the amount of high-pressure air injected into the face of the compressor. This research appears to be the first demonstration of dynamic control of rotating stall in an axial flow compressor using aeromechanical feedback.

Using a small amount of injection mass flow (4 percent of the mass flow through the compressor at a total pressure of approximately one dynamic head based on compressor wheel speed), aeromechanical feedback reduced the stalling flow coefficient of the compression system by 10 percent compared to the stalling flow coefficient with the same amount of steady-state injection.

The mechanism responsible for rotating stall can be viewed as the compressor feeding energy into disturbances due to a positive real part of the compressor pressure rise versus mass flow transfer function. In this context, the role of an effective dynamic control strategy to suppress rotating stall can be interpreted as adding a negative component to the real part of this transfer function, thus decreasing the effective local slope of the compressor pressure rise versus flow response to unsteady small disturbances.

A physical interpretation was given for the role of the structural dynamics in the aeromechanical control strategy. The reed dynamics were found to serve as a dynamic compensators; the reed displacement, although driven by pressure perturbations, remained roughly 180 deg out of phase with velocity perturbations in the upstream flow field over a large frequency range. This phase relation is similar to that found in the active control strategies that have been found, to date, to be most effective. It is thus useful to view the present strategy and that of active control as different implementations of the same overall concept.

Acknowledgments

The authors wish to thank N. A. Cumpsty, J. Dugundji, A. H. Epstein, G. J. Hendricks, K. U. Ingard, J. L. Kerrebrock, F. E. Marble, J. D. Paduano, P. D. Silkowski, J. S. Simon, and C. S. Tan for many useful discussions and helpful suggestions throughout this research program. This research was supported under Grant F49620-91-1-0032 from the U.S. Air Force Office of Scientific Research, Major D. B. Fant, contract monitor. The first author also received support from the Air Force Research in Aero Propulsion Technology (AFRAPT) Program, Grant AFOSR-91-0052. These sources of support are gratefully acknowledged.

References

Day, I. J., 1993, "Active Suppression of Rotating Stall and Surge in Axial Compressors," ASME JOURNAL OF TURBOMACHINERY, Vol. 115, pp. 40–47.

Den Hartog, J. P., 1956, *Mechanical Vibrations*, McGraw-Hill, New York.

Epstein, A. H., Ffowcs-Williams, J. E., and Greitzer, E. M., 1989, "Active Suppression of Compressor Instabilities," *Journal of Propulsion for Power*, Vol. 5, pp. 204–211.

Ffowcs Williams, J. E., and Huang, X. Y., 1989, "Active Stabilization of Compressor Surge," *Journal of Fluid Mechanics*, Vol. 204, pp. 245–269.

Greitzer, E. M., 1981, "The Stability of Pumping Systems, the 1980 Freeman Scholar Lecture," ASME *Journal of Fluids Engineering*, Vol. 103, pp. 193–243.

Gysling, D. L., et al., 1991, "Dynamic Control of Centrifugal Compressor Surge Using Tailored Structures," ASME JOURNAL OF TURBOMACHINERY, Vol. 113, pp. 710–722.

Gysling, D. L., 1993, "Dynamic Control of Rotating Stall in Axial Flow Compressors Using Aeromechanical Feedback," MIT Gas Turbine Laboratory Report No. 219, Sept.

Haynes, J. M., Hendricks, G. J., and Epstein, A. H., 1994, "Active Stabilization of Rotating Stall in a Three-Stage Axial Compressor," ASME JOURNAL OF TURBOMACHINERY, Vol. 116, pp. 226–239.

Hendricks, G. J., and Gysling, D. L., 1992, "A Theoretical Study of Sensor-Actuator Schemes for Rotating Stall Control," AIAA Paper No. 92-3486.

Moore, F. K., 1984, "A Theory of Rotating Stall of Multistage Axial Compressors, Parts I–III," ASME *Journal of Engineering for Gas Turbines and Power*, Vol. 106, pp. 313–336.

Moore, F. K., and Greitzer, E. M., 1986, "A Theory of Post Stall Transients in Axial Compression Systems: Parts I and II," ASME *Journal of Engineering for Gas Turbines and Power*, Vol. 108, pp. 68–76.

Paduano, J. D., 1992, "Active Control of Rotating Stall in Axial Compressors," MIT Gas Turbine Laboratory Report No. 208, Massachusetts Institute of Technology, Mar.

Paduano, J. P., et al., 1993, "Active Control of Rotating Stall in a Low Speed Compressor," ASME JOURNAL OF TURBOMACHINERY, Vol. 115, No. 1, pp. 48–56.

Simon, J. S., et al., 1993, "Evaluations of Approaches to Active Compressor Surge Stabilization," ASME JOURNAL OF TURBOMACHINERY, Vol. 115, pp. 57–67.

Wellstead, P. E., 1981, "Non-parametric Methods of System Identification," *Automatica*, Vol. 17, No. 1, pp. 55–69.

Aircraft Engine Committee Best 1993 Paper Award

Control-Oriented High-Frequency Turbomachinery Modeling: General One-Dimensional Model Development

O. O. Badmus
Graduate Student,
School of Chemical Engineering.

K. M. Eveker[1]
Air Force Laboratory Graduate Fellow,
School of Aerospace Engineering.

C. N. Nett[1]
Associate Professor and Director,
Laboratory for Identification and Control of
Complex Highly Uncertain Systems,
School of Aerospace Engineering.

Georgia Institute of Technology,
Atlanta, GA 30332-0150

In this paper, an approach for control-oriented high-frequency turbomachinery modeling previously developed by the authors is applied to develop one-dimensional unsteady compressible viscous flow models for a generic turbojet engine and a generic compression system. We begin by developing models for various components commonly found in turbomachinery systems. These components include: ducting without combustion, blading, ducting with combustion, heat soak, blading with heat soak, inlet, nozzle, abrupt area change with incurred total pressure losses, flow splitting, bleed, mixing, and the spool. Once the component models have been developed, they are combined to form system models for a generic turbojet engine and a generic compression system. These models are developed so that they can be easily modified and used with appropriate maps to form a model for a specific rig. It is shown that these system models are explicit (i.e., can be solved with any standard ODE solver without iteration) due to the approach used in their development. Furthermore, since the nonlinear models are explicit, explicit analytical linear models can be derived from the nonlinear models. The procedure for developing these analytical linear models is discussed. An interesting feature of the models developed here is the use of effective lengths within the models, as functions of axial Mach number and nondimensional rotational speed, for rotating components. These effective lengths account for the helical path of the flow as it moves through a rotating component. Use of these effective lengths in the unsteady conservation equations introduces a nonlinear dynamic lag consistent with experimentally observed compressor lag and replaces less accurate linear first-order empirical lags proposed to account for this phenomenon. Models of the type developed here are expected to prove useful in the design and simulation of (integrated) surge control and rotating stall avoidance schemes.

1 Introduction

In [1, 2] the authors presented the theoretical foundations of a new approach for control-oriented high-frequency turbomachinery modeling. The approach in [1] was based on an assumption of calorically perfect single species gas (i.e., γ and R constant); however, in [2] some preliminary results are given for a system of dimensionless equations, which is valid in the case of flow of a thermally perfect multiple species gas present in high-temperature flows involving combustion in some turbomachinery systems. The turbomachinery modeling approach developed in [1, 2] can be outlined as follows: First, the turbomachinery system is conceptually divided into distinct components. The component boundaries represent natural points of demarcation for the various forcing terms present in the governing flow equations. The components are then subdivided, if necessary, into elements to form an appropriate grid of the spatial domain. A set of dimensionless flow equations developed in [1, 2] is then applied to each element of the system. For each element, a decision is made to either retain or residualize the flow dynamics. This decision is based on the value of a singular perturbation parameter, ϵ, a naturally occurring parameter of the dimensionless equations. In either case, a novel discretization of the dimensionless equations is then utilized to obtain a lumped-parameter model for each element. Now, for elements in which forcing terms are nonzero, relations to describe the forcing terms are either determined from first principles or identified from experimental data. When these terms cannot be determined from first principles, techniques developed in [1, 2] for rigorous identification of these terms from steady-state experiments are employed. Once models have been developed for each of the system elements, they are aggregated to form the overall nonlinear system model. An important feature of models developed using this approach is that they are explicit (i.e., can be solved with any standard ODE solver without iteration). This results because the novel discretization of the dimensionless equations used in this modeling approach is matched to the natural turbomachinery inputs [1, 2].

The focus in [1, 2] was on the element equations. It was argued that the models developed using the approach are explicit, and that explicit analytical linear models can be developed from these models. However, a demonstration of system model development using this approach was not given. The goal of this paper is to show how the element equations are used to build system models and to demonstrate explicitly that

---

[1] Current address: United Technologies Research Center, East Hartford, CT 06108.

Contributed by the International Gas Turbine Division and based on a paper presented at the 38th International Gas Turbine and Aeroengine Congress and Exposition, Cincinnati, Ohio, May 24–27, 1993. Manuscript received at ASME Headquarters March 17, 1993. Paper No. 93-GT-385. Associate Technical Editor: H. Lukas.

these models exhibit the features claimed in [1, 2]. To achieve this goal, the approach in [1, 2] is applied to develop one-dimensional unsteady compressible viscous flow models for a calorically perfect single species gas in a generic turbojet engine and a generic compression system. The case of calorically perfect single species gas was selected for the model development in this paper since analytical component models can be developed for this case. However, some important computational issues pertaining to the development of models for a thermally perfect multiple species gas using the system of equations presented in [2] are also discussed.

We begin by developing models for various components commonly found in turbomachinery systems. These components include: ducting without combustion, blading, ducting with combustion, heat soak, blading with heat soak, inlet, nozzle, abrupt area change with incurred total pressure losses, flow splitting, bleed, mixing, and the spool. Once the component models have been developed, they are combined to form system models for a generic turbojet engine and a generic compression system. These models are developed so that they can be easily modified and used with appropriate maps to form a model for a specific rig. It is shown that these system models are explicit due to the approach used in their development. Furthermore, since the nonlinear models are explicit, analytical linear models can be derived from the nonlinear models. The procedure for developing these analytical linear models is discussed. The system models developed here give concrete indication that the claims made in [1, 2] are true.

An interesting feature of the models developed here is the use of effective lengths within the models, as functions of axial Mach number and nondimensional rotational speed, for rotating components. The use of effective lengths though implicit in [1, 2] is demonstrated explicitly here. These effective lengths account for the helical path of the flow as it moves through a rotating component. Use of these effective lengths in the unsteady conservation equations introduces a nonlinear dynamic lag consistent with experimentally observed compressor lag [3] and replaces less accurate linear first-order empirical lags proposed to account for this phenomenon in [4] and used in [5–9].

1.1 Historical Perspective. Many one-dimensional high-frequency turbomachinery models have been presented in the literature. For quasi-one-dimensional incompressible flow in compression systems, models of this type are given in [4, 10, 11, 8]. For quasi-one-dimensional compressible flow in compression systems, models of this type can be found in [12, 13, 5, 9]. For quasi-one-dimensional compressible flow in full engine systems, models of this type are given in [14–17, 7]. The generic models given in this paper are quasi-one-dimensional compressible flow models. The advantages of the models presented in this paper over others of this type presented in the literature include: (1) a rigorous procedure for embedding steady-state experimental data into the model, and (2) the ability to obtain explicit models that incorporate natural system boundary conditions. Models of this type are primarily used in the design of surge control and integrated surge control/rotating stall avoidance schemes, which have been reported in [6, 18–22] and [23], respectively.

For studying the two-dimensional phenomena of rotating stall, a two-dimensional model that can model and predict rotating stall is required. For incompressible flow, the models given in [24–28] have this capability. Extension of models of this type to compressible flow is discussed in [29]. These two-dimensional models are used in the design of rotating stall control schemes [18, 28, 30–33]. Extensions of the generic one-dimensional models presented in this paper to two-dimensional models will be undertaken in the future, using a parallel compressor concept [34], for use in the design of rotating stall control schemes.

2 Foundational Equations

In this section we list some foundational equations developed in [1, 2] that are used for model development in this paper. We first direct the reader to some notation in Tables 1 and 2 for dimensional and dimensionless variables, respectively. In addition, we define the notation that $\mathrm{M}_{k-1}(t) := \mathrm{M}(x_{k-1}, t)$ and $\mathrm{M}_k(t) := \mathrm{M}(x_k, t)$, where x_{k-1} is the position of the entrance of the kth element, and x_k is the position of the exit of the kth element. Similar notation is used for other variables unless otherwise specified. Now, the discretized form of the dimensionless equations for unsteady compressible viscous quasi-one-dimensional flow of a calorically perfect single species gas in the kth finite element of a component can be written as [2]:

$$\epsilon(s_{k-1}, p_{k-1}, L_k, \gamma)\frac{d}{dt}\begin{bmatrix}\mathrm{M}_{k-1}\\ p_k\\ s_k\end{bmatrix} = \Xi(\mathrm{M}_k, \gamma)\left\{\begin{bmatrix}\mathrm{M}_k - \mathrm{M}_{k-1}\\ p_k - p_{k-1}\\ s_k - s_{k-1}\end{bmatrix}\right.$$

$$\left. - \begin{bmatrix} m_4(\mathrm{M}_k, e^{A_{k-1}}/L_k^2, A_k - A_{k-1}, N_{k-1}, \gamma, \mathrm{Re}_{k-1}, \mathrm{Pr}, T_{w,k-1} - T_{k-1})\\ m_5(\mathrm{M}_k, e^{A_{k-1}}/L_k^2, A_k - A_{k-1}, N_{k-1}, \gamma, \mathrm{Re}_{k-1}, \mathrm{Pr}, T_{w,k-1} - T_{k-1})\\ m_6(\mathrm{M}_k, e^{A_{k-1}}/L_k^2, A_k - A_{k-1}, N_{k-1}, \gamma, \mathrm{Re}_{k-1}, \mathrm{Pr}, T_{w,k-1} - T_{k-1})\end{bmatrix}\right\} + \epsilon(s_{k-1}, p_{k-1}, L_k, \gamma)\begin{bmatrix}0\\ -1\\ \dfrac{\gamma-1}{\gamma}\end{bmatrix}\frac{d}{dt}A_k. \quad (1)$$

The matrix $\Xi(\mathrm{M}_k, \gamma)$ is made up of influence coefficient functions ξ_{ij}'s, which are known functions of M and γ defined in [1, 2], and

$$\epsilon(s_{k-1}, p_{k-1}, L_k, \gamma) = L_k e^{-(1/2)(T_{k-1})},$$

where, for brevity, the following definition is made:

$$T_{k-1} = s_{k-1} + \frac{\gamma - 1}{\gamma} p_{k-1}.$$

The maps, m_4, m_5, and m_6, in these equations account for the forcing terms Q, f_s, and f_w in the quasi-one-dimensional flow equations. They are equal in steady state to the differences $\mathrm{M}_k - \mathrm{M}_{k-1}$, $p_k - p_{k-1}$, and $s_k - s_{k-1}$ across the element, respectively. Identification of these functions is discussed further in [2].

3 Component Model Development

The first step of the modeling approach of [2] involves dividing the system into various components. The component boundaries represent natural points of demarcation for the various forcing terms present in the governing equations. In this way, we simplify model development by distinguishing between elements in the system in which certain forcing terms are nonzero and those in which they are zero. A discussion is now given on the development of models for various turbomachinery com-

Table 1 Dimensional variables

Variable	Description
$\tilde{x}$	position
$\tilde{t}$	time
$\tilde{L}$	length
$\tilde{A}(\tilde{x},\tilde{t})$	area
R	ideal gas constant
c_v	heat capacity at constant volume
c_p	heat capacity at constant pressure
$\tilde{u}(\tilde{x},\tilde{t})$	fluid velocity
$\tilde{\rho}_s(\tilde{x},\tilde{t})$	static density
$\tilde{p}_s(\tilde{x},\tilde{t})$	static pressure
$\tilde{T}_s(\tilde{x},\tilde{t})$	static temperature
$\tilde{e}(\tilde{x},\tilde{t})$	specific internal energy
$\tilde{w}(\tilde{x},\tilde{t})$	mass flow rate
$\tilde{Q}(\tilde{x},\tilde{t})$	volumetric heat transfer rate (into fluid)
$\tilde{f}_w(\tilde{x},\tilde{t})$	specific wall friction force (on fluid, does no work)
$\tilde{f}_s(\tilde{x},\tilde{t})$	specific force (on fluid, does work)
$\bar{t}$	reference time
$\bar{p}$	reference pressure
$\bar{T}$	reference temperature
$\tilde{N}(\tilde{t})$	shaft speed
μ	viscosity
k	thermal conductivity
$\tilde{T}_w(\tilde{x},\tilde{t})$	wall temperature

Table 2 Dimensionless variables

Variable	Description
$x = \tilde{x}/\tilde{L}$	dimensionless position
$t = \tilde{t}/\bar{t}$	dimensionless time
$A = ln\left[\tilde{A}/(\bar{t}^2\gamma R\bar{T})\right]$	dimensionless area
$L = \tilde{L}/\left(\bar{t}\sqrt{\gamma R\bar{T}}\right)$	dimensionless length
$\gamma = c_p/c_v$	ratio of specific heats
$M = \tilde{u}/\sqrt{\gamma R\tilde{T}_s}$	Mach number
$p = ln(\tilde{p}/\bar{p})$	dimensionless total pressure
$s = \tilde{s}/c_p$	dimensionless specific entropy
$T = ln(\tilde{T}/\bar{T})$	dimensionless total temperature
$Q = \tilde{Q}\tilde{L}/\left(\bar{p}\sqrt{\gamma R\bar{T}}\right)$	dimensionless volumetric heat transfer rate
$f_w = \tilde{f}_w\tilde{L}/\left(\gamma R\bar{T}\right)$	dimensionless specific wall friction force
$f_s = \tilde{f}_s\tilde{L}/\left(\gamma R\bar{T}\right)$	dimensionless specific force
$N = \tilde{N}\sqrt{\tilde{A}/\left(\gamma R\bar{T}\right)}$	dimensionless shaft speed
$Re = \tilde{\rho}_s\tilde{u}\sqrt{\tilde{A}}/\mu$	Reynolds number
$Pr = c_p\mu/k$	Prandtl Number
$T_w = ln(\tilde{T}_w/\bar{T})$	dimensionless wall temperature

ponents. Analytical model development for the various components is given, where possible, as a guide for more complicated case specific component models, which will be required for a model of a specific rig. In choosing which components to model, we attempt to cover all combinations of forcing that could be present in turbomachinery applications. Once the component models have been developed, a discussion is given on how they are used to form explicit system models for a generic turbojet engine and a generic compression system.

3.1 Components Modeled With Quasi-One-Dimensional Flow Equations. In this section, several component models are given that can be obtained by direct application of the quasi-one-dimensional flow equations developed in [2] and summarized above. In cases where analytical expressions for the forcing terms are known, analytical expressions are developed for the maps to include in Eq. (1).

Ducting Without Combustion. This component is used to model ducting in which no combustion is present. The maps for this component have the following form:

$$\chi_{M,k} = m_4(M_k, A_k - A_{k-1}, Re_{k-1})$$

$$\chi_{p,k} = m_5(M_k, A_k - A_{k-1}, Re_{k-1})$$

$$\chi_{s,k} = m_6(M_k, A_k - A_{k-1}, Re_{k-1}),$$

where $\chi_{M,k}$ is the map determined by the difference $M_k - M_{k-1}$ across the stage, $\chi_{p,k}$ is the map determined by the difference $p_k - p_{k-1}$ across the stage, and $\chi_{s,k}$ is the map determined by the difference $s_k - s_{k-1}$ across the stage. The dependence on the areas can be dropped if the areas are fixed. Analytical expressions for these maps are given in Appendix A.

Blading. This component is used to model fans, compressors, and turbines. Shaft forces, blade/wall friction forces, and area changes are all present. Accurate first principles modeling of these effects is difficult, so the maps for this component are usually identified through steady-state experiments. Further subdivision of the component into finite elements must be done with consideration of the requirement of experimental identification of these forcing terms. Although a hard practical limit for experimental measurement is probably a single row (rotor, stator, or guide vane), in most cases, a stage (rotor/stator pair or guide vane row) is the smallest division of the compressor considered for experimental measurement in a blading component. For this reason, the smallest element considered in modeling this component consists of a single stage. For the kth compressor stage, the following notation is used for the maps identified through steady-state experiments:

$$\pi_{M,k} = m_4(M_k, A_k - A_{k-1}, N_{k-1}, Re_{k-1}, \alpha)$$

$$\pi_{p,k} = m_5(M_k, A_k - A_{k-1}, N_{k-1}, Re_{k-1}, \alpha)$$

$$\pi_{s,k} = m_6(M_k, A_k - A_{k-1}, N_{k-1}, Re_{k-1}, \alpha),$$

where $\pi_{\mathrm{M},k}$ is the map determined by the difference $\mathrm{M}_k - \mathrm{M}_{k-1}$ across the stage, $\pi_{p,k}$ is the map determined by the difference $p_k - p_{k-1}$ across the stage, and $\pi_{s,k}$ is the map determined by the difference $s_k - s_{k-1}$ across the stage. A new term, α, is included in the functional dependence of these maps to account for the effects of variable guide vane/stator angles.

Ducting With Combustion. This component is used to model combustion chambers and afterburners. Combustion and wall friction forces are present with a possible area change as well. The combustion and friction forces usually cannot be modeled analytically, hence the maps for this component are usually identified through steady-state experiments. For the kth element of this component, the following notation is used for the maps identified through steady-state experiments:

$$\phi_{\mathrm{M},k} = m_4(\mathrm{M}_k, A_k - A_{k-1}, \mathrm{Re}_{k-1}, w_f)$$

$$\phi_{p,k} = m_5(\mathrm{M}_k, A_k - A_{k-1}, \mathrm{Re}_{k-1}, w_f)$$

$$\phi_{s,k} = m_6(\mathrm{M}_k, A_k - A_{k-1}, \mathrm{Re}_{k-1}, w_f),$$

where $\phi_{\mathrm{M},k}$ is the map determined by the difference $\mathrm{M}_k - \mathrm{M}_{k-1}$ across the stage, $\phi_{p,k}$ is the map determined by the difference $p_k - p_{k-1}$ across the stage, and $\phi_{s,k}$ is the map determined by the difference in $s_k - s_{k-1}$ across the stage. The term w_f is included in the functional dependence of these maps to account for the heat release of the fuel. An analytical model for this component is given in Appendix A.

Heat Soak. In this element, heat exchange occurs between the walls/blades and the flow. This component is used to model ducting downstream of a combustion chamber or in a recuperator. The maps for this component have the following form:

$$\chi_{\mathrm{M},k} = m_4(\mathrm{M}_k, A_k - A_{k-1}, \mathrm{Re}_{k-1}, \mathrm{Pr}, \mathrm{Nu}, T_{w,k-1} - T_{k-1})$$

$$\chi_{p,k} = m_5(\mathrm{M}_k, A_k - A_{k-1}, \mathrm{Re}_{k-1}, \mathrm{Pr}, \mathrm{Nu}, T_{w,k-1} - T_{k-1})$$

$$\chi_{s,k} = m_6(\mathrm{M}_k, A_k - A_{k-1}, \mathrm{Re}_{k-1}, \mathrm{Pr}, \mathrm{Nu}, T_{w,k-1} - T_{k-1}),$$

where $\chi_{\mathrm{M},k}$ is the map determined by the difference $\mathrm{M}_k - \mathrm{M}_{k-1}$ across the stage, $\chi_{p,k}$ is the map determined by the difference $p_k - p_{k-1}$ across the stage, and $\chi_{s,k}$ is the map determined by the difference $s_k - s_{k-1}$ across the stage. The Nusselt number, Nu, is added to the variable dependencies to account for convection heat transfer effects [35]. Analytical expressions for these maps are given in Appendix A. The wall temperature, $T_{w,k-1}$, is either an independent input of the model, or it is a state of the model. For the latter case, a dynamic equation is required for the wall temperature.

Blading With Heat Soak. This component is the same as the blading component with the addition of heat soak effects. This component is used to model the turbine when heat soak effects between the flow and blades are significant. The major change in the model of this component, compared to that of the blading component, is that the maps determined through steady-state experiments also include the effects of heat transfer to the walls and blades. Using the same notation as for the blading, the maps identified through steady-state experiments for the kth stage are:

$$\pi_{\mathrm{M},k} = m_4(\mathrm{M}_k, A_k - A_{k-1}, N_{k-1}, \mathrm{Re}_{k-1}, \mathrm{Pr}, \mathrm{Nu}, T_{w,k-1} - T_{k-1}, \alpha)$$

$$\pi_{p,k} = m_5(\mathrm{M}_k, A_k - A_{k-1}, N_{k-1}, \mathrm{Re}_{k-1}, \mathrm{Pr}, \mathrm{Nu}, T_{w,k-1} - T_{k-1}, \alpha)$$

$$\pi_{s,k} = m_6(\mathrm{M}_k, A_k - A_{k-1}, N_{k-1}, \mathrm{Re}_{k-1}, \mathrm{Pr}, \mathrm{Nu}, T_{w,k-1} - T_{k-1}, \alpha),$$

with the important difference that these maps depend on more variables. When turbine maps are obtained, however, the wall/blade temperature normally is not varied independently, and the entire map is not obtained. In this case, we would like to combine an analytical heat soak model with experimentally identified maps for the blade forcing. A discussion of how this is done is given in [2], and the maps for this component can be formed using this technique as follows:

$$\begin{bmatrix} m_4 \\ m_5 \\ m_6 \end{bmatrix} = \begin{bmatrix} m_{4,\mathrm{new}}(\mathrm{M}_k, A_k - A_{k-1}, N_{k-1}, \mathrm{Re}_{k-1}, \alpha) \\ m_{5,\mathrm{new}}(\mathrm{M}_k, A_k - A_{k-1}, N_{k-1}, \mathrm{Re}_{k-1}, \alpha) \\ m_{6,\mathrm{new}}(\mathrm{M}_k, A_k - A_{k-1}, N_{k-1}, \mathrm{Re}_{k-1}, \alpha) \end{bmatrix} - [\Xi(\mathrm{M}_k, \gamma)]^{-1}\Upsilon(\mathrm{M}_k, \gamma)\begin{bmatrix} Q_{hs} \\ 0 \\ 0 \end{bmatrix},$$

where Q_{hs} is an analytical model of the heat soak effects, equal to 0 at steady state, and $m_{4,\mathrm{new}}$, $m_{5,\mathrm{new}}$, and $m_{6,\mathrm{new}}$ are the experimental maps measured when the wall/blade temperature is allowed to equilibrate before measurements are taken.

Inlet. The inlet of the system is normally made up of either a compressor stage or a section of ducting. The model for this component differs only in that at the entrance of the first element of this component, p_i and s_i are model inputs, since they are natural boundary conditions of the system.

Nozzle. The nozzle is the main throttling device through which the flow exhausts to atmosphere. The nozzle usually consists of an isentropic area change in which a boundary condition is enforced at the exit. In this case, the equations for the nozzle would have the following form:

$$\mathrm{M}_{k-1} = m_4(A_e - A_{k-1}, p_e - p_{se})$$

$$p_e = p_{k-1}$$

$$s_e = s_{k-1},$$

where the term $p_e - p_{se}$ is accounts for the dependence on the model input, p_{se}, which determines the model boundary condition, M_e. Analytical equations for the nozzle are given in Appendix A.

3.2 Components Modeled With Other Equations.

In this section we develop models for components that cannot be modeled by a direct application of the quasi-one-dimensional flow equations developed in [2].

Abrupt Area Change With Incurred Total Pressure Losses. In this component, the flow encounters an abrupt area increase in which total pressure losses are incurred. This component is used to model the abrupt area change which sometimes occurs between the end of the ducting from the compressor and the combustion chamber. This process cannot be modeled using quasi-one-dimensional flow equations as they do not hold when the area increases abruptly. However, this area increase occurs over a very short axial distance, and the dynamics in this component are usually residualized. Analytical expressions for this process are given in Appendix A.

Flow Splitting. In this component, the flow is split into two streams, as is done in a turbofan engine. This occurs over a very short axial distance; hence, all dynamics are assumed to equilibrate quickly and are residualized. The equations for this element have the following form:

$$\mathrm{M}_{k-1} = g_{\mathrm{spl}}(\mathrm{M}_{k,1}, \mathrm{M}_{k,2}, A_{k,1} - A_{k-1}, A_{k,2} - A_{k-1}),$$

$$p_{k,1} = p_{k-1} \quad s_{k,1} = s_{k-1},$$

$$p_{k,2} = p_{k-1} \quad s_{k,2} = s_{k-1},$$

where the subscript $k-1$ denotes the flow entering this element, $k,1$ denotes the flow leaving the element in the first stream, and

k,2 denotes the flow leaving the element in the second stream. Analytical equations for this element are given in Appendix A.

Bleed. This component is a specialization of the flow splitting component just discussed. Here, the flow is split into two streams and a portion of the main flow is bled off to the atmosphere or another point in the system. The equations for this element have the following form:

$$\mathrm{M}_{k-1} = g_{\mathrm{bld}}(\mathrm{M}_k, A_k - A_{k-1}, A_{k,b} - A_{k-1}, p_{k-1} - p_{sk,b}),$$

$$p_k = p_{k-1} \quad s_k = s_{k-1},$$

where the term $p_{k-1} - p_{sk,b}$ accounts for the dependence on the input $p_{sk,b}$. Analytical expressions for this process are given in Appendix A.

Mixing. Mixing occurs when two streams are combined into one, as is done, for example, when bypass flow is recombined with the core flow in a turbofan engine. This phenomena cannot be modeled with quasi-one-dimensional flow equations. However, since this phenomenon occurs in a very short axial distance, the dynamics associated with it can be residualized. An often-used model for mixing is that the static pressure is equal at all points of the mixing plane. Analytical expressions for this process are given in Appendix A.

Wall/Blade Metal. A dynamic equation is required for the wall/blade metal temperature when it is a state of the model. This equation is developed using standard heat transfer analysis [35] and is given in Appendix A.

Spool. The model of the spool is developed since it is required for the generic turbojet engine model. This equation is developed through a power balance on the spool and is given in Appendix A.

3.3 Effective Lengths in Dynamic Equations. When developing the model for a component, care must be taken when computing the length required in the equations. The quasi-one-dimensional flow equations hold along a flow path as long as the flow properties in a plane normal to that flow path are essentially constant [36]. As the flow moves through a rotating element (e.g., a compressor rotor), it follows a helical path along which the quasi-one-dimensional flow equations hold. Thus, the correct length to use in the unsteady equations for this flow is the length of this helical path. The length of this path, called the effective length of the component ($L_{k,e}$), can be computed as follows:

$$L_{k,e} = L_k \sqrt{1 + \frac{N_{k-1}^2}{\mathrm{M}_k^2} r_{k-1}^2 e^{-A_{k-1}} e^{-(T_k - T_{k-1})} \left(1 + \frac{\gamma - 1}{2} \mathrm{M}_k^2\right)},$$

where r_{k-1} is the dimensionless radius of the component. This length is computed by first finding the time required for the flow to move axially through the rotating component. Then, this time is used to determine the distance the flow travels around the circumference of the rotating component as it moves through the component. The effective length is then computed as the magnitude of the vector sum of the axial and circumferential distances that the flow travels as it moves through the rotating component. Obviously, this length will become infinite if $\mathrm{M}_k = 0$, thus it is appropriate to set a threshold on the Mach number used in this equation.

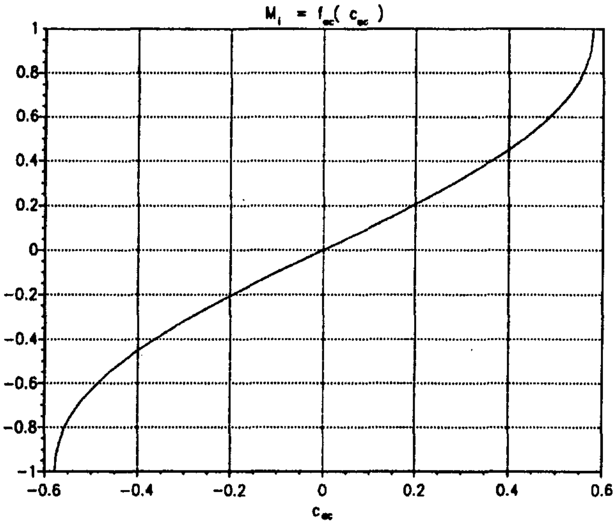

Fig. 1 Isentropic area change function $f_{ac}(c_{ac})$ for $\gamma = 1.4$

3.4 Choosing a Grid of the Spatial Domain. The issue of determining an appropriate grid of the spatial domain is important. In [37], a discussion is given on how the choice of the spatial discretization determines the models frequency response to a disturbance. Two criteria are given for the maximum frequency response of a model to disturbances, based on the spatial discretization. The first criterion is attributed to [38], and it requires that the minimum disturbance wavelength be limited by ten times the maximum length of a spatial element. Thus,

$$f_{\max} = \frac{(u + a)_{\min}}{10 \Delta x_{\max}},$$

where $f_{\max}$ is the maximum frequency response, u is the flow path velocity, a is the sonic velocity, and $\Delta x_{\max}$ is the maximum length of a spatial element. The second criterion is attributed to [39], and it requires that the propagation time through a spatial element be less than 1/3 the period of the disturbance. Thus,

$$f_{\max} \leq \frac{a}{6\pi \Delta x},$$

where a and Δx are average quantities.

Here, we suggest how these criteria can be used to determine the appropriate choice of spatial discretization. Now, if the smallest spatial discretization in the compressor is a compressor stage, these criteria can be used, with required effective lengths, to determine the maximum frequency response of the model to a disturbance based on one of the compressor stages. Having applied the criteria to a compressor stage, the corresponding sizes for elements in other components of the system can then be determined to give the same model frequency response to disturbances. Unfortunately, this can lead to models with a very high number of spatial elements and subsequently a high number of states. However, we consider this a good starting point and divide each component into finite elements in this manner. With this model, we can then look at the distribution of states along that component. A linear distribution of the states is assumed in each finite element [2]. If the distribution across the component modeled with several elements is linear, the component can be modeled equally well with a single element, thus reducing the number of states. The model can also be compared to experimental data in the form of both nonlinear and linear behaviors. Good agreement with experimental data also indicates the appropriateness of the spatial grid used. If the model compares well with experimental data, it is valid in spite of the fact that a coarser grid of the spatial domain is used in its development. Since the models developed using this technique are for use in control design, low model order is desirable. Therefore, the grid of the spatial domain is chosen as coarse as possible to achieve a good match of experimental data.

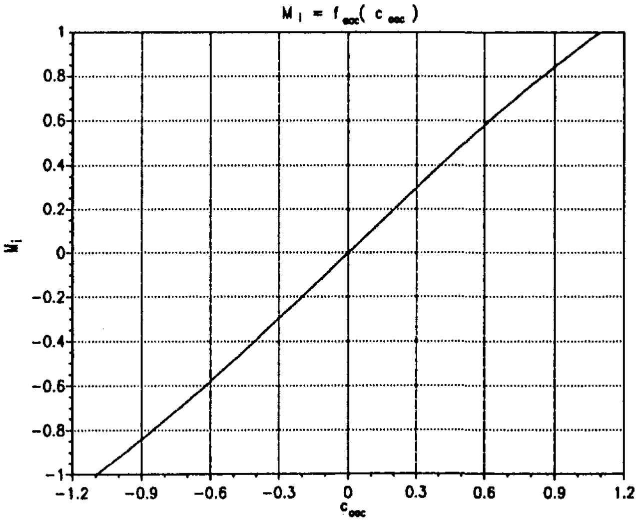

Fig. 2 Abrupt area change function $f_{aac}(c_{aac})$ for $\gamma = 1.4$

4 Generic Turbojet Engine

In this section a model of a generic turbojet engine is developed. Then, a discussion is given on how to use the nonlinear model to develop linear models for the generic turbojet engine.

4.1 Nonlinear Model. The generic turbojet shown in Fig. 3 is made up of the following components: inlet ducting, two-stage compressor with bleed after each stage, compressor discharge ducting, bleed, ducting with combustion, two-stage turbine with heat soak effects, nozzle ducting, and nozzle. Also, the dynamic spool equation is required to complete the model. A multispool machine would be modeled in the same way as a single-spool machine, with the exception of multiple spool equations. This model is developed so that it can be easily modified and used with maps for a specific turbojet engine to obtain a model for that particular rig. The number of elements making up each component is arbitrarily defined here so that an overall model can be developed; however, the number of elements making up each component in a model of a specific system must be determined by applying the procedure discussed previously.

Using the notation of Fig. 3, the model for the generic turbojet is developed as follows: The inlet consists of two elements of ducting with isentropic area change. The areas are assumed to be fixed so this map dependence is dropped. The following equations result:

$$\chi_{\mathrm{M},1} = m_{4,di1}(\mathrm{M}_1)$$

$$\chi_{p,1} = 0 \quad \chi_{s,1} = 0$$

$$\frac{d}{dt}\mathrm{M}_0 = \frac{e^{(1/2)(T_0)}}{L_1}\,[\xi_{11}(\mathrm{M}_1, \gamma)(\mathrm{M}_1 - \mathrm{M}_0 - \chi_{\mathrm{M},1})$$
$$+ \xi_{12}(\mathrm{M}_1, \gamma)(p_1 - p_0) + \xi_{13}(\mathrm{M}_1, \gamma)(s_1 - s_0)]$$

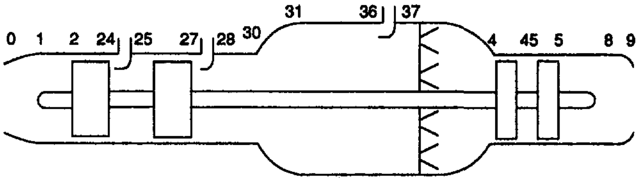

Fig. 3 Diagram of generic turbojet engine

$$\frac{d}{dt}p_1 = \frac{e^{(1/2)(T_0)}}{L_1}\,[\xi_{21}(\mathrm{M}_1, \gamma)(\mathrm{M}_1 - \mathrm{M}_0 - \chi_{\mathrm{M},1})$$
$$+ \xi_{22}(\mathrm{M}_1, \gamma)(p_1 - p_0) + \xi_{23}(\mathrm{M}_1, \gamma)(s_1 - s_0)]$$

$$\frac{d}{dt}s_1 = \frac{e^{(1/2)(T_0)}}{L_1}\,[\xi_{33}(\mathrm{M}_1, \gamma)(s_1 - s_0)].$$

For the second element,

$$\chi_{\mathrm{M},2} = m_{4,di2}(\mathrm{M}_2)$$

$$\chi_{p,2} = 0 \quad \chi_{s,2} = 0$$

$$\frac{d}{dt}\mathrm{M}_1 = \frac{e^{(1/2)(T_1)}}{L_2}\,[\xi_{11}(\mathrm{M}_2, \gamma)(\mathrm{M}_2 - \mathrm{M}_1 - \chi_{\mathrm{M},2})$$
$$+ \xi_{12}(\mathrm{M}_2, \gamma)(p_2 - p_1) + \xi_{13}(\mathrm{M}_2, \gamma)(s_2 - s_1)]$$

$$\frac{d}{dt}p_2 = \frac{e^{(1/2)(T_1)}}{L_2}\,[\xi_{21}(\mathrm{M}_2, \gamma)(\mathrm{M}_2 - \mathrm{M}_1 - \chi_{\mathrm{M},2})$$
$$+ \xi_{22}(\mathrm{M}_2, \gamma)(p_2 - p_1) + \xi_{23}(\mathrm{M}_2, \gamma)(s_2 - s_1)]$$

$$\frac{d}{dt}s_2 = \frac{e^{(1/2)(T_1)}}{L_2}\,[\xi_{33}(\mathrm{M}_2, \gamma)(s_2 - s_1)].$$

Since this is the inlet of the generic turbojet engine, p_0 and s_0 are inputs to the system and the model.

The compressor consists of two blading stages, each followed by a bleed valve. No heat soak effects are considered in the compressor, however these effects would be modeled in the same way as is done for the turbine stages. The areas at the inlet and exit of each compressor stage are assumed to be fixed, hence this dependence in the compressor maps is neglected. In terms of the notation of Figure 3, the following equations result:

$$\pi_{\mathrm{M},24} = m_{4,cs1}(\mathrm{M}_{24}, N_2, \mathrm{Re}_2, \alpha)$$

$$\pi_{p,24} = m_{5,cs1}(\mathrm{M}_{24}, N_2, \mathrm{Re}_2, \alpha)$$

$$\pi_{s,24} = m_{6,cs1}(\mathrm{M}_{24}, N_2, \mathrm{Re}_2, \alpha),$$

$$L_{24,e} = L_{24}\sqrt{1 + \frac{N_2^2}{\mathrm{M}_{24}^2}\,r_2^2 e^{-A_2 e^{-(T_{24}-T_2)}}\left(1 + \frac{\gamma - 1}{2}\,\mathrm{M}_{24}^2\right)}\,,$$

$$\frac{d}{dt}\mathrm{M}_2 = \frac{e^{(1/2)(T_2)}}{L_{24,e}}\,[\xi_{11}(\mathrm{M}_{24}, \gamma)(\mathrm{M}_{24} - \mathrm{M}_2 - \pi_{\mathrm{M},24})$$
$$+ \xi_{12}(\mathrm{M}_{24}, \gamma)(p_{24} - p_2 - \pi_{p,24})$$
$$+ \xi_{13}(\mathrm{M}_{24}, \gamma)(s_{24} - s_2 - \pi_{s,24})]$$

$$\frac{d}{dt}p_{24} = \frac{e^{(1/2)(T_2)}}{L_{24,e}}\,[\xi_{21}(\mathrm{M}_{24}, \gamma)(\mathrm{M}_{24} - \mathrm{M}_2 - \pi_{\mathrm{M},24})$$
$$+ \xi_{22}(\mathrm{M}_{24}, \gamma)(p_{24} - p_2 - \pi_{p,24})$$
$$+ \xi_{23}(\mathrm{M}_{24}, \gamma)(s_{24} - s_2 - \pi_{s,24})]$$

$$\frac{d}{dt}s_{24} = \frac{e^{(1/2)(T_2)}}{L_{24,e}}\,[\xi_{33}(\mathrm{M}_{24}, \gamma)(s_{24} - s_2 - \pi_{s,24})].$$

For the bleed valve after the first stage, we have

$$\mathrm{M}_{24} = g_{\mathrm{bld}}(\mathrm{M}_{25}, A_{25} - A_{24}, A_{24b} - A_{24}, p_{24} - p_{s24b})$$

$$p_{25} = p_{24} \quad s_{25} = s_{24}$$

p_{s24b} is an input to the model.

For the second stage,

$$\pi_{\mathrm{M},27} = m_{4,cs2}(\mathrm{M}_{27}, N_{25}, \mathrm{Re}_{25}, \alpha)$$

$$\pi_{p,27} = m_{5,cs2}(\mathrm{M}_{27}, N_{25}, \mathrm{Re}_{25}, \alpha)$$

$$\pi_{s,27} = m_{6,cs2}(\mathrm{M}_{27}, N_{25}, \mathrm{Re}_{25}, \alpha),$$

$$L_{27,e} = L_{27}\sqrt{1 + \frac{N_{25}^2}{\mathrm{M}_{27}^2}\, r_{25}^2 e^{-A_{25}} e^{-(T_{27}-T_{25})}\left(1 + \frac{\gamma - 1}{2}\mathrm{M}_{27}^2\right)},$$

$$\frac{d}{dt}\mathrm{M}_{25} = \frac{e^{(1/2)(T_{25})}}{L_{27,e}}\left[\xi_{11}(\mathrm{M}_{27}, \gamma)(\mathrm{M}_{27} - \mathrm{M}_{25} - \pi_{\mathrm{M},27})\right.$$
$$+ \xi_{12}(\mathrm{M}_{27}, \gamma)(p_{27} - p_{25} - \pi_{p,27})$$
$$\left.+ \xi_{13}(\mathrm{M}_{27}, \gamma)(s_{27} - s_{25} - \pi_{s,27})\right]$$

$$\frac{d}{dt}p_{27} = \frac{e^{(1/2)(T_{25})}}{L_{27,e}}\left[\xi_{21}(\mathrm{M}_{27}, \gamma)(\mathrm{M}_{27} - \mathrm{M}_{25} - \pi_{\mathrm{M},27})\right.$$
$$+ \xi_{22}(\mathrm{M}_{27}, \gamma)(p_{27} - p_{25} - \pi_{p,27})$$
$$\left.+ \xi_{23}(\mathrm{M}_{27}, \gamma)(s_{27} - s_{25} - \pi_{s,27})\right]$$

$$\frac{d}{dt}s_{27} = \frac{e^{(1/2)(T_{25})}}{L_{27,e}}\left[\xi_{33}(\mathrm{M}_{27}, \gamma)(s_{27} - s_{25} - \pi_{s,27})\right].$$

For the bleed valve after the second stage, we have:

$$\mathrm{M}_{27} = g_{\mathrm{bld}}(\mathrm{M}_{28}, A_{28} - A_{27}, A_{27b} - A_{27}, p_{27} - p_{s27b})$$

$$p_{28} = p_{27} \quad s_{28} = s_{27}$$

p_{s27b} is an input to the model.

The compressor discharge ducting is divided into three elements. Friction losses are present, but no particular form of friction loss is assumed. Experimentally identified maps are included in the equations to account for this forcing. As in the compressor, the dependency of the maps for these elements on the areas is neglected. The following equations result:

$$\chi_{\mathrm{M},3} = m_{4,dcd1}(\mathrm{M}_3, \mathrm{Re}_{28})$$

$$\chi_{p,3} = m_{5,dcd1}(\mathrm{M}_3, \mathrm{Re}_{28})$$

$$\chi_{s,3} = m_{6,dcd1}(\mathrm{M}_3, \mathrm{Re}_{28}),$$

$$\frac{d}{dt}\mathrm{M}_{28} = \frac{e^{(1/2)(T_{28})}}{L_3}\left[\xi_{11}(\mathrm{M}_3, \gamma)(\mathrm{M}_3 - \mathrm{M}_{28} - \chi_{\mathrm{M},3})\right.$$
$$+ \xi_{12}(\mathrm{M}_3, \gamma)(p_3 - p_{28} - \chi_{p,3})$$
$$\left.+ \xi_{13}(\mathrm{M}_3, \gamma)(s_3 - s_{28} - \chi_{s,3})\right]$$

$$\frac{d}{dt}p_3 = \frac{e^{(1/2)(T_{28})}}{L_3}\left[\xi_{21}(\mathrm{M}_3, \gamma)(\mathrm{M}_3 - \mathrm{M}_{28} - \chi_{\mathrm{M},3})\right.$$
$$+ \xi_{22}(\mathrm{M}_3, \gamma)(p_3 - p_{28} - \chi_{p,3})$$
$$\left.+ \xi_{23}(\mathrm{M}_3, \gamma)(s_3 - s_{28} - \chi_{s,3})\right]$$

$$\frac{d}{dt}s_3 = \frac{e^{(1/2)(T_{28})}}{L_3}\left[\xi_{33}(\mathrm{M}_3, \gamma)(s_3 - s_{28} - \chi_{s,3})\right].$$

For the second element,

$$\chi_{\mathrm{M},31} = m_{4,dcd2}(\mathrm{M}_{31}, \mathrm{Re}_3)$$

$$\chi_{p,31} = m_{5,dcd2}(\mathrm{M}_{31}, \mathrm{Re}_3)$$

$$\chi_{s,31} = m_{6,dcd2}(\mathrm{M}_{31}, \mathrm{Re}_3),$$

$$\frac{d}{dt}\mathrm{M}_3 = \frac{e^{(1/2)(T_3)}}{L_{31}}\left[\xi_{11}(\mathrm{M}_{31}, \gamma)(\mathrm{M}_{31} - \mathrm{M}_3 - \chi_{\mathrm{M},31})\right.$$
$$+ \xi_{12}(\mathrm{M}_{31}, \gamma)(p_{31} - p_3 - \chi_{p,31})$$
$$\left.+ \xi_{13}(\mathrm{M}_{31}, \gamma)(s_{31} - s_3 - \chi_{s,31})\right]$$

$$\frac{d}{dt}p_{31} = \frac{e^{(1/2)(T_3)}}{L_{31}}\left[\xi_{21}(\mathrm{M}_{31}, \gamma)(\mathrm{M}_{31} - \mathrm{M}_3 - \chi_{\mathrm{M},31})\right.$$
$$+ \xi_{22}(\mathrm{M}_{31}, \gamma)(p_{31} - p_3 - \pi_{p,31})$$
$$\left.+ \xi_{23}(\mathrm{M}_{31}, \gamma)(s_{31} - s_3 - \chi_{s,31})\right]$$

$$\frac{d}{dt}s_{31} = \frac{e^{(1/2)(T_3)}}{L_{31}}\left[\xi_{33}(\mathrm{M}_{31}, \gamma)(s_{31} - s_3 - \chi_{s,31})\right].$$

For the third element,

$$\chi_{\mathrm{M},36} = m_{4,dcd3}(\mathrm{M}_{36}, \mathrm{Re}_{31})$$

$$\chi_{p,36} = m_{5,dcd3}(\mathrm{M}_{36}, \mathrm{Re}_{31})$$

$$\chi_{s,36} = m_{6,dcd3}(\mathrm{M}_{36}, \mathrm{Re}_{31}),$$

$$\frac{d}{dt}\mathrm{M}_{31} = \frac{e^{(1/2)(T_{31})}}{L_{36}}\left[\xi_{11}(\mathrm{M}_{36}, \gamma)(\mathrm{M}_{36} - \mathrm{M}_{31} - \chi_{\mathrm{M},36})\right.$$
$$+ \xi_{12}(\mathrm{M}_{36}, \gamma)(p_{36} - p_{31} - \chi_{p,36})$$
$$\left.+ \xi_{13}(\mathrm{M}_{36}, \gamma)(s_{36} - s_{31} - \chi_{s,36})\right]$$

$$\frac{d}{dt}p_{36} = \frac{e^{(1/2)(T_{31})}}{L_{36}}\left[\xi_{21}(\mathrm{M}_{36}, \gamma)(\mathrm{M}_{36} - \mathrm{M}_{31} - \chi_{\mathrm{M},36})\right.$$
$$+ \xi_{22}(\mathrm{M}_{36}, \gamma)(p_{36} - p_{31} - \pi_{p,36})$$
$$\left.+ \xi_{23}(\mathrm{M}_{36}, \gamma)(s_{36} - s_{31} - \chi_{s,36})\right]$$

$$\frac{d}{dt}s_{36} = \frac{e^{(1/2)(T_{31})}}{L_{36}}\left[\xi_{33}(\mathrm{M}_{36}, \gamma)(s_{36} - s_{31} - \chi_{s,36})\right].$$

The governing equations for the bleed valve after the ducting are given as follows:

$$\mathrm{M}_{36} = g_{\mathrm{bld}}(\mathrm{M}_{37}, A_{37} - A_{36}, A_{36b} - A_{36}, p_{36} - p_{s36b})$$

$$p_{37} = p_{36} \quad s_{37} = s_{36}$$

p_{s36b} is an input to the model.

The ducting with combustion has only one element. The areas in this component are assumed to be fixed. Hence, this dependence in the maps is neglected, and the governing equations can be given as follows:

$$\phi_{\mathrm{M},4} = m_{4,dc}(\mathrm{M}_4, \mathrm{Re}_{37}, w_f)$$

$$\phi_{p,4} = m_{5,dc}(\mathrm{M}_4, \mathrm{Re}_{37}, w_f)$$

$$\phi_{s,4} = m_{6,dc}(\mathrm{M}_4, \mathrm{Re}_{37}, w_f)$$

$$\frac{d}{dt}\mathrm{M}_{37} = \frac{e^{(1/2)(T_{37})}}{L_4}\left[\xi_{11}(\mathrm{M}_4, \gamma)(\mathrm{M}_4 - \mathrm{M}_{37} - \phi_{\mathrm{M},4})\right.$$
$$+ \xi_{12}(\mathrm{M}_4, \gamma)(p_4 - p_{37} - \phi_{p,4})$$
$$\left.+ \xi_{13}(\mathrm{M}_4, \gamma)(s_4 - s_{37} - \phi_{s,4})\right]$$

$$\frac{d}{dt}p_4 = \frac{e^{(1/2)(T_{37})}}{L_4}\left[\xi_{21}(\mathrm{M}_4, \gamma)(\mathrm{M}_4 - \mathrm{M}_{37} - \chi_{\mathrm{M},4})\right.$$
$$+ \xi_{22}(\mathrm{M}_4, \gamma)(p_4 - p_{37} - \phi_{p,4})$$
$$\left.+ \xi_{23}(\mathrm{M}_4, \gamma)(s_4 - s_{37} - \phi_{s,4})\right]$$

$$\frac{d}{dt}s_4 = \frac{e^{(1/2)(T_{37})}}{L_4}\left[\xi_{33}(\mathrm{M}_4, \gamma)(s_4 - s_{37} - \chi_{s,4})\right].$$

The turbine consists of two blading stages with heat soak effects. The effects of variable guide vane angles are not considered in the turbine. As in the compressor stages, the dependency of the maps on the areas is neglected in the turbine stages. The governing equations are given as follows:

$$\pi_{\mathrm{M},45} = m_{4,ts1}(\mathrm{M}_{45}, N_4, \mathrm{Re}_4, \mathrm{Pr}, \mathrm{Nu}, T_{w,4} - T_4)$$

$$\pi_{p,45} = m_{5,ts1}(\mathrm{M}_{45}, N_4, \mathrm{Re}_4, \mathrm{Pr}, \mathrm{Nu}, T_{w,4} - T_4)$$

$$\pi_{s,45} = m_{6,ts1}(\mathrm{M}_{45}, N_4, \mathrm{Re}_4, \mathrm{Pr}, \mathrm{Nu}, T_{w,4} - T_4),$$

$$L_{45,e} = L_{45}\sqrt{1 + \frac{N_4^2}{\mathrm{M}_{45}^2}\, r_4^2 e^{-A_4} e^{-(T_{45}-T_4)}\left(1 + \frac{\gamma - 1}{2}\mathrm{M}_{45}^2\right)}\,,$$

$$\begin{aligned}\frac{d}{dt}\mathrm{M}_4 = \frac{e^{(1/2)(T_4)}}{L_{45,e}}\,&[\xi_{11}(\mathrm{M}_{45}, \gamma)(\mathrm{M}_{45} - \mathrm{M}_4 - \pi_{\mathrm{M},45}) \\ &+ \xi_{12}(\mathrm{M}_{45}, \gamma)(p_{45} - p_4 - \pi_{p,45}) \\ &+ \xi_{13}(\mathrm{M}_{45}, \gamma)(s_{45} - s_4 - \pi_{s,45})]\end{aligned}$$

$$\begin{aligned}\frac{d}{dt}p_{45} = \frac{e^{(1/2)(T_4)}}{L_{45,e}}\,&[\xi_{21}(\mathrm{M}_{45}, \gamma)(\mathrm{M}_{45} - \mathrm{M}_4 - \chi_{\mathrm{M},45}) \\ &+ \xi_{22}(\mathrm{M}_{45}, \gamma)(p_{45} - p_4 - \pi_{p,45}) \\ &+ \xi_{23}(\mathrm{M}_{45}, \gamma)(s_{45} - s_4 - \pi_{s,45})]\end{aligned}$$

$$\frac{d}{dt}s_{45} = \frac{e^{(1/2)(T_4)}}{L_{45,e}}\,[\xi_{33}(\mathrm{M}_{45}, \gamma)(s_{45} - s_4 - \pi_{s,45})]$$

$$\frac{d}{dt}T_{w,4} = h_{w,4}(e^{T_4 - T_{w,4}} - 1).$$

For the second stage we have

$$\pi_{\mathrm{M},5} = m_{4,ts2}(\mathrm{M}_5, N_{45}, \mathrm{Re}_{45}, \mathrm{Pr}, \mathrm{Nu}, T_{w,45} - T_{45})$$

$$\pi_{p,5} = m_{5,ts2}(\mathrm{M}_5, N_{45}, \mathrm{Re}_{45}, \mathrm{Pr}, \mathrm{Nu}, T_{w,45} - T_{45})$$

$$\pi_{s,5} = m_{6,ts2}(\mathrm{M}_5, N_{45}, \mathrm{Re}_{45}, \mathrm{Pr}, \mathrm{Nu}, T_{w,45} - T_{45}),$$

$$L_{5,e} = L_5\sqrt{1 + \frac{N_{45}^2}{\mathrm{M}_5^2}\, r_{45}^2 e^{-A_{45}} e^{-(T_5-T_{45})}\left(1 + \frac{\gamma - 1}{2}\mathrm{M}_5^2\right)}\,,$$

$$\begin{aligned}\frac{d}{dt}\mathrm{M}_{45} = \frac{e^{(1/2)(T_{45})}}{L_{5,e}}\,&[\xi_{11}(\mathrm{M}_5, \gamma)(\mathrm{M}_5 - \mathrm{M}_{45} - \pi_{\mathrm{M},5}) \\ &+ \xi_{12}(\mathrm{M}_5, \gamma)(p_5 - p_{45} - \pi_{p,5}) \\ &+ \xi_{13}(\mathrm{M}_5, \gamma)(s_5 - s_{45} - \pi_{s,5})]\end{aligned}$$

$$\begin{aligned}\frac{d}{dt}p_5 = \frac{e^{(1/2)(T_{45})}}{L_{5,e}}\,&[\xi_{21}(\mathrm{M}_5, \gamma)(\mathrm{M}_5 - \mathrm{M}_{45} - \chi_{\mathrm{M},5}) \\ &+ \xi_{22}(\mathrm{M}_5, \gamma)(p_5 - p_{45} - \pi_{p,5}) \\ &+ \xi_{23}(\mathrm{M}_5, \gamma)(s_5 - s_{45} - \pi_{s,5})]\end{aligned}$$

$$\frac{d}{dt}s_5 = \frac{e^{(1/2)(T_{45})}}{L_{5,e}}\,[\xi_{33}(\mathrm{M}_5, \gamma)(s_5 - s_{45} - \pi_{s,5})]$$

$$\frac{d}{dt}T_{w,45} = h_{w,45}(e^{T_{45} - T_{w,45}} - 1).$$

The nozzle ducting after the turbine has only one element. The areas are constant, hence this dependency is once again neglected in the maps. The governing equations in terms of experimentally measured maps for the friction are given as follows:

$$\chi_{\mathrm{M},8} = m_{4,dn}(\mathrm{M}_8, \mathrm{Re}_5)$$

$$\chi_{p,8} = m_{5,dn}(\mathrm{M}_8, \mathrm{Re}_5)$$

$$\chi_{s,8} = m_{6,dn}(\mathrm{M}_8, \mathrm{Re}_5),$$

$$\begin{aligned}\frac{d}{dt}\mathrm{M}_5 = \frac{e^{(1/2)(T_5)}}{L_8}\,&[\xi_{11}(\mathrm{M}_8, \gamma)(\mathrm{M}_8 - \mathrm{M}_5 - \chi_{\mathrm{M},8}) \\ &+ \xi_{12}(\mathrm{M}_8, \gamma)(p_8 - p_5 - \chi_{p,8}) \\ &+ \xi_{13}(\mathrm{M}_8, \gamma)(s_8 - s_5 - \chi_{s,8})]\end{aligned}$$

$$\begin{aligned}\frac{d}{dt}p_8 = \frac{e^{(1/2)(T_5)}}{L_8}\,&[\xi_{21}(\mathrm{M}_8, \gamma)(\mathrm{M}_8 - \mathrm{M}_5 - \chi_{\mathrm{M},8}) \\ &+ \xi_{22}(\mathrm{M}_8, \gamma)(p_8 - p_5 - \chi_{p,8}) \\ &+ \xi_{23}(\mathrm{M}_8, \gamma)(s_8 - s_5 - \chi_{s,8})]\end{aligned}$$

$$\frac{d}{dt}s_8 = \frac{e^{(1/2)(T_5)}}{L_8}\,[\xi_{33}(\mathrm{M}_8, \gamma)(s_8 - s_5 - \chi_{s,8})].$$

The nozzle is the last component of the model and consists of an isentropic area change, which occurs over a very short axial distance. The dynamics in the nozzle are assumed to equilibrate quickly and are residualized. The governing equations can be given as follows:

$$\mathrm{M}_8 = g_{\mathrm{noz}}(A_9 - A_8, p_8 - p_{s9})$$

$$p_9 = p_8 \quad s_9 = s_8$$

p_{s9} is an input to the model.

The equation for the spool is given as follows:

$$\begin{aligned}JN_{\mathrm{spl}}\frac{d}{dt}N_{\mathrm{spl}} = &- \frac{\gamma}{\gamma - 1}\, e^{A_{24}} e^{p_{24}} e^{(1/2)(T_{24})} \\ &\times \mathrm{M}_{24}\left(1 + \frac{\gamma - 1}{2}\mathrm{M}_{24}^2\right)^{-(\gamma+1)/[2(\gamma-1)]} \\ &+ \frac{\gamma}{\gamma - 1}\, e^{A_4} e^{p_2} e^{(1/2)(T_2)} \\ &\times \mathrm{M}_2\left(1 + \frac{\gamma - 1}{2}\mathrm{M}_2^2\right)^{-(\gamma+1)/[2(\gamma-1)]} \\ &- \frac{\gamma}{\gamma - 1}\, e^{A_{27}} e^{p_{27}} e^{(1/2)(T_{27})} \\ &\times \mathrm{M}_{27}\left(1 + \frac{\gamma - 1}{2}\mathrm{M}_{27}^2\right)^{-(\gamma+1)/[2(\gamma-1)]} \\ &+ \frac{\gamma}{\gamma - 1}\, e^{A_{25}} e^{p_{25}} e^{(1/2)(T_{25})} \\ &\times \mathrm{M}_{25}\left(1 + \frac{\gamma - 1}{2}\mathrm{M}_{25}^2\right)^{-(\gamma+1)/[2(\gamma-1)]} \\ &+ \eta_m\frac{\gamma}{\gamma - 1}\, e^{A_4} e^{p_4} e^{(1/2)(T_4)} \\ &\times \mathrm{M}_4\left(1 + \frac{\gamma - 1}{2}\mathrm{M}_4^2\right)^{-(\gamma+1)/[2(\gamma-1)]} \\ &- \eta_m\frac{\gamma}{\gamma - 1}\, e^{A_5} e^{p_5} e^{(1/2)(T_5)} \\ &\times \mathrm{M}_5\left(1 + \frac{\gamma - 1}{2}\mathrm{M}_5^2\right)^{-(\gamma+1)/[2(\gamma-1)]}.\end{aligned}$$

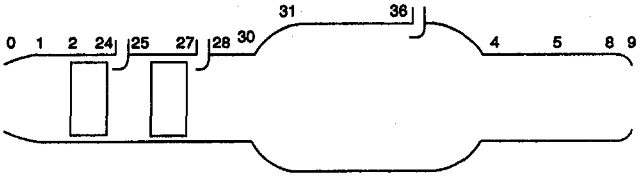

Fig. 4 Diagram of generic compression system

Now, the dimensionless spool speeds for the various maps are computed as follows:

$$N_2 = N_{\mathrm{spl}} e^{A_2/2} e^{-T_2/2},$$

$$N_{25} = N_{\mathrm{spl}} e^{A_{25}/2} e^{-T_{25}/2},$$

$$N_4 = N_{\mathrm{spl}} e^{A_4/2} e^{-T_4/2},$$

and

$$N_{45} = N_{\mathrm{spl}} e^{A_{45}/2} e^{-T_{45}/2}.$$

The aggregate of the component equations developed above represents the system model. A computational flow diagram for this model is given in Fig. 5. In this diagram, solid blocks represent elements that have dynamics associated with them, and dashed blocks represent elements in which dynamics have been residualized. All inputs to a dynamic element are required in order to do a state update, and all inputs to a static element are required to compute the outputs of the static element. Inputs that do not originate from any of the blocks are external inputs to the model. The states of the model are outputs of the solid blocks (dynamic elements). Multiple signal outputs, from various dynamic elements to the spool or heat soak elements, represent outputs available from the dynamic elements once the inputs have been obtained; thus, they should not be considered as defining the states of the model. Explicit model computation requires that all inputs to the dynamic elements can be computed without iteration using the initial conditions of the states (outputs of the dynamic blocks) and the various inputs to the model. Critical points for the development of an explicit model occur if there are two static blocks next to each other in the computational flow diagram requiring possible iteration to obtain the inputs to neighboring dynamic elements. For the generic turbojet engine model, there are no points where there are two static blocks next to each other. Thus, this model is explicit. If there were two static blocks next to each other, and if the equations of these two static blocks could not be solved without iteration, then one of two steps would have to be taken to develop an explicit model. First, the iterative solution of these algebraic equations could be done off line and implemented as maps in the model. In this case, these blocks are combined to form a single static block involving the new maps. Second, the dynamics of one of the blocks that have been residualized could be retained in the model, making the model explicit. This would, however, introduce relatively fast dynamics to the system and require an integration routine that can accommodate stiff systems.

4.2 Linear Model. Since the developed model for the generic turbojet is explicit, analytical expressions can be devel-

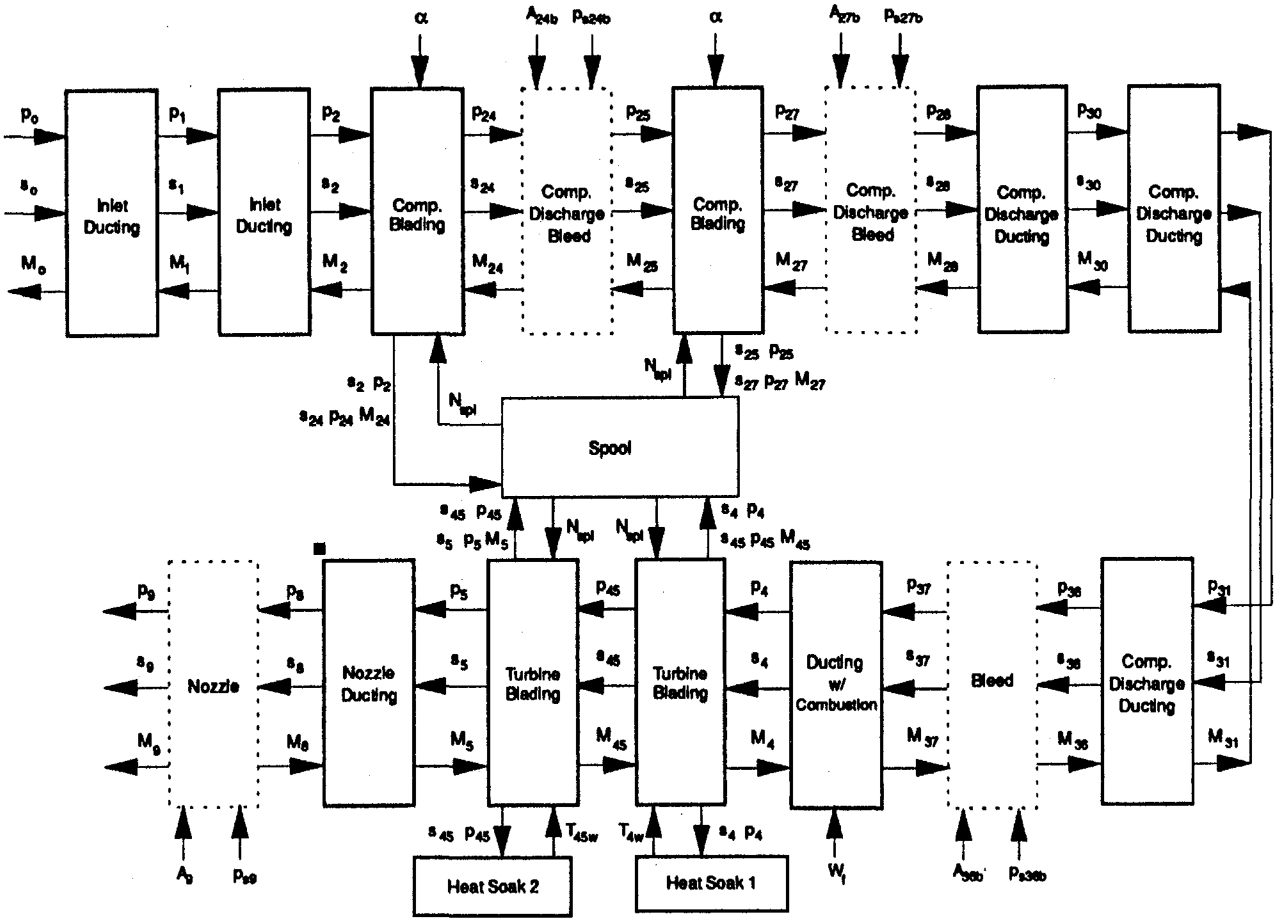

Fig. 5 Computational diagram for the generic turbojet engine model

oped for the linearized system model as a function of system operating condition. The linearized system model can then be used to determine the local stability of the system equilibria and to design control schemes that locally stabilize the system or enhance system damping.

The development of the analytical linearized system model requires that the derivatives of the right-hand side of each dynamic equation with respect to all states and inputs of the model be determined. This procedure is enhanced by the fact that the model equations can be put in the compact matrix form:

$$\dot{x} = P(x, u)f(x, u). \tag{2}$$

Here, x and u represent the vectors of system states and inputs respectively. Consider a system with n dynamic components, the matrix form representation of the system equations is:

$$\frac{d}{dt}\begin{bmatrix} M_0 \\ p_1 \\ s_1 \\ T_{w,1} \\ \vdots \\ M_{n-1} \\ p_n \\ s_n \\ T_{w,n} \\ N_{\text{spl}} \end{bmatrix} = \begin{bmatrix} & 0 & & 0\,0\,0 & 0\,0 \\ \dfrac{e^{(1/2)T_0}}{L_1}\,\Xi\,(\mathrm{M}_1, \gamma) & 0 & \ldots & 0\,0\,0 & 0\,0 \\ & 0 & & 0\,0\,0 & 0\,0 \\ 0\,0\,0 & 1 & \ldots & 0\,0\,0 & 0\,0 \\ \vdots & \vdots & \ddots & \vdots & \vdots\ \vdots \\ 0\,0\,0 & 0 & & & 0\,0 \\ 0\,0\,0 & 0 & \ldots & \dfrac{e^{(1/2)T_{n-1}}}{L_n}\,\Xi\,(\mathrm{M}_n, \gamma) & 0\,0 \\ 0\,0\,0 & 0 & & & 0\,0 \\ 0\,0\,0 & 0 & \ldots & 0\,0\,0 & 1\,0 \\ 0\,0\,0 & 0 & \ldots & 0\,0\,0 & 0\,1 \end{bmatrix} \begin{bmatrix} \mathrm{M}_1 - \mathrm{M}_0 - m_4^1 \\ p_1 - p_0 - m_5^1 \\ s_1 - s_0 - m_6^1 \\ h_{w,1}\,(e^{T_1 - T_{w,1}} - 1) \\ \vdots \\ \mathrm{M}_n - \mathrm{M}_{n-1} - m_4^n \\ p_n - p_{n-1} - m_5^n \\ s_n - s_{n-1} - m_6^n \\ h_{w,n}\,(e^{T_n - T_{w,n}} - 1) \\ f(\mathrm{M}_2, p_2, s_2, \ldots, N_{\text{spl}}) \end{bmatrix}$$

The notation, m_4^n, is used to represent the Mach number change map across the nth component, and the pressure and entropy change maps are similarly defined.

The matrix, $P(x, u)$, is nonsingular at all system operating conditions except when the flow Mach number at steady condition is 0 or 1 in any dynamic component [2]. These two conditions are exempted from this analysis. When this matrix is nonsingular, the equilibrium conditions correspond to $f(x^0, u^0) = 0$. Thus, the linear model for this system can be expressed as:

$$\delta\dot{x} = P(x^0, u^0)D_x f(x^0, u^0)\delta x + P(x^0, u^0)D_u f(x^0, u^0)\delta u.$$

The task of computing the linearized model equations is then reduced to evaluating the derivatives of the vector $f(x, u)$, with respect to the states and inputs of the system. As can be seen, this involves, for the most part, simply evaluating the derivatives of the maps, m_4^k, m_5^k and m_6^k for $k \in \{1, \ldots, n\}$, with respect to the states and inputs of the system.

5 Generic Compression System

In this section, the reduction of the model for the generic turbojet engine to form a model for a generic compression system is discussed. A model of this type is required for externally driven compression systems commonly found in the chemical process industry and externally driven experimental rigs built to study the phenomena of surge and rotating stall.

A diagram of the generic compression system is given in Fig. 4. From the generic turbojet engine model, we start by eliminating the ducting with combustion and the turbine stages. The spool speed, N_{spl}, becomes an independent input in this model since the compressor in the generic compression system is externally driven. For this model, points 37 and 4 of the generic turbojet engine are equivalent since the ducting with combustion is eliminated. Also, the flow temperatures are much lower due to lack of combustion, and heat soak effects are not considered. Between points 4 and 5 where there is a turbine in the generic turbojet engine, there is now another element of nozzle ducting.

A computational flow diagram of this model is given in Fig. 6. As in the case of the generic turbojet engine model, this diagram shows that the generic compression system model is explicit.

6 Thermally Perfect Multiple Species Gas

In this section, some important computational issues are discussed pertaining to the development of models for the case of a thermally perfect multiple species gas using the system of equations presented in [2]. The definitions for the dimensionless variables associated with this system of equations can be given as follows:

$$\begin{aligned} x &= \tilde{x}/\tilde{L} \\ t &= \tilde{t}/\bar{t} \\ A &= \ln\,[\tilde{A}/(\bar{t}^2 R_{\text{air}}\bar{T})] \\ L &= \tilde{L}/(\bar{t}\sqrt{R_{\text{air}}\bar{T}}) \\ u &= \tilde{u}/\sqrt{R_{\text{air}}\bar{T}} \\ p_s &= \ln\,(\tilde{p}_s/\bar{p}) \\ T_s &= \tilde{T}_s/\bar{T} \\ Q &= \tilde{Q}\tilde{L}/(\tilde{p}_s\sqrt{R_{\text{air}}\bar{T}}) \\ f_w &= \tilde{f}_w\tilde{L}/(R_{\text{air}}\bar{T}) \\ f_s &= \tilde{f}_s\tilde{L}/(R_{\text{air}}\bar{T}) \end{aligned}$$

$$\tau_h = g_h(T_s, x_c) = \tilde{h}_s/(R\bar{T}) \qquad \tau_{h,1} = \frac{\partial \tau_h}{\partial T_s} \qquad \tau_{h,2} = \frac{\partial \tau_h}{\partial x_c}$$

$$\tau_R = g_R(x_c) = R/R_{\text{air}} \qquad \tau_{R,1} = \frac{\partial \tau_R}{\partial x_c}$$

$$N = \frac{\tilde{N}\sqrt{\tilde{A}}}{\sqrt{R\tilde{T}_s}} \qquad \mathrm{Re} = \frac{\tilde{\rho}_s\tilde{u}\sqrt{\tilde{A}}}{\mu} \qquad \mathrm{Pr} = \frac{c_p\mu}{k} \qquad T_w = \tilde{T}_w/\bar{T}$$

Now, the discretized form of the dimensionless equations for unsteady compressible viscous quasi-one-dimensional flow of a thermally perfect multiple species gas in the kth finite element of a component can be written as [2]:

$$L_k \frac{d}{dt}\begin{bmatrix} u_{k-1} \\ p_{s,k} \\ T_{s,k} \end{bmatrix} = \Xi_T(u_k, T_{s,k-1}, x_{c,k-1})\left\{\begin{bmatrix} u_k - u_{k-1} \\ p_{s,k} - p_{s,k-1} \\ T_{s,k} - T_{s,k-1} \end{bmatrix}\right.$$

$$\left. - \begin{bmatrix} m_{T,1}(u_k, e^{A_{k-1}}/L_k^2, A_k - A_{k-1}, N_{k-1}, x_{c,k-1}, x_{c,k}, \mathrm{Re}_{k-1}, \mathrm{Pr}, T_{w,k-1}, T_{s,k-1}) \\ m_{T,2}(u_k, e^{A_{k-1}}/L_k^2, A_k - A_{k-1}, N_{k-1}, x_{c,k-1}, x_{c,k}, \mathrm{Re}_{k-1}, \mathrm{Pr}, T_{w,k-1}, T_{s,k-1}) \\ m_{T,3}(u_k, e^{A_{k-1}}/L_k^2, A_k - A_{k-1}, N_{k-1}, x_{c,k-1}, x_{c,k}, \mathrm{Re}_{k-1}, \mathrm{Pr}, T_{w,k-1}, T_{s,k-1}) \end{bmatrix}\right\}$$

$$+ L_k \begin{bmatrix} 0 \\ 1 \\ 0 \end{bmatrix} \frac{d}{dt} A_k + L_k \Phi_T(T_{s,k-1}, x_{c,k-1}) \frac{d}{dt} x_{c,k-1}, \quad (3)$$

where $\Xi_T(u_k, T_{s,k-1}, x_{c,k-1})$ and $\Phi_T(T_{s,k-1}, x_{c,k-1})$ are known functions of u_k, $T_{s,k-1}$, and $x_{c,k-1}$ defined in [2]. The maps, $m_{T,1}$, $m_{T,2}$, and $m_{T,3}$, in these equations account for the forcing terms Q, f_s, and f_w in the quasi-one-dimensional flow equations. They are equal in steady state to the differences $u_k - u_{k-1}$, $p_{s,k} - p_{s,k-1}$, and $T_{s,k} - T_{s,k-1}$ across the element, respectively. Identification of these functions is discussed further in [2].

The first computational issue associated with the development of models for this case involves the assumption made in developing this system of equations that the composition of the gas is known throughout the system. If this composition is to be determined in some way by the current state of the system (i.e., composition of the fluid downstream of the combustor is determined by the current composition in combustor), a technique must be determined to obtain this information in a manner that allows the model to be noniterative. As this technique will depend on the specific model, no further discussion is given here except to suggest a simple first approximation, which is to assume for the model a constant composition upstream and downstream of the combustor that does not depend on the current state of the system.

The second computational issue of interest involves obtaining a fully integrable model, which incorporates the system inputs. At the inlet, the system inputs are incorporated in a similar manner as for the case of a calorically perfect single species gas. At the system exhaust, some modification is required. Equa-

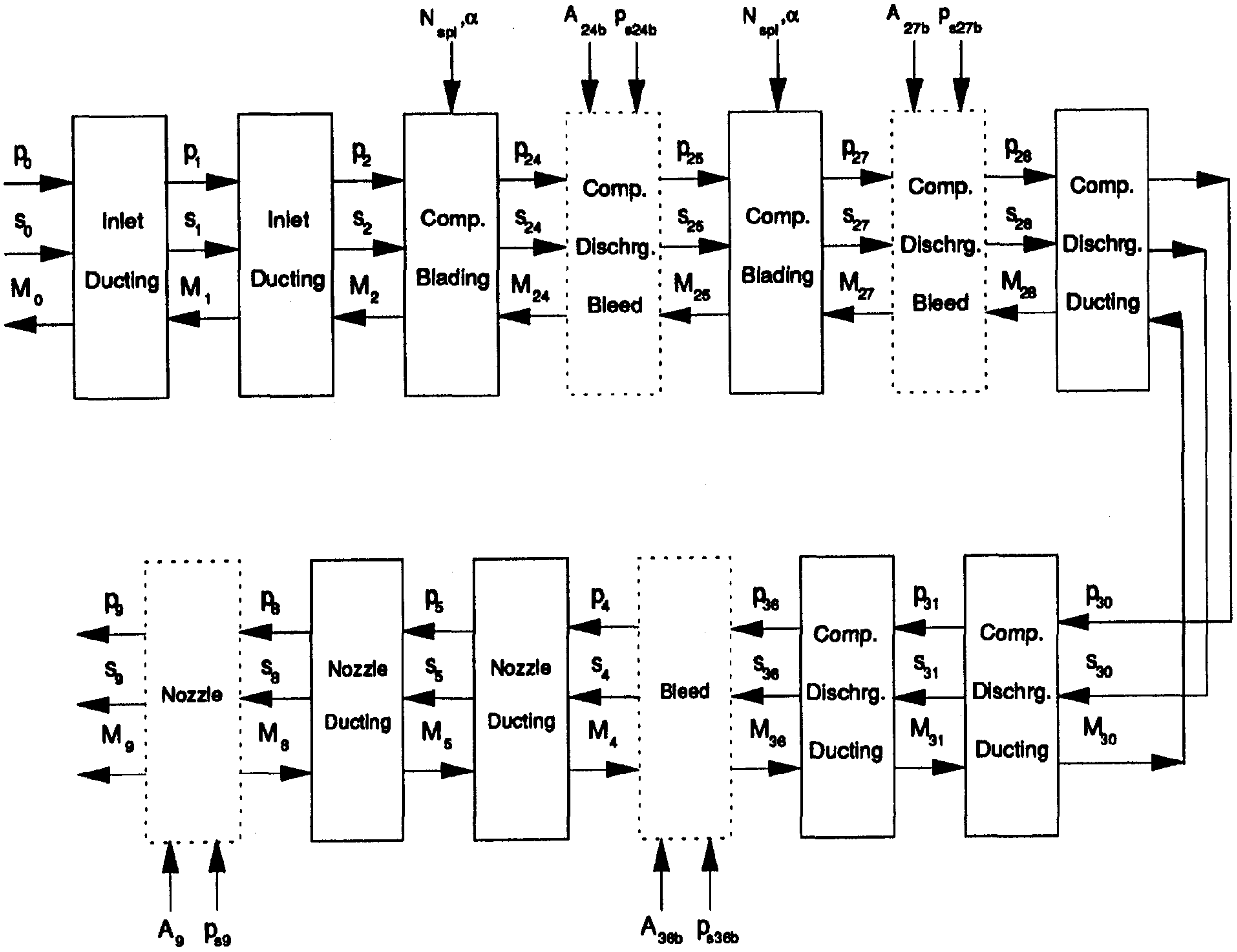

Fig. 6 Computational diagram for the generic compression system model

tion (3) indicates that the state at the exit of a dynamic element is p_s. This can cause problems if the dynamic element occurs where p_s at the exit of the element is also a system input (i.e., at the nozzle exit plane when the flow is subsonic). The problem arises if the state value and the input are not equal to each other, which is not the case in most situations. The simple solution to this problem is to have a static element between the dynamic element and the discharge plane. Of course, this static element must allow p_s at the exit of the dynamic element and p_s at the discharge plane to be unequal. At the exhaust of the generic turbojet engine, the nozzle, which consists of an isentropic area change, satisfies this constraint as long as the area changes across the nozzle. Hence, model development is not hindered by this requirement.

Another computational issue occurs at the mixing plane in a turbofan engine where the static pressure is assumed constant in the plane. In this case once again, there must be a static element between any upstream dynamic element and the element of the mixing plane that allows p_s to vary across it. This allows the static pressure in the dynamic element to vary independently while retaining the condition of constant static pressure in the mixing plane.

Besides these additional computational issues that must be considered, model development for the case of a thermally perfect multiple species gas is performed in the same manner as is discussed in this paper for the case of a calorically perfect single species gas.

7 Conclusions and Future Work

In this paper, a previously developed approach [2] for control-oriented high-frequency turbomachinery modeling was applied to develop one-dimensional unsteady compressible viscous flow models for a calorically perfect single species gas in a generic turbojet engine and a generic compression system. These models were developed so that they can be easily modified and used with appropriate maps to form a model of a specific rig. The system models are explicit (i.e., can be solved with any standard ODE solver without iteration) due to the approach used in their development. The procedure for developing analytical linear models from the nonlinear models was discussed. Models of the type developed here are expected to prove useful in the design and simulation of (integrated) surge control and rotating stall avoidance schemes.

In a companion paper [3], the generic compression system model given here was successfully applied to the LICCHUS[2] multistage axial compressor rig [3, 40] configured for single-stage operation. The model shows excellent comparison to experimental data for both open-loop uncontrolled and closed-loop controlled behaviors. The success of this model is believed to represent a positive first step toward a complete experimental validation of the approach to control-oriented high-frequency turbomachinery modeling being developed by the authors.

In future work, validated one-dimensional models will be developed for both the LICCHUS multistage axial compressor rig [40] configured for multistage operation and the LICCHUS turbojet engine rig [40] using the generic models developed here. Additionally, two-dimensional models that are capable of modeling and predicting both surge and rotating stall will be developed using this approach with a parallel compressor concept.

References

1 Badmus, O. O., Eveker, K. M., and Nett, C. N., "Control-Oriented High-Frequency Turbomachinery Modeling, Part 1: Theoretical Foundations," in: *Proceedings of the 1992 AIAA Joint Propulsion Conference,* AIAA Paper No. 92-3314, 1992.

2 Badmus, O. O., Eveker, K. M., and Nett, C. N., "Control-Oriented High-Frequency Turbomachinery Modeling: Theoretical Foundations," ASME JOURNAL OF TURBOMACHINERY, Vol. XX, pp. YY–ZZ.

3 Badmus, O. O., Chowdhury, S., Eveker, K. M., and Nett, C. N., "Control-Oriented High-Frequency Turbomachinery Modeling: Single-Stage Compression System One-Dimensional Model," ASME JOURNAL OF TURBOMACHINERY, Vol. 117, 1995, pp. 47–61.

4 Greitzer, E. M., "Surge and Rotating Stall in Axial Flow Compressors, Part 1: Theoretical Compression System Model," ASME *Journal of Engineering for Power,* Vol. 98, 1976, pp. 190–198.

5 Davis, M. W., and O'Brien, W. F., "A Stage-by-Stage Post-Stall Compression System Modeling Technique," AIAA Paper No. 87-2088, 1987.

6 Ffowcs-Williams, J. E., and Huang, X. Y., "Active Stabilization of Compressor Surge," *J. Fluid Mech.,* Vol. 204, 1989, pp. 245–262.

7 Sugiyama, Y., Tabakoff, W., and Hamed, A., "J85 Surge Transient Simulation," *J. Propulsion and Power,* Vol. 5, May–June 1989, pp. 375–381.

8 Tang, G. C., "Basic Features of Speed Induced Transient Behaviour of Axial Flow Compressors," ASME Paper No. 90-GT-211, 1990.

9 Davis, M., "Parametric Investigation into the Combined Effects of Pressure and Temperature Distortion on Compression System Stability," Paper No. AIAA-91-1895, 1991.

10 Greitzer, E. M., "Surge and Rotating Stall in Axial Flow Compressors, Part 2: Experimental Results and Comparison With Theory," ASME *Journal of Engineering for Power,* Vol. 98, 1976, pp. 199–217.

11 Stenning, A. H., "Rotating Stall and Surge," ASME *Journal of Fluids Engineering,* Vol. 102, 1980, pp. 14–21.

12 Fasol, K. H., "Recent Experiences With Modelling and Simulation of Some Industrial Plants," *Israel J. Technology,* Vol. 17, 1979, pp. 207–216.

13 Macdougal, I., and Elder, R. L., "Simulation of Centrifugal Compressor Transient Performance for Process Plant Applications," ASME *Journal of Engineering for Power,*, Vol. 105, 1983, pp. 885–890.

14 Wenzel, L. M., and Bruton, W. M., "Analytical Investigation of Nonrecoverable Stall," Technical Memorandum 82792, NASA, Feb. 1982.

15 Hosny, W. M., Bitter, S. J., and Steenken, W. G., "Turbofan Engine Nonrecoverable Stall Computer-Simulation Development and Validation," AIAA Paper No. 85-1432.

16 Chung, K., Leamy, K. R., and Collins, T. P., "A Turbine Engine Aerodynamic Model for In-Stall Transient Simulation," Paper No. AIAA-85-1429, 1985.

17 Steenken, W. G., "Turbofan Engine Post-instability Behavior: Computer Simulations, Test Validation, and Application of Simulations," in: *Engine Response to Distorted Inlet Flow Conditions,* AGARD-CP-400, 1987.

18 Epstein, A. H., Ffowcs-Williams, J. E., and Greitzer, E. M., "Active Suppression of Aerodynamic Instabilities in Turbomachines," *J. Propulsion and Power,* Vol. 5, 1989, pp. 204–211.

19 Ffowcs-Williams, J. E., and Graham, W. R., "Engine Demonstration of Active Surge Control," ASME Paper No. 90-GT-XX, 1990.

20 Gysling, D. L., Dugundji, J., Epstein, A. H., and Greitzer, E. M., "Dynamic Control of Centrifugal Compressor Surge Using Tailored Structures," ASME Paper No. 90-GT-XX.

21 Pinsley, J. E., Guenette, G. R., Epstein, A. H., and Greitzer, E. M., "Active Stabilization of Centrifugal Compressor Surge," ASME Paper No. 90-GT-XX.

22 Hosny, W. M., Leventhal, L., and Steenken, W. G., "Active Stabilization of Multistage Axial-Compressor Aerodynamic System Instabilities," ASME Paper No. 91-GT-403, 1991.

23 Badmus, O. O., Nett, C. N., and Schork, F. J., "An Integrated Full-Range Surge Control/Rotating Stall Avoidance Compressor Control System," *Proceedings of the 1991 American Control Conference,* June 1991.

24 Moore, F. K., "A Theory of Rotating Stall of Multistage Compressors, Parts I–III," ASME *Journal of Engineering for Power,* Vol. 106, 1984, pp. 313–336.

25 Moore, F. K., and Greitzer, E. M., "A Theory of Post-Stall Transients in Axial Compression Systems: Part 1, Development of Equations; Part 2, Application," ASME JOURNAL OF TURBOMACHINERY, Vol. 108, 1986, pp. 68–76; 1986, 231–239.

26 Moore, F. K., "Stall Transients of Axial Compression Systems With Inlet Distortion," *J. Propulsion and Power,* Vol. 2, 1986, pp. 552–561.

27 Paduano, J., Valavani, L., Epstein, A. H., Greitzer, E. M., and Guenette, G., "Modeling for Control of Rotating Stall," presented at the 29th IEEE Conference on Decision and Control, 1991.

28 Paduano, J., "Active Control of Rotating Stall in Axial Compressors," PhD thesis, Massachusetts Institute of Technology, Cambridge, MA, 1991.

29 Bonnaure, L., "Modelling High Speed Multistage Compressor Stability," Master's thesis, Department of Aeronautics and Astronautics, Massachusetts Institute of Technology, Cambridge, MA, 1991.

30 Dugundji, J., Garnier, V. H., Epstein, A. H., Greitzer, E. M., Guenette, G., Paduano, J., Silkowski, P., Simon, J., and Valavani, L., "A Progress Report on Active Control of Flow Instabilities: Rotating Stall Stabilization in Axial Compressors," AIAA Paper No. 89-1008, 1989.

31 Simon, J. S., and Valavani, L., "A Lyapunov Based Nonlinear Control Scheme for Stabilizing a Basic Compression System Using a Close-Coupled Valve," in: *Proceedings of the 1991 American Control Conference,* 1991.

32 Day, I. J., "Active Suppression of Rotating Stall and Surge in Axial Compressors," ASME JOURNAL OF TURBOMACHINERY, Vol. 115, 1993, pp. 40–47.

---

[2] Acronym for the Laboratory for Identification and Control of Complex Highly Uncertain Systems, School of Aerospace Engineering, Georgia Institute of Technology.

33 Liaw, D. C., and Abed, E. H., "Stability Analysis and Control of Rotating Stall," in: *Proceedings of the 2nd IFAC Nonlinear Control Systems Design Symposium,* June 1992.
34 Greitzer, E. M., "Review-Axial Compressor Stall Phenomena," ASME *Journal of Fluids Engineering,* Vol. 102, June 1980, pp. 134–151.
35 Holman, J. P., *Heat Transfer,* 6th ed., McGraw-Hill, New York, 1986.
36 Schreier, S., *Compressible Flow,* Wiley, New York, 1982.
37 Davis, M. W., "A Stage-By-Stage Post-Stall Compression System Modeling Technique: Methodology, Validation and Application," PhD thesis, Virginia Polytechnic Institute and State University, 1986.
38 Kimzey, W., "An Analysis of the Influence of Some External Disturbances on the Aerodynamic Stability of Turbine Engine Axial Flow Fans and Compressors," Tech. Rep. TR-77-80, Arnold Engineering Development Center, 1977.
39 Ward, G. G., "Compressor Stability Assessment Program (Techniques for Constructing Mathematical Models of Compression Systems and Propulsion Systems)," Tech. Rep. TR-74-107, Vol. II, Air Force Aero Propulsion Laboratory, Dec. 1974.
40 Nett, C. N., "LICCHUS Experimental Facilities Summary: September 1991 (Months 1–18)," Oct. 1991. Videotape presentation, available from School of Aerospace Engineering, Georgia Tech, 120 min.
41 Emanuel, G., *Gas Dynamics: Theory and Applications,* AIAA, New York; 1986.
42 Oates, G. C., *Aerothermodynamics of Gas Turbine and Rocket Propulsion,* AIAA, Washington, DC, 1988.
43 Cohen, H., Rogers, G. F. C., and Saravanaamuttoo, H. I. H., *Gas Turbine Theory,* 3rd ed., Longman Scientific & Technical; Wiley, 1990.
44 French, M. W., "Development of a Compact Real-Time Turbofan Engine Dynamic Simulation," SAE Tech. Rep. 821401, 1982.
45 Ballin, M. G., "A High Fidelity Real-Time Simulation of a Small Turboshaft Engine," Tech. Rep., NASA TM 100991, 1988.
46 Krikelis, N. J., and Papadakis, F., "Gas Turbine Modelling Using Pseudo-Bond Graphs," *Int. J. Systems Science,* Vol. 19, No. 4, 1988, pp. 537–550.
47 Dwyer, W. J., "Adaptive Model-Based Control Applied to a Turbofan Aircraft Engine," Master's thesis, Massachusetts Institute of Technology, Cambridge, MA, 1990.

APPENDIX A

Analytical Component Models

In this appendix, analytical models for various components are given. While some of the equations in these models become quite complicated, they can be implemented as precomputed maps for simplification when used in a developed model.

A.1 Ducting Without Combustion. Analytical maps for this component are developed by first obtaining an analytical or experimentally measured expression for the change in total pressure. For the Fanno flow case discussed in [1, 2], we could use:

$$p_k - p_{k-1} = -4c_f \frac{L_k}{D} \frac{\gamma \mathrm{M}_k^2}{2}.$$

where c_f is the skin-friction coefficient and D is the dimensionless hydraulic diameter [41]. The maps for the change in M and s are then computed by using conservation of mass and energy to obtain the following:

$$\mathrm{M}_{k-1}\left(1 + \frac{\gamma - 1}{2}\mathrm{M}_{k-1}^2\right)^{-(\gamma+1)/[2(\gamma-1)]}$$
$$= e^{p_k - p_{k-1}} e^{A_k - A_{k-1}} \mathrm{M}_k \left(1 + \frac{\gamma - 1}{2}\mathrm{M}_k^2\right)^{-(\gamma+1)/[2(\gamma-1)]},$$

or

$$\mathrm{M}_{k-1} = f_{\text{con}}(c_{\text{con}}),$$

where

$$c_{\text{con}} = e^{p_k - p_{k-1}} e^{A_k - A_{k-1}} \mathrm{M}_k \left(1 + \frac{\gamma - 1}{2}\mathrm{M}_k^2\right)^{-(\gamma+1)/[2(\gamma-1)]},$$

and

$$s_k - s_{k-1} = -\frac{\gamma - 1}{\gamma}(p_k - p_{k-1}).$$

The map $f_{\text{con}}(c_{\text{con}})$ is identical to the map $f_{ac}(c_{ac})$, which is plotted in Fig. 1. Using these relations, the maps m_4, m_5, and m_6 required in [1] can be given as:

$$m_5 = -4c_f \frac{L_k}{D} \frac{\gamma \mathrm{M}_k^2}{2}$$

$$m_4 = \mathrm{M}_k - f_{\text{con}}(c_{\text{con}})$$

where

$$c_{\text{con}} = e^{m_5} e^{A_k - A_{k-1}} \mathrm{M}_k \left(1 + \frac{\gamma - 1}{2}\mathrm{M}_k^2\right)^{-(\gamma+1)/[2(\gamma-1)]}$$

$$m_6 = -\frac{\gamma - 1}{\gamma}(m_5).$$

Note that if $m_5 = 0$, this component corresponds to an isentropic area change:

$$m_4 = \mathrm{M}_k - f_{ac}(c_{ac})$$

where

$$c_{ac} = e^{A_k - A_{k-1}} \mathrm{M}_k \left(1 + \frac{\gamma - 1}{2}\mathrm{M}_k^2\right)^{-(\gamma+1)/[2(\gamma-1)]}$$

$$m_5 = 0$$

$$m_6 = 0.$$

The function $f_{ac}(c_{ac})$ is plotted in Fig. 1.

A.2 Ducting With Combustion. An analytical form of the maps for this component can be developed for the kth element as follows:

$$\tilde{w}_{k-1} + \tilde{w}_f = \tilde{w}_k$$

$$\tilde{p}_k = \pi_b \tilde{p}_{k-1}$$

$$\tilde{w}_{k-1} c_p \tilde{T}_{k-1} + \tilde{w}_f c_p \tilde{T}_f + \eta_b \tilde{h}_f \tilde{w}_f = \tilde{w}_k c_p \tilde{T}_k,$$

where π_b, the burner pressure loss, η_b, the burner efficiency, and $\tilde{h}_f$, the heat release of the fuel, are experimentally determined constants [42, 43]. Also, $\tilde{w}_f$ is the fuel mass flow, and $\tilde{T}_f$ is the temperature of the fuel. In terms of dimensionless variables, the maps for the kth element become:

$$\phi_{p,k} = \ln\,[\pi_b]$$

$$\phi_{s,k} = 2\ln\left[\frac{1}{2}\left(-c_{k,1} + \sqrt{c_{k,1}^2 + 4}\right)\right] - \frac{\gamma - 1}{\gamma}\phi_{p,k}$$

where

$$c_{k,1} = -\frac{w_f\left(e^{T_f - T_{k-1}} - 1 + \eta_b h_f\right)}{\gamma e^{A_k - A_{k-1}} e^{\phi_{p,k}} \mathrm{M}_k \left(1 + \frac{\gamma - 1}{2}\mathrm{M}_k^2\right)^{-(\gamma+1)/[2(\gamma-1)]}},$$

and

$$\phi_{\mathrm{M},k} = \mathrm{M}_k - f_{\text{con}}(c_k, 2),$$

where $f_{\text{con}}(c_{\text{con}})$ is the same as $f_{ac}(c_{ac})$ plotted in Fig. 1, and

$$c_{k,2} = -\frac{w_f}{\gamma} + \frac{e^{A_k - A_{k-1}} e^{\phi_{p,k}}}{e^{(1/2)(\phi_{s,k} + [(\gamma-1)/\gamma]\phi_{p,k})}}$$
$$\times \mathrm{M}_k \left(1 + \frac{\gamma - 1}{2}\mathrm{M}_k^2\right)^{-(\gamma+1)/[2(\gamma-1)]}.$$

The definitions of T_f, h_f, and w_f are:

$$T_f = \ln\left(\frac{\tilde{T}_f}{\tilde{T}}\right), \quad h_f = \frac{\tilde{h}_f}{c_p \tilde{T}_{k-1}}, \quad \text{and} \quad w_f = \frac{\tilde{w}_f \sqrt{\gamma R \tilde{T}_{k-1}}}{\tilde{p}_{k-1} \tilde{A}_{k-1}}.$$

A.3 Heat Soak. The maps for this component can be modeled analytically using standard heat transfer analysis [35]. There are two types of heat transfer considered here, namely conduction and convection. For conduction between the flow and the wall/blade, the model in discretized form is

$$\tilde{q} = k \frac{\tilde{A}_{w,k-1}}{\tilde{L}_{w,k-1}} (\tilde{T}_{w,k-1} - \tilde{T}_{k-1}),$$

where $\tilde{q}$ is the heat transfer rate per unit volume, $\tilde{A}_{w,k-1}$ is the surface area of the wall, and $\tilde{L}_{w,k-1}$ is the length of the wall. In terms of dimensionless variables this can be given as

$$Q = \frac{e^{A_{w,k-1}-A_{k-1}}}{\hat{R}_{k-1}\,\mathrm{Pr}(\gamma - 1)} (e^{T_{w,k-1}-T_{k-1}} - 1),$$

where here

$$\widehat{\mathrm{Re}}_{k-1} = \frac{\tilde{p}_{k-1}\sqrt{\gamma R\tilde{T}_{k-1}}\,\tilde{L}_{w,k-1}}{R\tilde{T}_{k-1}\mu}.$$

For convection between the flow and the wall/blades, the model can be given as:

$$\tilde{q} = h\tilde{A}_{w,k-1}(\tilde{T}_{w,k-1} - \tilde{T}_{k-1}),$$

where h is the convection heat transfer coefficient. In terms of dimensionless variables we obtain

$$Q = \frac{\mathrm{Nu}\; e^{A_{w,k-1}-A_{k-1}}\gamma}{\hat{R}_{k-1}\,\mathrm{Pr}(\gamma - 1)} (e^{T_{w,k-1}-T_{k-1}} - 1),$$

where the Nusselt number, Nu, is defined as

$$\mathrm{Nu} = \frac{h\tilde{L}_{w,k-1}}{k}.$$

The convection model for heat soak effects is commonly used in turbomachinery modeling [44, 14, 45, 46, 47].

The maps required for this element can be developed by starting with the following dimensional equations:

$$\tilde{w}_{k-1} = \tilde{w}_k,$$

$$\tilde{p}_{k-1}(1 + \gamma \mathrm{M}_{k-1}^2) = \tilde{p}_k(1 + \gamma \mathrm{M}_k^2),$$

and

$$\tilde{w}_{k-1} c_p \tilde{T}_{k-1} - k \frac{\tilde{A}_{w,k-1}}{\tilde{L}_w} (\tilde{T}_{k-1} - \tilde{T}_{w,k-1}) = \tilde{w}_k c_p \tilde{T}_k.$$

These equations are cast into dimensionless form to give the following for the kth element:

$$\frac{\mathrm{M}_{k-1}\left(1 + \frac{\gamma - 1}{2}\mathrm{M}_{k-1}^2\right)^{-(\gamma+1)/[2(\gamma-1)]}}{1 + \gamma \mathrm{M}_{k-1}^2} \times \left[1 - \frac{c_{hs1}}{\mathrm{M}_{k-1}\left(1 + \frac{\gamma - 1}{\gamma}\mathrm{M}_{k-1}^2\right)^{-(\gamma+1)/[2(\gamma-1)]}}\right]^{1/2} = c_{hs2}, \quad (4)$$

where

$$c_{hs1} = \frac{e^{A_{w,k-1}-A_{k-1}}[1 - e^{(T_{w,k-1}-T_{k-1})}]}{\hat{R}_{k-1}\,\mathrm{Pr}},$$

and

$$c_{hs2} = e^{A_k - A_{k-1}} \frac{\mathrm{M}_k\left(1 + \frac{\gamma - 1}{2}\mathrm{M}_k^2\right)^{-(\gamma+1)/[2(\gamma-1)]}}{1 + \gamma \mathrm{M}_k^2}.$$

Equation (4) can be precomputed and implemented as the two-dimensional functional relation:

$$\mathrm{M}_{k-1} = f_{hs}(c_{hs1}, c_{hs2}).$$

Also,

$$p_k = p_{k-1} + \ln\left[\frac{1 + \gamma \mathrm{M}_{k-1}^2}{1 + \gamma \mathrm{M}_k^2}\right],$$

and

$$s_k = s_{k-1} + \ln \quad 1 - \frac{c_{hs1}}{\mathrm{M}_{k-1}\left(1 + \frac{\gamma - 1}{\gamma}\mathrm{M}_{k-1}^2\right)^{-(\gamma+1)/[2(\gamma-1)]}} - \frac{\gamma - 1}{\gamma} \ln\left[\frac{1 + \gamma \mathrm{M}_{k-1}^2}{1 + \gamma \mathrm{M}_k^2}\right].$$

If the convection model of heat transfer is used, the equations above are the same except that in this case

$$c_{hs1} = \frac{\mathrm{Nu}\; e^{A_{w,k-1}-A_{k-1}}[1 - e^{(T_{w,k-l}-T_{k-1})}]}{\widehat{\mathrm{Re}}_{k-l}\,\mathrm{Pr}}.$$

Using these relations, the maps m_4, m_5, and m_6 required in [1] can be given as:

$$m_4 = \mathrm{M}_k - f_{hs}(c_{hs1}, c_{hs2})$$

$$m_5 = \ln\left[\frac{1 + \gamma[f_{hs}(c_{hs1}, c_{hs2})]^2}{1 + \gamma \mathrm{M}_k^2}\right]$$

$$m_6 = \ln\left[1 - \frac{c_{hs1}}{\mathrm{M}_{k-1}\left(1 + \frac{\gamma - 1}{\gamma}\mathrm{M}_{k-1}^2\right)^{-(\gamma+1)/[2(\gamma-1)]}}\right] - \frac{\gamma - 1}{\gamma} m_5.$$

A.4 Nozzle. Analytical equations for the nozzle are developed here. First, the exhaust Mach number, M_e, is calculated using the input p_{se} as follows:

$$\mathrm{M}_e = \sqrt{\frac{2}{\gamma - 1}[e^{[(\gamma-1)/\gamma](p_e - p_{se})} - 1]}.$$

Of course, since the nozzle is a converging nozzle, the maximum value of M_e is 1, which must be considered in model computation. If this limit condition does occur, the exhaust plane static pressure will not be that given by the input p_{se}. Instead, it is given by:

$$p_{\mathrm{sep}} = p_e - \frac{\gamma}{\gamma - 1} \ln\left(1 + \frac{\gamma - 1}{2}\right).$$

Once M_e is computed, the equations for an isentropic area change, given earlier, are used to complete the model of the nozzle.

A.5 Abrupt Area Change With Incurred Total Pressure Losses. Analytical expressions for an abrupt area change are given here. Experimentally observed conditions for this process can be expressed for the kth element of a discretization with the following equations in dimensional form:

$$\tilde{w}_{k-1} = \tilde{w}_k,$$

$$\tilde{p}_{s,k-1} = \tilde{p}_{s,k},$$

and

$$\tilde{T}_{k-1} = \tilde{T}_k.$$

These equations are then cast into dimensionless variables to give the following:

$$\mathrm{M}_{k-1}\sqrt{1 + \frac{\gamma - 1}{2}\mathrm{M}_{k-1}^2} = e^{A_k - A_{k-1}}\mathrm{M}_k\sqrt{1 + \frac{\gamma - 1}{2}\mathrm{M}_k^2},$$

which can be solved for M_{k-1} to get the general function:

$$\mathrm{M}_{k-1} = f_{aac}(c_{aac}),$$

where

$$c_{aac} = e^{A_k - A_{k-1}}\mathrm{M}_k\sqrt{1 + \frac{\gamma - 1}{2}\mathrm{M}_k^2}.$$

Also,

$$p_k = p_{k-1} + \frac{\gamma}{\gamma - 1}\ln\left[\frac{1 + \dfrac{\gamma - 1}{2}\mathrm{M}_k^2}{1 + \dfrac{\gamma - 1}{2}\mathrm{M}_{k-1}^2}\right],$$

and

$$s_k = s_{k-1} - \ln\left[\frac{1 + \dfrac{\gamma - 1}{2}\mathrm{M}_k^2}{1 + \dfrac{\gamma - 1}{2}\mathrm{M}_{k-1}^2}\right].$$

The function $f_{aac}(c_{aac})$ is plotted in Fig. 2. For reverse flow in this component, when the flow is essentially static after the area increase, the flow can be modeled as an isentropic area decrease with the equations given earlier.

A.6 Flow Splitting. Analytical expressions for flow splitting are given here. Experimentally observed conditions for this component are listed in dimensional form as follows:

$$\tilde{w}_{k-1} = \tilde{w}_{k,1} + \tilde{w}_{k,2},$$

$$\tilde{p}_{k-1} = \tilde{p}_{k,1} = \tilde{p}_{k,2},$$

and

$$\tilde{T}_{k-1} = \tilde{T}_{k,1} = \tilde{T}_{k,2},$$

where subscript $k - 1$ denotes the flow entering this element, k,1 denotes the flow leaving the element in the first stream, and k,2 denotes the flow leaving the element in the second stream. These equations are cast into dimensionless variables to give the following:

$$\mathrm{M}_{k-1}\left(1 + \frac{\gamma - 1}{2}\mathrm{M}_{k-1}^2\right)^{-(\gamma+1)/[2(\gamma-1)]}$$
$$= e^{A_{k,1} - A_{k-1}}\mathrm{M}_{k,1}\left(1 + \frac{\gamma - 1}{2}\mathrm{M}_{k,1}^2\right)^{-(\gamma+1)/[2(\gamma-1)]}$$
$$+ e^{A_{k,1} - A_{k-1}}\mathrm{M}_{k,2}\left(1 + \frac{\gamma - 1}{2}\mathrm{M}_{k,2}^2\right)^{-(\gamma+1)/[2(\gamma-1)]},$$

which can be solved for M_{k-1} to give the general function:

$$\mathrm{M}_{k-1} = f_{\mathrm{spl}}(c_{\mathrm{spl}}),$$

where

$$c_{\mathrm{spl}} = e^{A_{k,1} - A_{k-1}}\mathrm{M}_{k,1}\left(1 + \frac{\gamma - 1}{2}\mathrm{M}_{k,1}^2\right)^{-(\gamma+1)/[2(\gamma-1)]}$$
$$+ e^{A_{k,2} - A_{k-1}}\mathrm{M}_{k,2}\left(1 + \frac{\gamma - 1}{2}\mathrm{M}_{k,2}^2\right)^{-(\gamma+1)/[2(\gamma-1)]}.$$

Also,

$$p_{k,2} = p_{k,1} = p_{k-1},$$

and

$$s_{k,2} = s_{k,1} = s_{k-1}.$$

As can be seen, the function f_{spl} is identical to f_{ac}, which is already plotted in Fig. 1.

A.7 Bleed. Analytical expressions for the bleed are given here for the kth element in a discretization:

$$\mathrm{M}_{k-1} = f_{\mathrm{spl}}(c_{\mathrm{spl}})$$

where

$$c_{\mathrm{spl}} = e^{(A_k - A_{k-1})}\mathrm{M}_k\left(1 + \frac{\gamma - 1}{2}\mathrm{M}_k^2\right)^{-(\gamma+1)/[2(\gamma-1)]}$$
$$+ e^{(A_{k,b} - A_{k-1})}\mathrm{M}_{k,b}\left(1 + \frac{\gamma - 1}{2}\mathrm{M}_{k,b}^2\right)^{-(\gamma+1)/[2(\gamma-1)]}$$

$$p_k = p_{k-1} \qquad s_k = s_{k-1}$$
$$p_{k,b} = p_{k-1} \qquad s_{k,b} = s_{k-1}.$$

Here, the subscript $k - 1$ refers to flow entering the component, the subscript k refers to the main flow leaving the component, and the subscript k,b refers to the bleed flow leaving the component. The bleed Mach number, $\mathrm{M}_{k,b}$, must also be calculated using the input $p_{sk,b}$ as follows:

$$\mathrm{M}_{k,b} = \sqrt{\frac{2}{\gamma - 1}\left[e^{[(\gamma-1)/\gamma](p_{k,b} - p_{sk,b})} - 1\right]}.$$

Of course, since the bleed valve is a converging nozzle, the maximum value of $\mathrm{M}_{k,b}$ is 1, which must be considered in model computation.

A.8 Mixing. Analytical expressions for mixing are given here. In terms of dimensional variables, we have:

$$\tilde{w}_{k-1,1} + \tilde{w}_{k-1,2} = \tilde{w}_k$$

$$\tilde{p}_{sk-1,1} = \tilde{p}_{sk-1,2} = \tilde{p}_{sk}$$

$$\tilde{w}_{k-1,1}c_p\tilde{T}_{k-1,1} + \tilde{w}_{k-1,2}c_p\tilde{T}_{k-1,2} = \tilde{w}_k c_p\tilde{T}_k,$$

where the subscript $k - 1$, 1 represents the flow entering from the first stream, $k - 1$, 2 represents the flow entering from the second stream, and k represents the flow leaving in a single stream. In terms of dimensionless variables, the following expression can be developed:

$$\left(1 + \frac{\gamma - 1}{2}\mathrm{M}_{k-1,1}^2\right)$$
$$\times \left\{\mathrm{M}_{k-1,1}^2 + e^{2(A_{k-1,2} - A_{k-1,1})}e^{2(p_{k-1,2} - p_{k-1,1})}\frac{2}{\gamma - 1}\right.$$
$$\times \left[e^{[(\gamma-1)/\gamma](p_{k-1,2} - p_{k-1,1})}\left(1 + \frac{\gamma - 1}{2}\mathrm{M}_{k-1,1}^2\right) - 1\right]$$

$$\begin{aligned}&\times e^{[-(\gamma+1)/\gamma](p_{k-1,2}-p_{k-1,1})} + e^{A_{k-1,2}-A_{k-1,1}}e^{p_{k-1,2}-p_{k-1,1}}\\ &\times \sqrt{\frac{2}{\gamma-1}\left[e^{[(\gamma-1)/\gamma](p_{k-1,2}-p_{k-1,1})}\left(1+\frac{\gamma-1}{2}\mathrm{M}_{k-1,1}^2\right)-1\right]}\\ &\times e^{[-(\gamma+1)/2\gamma](p_{k-1,2}-p_{k-1,1})}\mathrm{M}_{k-1,1}\\ &\left.\times \left(e^{(1/2)(T_{k-1,2}-T_{k-1,1})} + e^{-(1/2)(T_{k-1,2}-T_{k-1,1})}\right)\right\}\\ &= e^{2(A_k-A_{k-1,1})}\mathrm{M}_k^2\left(1+\frac{\gamma-1}{2}\mathrm{M}_k^2\right).\end{aligned}$$

This can put in terms of a map as follows:

$$\mathrm{M}_{k-1,1} = f_{\mathrm{mix}}(p_{k-1,2}-p_{k-1,1}, x_{k-1,2}-s_{k-1,1}, \mathrm{M}_k, A_{k-1,2}-A_{k-1,1}, A_k-A_{k-1,1}).$$

Once $\mathrm{M}_{k-1,1}$ has been computed, the remaining variables can be computed as follows:

$$\mathrm{M}_{k-1,2} = \sqrt{\frac{2}{\gamma-1}\left[e^{[(\gamma-1)/\gamma](p_{k-1,2}-p_{k-1,1})}\left(1+\frac{\gamma-1}{2}\mathrm{M}_{k-1,1}^2\right)-1\right]}$$

$$p_k = p_{k-1,1} + \frac{\gamma}{\gamma-1}\ln\left(\frac{1+\frac{\gamma-1}{2}\mathrm{M}_{k-1,1}^2}{1+\frac{\gamma-1}{2}\mathrm{M}_k^2}\right)$$

$$\begin{aligned}T_k = T_{k-1,1} + 2\ln\Bigg[&\mathrm{M}_{k-1,1}\left(1+\frac{\gamma-1}{2}\mathrm{M}_{k-1,1}^2\right)^{-(\gamma+1)/[2(\gamma-1)]}\\ &+ e^{A_{k-1,2}-A_{k-1,1}}e^{p_{k-1,2}-p_{k-1,1}}e^{(1/2)(T_{k-1,2}-T_{k-1,1})}\mathrm{M}_{k-1,2}\\ &\times\left(1+\frac{\gamma-1}{2}\mathrm{M}_{k-1,2}^2\right)^{-(\gamma+1)/[2(\gamma-1)]}\Bigg]\\ -2\ln\Bigg[&e^{A_k-A_{k-1,1}}e^{p_k-p_{k-1,1}}\mathrm{M}_k\\ &\times\left(1+\frac{\gamma-1}{2}\mathrm{M}_k^2\right)^{-(\gamma+1)/[2(\gamma-1)]}\Bigg].\end{aligned}$$

A.9 Wall/Blade Metal. An analytical expression for the dynamics of the wall/blade metal temperature is given here. Based on the conduction model for the heat soak effects, the following equation in dimensional form can be used [35]:

$$\tilde{m}_{w,k-1}c_{w,k-1}\frac{d}{d\tilde{t}}\tilde{T}_{w,k-1} = k\frac{\tilde{A}_{w,k-1}}{\tilde{L}_{w,k-1}}(\tilde{T}_{k-1}-\tilde{T}_{w,k-1}),$$

where $\tilde{m}_{w,k-1}$ is the mass of the metal in the wall/blade, and $c_{w,k-1}$ is the specific heat of the metal. In terms of dimensionless variables, this equation becomes:

$$\frac{d}{dt}T_{w,k-1} = k_{w,k-1}(e^{T_{k-1}-T_{w,k-1}}-1),$$

where $k_{w,k-1} = (\bar{t}k\tilde{A}_{w,k-1})/(\tilde{m}_{w,k-1}c_{w,k-1}\tilde{L}_{w,k-1})$. If the convection model for heat soak effects is used, the following equation for the wall/blade temperature can be used:

$$\frac{d}{dt}T_{w,k-1} = h_{w,k-1}(e^{T_{k-1}-T_{w,k-1}}-1),$$

where $h_{w,k-1} = (\bar{t}h\tilde{A}_{w,k-1})/(\tilde{m}_{w,k-1}c_{w,k-1})$.

The equations above for the wall temperature assume that there is only heat transfer between the wall and a single fluid flow. There are some cases in which there can be heat transfer between the wall and two different flows, for example if there is a heat exchanger or a wall between core flow and bypass flow in a turbofan. In these cases, there is another term in the equations for the wall temperature. For the conduction model this becomes

$$\frac{d}{dt}T_{w,k-1} = k_{w1}(e^{T_{k-1,1}-T_{w,k-1}}-1) + k_{w2}(e^{T_{k-1,2}-T_{w,k-1}}-1),$$

and for the convection model we have

$$\frac{d}{dt}T_{w,k-1} = h_{w1}(e^{T_{k-1,1}-T_{w,k-1}}-1) + h_{w2}(e^{T_{k-1,2}-T_{w,k-1}}-1),$$

where $T_{k-1,1}$, k_{w1}, and h_{w1} are associated with the first flow, and $T_{k-1,2}$, k_{w2}, and h_{w2} are associated with the second flow.

A.10 Spool. An analytical expression for the power balance on the spool is given here. Across the jth compressor stage, the power added to the flow from the spool is given by

$$\tilde{P}_{cs,j} = \tilde{w}_{cs,j}c_{p_{cs,j}}\tilde{T}_{cs,j} - \tilde{w}_{cs,j-1}c_{p_{cs,j-1}}\tilde{T}_{cs,j-1},$$

and across the kth turbine stage, the power extracted from the flow by the spool is given by

$$\tilde{P}_{ts,k} = \tilde{w}_{ts,k-1}c_{p_{ts,k-1}}\tilde{T}_{ts,k-1} - \tilde{w}_{ts,k}c_{p_{ts,k}}\tilde{T}_{ts,k}.$$

The equation for the power balance can then be given as:

$$\begin{aligned}\tilde{J}\tilde{N}\frac{d\tilde{N}}{d\tilde{t}} = &-\sum_{j-1}^{n_{cs}}(\tilde{w}_{cs,j}c_{p_{cs,j}}\tilde{T}_{cs,j} - \tilde{w}_{cs,j-1}c_{p_{cs,j-1}}\tilde{T}_{cs,j-1})\\ &+ \eta_m\sum_{k=1}^{n_{ts}}(\tilde{w}_{ts,k-1}c_{p_{st,k-1}}\tilde{T}_{ts,k-1} - \tilde{w}_{ts,k}c_{p_{ts,k}}\tilde{T}_{ts,k}),\end{aligned}$$

where $\tilde{J}$ is the spool inertia, and η_m is a mechanical efficiency factor which accounts for the effects of spool friction. In terms of dimensionless variables we have:

$$\begin{aligned}JN_{\mathrm{spl}}\frac{d}{dt}N_{\mathrm{spl}} = &-\sum_{j-1}^{n_{cs}}\Bigg[\frac{\gamma}{\gamma-1}e^{A_{cs,1}}e^{p_{cs,1}}e^{(1/2)T_{cs,1}}\mathrm{M}_{cs,j}\\ &\times\left(1+\frac{\gamma-1}{2}\mathrm{M}_{cs,j}^2\right)^{-(\gamma+1)/[2(\gamma-1)]}\\ &-\frac{\gamma}{\gamma-1}e^{A_{cs,j-1}}e^{p_{cs,j-1}}e^{(1/2)T_{cs,j-1}}\mathrm{M}_{cs,j-1}\\ &\times\left(1+\frac{\gamma-1}{2}\mathrm{M}_{cs,j-1}^2\right)^{-(\gamma+1)/[2(\gamma-1)]}\Bigg]\\ &+\eta_m\sum_{k=1}^{n_{cs}}\Bigg[\frac{\gamma}{\gamma-1}e^{A_{ts,k-1}}e^{p_{ts,k-1}}e^{(1/2)T_{ts,k-1}}\mathrm{M}_{ts,k-1}\\ &\times\left(1+\frac{\gamma-1}{2}\mathrm{M}_{ts,k-1}^2\right)^{-(\gamma+1)/[2(\gamma-1)]}\\ &-e^{A_{ts,k}}e^{p_{ts,k}}\frac{\gamma}{\gamma-1}\times e^{(1/2)T_{ts,k}}\mathrm{M}_{ts,k}\\ &\times\left(1+\frac{\gamma-1}{2}\mathrm{M}_{ts,k}^2\right)^{-(\gamma+1)/[2(\gamma-1)]}\Bigg],\end{aligned}$$

where $N_{\mathrm{spl}} = \tilde{N}\bar{t}$ and $J = \tilde{J}/\bar{t}^5\bar{p}(\gamma R\bar{T})^{3/2}$. Now, the dimensionless spool speed at the inlet of a compressor stage is simply:

$$N_{cs,j-1} = N_{\mathrm{spl}}e^{(1/2)A_{cs,j-1}}e^{-(1/2)T_{cs,j-1}},$$

and similarly for a turbine stage.

The Structure of Tip Clearance Flow in Axial Flow Compressors

B. Lakshminarayana

M. Zaccaria

B. Marathe

The Pennsylvania State University,
Department of Aerospace Engineering,
University Park, PA 16802

Detailed measurements of the flow field in the tip region of an axial flow compressor rotor were carried out using a rotating five-hole probe. The axial, tangential, and radial components of relative velocity, as well as the static and stagnation pressures, were obtained at two axial locations, one at the rotor trailing edge, the other downstream of the rotor. The measurements were taken up to about 26 percent of the blade span from the blade tip. The data are interpreted to understand the complex nature of the flow in the tip region, which involves the interaction of the tip leakage flow, the annulus wall boundary layer and the blade wake. The experimental data show that the leakage jet does not roll up into a vortex. The leakage jet exiting from the tip gap is of high velocity and mixes quickly with the mainstream, producing intense shearing and flow separation. There are substantial differences in the structure of tip clearance observed in cascades and rotors.

Introduction

The flow field in the tip clearance region of a turbomachinery rotor is complex due to interaction of leakage flow, annulus wall boundary layer, and the blade boundary layer (or wakes). A survey of literature and the correlations used by the industry are given in the von Karman Institute Lecture Series (1985). Most of the earlier basic research was confined to cascades and it is only recently that several attempts have been made to understand this flow through comprehensive measurement in a compressor rotor (Hunter and Cumpsty, 1982; Pandya and Lakshminarayana, 1983; Inoue et al., 1986; Inoue and Kuroumaru, 1989; Murthy and Lakshminarayana, 1986; Lakshminarayana et al., 1990; Cho et al., 1990; Goto, 1992; Moyle et al., 1992). The configuration and the flow variables for various compressors used in the tip clearance flow studies by several investigators are tabulated in Table 1. No attempt will be made in this paper to compare the results from other compressors as the configuration and loading differ widely. Whenever possible, attempts will be made to compare qualitative trends observed by various investigators.

The objective of the present study is to measure the three-dimensional flow field in the tip clearance region of a rotor, and derive a detailed understanding of the flow structure in this region. None of the previous investigators, with the exception of Inoue et al. (1986), Inoue and Kuroumaru (1989), Hunter and Cumpsty (1982), Goto (1992), and Lakshminarayana et al. (1982), have acquired data on all three components of velocity. The emphasis of the present investigation is to acquire comprehensive data at the trailing edge and downstream of a compressor rotor in the tip clearance region and to resolve such issues as roll-up (if any) of the leakage flow into a discrete combined vortex, the nature of three-dimensional velocity and pressure field, generation of vorticity by leakage flow and the nature and magnitude of flow losses.

The leakage flow, in simulated cascades with tip clearance, rolls up into a discrete vortex near the suction surface. Some of the investigators have observed similar phenomena in rotors (e.g., Inoue et al. (1986), Inoue and Kuroumaru (1989)). But other investigations reveal that the leakage flow diffuses before it has a chance to roll up into a discrete combined vortex. This is one of the issues to be addressed in this paper in addition to a detailed understanding of the structure of the flow. The earlier measurements at Penn State were carried out with a Laser Doppler Velocimeter and a kiel probe and only two components of velocities were resolved near the design flow coefficient and at two different tip clearances (Lakshminarayana et al., 1990; Murthy and Lakshminarayana, 1986). The present measurement is carried out at the peak pressure rise coefficient, with a miniature five-hole probe.

Experimental Facility, Technique, Program, and Measurement Error

The measurements reported in this paper were performed in a single-stage axial flow compressor facility. The compressor stage consists of an inlet guide vane row followed by a rotor row and a stator row. The number of blades in these three rows is 43, 21, and 25, respectively. The hub/annulus-wall diameter ratio of the facility is 0.5, with the annulus-wall diameter equal to 0.939 m and the blade tip diameter of 0.932 m. All radii are nondimensionalized by the tip radius ($R = 1$ at the annulus wall). Hence the tip of the blade is located at $R = 0.9925$. The average tip clearance of the rotor

---

Contributed by the International Gas Turbine Institute for publication in the JOURNAL OF TURBOMACHINERY. Manuscript received at ASME Headquarters October 1993. Associate Technical Editor: H. Lukas.

is 3.5 mm,[1] or λ (based on chord) of 2.27 percent, or τ (based on blade height) of 1.52 percent. The measurements at lower tip clearances and other blade loading are reported by Lakshminarayana et al. (1990). The blade section at the rotor blade tip corresponds to a NACA 65 series, where the chord length is 15.41 cm, blade spacing 14.12 cm, maximum thickness, 5.1 percent of chord, stagger angle 45.0 deg, and maximum camber 8 percent of the chord.

The operating conditions are: inlet velocity, $\overline{W}_{x1}$, 25.4 m/s; flow coefficient $\underline{\phi}$ (based on tip speed) of 0.513; stage loading coefficient $\bar{\bar{\psi}}$ (based on tip speed) of 0.514; blade tip speed U_{tip} is 49.8 m/s and rotor speed is 1020 rpm. This operating condition is the peak pressure rise coefficient and is higher than the operating condition for which earlier data were reported (Lakshminarayana et al., 1990). The measured data are compared with earlier data, by Lakshminarayana et al. (1990), which were taken at a flow coefficient ϕ of 0.56 and a stage loading coefficient $\bar{\bar{\psi}}$ of 0.4864. The operating conditions for the two experiments are shown in Table 1. The radial distributions of velocity, absolute and relative pressures at the inlet (0.73 chord upstream) are shown in Fig. 1. The annulus wall boundary layer thickness is about 8 percent of the blade span.

The facility is equipped with a rotating-probe traverse mechanism that permits a circumferential traverse to be done while the rotor is in motion. The circumferential stepping is 0.0166 deg/step which represents 1032 steps per blade passage. A rotating five-hole probe (1.65 mm dia) was employed for the measurement of the flow downstream of the rotor. The output from the transducer is carried from a rotating frame to a stationary frame through a mercury slip-ring unit. The data were processed using the technique developed by Treaster and Yocum (1979).

The measurements were carried out at two axial stations, 4 percent chord downstream and 64 percent chord downstream ($X = 1.04$ and $X = 1.64$) of the trailing edge. At $X = 1.04$, the measurements were performed at 15 radial stations and 54 tangential locations (in one passage) at each radial station. At this axial station, the radial measurement station nearest to the casing wall was at $R = 0.9883$ and the one farthest from the casing wall was at $R = 0.9095$. No data were taken in the tip clearance region $R = 0.9925$ to 1.0, due to mechanical limitations of the rotating probe. At $X = 1.64$, the measurements were performed at 17 radial stations and 27 tangential locations at each radial station. At this axial station, the radial measurement station nearest to the casing wall was at $R = 0.9787$ and the one farthest from the casing wall was at $R = 0.8701$. Hence the data represent a comprehensive survey involving about 800 data points at $X = 1.04$ and 460 data points at $X = 1.64$ in about 20–26 percent of the span within the tip region.

A review of the various methods of estimating five-hole probe measurement errors is given by Sitaram (1983). The wall and blade vicinity effects are negligible, as the probe was located at least three diameters away from the annulus wall. The probe alignment is accurate to within ±1 deg, and the probe calibration is accurate to ±0.5 deg, hence the yaw and pitch angle accuracy is about ±2 deg. The probe alignment in the yaw direction is varied to improve the accuracy of yaw angle measurement while the alignment in the pitchwise (spanwise) direction is fixed. Hence, the measurement in the

---

[1] Tip clearance height quoted as 5 to 5.5 mm in the earlier paper (Lakshminarayana et al., 1990) is erroneous. The largest tip clearance height employed in the Penn State program is 3.5 mm.

Nomenclature

C = chord length
C_p = static pressure rise coefficient (Eq. (5))
h = blade height
N = number of rotor blades (= 21)
p = static pressure
P_{0R} = relative stagnation pressure normalized by $\rho \cdot U_t^2/2$
PS = pressure surface
P_0 = absolute stagnation pressure (normalized by $\rho U_t^2/2$)
R = radius normalized by annulus wall radius (0.4695 m)
r, θ, x = radial, tangential, and axial coordinates
S = spacing = $2\pi r/N$
SS = suction surface
t = tip clearance height
U = blade speed
V = absolute velocity/U_t
W_x, W_θ, W_r = relative axial, tangential, and radial velocity components normalized by the blade-tip speed (49.8 m/s)
W = relative velocity
W_{sec} = secondary velocity (Eq. (2))
X = distance from rotor leading edge normalized by axial chord at tip (0.109 m)
Y = tangential distance measured from wake center normalized by local blade spacing (Y is positive on suction side and negative on the pressure side)
α = relative pitch angle; measured from the axisymmetric surfaces
β = relative airflow (yaw) angle; measured from the axial direction
Γ = circulation = $S(W_{\theta 1} - W_{\theta 2})$
λ = $100t/c$
ν = kinematic viscosity
ρ = fluid density
τ = $100t/h$
ϕ = mass-averaged flow coefficient (based on U_t)
ψ_A = absolute pressure rise coefficient (Eq. (6))
ψ_E = Euler pressure rise coefficient (Eq. (7))
ψ_R = relative stagnation pressure coefficient = $2(P_{R1} - P_a)/\rho U_t^2$
$\bar{\bar{\psi}}$ = mass-averaged stagnation pressure rise coefficient (normalized by $\rho U_t^2/2$)
$\bar{\psi}$ = passage (mass) averaged stagnation pressure rise coefficient (normalized by $\rho U_t^2/2$)
ψ_L = relative stagnation pressure loss coefficient (Eq. (8))
ω_x = axial vorticity (Eq. (3))

Subscripts

A = absolute frame of reference
a, ∞ = atmosphere, far upstream
1, 2 = rotor inlet and exit
h, t = hub, tip
r, θ, x = components in r, θ, and x directions
R = relative frame of reference
s, p = suction and pressure surface

Superscripts

$^{-}$ = blade-to-blade mass average

Table 1 Various configurations used for tip clearance flow study in a compressor rotor

	Hunter & Cumpsty(1982)	Inoue (1989, 1986)	Cho, et al. (1990)	Lakshminarayana, et al. (1990)	Lakshminarayana (present)	Goto (1990)
ϕ	0.28 to 0.49	0.5	NA	0.56	0.513	0.459
$\bar{\psi}$	0.15 to 0.39	0.4	NA	0.486	0.514	0.38 to 0.43*
N rpm	525	1300	1380	1080	1020	500
Flow Turning Angle (Design)	8.2° (camber angle)	6.8°	NA	16°	16°	26.5° (camber angle)
Blading	C4	NACA 65	NACA 65	NACA 65	NACA 65	C4
τ/h percent	0.22 to 3.06	0.56 to 5.6	2.2	1.1 and 1.52	1.52	0.57 to 2.43
Reynolds Number $(\frac{WC_t}{\nu})$	4.4×10^5 to 5.0×10^5 (based on relative inlet velocity)	2.4×10^5	NA	5.3×10^5	5.0×10^5	3.1×10^5 (based on relative inlet velocity)
Configuration	rotor alone (no inlet swirl, low inlet turbulence level)	rotor alone (no inlet swirl, low inlet turbulence level)	rotor alone (no inlet swirl, low inlet turbulence level)	with IGV (inlet swirl and high inlet turbulence level)	with IGV (inlet swirl and high inlet turbulence level)	rotor alone
Data	only exit flow data	only exit flow data	only exit flow data	data inside and exit of rotor passage	only exit flow data	only exit flow data

NA Not available; *Total-to-static pressure rise coefficient.

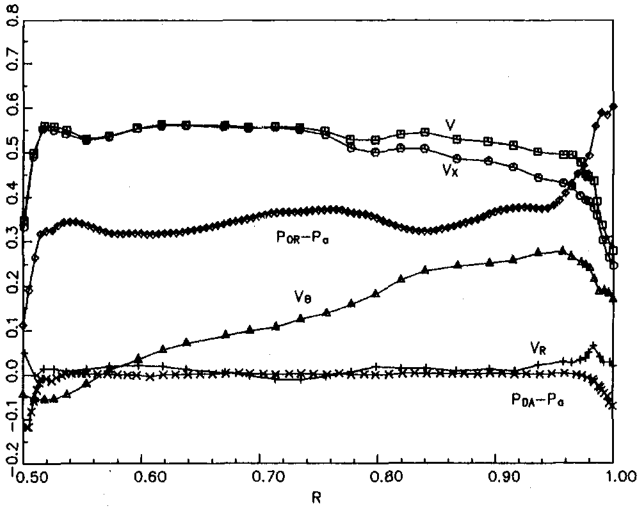

Fig. 1 Radial distribution of rotor inlet flow properties ($x = -0.73$)

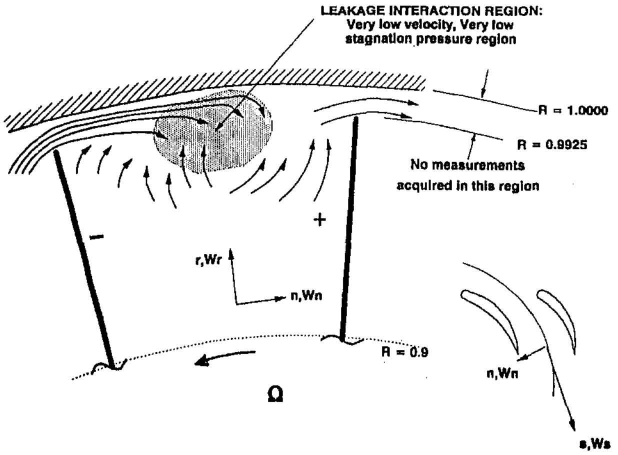

Fig. 2 Schematic of leakage flow and its interaction with the main flow

high pitch angle region (> 35 deg) is not accurate. The error due to turbulence effect is estimated to be 0.33 percent on the total velocity, based on 10 percent turbulence intensity. The probe is calibrated for the same range of Reynolds numbers as the values encountered in the experiment, hence this error is negligible. The error due to probe blockage and probe stem is included in the calibration data. Since the probe is a miniature five-hole probe, the spatial error is small (displacement effect $\delta = 0.21d = 0.35$ mm). The error due to pressure and velocity gradients (based on typical data at the tip) is estimated to be less than 1 percent on the pressure and velocity. Hence the cumulative error (maximum) on the total velocity is estimated to be less than ±1.33 percent. The maximum radial velocity reported in this paper is 4–5 m/s, which is small compared to the total velocity. Thus the error in radial velocities is higher than the error in the axial and tangential components.

All the velocities are normalized by blade tip speed U_t, pressures by $\rho U_t^2/2$. The passage average properties are defined by

$$\bar{A} = \int_{-0.5}^{+0.5} A W_x dY \Big/ \int_{-0.5}^{+0.5} W_x dY$$

$$\text{where } A = W_\theta,\ W_r,\ \psi_L,\ \psi_R,\ \psi_A,\ \psi_E \quad (1)$$

Total and Axial Velocity

A schematic describing the nature of leakage flow derived from the data reported in this paper is shown in Fig. 2. The blade tip is immersed within the annulus wall boundary layer,

TOTAL VELOCITY VARIATION (X=1.04)

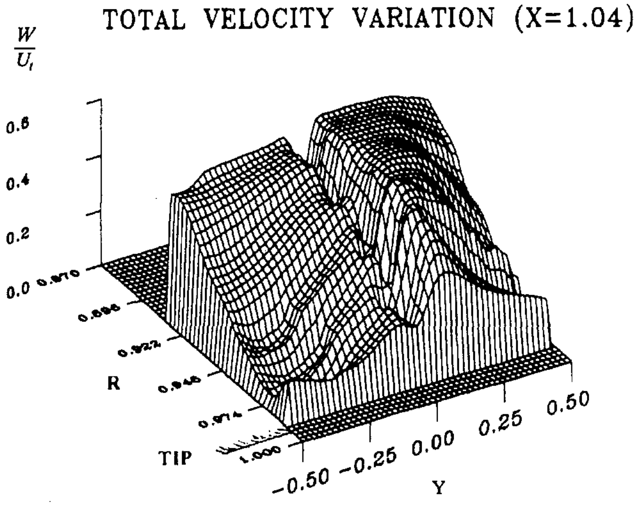

TOTAL VELOCITY VARIATION (X=1.64)

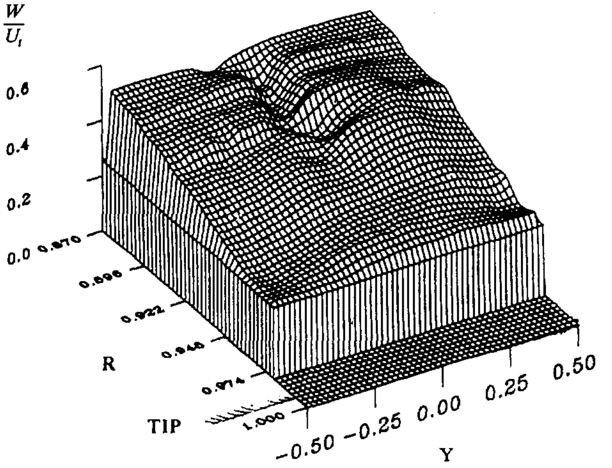

Fig. 3 Total velocity distribution at $x = 1.04$ and $x = 1.64$

CONTOURS OF ISO-AXIAL VELOCITY AT X=1.04

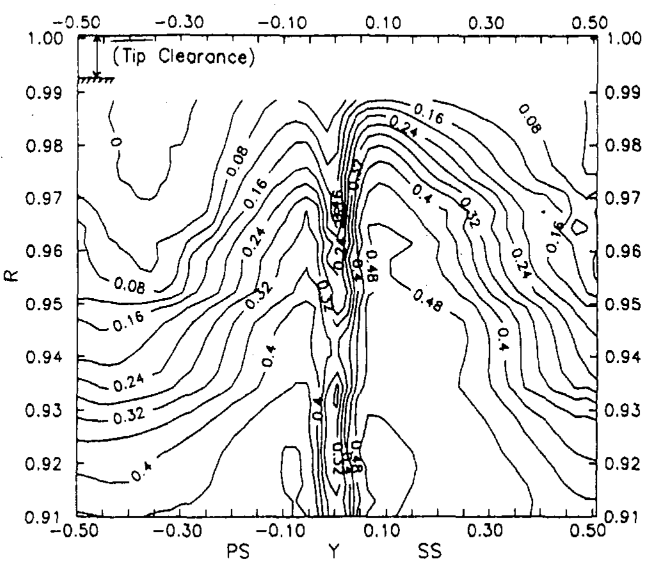

CONTOURS OF ISO-AXIAL VELOCITY AT X=1.64

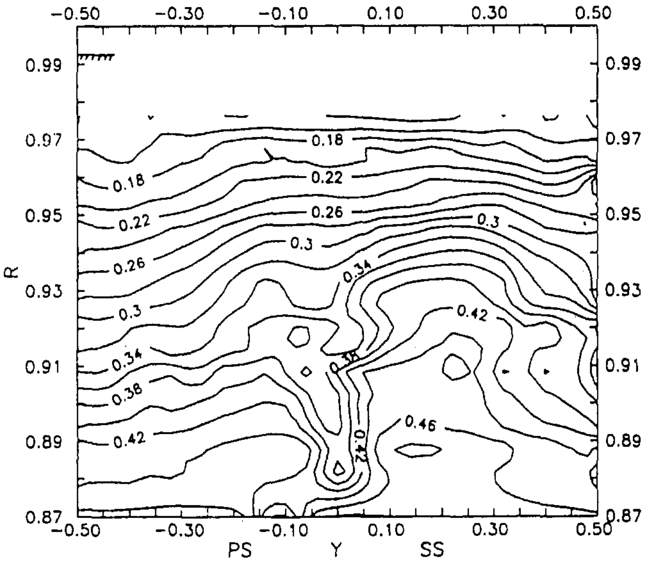

Fig. 4 Contours of iso-axial velocity (W_x) at $x = 1.04$ and $x = 1.64$

hence the leakage jet penetrates deep into the passage before diffusing and interacting with the main flow. The leakage jet moves farther toward the pressure surface due to the blade motion. The leakage jet, located in the highly viscous region, tends to diffuse rapidly. The resulting interaction and mixing region has very low velocities and stagnation pressure and behaves like a separated zone. This region is shown in the shaded area. This region of low stagnation pressure and velocity tends to entrain fluid from regions away from the tip region resulting in outward flow in this region as shown in Fig. 2. The data presented below confirm the flow physics shown in Fig. 2. In an inviscid flow, the leakage jet and the mainflow, which are of similar magnitudes but at widely differing angles, tend to roll up quickly into a vortex.

A three-dimensional plot of the total relative velocity is shown in Fig. 3. In this and subsequent figures, $Y = 0$ at the trailing edge (or blade wake centerline) and Y is negative on the pressure side and positive on the suction side. Dominant influence of leakage flow is evident from this figure. Unlike those in a cascade, the interaction region is closer to the pressure surface. The data presented later indicate that the flow at $X = 1.04$ in the region $0.96 < R < 0.98$ and $Y = -0.3$ to -0.5 has very low velocities and exhibits the characteristic features of separation. The wake edge velocities are low on this pressure side. The influence of leakage is felt as far as $R = 0.93$. On the other hand the velocities on the suction side are generally higher, with relatively high velocities at the edge of the suction surface wake. The interaction region is located near midpassage, closer to the pressure side indicating the influence of blade motion. The flow redistribution from $X = 1.04$ to $X = 1.64$ is very rapid and dramatic. The wake decays very rapidly in the region $R > 0.900$ and the flow becomes nearly axisymmetric. This is unlike cascade where the decay of leakage vortex and its influence is much slower and felt far downstream.

The contours of iso-axial velocity at $X = 1.04$ and 1.64 are shown in Fig. 4. At $X = 1.04$, the blade-to-blade distribution of axial velocity is highly nonuniform, especially in the outer 10 percent of the span, becoming nearly uniform (except in the wake) at $R = 0.91$. In addition, a substantial region closer to the pressure surface near the tip, has zero axial velocity. The interaction between the leakage flow and the main flow will result in low velocities regions as shown in Figs. 2–4. Further evidence of this phenomenon will be presented later. Higher axial velocities are observed near the suction surface in the tip region, while the velocities are lower near the pressure surface. In general, the blade-to-blade distribution of W_x in the tip region shows high axial velocities

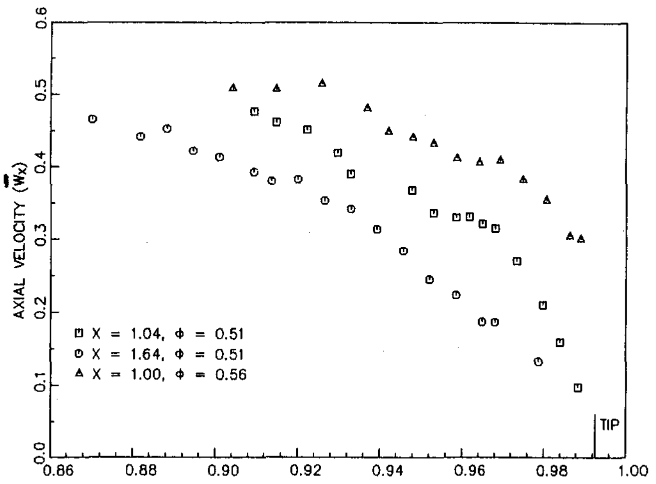

Fig. 5 Comparison of radial distribution of passage-averaged axial velocity ($\overline{W}_x$) at $\phi = 0.51$ and $\phi = 0.56$

near the edges of the wake, decreasing to low values near the midpassage. There is no evidence of interaction between the wake and the leakage flow at $X = 1.04$. The wakes are distinct at $X = 1.04$. These results are similar to the data reported at lower loading ($\phi = 0.56$), with the same clearance, by Lakshminarayana et al. (1990), but the magnitudes of axial velocities are generally lower for the higher loading case.

Considerable mixing occurs downstream of the rotor, including the wake-leakage flow interaction between $X = 1.04$ and 1.64. The flow becomes nearly uniform at $X = 1.64$, with no trace of low velocity region observed at $X = 1.04$. In addition, the wake in the outer 10 percent of the span has mixed out completely.

The passage average axial velocity at $X = 1.04$ and $X = 1.64$ is shown compared with earlier data at $X = 1.0$ and $\phi = 0.56$ in Fig. 5. The annulus wall boundary layer is well behaved very close to the tip at $X = 1.04$ ($R = 0.97$ to 0.99), but considerable distortion is observed in the outer layer ($R = 0.92$ to 0.97). Two distinct profiles are observed: The inner region of the annulus wall boundary layer shows a rather smooth distribution with high velocity gradients, and the outer layer has distorted velocity profile. The axial velocity distribution at lower loading ($\phi = 0.56$) with the same tip clearance shows very similar distribution and behavior, but the axial velocities are generally higher than the present case and the boundary layer and momentum thicknesses are lower. As the flow progresses downstream ($X = 1.64$), the annulus wall boundary layer grows rapidly and the interaction region and the wake disappear giving rise to a smooth velocity distribution. Comparing the passage mean axial velocities with those at inlet (Fig. 1), it is clear that the axial velocities inside the annulus wall/boundary layer are substantially reduced, with appreciable increase in the boundary layer growth from inlet to exit.

Relative Tangential Velocity and Yaw Angles

The contours of iso-relative tangential velocities are shown in Fig. 6. These distributions are similar to the iso-axial velocity contours shown in Fig. 2. The leakage flow phenomenon, shown schematically in Fig. 2, is confirmed by this plot. The relative tangential velocities are low at $X = 1.04$ in most of the leakage flow interaction region. This does not necessarily mean a higher flow turning angle, as the axial velocities are also very low in these regions. The flow is underturned in most of these regions as observed later. The axial and relative tangential velocity components are very low (Figs. 4 and 6) in the tip region ($R = 0.94$ to 0.99) and this region extends to nearly half the blade passage width near the midpassage. The core of the interaction region, where both the axial and the relative tangential velocities are nearly zero, covers nearly 30 percent of the passage from $R = 0.95$ to 0.99 (about 8 percent of span). Very high relative tangential velocities occur near the edges of the wake, and there is no evidence of wake-leakage flow interaction at $X = 1.04$. As the flow progresses downstream ($X = 1.64$), the low relative tangential velocity region mixes out rapidly with the mainstream to provide nearly uniform relative tangential velocity distribution, especially in the tip region.

The blade-to-blade distribution of W_θ, plotted in Fig. 7, clearly reveals the influence of leakage flow. The relative tangential velocities are high near the blade surfaces and reach their lowest values at about 30 percent of the passage width from the pressure surface. The influence of leakage flow is evident across the entire passage, away from the blade

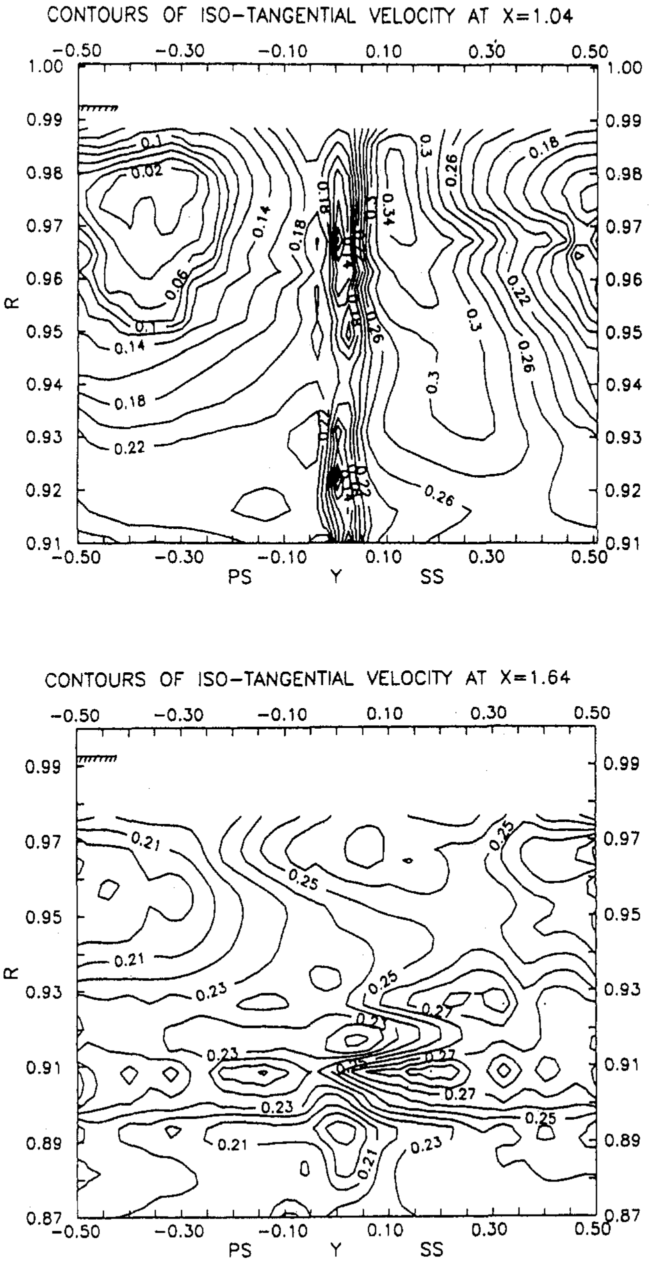

Fig. 6 Contours of iso-relative tangential velocity at x = 1.04 and x = 1.64 (the numbers denote tangential velocity, W_θ)

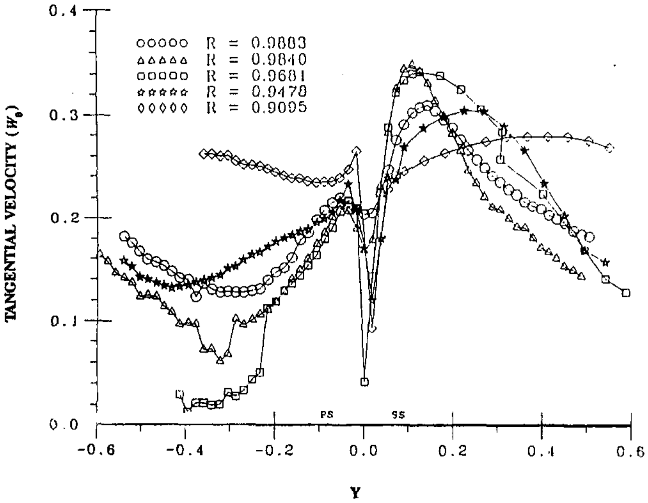

Fig. 7 Blade-to-blade distribution of relative tangential velocity (W_θ) at x = 1.04

surfaces and wake regions, extending to almost 14 percent of span from the tip. The blade wakes are distinct up to the blade tip.

Iso-contours of relative yaw angles are shown in Fig. 8. The plot at $X = 1.04$ shows the dramatic effects of the leakage flow in the tip region from $R = 0.96$ to 0.99, $Y = -0.3$ to -0.5 (in the shaded area marked in Fig. 2). In this region, the flow is nearly tangential (in absolute frame) and is separated (as evident from Fig. 4) with very low axial, relative tangential, and radial velocities. Flow is underturned in all regions away from the blade tip, with no indication of the presence of a strong leakage vortex; where one would encounter both underturning and overturning of the flow in the vortex region, as reported in a cascade (Lakshminarayana and Horlock, 1967, Fig. 24*b*). The mixing of the main flow and the leakage jet, which are at different angles, results in flow separation. The evidence presented later indicates that the vorticity is not high in this region, and there is no substantial static pressure variation. This seems to indicate that the leakage flow has not rolled up into a strong vortex at $X = 1.04$. The relative flow angles are low near the edge of the wake at $X = 1.04$, indicating that the flow is well behaved near both surfaces. The relative flow angles achieve design values at $R = 0.96$ near the blade surfaces, and near the midpassage at $R = 0.92$.

As the flow progresses downstream ($X = 1.64$), the separated region, wake flow, and the leakage flow mix out almost completely, resulting in uniform relative angle distribution across the passage in the tip region (Fig. 8). The flow is underturned in the entire region from $R = 0.92$ to 0.99. The leakage flow and interaction region mix and spread out across the entire passage, with no substantial inward movement. In many simulated cascades, the leakage vortex is observed to move inward downstream, influencing larger spanwise regions. In the present case, the leakage vortex is not observed, and the influence of interaction between the main flow and leakage jet does not spread substantially inward. The passage-averaged values of yaw angle, shown plotted in Fig. 9, confirm this conclusion. The passage-averaged values of yaw angle at $X = 1.04$ and 1.64 are shown compared with the earlier data at $X = 1.00$ and $\phi = 0.56$. The underturning of the flow is lower at all radial locations at lower loading. The average relative flow yaw angles increase as the flow progresses downstream from $X = 1.04$ to 1.64. The average underturning angle near the tip ($R > 0.985$) remains nearly the same, indicating that the inner layer of the annulus wall boundary layer is not disturbed. Major changes in average underturning angle occurs from $R = 0.94$ to 0.98. Near the trailing edge, the underturning angles are nearly identical at both loadings, except at the very tip ($R > 0.98$).

CONTOURS OF ISO-YAW ANGLE AT X=1.04

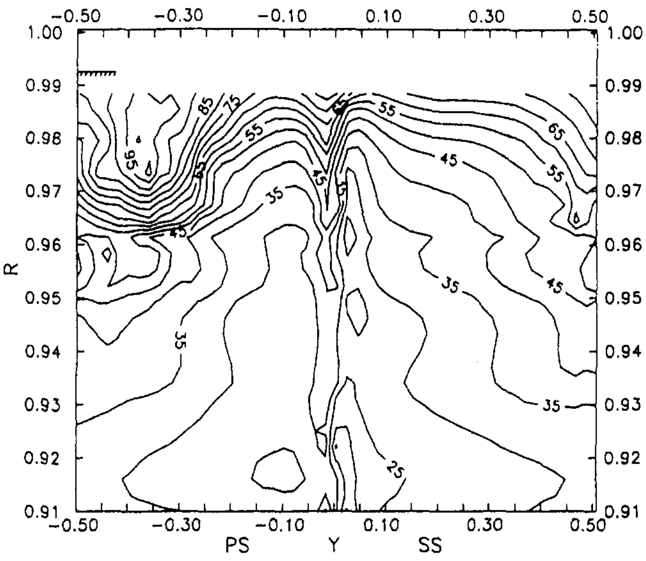

CONTOURS OF ISO-YAW ANGLE AT X=1.64

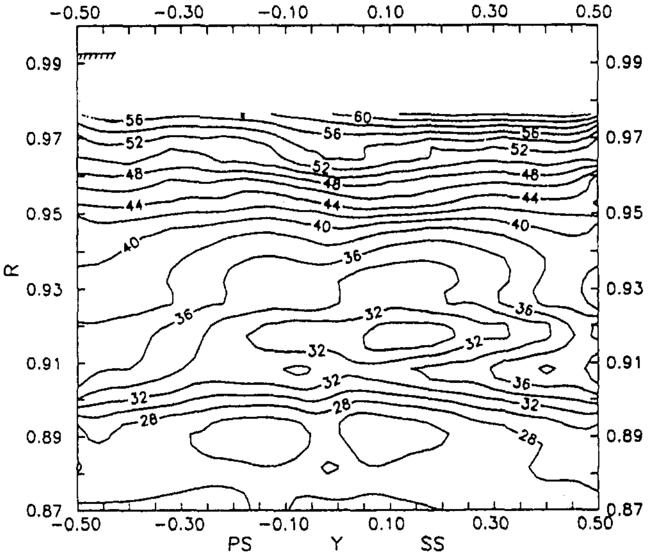

Fig. 8 Contours of iso-yaw angle at x = 1.04 and x = 1.64 (the numbers denote yaw angle, β, in deg)

Radial Velocity

Iso-radial velocity contours are shown in Fig. 10. At $X = 1.04$, the radial velocity is outward everywhere from $R = 0.91$ to $R = 0.98$, except a small region near the suction surface. Inward radial velocities are observed at the blade tip from $R = 0.985$ to $R = 0.99$. The radial flow is predominantly outward (indicated by positive values) outside the separated region (Figs. 4 and 10) and very small in the interaction or nearly separated region. The interaction of the leakage flow with the main flow tends to entrain fluid from the regions away from it. This is evident from $R = 0.95$ to 0.97, $Y = -0.10$ to -0.30 (near the pressure surface). The radial velocities are small in other regions. The radial velocities are generally lower near the suction surface from $Y = 0.1$ to 0.5. The absence of significant radial inward velocity elsewhere

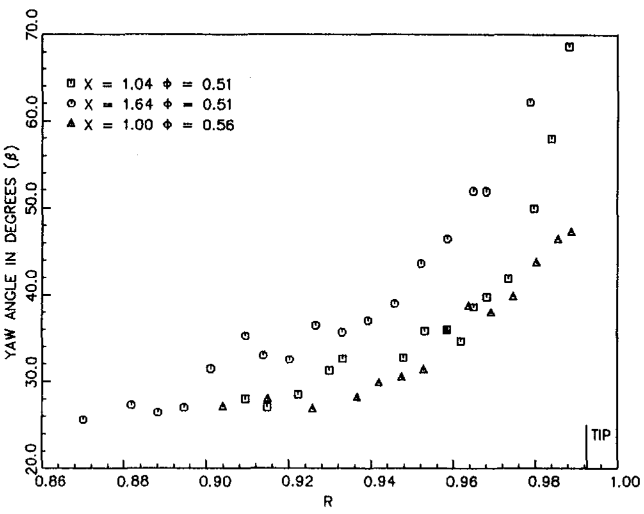

Fig. 9 Comparison of radial distribution of passage-averaged yaw angle ($\bar{\beta}$) at $\phi = 0.56$ and $\phi = 0.51$

indicates that the leakage flow has not rolled up to form a discrete vortex, a conclusion contrary to those drawn by other investigators (e.g., Inoue et al., 1986).

As the flow progresses downstream, the radial velocity across the passage becomes uniform across the passage due to rapid mixing of the leakage flow, separated flow, and the wake flow, except near the inner radius (Fig. 10). The maximum radial velocities measured is about 7 percent of the blade tip speed, decreasing to negligible values near $R = 0.87$.

Secondary Flow and Axial Vorticity

The secondary velocities in the $r-\theta$ plane are derived from the measured data by estimating the design flow angle (blade angle at outlet plus the deviation angle based on empirical correlations) and the measured pitch and yaw angles. Using this procedure, the secondary velocities were derived from the equation

$$\mathbf{W}_{\mathrm{sec}} = \mathbf{r}W_r + \mathbf{n}W_n \qquad (2)$$

where W_r is the radial velocities measured and reported earlier, and W_n is the velocity normal to the streamwise direction (estimated as indicated above). These velocity components are shown in Fig. 2. The secondary velocity vectors ($\mathbf{W}_{\mathrm{sec}}$) provide valuable information on the leakage and the shear-induced secondary flows. The secondary velocity vectors derived from the data are shown in Fig. 11 for $X = 1.04$ and $X = 1.64$.

At $X = 1.04$, the flow in the tip region ($R = 0.98$–0.99) is dominated by leakage flow with very little trace of secondary flow induced by the shear gradients. The secondary flow is predominantly radial, with large outward velocity, near the outer edge of the interaction or separated region. It should be emphasized here that the values of W_n are based on an empirical correlation for the deviation angle, and this is an estimated value. Hence the magnitude and the direction of W_n, especially when these values are low, should be viewed with caution. The secondary velocity vectors near the suction surface $Y = 0.0$ to 0.5 are usually small, and are of the same order of magnitude as the accuracy of measurement and estimation. The data at $X = 1.64$ indicates that W_n is significantly reduced at this station, with no appreciable decrease in radial velocities, except near the suction surface. The secondary velocity is outward everywhere, except in the tip region, where the annulus boundary layers are three dimensional (or skewed), with substantial velocity in the normal direction.

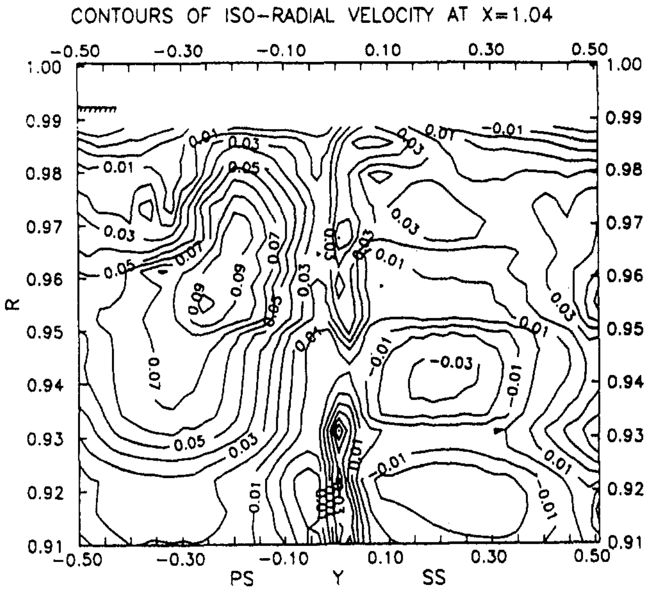

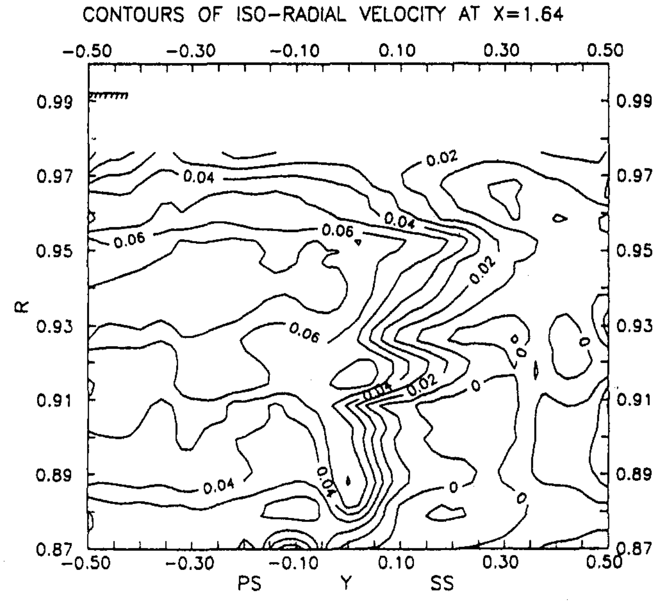

Fig. 10 Contours of iso-radial velocity at $x = 1.04$ and $x = 1.64$ (the numbers denote radial velocity, W_r)

Axial and Tangential Vorticity

The axial vorticity is calculated from the measured data using the equation

$$\omega_x = \frac{1}{r}\left[\frac{\partial}{\partial r}(rW_\theta) - \frac{\partial W_r}{\partial \theta}\right] \qquad (3)$$

where W_θ and W_r are the local relative tangential and radial velocities and θ is the tangential direction. The measurement program includes direct (as opposed to the derived values) measurement of W_r and W_θ at a large number of r and θ locations. Hence the axial vorticity can be calculated accurately. Furthermore, no attempt is made to derive the streamwise vorticity as it involves gradients of $\partial W_n/\partial r$ where W_n is based on an estimated design flow angle. Hence, only axial vorticity can be derived with confidence. The axial vorticity is related to the magnitude of the streamwise vorticity, induced by secondary and leakage flows. Furthermore, it

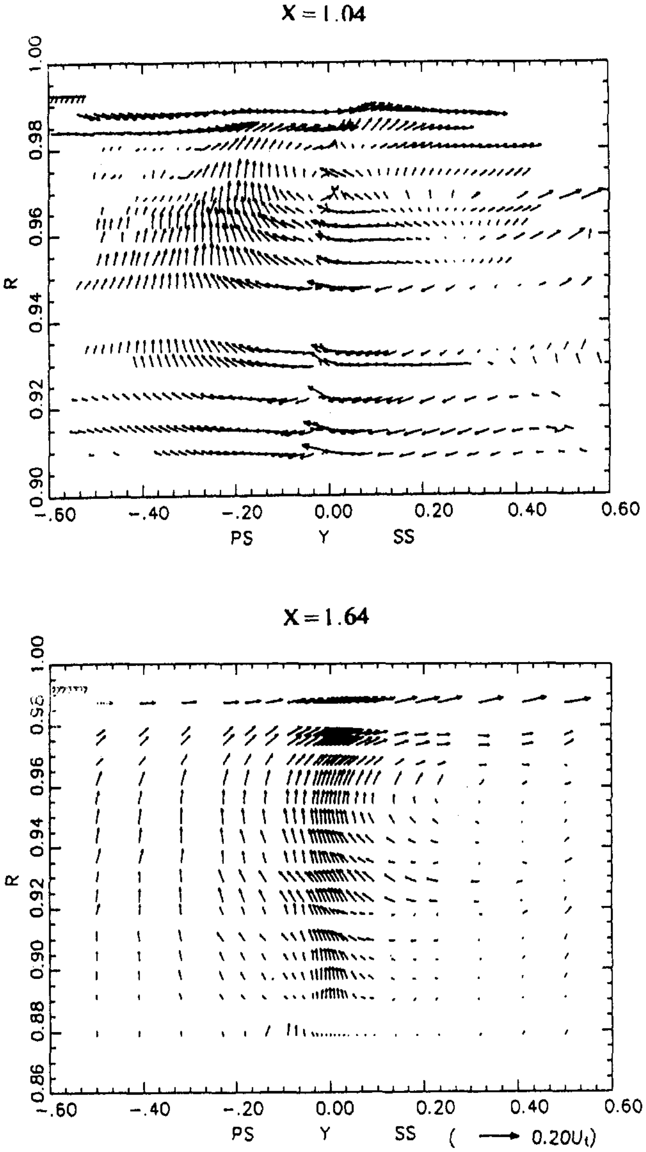

Fig. 11 Secondary velocity vectors ($nW_n + rW_r$) at $x = 1.04$ and $x = 1.64$

provides conclusive evidence on the presence, if any, of a leakage vortex. The contours of iso-axial vorticity, shown in Fig. 12, are based on vorticity generation inside the rotor given by

$$\omega_x = \omega_{x_2} - \omega_{x_1} \tag{4}$$

where ω_{x_1} is the inlet axial vorticity. The vorticity is nondimensionalized by 2Ω.

The iso-axial vorticity (ω_x) plot shows some very interesting features at $X = 1.04$. The vorticity has moderate values in the separated or interaction region. Very high values of vorticity occur from $R = 0.965$ to 0.975 in the passage from $Y = 0.31$ to 0.39, located close to the midpassage. The main contribution to the vorticity comes from $\partial W_\theta/\partial r$, which is large in this region (Fig. 6). This is probably caused by the interaction of the high-speed leakage jet with the main flow. Sudden reversal of the vorticity seems to confirm this hypothesis. The vorticity in the wake is of the same order of magnitude as the vorticity in the separated region.

As the flow progresses downstream ($X = 1.64$), the magnitude of axial vorticity decreases to very small values, especially in the leakage interaction regions. The jet mixing region as well as the separated regions have mixed out completely to provide very low values for the axial vorticity. But, axial velocity has increased substantially from $R = 0.91$ to 0.93, where high radial gradients in tangential velocity are also observed (Fig. 6). This may have been caused by the radial outward flow inside the wake in this region.

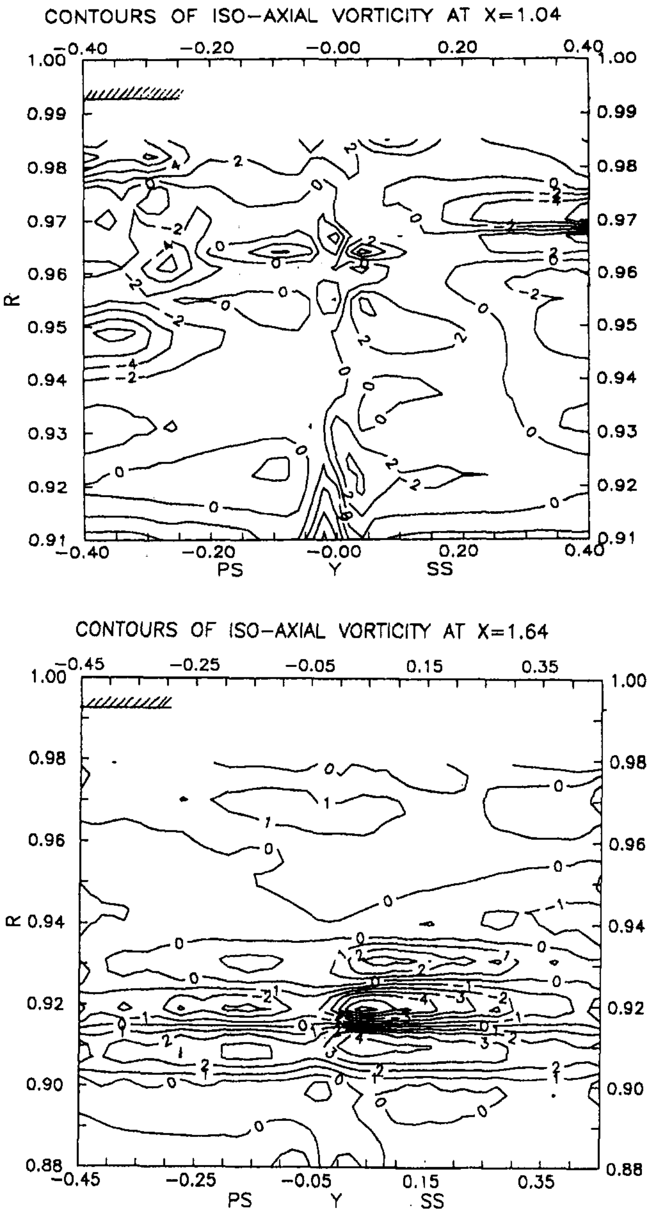

Fig. 12 Contours of iso-axial vorticity at $x = 1.04$ and $x = 1.64$ (the numbers denote ($\omega_x/2\Omega$))

The relative tangential vorticity can be approximated by

$$\omega_\theta = \frac{\partial W_x}{\partial r}$$

The gradient $\partial W_r/\partial x$ is neglected. This gradient may be much smaller than the gradient $\partial W_x/\partial r$. Nevertheless, an evaluation of approximate ω_θ for this flow provides additional information on the vorticity field and evidence on the presence or absence of the leakage vortex. The values of ω_θ are shown plotted in contour form in Fig. 13. The data in this plot are similar to the axial vorticity. The axial and tangential vorticity are low in the tip clearance region and high values occur near the midpassage in the region of $R = 0.93-0.97$. This again confirms lack of well-developed vortex system.

To check the hypothesis about the absence of a leakage

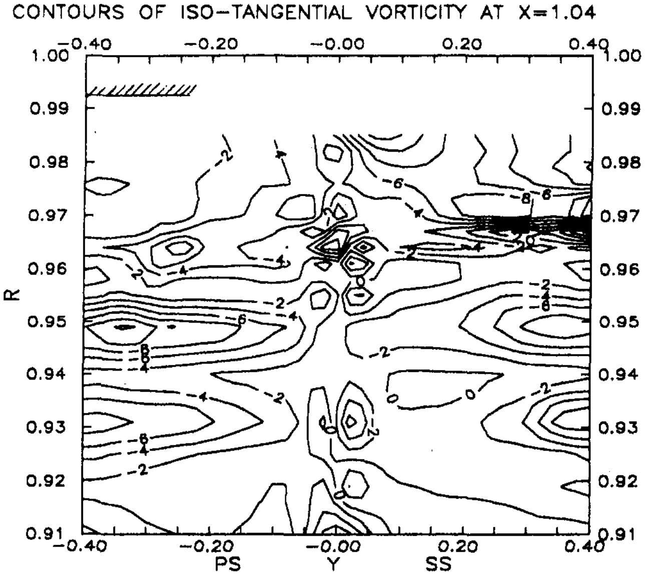
CONTOURS OF ISO-TANGENTIAL VORTICITY AT X=1.04

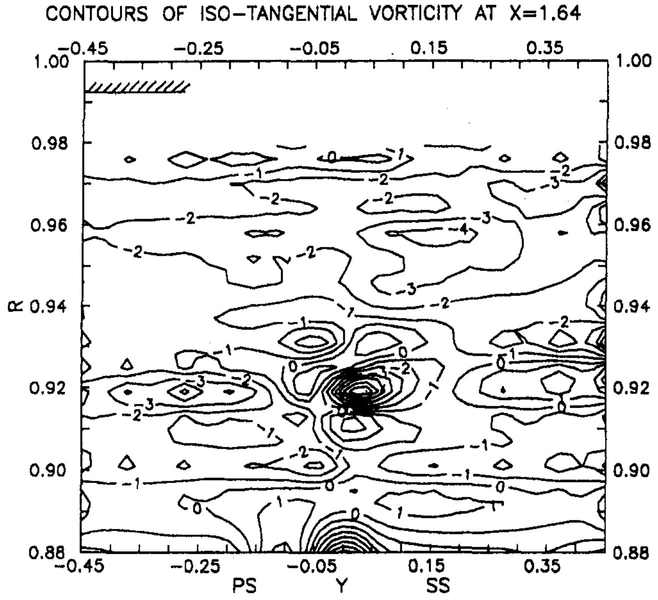
CONTOURS OF ISO-TANGENTIAL VORTICITY AT X=1.64

Fig. 13 Contours of iso-tangential vorticity at $x = 1.04$ and $x = 1.64$ (the numbers denote $(\omega_\theta/2\Omega)$)

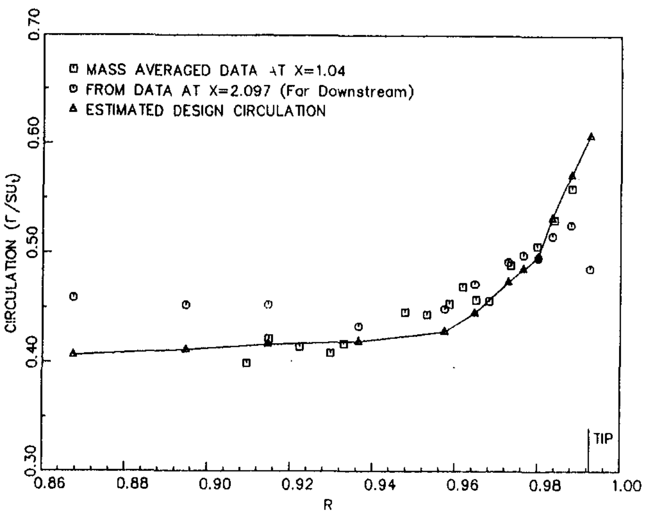

Fig. 14 Radial distribution of circulation

vortex, an attempt was made to assess the magnitude of shed vorticity due to the gap. This is related to the difference in circulation between the design values and the measured values, shown in Fig. 14. The actual (measured) values are based on the data at $X = 1.64$ and 2.097 using the actual (measured) inlet relative tangential velocity and the mass-averaged exit relative tangential velocity. This is an approximation and assumes two dimensionality in the flow. Hence the magnitude of Γ is plotted only to support the hypothesis. The design values are based on the measured inlet W_θ and the outlet $W_{\theta 2}$ based on the blade outlet angle. The far downstream values are based on the measurement at $X -$ 2.097, where the flow is nearly axisymmetric. It is clear that the circulation drops only in the outer 2–3 percent of the span from the tip. This is consistent with the data (at different loadings and tip clearance) presented earlier (Lakshminarayana and Pandya, 1984 (Fig. 6); Lakshminarayana and Murthy, 1988 (Fig. 16); Sitaram and Lakshminarayama, 1983 (Fig. 21)). The analysis of the data quoted in the earlier papers by the Penn State groups are based on the blade static, laser, and hot-wire measurements near the tip region. These data have been used to derive the magnitude of the retained lift or circulation in the tip region. All the earlier data as well as the present data (with larger tip clearance) indicate no noticeable decrease in lift or circulation along the blade; most of the decrease is confined to about 2–3 percent of the blade span from the tip. The value of Γ near the tip is about 20–30 percent less than the design values. This again confirms the retained lift concept introduced by Lakshminarayana and Horlock (1967).

Static Pressure Rise and Stagnation Pressure Rise Coefficient

The static pressure rise coefficient is defined by

$$C_p = \frac{p_2 - p_1}{\frac{1}{2}\rho U_t^2} \qquad (5)$$

Iso-contours of C_p are plotted in Fig. 15. It is evident from the C_p contours at $X = 1.04$ that the exit static pressure and the static pressure rise are nearly uniform across the passage, except in the wake, decreasing gradually toward the inner radius. Contrary to velocity and stagnation pressures, which vary substantially from blade to blade in the tip region, the static pressure is fairly uniform. The static pressure variation in the separated and the interaction zone (Fig. 2) is very small. On the basis of this, it is concluded that the leakage flow has not rolled up into a discrete vortex to form a core (solid body rotation), where the static pressures are likely to be much lower.

The measured stagnation pressure rise coefficient is defined by

$$\psi_A = \frac{P_{02} - P_{01}}{\frac{1}{2}\rho U_t^2} \qquad (6)$$

and the ideal pressure rise is defined by the Euler's equation

$$\psi_E = \frac{2U(V_{\theta 2} - V_{\theta 1})}{U_t^2} \qquad (7)$$

The difference between the two $(\psi_A - \psi_E)$ is a measure of the aerodynamic loss. The highest value of ψ_A occurs at the location where relative velocities are also minimum. Higher values also occur within the wake, where the relative velocities are low. These large values are caused by viscous and mixing effects. The relative velocities are reduced through the viscous dissipation of the relative kinetic energy. The

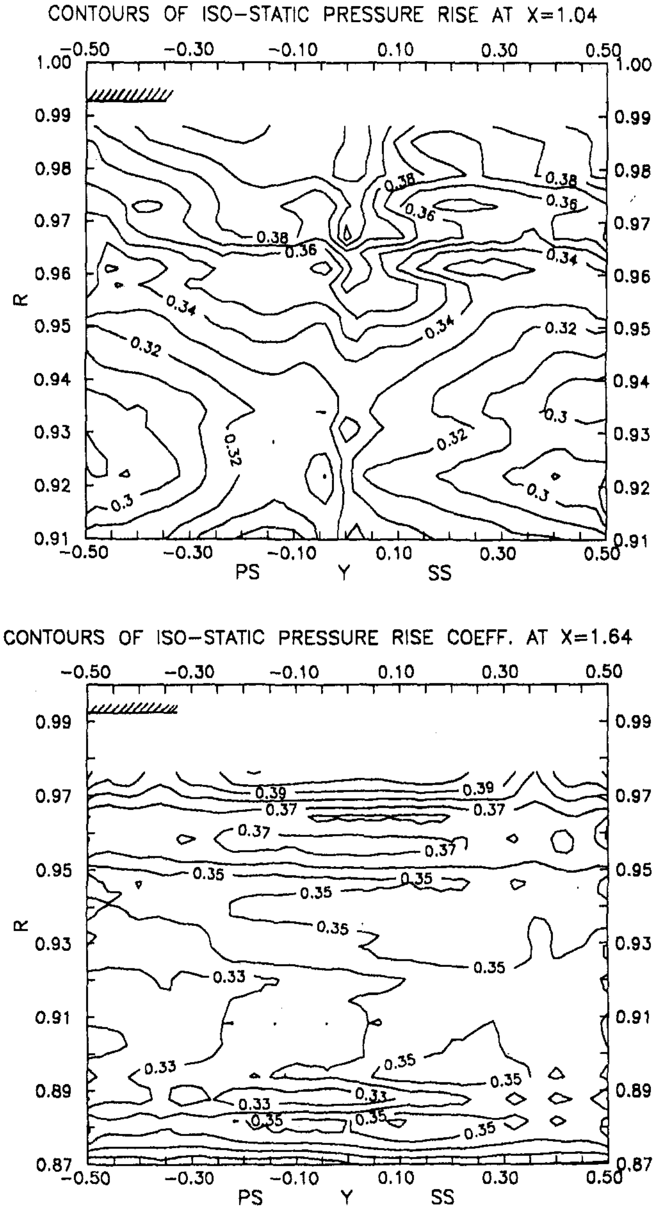

Fig. 15 Contours of iso-static pressure rise coefficient at $x = 1.04$ and $x = 1.64$ (the numbers denote static pressure rise coefficient, C_p)

mechanism causing such a high pressure rise is different from that caused by the flow turning, an inviscid effect. Such a phenomenon has been measured by many. A measure of how efficiently this pressure rise occurs is revealed by the Euler pressure rise coefficient and the difference between the two. The Euler pressure rise also shows very high values in the interaction region; the maximum difference $(\psi_A - \psi_E)$ was found to be as high as 40 percent in the interaction region. Hence the pressure rise achieved through pure viscous and mixing effects is very inefficient.

A proper measure of the pressure rise is the passage (mass) averaged values, as the axial velocities are very low or zero in regions where the stagnation pressure rise is high. The passage average values are based on Eq. (1) with $A = \psi_A$ or ψ_E. The radial distribution of passage-averaged pressure rise coefficient is plotted in Fig. 16. This plot shows a more realistic distribution of the $\bar{\psi}_A$, which is nearly constant along the radius, their values decreasing as the flow proceeds downstream. On the contrary, the passage-averaged Euler pressure rise near the tip is very high, and nearly constant from $X = 1.04$ to $X = 1.64$. The difference, $\bar{\psi}_E - \bar{\psi}_A$, represent the losses, which are very high near the tip.

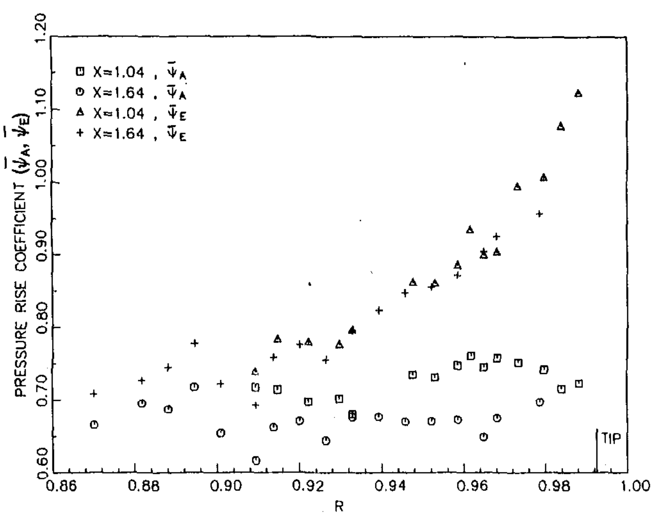

Fig. 16 Radial distribution of passage-averaged measured and Euler pressure rise coefficient $(\bar{\psi}_A, \bar{\psi}_E)$ at $\phi = 0.51$

Stagnation Pressure Loss Coefficient

The stagnation pressure loss coefficient, based on the equation

$$\psi_L = \frac{(P_{02})_R - (P_{01})_R}{\frac{1}{2}\rho U_t^2} \qquad (8)$$

is shown plotted in contour form in Fig. 17. The loss coefficient defined by Eq. (8) and the difference between $(\psi_E - \psi_A)$ are found to be nearly identical, as they should be. At $X = 1.04$, very high losses in relative stagnation pressure are evident in the interaction zone and these are much higher than the loss coefficients in the wake region. The losses near the pressure surface (midpassage to pressure surface) are generally much higher than the losses in the corresponding region on the suction side, except in the tip region from $R = 0.97$ to 0.99, where the magnitudes are similar. Downstream of the trailing edge ($X = 1.64$), the loss core in the tip region tends to mix out, providing nearly constant losses across the passage, with the exception of wake region, which extends from $R < 0.9$.

Blade-to-blade variations of the loss coefficient at five typical radii are shown in Fig. 18 to demonstrate the complex nature of loss distribution. Close to the tip, $R = 0.9883$, the losses are nearly uniform, except very near the suction side, where the radial outward flow has washed away the low energy region and convected it to other parts of the passage. Slightly away from $R = 0.9883$, the losses decrease substantially very near the suction side, but remain high everywhere else. At the lowest radius ($R = 0.9095$), the wake losses dominate the flow field. This tends to confirm the schematic nature of flow field shown in Fig. 2. The leakage flow emanating from the gap travels farther into the passage, mixing with the mainstream closer to the pressure surface. This sets up substantial radial outward flow near the suction surface as well as near the interaction region. The radial outward flow near the suction surface tends to energize the fluid in this region, decreasing the boundary layer growth and the wake width. Hence the leakage flow has a beneficial effect on the suction side. This is contrary to the phenomena observed in cascades, where the vortex tends to roll up near the suction side, causing considerable losses and flow separation. Furthermore, absence of a discrete and well-defined

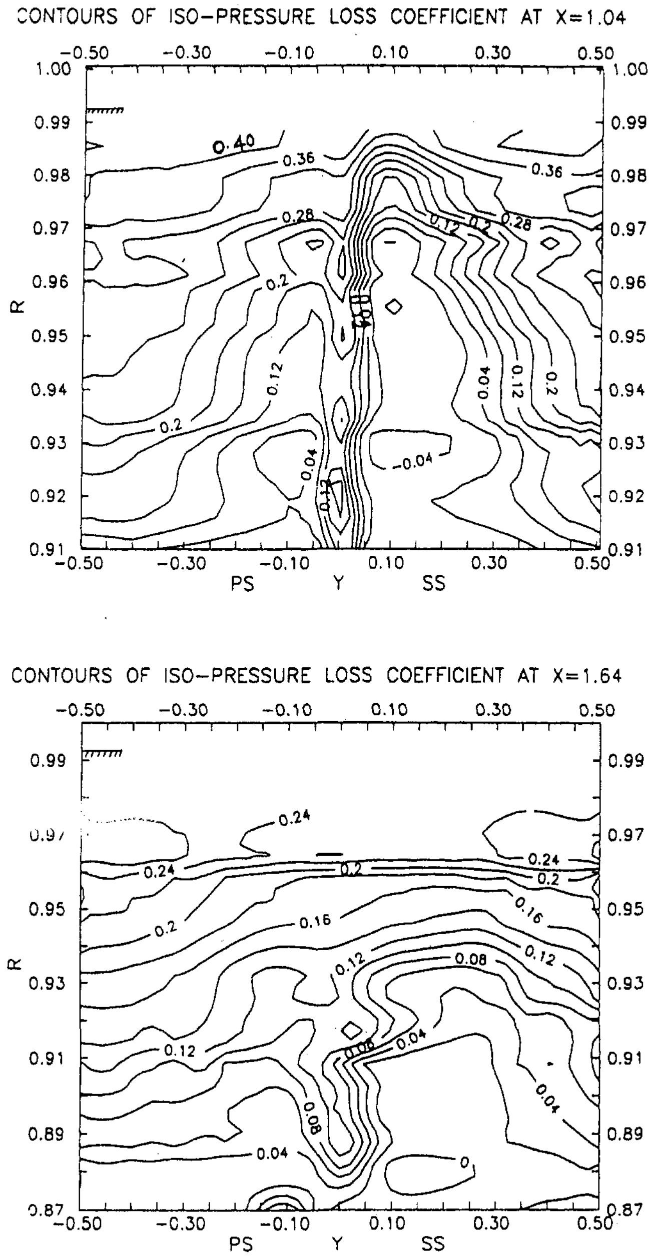

Fig. 17 Contours of iso-pressure loss coefficient at $x = 1.04$ and $x = 1.64$ (the numbers denote pressure loss coefficient, ψ_L)

loss core region at $X = 1.04$ seems to indicate the absence of a combined vortex, where very high losses occur within the core with solid body rotation.

The passage-averaged stagnation pressure loss coefficient is plotted and compared with the earlier data at $\phi = 0.56$ (with the same tip clearance) in Fig. 19. The losses are higher for the higher loading case. At $X = 1.04$, $\phi = 0.51$, the losses increase rapidly from $R = 0.96$ to 0.99. As the flow progresses downstream, the loss core tends to mix out, increasing the losses at inner radii and decreasing it in the outer radii. One of the interesting observations is the similarity in the radial distribution of losses at $\phi = 0.51$ (taken with a five-hole probe) and $\phi = 0.56$ (taken with a kiel probe). Both of_them show discontinuity in the radial loss gradient $(\partial\psi_L/\partial r)$. For example, both distribution show reduced losses near $R = 0.98$. This may be the location of the peak velocity in the leakage flow jet. The mixing would be intense in the periphery of the leakage jet, initially, before the main flow starts interacting with the core of the leakage jet. It is also evident from this plot that the loss near the tip doubled when the flow coefficient decreased from 0.56 to the peak pressure rise condition at $\phi = 0.51$.

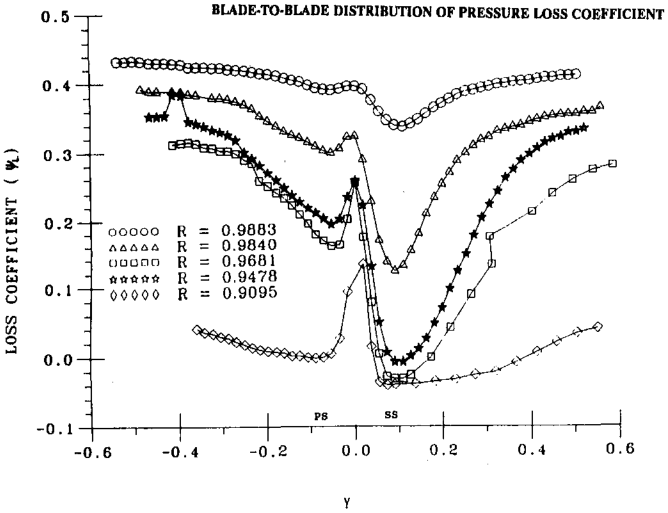

Fig. 18 Blade-to-blade distribution of pressure loss coefficient

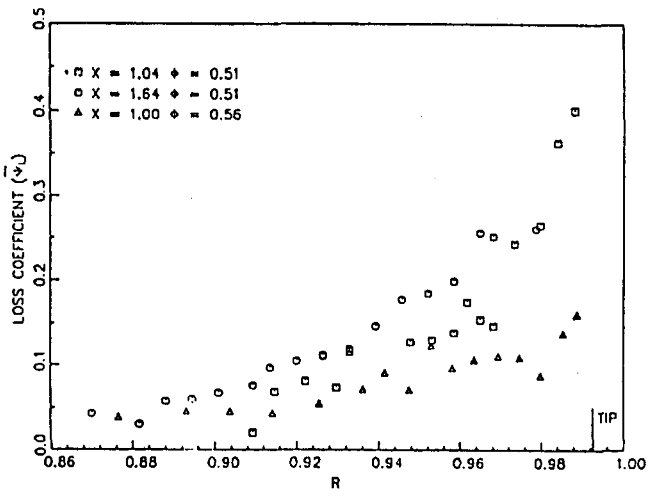

Fig. 19 Comparison of radial distribution of passage-averaged pressure loss $(\bar{\psi}_L)$ at $\phi = 0.51$ and $\phi = 0.56$

Discussion and Conclusions

There are substantial differences in the structure of tip clearance flow observed in cascades and rotors. In cascades (Lakshminarayana and Horlock, 1967; Storer and Cumpsty, 1991), the leakage flow rolls up into a discrete vortex, which is located near the suction surface and slightly inward from the tip. This increases the peak suction pressures on the blade and introduces very high losses with a discrete loss core located close to the suction surface. Inoue et al. (1986) provided detailed data near the tip region and observed the presence of a discrete vortex. One possible difference between this experiment and the present data is that Inoue's data are from a rotor alone configuration with very low turning, but comparable blade speed. It is possible that inlet swirl, high turbulence, and high blade loading present in the author's experiment cause intense mixing of the leakage jet before it had a chance to roll up into a discrete vortex. Inoue's data clearly show both the underturning and overturning regions in the flow, near the tip, but the present data reveal no such features. The leakage jet issuing from the gap is of high velocity and mixes rapidly with the mainstream.

Intense mixing between these two dissimilar and high-speed jets, with widely varying flow angle, produce intense shearing and flow separation, which is consistent with Storer and Cumpsty's (1991) remarks. Similar conclusions can be drawn from the data reported by Goto (1992). Hence the formation of a vortex depends on various parameters, some of which are: configuration (single stage, multistage, cascade, rotor alone), inlet flow turbulence and the annulus wall boundary layer thickness, the difference in magnitude and direction of the velocity in the leakage jet and in the mainstream flow, blade speed, and stagger angle. These are in addition to the widely accepted parameters such as tip clearance height, Reynolds number, Mach number, thickness of the blade, blade loading, etc. In a recent paper, Moyle et al. (1992) express similar doubts about the role of tip leakage vortex, but their results, based on casing pressure data alone, are not conclusive.

The data by Hunter and Cumpsty (1982) show some of the features described in the present experiment. But there are substantial differences in the structure of tip clearance flow between the two experiments. It should be remarked here again that Hunter and Cumpsty's experiment is rotor alone configuration, with low turbulence and lower loading (Table 1). Neither the present data nor Hunter and Cumpsty's (1982) data show large radial inward flows near the tip region measured by Inoue in his rotor. This seems to confirm the absence of a Rankine type of combined vortex in a realistic configuration. One of the objectives of this investigation was to resolve discrepancies in the phenomena reported by various authors, and the present measurement program was designed to cover data on a very detailed experimental grid to resolve this issue. The absence of a discrete Rankine combined vortex in this configuration has been clearly established. The flow in a multistage environment should be closer to these data than the flow in a cascade.

Based on the data reported in this paper, a schematic of the structure of tip clearance flow in an axial flow compressor can be drawn, as shown in Fig. 2. The leakage jet emerging from the tip clearance travels toward the pressure surface. The mixing of this high-speed leakage jet with the main flow, both of which involve large flow angle changes at the interface, produces a separated region as shown in Fig. 2. This separated region entrains fluid from across the passage as well as from the lower radii. This region has very low axial, tangential, and radial velocities, and the losses are very high. The radial flow is outward everywhere in the tip clearance region, with the exception of the region very close to the tip of the blade and at inner radii near the suction surface.

References

Cho, S. O., Kang, D. J., and Cho, K. R., 1990, "An Experimental Study on the Vorticity Distribution in Flows Behind an Axial Flow Rotor," *Proc. 2nd KSME–JSME Fluids Engineering Conference*, Seoul, Korea, Vol. 2, pp. 2–81.

Goto, A., 1992, "Three-Dimensional Flow and Mixing in an Axial Flow Compressor With Different Rotor Tip Clearances," ASME JOURNAL OF TURBOMACHINERY, Vol. 114, pp. 675–685.

Hunter, I. H., and Cumpsty, N. A., 1982, "Casing Wall Boundary Layer Development Through an Isolated Compressor Rotor," ASME *Journal of Engineering for Power*, Vol. 104, pp. 805–818.

Inoue, M., et al., 1986, "Behavior of Tip Leakage Flow Behind an Axial Compressor Rotor," ASME *Journal of Engineering for Gas Turbines and Power*, Vol. 108, pp. 7–14.

Inoue, M., and Kuroumaru, M., 1989, "Structure of Tip Clearance Flow in an Isolated Axial Compressor Rotor," ASME JOURNAL OF TURBOMACHINERY, Vol. 111, pp. 250–256.

Lakshminarayana, B., and Horlock, J. H., 1967, "Leakage and Secondary Flows in Compressor Cascades," ARC R & M 3483.

Lakshminarayana, B., et al., 1982, "Three-Dimensional Flow Field in the Tip Region of a Compressor Rotor Passage, Parts I and II," ASME *Journal of Engineering for Power*, Vol. 104, pp. 760–781.

Lakshminarayana, B., and Pandya, A., 1984, "Tip Clearance Flow in a Compressor Rotor Passage at Design and Off Design Conditions," ASME *Journal of Engineering for Gas Turbines and Power*, Vol. 106, p. 570.

Lakshminarayana, B., and Murthy, K. N. S., 1988, "Laser-Doppler Velocimeter Measurement of Annulus Wall Boundary Layer Development in a Compressor Rotor," ASME JOURNAL OF TURBOMACHINERY, Vol. 110, p. 377–385.

Lakshminarayana, B., Zhang, J., and Murthy, K. N. S., 1990, "The Effects of Tip Clearance on Flow Field and Losses in a Compressor Rotor," *Z. Flugwiss. Weltram.*, Vol. 14, pp. 273–281.

Moyle, I. N., Walker, G. J., and Shreeve, R. P., 1992, "Stator Averaged, Rotor Blade-to-Blade Near Wall Flow in a Multistage Axial Compressor With Tip Clearance Variation," ASME JOURNAL OF TURBOMACHINERY, Vol. 114, pp. 668–674.

Murthy, K. N. S., and Lakshminarayana, B., 1986, "Laser Doppler Velocimeter Measurement in the Tip Region of a Compressor Rotor," *AIAA Journal*, Vol. 24, pp. 807–814.

Pandya, A., and Lakshminarayana, B., 1983, "Investigation of the Tip Clearance Flow Inside and at the Exit of a Compressor Rotor Passage, Parts I and II," ASME *Journal of Engineering for Power*, Vol. 105, pp. 1–17.

Ravindranath, A., and Lakshminarayana, B., 1980, "Mean Velocity and Decay Characteristics of the Near and Far Wake of a Moderately Loaded Compressor," ASME *Journal of Engineering for Power*, Vol. 103, pp. 131–141.

Sitaram, N., and Lakshminarayama, B., 1983, "End Wall Flow Characteristics and Overall Performance of an Axial Flow Compressor Stage," NASA CR 3671.

Storer, J. A., and Cumpsty, N. A., 1991, "Tip Leakage Flow in Axial Compressors," ASME JOURNAL OF TURBOMACHINERY, Vol. 113, pp. 252–259.

Treaster, A. L., and Yocum, A. M., 1979, "The Calibration and Application of Five-Hole Probes," *ISA Transactions*, Vol. 18, No. 3.

von Karman Institute, 1985, "Tip Clearance Effects in Axial Turbomachines," VKI LS 1985-05.

Numerical Simulation of Tip Clearance Effects in Turbomachinery

A. Basson

B. Lakshminarayana

Dept. of Aerospace Engineering,
The Pennsylvania State University,
University Park, PA 16802

The numerical formulation developed here includes an efficient grid generation scheme, particularly suited to computational grids for the analysis of turbulent turbomachinery flows and tip clearance flows, and a semi-implicit, pressure-based computational fluid dynamics scheme that directly includes artificial dissipation, and is applicable to both viscous and inviscid flows. The value of this artificial dissipation is optimized to achieve accuracy and convergency in the solution. The numerical model is used to investigate the structure of tip clearance flows in a turbine nozzle. The structure of leakage flow is captured accurately, including blade-to-blade variation of all three velocity components, pitch and yaw angles, losses and blade static pressures in the tip clearance region. The simulation also includes evaluation of such quantities as leakage mass flow, vortex strength, losses, dominant leakage flow regions, and the spanwise extent affected by the leakage flow. It is demonstrated, through optimization of grid size and artificial dissipation, that the tip clearance flow field can be captured accurately.

Introduction

Tip leakage flows are an important source of unsteadiness and three dimensionality of the flow in turbomachines, while contributing significantly to loss of efficiency and useful work in turbomachines. They have therefore been the subject of many studies. The earliest contributions to the quantification of the effects of tip leakage flows were based on analytical and semi-empirical approaches, e.g., Lakshminarayana (1970), Lakshminarayana and Horlock (1965), and more recently, Moore and Tilton (1988), and Chen et al. (1991).

Although a large number of numerical models of fluid flow have been published, their applications to the complex flows encountered in turbomachinery bladerows have had mixed success (Lakshminarayana, 1991). In a general sense, the purpose of the present paper is to contribute to the knowledge of the approximations inherent in numerical models, to consider ways in which to improve the efficiency and accuracy of the models, and to demonstrate the usefulness of such a model in understanding the physical phenomena involved in complex turbomachinery flows, especially the tip clearance flows.

In the present development, concepts that are common in time-marching methods have been introduced into the SIMPLE type formulation to improve its accuracy significantly. The most significant extension to the SIMPLE type methods is in the direct use of artificial dissipation terms. The effect of the artificial dissipation is demonstrated quantitatively for a number of internal flow cases (Basson, 1992).

The numerical model developed here and the new grid topology developed earlier (Basson et al., 1993), are applied in an investigation of the tip leakage vortex in a turbine nozzle bladerow. This phenomenon was chosen, in the first place, to test the ability of the model to capture such complex flow structures, but also to gain a better understanding of the physical phenomena involved in the origin, development, and decay of the tip leakage flows. The complexity of the flow, and the associated strong gradients in flow properties, limit the ability of experimental investigations to quantify the flow structure fully. By necessity, numerical solutions are of a more global nature, thus allowing more detailed investigations of the physical phenomena involved.

Numerical Technique

The numerical scheme employed for the investigation of the tip clearance flow discussed here is the extension of the SIMPLE scheme (Patankar, 1980). The scheme differs from previous SIMPLE-type schemes (e.g., Rhie and Chow, 1983; Hah, 1984; Pouagare and Delaney, 1986; Bansod and Rhie, 1990; Hobson and Lakshminarayana, 1991) in its use of central differencing of the convective terms with direct addition of artificial dissipation. In the extensive review by Patankar (1988), no reference is made to SIMPLE schemes that include artificial dissipation terms directly. SIMPLE type methods commonly use schemes such as the powerlaw and quadratic upwind schemes, which include artificial dissipation indirectly, as demonstrated by Basson and Lakshminarayana (1994). The direct inclusion of artificial dissipation terms is more common in methods that can be termed "time-marching" (e.g., Pulliam, 1986).

In the tradition of semi-implicit methods, the momentum, energy, and turbulence equations are considered to be specific cases of a general convection-diffusion scalar transport equation. The resulting form, for a steady flow and an isotropic diffusion coefficient in generalized coordinate systems, is given by

$$\frac{\partial(\rho J G_1 \phi)}{\partial \xi} + \frac{\partial(\rho J G_2 \phi)}{\partial \eta} + \frac{\partial(\rho J G_3 \phi)}{\partial \zeta}$$
$$= \frac{\partial}{\partial \xi}\left(\Gamma \alpha J \frac{\partial \phi}{\partial \xi} + \Gamma \theta_1 J \frac{\partial \phi}{\partial \eta} + \Gamma \theta_2 J \frac{\partial \phi}{\partial \zeta}\right)$$
$$+ \frac{\partial}{\partial \eta}\left(\Gamma \beta J \frac{\partial \phi}{\partial \eta} + \Gamma \theta_1 J \frac{\partial \phi}{\partial \xi} + \Gamma \theta_3 J \frac{\partial \phi}{\partial \zeta}\right)$$
$$+ \frac{\partial}{\partial \zeta}\left(\Gamma \gamma J \frac{\partial \phi}{\partial \zeta} + \Gamma \theta_2 J \frac{\partial \phi}{\partial \xi} + \Gamma \theta_3 J \frac{\partial \phi}{\partial \eta}\right) + JS \quad (1)$$

The following second and fourth-order artificial dissipation terms are added to the right-hand side of Eq. (1):

Contributed by the International Gas Turbine Institute and presented at the 38th International Gas Turbine and Aeroengine Congress and Exposition, Cincinnati, Ohio, May 24–27, 1993. Manuscript received at ASME Headquarters March 17, 1993. Paper No. 93-GT-316. Associate Technical Editor: H. Lukas.

$$+\frac{1}{2}\epsilon_2\left[\frac{\partial}{\partial\xi}\left(|\rho JG_1|\frac{\partial\phi}{\partial\xi}\right)+\frac{\partial}{\partial\eta}\left(|\rho JG_2|\frac{\partial\phi}{\partial\eta}\right)+\frac{\partial}{\partial\zeta}\left(|\rho JG_3|\frac{\partial\phi}{\partial\zeta}\right)\right] \qquad (2a)$$

$$-\frac{1}{8}\epsilon_4\left[\frac{\partial}{\partial\xi}\left(|\rho JG_1|\frac{\partial^3\phi}{\partial\xi^3}\right)+\frac{\partial}{\partial\eta}\left(|\rho JG_2|\frac{\partial^3\phi}{\partial\eta^3}\right)+\frac{\partial}{\partial\zeta}\left(|\rho JG_3|\frac{\partial^3\phi}{\partial\zeta^3}\right)\right] \qquad (2b)$$

The central difference scheme used here is unstable when solely used for the convection term for high Reynolds number flows. The main reason is that the central differencing is not dissipative and the physical viscous terms cannot damp the error at high wave numbers, even in viscous flow computations with small grid spacing (Kunz et al., 1993).

Higher order upwinding schemes used in the time-marching methods are generally more accurate than the first-order upwind scheme, but inherently include certain amount of artificial dissipation (Pulliam, 1986). Basson and Lakshminarayana (1994) showed that the more accurate QUICK scheme (Leonard, 1979) is equivalent to central differencing plus third-order and fourth-order dissipation. Thus, the disadvantage of these higher order upwind schemes is the lack of control on the amount of numerical dissipation. In the scheme developed here, a second-order and a fourth-order artificial dissipation term are added explicitly to control the numerical dissipation (Eq. (2)).

The use of a nonstaggered grid will introduce pressure solutions that have decoupled odd and even grid points. In order to circumvent this problem, Rhie and Chow (1983) proposed a pressure-weighting scheme to link the odd and even grid points. Basson and Lakshminarayana (1994) has proved that this scheme is equivalent to addition of a fourth-order artificial dissipation to the pressure correction equation with proper coefficients. The original pressure-weighting method has too much dissipation and this affects the accuracy of the solution. Therefore, in the present work, a 20 to 30 percent value of the original pressure weighting is used to provide a smooth pressure field.

Second-order dissipation terms have a stronger smoothing effect than fourth-order dissipation terms, because the second-order dissipation terms are sensitive to nonzero second derivatives, thus opposing variations from linear distributions. The fourth-order dissipation terms only react to nonzero fourth derivatives, thus allowing distributions represented by cubic or lower order polynomials. The smoothing effects of fourth-order dissipation terms are therefore less severe than those of second-order dissipation terms.

The advantage of the inclusion of these terms directly, rather than indirectly through one-sided differencing schemes, is that the amount of artificial dissipation is clear and can be controlled. Basson and Lakshminarayana (1994) showed that the control provided by the direct inclusion of these terms is essential for the accurate modeling of complex flows on current practical grids.

The finite difference approximation to Eqs. (1) and (2) is obtained by applying the second-order central difference approximations of first and second derivatives to the respective terms. The cross derivative terms (i.e., those terms containing θ_1, θ_2, or θ_3) and the source term in Eq. (1) are treated explicitly, in other words they are calculated from the latest estimate of the solution. The remaining terms in Eq. (1) and the second-order artificial dissipation terms in Eq. (2) are treated implicitly.

The second-order difference approximation of the fourth-order artificial dissipation terms involve 13 grid points. If all the grid points' contributions are treated implicitly, a line relaxation procedure would involve the solution of a sparse-banded matrix. The solution of tridiagonal matrix equations is far more economical, particularly when considering the number of times that the matrix equations have to be solved. The fully explicit treatment of the fourth-order artificial dissipation terms, however, introduces stability limits on the amount of second-order artificial dissipation that can be used. As a compromise, the difference approximation of these dissipation terms is split into two parts, respectively, the three-point and five-point difference approximations of a second derivative. To demonstrate this approach, consider the difference stencil for the following artificial dissipation term (assuming unit grid spacing; refer to Fig. 1 for grid vortex notation):

$$\left(\frac{\partial^4\phi}{\partial\xi^4}\right)_P \approx -\phi_{ww} - 4\phi_w + 6\phi_P - 4\phi_E + \phi_{EE}$$

$$= (\phi_{ww} - 2\phi_P + \phi_{EE}) - 4(\phi_w - 2\phi_P + \phi_E) \qquad (3)$$

To retain the conservative form of Eq. (3), this split has to be formulated in terms of the difference approximation for a

Nomenclature

C_p = pressure coefficient = $(p_{in} - p)/Q_{in}$
E_R = nondimensional local timestep (Eq. (6))
$\hat{e}_n$, $\hat{e}_r$ = normal and radial direction unit vectors
G_1 = contravariant velocity in ξ direction = $\xi_x u + \xi_y v + \xi_z w$
G_2 = contravariant velocity in η direction = $\eta_x u + \eta_y v + \eta_z w$
G_3 = contravariant velocity in ζ direction = $\zeta_x u + \zeta_y v + \zeta_z w$
J = Jacobian of coordinate transformation
k = turbulent kinetic energy
K = leakage mass flow parameter (Eqs. (10) and (11))
$\dot{m}_L$ = leakage mass flow in the gap region
$\dot{m}_1$ = inlet mass flow in the gap region
P_0 = total pressure
PS = pressure side of blade
p = static pressure
Q_{in} = inlet dynamic pressure
S = source term/blade spacing
SS = suction side of blade
u, v, w = Cartesian velocity components
$\underline{V}$ = total velocity
V_θ = absolute tangential velocity
x, y, z = Cartesian coordinates (axial, tangential and spanwise)
Z = spanwise distance (measured from endwall)
α, β, γ = $\nabla\xi\cdot\nabla\xi$, $\nabla\eta\cdot\nabla\eta$, $\nabla\zeta\cdot\nabla\zeta$
Γ = diffusion coefficients
ϵ = dissipation rate per unit mass of k
ϵ_2, ϵ_4 = coefficient for second and fourth-order artificial dissipation
ζ_L = total pressure loss coefficient = $((P_0)_{in} - P_0)/Q_{in}$
$\bar{\zeta}_L$ = passage-averaged total pressure loss coefficient
θ_1, θ_2, θ_3 = $\nabla\xi\cdot\nabla\eta$, $\nabla\xi\cdot\nabla\zeta$, $\nabla\eta\cdot\nabla\zeta$
μ, μ_e, μ_t = absolute, effective $(\mu + \mu_t)$, and eddy viscosity
ν = kinematic viscosity
ξ, η, ζ = generalized coordinates (unit increments in computational domain)
ρ = density
τ = tip clearance height
ϕ = general scalar dependent variable

Subscripts

in = inlet

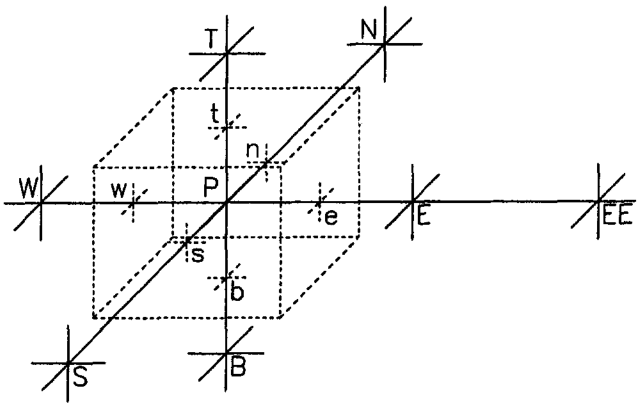

Fig. 1 Grid vortex and control volume face notation

third derivative at a control volume face. This is accomplished as follows:

$$\left(\frac{\partial^3\phi}{\partial\xi^3}\right)_e \approx -\phi_w + 3\phi_P - 3\phi_E + \phi_{EE}$$

$$= (-\phi_w - \phi_P + \phi_E + \phi_{EE}) - 4(-\phi_P + \phi_E) \quad (4)$$

By treating the terms in the first brackets on the right-hand side of Eq. (4) explicitly and the remainder implicitly, the use of tridiagonal matrix solution techniques can be retained, but the stability limitations associated with a fully explicit treatment would be relaxed.

The difference form of the general convection-diffusion Eq. (1) is derived in Basson and Lakshminarayana (1994). The final form is as follows:

$$(a^P)^*\phi_P = a^E\phi_E + a^W\phi_W + a^N\phi_N + a^S\phi_S + a^T\phi_T + a^B\phi_B + (S_\phi)^* \quad (5)$$

The coefficients $a^P, a^E \ldots$ are given by Basson and Lakshminarayana (1994).

Underrelaxation of the difference equations is implemented in the present formulation according to the E-factor scheme of Van Doormaal and Raithby (1984). This factor fulfills the role equivalent to that of the local timestepping scheme commonly used in time-marching formulations. According to this scheme, Eq. (5) is modified as follows:

$$a^P\phi_P = a^E\phi_E + a^W\phi_W + a^N\phi_N + a^S\phi_S + a^T\phi_T + a^B\phi_B + S_\phi \quad (6)$$

$$a^P = (a^P)^*\left(1 + \frac{1}{E_R}\right), \quad S_\phi = (S_\phi)^* + \frac{(a^P)^*}{E_R}\phi_P^o$$

where ϕ_P^o is the current estimate of ϕ_P.

Experience has shown that the overall convergence rate of whole system of equations is dominated by the pressure equation's convergence rate. The total iteration time is therefore not very sensitive to how close the value of E_R is to the optimum.

Continuity and Pressure Correction Equation. In the formulation used here, the continuity equation is enforced through a pressure correction equation formulated for a nonstaggered grid.

The pressure correction equation, as used in the present formulation, is given in Basson and Lakshminarayana (1994) and will not be repeated here for brevity. Similar developments have been given, e.g., Rhie and Chow (1983), Hah (1984), and Hobson and Lakshminarayana (1991). To obtain control over the amount of dissipation added, the pressure-weighting approach is replaced by the direct inclusion of fourth-order artificial dissipation terms in the continuity equation. Adding terms for the η- and ζ-directions, the artificial dissipation term for pressure is as follows:

$$0.25\epsilon_{pw}\left[\frac{\partial}{\partial\xi}\left(a^{ew}\frac{\partial^3 p}{\partial\xi^3}\right) + \frac{\partial}{\partial\eta}\left(a^{ns}\frac{\partial^3 p}{\partial\eta^3}\right) + \frac{\partial}{\partial\zeta}\left(a^{th}\frac{\partial^3 p}{\partial\zeta^3}\right)\right] \quad (7)$$

where a^{ew}, a^{ns}, a^{th} are coefficients of the pressure equation (Basson and Lakshminarayana, 1994).

Note that when $\epsilon_{pw} = 1$, this dissipation term will result in a formulation equivalent to the original pressure weighting scheme.

Turbulence Model and Boundary Conditions. The turbulence model employed in the numerical model is the low-Reynolds-number $k-\epsilon$ model of Chien (1982). This model was found to be accurate and gave good numerical stability in the present development.

Although it may not be first obvious, both the production and the dissipation term in the k equation depend indirectly on k. The approach that has been followed in the implementation of the model is to ensure that the dissipation term reacts as rapidly as possible to changes in the production term. The dissipation term is therefore calculated implicitly, while the production term is calculated explicitly.

All the properties are specified at inlet boundary, located far upstream. At the outlet boundary, located far downstream, all the flow gradients are assumed to be zero. The treatment of the periodic boundaries was aimed at making the numerical boundary invisible to the solution. This is accomplished fully by the use of a periodic solution scheme where the coupling between the opposite periodic boundaries is coded directly.

The boundary condition on the solid walls depends on the physical property being transported. In the case of u, v, w, and k the only physically correct boundary condition is the no-slip wall condition, whereby the values of these properties are identically zero on the solid walls. The boundary condition for ϵ depends on the turbulence model being used. In the model used here, the value of $(\epsilon - 2\nu k/y^2)$ is zero at the walls. The boundary layer approximations provide a good basis for setting the pressure gradient normal to the wall to zero. In more complex flows with appreciable turbulence, rotation, or gravitation effects, the appropriate Neumann boundary condition used is as follows:

$$\frac{\partial p}{\partial n} = \rho\frac{(V_\theta)^2}{r}\hat{e}_n\cdot\hat{e}_r + \rho g\cdot\hat{e}_n - \frac{2}{3}\frac{\partial\rho k}{\partial n} \quad (8)$$

Overall Solution Scheme and Validation. The concepts presented above were used to develop a new three-dimensional, semi-implicit pressure correction code aimed at the modeling of complex flows in turbomachinery bladerows. The artificial dissipation scheme presented above is applied to the momentum and pressure correction equations. The powerlaw scheme is applied to the $k-\epsilon$ model to maintain numerical stability of the model, which requires large artificial terms.

The formulation was also modified to be able to compute inviscid two-dimensional flows, through the elimination of viscous effects and by the replacement of the no-slip wall boundary condition by a slip wall boundary condition. The development of such an inviscid flow formulation was necessary for the evaluation of artificial dissipation effects (Basson and Lakshminarayana, 1994).

The momentum and other convection-diffusion equations all use the same routine for the calculation of the coefficients of the finite difference equation. The source terms for each equation are, however, coded separately. In the ADI solution scheme, the change in the convected property is calculated by using only the residual of the equation as source term in the difference equation. This approach is less susceptible to rounding errors, because the source term will be zero in the converged solution, thus producing zero corrections to the convected property.

The formulation presented here was implemented in a code that has subsequently been tested and validated for a number of applications. The model has been validated against benchmark quality data for a three-dimensional flow field in a 90 deg bend, and a two-dimensional flow field in a turbine cascade. These and a quantitative assessment of the effect of artificial dissipation in SIMPLE-type schemes are given by Basson and Lakshminarayana (1994). In this assessment, it is shown that the excessive artificial dissipation inherent in some commonly used schemes, such as the power-law scheme, prohibits the accurate capturing of detailed flow structures in some complex flows. Significant improvement in the accuracy of the flow modeling was obtained by the use of smaller amounts of artificial dissipation, which was achieved by retaining control over the amount of artificial dissipation through the inclusion of direct artificial dissipation terms.

Numerical Modeling of Tip Clearance Flow Effects

The case chosen to evaluate the ability of the present formulation to model complex turbomachinery flows is the investigation of tip clearance effects documented by Bindon (1987, 1989, 1990) and Bindon and Morphis (1992). This investigation is one of the most extensive in this area. The results presented in the two research reports Bindon (1986a, 1986b), were obtained in a geometrically similar cascade and can, therefore, also be used for comparison with the computational results. Bindon (1990) provided the tabulated results from which the information was drawn for the papers mentioned previously.

The flow measurements used for comparison here were taken in a linear turbine nozzle cascade, with a chord of 0.186 m, a span equal to one chord, a pitch/chord ratio of 0.7, and a tip gap of 2.5 percent chord. The exit Reynolds number based on chord length was 470,000 and the incoming endwall boundary layer was thickened by a trip wire about $1\frac{1}{2}$ chord upstream of the cascade. The inlet angle was 0 deg and the outlet angle was about 68 deg (measured from axial direction). The turning angle is therefore representative of typical turbine nozzles. The maximum blade thickness was about 15 percent of the chord length. The numerical model's inlet velocity distribution corresponded to that measured downstream of the boundary layer trip in the experimental setup.

The stability limitations on the choice of artificial dissipation parameters for a two-dimensional turbine stator considered earlier (Basson and Lakshminarayana, 1994), lead to the selection of the following artificial dissipation settings (Eqs. (2) and (7)):

$$\epsilon_2 = 0.4 \quad \epsilon_4 = 0.5 \quad \epsilon_{pw} = 0.3$$

The E_R value was set at 0.3 for the momentum and turbulence equations. The inlet turbulence intensity was not measured, but was estimated to be at least 2 percent.

Embedded Mesh Technique. The resolution of tip clearance flows requires specialized grids. The abrupt transition from the blade passage to the tip gap, with the sharp corners at the blade tip and the large gradients in flow properties, make the use of typical H- or C-grids impractical. A commonly used approach, sometimes called the "thin blade approximation" or "pinched tip approximation," is to cusp the blade tip, e.g., Pouagare and Delaney (1986), Bansod and Rhie (1990), Kunz et al. (1993), Storer and Barton (1991). This approach is reasonable for thin blade tips (e.g., compressors and pumps) and is only suitable for modeling the gross effects of the tip clearance flows as the tip geometry is not modeled correctly. Nonsmooth grid lines in the tip region also reduce the accuracy of the solution. Better modeling of the tip gap has been obtained by embedding an O-grid within the main grid in the tip gap (Beach, 1990), or embedding an H-grid inside a C-grid (Watanabe et al., 1991). These methods provide better resolution and accurate modeling of the actual geometry, but introduce singularities in the case of the embedded O-grid where the innermost line of the O-grid doubles back near the leading and trailing edges. The solution algorithm for these embedded grids must further be formulated for the block-structured nature of the grid. To overcome these difficulties, an embedded H-grid topology was developed. This topology eliminates the singularities, while retaining the advantages of good resolution and accurate modeling of the geometry. The embedded H-grid topology, which retains the H-grid connectivity pattern, does not require a block-structured solution algorithm and is well suited to ADI solution procedures. A complete description of embedded H-grid technique and its application to turbomachinery, and improved accuracy obtained from that is described in Basson et al. (1991). An example of the embedded mesh generated for C4 profile (Basson et al., 1993) is shown in Fig. 2.

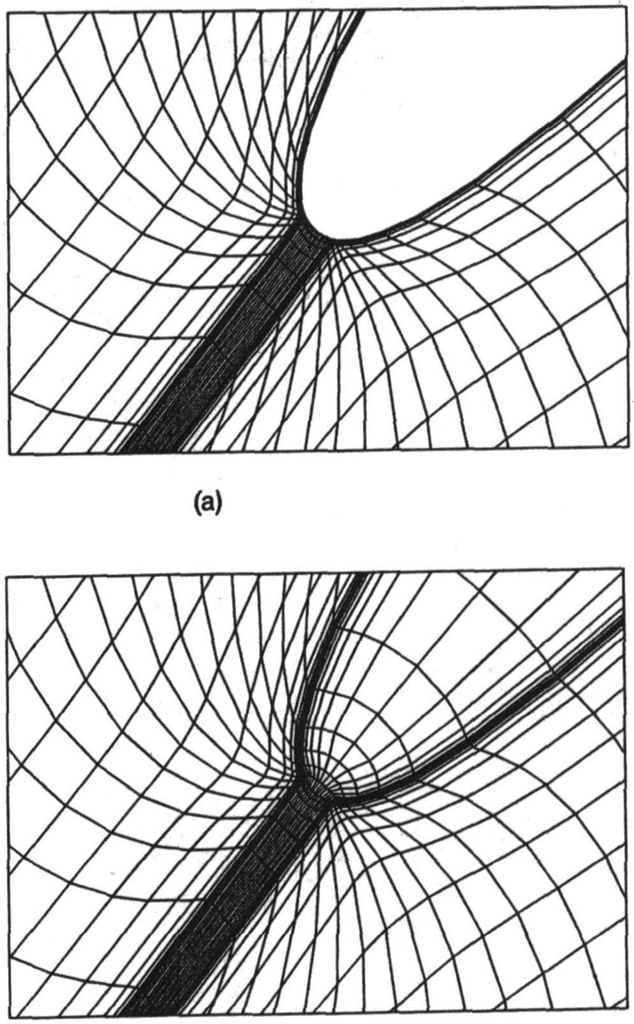
(a)

(b)

Fig. 2 Leading edge grid detail for embedded H-grid for a C4 cascade blade row: (a) grid below tip gap; (b) grid in tip gap

The numerical model for the turbine cascade had 81 × 57 × 57 grid points in the streamwise, pitchwise, and spanwise directions, respectively, of which 41 × 21 × 15 grid points were located in the tip gap. The number of grid points is the

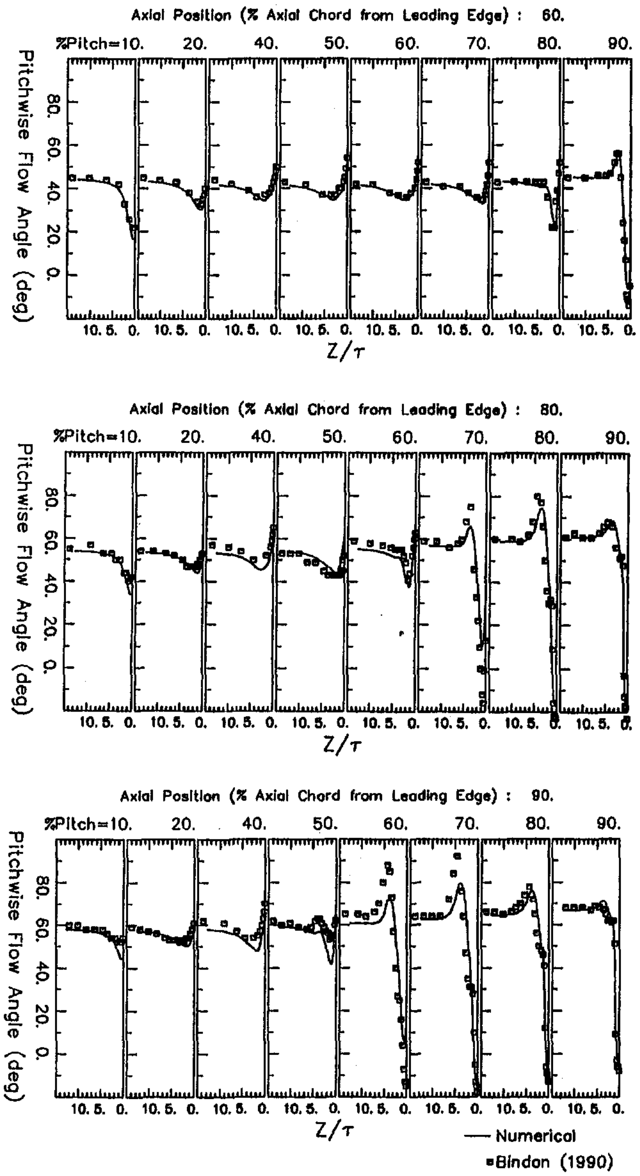

Fig. 3 Comparison of measured and predicted pitchwise flow angles

maximum that could be used with the present formulation on the available supercomputer facilities. The grid at the hub wall, i.e., the endwall without tip clearance, was kept fairly coarse to be able to resolve the tip clearance region as well as possible.

The grid resolution is insufficient to capture the endwall secondary flow here. The small number of grid points, however, severely limited the resolution that could be obtained. In a previous computation with the same overall number of grid points, but more points in the spanwise direction in the tip gap region, the results were markedly poorer in the main flow region due to insufficient spatial resolution.

Predictions and Comparison With Data. The distance from the endwall is referred to below in terms of the number of tip gaps. This measure was chosen because the spanwise extent of the tip leakage phenomena is expected to scale primarily with the height of the tip gap. The flow over most of the blade span is not affected by the tip leakage flow, with the result that the spanwise extent of the leakage phenomena would not be affected by changes in the span.

The accuracy with which the numerical model captures the flow angles, total pressure losses, and pressure distributions is a good indication of the accuracy and validity of the numerical model. A direct quantitative comparison can be seen in the plot of pitchwise (blade-to-blade measured from the axial direction) and spanwise (hub to tip) flow angles (zero in a two-dimensional flow) shown in Figs. 3 and 4, respectively. These graphs compare the spanwise distribution of the measured and computed flow angles at various pitchwise and axial positions. The pitchwise positions of each graph indicate the distance from the pressure to the suction side, i.e., 10 percent pitch is near the pressure side, while 90 percent pitch is near the suction side. The pitchwise flow angle plots indicate the spanwise position of the leakage vortex, i.e., the spanwise position near the endwall where the pitchwise angle crosses through the midspan value. Figure 3 shows that the leakage flow effects are captured very accurately up to about 80 percent of the axial chord, including both the magnitude and the extent of under- and overturning. However, already at the 80 percent axial chord position, the numerical solution fails to capture the maximum pitchwise flow angle (overturning) at the 70 and 80 percent pitch positions. These discrepancies are larger at the 90 percent axial chord

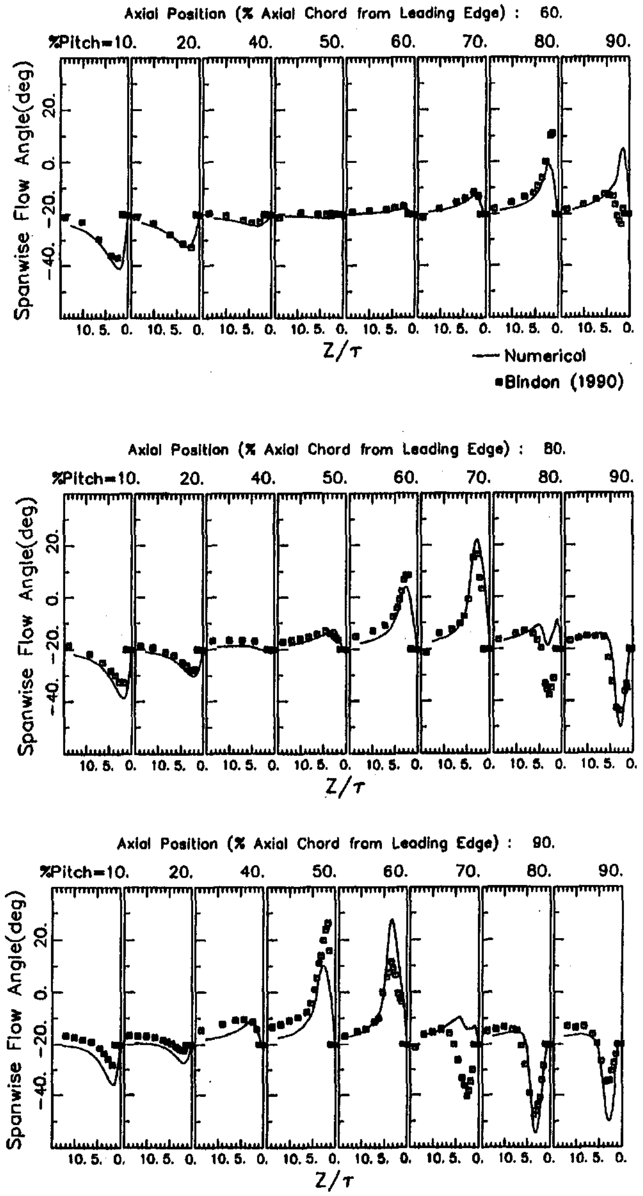

Fig. 4 Comparison of measured and computed spanwise flow angles (positive angle when flow directed toward endwall)

position. The lack of sufficient spatial resolution is the most likely cause for the inability of the numerical model to capture the peaks of pitchwise flow angle.

As mentioned earlier, another computation with less resolution near the endwall was performed. This computation was incapable of capturing any of the overturning region of the leakage vortex (where the pitchwise flow angle exceeds the midspan value). By increasing the grid resolution where the overturning was expected, the computation was capable of capturing some of the overturning, as shown in Fig. 3. The extremely large gradients exhibited by the experimental data clearly require a large number of grid points to be resolved accurately. Further possible contributions to the inability of the numerical model to capture the magnitude of the pitchwise flow angles accurately are the use of too much second-order artificial dissipation (thus bringing the numerical scheme closer to a first-order scheme) and the inability of the isotropic $k-\epsilon$ turbulence model to represent the anisotropic turbulence effects in vortical flows. Even within these limitations, however, the numerical model succeeded in capturing the spanwise location and extent of the leakage vortex. The underturning near the tip gap close to the pressure and suction surfaces, and overturning away from the surfaces, are captured accurately at all three axial positions.

Figure 4 shows plots of spanwise flow angle for the computed and experimental results. The experimental results shown very near the endwall are not from actual measurements, but extrapolated to zero angle. In general, the computed spanwise flow angles are in good agreement with experimental results. The spanwise flow angle gives an indication of the pitchwise location of the leakage vortex, as indicated by the pitchwise position where the spanwise flow angle reverses in sign. The computation captures the spanwise flow toward the blade tip on the pressure side quite accurately at all three axial positions shown in Fig. 4. The pitchwise location of the leakage vortex given by the computation is, however, in error by about 5–10 percent pitch. For example, at 60 percent axial chord the measured spanwise flow angles reverses in sign between the 80 and the 90 percent pitch positions. This indicates that the core of the leakage vortex is located between these two pitchwise positions. The computed spanwise flow angle, however, shows no reversal before 90 percent pitch, indicating the leakage vortex core is between the 90 and 100 percent pitch positions in the computational results. A similar discrepancy between the computed and measured pitchwise position of the leakage vortex can be seen at 80 and 90 percent chordwise positions. Contrary to what was observed in the pitchwise flow angle graphs of Fig. 3, the computed spanwise flow angles peaked at somewhat larger values than those measured by Bindon (1990). When taking into account the differences between the pitchwise locations of the leakage vortex in the computed and experimental results, however, the values of spanwise flow angles agree very well with the measured values. The strength and extent of the vortex are captured accurately. For example, at 90 percent axial chord, the vortex spans from 50 percent pitchwise position to 90 percent pitchwise position. This is captured accurately by the numerical simulation.

In addition to flow angles, the total pressure loss coefficient (ζ_L) provide another means of validating the numerical model. Figure 5 gives contour plots of numerical and experimentally determined ζ_L values at various axial positions (no experimental results were available at the positions downstream of the trailing edge). The contour plots for ζ_L are drawn for two adjacent bladerows, with the space between the respective contour plots for the numerical and experimental ζ_L values indicating the local blade thickness to scale. Total pressure losses are very difficult to capture accurately in a numerical model. The small differences between the local total pressure and the inlet total pressure relative to the inlet dynamic head, which are used to compute the loss coefficients, lead to amplification of the numerical errors in the calculation of ζ_L.

However, the loss coefficient is a very important parameter and it is highly desirable that the numerical model be able to capture the extent and magnitude of total pressure losses associated with the important flow structures. The accuracy of these total pressure losses is affected by many aspects of the numerical model, e.g., grid resolution, order of approximation of the governing equations, and the validity of the turbulence model. Given all these factors contributing to errors in the modeling of the total pressure losses, the computational results shown in Fig. 5 compare very well with the experimental results. The spanwise extent of the total pressure loss core associated with the leakage vortex, the overall extent and magnitude of total pressure losses are captured accurately up to 90 percent of chord. The differences between the computed and experimental results are larger at the further downstream positions. At the 90 and 100 percent axial chord positions, the movement of the loss core away from the endwall is not captured by the computation. The magnitude and location of peak losses, as high as 300 to 400 percent of the inlet dynamic head, is predicted very well. It should be observed here that the values are very high due to normalization by inlet dynamic head. Since this is a highly accelerating flow, the losses based on the local free-stream velocity will be much lower.

In a previous calculation, not shown here, with fewer grid points in the region where the loss core is observed, the accuracy of the computed loss core's position and spanwise extent was significantly poorer than that shown in Fig. 5. This indicates that a further increase in the grid resolution in the near endwall region (within about eight tip gaps from the endwall) could result in even more accurate modeling of the loss core. The inability of the turbulence model to represent the anisotropic effects in the leakage vortex further contributes to the loss in accuracy of the computed ζ values.

Figure 6 shows the development of the mass-averaged loss coefficient as the flow passes through the blade passage. Also shown in Fig. 6 are averaged values obtained from Bindon's measurements (Bindon, 1990). The latter measurements did not extend over the whole blade pitch or span, with the result that the averaged experimental results shown in Fig. 6 do not include the effect of the blade and lower endwall boundary layers. These boundary layers are relatively thin, and should therefore not affect the averaged values significantly. The numerical model captures the early development of the loss accurately, but not in the last 25 percent of the blade passage. In this latter part, the strong gradients are affected more by the numerical diffusion, thus limiting the development of the leakage vortex. The losses are therefore underpredicted in this part of the blade passage. It is nevertheless surprising that the experimental data show no increase in the average loss coefficient from 80 to 90 percent axial chord. The predicted losses increase down stream of trailing edge due to mixing of the leakage vortex and the wake.

Bindon (1986b) provides contours of static pressure at the endwall. Figure 7 compares these contours to those obtained from the numerical model results (note that larger values of pressure coefficient $[(p_{in} - p)/Q_{in}]$ correspond to lower values of pressure, as defined by Bindon, 1986b). The numerical model succeeded in capturing the pressure levels in the blade passage. This serves to validate the blade surface pressure distribution given in Fig. 8. Inside the tip gap, the pressure contours from the numerical results are straight in the leading half of the blade chord, while the contours given by Bindon (1986b) are smoother. Interpolations between measurements from the very coarse grid on which Bindon took his pressure measurements, required for generating the contour plot, may however have lead to excessive smoothing of the contours given by Bindon (1986b). Insufficient grid resolution in the numerical model and excessive numerical dissipation, on the other hand, prevented the numerical model from capturing the extremes of low pressure observed in the measurements.

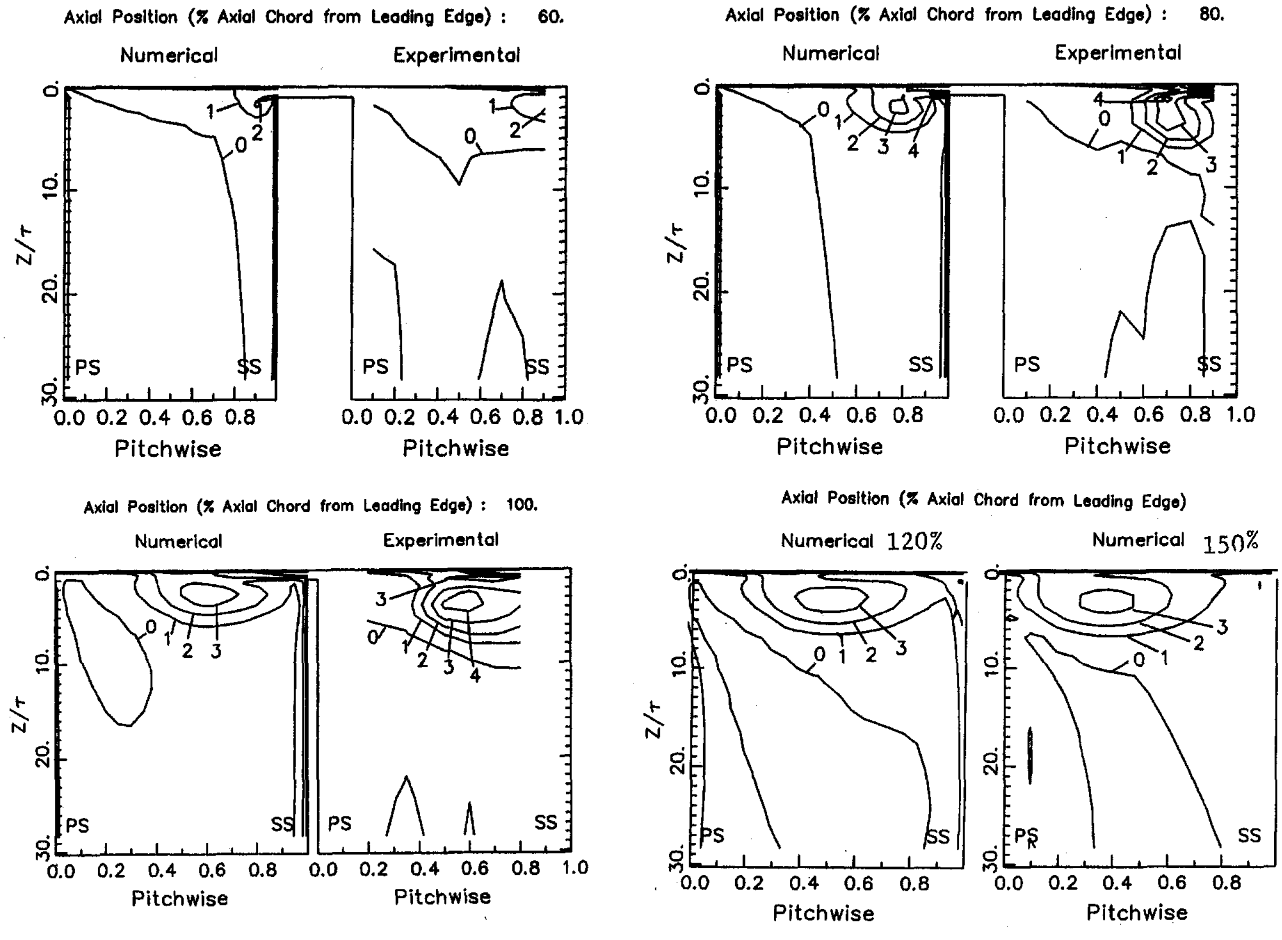

Fig. 5 Contours of loss coefficient (ζ_L) predicted and measured

The comparison of the results obtained with the numerical model and with the experimental results, discussed above, indicates that the numerical model succeeds in capturing most of the flow phenomena associated with the tip leakage flow. The differences that were pointed out can be accounted for primarily by insufficient grid resolution. Excessive artificial dissipation and the limitations of the isotropic turbulence model further contribute to the loss of some details of the flow phenomena. The computed results are however in very good agreement with measured results to give sufficient confidence in the computational results for it to be used to investigate tip clearance flow phenomena, through numerical simulation.

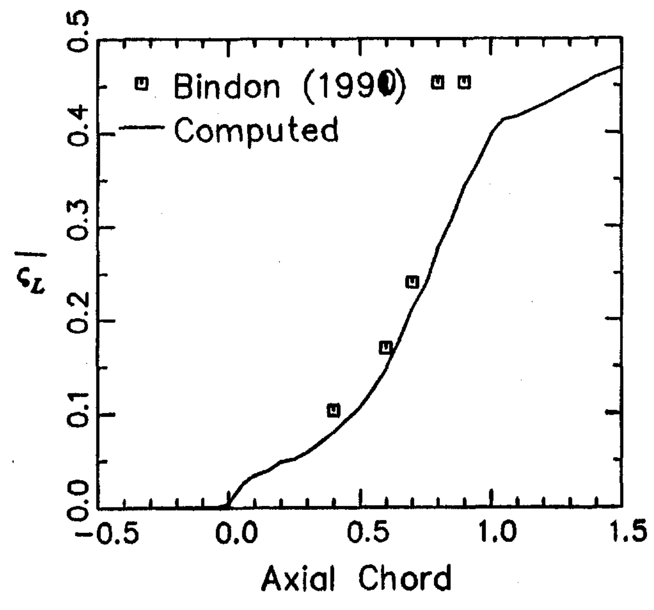

Fig. 6 Axial development of mass-averaged loss coefficient ($\bar{\zeta}_L$)

Additional Simulation and Discussion. In the previous section, the present numerical model was shown to capture the major flow phenomena associated with tip clearance flows accurately. The results obtained from the numerical model can therefore be used to investigate the effect of the tip clearance flows. The aspects of tip clearance flows that are of most interest are the following:

(*a*) The effect of the leakage flow on the loss of flow turning (underturning reduces the useful work done by a bladerow).
(*b*) Stagnation pressure losses incurred in the mixing of the leakage jet with the main flow, which reduces the overall efficiency of the bladerow.
(*c*) Loss of loading near the blade tip, which is associated with the loss of flow turning.
(*d*) The creation of regions of very high velocity on the pressure side corner of the blade tip, leading to a high heat transfer rate and surface erosion.
(*e*) The introduction of three dimensionality and unsteadiness into the flow entering downstream bladerows, in terms of flow angle, velocity magnitude and total pressure.

The results of the numerical simulation shown in Figs. 3 to 7, discussed in the previous paragraph, illuminate many of these

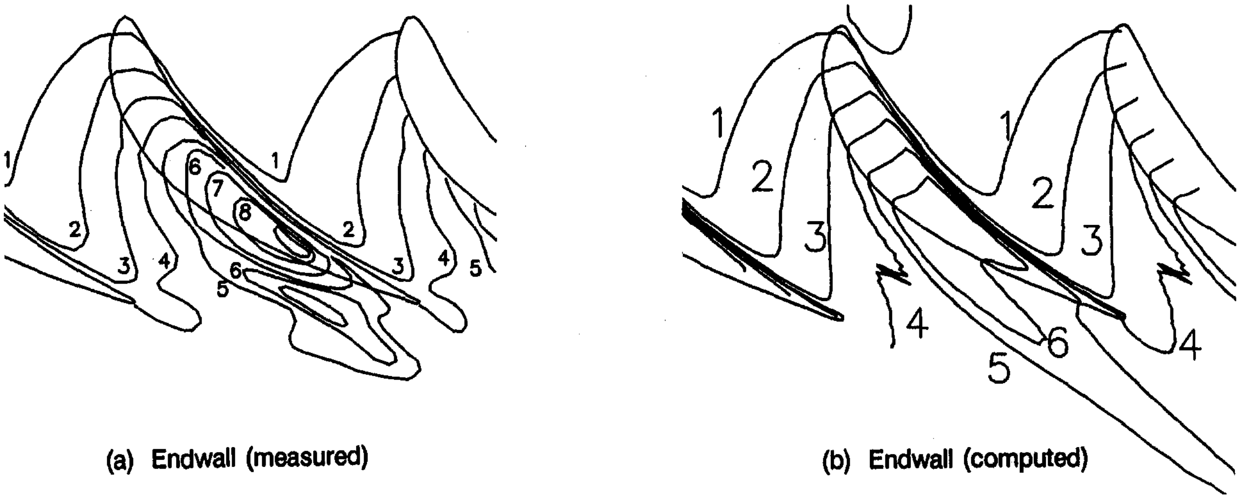

(a) Endwall (measured)

(b) Endwall (computed)

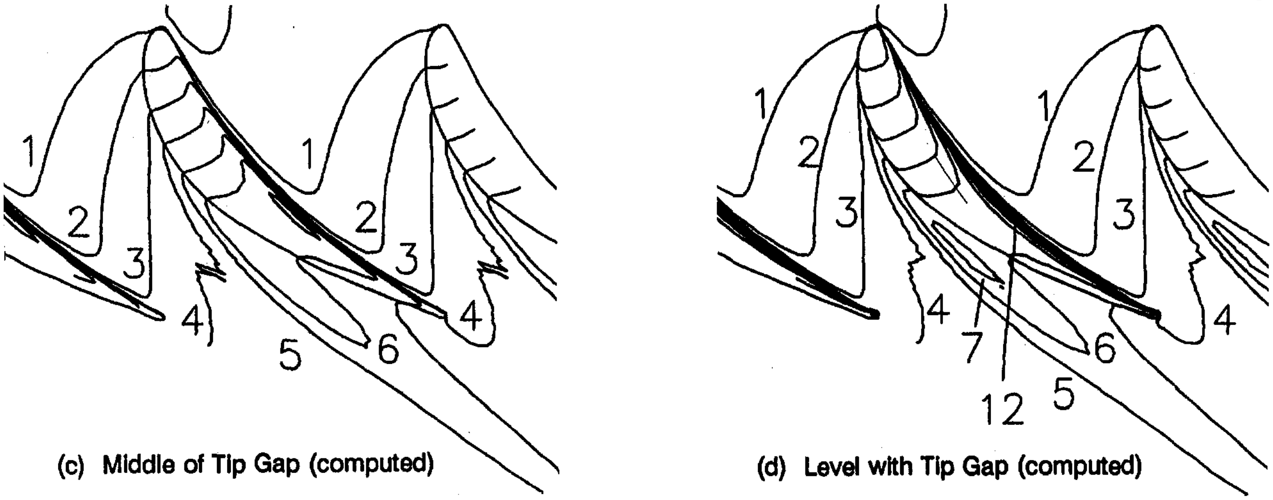

(c) Middle of Tip Gap (computed)

(d) Level with Tip Gap (computed)

Fig. 7 Contours of pressure coefficient (C_p)

aspects of tip clearance flows. Additional results from the numerical simulation that can be used to investigate the effects of the tip leakage flows are given in this section.

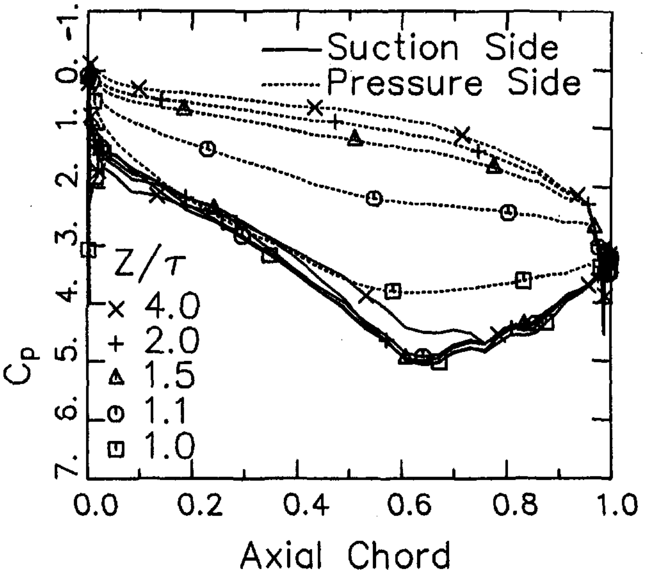

Fig. 8 Blade surface pressure (C_p) distribution at various spanwise positions

Figure 8 shows the blade surface pressure distribution at a number of spanwise positions. At four tip gaps from the endwall, the blade surface pressure distribution is virtually identical to the midspan distribution. The effect of the leakage flow is therefore limited to a small region near the blade tip. Near the tip, the pressure on the suction side is reduced below the midspan values. This is caused by the presence of the leakage vortex and low pressures that exit in the core of the vortex. The pressure distribution on the suction side remains unchanged from two tip gaps below the endwall to just below the tip itself. The pressure distribution on the pressure side, however, gradually changes from the midspan distribution at about four tip gaps from the endwall, to a slightly lighter loading distribution at about $1\frac{1}{2}$ tip gaps from the endwall. Thereafter the pressure on the pressure side drops rapidly, until there is only a small residual loading at the blade tip over the trailing half of the axial chord.

Figure 7 shows pressure contours in a blade-to-blade plane in the level of the blade tip. The extremely low pressure on the pressure side edge of the blade tip is associated the sharp turning of the flow entering the tip gap from the pressure side of the blade. This low-pressure region will lead to spanwise flow accelerating along the pressure side blade surface near the tip. This can be seen in the velocity vectors close to pressure surface (95 percent of pitchwise distance from the suction side) shown in Fig. 9. The accelerating flow will reduce the local boundary layer thickness, thus enhancing the heat transfer and erosion processes in this region.

The velocity vectors projected on to the x–z plane at various distances from the suction side are shown in Fig. 9. The span-

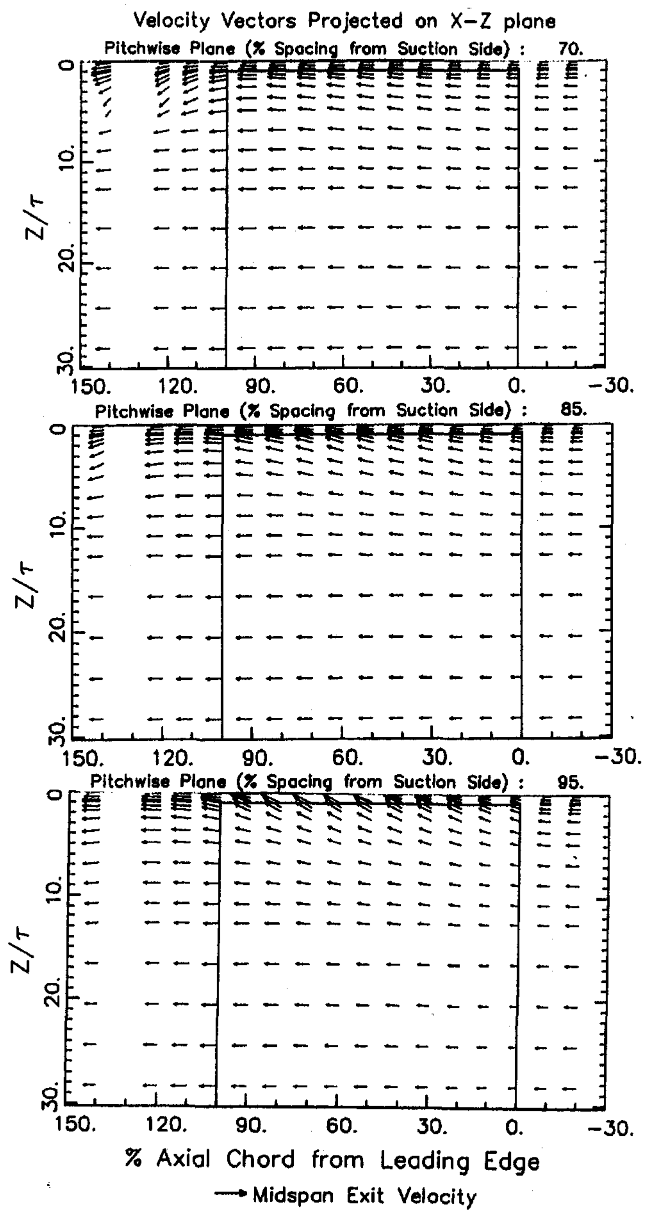

Fig. 9 Velocity vector in planes at constant pitchwise positions projected on to a hub-to-tip (x–z) plane

wise flow is large up to about 5τ from the wall inside the passage close to the pressure surface (95 percent spacing from the suction side) reducing gradually to very small values at 70 percent of spacing from the suction side. Spanwise inward flow occurs downstream at 70 percent blade spacing. This is caused by the entrainment and blockage of the flow caused by the leakage vortex.

The velocity vectors in the x–y plane (blade-to-blade) at various spanwise locations are plotted in Fig. 10. It is clear that appreciable leakage flow exists even at 10 percent of gap from the wall, increasing gradually to very high values at $z = 0.9\tau$, just above the tip. A dramatic effect of mixing of the leakage flow and the main flow, which are at differing angles, is also clear from this figure. The underturning is very strong. An additional feature seen at $z = 0.1\tau$ is the "blowing" effect of leakage flow on annular wall boundary layer. The leakage flow tends to energize the wall boundary layer flows, giving rise to "jet-wake" type flows at the exit. This effect persists up to $z = \tau$. The passage region affected by the leakage flow also increases gradually from leading edge and covers almost half the passage at trailing edge. The underturning is strong up to $z = \tau$, and is already weak at $z = 2\tau$. At $z = 4\tau$, the velocity vectors almost follow the main flow direction inside the passage. But the exit flow is overturned due to the vortex. The flow from the core to the top of the leakage vortex is underturned and the flow from the core to the bottom of the vortex is overturned. The underturning of the flow is evident from $z = 0.1$ to 2τ and small overturning is evident from $z = 4$ to 6τ. Hence the core of this leakage vortex is located between $z = 2$ to 4τ. The spanwise extent of the underturning grows from about 2τ at 60 percent axial chord to 3τ at the trailing edge plane. The underturning therefore remains localized near the end wall, but the magnitude of overturning is much smaller than the underturning.

The pitchwise extent of the region effected by underturning is clearly noticeable. Figures 3 and 10 show that the region affected by underturning inside the blade passage extends from the suction side and grows from about 30 percent pitch at 60 percent axial chord, to about 60 percent pitch at the trailing edge plane. Downstream of the bladerow, the effect of the leakage flow dissipates slowly, so that the region affected by underturning extends over about half of the pitch at the 150 percent axial chord position. Figure 10 shows that, at 50 percent tip gap away from the endwall, the leakage flow leaves the bladerow in a nearly axial direction. No turning has therefore been imparted to this flow. The region affected by overturning has a much smaller pitchwise extent of about 30 percent of the pitch at the trailing edge plane, as can be seen in Figs. 3 and 10.

A striking feature of the leakage jet is that its pitchwise penetration ceases abruptly. The jet does not gradually loose pitchwise velocity, but penetrates up to a certain pitchwise position and then abruptly turns toward the main flow direction. The secondary velocity vectors reveal (not shown) that the leakage jet only turns weakly away from the endwall in a spanwise direction. This is confirmed by the spanwise flow angles shown in Fig. 4, where the spanwise flow angles rarely exceed 30 deg. The axial component of the velocity therefore is always much greater than the spanwise component. These results indicate that the "roll up" of the leakage flow into a vortex is overshadowed by the turning of the leakage flow toward the main flow direction.

The chordwise pressure gradient on the blade tip supports Bindon's supposition that there is a chordwise flow over the leading part of the blade tip (Bindon, 1989). The flow over the sharp pressure side edge of the blade tip, will likely to separate at the edge. The fluid in the separation zone will be subject to this chordwise pressure gradient and therefore tend to move towards the center of the blade. This supposition is further supported by the velocity vectors shown in Fig. 10 ($z = 0.9\tau$), where the row of vectors just inside the tip gap near the blade's pressure side, is directed in a nearly chordwise direction.

The mass-averaged outlet angle (pitch angle) is shown in Figure 11. It is clear from this plot that the flow underturning is confined to four gaps from the wall, with highest values near the wall, where the average underturning is as high as 35 deg. As the flow proceeds downstream the underturning near the wall is reduced due to mixing. The underturning is very small at $z = 4\tau$. The overturning, as explained earlier, is very small and is confined to the outer edge of the leakage flow region.

The strength of secondary vorticity is defined as the difference between the local vorticity ($\nabla \times \underline{V}$) and the midspan vorticity (at the same pitchwise and chordwise location). $\nabla \times (\underline{V} - \underline{V}_{\text{midspan}})$ is shown in vector form in Fig. 12. The anticlockwise rotation is positive, representing the vector pointing in the exit direction. This plot also indicates that the vertical motion associated with leakage flow is limited to the region between the endwall and $z = 4\tau$. The strength of the secondary vorticity is very high inside the gap and near the tip, decreasing to insignificant values at $z = 4\tau$. Furthermore, there is a close resemblance (as expected) between the velocity vectors shown in

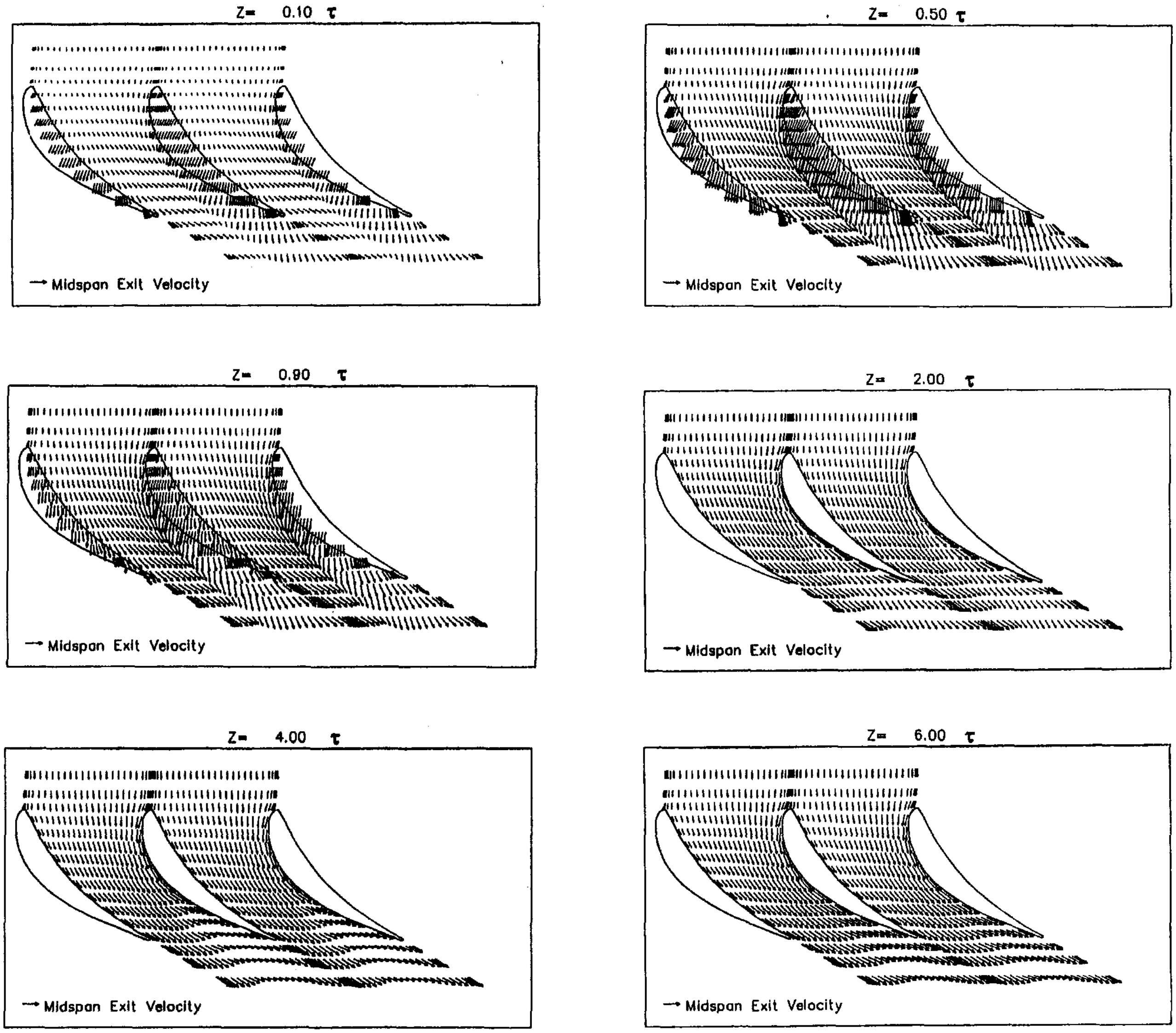

Fig. 10 Velocity vectors at constant spanwise positions projected on to a blade-to-blade (*x*–*y*) plane

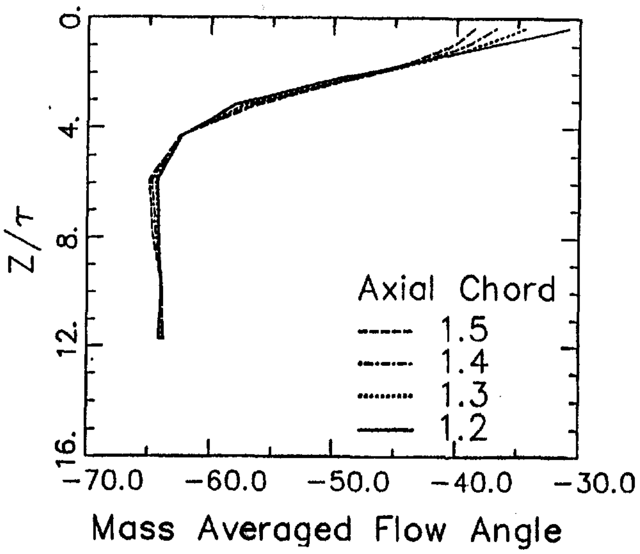

Fig. 11 Spanwise distribution of mass-averaged outlet angle

Fig. 10 and the vorticity vectors shown in Fig. 12. The secondary vorticity is high across most of the passage at exit at $z = \tau$ and is confined to less than 50 percent of passage width at $z = 4\tau$.

The leakage mass flow is one of the important parameters in assessing the aerodynamic loss and performance. The chordwise distribution of leakage mass flow also provides valuable information on regions of high leakage flow and losses. The leakage mass flow is given by

$$\underline{\dot{m}_L} = \int_{LE}^{s} \underbrace{\left[\rho \int_0^{\tau} (V_L \, dz)\right]}_{\Delta \dot{m}_L} ds \qquad (9)$$

where V_L is the leakage velocity normal to the blade surface, and s is the distance along the blade surface. The inlet mass flow in this region is given by

$$\frac{\dot{m}_I}{S} = \rho \int_0^{\tau} V_x dz \qquad (10)$$

The parameter

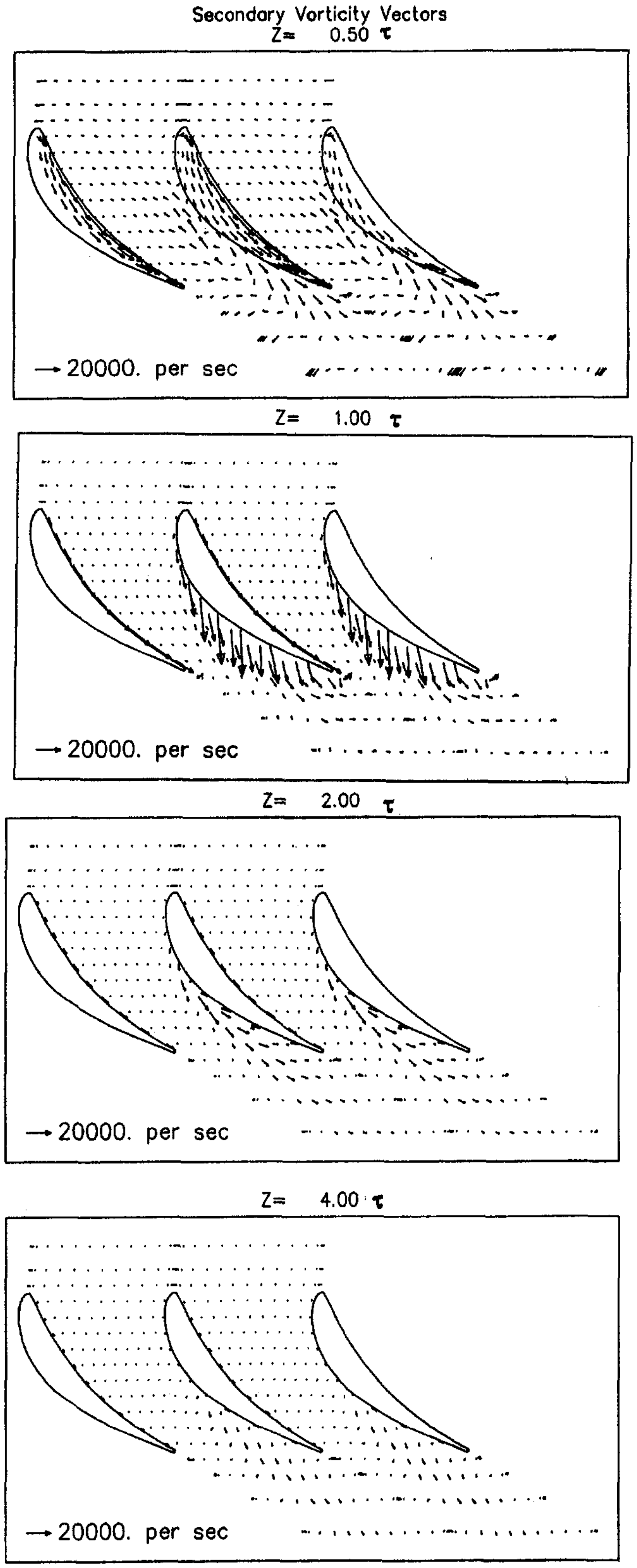

Fig. 12 Computed secondary vorticity vectors $[(\nabla x(V - V_{\text{midspan}}))]$

$$K = (\Delta \dot{m}_L) \frac{S}{\dot{m}_1} \tag{11}$$

is a nondimensional quantity and is a measure of the mass flow through the gap caused by blade unloading at the tip. This does not include direct mass flow through the gap in the absence of leakage flow and loading.

The chordwise distribution of leakage flow parameter K, shown plotted in Fig. 13, indicates the development of the leakage mass flow. The leakage mass flow was computed as follows: The tip gap "boundaries" were chosen to correspond to the extension of the blade profile, i.e., where the blade surfaces would have been if there was no tip gap. The mass flow passing through these boundaries was calculated from the velocity component normal to the surfaces. The suction and pressure sides were split at the leading and trailing edge branch points in the grid. The mass flow was integrated along these respective sides, with positive values attributed to the flow entering the tip gap on the pressure side and to the flow leaving the tip gap on the suction side. The blade surface pressure distribution shown in Fig. 8 indicates that the blade section is highly loaded over the aft half of the blade. The increased loading, added to the reduced blade thickness toward the trailing edge, increases the leakage flow over that part of the blade tip. The leakage mass flow is almost linear from the leading to the trailing edge and decreases near the trailing edge. The difference between the two curves represents the accumulation of mass flow within the gap and this is negligibly small, as expected.

The value of $(\dot{m}_L/\dot{m}_1)$ is the cumulative leakage flow passing through the gap as a fraction of the inlet flow. This quantity plotted versus axial distance in Fig. 14 shows that the cumulative leakage flow increases rapidly from about 40 percent axial chord onward, only 10 percent of the leakage flow passes through the gap between leading edge and 40 percent on chord. This is also consistent with the passage-averaged aerodynamic losses plotted in Fig. 6, which shows that losses increase rapidly from 40 percent of axial chord onward. This increase in losses coincides with the increase in the leakage flow from 40 percent axial chord onward.

Conclusions

The successful development and application of a numerical model for three-dimensional, steady, viscous flow through turbomachinery bladerows are presented in this paper. Together with the embedded grid generation techniques, the numerical model has been shown to be capable of producing an accurate simulation of the physical flow phenomena. Computational experiments showed that the embedded grid topology produced very good quantitative modeling of the tip clearance vortex. Second-order and fourth-order artificial dissipation terms for direct use in the convection-diffusion equations of pressure-based semi-implicit (SIMPLE-type) schemes, were successfully formulated and implemented in a three-dimensional vis-

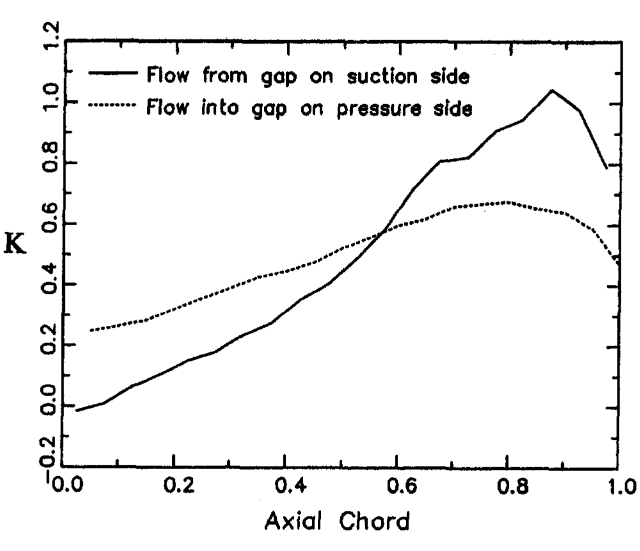

Fig. 13 Chordwise distribution of tip leakage mass flow parameter K

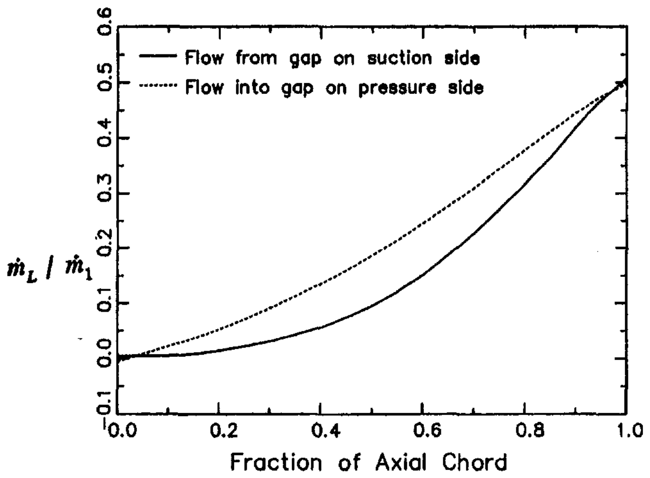

Fig. 14 Chordwise distribution of cumulative leakage flow ($\dot{m}_L/\dot{m}_1$)

cous code. The validation studies indicated that by controlling the amount of artificial dissipation, the spurious effects of the dissipation could be minimized. The numerical simulation results presented and interpreted in this paper have revealed how valuable such a numerical simulation can be in understanding the complex flow structure associated with tip leakage. Even with the known limitations in the accuracy of the numerical model, it provides a wealth of information that can contribute significantly to an understanding of the physical phenomena associated with tip clearance phenomena.

The pitchwise and spanwise angles as well as losses are predicted accurately. Additional simulation studies indicate that major leakage flow and losses occur beyond midchord due to increased loading and decreased blade thickness in this region. The influence of tip leakage flow as discerned by secondary vorticity, spanwise, and pitchwise velocity components does not extend beyond about four gap heights for the particular geometry investigated.

Acknowledgments

The first author was supported by the Bureau for Mechanical Engineering of the University of Stellenbosch, South Africa. The use of supercomputer facilities at NASA Ames Research Center (National Aerospace Simulation Facility) and NASA Lewis Research Center is gratefully acknowledged. The authors are indebted to J. Bindon for providing published and unpublished data.

References

Bansod, P., and Rhie, C. M., 1990, "Computation of Flow Through a Centrifugal Impeller With Tip Leakage," AIAA Paper No. 90-2021.

Basson, A. H., Kunz, R. F., and Lakshminarayana, B., 1993, "Grid Generation for Three-Dimensional Turbomachinery Geometries Including Tip Clearance," *J. Propulsion and Power*, Vol. 9, p. 59.

Basson, A. H., and Lakshminarayana, B., 1994, "An Artificial Dissipation Formulation for Semi-implicit Pressure Based Solution Scheme for Inviscid and Viscous Flows," *Int. J. Comp. Fluid Dynamics*, Vol. 2, p. 253.

Beach, T. A., 1990, "An Interactive Grid Generation Procedure for Axial and Radial Flow Turbomachinery," AIAA Paper No. 90-0344.

Bindon, J. P., 1986a, "Visualization of Axial Turbine Tip Clearance Flow Using a Linear Cascade," CUED/A-Turbo TR 122, Engineering Department, Cambridge University, United Kingdom.

Bindon, J. P., 1986b, "Pressure and Flow Field Measurements of Axial Turbine Tip Clearance Flow in a Linear Cascade," CUED/A-Turbo TR 123, Engineering Department, Cambridge University, United Kingdom (also see *Proc. I. Mech. E 1987-6*, pp. 43–52, 1987).

Bindon, J. P., 1987, "Pressure Distributions in the Tip Clearance Region of an Unshrouded Axial Turbine as Affecting the Problem of Tip Burnout," ASME Paper No. 87-GT-230.

Bindon, J. P., 1989, "The Measurement and Formation of Tip Clearance Loss," ASME JOURNAL OF TURBOMACHINERY, Vol. 111, pp. 257–263.

Bindon, 1990, private communication.

Bindon, J. P., and Morphis, G., 1992, "The Development of Axial Turbine Leakage Loss for Two Profiled Tip Geometries Using Linear Cascade Data," ASME JOURNAL OF TURBOMACHINERY, Vol. 114, No. 7, p. 198.

Chen, G. T., et al., 1991, "Similarity Analysis of Compressor Tip Clearance Flow Structure," ASME JOURNAL OF TURBOMACHINERY, Vol. 113, pp. 260–271.

Chien, K.-Y., 1982, "Predictions of Channel and Boundary-Layer Flows With a Low-Reynolds-Number Turbulence Model," *AIAA Journal*, Vol. 20, No. 1, pp. 33–38.

Hah, C., 1984, "A Navier–Stokes Analysis of Three-Dimensional Turbulent Flows Inside Turbine Blade Rows at Design and Off-Design Conditions," ASME *Journal of Engineering for Gas Turbines and Power*, Vol. 106, pp. 421–429.

Hobson, G. V., and Lakshminarayana, B., 1991, "Prediction of Cascade Performance Using an Incompressible Navier–Stokes Technique," ASME JOURNAL OF TURBOMACHINERY, Vol. 113, pp. 561–572.

Kunz, R. F., Lakshminarayana, B., and Basson, A. H., 1993, "Investigation of Tip Clearance Phenomena in an Axial Compressor Cascade Using Euler and Navier–Stokes Procedures," ASME JOURNAL OF TURBOMACHINERY, Vol. 115, pp. 453–467.

Lakshminarayana, B., 1970, "Methods of Predicting Tip Clearance Effects in Axial Flow Turbomachinery," ASME *Journal of Basic Engineering*, Vol. 94, p. 777.

Lakshminarayana, B., 1991, "An Assessment of Computational Fluid Dynamic Techniques in the Analysis and Design of Turbomachinery—The 1990 Freeman Scholar Lecture," ASME *Journal of Fluids Engineering*, Vol. 113, pp. 315–352.

Lakshminarayana, B., and Horlock, J. H., 1965, "Leakage and Secondary Flows in Compressor Cascades," Aeronautical Research Council, UK, R&M 3483.

Leonard, B. P., 1979, "A Stable and Accurate Convective Modelling Procedure Based on Quadratic Upstream Interpolation," *Computer Methods in Applied Mechanics and Engineering*, Vol. 19, pp. 59–98.

Moore, J., and Tilton, J. S., 1988, "Tip Leakage Flow in a Linear Turbine Cascade," ASME JOURNAL OF TURBOMACHINERY, Vol. 110, pp. 18–26.

Patankar, S. V., 1980, *Numerical Heat Transfer and Fluid Flow*, Hemisphere Publishing Corp., New York.

Patankar, S. V., 1988, "Recent Developments in Computational Heat Transfer," ASME *Journal of Heat Transfer*, Vol. 110, pp. 1037–1045.

Pouagare, M., and Delaney, R. A., 1986, "Study of Three-Dimensional Viscous Flows in an Axial Compressor Cascade Including Tip Leakage Effects Using a SIMPLE-Based Algorithm," ASME JOURNAL OF TURBOMACHINERY, Vol. 108, pp. 51–58.

Pulliam, T. H., 1986, "Artificial Dissipation Models for the Euler Equations," *AIAA Journal*, Vol. 24, No. 12, pp. 1931–1940.

Rhie, C. M., and Chow, W. L., 1983, "Numerical Study of the Turbulent Flow Past an Airfoil With Trailing Edge Separation," *AIAA Journal*, Vol. 21, No. 11, pp. 1525–1532.

Storer, J. A., and Barton, J. P., 1991, "An Investigation of the Flow Within the Clearance Space of a Compressor Rotor Tip," *Proc. Tenth Int. Sym. Airbreathing Engines*, Nottingham, Vol. 1, p. 143.

Van Doormaal, J. P., and Raithby, G. D., 1984, "Enhancements of the SIMPLE Method for Predicting Incompressible Fluid Flows," *Numerical Heat Transfer*, Vol. 7, pp. 147–163.

Watanabe, T., Nozaki, O., Kikuchi, K., and Tamura, A., 1991, "Numerical Simulations of the Flow Through Cascades With Tip Clearance," in: *Numerical Simulations in Turbomachinery*, ASME FED-Vol. 20, pp. 131–139.

Mean Streamline Aerodynamic Performance Analysis of Centrifugal Compressors

R. H. Aungier
Product Development,
Elliott Company,
Jeannette, PA 15644

Aerodynamic performance prediction models for centrifugal compressor impellers are presented. In combination with similar procedures for stationary components, previously published in the open literature, a comprehensive mean streamline performance analysis for centrifugal compressor stages is provided. The accuracy and versatility of the overall analysis is demonstrated for several centrifugal compressor stages of various types, including comparison with intrastage component performance data. Detailed validation of the analysis against experimental data has been accomplished for over a hundred stages, including stage flow coefficients from 0.009 to 0.15 and pressure ratios up to about 3.5. Its application to turbocharger stages includes pressure ratios up to 4.2, but with test uncertainty much greater than for the data used in the detailed validation studies.

Introduction

Mean streamline aerodynamic performance analysis continues to play a key roll in the design and application of centrifugal compressors. Despite impressive progress in computational fluid dynamics procedures, mean streamline methods continue to be the most accurate and the most practical method of predicting the performance of a stage or a component of a stage. Whitfield and Baines (1990) and Cumpsty (1989) contain good recent overviews of mean streamline methods. The analysis described here has been under development for over twenty years. Literally hundreds of different stages have been analyzed with it.

Detailed comparison of experimental data with predicted results has been accomplished for over a hundred stages. However, the best test of a performance analysis is its application to design activity. Weaknesses in the analysis are most clearly exposed when designers use it to guide them to better performing stages or components. This analysis has been revised and requalified each time sufficient test results from stage development programs were available to define significant deficiencies. The seventh major revision of the analysis is now in use. It has been successfully supporting stage development activity for over four years. It is applied to a variety of stage types, including process compressors, air compressors, and turbochargers. The detailed validation studies include stage flow coefficients, ϕ, from 0.009 to 0.15 and pressure ratios up to about 3.5. Good results have also been obtained on applications to turbocharger stages for pressure ratios up to about 3.5. Good results have also been obtained on applications to turbocharger stages for pressure ratios up to 4.2. However, test uncertainty for these units is much greater than for data used in the detailed validation studies.

Methods used in this analysis to predict performance for stationary components have previously been published in the open literature. These include prediction methods for vaned diffusers (Aungier, 1990), vaneless diffusers and return systems (Aungier, 1993), and volutes (Weber and Koronowski, 1986). The present paper provides a description of the impeller performance prediction methods to complete the description of the overall analysis. The overall centrifugal compressor stage performance analysis is compared to experiment for a series of stages of widely varying type.

The mean streamline performance analysis is a modular structured computer program. It has modules to analyze the various stage components as they appear in the stage. Figure 1 illustrates a general return channel style stage with the key computing stations numbered 1 through 7. The analysis provides detailed mean streamline fluid dynamic and performance data at each numbered station. Figures 2 and 3 illustrate some of the more important impeller geometric parameters.

Impeller Work Input

The general form of the impeller work input equation is

$$(\mu/\eta) = \Delta H/U_2^2 = I_B + I_{DF} + I_L + I_R \qquad (1)$$

where the terms on the right-hand side are (in order) the contributions due to the blades, windage and disk friction, seal leakage, and recirculation. The blade work input is given by

$$I_B = \sigma(1 - \lambda\phi_2 \cot \beta_2) - U_1 C_{u1}/U_2^2 \qquad (2)$$

The last term in Eq. (2) accounts for prewhirl effects. The term in parentheses can be recognized as the ideal (perfect blade guidance) dimensionless tip tangential velocity, $C_{u2\ \mathrm{ideal}}$. The slip factor formulation of Wiesner (1967) is used

$$\sigma = 1 - \frac{\sin \alpha_{c2}\sqrt{\sin \beta_2}}{z^{0.7}} \qquad (3)$$

which holds up to the limiting radius ratio given by

$$\epsilon_{\mathrm{LIM}} \doteq \frac{\sigma - \sigma_*}{1 - \sigma_*}$$

$$\sigma_* = (19\ \mathrm{deg} + 0.2\beta_2) \qquad (4)$$

When the actual radius ratio exceeds the limiting value, a corrected slip factor is computed by

$$\sigma_{\mathrm{COR}} = \sigma\left[1 - \left(\frac{\epsilon - \epsilon_{\mathrm{LIM}}}{1 - \epsilon_{\mathrm{LIM}}}\right)^{\sqrt{\beta_2/10}}\right] \qquad (5)$$

When splitter blades are present, the effect of the limiting radius ratio is checked independently for full and splitter blades. Hence, extremely short splitter blades will be recognized as ineffective in contributing to the impeller work input.

Contributed by the International Gas Turbine Institute and presented at the ASME–NJIT–HI–STLE Rotating Machinery Conference and Exposition (ROCON'93), Somerset, New Jersey, November 10–12, 1993. Manuscript received at ASME Headquarters July 1994. Associate Technical Editor: N. A. Cumpsty.

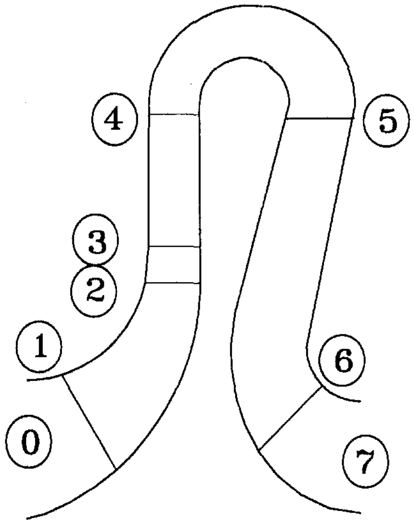

Fig. 1 Stage computing stations

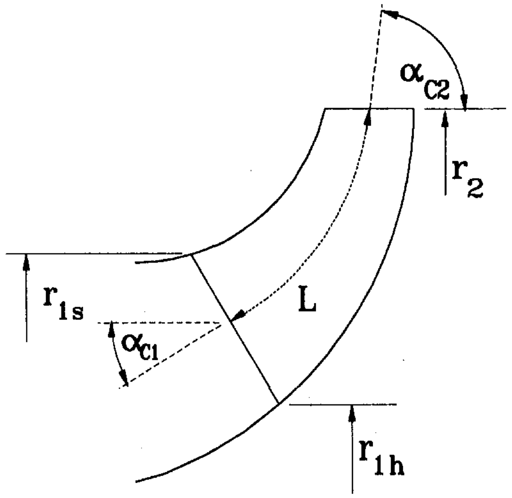

Fig. 2 Impeller Gaspath geometry

The impeller distortion factor, λ, is related to the tip aerodynamic blockage, B_2, by

$$\lambda = 1/(1 - B_2) \qquad (6)$$

The equation used to predict the impeller tip blockage is

$$B_2 = (\Delta q_{SF} + \Delta q_{HS}) \frac{U_2^2}{W_2^2} + \left[0.3 + \frac{b_2^2}{L_B^2}\right] \frac{A_R^2 v_1 b_2}{v_2 L_B} + \frac{s_{CL}}{2b_2} \qquad (7)$$

where the first term on the right-hand side contains skin friction and hub-to-shroud distortion loss coefficients to be presented later. The area ratio, A_R, is given by

$$A_R = A_2 \sin \beta_2/(A_1 \sin \beta_{th}) \qquad (8)$$

where β_{th} is suction surface blade angle at the impeller throat. A_R is similar to the ratio of the discharge area to the throat area. Throat area was not used directly because users of the analysis occasionally have chosen to adjust the input throat area to match an experimental choke limit. To avoid false variations in work input when this is done, the form given above was used to develop the empirical correlation. An equally accurate correlation could be developed using the throat area, but the present

Nomenclature

A = an area inside the blade passage
a = sound speed
B = fractional area blockage
b = hub-to-shroud passage width
C = absolute velocity
C_M = disk torque coefficient
C_m = absolute meridional velocity
C_r = throat contraction ratio, Eq. (20)
C_u = absolute tangential velocity
c_f = skin friction coefficient
D_{eq} = equivalent diffusion factor, Eq. (11)
d = diameter
d_h = hydraulic diameter
f_c = head loss correction factor, Eq. (31)
H = total enthalpy
h = static enthalpy
h_{th} = blade-to-blade throat width
I = work input coefficients, Eq. (1)
K = clearance gap swirl parameter = $C_u/(\omega r)$
L = blade mean streamline meridional length = $m_2 - m_1$
L_{SB} = splitter blade mean streamline meridional length
L_B = length of blade mean camberline
M = Mach number
M_u = rotational Mach number = U_2/a_{0T}
m = meridional coordinate
$\dot{m}$ = mass flow
P = pressure
R = rothalpy, Eq. (29)
r = radius
S = entropy
s = clearance gap width
U = blade speed = ωr; leakage tangential velocity
v = gas specific volume
W = relative velocity
W_u = relative tangential velocity
z = effective number of blades = $z_{FB} + z_{SB} L_{SB}/L$
z_{FB} = number of full-length blades
z_{SB} = number of splitter blades
α = flow angle with respect to tangent
α_c = streamline slope angle with axis
β = blade angle with respect to tangent
Δq = adiabatic head loss coefficient = $\Delta H/U_2^2$
ϵ = impeller meanline radius ratio = r_1/r_2
η = adiabatic efficiency
κ = streamline curvature, Eq. (15)
λ = tip distortion factor, Eq. (6)
μ = adiabatic head coefficient and gas viscosity
ξ = distance along blade mean camberline
ρ = gas density
σ = slip factor = $C_{u2}/C_{u2\,ideal}$
ϕ = stage flow coefficient = $\dot{m}/(\pi \rho_{T0} r_2^2 U_2)$
ϕ_2 = tip flow coefficient = C_{m2}/U_2
ω = rotation speed

Subscripts

B = a blade parameter
C = cover parameter
CL = clearance gap parameter
D = disk parameter
DF = disk friction parameter
h = parameter on the hub contour
L = leakage parameter
p = blade pressure surface parameter
R = recirculation parameter
s = shroud contour or blade suction surface parameter
T = total thermodynamic condition
th = throat parameter
0 = impeller eye condition
1 = impeller blade leading edge condition
2 = impeller tip condition
4 = diffuser exit condition
7 = stage exit condition

Superscripts

* = sonic flow condition
′ = value relative to rotating frame of reference

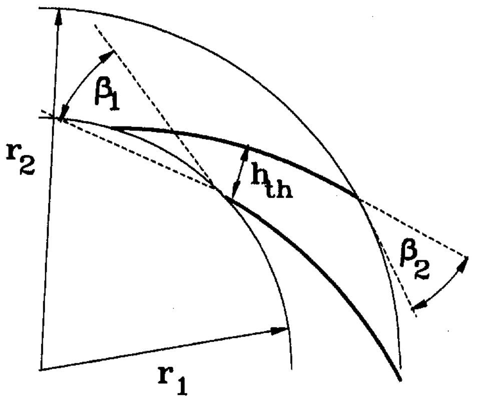

Fig. 3 Impeller blade geometry

model uses the form in Eq. (8). Equation (7) is the product of many years of development, directed to work input prediction for over a hundred different impellers. It is deceptively simple, but it is very effective in modeling the complex distortion effect for a broad range of impeller types. It seeks to model a number of different mechanisms, such as skin friction, hub-to-shroud flow distortion, volume ratio, flow diffusion, clearance (for open impellers) and blade aspect ratio. These various mechanisms assume vastly different significance for different impeller types. For example, dominant terms for low-specific-speed impellers are negligible for high-specific-speed impellers, and inversely.

Impeller windage and disk friction and cover seal leakage work input for covered impellers are given by

$$I_{DF} + I_L = \frac{(C_{MD} + C_{MC})\rho_2 U_2 r_2^2}{2\dot{m}} + \frac{\dot{m}_L I_B}{\dot{m}} \tag{9}$$

For open impellers, they are given by

$$I_{DF} + I_L = \frac{C_{MD}\rho_2 U_2 r_2^2}{2\dot{m}} + \frac{\dot{m}_{CL} U_{CL}}{2\dot{m} U_2} \tag{10}$$

which assumes half of the clearance gap leakage flow is re-entrained into the blade passage flow and re-energized by the impeller. The appendix describes the calculation of the torque coefficients and leakage parameters in Eqs. (9) and (10).

Impeller tip flow recirculation is observed to contribute to the impeller work input for some impellers, particularly high head coefficient impellers with excessive blade loading levels and at low tip relative flow angles. Impeller blade loading levels are evaluated with a generalization of the equivalent diffusion factor, D_{eq}, of Lieblein (1959) given by

$$W_{\max} = (W_1 + W_2 + \Delta W)/2$$

$$D_{eq} = W_{\max}/W_2 \tag{11}$$

where the average blade velocity difference, ΔW, is computed from standard irrotational flow relations, assuming an ideal or optimum blade loading style.

$$\int_0^{L_B} (W_s - W_p)d\xi = 2\pi(r_2 C_{U2} - r_1 C_{U1})/z$$

$$W_s - W_p = \Delta W[1 - |2\xi/L_b - 1|]$$

$$\Delta W = 2\pi d_2 U_2 I_B/(zL_B) \tag{12}$$

The blade stall limit of Lieblein ($D_{eq} = 2$) has been found to be appropriate for impellers also. Hence, when $D_{eq} > 2$, the recirculation work input coefficient is computed from

$$I_R = (D_{eq}/2 - 1)[W_{u2}/C_{m2} - 2 \cot \beta_2]$$

$$I_R \geq 0 \tag{13}$$

Impeller Internal Losses

The adiabatic head loss coefficient in the inlet passage (stations 0 to 1) can be computed with the vaneless passage performance analysis of Aungier (1993). A simple approximation to that analysis has also been found to be sufficient for this purpose.

$$\Delta q_0 = \frac{C_{m1}^2}{2U_2^2}\left[\frac{2c_f(m_1 - m_0)}{b_1} + \frac{\alpha_{c1} - \alpha_{c2}}{13}\right] \tag{14}$$

Equation (14) approximates the friction and curvature loss models of the more exact analysis. The skin friction coefficient is computed from an empirical correlation of pipe friction factors for laminar, transitional and turbulent flow, including surface roughness effects (e.g., see Schlichting, 1979).

Entrance losses are computed for the hub, shroud, and mean streamline positions. The mean streamline entrance velocity is computed from the specified inlet prewhirl, C_{u1}, and conservation of mass. The hub and shroud entrance meridional velocities are estimated from the inlet streamline curvature, κ_1,

$$\kappa = \frac{\partial \alpha_c}{\partial m}$$

$$C_{mh1} = C_{m1}[1 - \kappa_1 b_1/2]$$

$$C_{ms1} = C_{m1}[1 + \kappa_1 b_1/2] \tag{15}$$

If any of the three entrance relative velocities exceeds sonic conditions, normal shock wave relations are used to reduce it to a subsonic value and compute a shock loss, Δq_{sh}. Fundamental shock wave mass and momentum conservation relations are used for this purpose to permit analysis of nonideal gas mixtures. The incidence loss is computed by

$$\Delta q_{\text{inc}} = 0.4(W_1 - C_{m1}/\sin \beta_1)^2/U_2^2 \tag{16}$$

Equation (16) is applied at the hub, shroud, and mean surfaces. The overall incidence and shock losses are then combined in a weighted average, with the mean streamline values weighted 10 times as heavy as the hub and shroud values. At positive incidence angles, Eq. (16) occasionally underestimates the entrance loss. For some impellers, the flow adjustment between the leading edge and the throat is the more significant effect. An entrance diffusion loss is computed to account for these situations:

$$\Delta q_{\text{DIF}} = 0.4(W_1 - W_{th})^2/U_2^2 - \Delta q_{\text{inc}}$$

$$\Delta q_{\text{DIF}} \geq 0 \tag{17}$$

The flow diffusion from the blade inlet to the throat has been found to be a primary indicator of inducer stall. The specific stall criterion derived from available test data is

$$W_{1s}/W_{th} > 1.75 \tag{18}$$

Kosuge et al. (1982) have used the same parameter to correlate the onset of impeller rotating stall as a function of throat Mach number. When inducer stall is predicted, the diffusion loss is limited by

$$\Delta q_{\text{DIF}} \geq 0.5(W_{1s} - 1.75W_{th})^2/U_2^2 - \Delta q_{\text{inc}} \tag{19}$$

Aerodynamic blockage in the throat is modeled by a contraction ratio computed from

$$C_r = \sqrt{A_1 \sin \beta_1/A_{th}}$$

$$C_r \leq 1 - (A_1 \sin \beta_1/A_{th} - 1)^2 \tag{20}$$

The contracted throat area and the sonic flow throat area, A^*_{th}, are used to compute a choking loss:

$$x = 10(1.1 - A^*_{th}/(C_r A_{th})$$
$$\Delta q_{CH} = 0; \quad x \leq 0$$
$$\Delta q_{CH} = (W_1/U_2)^2(0.05x + x^7)/2; \quad x > 0 \qquad (21)$$

The friction factor correlation mentioned earlier is used to compute the impeller friction loss using a hydraulic diameter, d_H, that is the average of the throat and discharge values.

$$\Delta q_{SF} = 2c_f(\bar{W}/U_2)^2 L_B/d_H$$
$$\bar{W}^2 = (W_1^2 + W_2^2)/2$$
$$\bar{W}^2 \geq (W_{th}^2 + W_2^2)/2 \qquad (22)$$

Blade loading and hub-to-shroud loading losses are computed as mixing losses derived from the integrated difference between the average and mass-averaged relative velocity squared for the distorted profiles. The relations used are

$$\Delta q_{BL} = (\Delta W/U_2)^2/48$$
$$\Delta q_{HS} = (\bar{\kappa}\bar{b}\bar{W}/U_2)^2/12$$
$$\bar{\kappa} = (\alpha_{c2} - \alpha_{c1})/L$$
$$\bar{b} = (b_1 + b_2)/2$$
$$\bar{W} = (W_1 + W_2)/2 \qquad (23)$$

where ΔW is given in Eq. (12). Similarly, a discharge profile distortion loss is computed from

$$\Delta q_\lambda = 0.5(\lambda - 1)^2\phi_2^2 \qquad (24)$$

For open impellers, the clearance loss is given by

$$\Delta q_{CL} = \frac{\dot{m}_{CL}\Delta P_{CL}}{\dot{m}\rho U_2^2} \qquad (25)$$

where the calculation of the clearance gap leakage parameters is described in the appendix. A wake mixing loss is computed, assuming that the wake contains stagnant fluid, which mixes with free stream fluid with velocity W_{SEP}. Separation is assumed to occur inside the blade passage if $D_{eq} > 2$. The loss is given by

$$\Delta q_{\text{MIX}} = 0.5[(W_{\text{SEP}} - W_{\text{OUT}})/U_2]^2$$
$$W_{\text{SEP}} = W_2; \quad D_{eq} \leq 2$$
$$W_{\text{SEP}} = W_2 D_{eq}/2; \quad D_{eq} > 2$$
$$W_{\text{OUT}}^2 = [C_{m2}A_2/(\pi d_2 b_2)]^2 + W_u^2 \qquad (26)$$

where A_2 is the discharge area inside the blades. Using relative total thermodynamic conditions at the blade midpassage, the local value of sonic velocity is computed. From the maximum blade surface velocity from Eq. (11), the inlet critical Mach number (corresponding to locally sonic flow on the blade surfaces) is given by

$$\text{M}'_{cr} = \text{M}'_1 W^*/W_{\max} \qquad (27)$$

If the inlet relative Mach number exceeds this critical Mach number, a supercritical Mach number loss is computed by

$$\Delta q_{cr} = 0.2[(\text{M}'_1 - \text{M}'_{cr})W_{\max}/U_2]^2 \qquad (28)$$

Thermodynamic and Compressibility Effects

The analysis employs a general thermodynamic model suitable for one of several alternate nonideal gas equations of state (e.g., Aungier, 1994). The adjustment of total thermodynamic conditions relative to the rotating frame of reference is accomplished with the usual rothalpy parameter, R, which is constant along a stream surface:

$$R = H - UC_u \qquad (29)$$

R can be evaluated at the impeller inlet from the specified operating conditions. The conversion between R and the various total and static enthalpy values required is governed by

$$H' = h + W^2/2 = R + U^2/2$$
$$H = h + C^2/2 = R + UC_u \qquad (30)$$

These relations and isentropic state change logic offered by the various equations of state permit fluid dynamic calculations at the various locations in the impeller passage.

Largely due to historical reasons, the impeller loss models have been developed as adiabatic head (enthalpy) losses. This is strictly valid for incompressible flow, only. Since adiabatic head is not a state point parameter, a given head loss will produce different results when imposed at different locations. In this analysis, the losses occur in the blade passage, but are imposed at the impeller tip. Similarly, the loss formulations are based on relevant velocity heads, rather than the more correct velocity pressure, $P_t - P$. Again, this is strictly correct only for incompressible flow. The consequence of these two factors is a deterioration in prediction accuracy as rotational Mach number (or pressure ratio) increases.

The adiabatic head loss formulation imposes an enthalpy loss at constant entropy to predict the stage discharge total pressure. The correct approach is to impose an entropy rise at constant total enthalpy. From the basic thermodynamic relation,

$$TdS = dH - vdP \qquad (31)$$

it can be seen that a constant $\Delta q/T'_T$ provides the equivalent of a constant entropy rise. Consequently, the weaknesses of the head loss formulation are correctable by a head loss multiplying factor, f_c, given by

$$f_c = \frac{2T'_{T2}}{T'_{T1} + T'_{T2}} \frac{2(P'_{T1} - P_1)}{\rho_1 W_1^2} \qquad (32)$$

Then, the adiabatic head coefficient is given by

$$\mu_{2T} = I_B - f_c \Sigma \Delta q \qquad (33)$$

where the summation applies to the various loss coefficients presented in this paper. With this head loss correction procedure, the analysis has been used for stage pressure ratios up to 3.5 with no observable difference in prediction accuracy for different pressure ratios. Without this procedure, the deterioration of prediction accuracy with pressure ratio was quite noticeable.

Solution Procedure

The analysis of the impeller is conducted by an iterative solution to converge on the impeller tip mass flow. The impeller work input, losses and seal leakage are computed for each iteration. For covered impellers, the impeller mass flow is corrected

Table 1 Compressor stage data

STAGE	ϕ_{DES}	M_u	DISCHARGE	DIFFUSER
A	0.0093	0.50	RETURN CHANNEL	VANELESS
B	0.0525	0.70	RETURN CHANNEL	VANED
C	0.0950	1.38	VOLUTE	VANELESS
D	0.0950	1.38	VOLUTE	VANED
E	0.0860	0.70	RETURN CHANNEL	VANELESS
F	0.1250	0.70	RETURN CHANNEL	VANELESS

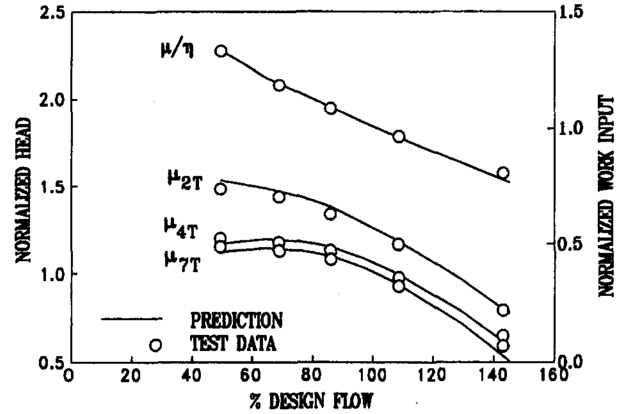

Fig. 4 Performance of Compressor A

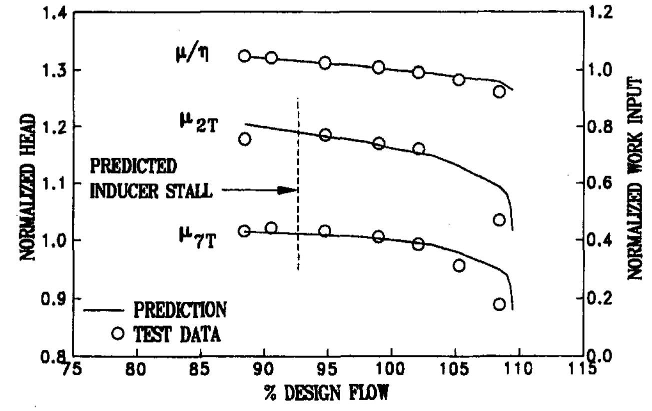

Fig. 6 Performance of Compressor C

to include the cover seal leakage flow. The total work input and tip adiabatic head coefficients define the tip thermodynamic conditions. The computed tip mass flow, $(\rho C_m A)_2$, is compared to the actual impeller mass flow and C_{m2} is updated until the process converges. Once convergence is achieved, the diffuser entrance mass flow is computed by adjusting the impeller mass flow for the seal leakage flows.

Results

The overall centrifugal compressor performance analysis is applicable to a broad range of stage types and operating conditions. Table 1 lists the particular stages for which predictions and test performance are compared in this paper. This performance analysis does not permit any "user adjustments" to the performance models. Hence, the results show predictions directly from the reported models for the precise stage geometry. With the exception of compressor A, these stages have been selected due to their very limited role in the development of the performance models used. The high quality of the test data and ultralow flow coefficient of Compressor A has made it a very valuable test of models relating to friction losses, windage and disk friction, and seal leakage for many years. Compressors B and D were used in the development of the vaned diffuser performance analysis (Aungier, 1990). Compressors C, D, and E were used to validate the head loss correction, Eq. (32), over the wide range of speeds for which they were tested. Compressor F was not used in the development of this analysis.

Figure 4 shows a comparison of predictions and test data for the ultralow flow coefficient compressor A. This stage experiences unusually high parasitic work (cover leakage, windage, and disk friction). The analysis does an excellent job of predicting both work and head, including impeller and diffuser exit heads.

Figure 5 compares predictions with test data for a medium-low flow coefficient vaned diffuser stage. This stage showed a pronounced stall on test with unstable operation at all flows lower than the peak head flow. The onset of this "stall" almost exactly corresponds to the predicted vaned diffuser stall. Tests on this stage with a vaneless diffuser confirm that the vaned diffuser is the source of this unstable operation.

Figure 6 compares predictions with test data for compressor C, a moderately high flow coefficient air compressor stage. This is a volute-type stage with a stage pressure ratio of 3.4, tested with a vaneless diffuser. Figure 7 shows results for the same compressor stage, but with a vaned diffuser. Clearly, the analysis models both stage configurations very well. Again, predicted vaned diffuser stall is shown on Fig. 7, which is almost exactly at the stage test surge flow. For the vaneless diffuser version, inducer stall is predicted in the test operating range. While the impeller tip head coefficient curve suggests a possible impeller stall in this region, intrastage component data for volute stages are rather unreliable due to the circumferential distortion imposed upon the stage by the volute.

Figure 8 shows results for compressor E, a medium flow coefficient return channel stage. It can be seen that agreement between predictions and test data is quite good, including the intrastage component discharge head coefficient curves.

Figure 9 shows results for the very high flow coefficient compressor stage F. This comparison is particularly significant since it is a recent design never used in the development of the analysis. Indeed, Fig. 9 is the projected performance provided by this analysis with actual test performance added. It can be seen that the analysis is quite accurate in its prediction of overall

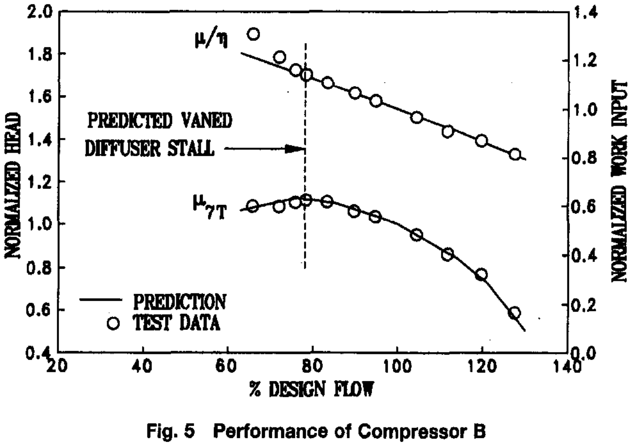

Fig. 5 Performance of Compressor B

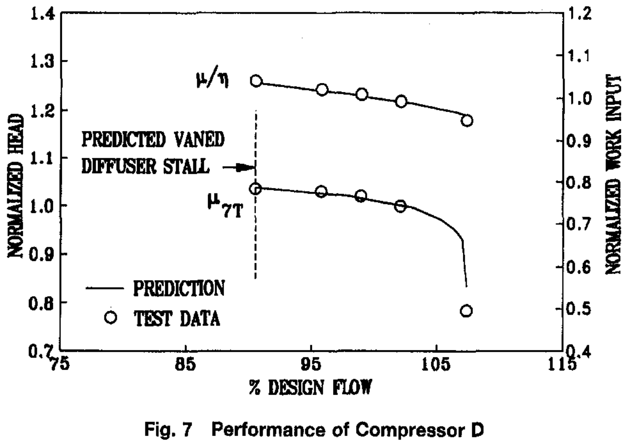

Fig. 7 Performance of Compressor D

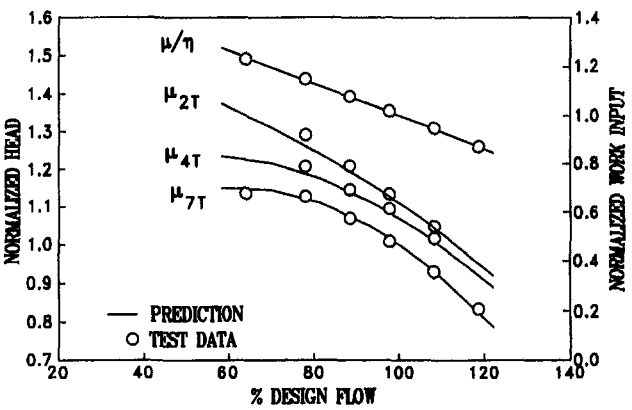

Fig. 8 Performance of Compressor E

and internal component performance. Note that the predicted inducer stall is quite close to the apparent impeller stall indicated by the impeller tip head curve. Further confirmation was obtained in a subsequent test where the vaneless diffuser width was significantly reduced, with no change in the surge flow. That strongly suggests that the impeller, rather than the diffuser, is the component governing surge.

Many additional detailed comparisons of test data with performance predictions from this analysis can be found in Aungier (1990, 1993), where the accuracy of the vaned diffuser, vaneless diffuser, and return system performance analyses is demonstrated.

Conclusions

The impeller analysis presented here, together with the stationary component analyses in the cited open literature, provide a comprehensive mean streamline aerodynamic performance prediction procedure for centrifugal compressor stages. This analysis has been qualified against experimental test data for over one hundred different stages, of widely varying types. Its prediction accuracy is generally excellent for any reasonably well-designed stage. On some very old designs (considered poorly designed by modern standards) the analysis can be less accurate. However, even then, it correctly identifies the weaknesses in those designs and it correctly predicts their performance to be poor. The minimal geometric data needed to apply these performance models is simply not sufficient to identify poor detailed design practice.

Detailed validation of the analysis against experiment has included stage flow coefficients from 0.009 to 0.15 and pressure ratios up to about 3.5. Good results have also been obtained for turbocharger stages at pressure ratios up to 4.2, but test data uncertainty for these units is much greater than for the data used in the detailed validation studies. Application of this analysis significantly beyond this range of experience would require additional validation studies.

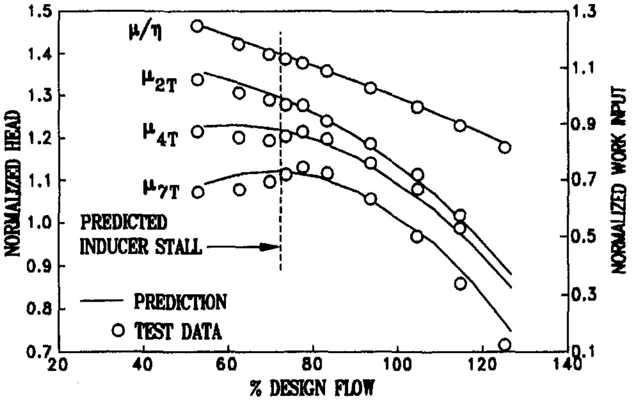

Fig. 9 Performance of Compressor F

References

Aungier, R. H., 1990, "Aerodynamic Performance Analysis of Vaned Diffusers," *Fluid Machinery Components*, ASME FED-Vol. 101, pp. 27–44.

Aungier, R. H., 1993, "Aerodynamic Design and Analysis of Vaneless Diffusers and Return Channels," ASME Paper No. 93-GT-101.

Aungier, R. H., 1994, "A Fast, Accurate Real Gas Equation of State for Fluid Dynamic Analysis Applications," *Contributed Papers in Fluids Engineering 1994*, ASME FED-Vol. 182, pp. 1–6; to be published in ASME *Journal of Fluids Engineering*.

Cumpsty, N. A., 1989, *Compressor Aerodynamics*, Longman Scientific and Technical, Essex, United Kingdom.

Daily, J. W., and Nece, R. E., 1960a, "Chamber Dimension Effects on Induced Flow and Frictional Resistance of Enclosed Rotating Disks," ASME *Journal of Basic Engineering*, Vol. 82, pp. 217–232.

Daily, J. W., and Nece, R. E., 1960b, "Roughness Effects on Frictional Resistance of Enclosed Rotating Disks," ASME *Journal of Basic Engineering*, Vol. 82, pp. 553–562.

Egli, A., 1935, "The Leakage of Steam Through Labyrinth Glands," *Trans. ASME*, Vol. 57, pp. 115–122.

Kosuge, H., Ito, T., and Nakanishi, K., 1982, "A Consideration Concerning Stall and Surge Limitations Within Centrifugal Compressors," ASME *Journal of Engineering for Power*, Vol. 104, pp. 782–787.

Lieblein, S., 1959, "Loss and Stall Analysis of Compressor Cascades," ASME *Journal of Basic Engineering*, Vol. 81, pp. 387–400.

Moussa, Z. M., 1978, "Impeller Casing Clearance Gap Flow Prediction Program," Carrier Corp. Technical Report 9-1030-05, No. 9 (proprietary).

Schlichting, H., 1979, *Boundary Layer Theory*, 7th ed., McGraw-Hill, New York, Chap. 20.

Weber, C. R., and Koronowski, M. E., 1986, "Meanline Performance Prediction of Volutes in Centrifugal Compressors," ASME Paper No. 86-GT-216.

Whitfield, A., and Baines, N. C., 1990, *Design of Radial Turbomachines*, Longman Scientific and Technical, Essex, United Kingdom.

Wiesner, F. J., 1967, "A Review of Slip Factors for Centrifugal Impellers," ASME *Journal of Engineering for Power*, Vol. 89, pp. 558–572.

APPENDIX

Clearance Gap Flows

Leakage, windage, and disk friction effects all require models of the clearance gap flows. This includes the disk/housing gap for the disk side and the shroud side for covered impellers, and the blade/housing clearance gap for open impellers. The flow in the disk/housing gap is modeled as a forced vortex:

$$\frac{\partial P}{\partial r} = K^2\omega^2\rho r \qquad (34)$$

where $K = C_u/(\omega r)$ is assumed constant in the gap. An internal flow analysis for clearance gap flows (Moussa, 1978) was used to develop empirical relations for K, including the effects of seal leakage. Leakage was found to be quite significant due to the influx of angular momentum into the gap. In the absence of seal leakage, the data of Daily and Nece (1960a) suggest the following empirical equation:

$$K_0 = 0.46/(1 + 2s/d) \qquad (35)$$

When leakage flow enters the gap with a swirl parameter K_F, the value of K in the gap is given by

$$K = K_0 + C_q(1.75K_F - 0.316)r_2/s$$

$$C_q = \frac{\dot{m}_L(\rho r_2 U_2/\mu)^{1/5}}{2\pi\rho r_2^2 U_2} \qquad (36)$$

Typically, seal leakage from the tip employs $K_F = C_{u2}/U_2$ while leakage toward the tip uses $K_F = 0$. The validity of these approximations has been reasonably well established by comparing predicted and measured clearance gap radial static pressure profiles for select compressor stages. The resulting pressure distributions are used for predicting the seal leakage and for impeller thrust force calculations. Seal leakage is computed by the method of Egli (1935), although any other suitable formulation could be substituted. Windage and disk friction is calculated with the Daily and Nece (1960a, 1960b) model with a correction for the clearance gap leakage flow. If the Daily and Nece torque coefficient is denoted as C_{M0}, the corrected value is given by

$$C_M = \frac{C_{M0}(1 - K)^2}{(1 - K_0)^2} \tag{37}$$

Equation (37) is somewhat intuitive, but has proven to yield very accurate work input predictions for ultralow flow coefficient stages (e.g., Compressor A) where leakage, windage, and disk friction play a very dominant roll. The torque coefficient is computed for each side of the disk and the disk and cover side values adjusted by

$$C_{MD} = 0.8C_M$$

$$C_{MC} = 0.8C_M \frac{L[1 - (d_{1s}/d_2)^5]}{r_2 - r_1} \tag{38}$$

where the constant 0.8 is an ''experience'' factor selected from correlation with numerous experimental stage work input curves. Since the Daily and Nece C_M refers to both sides of the disk, the factor of 0.8 actually imposes a torque coefficient about 60 percent higher than the Daily and Nece ideal disk flow correlation. Note that C_{MS} includes a correction for the different surface area (relative to a flat disk) for the impeller cover.

For the blade/housing clearance gap of open impellers, the velocity of the leakage flow through the clearance gap is given by

$$U_{CL} = 0.816\sqrt{2\Delta P_{CL}/\rho_2} \tag{39}$$

where the constant throttling coefficient of 0.816 was estimated by assuming an abrupt contraction followed by an abrupt expansion as the flow passes through the gap. The average pressure difference across the gap is estimated from the change in fluid angular momentum through the impeller:

$$\Delta P_{CL} = \frac{\dot{m}(r_2C_{u2} - r_1C_{u1})}{z\bar{r}\bar{b}L}$$

$$\bar{r} = (r_1 + r_2)/2$$

$$\bar{b} = (b_1 + b_2)/2 \tag{40}$$

Then the leakage flow is computed from

$$\dot{m}_{CL} = \rho z s L U_{CL} \tag{41}$$

An Asymptotic Analysis of Mixing Loss[1]

G. Fritsch
MTU Motoren- und Turbinen-Union
München GmbH,
München, Federal Republic of Germany

M. B. Giles
Oxford University Computing Laboratory,
Oxford, United Kingdom

The objective of this paper is to establish, in a rigorous mathematical manner, a link between the dissipation of unsteadiness in a two-dimensional compressible flow and the resulting mixing loss. A novel asymptotic approach and a control-volume argument are central to the analysis. It represents the first work clearly identifying the separate contributions to the mixing loss from simultaneous linear disturbances, i.e., from unsteady entropy, vorticity, and pressure waves. The results of the analysis have important implications for numerical simulations of turbomachinery flows; the mixing loss at the stator/rotor interface in steady simulations and numerical smoothing are discussed in depth. For a transonic turbine, the entropy rise through the stage is compared for a steady and an unsteady viscous simulation. The large interface mixing loss in the steady simulation is pointed out and its physical significance is discussed. The asymptotic approach is then applied to the first detailed analysis of interface mixing loss. Contributions from different wave types and wavelengths are quantified and discussed.

Introduction

Turbomachinery flows are inherently unsteady in the absolute as well as in the relative frame of reference. In the absolute frame, the unsteadiness is a necessary condition for the rotor to extract work from the fluid. In the relative frame, the flow can only be steady in the limit of infinite gaps between blade rows when viscous effects mix out the incoming flow.

A multitude of sources contributes to the unsteadiness. The relative motion of neighboring blade rows, in conjunction with the spatially nonuniform pressure fields locked to loaded blades, leads to an unsteady pressure distribution in both through so-called potential interaction. A blade may move through, and interact with, shock wave systems originating in its own or in a neighboring blade row. Stator wakes, convected downstream with the mean flow, cause unsteadiness in the rotor frame of reference. A related phenomenon is hot streak/rotor interaction due to nonuniformities in the temperature of the combustor outflow. Similarly, secondary flow phenomena like horseshoe vortices, passage vortices, and tip-clearance vortices contribute to unsteadiness. The viscous flow past a blunt turbine trailing edge results in vortex shedding. Trailing-edge vortex shedding has also been found in compressors operating in the supersonic or transonic regime. Shock wave/boundary layer interaction can also be a contributor. Finally, there is unsteadiness induced by the motion of the blades themselves, i.e., blade flutter.

Due to restrictive conditions on the rectification of energy associated with the part of the flow field unsteady in the relative frame (Fritsch, 1992), it is important to know the mixing loss resulting from the dissipation of this energy. This approach, i.e., relating the energy associated with unsteadiness in the relative frame to a mixing loss, is conceptually similar to considerations in turbulence. There, energy is fed into turbulent motion on the length scale of the largest turbulent eddies in a flow. The turbulent kinetic energy is dissipated only after it has cascaded down to eddies of the smallest length scale. Nevertheless, the energy must be regarded as lost upon entering the energy cascade.

In the early 1980's Adamczyk (1985) pointed out the impracticality of unsteady multistage simulations for turbomachinery flows. Such simulations will take orders of magnitude more CPU time than current single-stage simulations. This is not only because there are more blade rows but also because the techniques developed to treat arbitrary pitch ratios, see for example Giles (1990a, 1992), will not work in multistage situations and so the only correct treatment in many situations would be to include every single blade in the engine. For routine design purposes, steady simulations with mixing planes at the stator/rotor interfaces will therefore remain the standard approach for many years. The detailed investigation of the mixing loss associated with this interface model was another driving factor behind the development of the asymptotic analysis.

Nonlinear and Linear Euler Equations

This section briefly introduces the nonlinear Euler equations and their first-order perturbation equations, linearized about a time-mean flow state. They are essential to the theoretical developments in the following two sections.

The nonlinear Euler equations are usually expressed in a form based on the conservation of mass, momentum, and energy:

$$\frac{\partial U}{\partial t} + \frac{\partial F}{\partial x} + \frac{\partial G}{\partial y} = 0 \tag{1}$$

The state vector U and the flux vectors F and G are defined by

$$U = \begin{bmatrix} \rho \\ \rho u \\ \rho v \\ \rho e_t \end{bmatrix}, \quad F = \begin{bmatrix} \rho u \\ \rho u^2 + p \\ \rho uv \\ \rho u h_t \end{bmatrix}, \quad \text{and}$$

$$G = \begin{bmatrix} \rho v \\ \rho uv \\ \rho v^2 + p \\ \rho v h_t \end{bmatrix}. \tag{2}$$

The variables e_t and $h_t = (e_t + p/\rho)$ denote the total energy and the stagnation enthalpy per unit mass, respectively.

From the nonlinear Euler equations in the *conservation* form

---

[1] This research was conducted during the authors' affiliation with the Department of Aeronautics & Astronautics at the Massachusetts Institute of Technology, Cambridge, MA 02139.

Contributed by the International Gas Turbine Institute and presented at the 38th International Gas Turbine and Aeroengine Congress and Exposition, Cincinnati, Ohio, May 24–27, 1993. Manuscript received at ASME Headquarters March 17, 1993. Paper No. 93-GT-345. Associate Technical Editor: H. Lukas.

given above, the linear Euler equations in so-called *primitive* form are easily derived:

$$\frac{1}{a_0}\frac{\partial U_1}{\partial t} + A_0 \frac{\partial U_1}{\partial x} + B_0 \frac{\partial U_1}{\partial y} = 0 \tag{3}$$

The state vector

$$U_1 = [\tilde{\rho}, \tilde{u}, \tilde{v}, \tilde{p}]^T \tag{4}$$

contains the perturbations in primitive form, nondimensionalized by the mean density ρ_0 and the mean speed of sound a_0. Note that the energy equation has been replaced by an equation for the pressure. The matrices A_0 and B_0 are based on the mean flow state $U_0 = [\rho, u, v, p]_0^T$ about which the nonlinear Euler equations were linearized; they are found in the appendix.

Searching for wave-type solutions of the form

$$U_1 = \hat{U}_{r,l} \exp\{i(k_{x,l}x + k_y y - \omega t)\} \tag{5}$$

to the linear Euler equations, one is led to an eigenvalue problem, a detailed derivation of which is found in Giles (1990b). The symbol $\hat{U}_r$ denotes a right eigenvector corresponding to one of four linear waves that satisfy Eq. (3). The real part is implied by complex notation. With the asymptotic analysis in the following sections in mind, the wavenumber k_y (or equivalently the wavelength λ_y) and the frequency ω are assumed to be known a priori; the wavenumbers $k_{x,l}$ corresponding to the four waves are set via a dispersion relation in the eigenvalue problem.

The first two of these waves, the entropy wave ($l = 1$), with a perturbation in the density (temperature) only, and the vorticity wave ($l = 2$), with perturbations in the velocity components only, are convected with the mean flow. The corresponding axial wavenumbers $k_{x,1/2}$ and right eigenvectors $\hat{U}_{r,1/2}$ are

$$k_{x,1} = k_{x,2} = k_y \frac{(\Omega - \mathrm{M}_{y,0})}{\mathrm{M}_{x,0}} \quad \text{where} \quad \Omega = \frac{\omega}{a_0 k_y}, \tag{6}$$

$$\hat{U}_{r,1} = \begin{bmatrix} 1 \\ 0 \\ 0 \\ 0 \end{bmatrix}, \quad \text{and} \quad \hat{U}_{r,2} = \begin{bmatrix} 0 \\ -\mathrm{M}_{x,0} \\ \Omega - \mathrm{M}_{y,0} \\ 0 \end{bmatrix}. \tag{7}$$

$\mathrm{M}_{x,0}$ and $\mathrm{M}_{y,0}$ stand for the mean Mach numbers in the axial and the circumferential direction. The remaining two waves are pressure waves ($l = 3, 4$) corresponding to the axial wavenumbers

$$k_{x,3/4} = k_y \frac{(\Omega - \mathrm{M}_{y,0})(\pm R - \mathrm{M}_{x,0})}{1 - \mathrm{M}_{x,0}^2} \tag{8}$$

where

$$R = \sqrt{1 - \frac{1 - \mathrm{M}_{x,0}^2}{(\Omega - \mathrm{M}_{y,0})^2}}\,. \tag{9}$$

For a negative discriminant of R, the root with positive imaginary part is implied. The corresponding eigenvectors are

$$\hat{U}_{r,3/4} = \begin{bmatrix} -(\Omega - \mathrm{M}_{y,0})(\pm \mathrm{M}_{x,0}R - 1) \\ (\Omega - \mathrm{M}_{y,0})(\pm R - \mathrm{M}_{x,0}) \\ (1 - \mathrm{M}_{x,0}^2) \\ -(\Omega - \mathrm{M}_{y,0})(\pm \mathrm{M}_{x,0}R - 1) \end{bmatrix}. \tag{10}$$

In axially subsonic flow ($|\mathrm{M}_{x,0}| < 1$), they represent isentropic evanescent pressure waves ("cut-off" sound waves) with amplitudes decaying axially upstream and downstream for a reduced frequency $(\mathrm{M}_{y,0} - \sqrt{1 - \mathrm{M}_{x,0}^2}) \leq \Omega \leq (\mathrm{M}_{y,0} + \sqrt{1 - \mathrm{M}_{x,0}^2})$. The evanescent nature is due to the complex conjugate wavenumbers $k_{x,3}$ and $k_{x,4}$. Outside this range, they represent isentropic propagating pressure waves. In axially supersonic flow ($|\mathrm{M}_{x,0}| > 1$), both waves are of propagating nature traveling downstream.

Asymptotic Analysis

A novel asymptotic approach and a control volume argument are central to the analysis. The analysis is split into two steps. In the first, the change in the time-mean flow due to dissipation of unsteadiness is calculated. The second step links the mean-flow change to the corresponding rise in the flux-average entropy.

Mean Flow Changes Due to Mixing. Figure 1 shows the control volume. At the right-hand side, the outflow boundary, the uniform and steady mean flow is described by the state vector $U_{p,\mathrm{out}}$ in primitive form:

$$U_{p,\mathrm{out}} = U_0 = [\rho, u, v, p]_0^T \tag{11}$$

At the left-hand side, the inflow boundary, the spatially and temporally varying flow is described by

$$U_{p,\mathrm{in}}(x, y, t) = U_0 + \Delta U(x, y, t). \tag{12}$$

The top and bottom surfaces are periodic boundaries. In a turbomachine, the control volume may be thought as being located in a blade row gap or downstream of the last blade row.

The perturbation ΔU is described by an asymptotic expression in the small parameter ϵ.

$$\Delta U(x, y, t) = \epsilon U_1(x, y, t) + \epsilon^2 U_2(x, y, t) + \ldots \tag{13}$$

For the objectives of this paper, it will suffice to include terms

Nomenclature

a = speed of sound
c_p = specific heat at constant pressure
$\hat{e}_j$ = jth unit vector = $[\delta_{1j}, \delta_{2j}, \delta_{3j}, \delta_{4j}]^T$
e_t = total internal energy
h_t = stagnation enthalpy
k = wave number
p, s = pressure, entropy
u/v = velocity in the direction of the coordinate x/y
x = axial coordinate
y = circumferential coordinate
A, B = coefficient matrices, defined in the appendix
F, G = flux vectors, defined in Eq. (2)
M = Mach number
P = pitch
S = entropy flux = ρus
T = period, temperature
U = state vector in primitive or conservative form
$\hat{U}_r$ = complex right eigenvector in primitive form
V_R = rotor speed
γ = ratio of specific heats for an ideal gas
ρ = density
ω/Ω = frequency/reduced frequency, defined in Eq. (6)

Subscripts/Superscripts

l, m, n = wave type, spatial harmonic, temporal harmonic
p = in primitive form
x/y = in the direction of the coordinate x/y
0 = mean state
1 = first-order (perturbation), or entropy wave
2 = second-order (perturbation), or vorticity wave
3/4 = pressure wave
$\tilde{*}$ $\triangleq$ unsteady first-order perturbation
$\overline{*}$ $\triangleq$ temporal and spatial mean

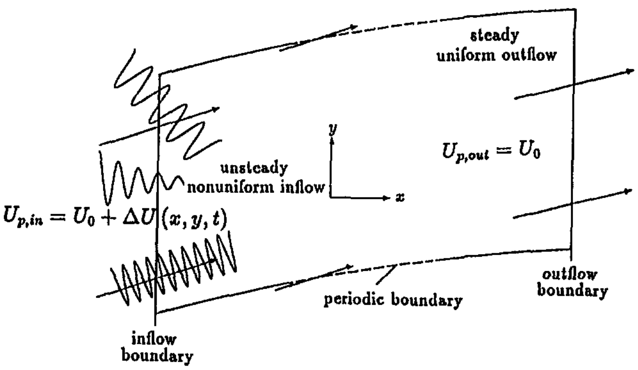

Fig. 1 Control volume for the asymptotic analysis

up to second order. A similar asymptotic approach to the Euler equations is taken in Giles (1992) for the simulation of unsteady flows through multistage turbomachinery.

The first-order perturbation, $U_1(x, y, t)$, is described by a superposition of the four linear waves that were introduced in the previous section:

$$U_1(x, y, t) = \sum_m \sum_n U_{1,mn}(x, y, t)$$

where

$$U_{1,mn} = \sum_{l=1}^{4} b_{lmn} \bar{U}_{r,lmn} \exp\{i(k_{x,lmn}x + k_{y,m}y - \omega_n t + \varphi_{lmn})\} \quad (14)$$

By linear superposition of waves of different physical nature, wavenumber $k_{y,m}$ along the interface, and frequency ω_n, any finite periodic disturbance can be build up. The scalar b denotes a wave amplitude, the variable φ a phase angle. The subscript l distinguishes different wave types, the subscript m different wavenumbers k_y, and the subscript n different frequencies ω.

Integrating the Euler equations in conservation form (1) over the control volume of Fig. 1 and averaging over a period yield

$$\bar{F}_{\text{out}} = \bar{F}_{\text{in}}, \quad (15)$$

where the overbar $(\bar{*}) = 1/T \int_0^T [1/P \int_0^P (*)dy]dt$ denotes an operator combining both spatial and temporal averaging.

A formal Taylor series expansion for the components of the flux vector, F_j, yields:

$$F_j(U_0 + \Delta U) = F_j(U_0) + \left.\frac{dF_j}{dU_p}\right|_{U_p=U_0} \Delta U + \frac{1}{2} \Delta U^T \left.\frac{d^2F_j}{dU_p^2}\right|_{U_p=U_0} \Delta U + \ldots \quad (16)$$

The second derivatives of the flux vector elements F_j, i.e., the matrices d^2F_j/dU_p^2, along with the matrix of first derivatives dF/dU_p, are found in the appendix. Substituting the asymptotic expression (13) into Eq. (16) and averaging, one obtains

$$\bar{F}_j(U_0 + \Delta U) = F_j(U_0) + \epsilon^2 \left[\overline{\frac{1}{2} U_1^T \left.\frac{d^2F_j}{dU_p^2}\right|_{U_p=U_0} U_1} + \left.\frac{dF_j}{dU_p}\right|_{U_p=U_0} \bar{U}_2 \right] + \ldots \quad (17)$$

Note that terms linear in U_1 have dropped out upon averaging.

Equating fluxes as in Eq. (15) and collecting terms in ϵ^2, one obtains a linear system of equations that can solved for $\bar{U}_2(x)$, the time-mean part of U_2:

$$\bar{U}_2 = -\frac{1}{2} \left[\left.\frac{dF}{dU_p}\right|_{U_p=U_0} \right]^{-1} \sum_{j=1}^{4} \vec{e}_j \sum_m \sum_n \overline{U_{1,mn}^T \left.\frac{d^2F_j}{dU_p^2}\right|_{U_p=U_0} U_{1,mn}} \quad (18)$$

The vector $\vec{e}_j$ is the jth unit column vector with a unit entry in the jth row. To arrive at Eq. (18), the orthogonality of trigonometric functions has been employed to replace the two double sums implicitly contained in Eq. (17) via U_1 by a single double sum over m and n. Equation (18) shows the separate contributions to the mean-flow change from waves of different wavenumbers $k_{y,m}$ and/or frequencies ω_n. Waves in U_1 of different physical nature but of the same wavenumber k_y and the same frequency ω cannot be separated in the mean-flow change.

It is also interesting to note that the mean flow change $\bar{U}_2$ and the mean inflow state $\bar{U}_{p,\text{in}} = U_0 + \bar{U}_2$ depend on the axial location of the inflow boundary. They vary periodically because the phase angles among waves of different physical nature (and therefore different axial wavenumber $k_{x,l}$) contained in $U_{1,mn}$ change periodically in the axial direction, causing the elements of $U_{1,mn}$, and consequently $\bar{U}_2$, to vary periodically.

Entropy Rise Due to Mixing. The entropy is the only measure of irreversibility in an unsteady nonuniform flow with a sound physical foundation. For an inviscid adiabatic flow, the substantial derivative of the specific entropy is zero. Combined with the continuity equation, this statement can be expressed as

$$\frac{\partial(\rho s)}{\partial t} + \frac{\partial(\rho u s)}{\partial x} + \frac{\partial(\rho v s)}{\partial y} = 0. \quad (19)$$

For an inviscid adiabatic flow, integration of Eq. (19) over the control volume in Fig. 1 leads to $\partial\overline{\rho us}/\partial x = 0$. The average of the entropy flux $\overline{\rho us}$ is conserved in the axial direction. Note that no such condition holds in unsteady nonuniform flows for the average of the total pressure flux $\overline{\rho u p_t}$, which is often used as an alternate indicator of loss.

Analogous to Eq. (17), one can derive an equation for the entropy flux.

$$\bar{S}(U_0 + \Delta U) = S(U_0) + \epsilon^2 \left[\overline{\frac{1}{2} U_1^T \left.\frac{d^2S}{dU_p^2}\right|_{U_p=U_0} U_1} + \left.\frac{dS}{dU_p}\right|_{U_p=U_0} \bar{U}_2 \right] + \ldots \quad (20)$$

The first and second derivatives of the entropy flux are given in the appendix. With the mean flow change $\bar{U}_2$ known from Eq. (18), the change in the mean specific entropy $\bar{s}$ due to mixing can be calculated from Eq. (20). For physical interpretation, it is better to write $\Delta\bar{s}$ in explicit form rather than in vector/matrix form:

$$\Delta\bar{s} = \frac{(\rho us)_{\text{out}} - (\overline{\rho us})_{\text{in}}}{\rho_0 u_0 c_p} = \sum_m \sum_n \Delta\bar{s}_{mn}$$

where

$$\Delta\bar{s}_{mn} = \frac{1}{2} \left[(\gamma - 1) \left(\overline{\tilde{u}^2} + \overline{\tilde{v}^2} + \overline{\tilde{p}^2} + 2 \frac{\overline{\tilde{p}\tilde{u}}}{M_{x,0}} \right)_{mn} + \overline{(\tilde{p} - \tilde{\rho})^2_{mn}} \right] \quad (21)$$

Equation (21) is in terms of the incoming first-order perturbations contained in $U_{1,mn} = [\tilde{\rho}, \tilde{u}, \tilde{v}, \tilde{p}]^T_{mn}$. The vector $U_{1,mn}$ still is a superposition; it contains waves of the same frequency ω_n and wavenumber $k_{y,m}$ but of different physical nature. Equation (22), the final result of the analysis, has been rewritten in a form showing the separate contributions to the mixing loss from waves of different physical nature. Details are found in Fritsch (1992).

$$\Delta\bar{s}_{mn} = \underbrace{\frac{\overline{\tilde{\rho}^{2}}_{1,mn}}{2}}_{\text{entropy wave}} + \underbrace{\frac{\gamma-1}{2}[\overline{\tilde{u}_2^2}+\overline{\tilde{v}_2^2}]_{mn}}_{\text{vorticity wave}}$$

$$+ \underbrace{\frac{\gamma-1}{2}\left[\overline{\tilde{u}_3^2}+\overline{\tilde{v}_3^2}+\overline{\tilde{p}_3^2}+2\,\frac{\overline{\tilde{p}_3\tilde{u}_3}}{\mathrm{M}_{x,0}}\right]_{mn}}_{\text{pressure wave propagating downstream}}$$

$$+ \underbrace{\frac{\gamma-1}{2}\left[\overline{\tilde{u}_4^2}+\overline{\tilde{v}_4^2}+\overline{\tilde{p}_4^2}+2\,\frac{\overline{\tilde{p}_4\tilde{u}_4}}{\mathrm{M}_{x,0}}\right]_{mn}}_{\text{... propagating upstream or downstream}} \quad (22)$$

Note that the entropy rise $\Delta\bar{s}$, unlike the mean flow change $\bar{U}_2$, is independent of the axial location of the inflow boundary. While the vector of perturbations $U_{1,mn}$, containing a superposition of perturbations from four different wave types, changes with the axial location of the inflow boundary, the entropy rise upon mixing is unaffected. Conceptually, the inflow boundary is located in a region of inviscid adiabatic flow and no mechanism of entropy generation exists between two different axial locations. Therefore, the waves of different physical nature have to discouple in the calculation of the entropy rise in order to render it independent of the inflow boundary location.

At this point it is appropriate to point out that Eq. (22) assumes a constant mean flow state U_0, i.e., constant area, during mixing. If the flow undergoes expansion before or during mixing, the mixing loss will be less. The opposite holds if the flow undergoes diffusion; see for example Denton and Cumpsty (1987).

Physical Interpretation

Entropy and Vorticity Waves. The first term on the right-hand side of (22) represents the entropy increase through mixing of density variations associated with entropy waves. Hot streaks resulting from a nonuniform combustion are an example of entropy waves in turbomachinery.

The second term represents the effect of the mixing-out of velocity fluctuations associated with vorticity waves. This term's contribution to the entropy rise is related to the average kinetic energy per unit mass in a frame of reference convected with the mean flow. It is independent of the mean Mach numbers and can also be derived from $\Delta\bar{s} = \Delta\bar{q}/(c_pT_0)$ with the specific heat release $\Delta\bar{q}$ replaced by the average kinetic energy $(\tilde{u}^2 + \tilde{v}^2)/2$ per unit mass in the convected frame. Note that this term coincides with an earlier result of Kemp and Sears (1956) for the energy transfer to a vorticity wake in an incompressible flow.

Propagating Pressure Waves. The pressure wave contributions on the right-hand side of Eq. (22) are in terms of the axial component of an acoustic energy flux originally put forward by Ryshov and Shefter (1962) and are appropriate for an observer moving with the mean flow. Eversman (1979) showed this energy flux and the corresponding acoustic energy density $E = (\tilde{p}_3^2 + \tilde{u}_3^2 + \tilde{v}_3^2)/2$, which is the sum of potential and kinetic energy, to be consistent with the energy equation in a uniform mean flow. In the limit of very high axial Mach numbers, the pressure waves are essentially convected with the mean flow and their main contribution to the entropy rise stems from the dissipation of their potential and kinetic energy. For small axial Mach numbers, the term containing a factor $(1/\mathrm{M}_{x,0})$, representing the axial flux of acoustic energy across the inflow boundary of the control volume, dominates.

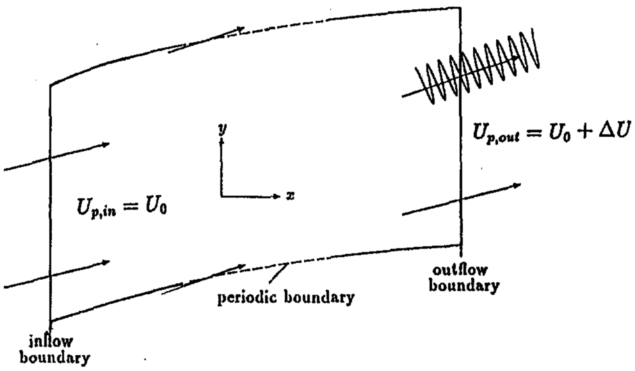

Fig. 2 Control volume, revisited for pressure waves

It is important to recall that weak shock waves can be modeled as a superposition of isentropic pressure waves with the vector sum of local propagation velocity (speed of sound) and local convection velocity along the shock front. Thus, the presence of weak shock waves at the inflow boundary will also cause a mixing loss. Its magnitude is correctly captured by the first pressure wave contribution in Eq. (22).

Also note the analogy with the wave drag acting on a supersonic airfoil. Energy fed into Mach waves originating at the airfoil surface is eventually dissipated and leads to a corresponding increase in entropy. In inviscid flow, the rate of energy transfer to the moving airfoil and the rate of energy dissipation equal the wave drag times the airfoil speed.

The physical interpretation of the pressure wave contributions depends on the axial Mach number of the mean flow. The first pressure wave contribution, identified by a subscript "3" in Eq. (22), always propagates downstream, entering the control volume at the inflow boundary. So does the second pressure wave, identified by a subscript "4," for an axially supersonic mean flow ($\mathrm{M}_{x,0} > 1$). In axially subsonic flow ($\mathrm{M}_{x,0} < 1$), a situation can arise in which a pressure wave leaves the control volume at the upstream boundary, the inflow boundary of the mean flow. Since, by way of the problem definition in Fig. 1, no waves enter at the downstream boundary and propagate upstream, a wave leaving the control volume at the inflow boundary leads to difficulties in physical interpretation. There are two ways to understand the contribution of this wave.

The first is to interpret the wave as a reflected wave, in which case a corresponding downstream propagating wave must also be present at the inflow boundary. Its negative contribution to the entropy rise reflects the fact that not all of the incoming wave is dissipated. This is the appropriate point of view in the analysis of the steady numerical simulation to be considered later on.

The second way is to reformulate the problem, as is illustrated in Fig. 2. The flow is now uniform at the inflow boundary and the unsteady pressure waves enter at the outflow boundary. A physical example of this situation is a shock wave ahead of a supersonic fan. The entropy rise between inflow and outflow boundary due to dissipation of an upstream propagating pressure wave or a weak shock wave is then given by the negative of the second pressure wave contribution in Eq. (22).

Evanescent Pressure Waves. For single evanescent pressure waves the last two terms in Eq. (22) are zero. They do not contribute to the mixing loss. The simultaneous presence of both evanescent pressure waves, one decaying upstream and the other one downstream, leads to a change in the entropy flux between inflow and outflow through crosscoupling terms upon transformation of Eq. (21) into Eq. (22). This case, however,

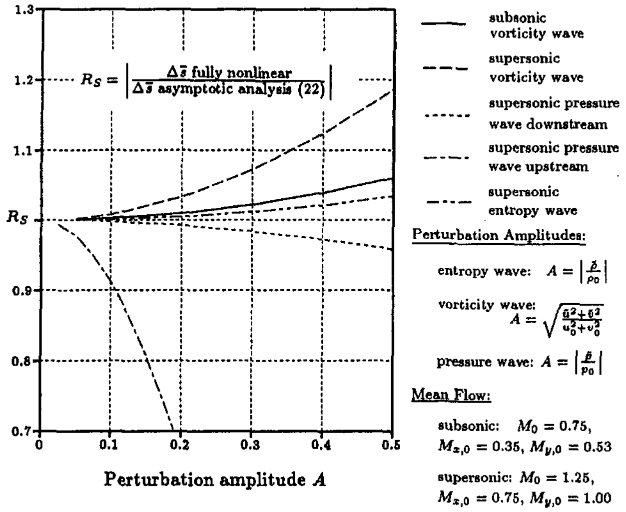

Fig. 3 *Accuracy of the second-order entropy rise ($\Omega = 0$)*

represents an ill-posed problem because the postulated mean flow state U_0 does not exist.

Numerical Check and Accuracy

The analytical results for the mean-flow change $\bar{U}_2$ (Eq. (18)) and the entropy rise $\Delta \bar{s}$ (Eq. (22)) were checked against a numerical simulation. The mean-flow change and the entropy rise were calculated using both the result of the asymptotic analysis and a fully nonlinear approach.

An arbitrary combination of waves of arbitrary amplitudes b_{lmn} and phase angles φ_{lmn} but the same reduced frequency Ω_{mn} was superimposed upon a mean flow of arbitrary Mach numbers $M_{x,0}$ and $M_{y,0}$. In the limit of infinitesimal wave amplitudes, the two approaches yield identical result regardless of the mean flow state, the composition of the disturbance vector, and the reduced frequency. For zero reduced frequency, Fig. 3 shows the accuracy of the entropy rise calculated from Eq. (22) versus the perturbation amplitude. Only a single wave was entering (or leaving) the control volume. While the choice of a single disturbance is necessarily arbitrary, it allows one to judge the degree of nonlinearity in the Euler equations and the range of applicability of the asymptotic analysis for different disturbance types and mean flows.

Implications for Flow Simulations

Mixing Loss at the Stator/Rotor Interface. Turbomachinery flows are inherently unsteady. Nevertheless, steady simulations prevail as routine design tools because they are easier to implement and less CPU-intensive than unsteady simulations. In steady simulations the nonuniform axial fluxes of mass, momentum, and energy, defined in Eq. (2), are mixed out at the stator outflow boundary and subsequently transferred to the rotor frame to provide uniform and steady inflow boundary conditions. Other approaches are possible and are used in practice but they are nonconservative, i.e., the fluxes are not conserved across the interface, and they defy physical interpretation. The interface mixing loss associated with a conservative approach can be examined with the help of the asymptotic analysis presented above. A detailed case study is found in the next section. Four important general findings, however, need to be pointed out first.

First, the entropy rise (Eq. (22)) is invariant to a circumferential translation of the control volume. Thus, it is independent of the frame of reference in which Eq. (22) is applied. It can be calculated in the absolute or in the relative frame. While the right eigenvectors (7) and (10), and therefore the perturbations of the primitive variables in Eq. (22), depend on the Mach number M_y, they do so only through a factor $(\Omega - M_y)$. With the reduced frequencies in stator and rotor related by

$$\Omega_R = \Omega_S - \frac{V_R}{a_0}, \tag{23}$$

the above-mentioned factor and the mixing loss remain constant upon changing the frame of reference.

Second, the interface entropy rise in a steady simulation is the same that would be observed if the flow were allowed to mix out completely at constant area in the limit of an infinite blade row gap. Since stator outflow and rotor inflow boundary are sliding past each other with zero axial gap, the mixing occurs at constant area and the results of the asymptotic analysis, Eqs. (18) and (22), apply.

Third, evanescent pressure waves (''cut-off'' sound waves) do not contribute a mixing loss. As a consequence, the potential field associated with an upstream blade row, which represents an evanescent pressure wave, does not lead to a mixing loss at the steady interface. Entropy and vorticity waves are simply convected with the mean flow and their contribution to the mixing loss is independent of the interface location within the blade row gap. Therefore, it is unnecessary to place the interface far downstream of the trailing edges to keep the mixing loss small. Barring the effects of numerical smoothing, the mixing loss is not affected by the interface position in an inviscid simulation. This statement carries over qualitatively to viscous simulations.

Fourth, the interface model gives the ''physically correct'' mixing loss for propagating pressure waves as well as for weak shock waves. The presence of weak shock waves at the interface will cause a loss; it is the same the flow would experience if it were allowed to go through the corresponding, axially weakening, sequence of shocks in the limit of an infinite blade row gap.

Numerical Smoothing. The control volume argument and the asymptotic analysis made no assumption other than adiabatic mixing at constant area and the applicability of the linear/quadratic regime, i.e., the neglect of terms of order higher than two. In particular, no assumption was made about the mechanism mixing out the flow within the control volume. The results, Eqs. (18) and (22), are therefore valid for a physical flow mixed out by the action of laminar or turbulent viscosity and conductivity as well as for a simulated flow mixed out by the action of numerical smoothing. Smoothing is required to stabilize numerical simulations of the Euler equations. Equations (18) and (22) hold in the presence of second-difference smoothing, which mimics the action of physical viscosity, and in the presence of fourth-difference smoothing, which has no physical counterpart. The former is necessary to capture shock waves, the latter to dissipate high-wavenumber oscillations, which are solutions to the finite difference equations but not the partial differential equations.

Two conclusions can be drawn. First, as long as the basic formulation and the numerical implementation of algorithm plus smoothing are conservative, the results (18) and (22) hold in a numerical simulation. Second, the simulation of a flow in which waves are dissipated by way of numerical smoothing must essentially show the same integrated entropy rise as the corresponding physical flow in which the waves are dissipated by the action of physical viscosity and conductivity.

Application to a Turbine Stage

The asymptotic analysis can be used to investigate in detail the mixing loss at a steady interface in a numerical simulation. A viscous simulation of a highly loaded transonic high-pressure turbine stage, called the ACE turbine stage, which has been

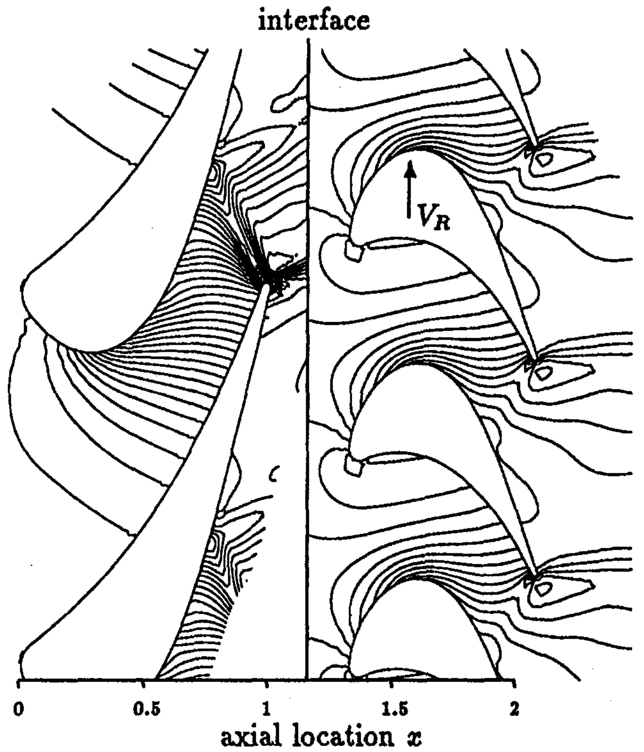

Fig. 4 Static pressure contours in a steady simulation of the ACE turbine stage

tested at MIT Guenette et al. (1989), was chosen as an example. The simulation was performed with the code UNSFLO by Giles (1991).

Global Analysis. Figure 4 shows the static pressure contours in a steady simulation of the flow through the ACE turbine stage. A detailed account of the unsteady interaction is found in Giles (1990a). The axial coordinate x has been nondimensionalized by the stator axial chord. The stator leading edge is located at $x = 0$, the trailing edge at $x = 1$. The shock waves originating at the stator trailing edge are seen to vanish at the interface. The outflow boundary conditions ensure that entropy, vorticity waves, and pressure waves leave the stator computational domain with very little reflection. Between the stator outflow and the rotor inflow, bounding a control volume of zero axial extent, the flow is first mixed out and then transferred to the rotor frame to provide steady and uniform inflow boundary conditions.

Figure 5 compares the time-mean flux average of the specific entropy $\bar{s}$ in the blade passages for a steady and for an unsteady simulation. It is defined analogous to Eq. (21):

$$\bar{s}(x) = \frac{\int_0^1 \left[\int_0^1 (\rho u s) \Big|_x d(y/P) \right] d(t/T)}{c_p \int_0^1 \left[\int_0^1 (\rho u) d(y/P) \right] d(t/T)}$$

The focus here is the steady interface. Of the total entropy rise in the steady simulation about 20 percent is caused by mixing loss at the stator/rotor interface. Although it was recognized previously that the interface treatment in steady simulations results in an entropy rise, see for example Denton (1992), its potentially large magnitude needs to be pointed out. While its level of unsteadiness and its level of mixing loss are high, the ACE stage is representative of modern high-pressure turbine design.

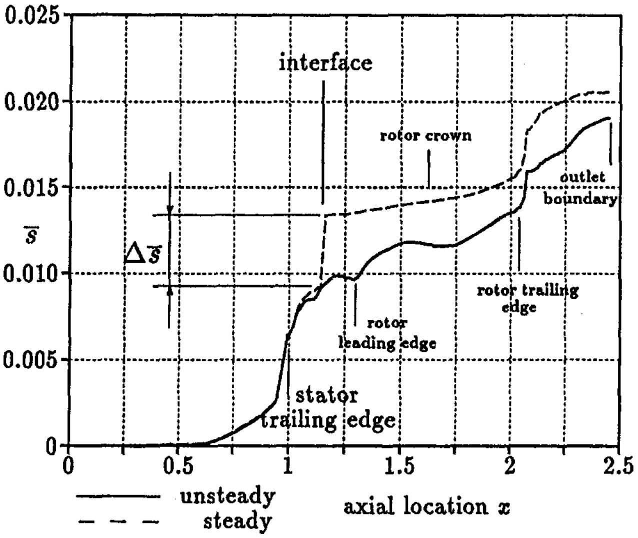

Fig. 5 Entropy rise in numerical simulations of the ACE stage (turbulent boundary layers/no free-stream turbulence)

Beyond the interface, the entropy rise is slower in the steady than in the unsteady simulation. All waves that could cause unsteadiness in the rotor frame, and additional entropy rise upon dissipation, have been mixed out at the interface already. As a consequence, the total entropy rise through the stage remains only 8 percent higher in the steady simulation despite the contribution at the interface. Part of the interface mixing loss must thus be viewed as being physically meaningful but having occurred prematurely at the interface; it is not merely a numerical artifact.

An important question remaining to be answered is whether the differing loci of dissipation in a real flow or an unsteady simulation thereof on the one side and in a steady simulation on the other side are quantitatively significant. The authors tend to believe that, in general, they are not. A note of caution is in order though because mixing at the steady interface occurs localized at constant mean flow state while mixing in the rotor passage of the unsteady simulation occurs in an expansion region. With the same wave amplitudes dissipated in both cases, the entropy rise at the steady interface is higher.

Detailed Asymptotic Analysis. The asymptotic analysis is now applied to the investigation of interface mixing loss; it is used to identify the contributors and the magnitude of their contributions. This kind of detailed information was not available previously.

To that end, the nonuniform stator outflow of the steady simulation is decomposed into its Fourier modes along the boundary. The wavenumbers $k_{y,m}$ are set by the stator pitch and the number of boundary nodes. The individual waves contained in these modes are determined with the help of the left eigenvectors corresponding to the right eigenvectors $\hat{U}_{r,l}$. With the individual waves amplitudes known, Eq. (22) is used to determine the magnitude of their contributions to the mixing loss.

Table 1 Mixing loss at the interface, by wave type

predicted entropy rise $\Delta\bar{s}$	0.00436
Entropy waves ($k_{x,1m}$)	4.3%
Vorticity waves ($k_{x,2m}$)	15.6%
Pressure waves ($k_{x,3m}$)	80.9%
Pressure waves ($k_{x,4m}$)	−0.8%

Table 2 Mixing loss at the interface, by wavenumber

entropy rise $\Delta\bar{s}$ in the simulation	0.00417
entropy rise $\Delta\bar{s}$ predicted	0.00436
wavenumber $k_{y,1}$	49.9%
$k_{y,2}$	32.5%
$k_{y,3}$	9.2%
$k_{y,4}$	5.2%
all higher modes	3.2%

Table 1 lists the contributions by wave type, regardless of wavenumber along the interface. Pressure waves propagating downstream (with wavenumber $k_{x,3m}$) are seen to account for the major part of the mixing loss. In a *steady subsonic* flow all pressure waves are of evanescent nature, as is easily deduced from Eq. (8); they do not contribute to the entropy rise. In a *steady supersonic* flow, like the outflow of the ACE stator, all pressure waves are of propagating nature and do contribute.

As was pointed out earlier, weak shock waves can be modeled as isentropic pressure waves. The analysis does exactly that; the shock waves present at the stator outflow boundary are interpreted as pressure waves propagating downstream. The asymptotic analysis yields the "physically correct" interface mixing loss upon their dissipation. The oblique shock waves introduce a relatively strong perturbation at the stator outflow boundary and are the primary cause of the large entropy rise at the interface.

Vorticity waves and entropy waves, primarily a consequence of the stator boundary layers, contribute the rest of the mixing loss. There is also a minor negative contribution to the entropy rise from pressure waves propagating upstream. The flow is *axially* subsonic and pressure waves can travel upstream against the mean flow. Since disturbances in the rotor frame do not make themselves felt upstream beyond the interface, these waves are reflections from the stator outlet boundary. While the boundary conditions are designed to pass through waves traveling downstream (Giles, 1990b), their linear nature produces weak reflections in the presence of nonlinear phenomena like shock waves.

Table 2 lists the contributions by wavenumber (or wavelength) along the interface, regardless of the wave type. The fundamental wavenumber along the interface, $k_{y,1}$, correspond to a wave with one period per stator pitch. The importance of higher harmonics is due to the presence of oblique shock waves.

Adding up the individual contributions, the asymptotic analysis is found to overpredict the mixing loss observed in the steady simulation by 4.5 percent. The discrepancy is explained by the nonlinearity of the mixing process in the presence of all but the weakest shock waves. Given the large amplitude of the disturbance at the stator outlet, the ACE turbine stage represents a difficult test for the asymptotic analysis and it exhibits surprising accuracy. Note that this discrepancy is consistent with Fig. 3, which shows that the asymptotic analysis overpredicts the entropy rise due to dissipation of a downstream propagating pressure wave of finite amplitude.

Conclusions

In a rigorous mathematical manner, a link has been established between the dissipation of unsteadiness in a two-dimensional compressible flow and the resulting mixing loss. A novel asymptotic approach and a control-volume argument are central to the analysis. The flux-average entropy rise was found to be the only physically sound measure of loss in an unsteady nonuniform flow. This paper presented the first work clearly identifying and explaining the separate contributions to the mixing loss from simultaneous linear disturbances. The result is consistent with previous work on single vorticity waves or single propagating pressure waves. It was expressed in a form that facilitates understanding of the flow physics involved. A comparison to a fully nonlinear approach shows the asymptotic approach to be accurate up to substantial disturbance levels.

An important result is the finding that evanescent pressure waves, unlike propagating pressure waves, do not contribute a mixing loss. This has important implications for steady numerical simulations of turbomachinery. The potential field of an upstream blade row does not contribute a mixing loss at the stator/rotor interface while weak shock waves and propagating pressure waves contribute the "physically correct" loss. Implications for numerical smoothing were also discussed.

The asymptotic approach was applied to the first detailed analysis of mixing loss at the interface of a steady simulation. In the stage examined, the transonic first stage of a high-pressure turbine, the interface mixing loss was found to account for a surprising 20 percent of the total losses in the stage. So far, the potentially large magnitude of this loss has found little detailed attention in the CFD community. The interface mixing loss is the same that would be observed if the flow were allowed to mix out completely in the limit of an infinite blade row gap. Contributions from different wave types and spatial and temporal harmonics were identified, quantified, and discussed.

References

Adamczyk, J. J., 1985, "Model Equations for Simulating Flows in Multistage Turbomachinery," ASME Paper No. 85-GT-226.

Denton, J. D., and Cumpsty, N. A., 1987, "Loss Mechanisms in Turbomachines," IMechE Paper No. C260/87.

Denton, J. D., 1992, "The Calculation of Three-Dimensional Viscous Flow Through Multistage Turbomachines," ASME JOURNAL OF TURBOMACHINERY, Vol. 114, pp. 18–26.

Eversman, W., 1979, "Acoustic Energy in Ducts: Further Observations," *Journal of Sound and Vibration,* Vol. 62, No. 4.

Fritsch, G., 1992, "An Analytical and Numerical Study of the Second-Order Effects of Unsteadiness on the Performance of Turbomachines," Sc. D. Thesis, Massachusetts Institute of Technology, Cambridge, MA, Apr.

Giles, M. B., 1990a, "Stator/Rotor Interaction in a Transonic Turbine," *Journal of Propulsion and Power,* Vol. 6, No. 5.

Giles, M. B., 1990b, "Non-reflecting Boundary Conditions for Euler Equation Calculations," *AIAA Journal,* Vol. 28, No. 12.

Giles, M. B., 1992, "An Approach for Multi-stage Calculations Incorporating Unsteadiness," ASME Paper No. 92-GT-282.

Giles, M. B., and Haimes, R., 1993, "Validation of a Numerical Method for Unsteady Flow Calculations," ASME JOURNAL OF TURBOMACHINERY, Vol. 115, pp. 110–117.

Guenette, G. R., Epstein, A. H., Giles, M. B., Haimes, R., and Norton, R. J. G., 1989, "Fully Scaled Transonic Turbine Rotor Heat Transfer Measurements," ASME JOURNAL OF TURBOMACHINERY, Vol. 111, pp. 1–7.

Kemp, N. H., and Sears, W. R., 1956, "On the Wake Energy of Moving Cascades," ASME *Journal of Applied Mechanics,* Vol. 23.

Ryshov, O. S., and Shefter, G. M., 1962, "On the Energy of Acoustic Waves Propagating in Moving Media," *Journal of Applied Mathematics and Mechanics,* Vol. 26.

APPENDIX

$$A_0 = \begin{bmatrix} \mathrm{M}_{x,0} & 1 & 0 & 0 \\ 0 & \mathrm{M}_{x,0} & 0 & 1 \\ 0 & 0 & \mathrm{M}_{x,0} & 0 \\ 0 & 1 & 0 & \mathrm{M}_{x,0} \end{bmatrix} \quad B_0 = \begin{bmatrix} \mathrm{M}_{y,0} & 0 & 1 & 0 \\ 0 & \mathrm{M}_{y,0} & 0 & 0 \\ 0 & 0 & \mathrm{M}_{y,0} & 1 \\ 0 & 0 & 1 & \mathrm{M}_{y,0} \end{bmatrix}$$

$$\frac{dF}{dU} = \begin{bmatrix} u & \rho & 0 & 0 \\ u^2 & 2\rho u & 0 & 1 \\ uv & \rho v & \rho u & 0 \\ \frac{u}{2}(u^2 + v^2) & \frac{\gamma}{\gamma - 1} p + \frac{\rho}{2}(3u^2 + v^2) & \rho uv & \frac{\gamma}{\gamma - 1} u \end{bmatrix}$$

$$\frac{d^2F_1}{dU^2} = \begin{bmatrix} 0 & 1 & 0 & 0 \\ 1 & 0 & 0 & 0 \\ 0 & 0 & 0 & 0 \\ 0 & 0 & 0 & 0 \end{bmatrix} \quad \frac{d^2F_2}{dU^2} = \begin{bmatrix} 0 & 2u & 0 & 0 \\ 2u & 2\rho & 0 & 0 \\ 0 & 0 & 0 & 0 \\ 0 & 0 & 0 & 0 \end{bmatrix} \quad \frac{d^2F_3}{dU^2} = \begin{bmatrix} 0 & v & u & 0 \\ v & 0 & \rho & 0 \\ u & \rho & 0 & 0 \\ 0 & 0 & 0 & 0 \end{bmatrix}$$

$$\frac{d^2F_4}{dU^2} = \begin{bmatrix} 0 & \left(u^2 + \frac{u^2 + v^2}{2}\right) & uv & 0 \\ \left(u^2 + \frac{u^2 + v^2}{2}\right) & 3\rho u & \rho v & \frac{\gamma}{\gamma - 1} \\ uv & \rho v & 0 & 0 \\ 0 & \frac{\gamma}{\gamma - 1} & 0 & 0 \end{bmatrix}$$

$$\frac{dS}{dU_p} = \begin{bmatrix} u(s - c_p) \\ \rho \\ 0 \\ \frac{\mathrm{M}_x c_p}{a} \end{bmatrix}^T \quad \frac{d^2S}{dU_p^2} = \begin{bmatrix} -\frac{uc_p}{\rho} & (s - c_p) & 0 & \frac{\mathrm{M}_x c_p}{\rho a} \\ (s - c_p) & 0 & 0 & \frac{c_p}{a^2} \\ 0 & 0 & 0 & 0 \\ \frac{\mathrm{M}_x c_p}{\rho a} & \frac{c_p}{a^{\mathrm{a}}} & 0 & -\frac{\mathrm{M}_x c_p}{ap} \end{bmatrix}$$

DISCUSSION

L. H. Smith, Jr.[1]

The authors are to be congratulated for treating a very complex phenomenon in a comprehensible fashion and distinguishing the effects of the several sources of unsteadiness.

It seems to be implied, although not actually stated, that the mixing loss (entropy rise) from stator exit nonuniformities that is calculated at the interface plane is largely inevitable regardless of what the downstream rotor does to the flow. I have always thought that a rotor could partially flatten a stator vane viscous wake through a reversible energy exchange process, thereby avoiding some of the entropy rise that would occur if the wake were flattened entirely by mixing. In a recent article (Smith, 1993), it is pointed out that the propulsive efficiency of a self-propelled craft can be increased by placing the propulsor in the wake of the craft. It can be shown that the energy thereby saved is just equal to the reduction of wake mixing loss, the wake having been flattened by reversible energy addition rather than by viscous dissipation. This case can be related to the subject of the present paper by thinking of the propelled craft as a giant stator vane and the propulsor as an idealized rotor.

The amount of mixing loss that can be avoided in an actual turbine or compressor by this mechanism is probably not large, but it has been speculated that this may explain part of the gain in efficiency that is usually observed when the stages of a multistage compressor are spaced together more closely.

References

Smith, L. H., Jr., 1993, "Wake Ingestion Propulsion Benefit," *Journal of Propulsion and Power*, Vol. 9, No. 1, pp. 74–82.

---

[1] GE Aircraft Engines, Cincinnati, OH 45215.

$$\frac{dF}{dU} = \begin{bmatrix} u & \rho & 0 & 0 \\ u^2 & 2\rho u & 0 & 1 \\ uv & \rho v & \rho u & 0 \\ \frac{u}{2}(u^2 + v^2) & \frac{\gamma}{\gamma - 1} p + \frac{\rho}{2}(3u^2 + v^2) & \rho uv & \frac{\gamma}{\gamma - 1} u \end{bmatrix}$$

$$\frac{d^2F_1}{dU^2} = \begin{bmatrix} 0 & 1 & 0 & 0 \\ 1 & 0 & 0 & 0 \\ 0 & 0 & 0 & 0 \\ 0 & 0 & 0 & 0 \end{bmatrix} \quad \frac{d^2F_2}{dU^2} = \begin{bmatrix} 0 & 2u & 0 & 0 \\ 2u & 2\rho & 0 & 0 \\ 0 & 0 & 0 & 0 \\ 0 & 0 & 0 & 0 \end{bmatrix} \quad \frac{d^2F_3}{dU^2} = \begin{bmatrix} 0 & v & u & 0 \\ v & 0 & \rho & 0 \\ u & \rho & 0 & 0 \\ 0 & 0 & 0 & 0 \end{bmatrix}$$

$$\frac{d^2F_4}{dU^2} = \begin{bmatrix} 0 & \left(u^2 + \frac{u^2 + v^2}{2}\right) & uv & 0 \\ \left(u^2 + \frac{u^2 + v^2}{2}\right) & 3\rho u & \rho v & \frac{\gamma}{\gamma - 1} \\ uv & \rho v & 0 & 0 \\ 0 & \frac{\gamma}{\gamma - 1} & 0 & 0 \end{bmatrix}$$

$$\frac{dS}{dU_p} = \begin{bmatrix} u(s - c_p) \\ \rho \\ 0 \\ \frac{\mathrm{M}_x c_p}{a} \end{bmatrix}^T \quad \frac{d^2S}{dU_p^2} = \begin{bmatrix} -\frac{uc_p}{\rho} & (s - c_p) & 0 & \frac{\mathrm{M}_x c_p}{\rho a} \\ (s - c_p) & 0 & 0 & \frac{c_p}{a^2} \\ 0 & 0 & 0 & 0 \\ \frac{\mathrm{M}_x c_p}{\rho a} & \frac{c_p}{a^{\mathrm{a}}} & 0 & -\frac{\mathrm{M}_x c_p}{ap} \end{bmatrix}$$

DISCUSSION

L. H. Smith, Jr.[1]

The authors are to be congratulated for treating a very complex phenomenon in a comprehensible fashion and distinguishing the effects of the several sources of unsteadiness.

It seems to be implied, although not actually stated, that the mixing loss (entropy rise) from stator exit nonuniformities that is calculated at the interface plane is largely inevitable regardless of what the downstream rotor does to the flow. I have always thought that a rotor could partially flatten a stator vane viscous wake through a reversible energy exchange process, thereby avoiding some of the entropy rise that would occur if the wake were flattened entirely by mixing. In a recent article (Smith, 1993), it is pointed out that the propulsive efficiency of a self-propelled craft can be increased by placing the propulsor in the wake of the craft. It can be shown that the energy thereby saved is just equal to the reduction of wake mixing loss, the wake having been flattened by reversible energy addition rather than by viscous dissipation. This case can be related to the subject of the present paper by thinking of the propelled craft as a giant stator vane and the propulsor as an idealized rotor.

The amount of mixing loss that can be avoided in an actual turbine or compressor by this mechanism is probably not large, but it has been speculated that this may explain part of the gain in efficiency that is usually observed when the stages of a multistage compressor are spaced together more closely.

References

Smith, L. H., Jr., 1993, "Wake Ingestion Propulsion Benefit," *Journal of Propulsion and Power*, Vol. 9, No. 1, pp. 74–82.

---

[1] GE Aircraft Engines, Cincinnati, OH 45215.

A Reduced Order Model of Unsteady Flows in Turbomachinery

K. C. Hall

R. Florea

Department of Mechanical Engineering
and Materials Science,
Duke University,
Durham, NC 27708

P. J. Lanzkron

Raytheon Company,
Marlborough, MA 01752

A novel technique for computing unsteady flows about turbomachinery cascades is presented. Starting with a frequency domain CFD description of unsteady aerodynamic flows, we form a large, sparse, generalized, non-Hermitian eigenvalue problem that describes the natural modes and frequencies of fluid motion about the cascade. We compute the dominant left and right eigenmodes and corresponding eigenfrequencies using a Lanczos algorithm. Then, using just a few of the resulting eigenmodes, we construct a reduced order model of the unsteady flow field. With this model, one can rapidly and accurately predict the unsteady aerodynamic loads acting on the cascade over a wide range of reduced frequencies and arbitrary modes of vibration. Moreover, the eigenmode information provides insights into the physics of unsteady flows. Finally we note that the form of the reduced order model is well suited for use in active control of aeroelastic and aeroacoustic phenomena.

Introduction

In this paper, we present a new approach for computing unsteady flows through turbomachinery cascades. In particular, we first compute the dominant eigenmodes of the fluid motion. We then use these eigenmodes to construct a compact and efficient dynamic model of the unsteady flow.

Numerous analyses have been developed in recent years to predict the unsteady flows about cascades due to wake interaction and vibratory blade motion. Most of these analyses compute the unsteady flow in the time domain or frequency domain. In time domain analyses (Hodson, 1985; Whitfield et al., 1987; Giles, 1988; Rai, 1989a, 1989b; He, 1990, 1993; Huff et al., 1991; Gerolymos, 1993), one time accurately "time marches" the unsteady flow solution from one time level to the next using conventional computational fluid dynamic (CFD) algorithms. The time domain approach is particularly well suited for solution of nonlinear hyperbolic and parabolic equations such as the potential, Euler, and Navier–Stokes equations. The main drawback is the high computational cost. Because of the requirement that the scheme be accurate and stable, the maximum allowable time step is usually quite small—especially for very fine computational grids—leading to large computational times.

In so-called time linearized analyses (Whitehead and Grant, 1981; Verdon, 1987; Hall and Crawley, 1989; Hall and Clark, 1993; Hall and Lorence, 1993; Hall, 1993; Holmes and Chuang, 1993; Lindquist and Giles, 1994), one assumes that the unsteady flow field is the sum of a time invariant mean flow plus a harmonically varying small disturbance flow. The resulting equations for the small disturbance flow are linear, time invariant variable coefficient equations for the complex amplitude of the unknown small disturbance flow. These small disturbance equations are discretized and solved very efficiently via LU decomposition or an appropriate iterative technique. Typical time-linearized calculations require close to two orders of magnitude less computational time than time-accurate time-marching algorithms. For this reason, the time-linearized approach is widely used in the turbomachinery industry for flutter and forced response calculations.

One criticism of both the time marching and time linearized approaches is that they provide predictions for a single condition only, e.g., a single reduced frequency, interblade phase angle, and mode shape. Other than through extensive parametric studies, these analyses provide little physical insight into the behavior of the unsteady flow. A number of investigators have used the "indicial response" technique to partially alleviate these difficulties for external flows [see for example Nixon (1989)]. More recently, Bakhle et al. (1991) have developed the indicial response technique for use in turbomachinery applications. Using a time-marching analysis, Bakhle et al. computed the time history of the unsteady forces acting on the airfoils in a cascade due to a small indicial step motion of the airfoils. They then Laplace transformed the resulting lift history to find a transform from which they could quickly compute the unsteady lift at any desired frequency. This technique, while providing a somewhat more generally applicable solution from a single time domain calculation, still only provides a solution for a single mode shape of blade vibration. Furthermore, the method obscures the influence of the input (the mode shape of vibration) and the dynamics of the fluid flow on the output (the unsteady force acting on the airfoil).

Parker (1967) noted that cascade acoustic resonances (i.e., eigenmodes) could be excited in cascades resulting in large unsteady forces acting on the airfoils of cascades. He calculated both the natural frequencies and mode shapes of these resonances for low-speed flows about a cascade of unstaggered flat plate airfoils. Parker found that the numerically predicted natural frequencies compared quite well with those he measured experimentally.

More recently, Mahajan et al. (1991a, 1991b) have computed the eigenfrequencies of fluid flow about an isolated airfoil modeled with a Navier–Stokes CFD algorithm to understand better the influence of artificial viscosity on numerical stability. The eigenvalue information was computed using a Lanczos procedure. In a later paper, Mahajan et al. (1993) applied a similar technique to compute the aeroelastic stability of the SR5 propfan. In their analysis, the eigenfrequencies were extracted from a time domain potential model of the unsteady flow field. The airfoils were modeled as "typical sections" with one bending and one torsional degree of freedom. The method predicted the aeroelastic damping of the system directly, rather than the less meaningful "required damping" one would compute using a conventional V-g analysis.

Contributed by the International Gas Turbine Institute and presented at the 39th International Gas Turbine and Aeroengine Congress and Exposition, The Hague, The Netherlands, June 13–16, 1994. Manuscript received by the International Gas Turbine Institute February 25, 1994. Paper No. 94-GT-291. Associate Technical Editor: E. M. Greitzer.

In this paper, we extend the previous eigenmode analyses by using the mode displacement method to construct reduced order models of unsteady compressible flow about airfoils in cascade. The eigenmode information is obtained by first discretizing the time-linearized small-disturbance form of the full potential equation. Because the discretized equations are quadratic in the eigenfrequency, we must solve a quadratic, complex, generalized, non-Hermitian eigenvalue problem to obtain the eigenmode information. To solve this problem, we have implemented a generalized non-Hermitian Lanczos algorithm that takes into account the quadratic nature of the problem. Using the computed eigenmodes, we construct reduced order models, which can be used to describe the dynamic behavior of the unsteady flow over a wide range of reduced frequencies and arbitrary vibrational mode shapes. In addition, we develop the "method of multiple corrections" to improve the accuracy of the basic reduced order model. The method is a generalization of the static correction and acceleration methods commonly used in structural dynamics (Bisplinghoff and Ashley, 1962; Cornwell et al., 1983). Finally, we demonstrate that the unsteady flow about a cascade of airfoils can be accurately modeled using just a few dominant fluid eigenmodes.

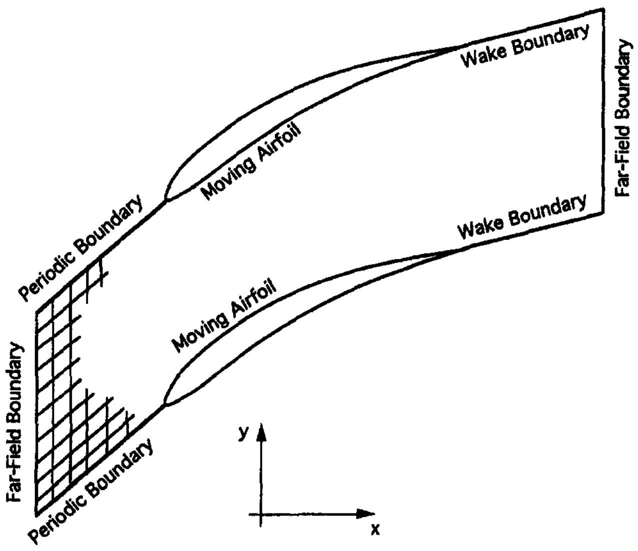

Fig. 1 Computational domain showing various computational boundary types; portion of *H*-grid is shown at left

Theory

Time-Linearized Potential Model. The reduced order modeling technique developed in this paper is quite general and can be applied to a variety of flow models. In this paper, we have applied the technique to the two-dimensional linearized full potential equation. Hall (1993) has previously described this model in detail. Hence, only the essential features are described here for completeness.

The flow through a compressor or turbine blade row is assumed to be inviscid, isentropic, irrotational, and two dimensional. Any boundary layers are assumed to be thin and attached. Under these circumstances, the full potential equation provides a reasonable description of the unsteady flow. The nonlinear full potential equation is given by

$$\nabla^2\hat{\phi} = \frac{1}{\hat{c}^2}\left[\frac{\partial^2\hat{\phi}}{\partial t^2} + 2\nabla\hat{\phi}\cdot\frac{\partial\hat{\phi}}{\partial t} + \frac{1}{2}\nabla\hat{\phi}\cdot(\nabla\hat{\phi})^2\right] \quad (1)$$

where $\hat{\phi}$ is the velocity potential, and $\hat{c}$ is the local speed of sound. The static pressure and density, as a function of the velocity potential, are

$$\hat{p} = P_T\left\{1 - \frac{\gamma - 1}{C_T^2}\left[\frac{1}{2}(\nabla\hat{\phi})^2 + \frac{\partial\hat{\phi}}{\partial t}\right]\right\}^{\gamma/\gamma-1} \quad (2)$$

$$\hat{\rho} = \rho_T\left\{1 - \frac{\gamma - 1}{C_T^2}\left[\frac{1}{2}(\nabla\hat{\phi})^2 + \frac{\partial\hat{\phi}}{\partial t}\right]\right\}^{1/\gamma-1} \quad (3)$$

where P_T and ρ_T are the total pressure and total density, respectively, C_T is the total speed of sound, and γ is the ratio of specific heats.

In the direct problem, we calculate the unsteady forces acting on the airfoils due to small harmonic vibrations of the airfoil with frequency ω. Toward that end, the solution to Eq. (1) will be found computationally using a finite element method implemented on an *H*-grid. For accuracy, a deforming computational grid that conforms to the motion of the vibrating airfoils is used. The grid motion is defined by the coordinate transformation

$$x(\xi, \eta, \tau) = \xi + f(\xi, \eta)e^{j\omega\tau} \quad (4)$$

$$y(\xi, \eta, \tau) = \eta + g(\xi, \eta)e^{j\omega\tau} \quad (5)$$

$$t(\xi, \eta, \tau) = \tau \quad (6)$$

where ξ and η may be thought of as the mean coordinate system, or alternatively, the coordinates of the undeformed grid. The perturbation functions f and g describe the small deformation motion of the grid about its mean or undeformed position.

Having defined the unsteady coordinate system, we next define the unsteady flow field. The unsteady potential is given by

$$\hat{\phi}(\xi, \eta, \tau) = \Phi(\xi, \eta) + \phi(\xi, \eta)e^{j\omega\tau} \quad (7)$$

where here $\Phi(\xi, \eta)$ is the steady flow potential function, and $\phi(\xi, \eta)$ is a small perturbation potential. Note, however, that there are two sources of unsteadiness in Eq. (7). If one observes the flow field at a point fixed in physical space (constant x, y), one sees not only an unsteadiness from the unsteady perturbation potential ϕ, but also from the "steady" potential Φ being convected past the fixed observer due to the deformation of the grid.

Substitution of Eqs. (2)–(7) into the full potential equation, Eq. (1), and collection of zeroth and first-order terms results in the steady (zeroth-order) flow equation, and the unsteady small disturbance (first-order) equation. The steady flow potential equation is given by

$$\nabla'^2\Phi = \frac{1}{C^2}\left[\frac{1}{2}\nabla'\Phi\cdot\nabla'(\nabla'\Phi)^2\right] \quad (8)$$

where C is the steady speed of sound, and ∇' is del operator in the ξ, η coordinate system.

The linearized potential equation is given by

$$\nabla'\cdot R\nabla'\phi - \nabla'\cdot\left[\frac{R}{C^2}(\nabla'\Phi^T\nabla'\phi + j\omega\phi)\nabla'\Phi\right] - \frac{R}{C^2}(j\omega\nabla'\Phi^T\nabla'\phi - \omega^2\phi) = b \quad (9)$$

where R is the steady density and b is an inhomogeneous term that arises from the prescribed vibratory motion of the computational grid.

In addition to the basic governing equations, appropriate boundary conditions must be applied around the boundary of the computational domain (see Fig. 1). For example, on airfoil surfaces, the velocity normal to the airfoil surface must equal the upwash arising from the vibration of the airfoil. On the wake surface, no mass can flow through the wake, and the pressure jump across the wake must be zero. Additionally, upstream and downstream of the airfoil along the periodic and wake boundaries, periodicity conditions are imposed that allow the computational domain to be reduced to a single blade passage. Finally, on the upstream and downstream far-field boundaries, nonreflecting boundary conditions are imposed to prevent spurious reflections of outgoing pressure waves for the linearized flow analysis. For the present analysis, we use approximate nonreflecting boundary conditions based on pseudo-differential operator techniques (Engquist and Majda, 1977; Higdon, 1986). We use approximate rather than exact nonreflecting boundary conditions (Hall et al., 1993; Verdon, 1989) for reasons to be explained shortly.

The general procedure in the direct frequency domain approach is to first compute the steady flow through the cascade. The resulting steady flow solution is used to form the variable coefficient equation, Eq. (9), that describes the unsteady flow field. The linearized potential equation is then discretized and solved using LU decomposition. Finally, the unsteady surface pressure is calculated using a linearized version of the Bernoulli equation, Eq. (2), and the unsteady pressure is integrated to obtain the unsteady force acting on the airfoils.

Following Hall (1993), we solve both the steady and unsteady flow problems using a variational finite element method based on an extension to Bateman's variational principle for compressible flow (Bateman, 1930). The resulting discretized equations for the unsteady flow field are of the form

$$\mathbf{A}\underline{\phi} = \mathbf{b} \tag{10}$$

where the matrix $\mathbf{A}$ is a large, sparse, complex, non-Hermitian matrix of order n, and $\mathbf{b}$ is an inhomogeneous vector that arises from the prescribed airfoil and grid motion. The vector $\underline{\phi}$ is the vector of unknown nodal values of the unsteady velocity potential ϕ.

Eigenmode Analysis

State Space Formulation. Considering the discretized time-linearized small disturbance equations, Eq. (10), we note that every element in the matrix $\mathbf{A}$ is quadratic in $j\omega$. (If we had used exact nonreflecting boundary conditions rather than approximate boundary conditions, the terms in the matrix equation associated with the far-field boundary conditions would not be quadratic.) Hence, Eq. (10) may be written as

$$[\mathbf{A}_0 + j\omega\mathbf{A}_1 + \omega^2\mathbf{A}_2]\underline{\phi} = \mathbf{b} \tag{11}$$

where the matrices $\mathbf{A}_0$, $\mathbf{A}_1$, and $\mathbf{A}_2$ are matrices that are not functions of ω. Such quadratic matrix equations are common in structural dynamic problems. In structural dynamic problems, the matrices $\mathbf{A}_0$ and $\mathbf{A}_2$ are usually real symmetric and positive definite, or occasionally complex Hermitian and positive definite. Additionally, in structural dynamics problems, the matrix $\mathbf{A}_1$ is often small, and the simplifying assumption is made that $\mathbf{A}_1$ is zero or the identity matrix, or alternatively, is a linear combination of the matrices $\mathbf{A}_0$ and $\mathbf{A}_2$. In the present unsteady flow analysis, the matrices $\mathbf{A}_0$, $\mathbf{A}_1$, and $\mathbf{A}_2$ are all the same order, complex, and non-Hermitian so that none of the above simplifying assumptions can be made.

For convenience, we convert Eq. (11) to a form that is first order in $j\omega$ by recasting in state-space form. Let $\mathbf{\Phi}$ be the system "state" defined by

$$\mathbf{\Phi} = \begin{Bmatrix} j\omega\underline{\phi} \\ \underline{\phi} \end{Bmatrix} \tag{12}$$

Equation (11) may then be rewritten as

$$\mathcal{A}\mathbf{\Phi} - j\omega\mathcal{B}\mathbf{\Phi} = \bar{\mathbf{b}} \tag{13}$$

where

$$\mathcal{A} = \begin{bmatrix} \mathbf{G} & \mathbf{0} \\ \mathbf{A}_1 & \mathbf{A}_0 \end{bmatrix}, \quad \mathcal{B} = \begin{bmatrix} \mathbf{0} & \mathbf{G} \\ \mathbf{A}_2 & \mathbf{0} \end{bmatrix}, \quad \bar{\mathbf{b}} = \begin{Bmatrix} \mathbf{0} \\ \mathbf{b} \end{Bmatrix}$$

and where $\mathbf{G}$ is any nonsingular matrix. We chose for the present analysis $\mathbf{G} = \mathbf{A}_0$.

To solve the inhomogeneous problem, Eq. (13), one can solve the homogeneous part of the problem first—a generalized eigenvalue problem—to determine the natural mode shapes (eigenmodes) and the corresponding natural frequencies (eigenvalues). This modal information may then be used to diagonalize Eq. (13) and solve the inhomogeneous problem.

Consider the solution of the generalized eigenvalue problem. The ith eigenvalue λ_i and corresponding right eigenvector $\mathbf{x}_i$ are defined by the eigenvalue problem

$$\mathcal{A}\mathbf{x}_i = \lambda_i\mathcal{B}\mathbf{x}_i \tag{14}$$

More generally, we may write

$$\mathcal{A}\mathbf{X} = \mathcal{B}\mathbf{X}\mathbf{\Lambda} \tag{15}$$

where now $\mathbf{X}$ is the matrix containing the $2n$ eigenvectors. The ith eigenvector is stored in the ith column. The matrix $\mathbf{\Lambda}$ is a diagonal matrix whose ith entry is the eigenvalue λ_i. For convenience, the eigenvalues λ_i are ordered from smallest to largest in magnitude. Similarly, the left eigenvectors are defined by

$$\mathcal{A}^T\mathbf{Y} = \mathcal{B}^T\mathbf{Y}\mathbf{\Lambda} \tag{16}$$

The eigenvectors, suitably normalized, are $\mathcal{B}$-orthonormal,

$$\mathbf{Y}^T\mathcal{B}\mathbf{X} = \mathbf{I} \tag{17}$$

$$\mathbf{Y}^T\mathcal{A}\mathbf{X} = \mathbf{\Lambda} \tag{18}$$

where $\mathbf{I}$ is the $2n$ by $2n$ identity matrix.

The Reduced Order Model. Because the number of degrees of freedom in our unsteady flow model is quite large, it would be prohibitively expensive to compute all of the eigenvectors. Therefore, we will model the dynamic behavior of the fluid using the "mode displacement method" with a small number of eigenvectors. We represent the solution $\mathbf{\Phi}$ as a linear combination of the eigenvectors $\mathbf{X}$ so that

$$\mathbf{\Phi} = \mathbf{X}\mathbf{c} \tag{19}$$

where $\mathbf{c}$ is the vector of modal coordinates. Substitution of Eq. (19) into Eq. (13) gives

$$\mathcal{A}\mathbf{X}\mathbf{c} - j\omega\mathcal{B}\mathbf{X}\mathbf{c} = \bar{\mathbf{b}} \tag{20}$$

Multiplying Eq. (20) by $\mathbf{Y}^T$, and making use of Eqs. (17) and (18), we obtain $2n$ decoupled equations for the modal coordinates,

$$\lambda_i c_i - j\omega c_i = \delta_i, \quad i = 1, 2n \tag{21}$$

where δ_i is the ith participation factor, the ith entry of the vector $\mathbf{Y}^T\bar{\mathbf{b}}$. Finally then, we may write the system state as

$$\mathbf{\Phi} = \sum_{i=1}^{2n} c_i\mathbf{x}_i = \sum_{i=1}^{2n} \frac{\delta_i}{\lambda_i - j\omega}\mathbf{x}_i \tag{22}$$

Generally speaking, the coefficient c_i multiplying $\mathbf{x}_i$ gets small for large i (large λ_i). Hence, as is commonly done in structural dynamics, we truncate the above series at $i = m \ll 2n$.

Static Correction Technique. To improve the convergence of the series of Eq. (22), we use a variation of the "static correction" or "modal acceleration" techniques originally developed for structural dynamics problems (Bisplinghoff and Ashley, 1962; Cornwell et al., 1983). One notes that as i gets large, so does λ_i. If λ_i is large, then the term $j\omega$ in the denominator of c_i may to a good approximation be neglected. In other words, the higher modes respond in a quasi-static way. This naturally leads one to let

$$\mathbf{\Phi} = \tilde{\mathbf{\Phi}} + \mathbf{\Phi}_{\text{static}} \tag{23}$$

where

$$\mathcal{A}\mathbf{\Phi}_{\text{static}} = \bar{\mathbf{b}} \tag{24}$$

Substitution of Eq. (23) and (24) into Eq. (13) gives

$$\mathcal{A}\tilde{\mathbf{\Phi}} - j\omega\mathcal{B}\tilde{\mathbf{\Phi}} = j\omega\mathcal{B}\mathbf{\Phi}_{\text{static}} \tag{25}$$

Again making use of the bi-orthogonality conditions, and after some manipulation, one finds that

$$\mathbf{\Phi} = \sum_{i=1}^{m} \frac{j\omega}{\lambda_i}\frac{\delta_i}{\lambda_i - j\omega}\mathbf{x}_i + \mathbf{\Phi}_{\text{static}} \tag{26}$$

Each term in the series in Eq. (26) differs from the terms in the series in Eq. (22) by a factor of $j\omega/\lambda_i$. Thus, since $|j\omega/\lambda_i| < 1$ for large i, the series in Eq. (26) converges faster than that in Eq. (22), and fewer terms need to be retained to obtain an accurate solution.

The Method of Multiple Corrections. Equation (26) may be generalized to multiple levels of corrections. Without derivation, we write that the method of multiple corrections is given by

$$\mathbf{\Phi} = \tilde{\mathbf{\Phi}}^{N_c} + \mathbf{\Phi}^{N_c}_{\text{static}} \tag{27}$$

where N_c is the number of corrections. Also,

$$\tilde{\mathbf{\Phi}}^{N_c} = \sum_{i=1}^{m}\left(\frac{j\omega}{\lambda_i}\right)^{N_c}\cdot\frac{\delta_i}{\lambda_i - j\omega}\mathbf{x}_i \tag{28}$$

$$\mathbf{\Phi}^{N_c}_{\text{static}} = \sum_{k=0}^{N_c-1}(j\omega)^k\mathbf{s}_k \tag{29}$$

and

$$\mathbf{s}_0 = \mathcal{A}^{-1}\bar{\mathbf{b}} = \mathbf{\Phi}^1_{\text{static}}$$

$$\mathbf{s}_k = \mathcal{A}_R\mathbf{s}_{k-1}, \quad k \geq 1$$

where $\mathcal{A}_R = \mathcal{A}^{-1}\mathcal{B}$.

This method of multiple corrections converges even more quickly than Eq. (26) because for large i (large λ_i), the term $(j\omega/\lambda_i)^N$ is quite small. Nevertheless, the method of multiple corrections may break down for large N_c. This is because the leading order term (proportional to $(j\omega/\lambda_1)^N$) in this series will be very large for large N_c. Hence, $\tilde{\mathbf{\Phi}}^N$ will be numerically large, as will the term $\mathbf{\Phi}^{N_c}_{\text{static}}$. The sum of the two, however, will be of order unity. In finite precision arithmetic, such operations can lead to significant roundoff errors. We have found that for problems considered thus far, using about five corrections generally produces the best results.

Eigenvalue Computation. For the reduced order model described above to be of practical use, one must be able to calculate efficiently the eigenvalues and eigenmodes of those modes with $|\lambda_i| < \lambda_{\text{specified}}$ where $\lambda_{\text{specified}}$ is somewhat larger than the maximum frequency ω of interest. Note further that for our problem, the eigenvalue problem is a large, sparse, complex, non-Hermitian, quadratic, generalized problem.

In recent years, investigators have had success solving the quadratic, real, nonsymmetric, generalized eigenvalue problem (e.g., Zheng et al., 1989; Rajakumar, 1993). Others have solved certain complex, non-Hermitian, generalized (but nonquadratic) eigenvalue problems (Cullum et al., 1989; Saad, 1992). However, we have not found in the literature applications of efficient eigensolvers to the quadratic, complex, fully non-Hermitian, generalized eigenvalue problem. Thus, as part of the present work, we have developed a number of computer codes to solve this eigenvalue problem including a method using subspace iteration with projection and deflation (Stewart, 1976; Jennings, 1978; Stewart and Jennings, 1981), an Arnoldi Gram-Schmidt method (Wilkinson, 1965; Zheng et al., 1989), and a generalized nonsymmetric Lanczos method with full re-orthogonalization (Wilkinson, 1965; Cullum et al., 1989; Rajakumar, 1993). The last of these methods was found to be the most efficient, and is described briefly below.

The left and right generalized eigenvalue problems may be rewritten as

$$\mathbf{X}\mathbf{\Lambda}^{-1} = \mathcal{A}_R\mathbf{X} \tag{30}$$

$$\mathbf{Y}\mathbf{\Lambda}^{-1} = \mathcal{A}_L\mathbf{Y} \tag{31}$$

where $\mathcal{A}_R = \mathcal{A}^{-1}\mathcal{B}$ and $\mathcal{A}_L = \mathcal{A}^{-T}\mathcal{B}^T$.

Next, as is usually done in eigenvalue computations, we seek similarity transforms of the form

$$\mathcal{A}_R\mathbf{V} = \mathbf{V}\mathbf{H}_R \tag{32}$$

$$\mathcal{A}_L\mathbf{W} = \mathbf{W}\mathbf{H}_L \tag{33}$$

where $\mathbf{H}_R$ and $\mathbf{H}_L$ are upper Hessenberg matrices. Within this constraint, however, there is great flexibility in the choice of **V** and **W**. It is convenient to impose the additional constraint that **V** and **W** be orthonormal with respect to $\mathcal{B}$. Under these conditions, one can easily show that

$$\mathbf{H}_R = \mathbf{H}_L^T \tag{34}$$

Hence, because both $\mathbf{H}_R$ and $\mathbf{H}_L$ are upper Hessenberg, they must also be tridiagonal. Cullum and Willoughby (1985) have shown that any tridiagonal matrix can be reduced to a symmetric tridiagonal matrix. Therefore, without loss of generality, we can assume that both $\mathbf{H}_R$ and $\mathbf{H}_L$ are in fact equal to the symmetric tridiagonal matrix **T**.

Next, we make the change of variables

$$\mathbf{X} = \mathbf{V}\mathbf{Z} \tag{35}$$

$$\mathbf{Y} = \mathbf{W}\mathbf{Z} \tag{36}$$

Using these transformations, one can show both the right and left eigenvalue problems, Eqs. (30) and (31), reduce to

$$\mathbf{Z}\mathbf{\Lambda}^{-1} = \mathbf{T}\mathbf{Z} \tag{37}$$

Note that since the matrix **T** is symmetric, the left and right eigenvectors of Eq. (37) are identical. Furthermore, because **T** is tridiagonal, the eigenvalues and eigenvectors can be efficiently computed. The eigenvalues of **T** are equal to the eigenvalues of $\mathcal{A}_R$ and $\mathcal{A}_L$, and the eigenvectors of **T** are related to the eigenvectors of $\mathcal{A}_R$ and $\mathcal{A}_L$ through Eqs. (35) and (36).

The last remaining task, then, is to compute the matrices **T**, **V**, and **W**. This is accomplished using the Lanczos recursion. To begin the recursion, one picks initial right and left vectors $\mathbf{v}_1$ and $\mathbf{w}_1$ (the first columns of the matrices **V** and **W**), which are $\mathcal{B}$-orthonormal, i.e.,

$$\mathbf{w}_1^T\mathcal{B}\mathbf{v}_1 = 1 \tag{38}$$

In pseudo-code, the generalized Lanczos algorithm may then be written as

```
$\beta_0 = 0$
for $j = 1, 2n - 1$
  $\mathbf{r}$       $:= \mathcal{A}_R\mathbf{v}_j$
  $\mathbf{s}$       $:= \mathcal{A}_L\mathbf{w}_j$
  $\mathbf{r}$       $:= \mathbf{r} - \beta_j\mathbf{v}_{j-1}$
  $\mathbf{s}$       $:= \mathbf{s} - \beta_j\mathbf{w}_{j-1}$
  $\alpha_j$      $:= \mathbf{w}_j^T\mathcal{B}\mathbf{r}$
  $\mathbf{r}$       $:= \mathbf{r} - \alpha_j\mathbf{v}_j$
  $\mathbf{s}$       $:= \mathbf{s} - \alpha_j\mathbf{w}_j$
  $\beta_{j+1}$  $:= (\mathbf{s}^T\mathcal{B}_{\mathbf{r}})^{1/2}$
  $\mathbf{v}_{j+1}$  $:= \mathbf{r}/\beta_{j+1}$
  $\mathbf{w}_{j+1}$  $:= \mathbf{s}/\beta_{j+1}$
next $j$
```

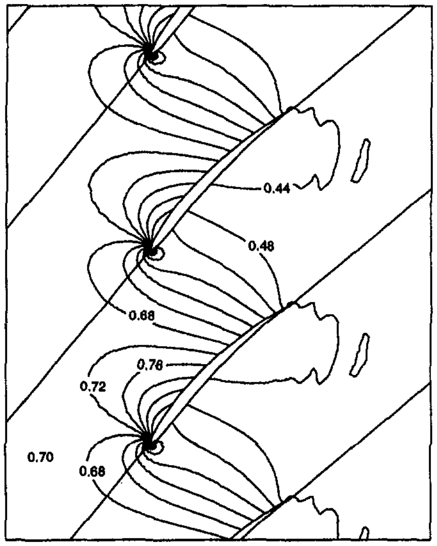

Fig. 2 Mach number contours for Tenth Standard Configuration test case: $\Theta = 45$ deg, $G = 1.0$, $M_{-\infty} = 0.7$, $\Omega_{-\infty} = 55$ deg

Note that the matrices $\mathcal{A}_R$ and $\mathcal{A}_L$ are never actually computed. Instead, the matrix $\mathcal{A}$ is LU-decomposed,

$$\mathcal{A} = \mathcal{L}\mathcal{U} = \begin{bmatrix} \mathbf{L} & \mathbf{0} \\ \mathbf{A}_1\mathbf{U}^{-1} & \mathbf{L} \end{bmatrix} \begin{bmatrix} \mathbf{U} & \mathbf{0} \\ \mathbf{0} & \mathbf{U} \end{bmatrix} \tag{39}$$

where

$$\mathbf{A}_0 = \mathbf{LU} \tag{40}$$

Then, whenever the product $\mathbf{r} = \mathcal{A}_R\mathbf{v}$ is required, one simply performs one forward and one back substitution to solve the linear equation

$$\mathcal{L}\mathcal{U}\mathbf{r} = \mathcal{B}\mathbf{v} \tag{41}$$

A similar technique is used to compute $\mathbf{s} = \mathcal{A}_L\mathbf{v}$.

In principle, the basic Lanczos algorithm produces $\mathcal{B}$-orthonormal matrices $\mathbf{V}$ and $\mathbf{W}$. Unfortunately, using finite precision arithmetic, $\mathcal{B}$-orthogonality can be lost. We attempt to maintain orthogonality by checking for $\mathcal{B}$-orthogonality at each step of the Lanczos algorithm and, if necessary, performing a Gram-Schmidt reorthogonalization.

Having computed the α_j and β_j, one forms the matrix

$$\mathbf{T} = \begin{bmatrix} \alpha_1 & \beta_2 & & \\ \beta_2 & \alpha_2 & \beta_3 & \\ & \ddots & \ddots & \ddots \\ & & \beta_{2n} & \alpha_{2n} \end{bmatrix} \tag{42}$$

which shares the same eigenvalues with the matrix $\mathcal{A}_R$ (and $\mathcal{A}_L$). If carried to completion, however, the Lanczos algorithm would be computationally quite expensive. Fortunately, the process can be stopped part way. Let $\mathbf{T}_p$ be the tridiagonal matrix obtained by performing only p steps of the Lanczos recursion. Then it happens that the largest eigenvalues of $\mathbf{T}_p$ (largest $1/\lambda$, smallest λ) are very nearly equal to the largest eigenvalues of $\mathbf{T}$.

The Lanczos algorithm's computational cost is driven by the cost of performing a single LU-decomposition of the matrix $\mathbf{A}_0$, and then two forward and two backward substitutions using the matrices $\mathcal{L}$ and $\mathcal{U}$ for each j, and also by the reorthogonalization of the Lanczos vectors. If more than about a dozen eigenvectors are required, we have found that it is more efficient to perform an eigenvalue shift and repeat the algorithm on the shifted problem. To compute approximately one dozen eigenvalues and corresponding left and right eigenvectors using the Lanczos method requires only about 20 to 50 times the CPU time required to perform a single direct time-linearized calculation. Once the eigenmode information has been found, however, the unsteady flow about the cascade may be computed at virtually no additional cost for arbitrary mode shapes over a wide range of reduced frequencies. Moreover, the modal information gives important insights into the physics of the unsteady flow.

Results

To demonstrate the reduced order modeling techniques developed in this paper, we apply the technique to two of the so-called Standard Configurations (Bölcs and Fransson, 1986). The Standard Configurations are cascades that were either experimentally tested, or defined analytically, for the purpose of validating unsteady aerodynamic theories. In this paper, we consider the Tenth and Fourth Standard Configurations, compressor and turbine geometries respectively. For both cases, the computational grids used were H-grids containing 65 nodes in the streamwise direction, and 17 nodes in the cross-stream direction.

Tenth Standard Configuration. The Tenth Standard Configuration is a two-dimensional compressor cascade (Fransson, 1991). The airfoils of this cascade have a slightly modified NACA 0006 thickness distribution, and a circular arc camber line. The maximum camber is 5 percent of the chord. The stagger angle Θ is 45 deg, and the gap-to-chord ratio G is 1.0. For the case considered in this paper, the inflow Mach number $M_{-\infty}$ is 0.7, and the inflow angle $\Omega_{-\infty}$ is 55 deg. Shown in Fig. 2 are the computed Mach number contours for the steady flow. Note that for this subsonic case, the maximum Mach number is about 0.92 and occurs near the leading edge of the suction surface of the airfoil.

Next, we computed the eigenvalues and eigenvectors for the case where the airfoil motion has an interblade phase angle σ of 180 deg. The smallest 28 eigenvalues are shown in Fig. 3 (the eigenvalues are nondimensionalized by the upstream velocity $V_{-\infty}$ and the blade chord c). The eigenvalues and corresponding eigenmodes can be roughly grouped into one of three types: acoustic modes, a "cascade simple pole" mode, and branch cut modes. Note that in this example, all of the eigenvalues are in the left-half complex plane indicating that the fluid flow through the cascade is stable.

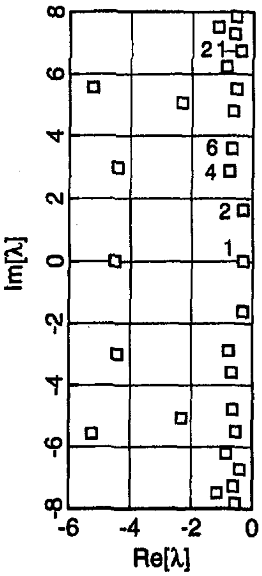

Fig. 3 Eigenvalues of compressible flow about Tenth Standard Configuration: $\sigma = 180$ deg

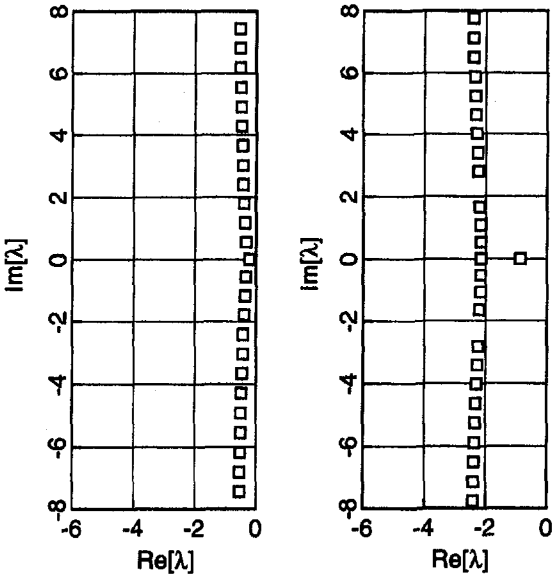

Fig. 4 Eigenvalues computed using unsteady incompressible vortex lattice model; left: flat plate airfoil; right: cascade of flat plate airfoils with Θ = 45 deg, G = 1.0, and σ = 180 deg

First, there are a number of eigenvalues that are complex and lightly damped—that is, the real part is small and negative. These eigenvalues correspond to acoustic modes that only appear in the case of compressible flow. The acoustic modes are analogous to the unsteady acoustic eigenmodes described by Parker (1967) for low-speed flows. Next, note in Fig. 3 the eigenvalue located at $\lambda = -0.322 + 0.00j$. We denote the corresponding eigenmode as the cascade simple pole mode. This mode is damped and nonoscillatory (at least for the σ = 180 deg case). Finally, note the line of eigenvalues with real part approximately equal to -5. This line of poles is a finite state approximation of a branch cut.

A branch cut in the aerodynamic transfer function indicates that the impulse response contains nonexponential behavior. For instance, the well-known Theodorsen function contains a branch cut with a branch point at the origin. The equivalent incompressible cascade transfer function also contains a branch cut, but the branch point is shifted to the left in the complex plane. To illustrate this point more clearly, we have computed the eigenvalues of an unsteady incompressible vortex lattice model [for a complete description of the vortex lattice model, see Hall (1994)]. Shown in Fig. 4 are the computed eigenvalues for the case of incompressible flow about an isolated flat plate airfoil. The branch cut in the Theodorsen function is approximated by a dense line of eigenvalues, which passes very near the origin. As more and more vortex elements are added to the model, the line of eigenvalues gets more and more dense. Also shown in Fig. 4 are the computed eigenvalues for the case of incompressible flow about a cascade of flat plate airfoils. For this example, we have picked the gap, stagger angle, and interblade phase angle to be the same as the Tenth Standard Configuration example. Note that again a branch cut is predicted, but the cut is shifted to the left. Furthermore, a simple pole now appears on the negative real axis. Except for the lack of acoustic modes, the incompressible cascade results are qualitatively similar to the results predicted for the Tenth Standard Configuration using the compressible potential flow model.

Returning again to the Tenth Standard Configuration example, the real and imaginary parts of the unsteady surface pressure for five of the eigenmodes are shown in Fig. 5. Note the "beam-like" behavior of the modes. As the mode number increases, one observes that the pressure distribution has more and more zero crossings. One interesting feature of the present analysis is that the mode shapes are actually mode shapes of potential, not pressure. The pressures shown in Fig. 5 are the pressures associated with the five modes at the natural frequencies of each of the modes. When these modes are used to compute the response at some other specified frequency, the unsteady pressure mode shapes (but not the potential mode shapes) will be different since the unsteady pressure depends on the frequency through the small disturbance form of the Bernoulli equation. In particular, the contribution from a particular mode will not in general satisfy the Kutta condition. However, in the limit as many modes are added to the mode displacement method series [Eq. (22) or Eq. (26)], the Kutta condition will be satisfied.

Next, we consider the unsteady aerodynamic response of the cascade due to plunging motion of the airfoils with a reduced frequency ω of 1.0. Shown in Fig. 6 are the real and imaginary parts of the unsteady surface pressure distribution (the pressure is nondimensionalized by dividing the dimensional pressure by $\bar{p}_{-\infty}V^2_{-\infty}h/c$ where $\bar{p}_{-\infty}$ is the upstream density and h is the amplitude of the blade vibration). Shown is the exact solution, along with the solutions computed with the reduced order model using a single static correction and one, five, or ten eigenmodes corresponding to the eigenvalues closest to the origin. With just five eigenmodes, the reduced order model reproduces the exact solution fairly well; with ten eigenmodes, the agreement is nearly exact. Physically, this demonstrates that the unsteady response is dominated by just a few of the thousands of eigenmodes in the model. This is an important result. What appears to be very complex behavior can be modeled using a reduced order model with just a few degrees of freedom.

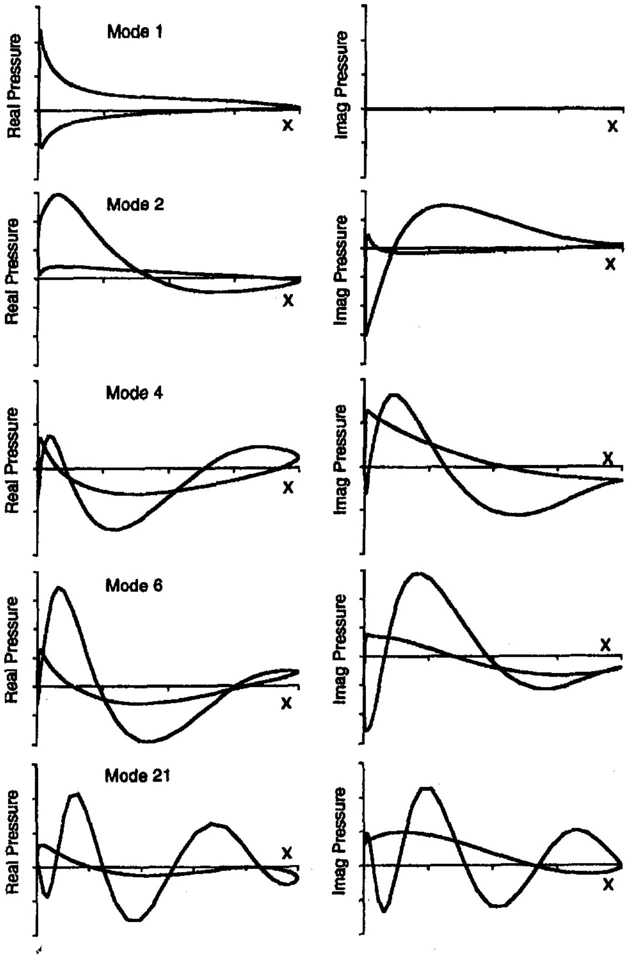

Fig. 5 Surface pressure distributions for five eigenmodes of compressible flow about Tenth Standard Configuration: σ = 180 deg

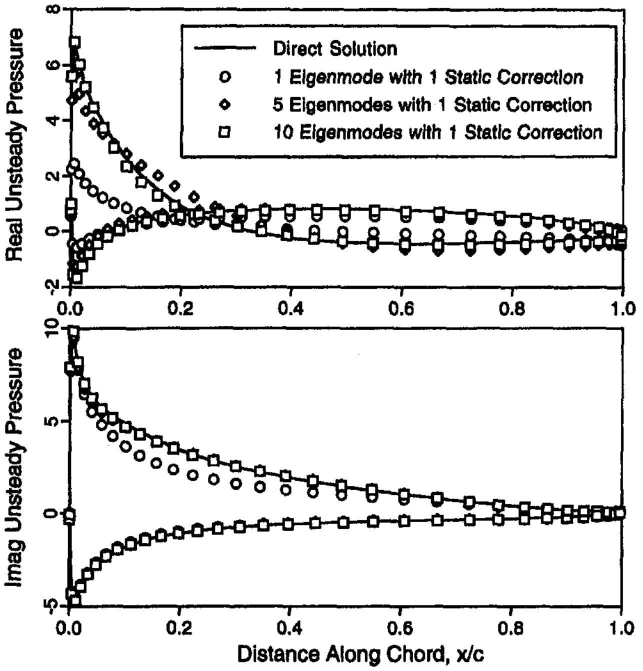

Fig. 6 Modal contributions to unsteady surface pressure; Tenth Standard Configuration, plunging motion, σ = 180 deg, ω = 1.0

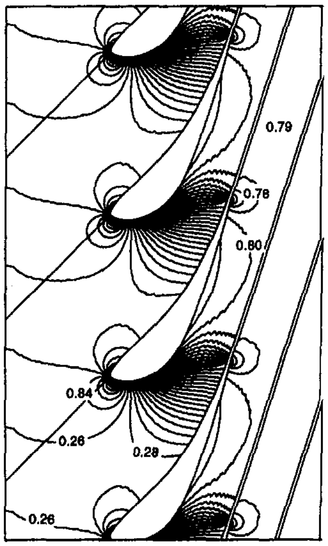

Fig. 8 Mach number contours for Fourth Standard Configuration test case: Θ = 56.6 deg, G = 0.76, $M_{-\infty}$ = 0.26, $\Omega_{-\infty}$ = 50 deg

Next, using the three eigenmodes corresponding to the three eigenvalues closest to the origin, we constructed a reduced order model of the unsteady flow due to plunging motion of the airfoils. The resulting unsteady lift is plotted in Fig. 7 (the lift is nondimensionalized by dividing the dimensional lift by $\bar{p}_{-\infty} V^2_{-\infty} h$). Also shown is the "exact solution" computed by solving the frequency domain equations directly. Note that with no static corrections, the error in the reduced order model is fairly large, but the model correctly predicts the qualitative behavior of the unsteady lift for frequencies less that 2.0. With five corrections, the prediction is quite good for reduced frequencies smaller that the largest eigenfrequency in the reduced order model ($\lambda = -0.304 + 1.620j$). With nine corrections, the prediction is accurate for frequencies as high as 1.8, but the method breaks down for higher frequencies due to the roundoff error associated with higher order corrections. Also note the abrupt change in magnitude and phase of the unsteady lift at a reduced frequency of about 1.6. Clearly, this is due to a resonant response of the fluid flow associated with the lightly damped eigenvalue at $\lambda = -0.304 + 1.620j$ (see Fig. 3).

Fourth Standard Configuration. The Fourth Standard Configuration is a high-speed turbine geometry, which has been tested extensively by Bölcs and Fransson (1986). The stagger angle Θ is 56.6 deg, and the gap-to-chord ratio G is 0.76. For the case considered here, the blades are assumed to vibrate with an interblade phase angle σ of 180 deg. The inflow Mach number $M_{-\infty}$ is 0.26, and the inflow angle $\Omega_{-\infty}$ (measured from the axial direction) is 50 deg. Shown in Fig. 8 are the computed steady flow Mach contours. The flow remains subsonic throughout, and exits with a Mach number M_{∞} of approximately 0.79.

Shown in Fig. 9 are the nine smallest eigenvalues for the case where the unsteady blade motion has an interblade phase

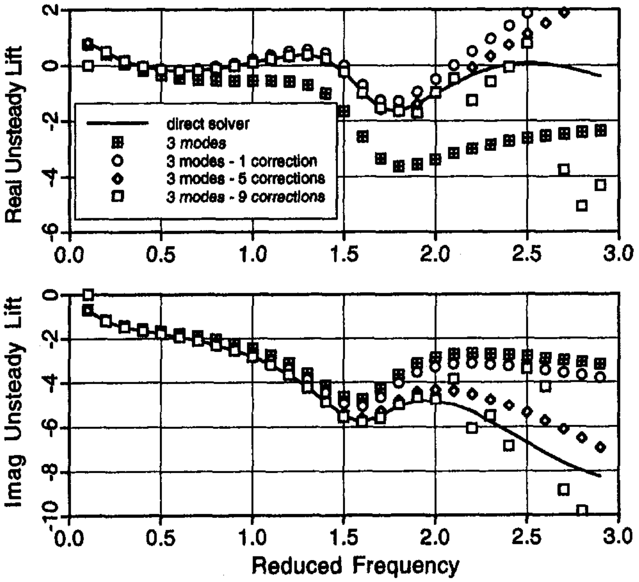

Fig. 7 Unsteady lift due to plunging motion of Tenth Standard Configuration airfoils: σ = 180 deg

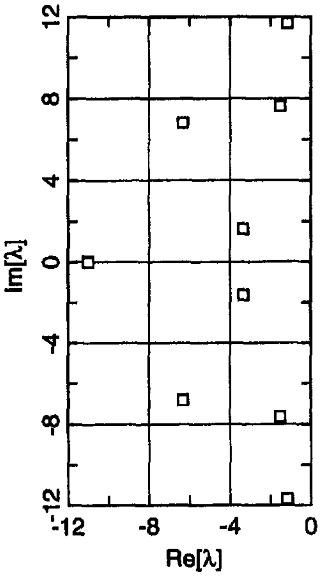

Fig. 9 Eigenvalues of compressible flow about Fourth Standard Configuration: σ = 180 deg

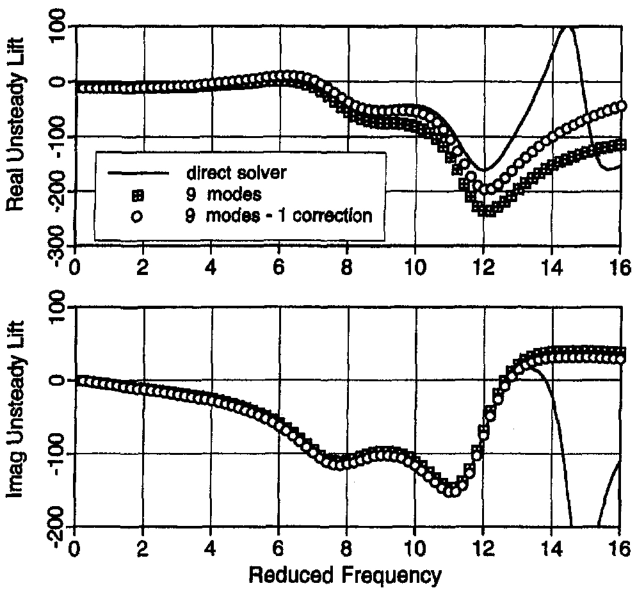

Fig. 10 Unsteady lift due to plunging motion of Fourth Standard Configuration airfoils: σ = 180 deg

angle σ of 180 deg. Again, all of the eigenvalues are in the left-half plane indicating that the flow is stable. The eigenvalue pattern is less distinctive that the Tenth Standard Configuration example. However, there are several lightly damped acoustic modes ($\lambda = -1.51 \pm 7.65$ and $\lambda = -1.18 \pm 11.7$). Interestingly, no lightly damped simple pole mode appears in this case. Although not shown here, the incompressible vortex lattice code also predicts that the cascade simple pole disappears for cascades with small gap to chord ratio and large stagger angle.

Figure 10 shows the computed unsteady lift due to plunging motion of the airfoils for a range of frequencies. Shown is the "exact" solution computed using the direct frequency domain approach. Also shown is the unsteady lift predicted using the reduced order model with nine eigenmodes with and without a single static correction. Again, the agreement between the exact solution and the reduced order model is quite good until the frequency approaches that of the largest natural frequency used in the reduced order model, and the static correction significantly improves the accuracy. It is remarkable that the complex behavior of the unsteady lift can be represented using just nine eigenmodes.

Finally, a word about computational efficiency. To compute 18 eigenfrequencies and corresponding right and left eigenmodes for the Fourth Standard Configuration case required about 345 seconds of CPU time on a Stardent 3000 workstation. This compares to about 8.3 seconds to compute the steady flow field, and 12.4 seconds to compute the unsteady flow at a single frequency for a single mode shape using the direct frequency domain approach. Thus, the present method is somewhat more expensive than a single direct frequency domain solution, but still less expensive than a single time-accurate time-marching solution. Once the eigenmode information has been computed, however, the unsteady lift for a number of frequencies and mode shapes can be computed very efficiently. For the present example, the lift at 80 different frequencies was computed in just 33.0 seconds. Finally, we note that the finite element scheme used in this investigation is not particularly well suited for eigenvalue extraction. It may be possible to extract eigenvalue information from other CFD schemes, particularly approximately factored time marching schemes, much more efficiently than from the frequency domain techniques (Mahajan et al., 1993), further improving the efficiency of the reduced order modeling technique.

Summary

A reduced order model that describes the unsteady flow in terms of fluid eigenmodes has been presented. The reduced order model was shown to predict accurately the unsteady loads acting on a cascade of blades using just a few eigenmodes. Furthermore, the accuracy can be improved substantially using the static correction and multiple static correction techniques. The method is reasonably efficient. For example, to compute one dozen eigenvalues and corresponding eigenmodes requires about 20 to 50 times the computational time of a single direct frequency domain calculation, but still less than a single time-domain calculation would require. Once the eigenmode information has been found, the unsteady aerodynamics response can be found quite inexpensively for any number of different vibrational frequencies and mode shapes.

The eigenmode information provides important insights into the physics of the unsteady flow field. For example, the abrupt changes in phase and magnitude of the unsteady lift due to plunging motion with increasing vibrational frequency are seen to be the result of passing through fluid resonances. When applied to viscous flow models, the present method may be useful for prediction of flow instabilities since the damping of each fluid mode is obtained explicitly. The method may also prove useful for aeroacoustic problems where the unsteady aeroacoustic response is required at a large number of discrete frequencies as in the case of tonal noise, or over a continuous range of frequencies as in the case of broad band noise.

Finally, we note that the form of the reduced order model, that is, a low-order model with pole/zero behavior of the individual modes, is ideally suited for use in applications of active control of aeroelastic or aeroacoustic phenomena.

Acknowledgments

This work was supported in part by a Presidential Young Investigator Award from the National Science Foundation. The authors wish to thank Professor Earl H. Dowell, Dean of the School of Engineering at Duke University, and Mr. Michael Romanowski, a Research Assistant in the Department of Mechanical Engineering and Materials Science at Duke University, for their helpful comments on reduced order modeling. The authors would also like to thank Dr. Jane Cullum of the IBM T. J. Watson Research Center for her helpful advice on eigenvalue calculation methods.

References

Bakhle, M. A., Mahajan, A. J., Keith, T. G. Jr., and Stefko, G. L., 1991, "Cascade Flutter Analysis With Transient Response Aerodynamics," *Computers and Structures,* Vol. 41, pp. 1073–1085.

Bateman, H., 1930, "Irrotational Motion of a Compressible Fluid," *Proc. National Academy of Sciences,* Vol. 16, pp. 816–825.

Bisplinghoff, R. L., and Ashley, H., 1962, *Principles of Aeroelasticity,* Wiley, New York, p. 350.

Bölcs, A., and Fransson, T. H., 1986, "Aeroelasticity in Turbomachines Comparison of Theoretical and Experimental Results," AFOSR-TR-87-0605, Air Force Office of Scientific Research, Washington, DC.

Cornwell, R. E., Craig, R. R., Jr., and Johnson, C. P., 1983, "On the Application of the Mode-Acceleration Method to Structural Engineering Problems," *Earthquake Engineering and Structural Dynamics,* Vol. 11, pp. 679–688.

Cullum, J., and Willoughby, R., 1985, "Lanczos Algorithms for Large Symmetric Eigenvalue Computations, Vol. 1, Theory," in: *Progress in Scientific Computing,* Vol. 3, S. Abarbanel et al., eds., Birkhäuser, Boston, pp. 76–163.

Cullum, J., Kerner, W., and Willoughby, R., 1989, "A Generalized Nonsymmetric Lanczos Procedure," *Computer Physics Communications,* Vol. 53, pp. 19–48.

Engquist, B., and Majda, A., 1977, "Absorbing Boundary Conditions for the Numerical Simulation of Waves," *Mathematics of Computation,* Vol. 31, pp. 629–651.

Fransson, T. H., 1991, private communication.

Gerolymos, G. A., 1993, "Advances in the Numerical Integration of the Three-Dimensional Euler Equations in Vibrating Cascades," ASME JOURNAL OF TURBOMACHINERY, Vol. 115, pp. 781–790.

Giles, M. B., 1988, "Calculation of Unsteady Wake/Rotor Interaction," *Journal of Propulsion and Power,* Vol. 4, pp. 356–362.

Hall, K. C., and Crawley, E. F., 1989, "Calculation of Unsteady Flows in Turbomachinery Using the Linearized Euler Equations," *AIAA Journal*, Vol. 27, pp. 777–787.

Hall, K. C., 1993, "Deforming Grid Variational Principle for Unsteady Small Disturbance Flows in Cascades," *AIAA Journal*, Vol. 31, pp. 891–900.

Hall, K. C., and Clark, W. S., 1993, "Linearized Euler Predictions of Unsteady Aerodynamic Loads in Cascades," *AIAA Journal*, Vol. 31, pp. 540–550.

Hall, K. C., and Lorence, C. B., 1993, "Calculation of Three-Dimensional Unsteady Flows in Turbomachinery Using the Linearized Harmonic Euler Equations," ASME JOURNAL OF TURBOMACHINERY, Vol. 115, pp. 800–809.

Hall, K. C., Lorence, C. B., and Clark, W. S., 1993, "Nonreflecting Boundary Conditions for Linearized Unsteady Aerodynamic Calculations," AIAA Paper No. 93-0882.

Hall, K. C., 1994, "Eigenanalysis of Unsteady Flows About Airfoils, Cascades, and Wings," *AIAA Journal*, Vol. 32, pp. 2426–2432.

He, L., 1990, "An Euler Solution or Unsteady Flows Around Oscillating Blades," ASME JOURNAL OF TURBOMACHINERY, Vol. 112, pp. 714–722.

He, L., 1993, "New Two-Grid Acceleration Method for Unsteady Navier–Stokes Calculations," *Journal of Propulsion and Power*, Vol. 9, pp. 272–280.

Higdon, R. L., 1986, "Absorbing Boundary Conditions for Difference Approximations to the Multi-dimensional Wave Equation," *Mathematics of Computation*, Vol. 47, pp. 437–459.

Hodson, H. P., 1985, "An Inviscid Blade-to-Blade Prediction of a Wake-Generated Unsteady Flow," ASME *Journal of Engineering for Gas Turbines and Power*, Vol. 107, pp. 337–344.

Holmes, D. G., and Chuang, H. A., 1993, "2D Linearized Harmonic Euler Flow Analysis for Flutter and Forced Response," in: *Unsteady Aerodynamics, Aeroacoustics, and Aeroelasticity of Turbomachines and Propellers*, H. M. Atassi, ed., Springer-Verlag, New York, pp. 213–230.

Huff, D. L., Swafford, T. W., and Reddy, T. S. R., 1991, "Euler Flow Predictions for an Oscillating Cascade Using a High Resolution Wave-Split Scheme," ASME Paper No. 91-GT-198.

Jennings, A., 1978, *Matrix Computation for Engineers and Scientists*, Wiley, New York, pp. 289–320.

Lindquist, D. R., and Giles, M. B., 1994, "On the Validity of Linearized Euler Equations With Shock Capturing," *AIAA Journal*, Vol. 32, pp. 46–53.

Mahajan, A. J., Dowell, E. H., and Bliss, D. B., 1991a, "Eigenvalue Calculation Procedure for Euler/Navier–Stokes Solvers With Application to Flows Over Airfoils," *Journal of Computational Physics*, Vol. 97, pp. 398–413.

Mahajan, A. J., Dowell, E. H., and Bliss, D. B., 1991b, "Role of Artificial Viscosity in Euler and Navier–Stokes Solvers," *AIAA Journal*, Vol. 29, pp. 555–559.

Mahajan, A. J., Bakhle, M. A., and Dowell, E. H., 1993, "An Efficient Procedure for Cascade Aeroelastic Stability Determination Using Nonlinear, Time-Marching Aerodynamic Solvers," AIAA Paper No. 93-1631.

Nixon, D., 1989, "Alternative Methods for Modeling Unsteady Transonic Flows," in: *Unsteady Transonic Aerodynamics*, D. Nixon, ed., Progress in Astronautics and Aeronautics, Vol. 120, American Institute of Aeronautics and Astronautics, Washington, DC, pp. 349–376.

Parker, R., 1967, "Resonance Effects in Wake Shedding From Parallel Plates: Calculation of Resonant Frequencies," *Journal of Sound and Vibration*, Vol. 5, pp. 330–343.

Rai, M. M., 1989a, "Three-Dimensional Navier–Stokes Simulations of Turbine Rotor-Stator Interaction: Part I—Methodology," *Journal of Propulsion and Power*, Vol. 5, pp. 305–311.

Rai, M. M., 1989b, "Three-Dimensional Navier–Stokes Simulations of Turbine Rotor-Stator Interaction: Part II—Results," *Journal of Propulsion and Power*, Vol. 5, pp. 312–319.

Rajakumar, C., 1993, "Lanczos Algorithm for the Quadratic Eigenvalue Problem in Engineering Applications," *Computer Methods in Applied Mechanics and Engineering*, Vol. 105, pp. 1–22.

Saad, Y., 1992, *Numerical Methods for Large Eigenvalue Problems*, Wiley, New York, pp. 156–162, 186–194.

Stewart, G. J., 1976, "Simultaneous Iteration for Computing Invariant Subspaces of Non-Hermitian Matrices," *Numerische Mathematik*, Vol. 25, pp. 123–136.

Stewart, W. J., and Jennings, A., 1981, "Simultaneous Iteration Algorithm for Real Matrices," *ACM Transaction on Mathematical Software*, Vol. 7, pp. 184–198.

Verdon, J. M., 1987, "Linearized Unsteady Aerodynamic Theory," *AGARD Manual on Aeroelasticity in Axial Flow Turbomachines, Vol. 1, Unsteady Turbomachinery Aerodynamics* (AGARD-AG-298), M. F. Platzer and F. O. Carta, eds., Neuilly sur Seine, France, Chap. 2.

Verdon, J. M., 1989, "The Unsteady Flow in the Far Field of an Isolated Blade Row," *Journal of Fluids and Structures*, Vol. 3, pp. 123–149.

Whitehead, D. S., and Grant, R. J., 1981, "Force and Moment Coefficients of High Deflection Cascades," *Proceedings of the 2nd International Symposium on Aeroelasticity in Turbomachines*, P. Suter, ed., Juris-Verlag, Zurich, pp. 85–127.

Whitfield, D. L., Swafford, T. W., and Mulac, R. A., 1987, "Three-Dimensional Unsteady Euler Solutions for Propfans and Counter-rotating Propfans in Transonic Flow," AIAA Paper No. 87-1197.

Wilkinson, J. H., 1965, *The Algebraic Eigenvalue Problem*, Clarendon Press, Oxford, pp. 377–404.

Zheng, T. S., Liu, W. M., and Cai, Z. B., 1989, "A Generalized Inverse Iteration Method for the Solution of Quadratic Eigenvalue Problems in Structural Dynamic Analysis," *Computers and Structures*, Vol. 33, pp. 1139–1141.

Measurement of Turbine Blade-Tip Rotordynamic Excitation Forces

M. Martinez-Sanchez

B. Jaroux

S. J. Song

S. Yoo

Gas Turbine Laboratory,
Massachusetts Institute of Technology,
Cambridge, MA 02139

This paper presents results of a program to investigate the magnitude, origin, and parametric variations of destabilizing forces that arise in high power turbines due to blade-tip leakage effects. Five different unshrouded turbine configurations and one configuration shrouded with a labyrinth seal were tested with static offsets of the turbine shaft. The forces along and perpendicular to the offset were measured directly with a dynamometer, and were also inferred from velocity triangles and pressure distributions obtained from detailed flow surveys. These two routes yielded values in fair agreement in all cases. For unshrouded turbines, the cross-forces are seen to originate mainly (~ 2/3) from the classical Alford mechanism (nonuniform work extraction due to varying blade efficiency with tip gap) and about 1/3 from a slightly skewed hub pressure pattern. The direct forces arise mainly (3/4) from this pressure pattern, with the rest due to a slight skewness of the Alford mechanism. The pressure nonuniformity (lower pressures near the widest gap) is seen to arise from a large-scale redistribution of the flow as it approaches the eccentric turbine. The cross-forces are found to increase substantially when the gap is reduced from 3.0 to 1.9 percent of blade height, probably due to viscous blade-tip effects. The forces also increase when the hub gap between stator and rotor decreases. The force coefficient decreases with operating flow coefficient. In the case of the shrouded turbine, most of the forces arise from nonuniform seal pressures. This includes about 80 percent of the transverse forces. The rest appears to come from uneven work extraction (Alford mechanism). Their level is about 50 percent higher than in the unshrouded cases.

1 Introduction

The existing large body of literature on turbomachine tip leakage has been mainly motivated by the substantial contribution of these leakages to losses. H. J. Thomas [1], in 1958, and J. S. Alford [2], in 1964, independently pointed out that, in a turbine undergoing transverse vibrations (e.g., a whirling motion), the portion of the blading with the smaller tip gap would produce greater tangential driving force than its 180 deg opposite. Upon integration, this difference in work extraction results in a cross force tending to promote forward whirl. This can be a powerful positive feedback mechanism, leading to rotordynamic instability.

Both Alford and Thomas showed that, if the tangential force f per unit length is assumed to vary linearly with the ratio δ/H of local tip gap to blade height

$$f = f_0 - \beta \frac{\delta}{H} \tag{1}$$

and if the shaft is offset instantaneously by e_x along the ox direction, then a cross-force F_y equivalent to

$$F_y = \frac{\beta\eta}{2} \frac{Q_{id}}{R} \frac{e_x}{H} \tag{2}$$

arises where η is turbine efficiency, Q_{id} is the ideal turbine torque, and R its mean radius. The factor β has become known in the U.S. as the Alford coefficient, which is quoted as varying between 0 and 6. The German literature uses a factor called the "excitation coefficient," k_2, which is equivalent to $\eta\beta/2$. Implicit in the Alford/Thomas model is the assumption that the flow remains perfectly uniform up to the offset turbine, as well as downstream of it, so that only the local efficiency, as determined by the local tip gap, is of concern. Two of the consequences of these models are (a) the absence of a direct force component (in the offset direction), and (b) the absence of frequency dependence (no damping).

The rotordynamic importance of these forces can be brought up by a simple linear model of a symmetric rotor oscillating in the plane perpendicular to the shaft. If we assume that the aerodynamic forces can have both stiffness

---

Contributed by the International Gas Turbine Institute and presented at the 38th International Gas Turbine and Aeroengine Congress and Exposition, Cincinnati, Ohio, May 24–27, 1993. Manuscript received at ASME Headquarters March 1, 1993. Paper No. 93-GT-125. Associate Technical Editor: H. Lukas.

and damping forces, which contribute to direct and crosswise components, we have

$$F_x = -K_{xx}x + K_{xy}y - C_{xx}\dot{x} + C_{xy}\dot{y} \qquad (3)$$

$$F_y = -K_{xy}x - K_{xx}y - C_{xy}\dot{x} - C_{xx}\dot{y} \qquad (4)$$

where x, y are small displacements of the shaft. The dynamic analysis then yields x and y variations of the form $\exp(i\Omega t)$, with

$$\frac{\Omega}{\Omega_0} = \pm 1 \pm \frac{1}{2}k_{xx} - \zeta_{xy} - i\left(\pm\frac{1}{2}k_{xy}\text{-}\zeta_{xx}\right);$$

$$\Omega_0 = \sqrt{K_0/M} \qquad (5)$$

Here, K_0 is the shaft mechanical stiffness and M the rotor mass, and

$$k_{ij} = \frac{K_{ij}}{K_0} \ll 1, \qquad \zeta_{ij} = \frac{C_{ij}}{2\sqrt{K_0 M}} \ll 1 \qquad (6)$$

We note from Eq. (5) that K_{xx} and C_{xy} produce only small shifts in the natural frequency, while one of the two sign choices for k_{xy} leads to divergence if $|K_{xy}| > \Omega_0 C_{xx}$. Clearly, the *direct* damping C_{xx} counters the *cross stiffness* K_{xy}, and can in fact be due partly to aerodynamics, and partly to other mechanisms. If the machine is to be neutrally stable, the required damping factor is, therefore (from Eqs. (2), (5), and (6)):

$$\zeta_{\min} = \frac{1}{2}\frac{K_{xy}}{K_0} = \frac{\beta}{4}\frac{Q}{RHK_0} \qquad (7)$$

This can be very substantial in high-pressure turbines. For the SSME H_2 turbopump, $Q = 12{,}800$ Nm, $R = 0.129$ m, $H = 0.023$ m, and $K_0 = M\Omega_0^2 = 1.9 \times 10^8$ Nm, giving $\zeta_{\min} = 0.019$, or a log decrement of 12 percent.

Relatively little work on these forces has been done since the pioneering efforts of Alford and Thomas. Thomas' collaborators at the T.U. Munich produced the most detailed experimental data. Urlichs [3] used a relatively low power facility, with blade Reynolds number below 10^5, and measured cross-forces mainly on shrouded turbines, although one unshrouded case was also tested. He identified the shroud seal as the major contributor to the cross-forces. The mechanics of these seal-related forces has been more clearly elucidated since (see, for instance, [4, 5, 6]), and is distinct from the Alford–Thomas effect (uneven work extraction). In his unshrouded tests, Urlichs noted a cross-force reduction with increasing mean tip gap, and an increase with axial stator–rotor spacing. The measured forces were roughly compatible with the simple Alford argument. Wohlrab [7], used a larger, pressurized air turbine, capable of stator leaving Reynolds numbers up to 5×10^5, but tested only shrouded turbines. Strong nonlinearity of force versus displacement was noted in the cases with smaller forces, which raises questions about accuracy. Limited dynamic testing was accomplished as well. As in [3], the main mechanism in these tests was through seal pressure effects, rather than through uneven work extraction. Vance and Laudadio [8] did some very low power tests on a fan with movable casing, and reported measured cross-forces, but no aerodynamic data. Ehrich [9] has recently inferred Alford forces from compressor efficiency test data, and argues that these forces become backward-whirling at pressure ratios above the normal operating point.

We have performed extensive force measurements on an unshrouded turbine identical to the first stage of the Shuttle LH turbopump, and also on a shrouded derivative of it. These were supplemented by flow field measurements and theoretical analysis to clarify mechanisms. In this paper, we will describe the test facility (Sec. 2), and present the force and flow data (Secs. 3–6). A linearized theory that gives a good account of most of the observed effects [10] will be separately published.

2 Experimental Apparatus

The test facility is a pressurized closed loop, filled with Freon 12 gas, and equipped with a gas blower, heat exchanger/cooler, removable test section, power extraction generator, and data acquisition system. Nominal operating conditions are 2.0 atm mean pressure and 4.5 kg/s flow rate. Flow rate is mainly controlled by a manual series valve, with help from a bypass valve at low flow. Speed is controlled through generator excitation control.

The test section area is shown in Fig. 1. The upper section (12) of the casing can be rotated and carries the stator and the hub, as well as a variety of flow probes. The turbine shaft connects to the turbine via a four-post rotating dynamometer (14), and is supported by two bearings. The bearings are carried in a heavy cylindrical structure, which can be translated sideways by means of four stiff rods, two on each side. Static offsets are achieved (to an accuracy of ±0.5 mil) by insertion or removal of calibrated shims (11). Dynamic shaking was provided for by inertial shakers attached at (15), but the dynamic data proved inconsistent and will not be dis-

Nomenclature

C_x, C_y, C_z = fluid velocity components along x, y, z
C_θ = same as C_y
C_{ij} = fluid damping matrix for turbine displacements
e, e_x = turbine eccentricity
f, f_y = tangential force per unit length
F_x = net force on turbine in direction of offset
F_y = net force on turbine perpendicular to offset
H = blade height
K_{ij} = fluid stiffness matrix for turbine displacements
K_0 = structural stiffness for turbine displacements
M = rotor mass
P, P_t = pressure, total pressure
Q_{id} = turbine torque (ideal)
Q = turbine torque (actual)
R = turbine mean radius
U = turbine wheel speed = wR
x = axial coordinate
y = tangential coordinate
z = radial coordinate
α_x = force coefficient along offset (Eq. (8))
α_y = force coefficient perpendicular to offset (Eq. (8))
β = sensitivity of tangential force to relative gap = $-\partial f_y/\partial(\delta/H)$
β_η = sensitivity of local efficiency to relative gap = $-\partial\eta/\partial(\delta/H)$
δ = blade tip gap
η = thermodynamic efficiency
ζ = rotor damping factor
ρ = fluid density
θ = azimuth angle
ϕ = flow coefficient = C_x/U
ϕ_f, ϕ_p = phase angles for fluid force (Eq. (10)) and wall pressure (Eq. (13))
ω = angular frequency of turbine spin
Ω = whirl angular frequency

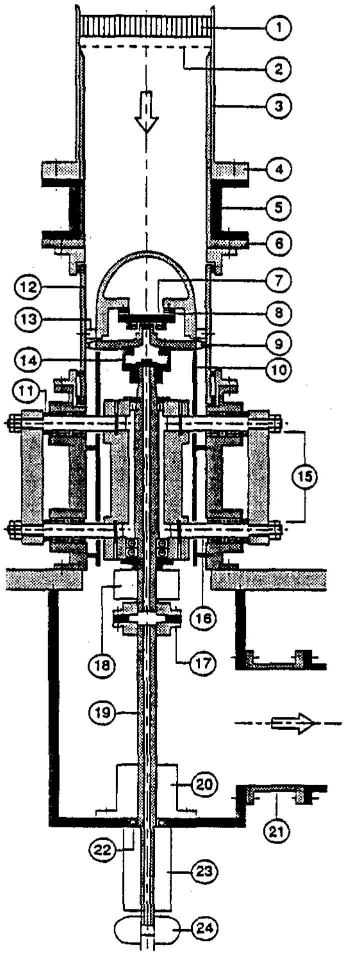

Fig. 1 Schematic of the turbine test section

cussed here. The dynamometer can sense all components of force and torque on the turbine, and the signals from its nine strain gage bridges are carried through the shaft to the slip-ring assembly (23). These signals were sampled 32 or 64 times per revolution, on a pattern, which was phase-locked to the rotor by means of signals from an auxiliary encoder (18). The data were ensemble-averaged over 128 or 256 revolutions, to reduce low-frequency noise, and were then numerically projected on fixed axes to extract the DC forces of interest (F_x along the displacement axis, F_y perpendicular to it). Despite sizable second harmonic contamination from the flex joints in the shaft, these DC components were extracted with an accuracy and repeatability of $\pm 0.05\ \ell b_f$ (the forces F_x and F_y ranged to a few ℓb_f).

The flow instrumentation is detailed in Fig. 2. The five-hole probes at stations 2 and 8 could traverse radially the outer 24 percent of the flow passage, while the three-hole probes at stations 1 and 9 could traverse the outer 75 percent, and sensed axial and tangential velocity components, plus total and static pressure. All these probes were precalibrated and then set at fixed yaw angles. The casing rotation allowed full coverage in the azimuthal direction. In addition to the probes, a variety of wall taps were provided for pressure mapping. All pressure data were read via a double 96 channel Scanivalve arrangement with central transducers. The flow instrumentation sensed time-averaged pressures. The absence of nonlinear bias in this averaging was verified for station 7 (where unsteadiness is most severe) by comparison to a flush-mounted fast response transducer.

The characteristics and design parameters of the unshrouded test turbine are summarized in Table 1. Due to the low pressure ratio, compressibility effects are minimal, and similarity would be ensured by matching flow and work coefficients, and Reynolds number. The first two are indeed matched to the SSME LH turbine. The Reynolds number (based on stator exit velocity and blade height) is 1.4×10^6,

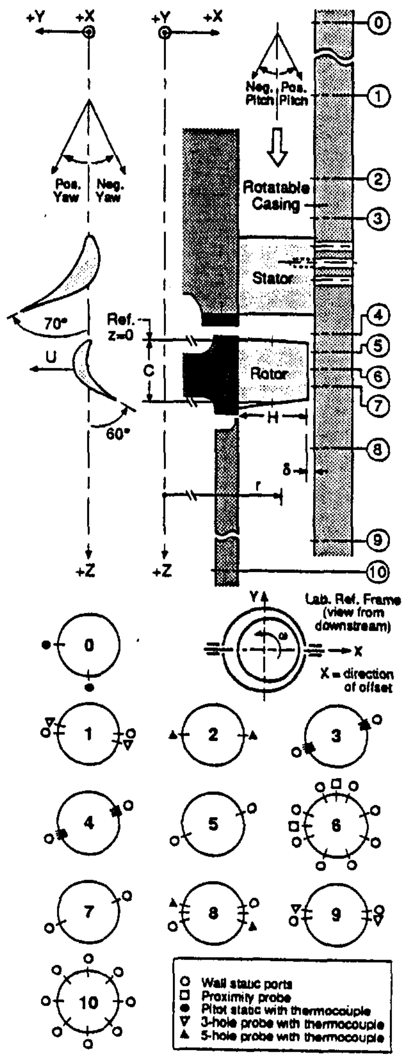

Fig. 2 Types of instrument used

Table 1 Design parameters for SSME fuel turbopump: first stage and test turbine

Parameter	SSME Stage	Test Turbine
Flow coefficient, ϕ	0.58	0.58
Work coefficient, Ψ	1.508	1.508
Stator exit angle	70°	-
Relative rotor inlet angle	43.9°	-
Rotor exit angle	60°	60°
Absolute exit angle	-3.1°	-3°
Degree of reaction	0.216	0.216
Rotor mean radius, cm (in)	12.88 (5.07)	12.88 (5.07)
Number of rotor blades	63	63
Rotor blade height, cm (in)	2.17 (0.854)	2.17 (0.854)
Rotor blade chord, cm (in)	2.21 (0.870)	2.21 (0.870)
Rotation Rate, rpm	34,560	3440
Axial flow velocity, m/s (in/s)	262 (10,300)	26 (1020)
Mass flow rate, kg/s (slug/s)	71.8 (4.92)	4.48 (0.307)
Inlet pressure, kPa (psi)	34,950 (5069)	224 (32.43)
Inlet temperature	1053 (1436)	300 (80)
Pressure ratio	1.192	1.231
Efficiency	0.821	0.80

Table 2 The test matrix

Conf #	t_m/H (%)	d/c (%)	d'/c (%)	Shroud (Y/N)	ω / ω_D (%)	e/t_m Range (%)
1	3.0	50	38	N	70 100 110	±67
2	3.0	26	15	N	70 100 110	±67
3	3.0	26	1.3	N	70 100 110	±67
4	1.9	26	15	N	70 100 110	±59
5	1.9	26	1.3	N	70 100 110	±59
6	4.5	26	1.3	Y	70 100 110	±59

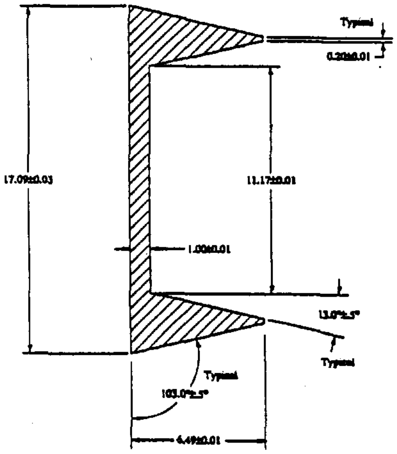

Fig. 3 Shroud-seal for turbine; dimensions in mm

compared to 5.6 × 10^6 in the SSME turbine; since both are well above transition ($10^5 - 2 \times 10^5$) no significant difference is expected. A limited test of this insensitivity was provided by comparison runs at 1 atm and 2 atm loop pressure, in which no difference was detected in the nondimensional cross-force characteristics.

After the unshrouded turbine tests, the same turbine was modified by removing the outer 6.5 mm (out of a blade height of 22.9 mm) and installing a continuous shroud band with a two-ridge labyrinth seal (as shown in Fig. 3). Due to the partial flow blockage of the unrecessed seal, the optimum flow rate at the design speed of 3440 rpm dropped to 3.16 kg/s, the optimum efficiency dropped to 74 percent, and the corresponding pressure ratio was reduced to 1.14.

The test matrix is summarized in Table 2, with the geometric notation contained in Fig. 4.

3 Force Data for the Unshrouded Turbine

Typical force versus displacement plots are shown in Fig. 5, which corresponds to configuration 1 of Table 2, at its design condition. The plots for configurations 2–5 are qualitatively similar. In these graphs, the negative F_x slope indicates a *restoring* direct force, while the positive F_y slope indicates a *forward-whirling* cross-force. Each test was repeated three times, and all test results are shown to illustrate the degree of repeatability of the data. The fact that the forces are not exactly zero at zero eccentricity is due to a combination of casing out-of-roundness and positioning error. Despite the relatively large offsets (±15 mil on a mean gap of 27 mil), the F_y data show no departure from linearity. By contrast, the F_x data show in all cases a slight s-shaped curvature, with the slope increasing with eccentricity.

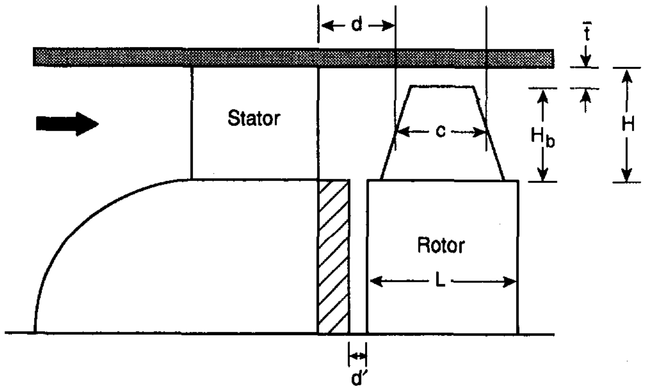

Fig. 4 Schematic of turbine's major dimensions of interest

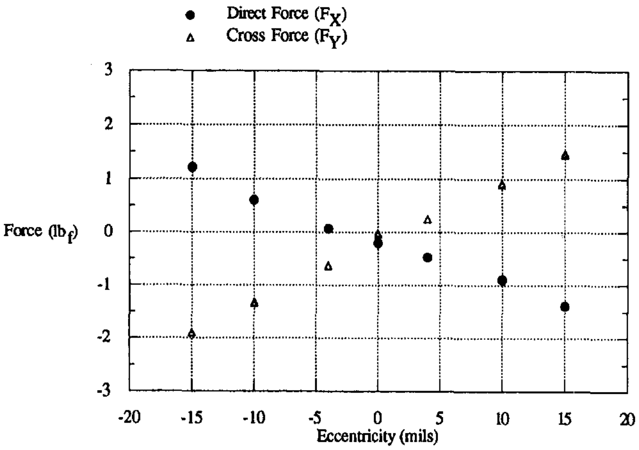

Fig. 5 F_x and F_y versus e (conf. 1, $\omega / \omega_D = 1.0$)

Table 3 Nondimensional force coefficients from dynamometer

Configuration	ω / ω_D	α_x	α_y
1	0.7	-2.12	2.43
1	1.0	-2.81	2.57
1	1.1	-3.42	3.66
2	0.7	-1.54	2.49
2	1.0	-2.14	2.96
2	1.1	-2.46	3.23
3	0.7	-1.47	2.87
3	1.0	-1.87	3.02
3	1.1	-2.04	3.43
4	0.7	-2.93	3.38
4	1.0	-3.42	3.55
4	1.1	-3.65	3.72
5	0.7	-2.82	3.83
5	1.0	-3.47	3.98
5	1.1	-3.50	4.04

As noted in the introduction, the simple Alford theory would predict $F_x = 0$. However, the data show $|F_x|$ of the same order as $|F_y|$, and a different mechanism, or a variation on Alford's postulated mechanism, must be involved.

The results of the measurements for all configurations are reported in nondimensional form in Table 3. The coefficients α_x and α_y are obvious generalizations of Alford's β:

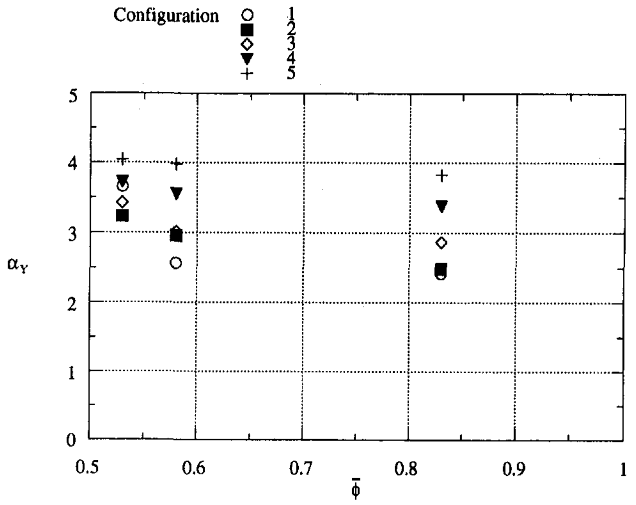

Fig. 6 Effect of ϕ on α_Y (conf. 1, $e/H = 0.019$

$$\alpha_x = \frac{2F_xR}{Q(e/H)}; \qquad \alpha_y = \frac{2F_yR}{Q(e/H)} \tag{8}$$

where the notation has been changed from β, which is strictly the sensitivity of blade tangential forces to tip gap, to α_y, which is a measure of the cross-forces, and may or may not be equal to β (indeed, there is no β counterpart to α_x). The forces at $e = 0$ have been subtracted from F_x and F_y in calculating α_x and α_y.

Table 3 indicates a general increase of α_y with speed at a fixed flow rate, or a decrease with the flow coefficient $\phi = C_x/\omega R$. This is displayed in Fig. 6.

A second trend in the data is a substantial increase of the force coefficient (both $|\alpha_x|$ and α_y) as the mean radial gap is reduced. This can be seen by comparing configurations 2 (gap 3 percent of blade height) and 4 (gap 1.9 percent), both with the widest axial hub gap d', and also by comparison of configurations 3 and 5, similarly related, but with a narrower axial hub gap. Averaging over the various speeds, the effect amounts to a 0.6 decrease in α_y (19 percent) per 1 percent increase in $\bar{\delta}/H$ (wide axial gap), or a 0.7 (21 percent) per 1 percent for the narrow axial gap. Of course, since only two gap values were tested, there is no confirmation of the linearity of this effect. There are some indications from the flow data (Sec. 4) that viscous flow effects in the narrow tip flow passages may be responsible. This trend had been previously reported by Urlichs [3] as well.

Configurations 2 and 3 differ only in the hub axial gap d', while configuration 1 differs from 2 and 3 in both, d', and the stator-to-rotor blade spacing, d. All three configurations have $\bar{\delta}/H = 3$ percent. Thus, if we postulate a *linear* variation of α_y with d and d', the data in Table 3 can be used to extract the separate sensitivities of α_y to these gap values. Similarly, comparison of configurations 4 and 5 can yield the d' sensitivity for the cases with the narrow radial tip gap. The results (Table 4) are inconclusive for d, but are unambiguous as to sign and general magnitude for the hub gap d'. We have not been able so far to find a satisfactory explanation for this effect. Opening the gap d' should have the direct effect of reducing the pressure nonuniformity in the stator–rotor space, and to the extent that this nonuniformity contributes to the cross-force (see Sec. 4), this would indeed reduce α_y. On the other hand, these pressure nonuniformities also redistribute the upstream flow in a manner that tends to dampen the Alford effect. The net result must then depend on the balance of these two effects. A more complete analysis of the flow data, and additional theoretical development are needed in this area. Urlichs [3] found the opposite trend (α_y increasing with axial gap), but his geometry was such that *both* d and d' were varied simultaneously.

Table 4 Cross-force sensitivity to axial stator–rotor spacing and hub axial gap

$\bar{\delta}/H$	ω/ω_D	$\partial\alpha_y/\partial(d/c)$	$\partial\alpha_y/\partial(d'/c)$
0.030	0.7	2.42	-2.78
0.030	1.0	-1.21	-0.44
0.030	1.1	-1.00	-1.44
0.019	0.7	-	-3.32
0.019	1.0	-	-3.13
0.019	1.1	-	-2.37

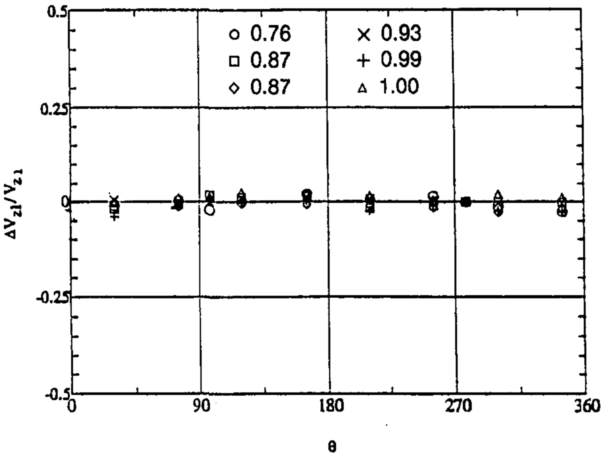

Fig. 7 Upstream axial velocity distribution (conf. 1, $e/H = 0.019$)

4 Flow Survey Results

Most of the discussion in this section is based on configuration 1, for which flow data were taken at all operating conditions.

Since our main interest is in the azimuthal nonuniformities due to the turbine offset, most of the probe data will be shown with the centered turbine values subtracted. This has the effect of eliminating artifacts, such as small probe misalignments, which make interpretation difficult. It also eliminates all radial and tangential variations of the basic (centered) data, while preserving those of the flow perturbations.

The surveys upstream of the stator indicated very small departures from tangential uniformity. As an example, Fig. 7 may show 1–2 percent axial velocity variation, with a maximum near 180 deg, where the widest rotor tip gap occurs, but the resolution is insufficient. This result is as expected, since the relative eccentricities e/H were 1–2 percent themselves.

The wall pressure surveys downstream of the stator do show a well-resolved nonuniformity. Figure 8 shows the pressure pattern for the interblade row region and the rotor blade tip region. For the region between stator and rotor a pressure fluctuation amplitude of about $0.0027\ P_{t0} = 0.22\ \rho C_{x0}^2/2 = 0.028\ \rho(\omega R)^2$ for $e/H = 0.019$. The pressure minimum is about 25 deg ahead of the maximum gap location. For $e/H = 0$, this variation is absent. Figure 9 shows concentric pressure patterns. As one advances downstream over the rotor blading, the amplitude of these nonuniformities increases, with the phase staying about constant. Downstream of the rotor the amplitude of the wall pressure nonuniformity reverts to $0.0027\ P_{t0}$ (Fig. 10), although with some rotation.

The question of whether the wall pressures measured over the rotor (stations 5, 6, 7) can be assumed to extend down to the blade roots and act on the hub cannot be answered directly. We did obtain static pressure data from the probe

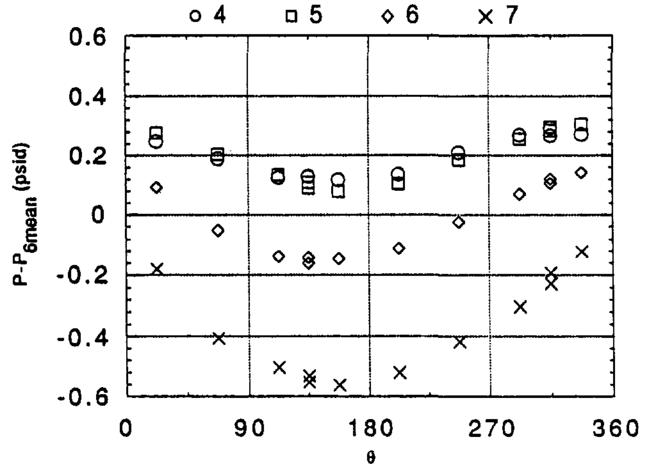

Fig. 8 Wall tap pressure between stator and rotor (4) and over the rotor blade tip (5, 6, and 7) (conf. 1, $e/H = 0.019$)

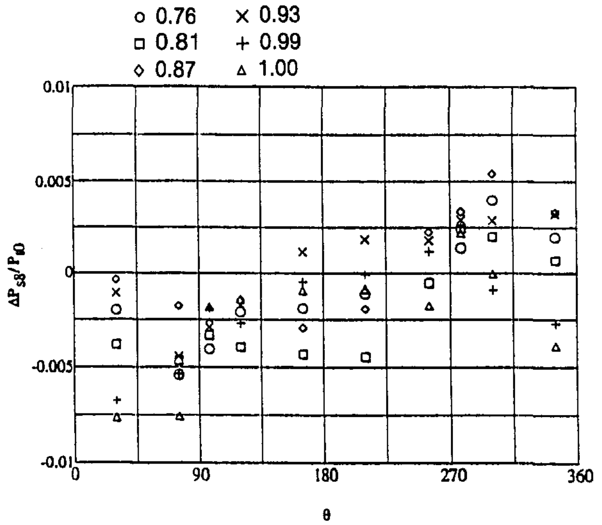

Fig. 11 A radial and tangential static pressure survey at station 8 (conf. 1 $e/H = 0.019$)

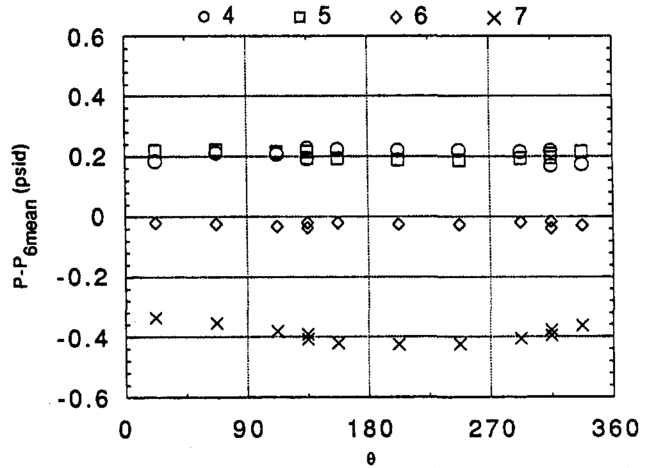

Fig. 9 Same as Fig. 8 for centered turbine (conf. 1, $e/H = 0.000$)

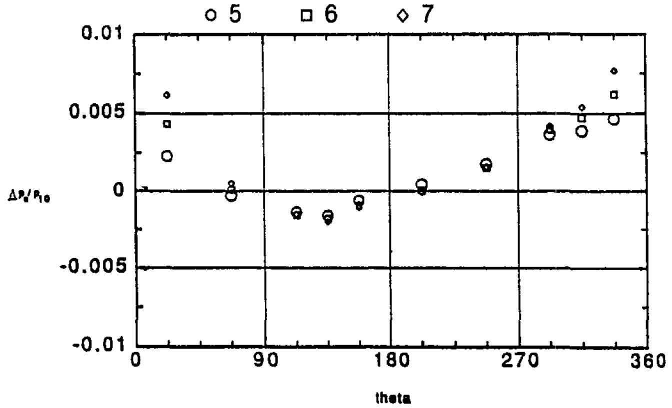

Fig. 12 Wall tap pressure for stations 5, 6, and 7 (conf. 1, $e/H = 0.019$)

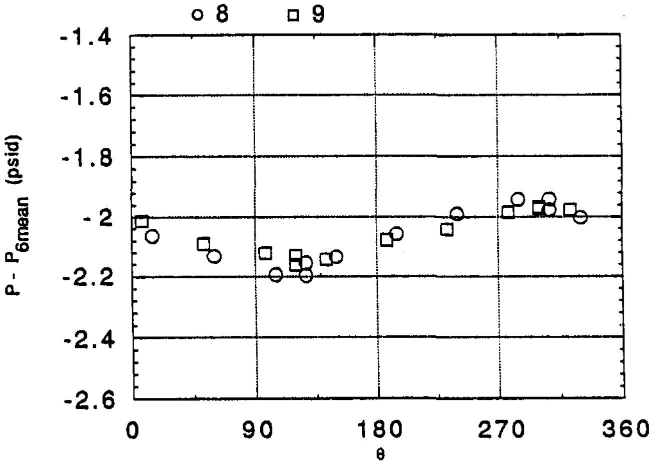

Fig. 10 Wall tap pressure downstream of rotor (conf. 1, $e/H = 0.019$)

traverses at stations 8 and 9, some distance downstream of the rotor. These are extracted from the frontal and angled hole readings, and are more prone to error than wall tap data, but the pattern (see Fig. 11 for station 8, for example) appears to indicate penetration of the wall pressure pattern, as shown in Fig. 10, throughout the radial depth surveyed. The same is true at station 9.

Related to this is the question as to the origin of the increasing wall pressure nonuniformity as one moves from station 4, to 5, 6, and 7, and why this additional nonuniformity appears to vanish past the rotor. Figure 12 sheds some light on this issue by showing together the measured tap pressure variations at stations 5, 6, and 7. There is no difference between these in the wide-gap sector (between 90 deg and 270 deg), but clear differences arise in the small-gap region, near 0 deg or 360 deg. This suggests a qualitatively different behavior of the leakage-dominant region near the blade tips when the local gap is less than about 10–12 mil. Perhaps this is the threshold for viscous effects (enhanced by counterflow relative motion of the casing wall) to become important. This question is being further investigated.

The tentative pattern that emerges from these pressure data is as follows. The turbine eccentricity is felt upstream and downstream of it through potential effects with a range of the order of the radius R. This produces a nonuniform pressure pattern that spans the passage depth and extends a few blade heights downstream. Superimposed on this, there is a second source of mean pressure variation, which appears to be localized toward the trailing edge region of the blades with the smallest tip gap. Although we have no direct indication of this, the rapid axial variation of this component would tend to show that its effect cannot extend radially to the hub. It is worth commenting here that, even though each of the trailing leakage vortices can be expected to be associated with a low-pressure footprint, averaging over a complete blade passage should cancel this pressure variation, because the leakage flow is not associated with any momentum transfer perpendicular to the casing wall. The observed pressure variations are on a broader scale, of order R, and must reflect the varying leakage rates.

The five-hole probes at station 8 (two chord lengths downstream of the rotor leading edge) were used to measure three

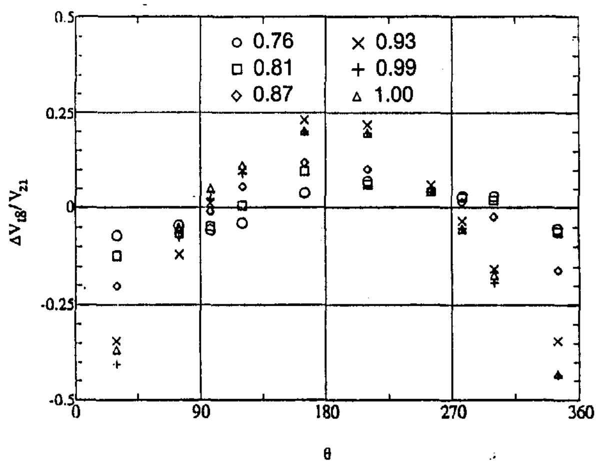

Fig. 13 Tangential velocity at station 8 (conf. 1, $e/H = 0.019$)

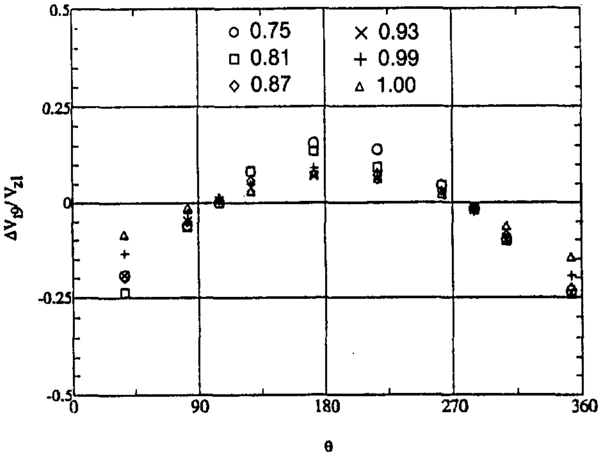

Fig. 14 Tangential velocity at station 9 (conf. 4, $e/H = 0.019$)

velocity components in the outer 24 percent of the span. The errors in the measurements are difficult to assess. However, based on consistency between the two probes used at each axial station, plus consistency of integrated forces (see below) between the two axial stations and also with the dynamometer data, the errors appear to be under 10 percent. The errors would be greater if the centered turbine data were not subtracted off, as there were alignment and other unaccounted-for biases. They were also greater for the axial and radial components of velocity; for this reason, and because of their smaller effect on cross force estimation, these other components are not reported. The downstream tangential velocity distribution is shown in Fig. 13, where the mean (centered turbine) tangential velocity has been subtracted out at each depth. The positive tangential velocity values seen near the bigger gap region (180 deg) indicate underturning by the rotor blades. The magnitude seems to be uniform in the outer 5 percent of the span, gradually decreasing to approximately zero at 76 percent span. Since the data are steady, they show a time-averaged shear flow pattern whose yaw angle varies with radius. The same tangential velocity distribution farther downstream, at station 9, is shown in Fig. 14. At this station, data were obtained (using the three-hole probes) to a depth of 75 percent span. The underturning magnitude has decreased but has penetrated farther toward the hub.

Thus, two main sources of lateral force on the turbine due to the flow properties can be identified: (1) a tangentially nonuniform flow turning, which leads to uneven work extraction; and (2) a nonuniform static pressure distribution. Both forces can be integrated around the perimeter to a direct force and a cross force.

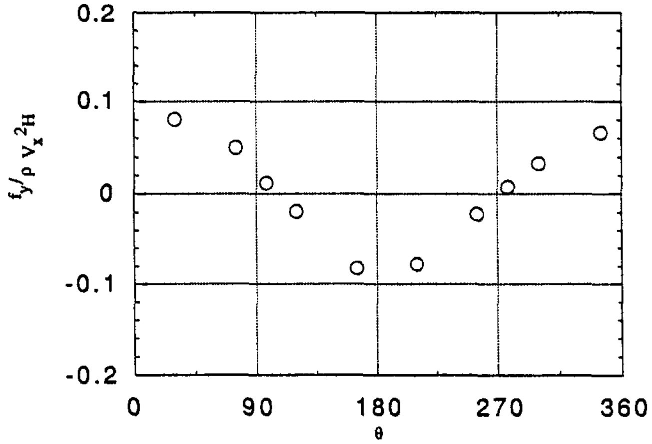

Fig. 15 Tangential force per unit length (conf. 1, $e/H = 0.019$)

5 Comparison of Fluid-Derived Forces and Dynamometer-Derived Forces

The force exerted on the turbine blades per unit perimeter by the fluid is given by the Euler turbine equation

$$f_y(\theta) = \int_0^H \rho C_x (C_{\theta 2} - C_{\theta 3}) dz \tag{9}$$

where $C_{\theta 2}$ and $C_{\theta 3}$ are tangential velocities upstream and downstream of the rotor, and ρC_x is the mass flux. Variations of mass flux and upstream velocity components are minor, and the major effect is due to the variation in the downstream tangential velocity distribution.

The difference in turning, $(C_{\theta 2} - C_{\theta 3})$, between eccentric and concentric cases was linearly extrapolated from the last measured radial station to zero at the hub. For station 8, the measurements extended down to the 76 percent span radial station (five-hole probes), while for station 9, in configurations 4 and 5, data were taken with three-hole probes down to the 25 percent span station.

The integrated force is shown in Fig. 15 for a particular case, and this force distribution can be expressed as a truncated Fourier series:

$$f_y(\theta) \cong \bar{f}_y + \Delta f_y \cos(\theta - \phi_f) \tag{10}$$

Upon projection onto x and y axes, the direct force (F_x) and the cross force (F_y) can be determined.

$$F_x = -\int_0^{2\pi} f_y \sin \theta R d\theta = -\pi R \Delta f_y \sin \phi_f \tag{11}$$

$$F_y = -\int_0^{2\pi} f_y \cos \theta R d\theta = -\pi R \Delta f_y \cos \phi_f \tag{12}$$

The F_x and F_y due to nonuniform pressure distribution can be determined similarly by projection of pressure forces onto X and Y axes. Assuming a pressure variation of the form

$$p(\theta) = \bar{p} + \Delta p \cos(\theta - \phi_p) \tag{13}$$

one can obtain

$$F_x = -\int_0^{2\pi} p \cos \theta R\theta = -\pi R W \Delta p \cos \phi_p \tag{14}$$

$$F_y = -\int_0^{2\pi} p \sin \theta R\theta = -\pi R W \Delta p \sin \phi_p \tag{15}$$

Table 5 Contributions from work defect (wd) and pressure (p) to the force coefficients α_x, α_y at design conditions, and comparison to dynamometer data. Pressure data from station 4 and tangential velocity from station 8.

Configuration	$(\alpha_x)_{wd}$	$(\alpha_x)_p$	$(\alpha_x)_{total}$	$(\alpha_x)_{dyn}$
1	-.4	-1.3	-1.7	-2.81
2	-.3	-1.3	-1.6	-2.61
4	-.5	-2.6	-3.1	-3.36
5	-.3	-2.3	-2.6	-3.47

Configuration	$(\alpha_y)_{wd}$	$(\alpha_y)_p$	$(\alpha_y)_{total}$	$(\alpha_y)_{dyn}$
1	1.2	.6	1.8	2.57
2	1.4	1.4	2.8	2.96
4	2.0	1.6	3.6	3.55
5	2.5	2.2	4.7	3.98

Table 6 Same as Table 5, but with velocity from station 9

Configuration	$(\alpha_x)_{wd}$	$(\alpha_x)_p$	$(\alpha_x)_{total}$	$(\alpha_x)_{dyn}$
4	-.6	-2.6	-3.2	-3.36
5	-.6	-2.3	-2.9	-3.47

Configuration	$(\alpha_y)_{wd}$	$(\alpha_y)_p$	$(\alpha_y)_{total}$	$(\alpha_y)_{dyn}$
4	2.1	1.6	3.7	3.55
5	1.9	2.2	4.1	3.98

Table 7 The pressure force compared to the dynamometer data for the shrouded turbine

$(\alpha_x)_p$	$(\alpha_x)_{dyn}$	$(\alpha_y)_p$	$(\alpha_y)_{dyn}$
-3.8	-5.58	5.6	6.00

The pressures used in Eqs. (14) and (15) were taken to be those at station 4 (between stator and rotor), since there are some local tip effects visible at stations 5, 6, and 7 (although their integrated effect turns out to be small). As for the blade forces for Eqs. (11) and (12), both station 8 and (for configurations 4 and 5) station 9 were used for comparison. The results are shown in Tables 5 and 6, where we report the separate pressure and work-defect contributions to α_x and α_y, their sum, and for reference, the dynamometer-measured data.

The results using either set of tangential velocity data are reasonably consistent with the dynamometer data. Most of the direct force is due to the pressure force while the cross force is caused by both the pressure force and blade force. The cross force coefficients, α_y, are larger than expected for this low-reaction turbine on the basis of work-defect arguments. Clearly, the pressure component, not previously identified, is an important factor.

6 Force Data for the Shrouded Turbine

The turbine was modified, as described in Section 2 of this paper, for the shrouded case, and dynamometer and pressure data were obtained. Velocity data were also obtained, but they were not conclusive due to the combined effects of radial traverse limit of probes and the separated flow behind the seal knife.

As in the unshrouded cases, the forces scale linearly with eccentricity, and a sinusoidal pressure pattern with a large amplitude develops over the shroud band. Table 7 shows the excitation coefficients from the dynamometer data and the pressure data.

Compared to the unshrouded cases, the excitation coefficients are larger by a factor ranging from 1.5 to 2.0. The nonuniform pressure distribution produces both direct and cross forces, which are smaller than those measured with the dynamometer. If it is assumed that the work defect mechanism contributes primarily to the cross force as in the unshrouded cases, the discrepancy in the direct force excitation coefficient cannot be explained. Furthermore, the small difference in the cross-force excitation coefficients for the shrouded case suggests that the pressure effect, instead of the work defect effect, is primarily responsible for the cross force. Last, the pressure nonuniformity, which can be detected upstream and downstream of the shroud, shows again a flow redistribution on the scale of the turbine radius.

A linear labyrinth seal model based on the work of Millsaps [6] was extended to include the effects of nonuniformities in the flow both upstream and downstream of the shroud and was used to analyze the shrouded data. It was found that the nonuniformities have a large effect on the model's predictions, essentially doubling the magnitude of both the direct and the cross force, but even after this correction, the model underpredicts the forces by about 40 percent. No complete theory exists of a seal interacting with the flow field of the turbine blading.

7 Conclusions

This work has confirmed the existence of the destabilizing forces suggested by Thomas and Alford. The general scaling and order of magnitude are also consistent with their insights. However, some new effects in the unshrouded cases include the following:

1 In addition to a nonuniform work extraction, a nonuniform pressure distribution also exists.

2 This pressure effect contributes almost all of the direct force and approximately 40 percent of the cross force.

3 The pressure nonuniformity extends over axial lengths on the order of the turbine radius. Therefore, it must result from azimuthal flow redistributions.

4 In addition to the large-scale pattern, some local effects occur, especially in the narrow-gap region. This, along with the increase in forces in small mean tip gap cases, calls for an examination of the viscous force and the relative wall motion.

5 The forces increase significantly as the mean tip gap is reduced, confirming an earlier result.

6 The lateral forces in shrouded turbines can be larger than those in unshrouded turbines. This is due to a large nonuniformity in the seal gland pressure, which now dominates over the work defect contribution.

7 For shrouded turbines, the upstream and downstream nonuniformities caused by flow redistribution increase the magnitude of the forces, by increasing the seal pressure nonuniformity.

Acknowledgments

This work was performed under Contract No. NAS 8-35018 from NASA, with Marshall SFC Glenn E. Wilmer, Jr., as Technical Monitor.

References

1 Thomas, H. J., "Instabile Eigenschwingungen von Turbinenlaeufern Angefacht durch die Spaltstroemung in Stopfubuchsen und Bechauchflug (Unstable Natural Vibrations of Turbine Rotors Induced by the Clearance Flows in Glands and Blading)," *Bull. de L.A.I.M.*, Vol. 71, No. 11/12, 1958, pp. 1039–1063.

2 Alford, J. S., "Protecting Turbomachinery From Self-Excited Rotor Whirl," ASME *Journal of Engineering for Power*, Vol. 87, 1965, pp. 333–334.

3 Urlichs, K., "Clearance Flow Generated Transverse Forces at the Rotors of Thermal Turbomachines," NASA TM-77292, Translation of Ph.D. Dissertation, Munich Technical University, 1975.

4 Iwatsubo, T., "Evaluation of Instability Forces of Labyrinth Seals in Turbines or Compressors," NASA CP-2133, 1980, pp. 139–169.

5 Scharrer, J. K., and Childs, D. W., "Theory Versus Experiment for the Rotordynamic Coefficients of Labyrinth Gas Seals: Parts 1 & 2, ASME *Journal of Vibration, Acoustics, Stress, and Reliability in Design*, Vol. 110, No. 3, 1989, pp. 270-1287,

6 Millsaps, K. T., and Martinez-Sanchez, M., "Dynamic Forces From Single-Gland Labyrinth Seals: Part I—Ideal and Viscous Decomposition," ASME JOURNAL OF TURBOMACHINERY, Vol. 116, 1994, pp. 686-693: "Part II—Upstream Coupling," ASME JOURNAL OF TURBOMACHINERY, Vol. 116, 1994, pp. 694—700.

7 Wohlrab, R., "Experimental Determination of Gap Flow Conditioned Forces at the Rotors of Thermal Turbomachines," NASA TM-77293, Translation of Ph.D. Dissertation, Munich Technical University, 1975.

8 Vance, J. M., and Laudadio, F. J., "Experimental Measurement of Alford's Force in Axial Flow Turbomachinery," ASME *Journal of Engineering for Gas Turbines and Power*, Vol. 106, 1984, pp. 585-590.

9 Ehrich, F., "Rotor Whirl Forces Induced by the Tip Clearance Effect in Axial Flow Compressors," ASME *Journal of Vibration and Acoustics*, Vol. 115, 1993, pp. 509-515.

10 Song, S. J., "An Investigation of Tip Clearance Flow Excitation Forces in a Single-Stage Unshrouded Turbine," Sc.D. Thesis, M.I.T., Feb. 1995.

Euler Solutions for Transonic Oscillating Cascade Flows Using Dynamic Triangular Meshes

C. J. Hwang

S. Y. Yang

Institute of Aeronautics and Astronautics,
National Cheng Kung University,
Tainan, Taiwan

The modified total-variation-diminishing scheme and an improved dynamic triangular mesh algorithm are presented to investigate the transonic oscillating cascade flows. In a Cartesian coordinate system, the unsteady Euler equations are solved. To validate the accuracy of the present approach, transonic flow around a single NACA 0012 airfoil pitching harmonically about the quarter chord is computed first. The calculated instantaneous pressure coefficient distribution during a cycle of motion compare well with the related numerical and experimental data. To evaluate further the present approach involving nonzero interblade phase angle, the calculations of transonic flow around an oscillating cascade of two unstaggered NACA 0006 blades with interblade phase angle equal to 180 deg are performed. From the instantaneous pressure coefficient distributions and time history of lift coefficient, the present approach, where a simple spatial treatment is utilized on the periodic boundaries, gives satisfactory results. By using this solution procedure, transonic flows around an oscillating cascade of four biconvex blades with different oscillation amplitudes, reduced frequencies, and interblade phase angles are investigated. From the distributions of magnitude and phase angle of the dynamic pressure difference coefficient, the present numerical results show better agreement with the experimental data than those from the linearized theory in most of the cases. For every quarter of one cycle, the pressure contours repeat and proceed one pitch distance in the upward or downward direction for interblade phase angle equal to −90 deg or 90 deg, respectively. The unsteady pressure wave and shock behaviors are observed. From the lift coefficient distributions, it is further confirmed that the oscillation amplitude, interblade phase angle, and reduced frequency all have significant effects on the transonic oscillating cascade flows.

Introduction

Recently, significant attention has been given to vibration problems. A number of Euler solutions of oscillating cascade flows were presented (Gerolymos, 1988; He, 1990; Huff et al., 1991; Bendiksen, 1991; Huff, 1992; Hsiao and Bendiksen, 1992). By utilizing the explicit MacCormack scheme, Gerolymos (1988) investigated both started and unstarted supersonic flows in vibrating cascades of fan blades. He (1990) developed sinusoidal shape and high-order shape corrections for phase-shifted periodic boundary conditions, so that the large computer storage required by the conventional direct parameter storage approach can be reduced. Huff et al. (1991) introduced a high-resolution wave-split scheme to predict the unsteady aerodynamics associated with transonic flows over oscillating cascades. Implementing a five-stage Runge–Kutta finite volume scheme on a deformable cascade mesh, Bendiksen (1991) calculated the unsteady transonic cascade flows. Based on the Beam–Warming block ADI algorithm, Huff (1992) studied the flows around an oscillating flat-plate cascade and biconvex airfoil cascades. Hsiao and Bendiksen (1992) introduced a Runge–Kutta Galerkin finite element method to solve the unsteady flow in cascade. Even though several works have been done, further research on the Euler solution procedure for solving the oscillating cascade flows with nonlinear effects is still necessary and worthwhile. To resolve the moving shocks and compression waves accurately, a modified locally implicit TVD scheme on the dynamic triangular mesh is presented in this work. Instead of using periodic boundary conditions from block to block for traditional structured grid systems, only a single block is used, and two different approaches to treat the periodic boundary conditions are evaluated. It is found that the simple spatial approach achieves more numerical stability than the direct parameter storage method.

In the oscillating cascade flow calculations, considerable efforts have been expended to develop the dynamic mesh algorithms on the structured (Gerolymos, 1988; He, 1990; Bendiksen, 1991; Huff, 1992) and unstructured grid systems

---

Contributed by the International Gas Turbine Institute and presented at the 38th International Gas Turbine and Aeroengine Congress and Exposition, Cincinnati, Ohio, May 24–27, 1993. Manuscript received at ASME Headquarters February 19, 1993. Paper No. 93-GT-93. Associate Technical Editor: H. Lukas.

(Hsiao and Bendiksen, 1992). Gerolymos (1988) presented a grid displacement procedure to conform with the position of vibrating blades. To save the computing effort, He (1990) created a zonal moving grid technique, where only the grids in local regions around blades are moved. In the calculations of oscillating cascade flows, Bendiksen (1991) indicated that the **H**-mesh solution produced numerical oscillation in the leading edge. Huff (1992) presented a deforming grid technique to generate a C-grid to fit with the moving blade. Even though the aforementioned structured grids can be applied to the oscillating cascade flow problems, the use of unstructured triangular meshes is more suitable for domain with complicated boundaries. By using the advancing front technique and conformal mapping procedure, Hsiao and Bendiksen (1992) created a globally unstructured but locally structured blade-fitted deformable mesh. In the present paper, a dynamic mesh algorithm, which was originally developed for solving oscillating airfoil flow (Hwang and Yang, 1993), is improved, so that the dynamic mesh can be in time to respond to the oscillating cascade of blades.

The objectives of this work are: (1) to develop a numerical solution procedure for studying the transonic oscillating cascade flows and (2) to investigate the effects of oscillation amplitude, interblade phase angle, and reduced frequency on unsteady flow phenomena. In the present numerical solution procedure, modification of a locally implicit TVD scheme on dynamic triangular mesh, improvement of a dynamic triangular mesh algorithm, triangular mesh generation, spatially periodic boundary treatment, and nonreflecting inlet/outlet boundary conditions are included. For the transonic flows around a single oscillating airfoil and oscillating cascade of two blades with 180 deg interblade phase angle, satisfactory results are obtained. In the calculations of transonic flows around an oscillating cascade of four biconvex blades, different values of oscillation amplitude, reduced frequency, and interblade phase angle are employed. The distributions of magnitude and phase angle of the first harmonic dynamic pressure difference coefficient, instantaneous pressure contours, and lift coefficient distributions are presented. In the comparison of magnitudes and phase angles with related data of experiment and linearized theory, the present Euler solutions are acceptable. For every quarter time period, the instantaneous pressure contours repeat and move one pitch distance in the upward or downward direction for interblade phase angle equal to -90 deg or 90 deg, respectively. The unsteady shock and pressure wave behaviors are observed. From the present numerical results, it is concluded that the oscillation amplitude, interblade phase angle, and reduced frequency all significantly affect the physical phenomena of transonic oscillating cascade flows.

Numerical Approach

For unsteady inviscid flows in a moving domain, the two-dimensional Euler equations including moving cell effects (Hwang and Yang, 1993) are solved in the X–Y Cartesian coordinate system. On the dynamic triangular mesh, a locally implicit TVD scheme, which was formulated on mixed quadrilateral-triangular dynamic mesh (Hwang and Yang, 1993), is modified by using an improved limiter function (Hwang and Liu, 1992). Because the utilization of this limiter function can compensate for the drawback, that high order TVD schemes reduce to first order at points of extrema, the unsteady shocks and pressure waves are accurately resolved.

On the oscillating airfoil or blade surfaces, no penetration condition with respect to the moving boundary is imposed. Pressure, density, and velocity components parallel to the moving surface are obtained by extrapolation from the values at the interior cells. For the single oscillating airfoil problem, one-dimensional characteristic analysis based on Riemann invariants is used to determine the values of the flow variables on the outer boundary of the computational domain. In the oscillating cascade flow calculations, the same number of cells and nodes are generated along the upper and lower boundaries of the computational domain. The nodes on both boundaries are located at the same position along the X axis, but with a fixed distance in the Y axis, which is equal to the height of computational domain. Then, both the corresponding cells at upper and lower periodical boundaries are assigned to be the neighbors of each other, and they are treated like interior cells. At the inlet and outlet boundaries, one-dimensional unsteady nonreflecting boundary condition, which was developed by Giles (1990), is utilized. For strong waves incident on the boundaries at highly oblique angles, the one-dimensional nonreflecting boundary conditions are not strictly nonreflective. In such cases, two-dimensional unsteady nonreflecting boundary conditions proposed by Giles (1990) are expected to be more appropriate. However, the application of two-dimensional unsteady nonreflecting boundary conditions will involve the solution of partial differential equations, which is more complicated and time-consuming than one-dimensional nonreflecting boundary conditions. Since no strong waves (such as shocks, etc.) are incident on both inlet and outlet boundaries at highly oblique angles in the present calculations, the utilization of one-dimensional nonreflecting boundary conditions is acceptable.

By using the mesh generation technique, which was developed by Hwang and Wu (1992), the unstructured triangular mesh systems for the isolated airfoil and blade cascade are created. According to the concept of Batina (1990), the mesh conforms to the instantaneous position of the body by modeling each edge of each cell by a spring, where the spring stiffness (K_l) for a given edge is taken to be inversely proportional to the length of the edge. Based on the modified Gauss–Seidel method, the displacements Δx_j and Δy_j at each interior node j of the grid are obtained by solving the static equilibrium equations (Hwang and Yang, 1993). Instead of calculating K_l explicitly (Hwang and Yang, 1993), the spring stiffness (K_l) is updated implicitly during each symmetric iteration cycle in the present work, so that the dynamic mesh can be improved to respond to the moving boundary immediately. In addition to the mass, momentum, and energy conservation laws that govern the physics of the flow, the geometric conservation (Marcel Vinokur, 1989) is satisfied numerically in the present paper.

Results and Discussion

To validate the accuracy of present approach, transonic flows around a single oscillating NACA 0012 airfoil and an oscillating cascade of NACA 0006 blades with σ equal to 180 deg are studied first. In the calculations of NACA 0006 cascade flow, the direct parameter storage method and the present spatial treatment are implemented on the periodic boundaries to compare the numerical characteristics. For transonic flows around an oscillating cascade of four biconvex blades, the computations with different oscillation amplitudes, reduced frequencies, and interblade phase angles are performed. The magnitude and phase angle of the first harmonic dynamic surface pressure difference coefficient (ΔC_p) are obtained by using the Fourier transform for the last cycle of oscillation. The dynamic surface pressure difference coefficient is normalized by the oscillation amplitude and the phase angle is referenced to the blade motion. In this work, the calculated magnitudes and phase angles are compared to those from experiment and linearized theory. Also, the lift coefficient distributions and unsteady behaviors related to moving shocks and pressure waves are presented.

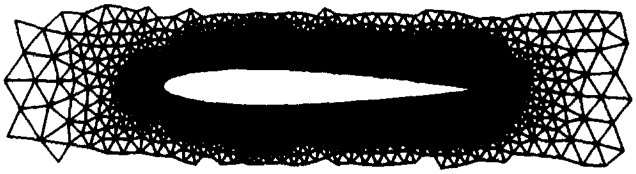

Fig. 1 Partial view of mesh (4888 elements and 2516 nodes) for the oscillating NACA 0012 airfoil

Code Validation

Transonic Flow Around Oscillating NACA 0012 Airfoil. To evaluate the present solution algorithm, the transonic flow, which is around a NACA 0012 airfoil pitching harmonically about the quarter chord with an oscillation amplitude of $\alpha_I = 2.51$ deg and a reduced frequency of $k = 0.0814$ based on semichord, is investigated. The motion of the oscillating airfoil is governed by the relation

$$\alpha = \alpha_0 + \alpha_I \sin(\omega t) \qquad (1)$$

where α is the instantaneous angle of attack. The frequency ω is related to the reduced frequency by the relation $k = \omega c/2V_\infty$, and c is the airfoil chord length. The computational domain is taken to be $21c \times 20c$, and the mesh (Fig. 1) contains 4888 elements and 2516 nodes. In this case, the solution for the airfoil at a free-stream Mach number of $M_\infty = 0.755$ and an angle of attack of $\alpha_0 = 0.016$ deg is taken as the initial condition. By choosing CFL as 30, three cycles of airfoil motion are processed to obtain a periodic solution. Comparing with the related numerical results (Kandil and Chuang, 1989; Batina, 1991) and experimental data (Landon, 1982), the calculated instantaneous pressure coefficient distributions during the third cycle of motion are shown in Fig. 2. Except for the pressure distributions for α equal to 1.09 deg, the results during the first part (α is positive) of the cycle demonstrate a shock wave on the upper surface of the airfoil, and the flow over the lower surface is predominantly subcritical. During the latter part (α is negative) of the cycle (except for α equal to -1.25 deg), the flow about the upper surface is subcritical, and a shock forms on the lower surface. The flow phenomena for α equal to 1.09 deg and -1.25 deg are due to the fact that the shock can't move with the airfoil motion in the same speed. In general, the trend of present results agrees well with the experimental data (Landon, 1982), and the profiles of pressure distribution are closer to the solutions of Batina (1991) than those of Kandil and Chuang (1989). Also, the presently predicted shock position ($\alpha = -2.0$ deg) matches with the adaptive solution (Rausch et al., 1992) than that of the nonadaptive result given by Batina (1991). From this discussion, it is concluded that the present solution algorithm is accurate for studying the unsteady flow problems with moving boundaries.

Transonic Flow Around Oscillating Cascade of NACA 0006 Blades. To further validate the present solution approach involving finite interblade phase angle σ, transonic flow around oscillating cascade of unstaggered NACA 0006 blades with σ equal to 180 deg is studied. In this case, the solidity is equal to one, and computational domain is extended to three chord lengths in both upstream and downstream directions. The meshes for two blades and single blade calculations are shown in Figs. 3(*a*) and 3(*b*), respectively. The steady-state solutions for both cases are obtained at inlet Mach number of $M = 0.77$, angle of attack of $\alpha_0 = 0$ deg, and static exit pressure of $P_e = 0.98\ P_\infty$, and they are chosen as the initial conditions of the unsteady calculations. The motion of the oscillating blades is governed by the relation

$$\alpha = \alpha_0 + \alpha_I \sin(2Mk\tau + m\sigma) \qquad (2)$$

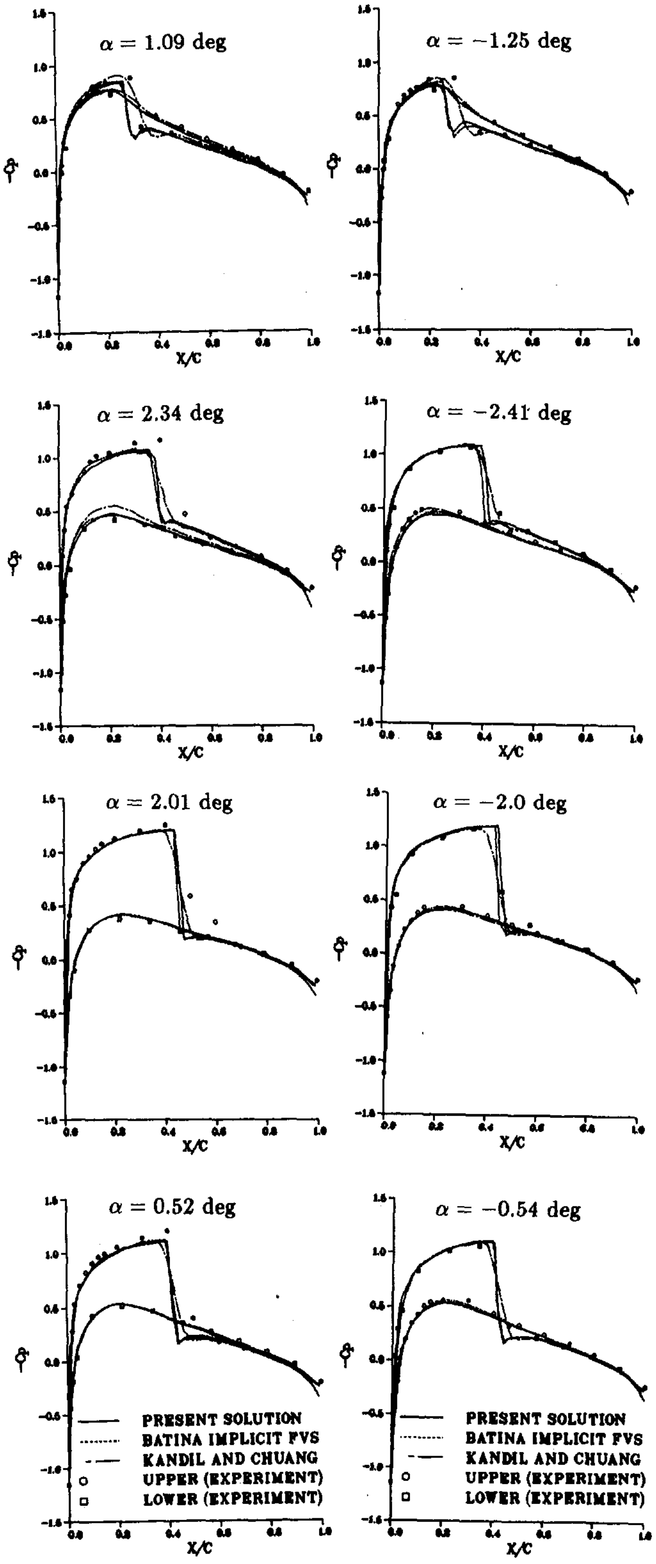

Fig. 2 Instantaneous pressure coefficient distributions for the oscillating NACA 0012 airfoil ($M_\infty = 0.755$, $k = 0.0814$, $\alpha_0 = 0.016$ deg, and $\alpha_I = 2.51$ deg)

where the values of oscillation amplitude α_I, reduced frequency k, and interblade phase angle σ are taken to be 2.0 deg, 0.2, and 180 deg, respectively. τ is the nondimensionalized time scale, and $m = 0, 1$ represent the upper and lower blades, respectively. In this case, nine cycles of blade motion are processed. From the time history of lift coefficient (Fig. 4), the two-blade calculation with spatial treatment of peri-

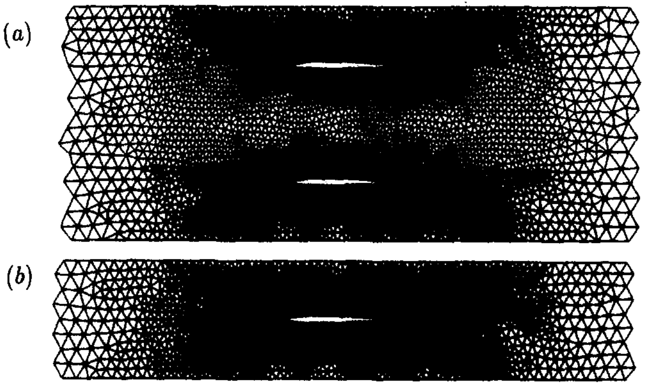

Fig. 3 Meshes for the oscillating cascade of NACA 0006 blades: (a) two blades (10378 elements and 5424 nodes) and (b) single blade (5279 elements and 2800 nodes)

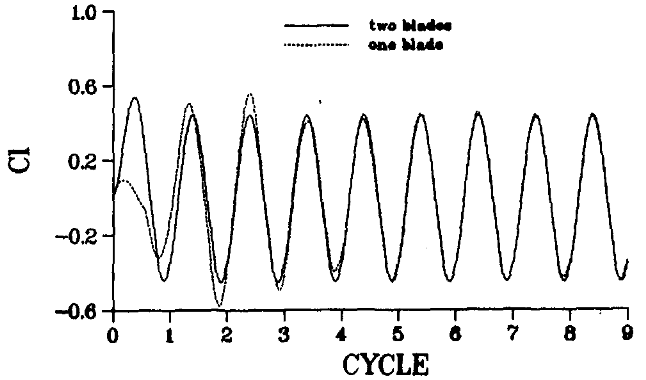

Fig. 4 Time history of lift coefficient for oscillating cascade of NACA 0006 blades (M = 0.77, $k = 0.2$, $\alpha_0 = 0$ deg, $\alpha_I = 2.0$ deg, and $\sigma = 180$ deg)

odic boundary conditions achieves better numerical stability than that of one blade calculation with direct parameter storage method for phase-shifted periodic boundary conditions. Comparing with the related numerical results (Bendiksen, 1991; Hsiao and Bendiksen, 1992), the initial and instantaneous pressure coefficient distributions are shown in Fig. 5. In general, the present results compare well with two related numerical data, except that the present scheme can capture shocks more sharply and the shock locations are between those of two related numerical solutions. For the present one-blade and two-blade calculations, the shock locations ($\alpha = 0.0$ deg) are different. It is believed that this numerical difference is due to the possible source of error when the direct parameter storage method is used. From this discussion, the present approach with spatial treatment of periodic boundary conditions can accurately and robustly simulate the realistic oscillating cascade flows with finite interblade phase angle.

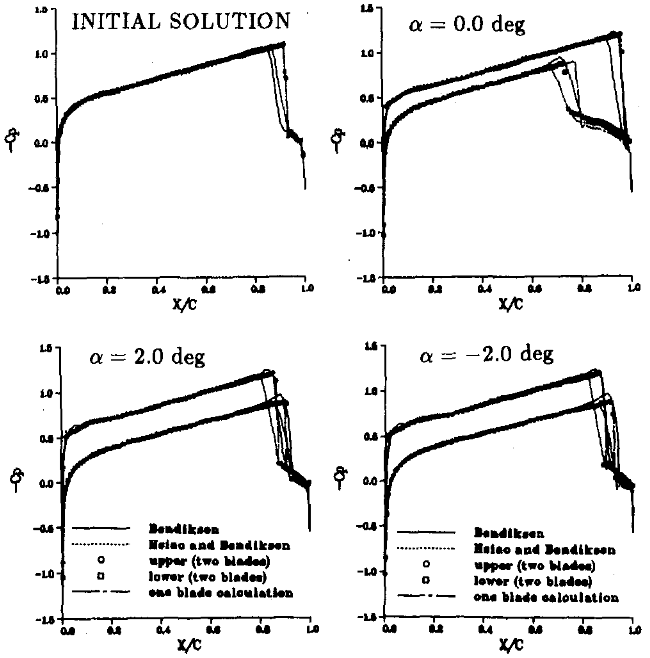

Fig. 5 Initial and instantaneous pressure coefficient distributions for oscillating cascade of NACA 0006 blades (M = 0.77, $k = 0.2$, $\alpha_0 = 0$ deg, $\alpha_I = 2.0$ deg, and $\sigma = 180$ deg)

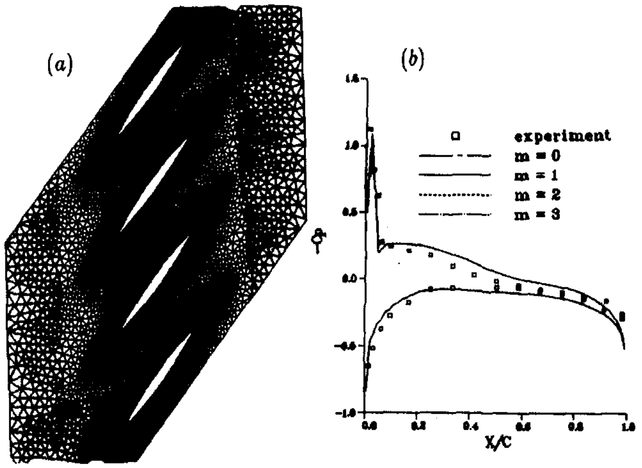

Fig. 6 (a) Partial view of mesh (12,462 elements and 6598 nodes) and (b) pressure coefficient distribution of the initial solution for oscillating cascade of four biconvex blades

Transonic Flow Around Oscillating Cascade of Four Biconvex Blades. For the transonic flows around an oscillating cascade of biconvex blades, the inlet Mach number and exit pressure ratio (static exit pressure divided by total pressure) are equal to 0.8 and 0.7322, respectively. The computational domain comprises four uncambered biconvex blades, in which the values of thickness-to-chord ratio, solidity (chord length divided by blade pitch), and stagger angle are 0.076, 1.3, and 53 deg, respectively. The motion of these four blades, which is executing torsional mode oscillations about midchord, is governed by Eq. (2), and $m = 0$, 1, 2, and 3 represent each blade from the lowest to the highest one, respectively. By setting α_0 to 7 deg, different values of oscillation amplitude (α_I), reduced frequency (k), and interblade phase angle (σ) are employed. The mesh (Fig. 6a) contains 12,462 elements and 6598 nodes, and there are 134 points that lie on each blade surface. From the pressure coefficient distribution of the initial solution (Fig. 6b), the weak leading edge shock appears on the upper surface of each blade. The present numerical results compare well with the experimental data given by Buffum and Fleeter (1990). In the computation of transonic flow with σ, k, and α_I equal to −90 deg, 0.462, and 1.2 deg, respectively, six cycles are processed to obtain a periodic solution. By choosing a constant marching time step of $\Delta\tau = 0.0236$ (CFL is about 20), it only takes 360 time steps to complete one cycle of motion. During the first cycle of blade motion, only the lowest blade ($m = 0$) is set to motion at the beginning, whereas the second ($m = 1$), the third ($m = 2$), and the highest ($m = 3$) blades are set to motion when $2Mk\tau$ reaches $\pi/2$, π, and $3\pi/2$, respectively. From the time history of lift coefficient in Fig. 7, the periodic solution is quickly achieved. The efficiency of the present numerical approach is confirmed.

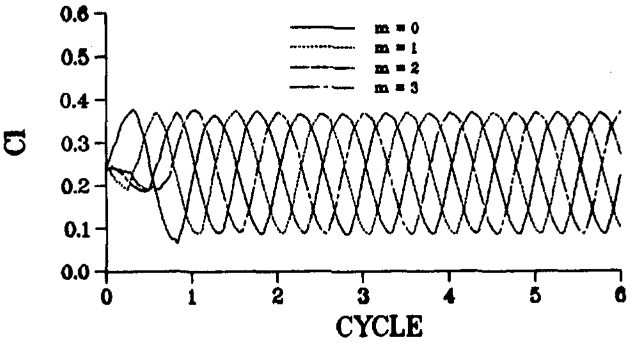

Fig. 7 Time history of lift coefficient for oscillating cascade of four biconvex blades (M = 0.8, $k = 0.462$, $\alpha_0 = 7$ deg, $\alpha_I = 1.2$ deg, and $\sigma = -90$ deg)

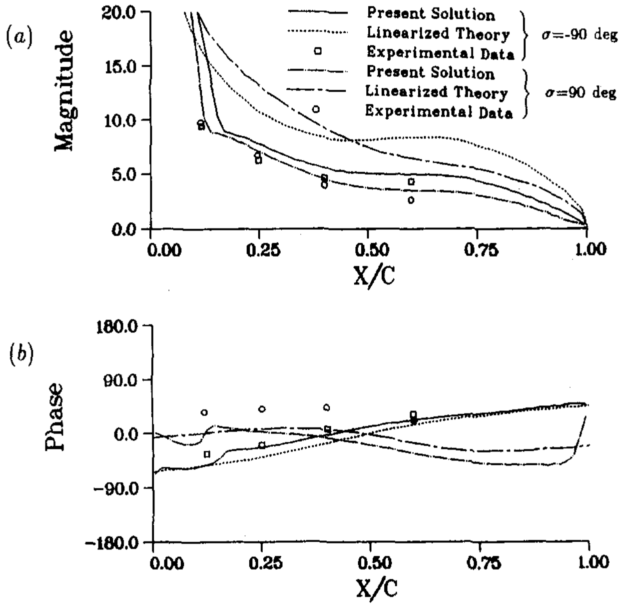

Fig. 8 (a) Magnitude and (b) phase angle of dynamic pressure difference coefficient (ΔC_p) for oscillating cascade of four biconvex blades (M = 0.8, $k = 0.185$, $\alpha_0 = 7$ deg, and $\alpha_I = 1.2$ deg)

When one value of α_I (1.2 deg) and two values of σ (90 deg and -90 deg) are chosen, the transonic oscillating cascade flows with k equal to 0.185 and 0.462 are studied. Magnitudes and phase angles of the first harmonic dynamic surface pressure difference coefficient (ΔC_P) are calculated and plotted in Figs. 8 and 9. To evaluate the present numerical solutions, the experimental data and results obtained by linearized theory (Buffum and Fleeter, 1990) are introduced. By choosing the experimental data as the reference values, the distributions of magnitude (Fig. 8*a*) indicate that the present Euler solver provides better results than does the linearized theory. For the phase angle distributions with σ equal to -90 deg (Fig. 8*b*), the same conclusion is drawn. If the value of σ is replaced by 90 deg, the difference between experimental data and present solution is significant (Fig. 8*b*). A similar phenomena was observed by Huff (1992), and he mentioned that it was difficult to access how many of the quantitative differences were due to the numerical error and how many were due to experimental error. For the magnitude distributions with $k = 0.462$ (Fig. 9*a*), the agreement with experimental data is worse than that in Fig. 8(*a*) for both interblade phase angles. In addition, the values of magnitude of present calculation are closer to those from linearized theory rather than those from experiment when σ is equal to 90 deg (Fig. 9*a*). Comparing the results of phase angle, the present calculation ($\sigma = -90$ deg, Fig. 9*b*) indicates better agreement with experimental data than those of linearized theory. Considering the case with σ replaced by 90 deg, the values of phase angle from both linearized theory and present calculation deviate a distance from those from experiment. As determined from the formula provided by Buffum and Fleeter (1993), the calculation ($k = 0.462$, $\sigma = 90$ deg, and $\alpha_I = 1.2$ deg) lies within the super-resonant region. In super-resonant flow, the pressure waves will propagate upstream and downstream to infinity without decay, which may account for some of the discrepancies. Furthermore, in this super-resonant case, the comparison between the present calculation and linearized theory is satisfactory. Except for the super-resonant case ($\sigma = 90$ deg ad $k = 0.462$) and one subresonant phase angle distribution ($\sigma = 90$ deg and $k = 0.185$), the present Euler solutions show better agreement with the experimental data than those from linearized theory. In the present calculations, no viscous effects are included. It is well known that the viscous effects may cause flow separation and change the unsteady behavior, and some of the discrepancies between the present calculations and experimental data may be attributed to viscous effects. Even though tremendous computational efforts will be involved, further research on a Navier–Stokes solver is inevitable in the future to resolve the unsteady shock/boundary layer interaction and flow separation accurately.

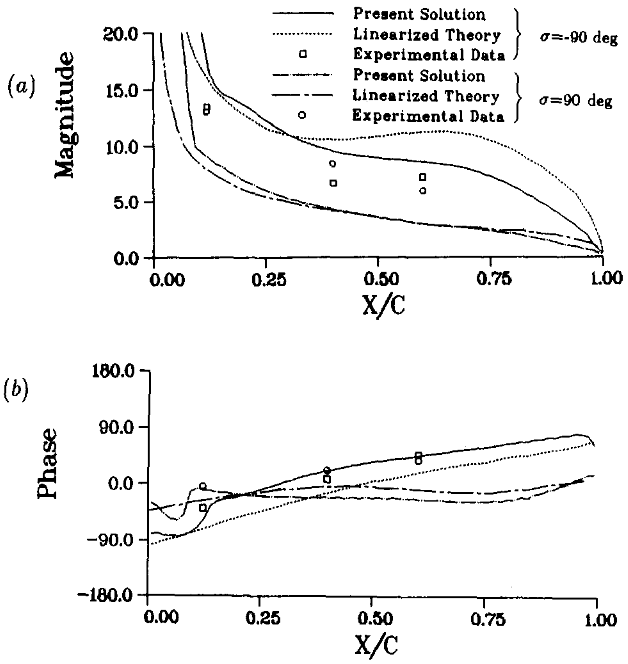

Fig. 9 (a) Magnitude and (b) phase angle of dynamic pressure difference coefficient (ΔC_p) for oscillating cascade of four biconvex blades (M = 0.8, $k = 0.462$, $\alpha_0 = 7$ deg, and $\alpha_I = 1.2$ deg)

To understand further the effects of oscillation amplitude and interblade phase angle on unsteady flow phenomena, instantaneous pressure contours for the transonic oscillating cascade flows with $k = 0.462$ are plotted in Figs. 10–13. It is observed that the contours repeat and proceed one pitch distance in the upward or downward direction for σ equal to -90 deg (Figs. 10 and 11) and 90 deg (Fig. 13), respectively. From the contours given in Figs. 10(*a*) and 11(*a*), the compression wave on the upper surface of the lowest blade in Fig. 10(*a*) becomes a shock located at the midchord of the upper surface of the lowest blade in Fig. 11(*a*). Also, the leading edge weak shock still appears on the upper surface of lowest blade. There is an additional shock on the lower surface of the second blade in Fig. 11(*a*). The weak shock on the upper surface of the third blade in Fig. 10(*a*) becomes

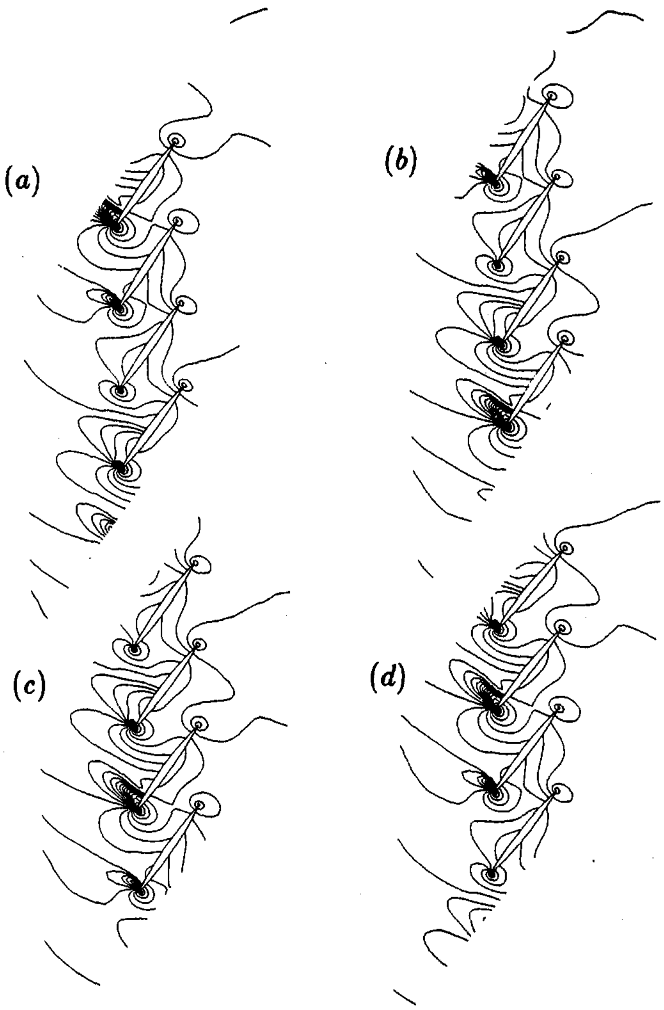

Fig. 10 Instantaneous pressure contours for oscillating cascade of four biconvex blades (M = 0.8, $k = 0.462$, $\alpha_0 = 7$ deg, $\alpha_l = 1.2$ deg, and $\sigma = -90$ deg): ($2Mk\tau - 10\pi$) equal to (a) $\pi/2$, (b) π, (c) $3\pi/2$, and (d) 2π

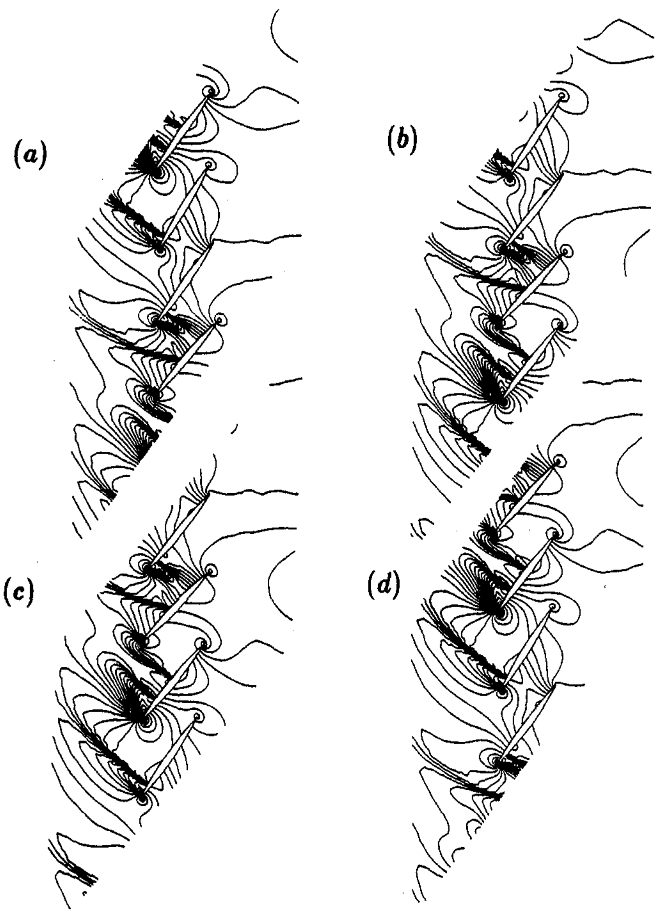

Fig. 11 Instantaneous pressure contours for oscillating cascade of four biconvex blades (M = 0.8, $k = 0.462$, $\alpha_0 = 7$ deg, $\alpha_l = 4.8$ deg, and $\sigma = -90$ deg): ($2Mk\tau - 10\pi$) equal to (a) $\pi/2$, (b) π, (c) $3\pi/2$, and (d) 2π

stronger, and it shifts slightly in the downstream direction. On the upper surface of the highest blade in Fig. 10(*a*), the wave compresses more closely and the original shock gets stronger and moves slightly in the downstream direction. Since different unsteady behaviors are observed in both figures, the nonlinearity of the oscillation amplitude with respect to the unsteady flow phenomena is confirmed. To understand further the unsteady behaviors during each quarter time period, the instantaneous pressure contours at four instant times (($2Mk\tau - 10\pi$) = $\pi/12$, $\pi/6$, $\pi/4$, and $\pi/3$) are plotted in Fig. 12. Due to the periodic characteristics, the pressure contour at Fig. 11(*d*) is the same as that at $2Mk\tau$ equal to 10π. From the sequence of contours given in Fig. 11(*d*), Figs. 12(*a–d*) and Fig. 11(*a*), the shock on the lower surface of the lowest blade in Fig. 11(*d*) keeps moving close to the leading edge and eventually passes through the leading edge to form a weak shock on the upper surface of the lowest blade in Fig. 11(*a*). Initially, there is no shock between the lowest and the second blades in Fig. 11(*d*). A shock on the upper surface of the second blade in Fig. 11(*d*) moves close to the leading edge, and it finally goes around the leading edge to interact with the pressure wave to form shocks on the lower surface of the second blade and on the midchord of the upper surface of the lowest blade (Fig. 11*a*). As shown in Fig. 11(*d*), there are one shock and one compression wave on the upper surface of the third blade. The latter compression wave moves close to the former shock, and eventually combines together to form a stronger shock on the upper surface of the third blade in Fig. 12(*c*). Then, this strong shock keeps moving upstream to be close to the leading edge (Fig. 11*a*). On the upper surface of the highest blade in Fig. 11(*d*), there exists a weak leading edge shock, a shock on the midchord, and the compression wave. During time evolution, this weak leading edge shock goes downstream and combines with the midchord shock, which is moving upstream. Then a strong shock is formed on the upper surface of the highest blade in Fig. 12(*d*). In the meantime, the rear compression wave merges to be stronger (Fig. 12*b*). Considering the case where σ and α_l are equal to 90 deg and 4.8 deg, respectively, the instantaneous pressure contours are shown in Fig. 13. The instantaneous locations and motion for the lowest blade are the same as those in the above case with α_l and σ equal to 4.8 deg and −90 deg, respectively. In Fig. 13(*a*), there exists a shock on the front portion of upper surface of the lowest blade. Also, a compression wave stands between the front part of lower surface of the highest blade and the rear part of upper surface of the third blade. On the lower surface of the third blade and on the upper surface of the highest blade, two compression waves are observed, respectively. Furthermore, a strong shock locates on the front part of the upper surface of the second blade. Comparing the results shown in Figs. 11(*a*) and 13(*a*), it is obvious that the unsteady flow behaviors are strongly related to the interblade phase angle.

To investigate the unsteady aerodynamic characteristics, the lift coefficients on the lowest blade during the sixth cycle are calculated. For the present oscillating cascade of four biconvex blades, the results given in Fig. 14 demonstrate the

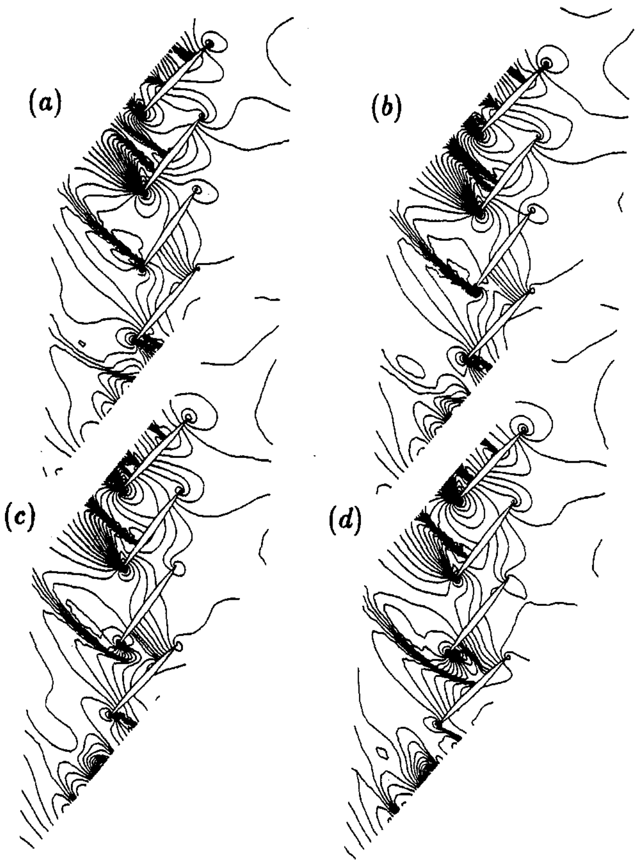

Fig. 12 **Instantaneous pressure contours for oscillating cascade of four biconvex blades (M = 0.8, $k = 0.462$, $\alpha_0 = 7$ deg, $\alpha_I = 4.8$ deg, and $\sigma = -90$ deg): ($2Mk\tau - 10\pi$) equal to (*a*) $\pi/12$, (*b*) $\pi/6$, (*c*) $\pi/4$, and (*d*) $\pi/3$**

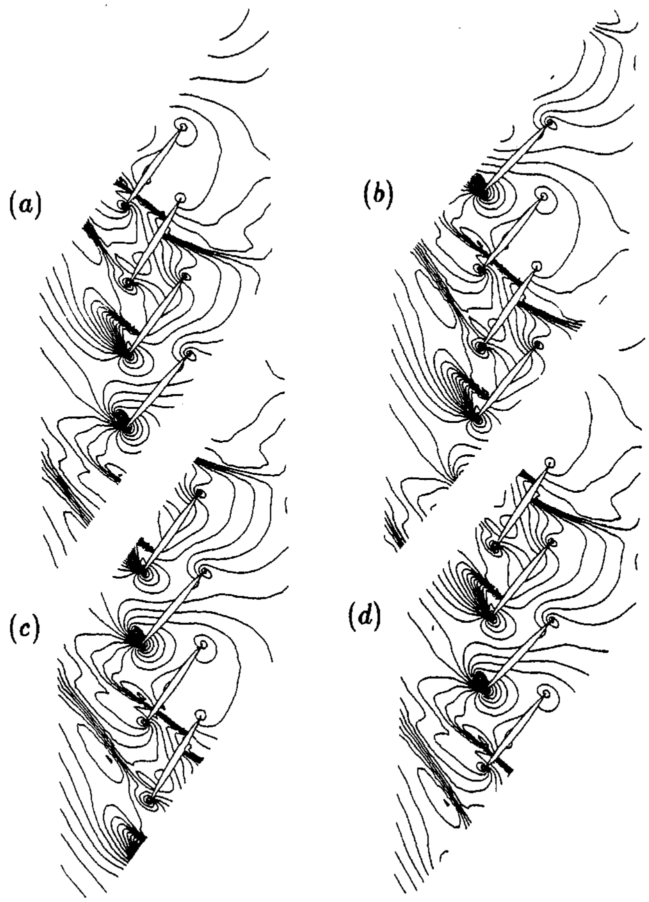

Fig. 13 **Instantaneous pressure contours for oscillating cascade of four biconvex blades (M = 0.8, $k = 0.462$, $\alpha_0 = 7$ deg, $\alpha_I = 4.8$ deg, and $\sigma = 90$ deg): ($2Mk\tau - 10\pi$) equal to (*a*) $\pi/2$, (*b*) π, (*c*) $3\pi/2$, and (*d*) 2π**

effects of k, σ, and α_I. At any instant positions (except the highest and lowest ones) of the lowest blade, the value of C_l for blade moving upward is smaller than that for blade moving downward. Also, the smallest C_l occurs a little late after the blade passes through its lowest position for all cases in Fig. 14, and the largest C_l happens a little late after blade passes its highest position (Fig. 14*b*, *c*). From the aforementioned magnitudes and phase angles of dynamic pressure difference coefficient, instantaneous pressure contours and lift coefficient distributions, it is found that oscillation amplitude, interblade phase angle, and reduced frequency all have significant effects on the oscillating cascade flows. The nonlinear phenomena, such as the shock formation, migration, strengthening, attenuation, and interaction with pressure wave, are observed in the present calculations. No matter how complicated the flowfields are, the periodic physical phenomena are still preserved. For every quarter time period, the pressure contours repeat and proceed one pitch distance in the upward or downward direction for σ equal to -90 deg or 90 deg, respectively.

Conclusions

A numerical solution procedure, which includes modification of a locally implicit total-variation-diminishing scheme on dynamic triangular mesh, improvement of a dynamic triangular mesh algorithm, triangular mesh generation, spatially periodic boundary treatment, and nonreflecting inlet/outlet boundary conditions, is introduced to study the transonic oscillating cascade flows. In a Cartesian coordinate system, the unsteady Euler equations are solved. For the transonic flow around an isolated NACA 0012 airfoil pitching harmonically about the quarter chord, the instantaneous pressure coefficient distributions during a cycle of motion are presented. By comparing with the related numerical and experimental results, the accuracy of the present approach is validated. In the computations of transonic flow around oscillating cascade of NACA 0006 blades with interblade phase angle equal to 180 deg, two kinds of computational domains, which include one and two blades, are used. To understand the numerical characteristics of the present spatial periodic boundary treatment, the direct parameter storage method for phase-shifted periodic boundary conditions is employed. From the time history of lift coefficient, the spatial periodic boundary treatment is more numerically stable than the direct parameter storage method. In the comparison of instantaneous pressure coefficient distributions with those of two other numerical methods, the present solution procedure is satisfactory. For the transonic flows around oscillating cascade of four biconvex blades, different values of oscillation amplitude, reduced frequency, and interblade phase angle are chosen to study the unsteady phenomena. Comparing the distributions of magnitude and phase angle of the dynamic pressure difference coefficient, the present Euler solutions show better agreement with experimental data than those from linearized theory in most of the cases. The nonlinear phenomena including shock formation, migration, strengthening, attenuation, and interaction with pressure wave are observed in the present calculations. For every quarter time period, the pressure contours repeat and proceed one pitch distance in the upward or downward direction for interblade phase angle equal to -90 deg or 90 deg,

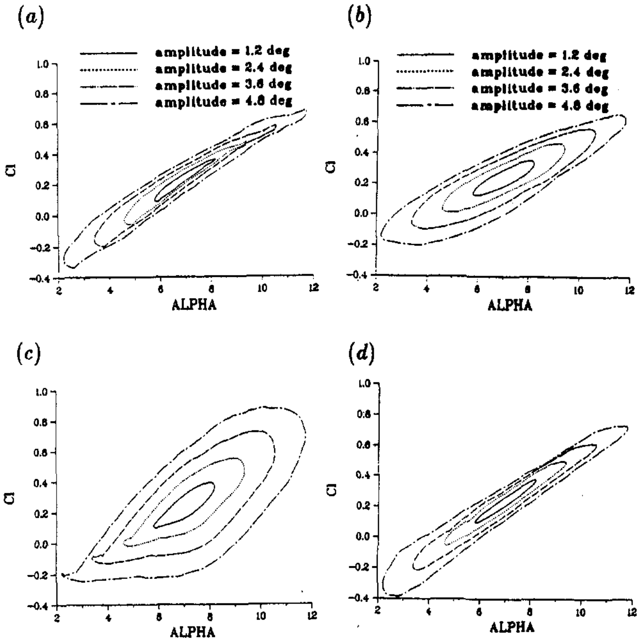

Fig. 14 Lift coefficient versus instantaneous angle of attack for the lowest blade of oscillating cascade of four biconvex blades: (*a*) $k = 0.462$, $\sigma = -90$ deg, (*b*) $k = 0.462$, $\sigma = 90$ deg, (*c*) $k = 0.185$, $\sigma = -90$ deg, and (*d*) $k = 0.185$, $\sigma = 90$ deg

respectively. From the lift coefficient distributions and this discussion, it is obvious that the oscillation amplitude, interblade phase angle, and reduced frequency all significantly affect the transonic oscillating cascade flows.

References

Batina, J. T., 1990, "Unsteady Euler Airfoil Solutions Using Unstructured Dynamic Meshes," *AIAA Journal*, Vol. 28, No. 8, pp. 1381–1388.

Batina, J. T., 1991, "Implicit Flux-Split Euler Schemes for Unsteady Aerodynamic Analysis Involving Unstructured Dynamic Meshes," *AIAA Journal*, Vol. 29, No. 11, pp. 1836–1843.

Bendiksen, O. O., 1991, "Euler Calculations of Unsteady Transonic Flow in Cascades," AIAA Paper No. 91-1104.

Buffum, D. H., and Fleeter, S., 1990, "The Aerodynamics of an Oscillating Cascade in a Compressible Flow Field," ASME JOURNAL OF TURBOMACHINERY, Vol. 112, pp. 759–767.

Buffum, D. H., and Fleeter, S., 1993, "Wind Tunnel Wall Effects in a Linear Oscillating Cascade," ASME JOURNAL OF TURBOMACHINERY, Vol. 115, pp. 147–156.

Gerolymos, G. A., 1988, "Numerical Integration of the Blade-to-Blade Surface Euler Equations in Vibrating Cascades," *AIAA Journal*, Vol. 26, No. 12, pp. 1483–1492.

Giles, M. B., 1990, "Nonreflecting Boundary Conditions for Euler Equation Calculations," *AIAA Journal*, Vol. 28, No. 12, pp. 2050–2058.

He, L., 1990, "An Euler Solution for Unsteady Flows Around Oscillating Blades," ASME JOURNAL OF TURBOMACHINERY, Vol. 112, pp. 714–722.

Hsiao, C., and Bendiksen, O. O., 1992, "Finite Element Euler Calculations of Unsteady Transonic Cascade Flows," AIAA Paper No. 92-2120-CP.

Huff, D. L., Swafford, T. W., and Reddy, T. S. R., 1991, "Euler Flow Predictions for an Oscillating Cascade Using a High Resolution Wave-Split Scheme," ASME Paper 91-GT-198.

Huff, D. L., 1992, "Numerical Analysis of Flow Through Oscillating Cascade Sections," *Journal of Propulsion and Power*, Vol. 8, No. 4, pp. 815–822.

Hwang, C. J., and Liu, J. L., 1992, "Locally Implicit Hybrid Algorithm for Steady and Unsteady Viscous Flows," *AIAA Journal*, Vol. 30, No. 5, pp. 1228–1236.

Hwang, C. J., and Wu, S. J., 1992, "Global and Local Remeshing Algorithms for Compressible Flows," *Journal of Computational Physics*, Vol. 102, No. 1, pp. 98–113.

Hwang, C. J., and Yang, S. Y., 1993, "Locally Implicit Total Variation Diminishing Schemes on Mixed Quadrilateral-Triangular Meshes," *AIAA Journal*, Vol. 31, No. 11, pp. 2008–2015.

Kandil, O. A., and Chuang, H. A., 1989, "Unsteady Transonic Airfoil Computation Using Implicit Euler Scheme on Body-Fixed Grid," *AIAA Journal*, Vol. 27, No. 8, pp. 1031–1037.

Landon, R. H., 1982, "NACA 0012. Oscillatory and Transient Pitching," *Compendium of Unsteady Aerodynamic Measurements*, Data Set 3, AGARD-R-702.

Marcel Vinokur, 1989, "An Analysis of Finite-Difference and Finite-Volume Formulations of Conservation Laws," *Journal of Computational Physics*, Vol. 81, No. 1, pp. 1–52.

Rausch, R. D., Batina, J. T., and Yang, H. T. Y., 1992, "Spatial Adaptation of Unstructured Meshes for Unsteady Aerodynamic Flow Computations," *AIAA Journal*, Vol. 30, No. 5, pp. 1243–1251.

Darryl E. Metzger Memorial Session Paper

An Account of Free-Stream-Turbulence Length Scale on Laminar Heat Transfer

K. Dullenkopf

R. E. Mayle[1]

Institut für Thermische
Strömungsmaschinen,
Universität Karlsruhe,
Karlsruhe, Federal Republic of Germany

The effect of length scale in free-stream turbulence is considered for heat transfer in laminar boundary layers. A model is proposed that accounts for an "effective" intensity of turbulence based on a dominant frequency for a laminar boundary layer. Assuming a standard turbulence spectral distribution, a new turbulence parameter that accounts for both turbulence level and length scale is obtained and used to correlate heat transfer data for laminar stagnation flows. The result indicates that the heat transfer for these flows is linearly dependent on the "effective" free-stream turbulence intensity.

Introduction

The effect of free-stream turbulence on laminar and turbulent boundary layers has been a topic of much interest for a long time. Its importance in gas turbines has been generally associated with large increases in heat transfer rates on turbine blades (e.g., see Turner, 1971) and large influences on boundary layer transition (e.g., see Mayle, 1991). These two effects are clearly shown in Fig. 1, where Nusselt number distributions for several free-stream turbulence levels are presented for a typical, fore-loaded, gas turbine airfoil (Schulz, 1986). On the suction surface of the airfoil ($x/c > 0$), the main effect of turbulence is to cause an earlier onset of transition to turbulent flow. Near the leading edge, however, and on the pressure surface ($x/c < 0$) where the boundary layer remains laminar, the main effect of turbulence is to cause a large increase in "laminar" heat transfer. It is this latter effect of free-stream turbulence that we will consider within this paper.

While some investigators examined this effect using a flat plate (Kestin et al., 1961; Smith and Kuethe, 1966; Junkhan and Serovy, 1967; Dyban and Epick, 1978; Rüd, 1985), most used cylinders in crossflow and examined the effect in the highly accelerated stagnation region (Zapp, 1950; Kestin, 1966; Dyban and Epick, 1970; Kestin and Wood, 1971; Lowery and Vachon, 1975; Yardi and Sukhatme, 1978; Van Dresar, 1987; Ames and Moffat, 1990). An interesting feature of stagnation flow is that the free-stream strain rate is constant (and nonzero), i.e., $a \equiv dU/dx = \text{const}$, which in turn produces a laminar boundary layer with constant viscous and thermal boundary layer thicknesses and, consequently, a constant heat transfer coefficient.[2] In this paper, for simplicity, we will consider only the effect of free-stream turbulence on laminar "stagnation-like" flow having a constant, nonzero, free-stream strain rate.

It should be pointed out, perhaps, that the results of this work may be applied directly to flow over gas turbine airfoils. The flow around the leading edge of a gas turbine airfoil is indeed a stagnation flow and, as seen in Fig. 1 near $x/c = 0$, produces the highest heat load on the airfoil. In fact, using the heat transfer results for cylinders in a turbulent crossflow, most gas turbine engine manufacturers apply a heat transfer augmentation factor of 1.5 to 2 to the calculated heat transfer coefficients on the leading edges of their turbine airfoils. Also, the free-stream flows on the pressure surfaces of many fore-loaded airfoils have a constant strain rate. This is evident for the airfoil used to obtain the data shown in Fig. 1 from the nearly constant Nusselt numbers measured over the forward portion of the pressure surface. The airfoils of Turner (1971) and Bayley and Priddy (1981), while not necessarily modern, are similar in this respect.

In the past, the effect of free-stream turbulence on stagnation heat transfer for cylinders in crossflow was usually correlated using the functional relation

$$\mathrm{Nu}_d/\sqrt{\mathrm{Re}_d} = \mathrm{fnc}\,(\mathrm{Pr},\ \mathrm{Tu}\sqrt{\mathrm{Re}_d}) \qquad (1)$$

where Nu_d is the Nusselt number based on the diameter of the cylinder, Re_d is the Reynolds number based on the incident flow velocity and the diameter of the cylinder, and $\mathrm{Tu} = u'/U_\infty$ is the incident turbulence level with u' the turbulence intensity. The parameter $\mathrm{Tu}\sqrt{\mathrm{Re}_d}$ was proposed initially by Smith and Kuethe (1966) upon applying their theoretical work on stagnation flow to cylinders in crossflow.

In 1992, however, the present authors showed that any correlation based on the cylinder's diameter incorrectly assumes that the strain rate is always in the same proportion to U_∞/d (Dullenkopf and Mayle, 1994). For flow around a cylinder where the velocity near stagnation varies according to $U = a_1 U_\infty x/d$, the free-stream strain rate is $a = a_1 U_\infty/d$. For potential flow around a circular cylinder, $a_1 = 4$. As shown by Dyban and Epick (1985), however, the parameter a_1 depends on the turbulence level, wind tunnel blockage, and Reynolds number.[3] In addition, it depends on the shape of the cylinder and, probably, on the turbulence length scale as well. To account correctly for this effect, Dullenkopf and Mayle introduced a Nusselt number and a dimensionless turbulence parameter based on the only length and velocity scales of the problem, namely, $\mathrm{Nu}_a \equiv h\sqrt{\nu/a}/k$ and $\mathrm{Tu}_a \equiv u'/\sqrt{a\nu} = \mathrm{Tu}U_\infty/\sqrt{a\nu}$ (where h is the heat transfer

---

[1] Present address: Department of Mechanical Engineering, Rensselaer Polytechnic Institute, Troy, NY.

[2] These results follow from the fact that there is only one viscous length scale and one thermal length scale to the problem, viz., $\sqrt{\nu/a}$ and $\sqrt{\alpha/a}$, where ν is the viscosity and α is the thermal diffusivity of the fluid (see Schlichting, 1979).

Contributed by the International Gas Turbine Institute and presented at the 39th International Gas Turbine and Aeroengine Congress and Exposition, The Hague, The Netherlands, June 13–16, 1994. Manuscript received by the International Gas Turbine Institute February 15, 1994. Paper No. 94-GT-174. Associate Technical Editor: E. M. Greitzer.

[3] These effects, particularly, on transition and the size of the ensuing wake, were very clearly pointed out by Kestin, 1966, but never considered further until Van Dresar (1987) showed that his results for $2.4 < a_1 < 3.8$ correlated well with others once the correct strain rate was used.

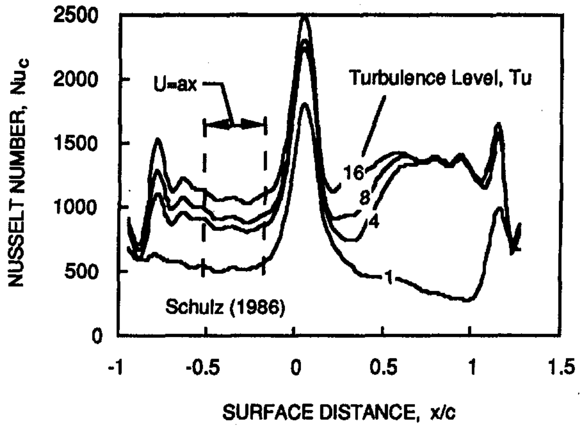

Fig. 1 Effect of incidence turbulence level on airfoil Nusselt numbers

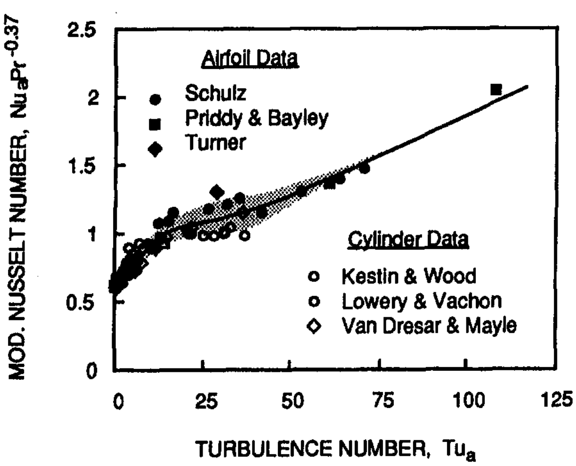

Fig. 2 Correlation of cylinder and airfoil Nusselt numbers for laminar flow with $U = ax + b$

coefficient and k is the thermal conductivity). For flow around a circular cylinder, one obtains $Nu_a = Nu_d/\sqrt{a_1 Re_d}$ and $Tu_a = Tu\sqrt{Re_d/a_1}$, which will properly account for different values of a_1. As a result, Eq. (1) is more correctly stated by

$$Nu_a = \text{fnc}\,(Pr, Tu_a) \qquad (2)$$

For nonturbulent stagnation flow, Eckert (1942) provided a relatively simple expression for Eq. (2), viz., $Nu_a = 0.571\ Pr^{0.37}$. With $Pr = 0.7$ this becomes $Nu_a = 0.5$, which provides the commonly known approximate result $Nu_d/\sqrt{Re_d} = 1$ when the potential flow value for a_1 is used.

While the functional relation given in Eq. (2) was obtained for stagnation heat transfer, it is also valid for gas turbine airfoils where the free-stream velocity varies linearly with distance, i.e., $U(x) = ax + b$. Dullenkopf and Mayle (1994) evaluated heat transfer data for both cylinders in crossflow and turbine airfoils and obtained the result shown in Fig. 2. In this figure, all the cylinder data are shown by the open symbols while all of the airfoil data are shown by filled-in symbols. Much of the cylinder data for small values of Tu_a are overlapped by the airfoil data there. A correlation of the results (stated incorrectly in the original paper[4]) is given by

$$Nu_a Pr^{-0.37} = 0.571 + 0.0125\ Tu_a \left\{ 1 + \frac{1.8}{[1 + (Tu_a/20)^3]} \right\}$$

where Tu_a is defined using the absolute value of the incident turbulence level, not percent. This correlation is also shown in the figure and, as pointed out by the authors, appears to indicate two separate effects of turbulence: one at small values of Tu_a, the other at high values. The region between contains a large scatter of data, which the authors then attributed to turbulence length scale effects.

Yardi and Sukhatme (1978) measured the effects of turbulence level and length scale on stagnation heat transfer. Their results, plotted as a function of the length scale parameter $(L/d)\sqrt{Re_d}$ where L is the integral length scale, are presented in Fig. 3 for various turbulence levels. The curves faired through their data have been drawn by the present authors anticipating the discussion in the following section, and differ slightly from Yardi and Sukhatme's curves (Fig. 3 in their paper), especially for small values of $(L/d)\sqrt{Re_d}$ where the data are scattered. Nevertheless, their results indicate a significant effect of turbulence length scale on heat transfer. In particular, it appears that the effect of free-stream turbulence on heat transfer is reduced at both the large and small extreme values of their length scale parameter. The maximum effect appears at a value of $(L/d)\sqrt{Re_d}$ somewhere between 5 and 15 (as marked by the vertical dashed lines in the figure). Assuming a typical value for a_1 of 3.6, this corresponds to a length scale-to-boundary layer thickness ratio between four and twelve, i.e., $4 < L/\delta < 12$, where $\delta \approx 2.4\sqrt{\nu/a}$ is the boundary layer thickness for stagnation flow.

Ames and Moffat (1990) proposed correlating the effects of turbulence including that of length scale by using the parameter $TuRe_d^{5/12}(L/d)^{-1/3}$. This parameter was obtained by applying the results of rapid distortion theory for flow around a cylinder to a turbulent eddy and equating the eddy size to the integral length scale. Although their parameter correlates their data, it is easy to show that their length scales, if L is considered the physically meaningful scale of turbulence, are much too large ($75 < L/\delta < 420$) to have anything but a negligible quasi-steady effect. This

---

[4] The authors must apologize for this error. The equation given there, Eq. (9), was mistakenly given as the best fit to the data, but actually corresponds to the upper limit of the data band. The equation given here corresponds to the best data fit.

Nomenclature

a = free-stream strain rate = dU/dx
a_1 = dimensionless strain rate
c = airfoil chord
d = cylinder diameter
E_1 = one-dimensional turbulence spectral energy density
h = heat transfer coefficient
k = thermal conductivity, turbulent kinetic energy per unit mass
L = integral length scale of turbulence
Nu = Nusselt number

Pr = Prandtl number
Re = Reynolds number
St = Stanton number = Nu/RePr
Tu = turbulence level = u'/U
u' = turbulence intensity = $\sqrt{2k/3}$
U = free-stream velocity = $U(x)$
U_∞ = incident velocity
x = surface coordinate in streamwise direction
α = thermal diffusivity

δ = boundary layer thickness
ν = kinematic viscosity
ρ = density
ϕ = dimensionless frequency

Subscripts

a = quantity based on dU/dx
c = quantity based on chord
d = quantity based on diameter
λ = quantity based on the dominant frequency

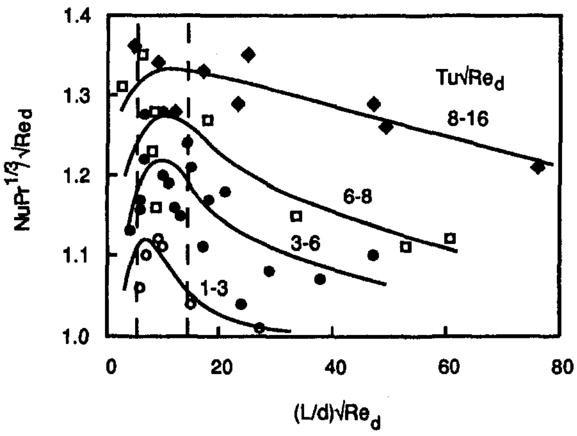

Fig. 3 Yardi and Sukhatma's (1978) data (Tu $\sqrt{Re_d}$ = 1–3, ○; 3–6, ●; 6–8, □; 8–16, ◆)

implies that the integral length scale of turbulence plays another role.

In the next section, an alternative role will be investigated, a simple model will be presented to account for the effect of turbulence on heat transfer, and a new correlation parameter based on an "effective" incident turbulence level for stagnation-like boundary layer flow will be introduced. Following this, data for both cylinders in crossflow and airfoils will be examined using the new turbulence parameter and a new correlation proposed.

A Simple Model

It is known from stability theory that a laminar boundary layer is sensitive to disturbances within a rather select band of frequencies. This may be reasoned by recognizing that fluctuations at high frequencies are viscously damped, while those at low frequencies appear quasi-steady. The representative frequency of this select band may be estimated roughly from stability theory as $f_\lambda \approx 0.03U_\infty/\delta$, where δ is the boundary layer thickness. The length scale of a eddy corresponding to this frequency is about 16δ.

Assuming that a laminar boundary layer is affected mostly by disturbances having a dominant frequency f_λ, a simple model to account for the effect of free-stream turbulence on heat transfer in a laminar boundary layer would be to presume that only the turbulent energy contained within a frequency band near this frequency is important. This energy may be called an "effective" turbulent energy. In other words, it is not the "overall" turbulence level, Tu, but some fraction of it that is important.

The turbulent energy in the free stream contained within any particular frequency band may be obtained from the frequency spectrum of turbulence. Considering only the spectrum of the longitudinal turbulent velocity component, one may use von Karman's distribution for the one-dimensional spectral energy density of turbulence E_1 (see Hinze, 1959). This distribution, which correlates the data quite well except at the very high frequencies, is given by

$$\frac{U_\infty E_1(\phi)}{u'^2 L} = \frac{4}{[1 + (8\pi\phi/3)^2]^{5/6}}$$

where $\phi = fL/U_\infty$ is the dimensionless frequency. For frequencies where $\phi \gg \frac{3}{8}\pi$, one obtains $E_1(\phi) \propto \phi^{-5/3}$ which corresponds to the well known result for the inertial subrange of turbulence. $E_1(\phi)$ is plotted in Fig. 4 and the energy contained with in a small bandwidth $\Delta\phi$ shown.

The effective turbulence level, $\mathrm{Tu_{eff}}$, is obtained by integrating the spectral energy density over a band width of frequencies centered about the dominant frequency. In terms of the dimensionless frequency ϕ, one obtains

$$\mathrm{Tu_{eff}} = \mathrm{Tu}\left\{\int_{\phi_\lambda-\Delta\phi/2}^{\phi_\lambda+\Delta\phi/2} \frac{4\,d\phi}{[1 + (8\pi\phi/3)^2]^{5/6}}\right\}^{1/2}$$

where $\phi_\lambda = f_\lambda L/U_\infty$. For a narrow bandwidth, $\Delta\phi/\phi_\lambda \ll 1$, the integral is simply the result shown in Fig. 4 and the expression above becomes

$$\mathrm{Tu_{eff}} = \frac{2\mathrm{Tu}\sqrt{\phi_\lambda}}{[1 + (8\pi\phi_\lambda/3)^2]^{5/12}}\sqrt{\frac{\Delta\phi}{\phi_\lambda}}$$

The errors in this expression are terms of order $(\Delta\phi/\phi_\lambda)^2$ which, in general, may be neglected.

Using a characteristic frequency corresponding to $f_\lambda = \lambda U_\infty/d$ where from stability considerations, λ is a multiplicative factor of the order of 0.01, one obtains

$$\phi_\lambda = \frac{f_\lambda L}{U_\infty} \approx 0.4\lambda L/\sqrt{\nu/a} = 0.4\lambda L_a$$

The last equality defines the important dimensionless integral length scale parameter of the problem, viz., $L_a \equiv L/\sqrt{\nu/a}$. This length scale parameter would also be obtained from dimensional considerations for flows with a constant free-stream strain rate. For flow around a cylinder $a = a_1 U_\infty/d$ near stagnation and $L_a = (L/d)\sqrt{a_1}\mathrm{Re}_d$ which differs from Yardi and Sukhatme's length scale parameter $(L/d)\sqrt{\mathrm{Re}_d}$ by the factor $\sqrt{a_1}$.

Substituting for ϕ_λ in terms of the new length scale parameter, one obtains

$$\mathrm{Tu_{eff}} \propto \frac{\mathrm{Tu}\sqrt{L_a}}{[1 + k_1 L_a^2]^{5/12}}$$

where the proportionality factor depends on the square root of band width ratio $\Delta f/f_\lambda$ and $k_1 \approx 10\lambda^2$. Since the fraction of the frequency band being considered is likely to be independent of the other parameters, the proportionality factor may be set equal to unity without any loss of generality. Defining a new turbulence parameter $\mathrm{Tu}_\lambda \equiv \mathrm{Tu_{eff}} U_\infty/\sqrt{a\nu}$, one then obtains

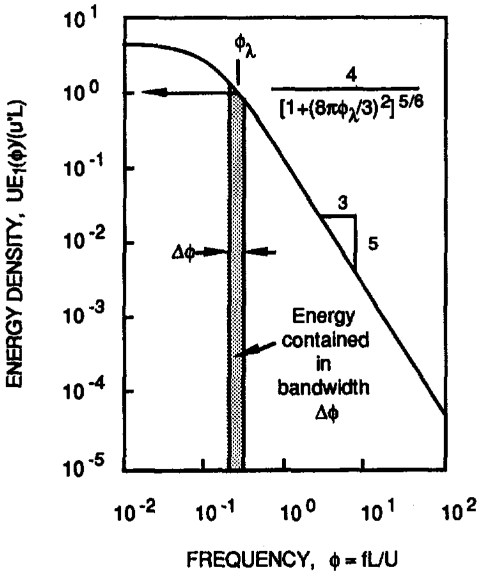

Fig. 4 Von Karman's power density distribution

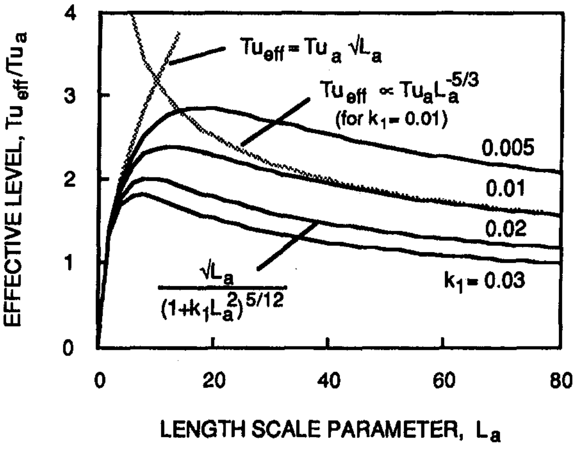

Fig. 5 Effective turbulence level as a function of the length scale parameter

$$\mathrm{Tu}_\lambda = \frac{\mathrm{Tu}_a\sqrt{L_a}}{[1 + k_1 L_a^2]^{5/12}} \qquad (3)$$

Curves of Eq. (3) are shown in Fig. 5 for several values of k_1. Each curve rises with increasing values of the length scale parameter L_a to a maximum and then decreases. It is easy to show that the maximum of $\mathrm{Tu}_\lambda/\mathrm{Tu}_a$ is obtained at $L_a = \sqrt{3/2k_1}$. For values of L_a much less than $\sqrt{3/2k_1}$, Eq. (3) yields $\mathrm{Tu}_\lambda \approx \mathrm{Tu}_a \sqrt{L_a}$, while for values much greater than $\sqrt{3/2k_1}$, Tu_λ is proportional to $\mathrm{Tu}_a L_a^{-1/3}$. These curves are also plotted in Fig. 5. While the last form, viz., $\mathrm{Tu}_a L_a^{-1/3}$, is similar to the correlating parameter proposed by Ames and Moffat (1990), it must be emphasized that the theories leading to this form are completely different.

The $\mathrm{Tu}_\lambda/\mathrm{Tu}_a$ curves in Fig. 5 are very similar to the heat transfer curves previously shown in Fig. 3 where the maximum effect of turbulence is seen to occur for $(L/d)\sqrt{\mathrm{Re}_d}$ roughly equal to ten. Using a typical value for a_1 of 3.6, this corresponds to an L_a of 20. Substituting this into the equation above relating L_a and k_1 at the maximum value of $\mathrm{Tu}_\lambda/\mathrm{Tu}_a$, one obtains $k_1 \approx 0.004$, which, in turn, provides $f_\lambda \approx 0.02 U_\infty/\delta$. It is interesting to note that this value for the dominant frequency is nearly the same as that obtained from stability considerations.

A New Correlation

Since the turbulence in the free stream is completely characterized by its level and length scale for a given spectral distribution, it is easy to show by dimensional analysis that the Nusselt number for turbulent free-stream flows with a constant strain rate is given by

$$\mathrm{Nu}_a = \mathrm{fnc}\,(\mathrm{Pr}, \mathrm{Tu}_a, L_a) \qquad (4)$$

This functional relation replaces Eq. (2). Normally, one would have to carry out an extensive set of experiments varying Tu_a and L_a independently to obtain the function, but according to Eq. (3) the parameters may be combined such that the functional becomes

$$\mathrm{Nu}_a = \mathrm{fnc}\,(\mathrm{Pr}, \mathrm{Tu}_\lambda)$$

In the following, a correlation relating Nu_a to Tu_λ according to this expression will be sought.

A review of the literature uncovered only four papers on stagnation heat transfer from cylinders in turbulent crossflow that report enough information to determine all of the parameters listed in Eq. (4). These papers are by Sikmanovic et al. (1974), Lowery and Vachon (1975), Van Dresar (1987), and Ames and Moffat (1990). Of these four, however, only Van Dresar reports the free-stream strain rates for his data. The strain rates for the other data were calculated using Dyban and Epick's (1985) correlation (see Dullenkopf and Mayle, 1994). The data of Yardi and Sukhatme (1978) could not be translated into the new form.

Table 1

Author	Pr	Tu_a	L_a
Lowery & Vachon	0.7	1-37	11-66
Sikmanovic, et al.	0.7	3-12	18-40
Van Dresar	2.5*	6-36	66-100
Ames & Moffat	0.7	6-28	176-1000

* Schmidt number

The values of Pr, Tu_a, and L_a for each of the four investigations cited above are given in Table 1. Considering that the maximum effect of turbulence occurs when $L_a \approx 20$, it is interesting to note that only the pre-1980 tests cover this range. Since Van Dresar attempted to model the turbulence in the wake of a typical gas turbine airfoil, it is seen that a typical "engine" length scale is somewhat larger than that which has the largest effect on heat transfer. It is also clear that Ames and Moffat, upon investigating the effects of large turbulence levels on heat transfer, investigated an effect where most of the turbulent energy was contained in eddies much too large to affect the boundary layer except in a quasi-steady manner. Their results are relevant, however, since they clearly support the idea of an "effective" turbulence level.

The data are plotted as Nu_a versus Tu_a in Fig. 6. This is as shown in Fig. 2, except that the data of Sikmanovic et al. and Ames and Moffat have been added and the airfoil data omitted. In an effort to eliminate any pollution from flow nonuniformities, data obtained where the test body is placed less than five mesh lengths downstream of turbulence grids are not presented. According to Baines and Peterson (1951), a distance of five to ten mesh lengths downstream from any screen is necessary to establish reasonably good flow. In addition, at least this distance is required to establish a spectral distribution such as shown in Fig. 4. The trend of the data in Fig. 6 shows that the effect of turbulence on heat transfer generally decreases with an increase in turbulence length scale. This behavior is indicated by the arrow.

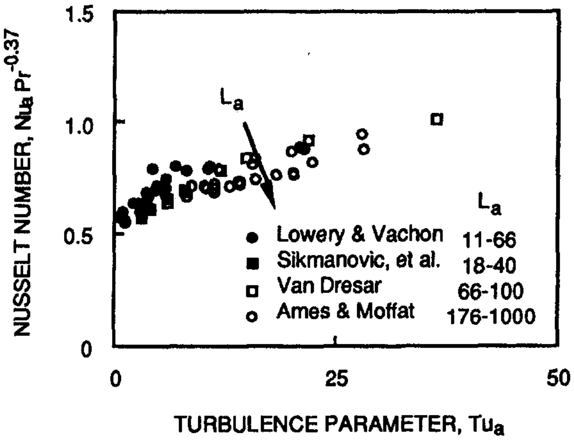

Fig. 6 Cylinder data for which length scale measurements are reported

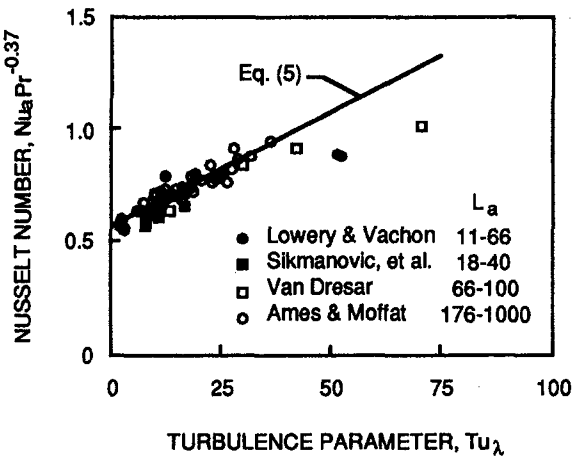

Fig. 7 Cylinder data plotted using the "effective" turbulence level parameter

Replotting the same data using the effective turbulence parameter Tu_λ with $k_1 = 0.004$ results in Fig. 7. Actually, this figure was plotted for various values of k_1 where it was found that any value between 0.002 and 0.007 produced a good correlation. Since it was difficult to distinguish a "best" value for k_1 using the present set of data, and until a better set becomes available, the value of k_1 arrived at from Yardi and Sukhatme's data was adopted. The data are correlated by

$$Nu_a Pr^{-0.37} = 0.571 + 0.01 Tu_\lambda \qquad (5)$$

where

$$Tu_\lambda = \frac{Tu_a \sqrt{L_a}}{[1 + 0.004 L_a^2]^{5/12}} \qquad (6)$$

Equation (5) is plotted in the figure and may be considered the new correlation for heat transfer in stagnation flow with a turbulent free stream. It is interesting to note that the theory first proposed by Smith and Kuethe (1966), which predicts a linear increase of stagnation heat transfer with increasing free-stream turbulence, and which originally did not predict much of the data for large turbulence levels and length scales, again appears correct if the concept of an effective turbulence level is accepted.

A Look at the Airfoil Data

Unfortunately, there are no length scale measurements for any of the airfoil results presented in Fig. 2. Schulz (1986), however, does present measurements of turbulence level at two streamwise locations downstream of his grids such that a length scale may be estimated from its decay. This was done assuming $Tu^{-2} \propto x$, evaluating the dissipation length scale L_ϵ from the decay of turbulent kinetic energy, and using the generally accepted relation $L = 2L_\epsilon/3$. Length scales obtained this way varied from one to one and one-half times the diameter of bars in the grid. The test cases with the smallest values of length scale were those where the airfoil row was about five mesh lengths downstream of the grid and, therefore, were not used. These test cases also happen to be the ones having the highest incident turbulence level. For flow over an airfoil with $U = a_1 U_\infty x/c + b$, $Tu_a = Tu\sqrt{Re_c/a_1}$ and $L_a = (L/c)\sqrt{a_1 Re_c}$. For the data of Schulz that could be used, Tu_a varied from 10 to 35 while L_a varied from 22 to 116. They correspond to data obtained on the pressure side of a turbine airfoil and should be compared to those given in Table 1 for stagnation flow on a cylinder.

The airfoil data are plotted in Fig. 8 (open circles) together with the cylinder data (filled circles) and the correlation given in Eqs. (5) and (6). The data fit the correlation surprisingly well.

Conclusions

The effect of free-stream turbulence on heat transfer in flows with a constant free-stream strain rate has been re-investigated by introducing the concept of an "effective" turbulence level. This led to the turbulence parameter Tu_λ, defined as

$$Tu_\lambda = \frac{Tu_a \sqrt{L_a}}{[1 + 0.004 L_a^2]^{5/12}}$$

which not only accounts for the overall level of free-stream turbulence, but also its integral length scale. As a result, a rather simple correlation of cylinder and airfoil data was obtained, namely,

$$Nu_a Pr^{-0.37} = 0.571 + 0.01\, Tu_\lambda$$

which describes a linear relation between laminar stagnation heat transfer and turbulence level as predicted by Smith and Kuethe (1966).

Introducing a Stanton number based on the "effective" turbulence intensity $(u')_{\text{eff}} = (u')\sqrt{L_a}[1 + 0.004 L_a^2]^{-5/12}$, the result above may also be written as

$$\Delta\ St = \Delta h/\rho c_p (u')_{\text{eff}} = 0.01 Pr^{-0.63}$$

which simply implies that the increase in heat transfer is directly proportional to the effective free-stream turbulence intensity $(u')_{\text{eff}}$. Physically, this is very attractive and similar to the result recently proposed for turbulent flow by Ames and Moffat (1990).

While the present work was concerned with the effect of free stream turbulence on laminar heat transfer, one cannot help thinking about its implications for laminar transition. As shown by Mayle (1991), the scale of turbulence in the free stream has an important effect on the onset of laminar–turbulent boundary layer transition which has not yet been taken into account. Perhaps, as for the present situation, an effective turbulence parameter similar to that defined above will also help correlate all the transition results.

Finally, it cannot be stressed too emphatically that experimenters studying the effects of free-stream turbulence on boundary flows should both measure and report turbulence levels and length scales. It is also suggested that their streamwise

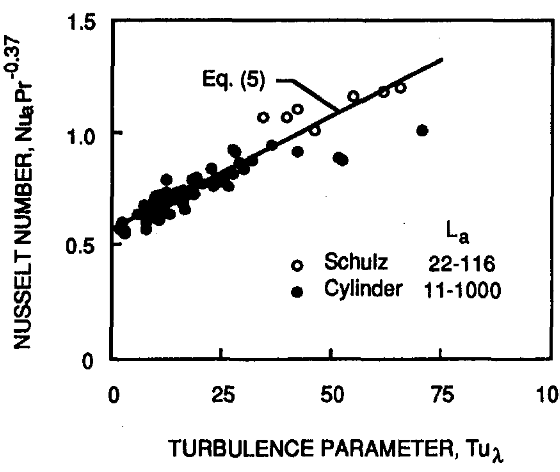

Fig. 8 Airfoil pressure side data of Schulz plotted with the cylinder data using the effective turbulence level parameter

distributions be provided together with the corresponding turbulent energy spectral distributions.

Acknowledgments

The second author wishes to express his gratitude to Professor S. Wittig for his continuing support and hospitality during many of author's visits to the Institut für Thermische Strömungsmaschinen as a Visiting Professor. The work presented herein was conducted during one of these visits in the summer of 1993. The same author is also grateful to the Sonderforschungsbereichs 167 which funded a portion of this work.

References

Ames, F. E., and Moffat, R. J., 1990, ''Heat Transfer With High Intensity, Large Scale Turbulence: The Flat Plate Turbulent Boundary Layer and the Cylindrical Stagnation Point,'' Dept. of Mech. Engng. Report No. HMT-44, Stanford University, Stanford, CA.

Baines, W. D., and Peterson, E. G., 1951, ''An Investigation of Flow Through Screens,'' *Trans. ASME,* Vol. 73, pp. 467–480.

Bayley, F. J., and Priddy, W. J., 1981, ''Effects of Free-Stream Turbulence Intensity and Frequency on Heat Transfer to Turbine Blading,'' ASME *Journal of Engineering for Power,* Vol. 103, pp. 60–64.

Dullenkopf, K., and Mayle, R. E., 1994. ''The Effects of Incident Turbulence and Moving Wakes on Laminar Heat Transfer in Gas Turbines,'' ASME JOURNAL OF TURBOMACHINERY, Vol. 116, pp. 23–28.

Dyban, E., and Epick, E., 1970, ''Some Heat Transfer Features in the Air Flow of Intensified Turbulence,'' *Proc. 4th Int. Heat Transfer Conf.,* Paris.

Dyban, E., and Epick, E., 1978, ''Heat Transfer in a Boundary Layer in Turbulized Air Flow,'' *Proc. 6th Int. Heat Transfer Conf.,* Vol. 2, Toronto.

Dyban, E., and Epick, E., 1985, *Thermal/Mass Transport and Hydrodynamics of Turbulent Flows,* Kiev (in Russian).

Eckert, E., 1942, ''Die Berechnung des Wärmeübergangs in der laminar Grenzschicht umströmter Körper,'' VDI-Forschungsheft 416.

Hinze, J. O., 1959, *Turbulence,* McGraw-Hill, New York.

Junkhan, G. H., and Serovy, G. K., 1967, ''Effects of Free-Stream Turbulence and Pressure Gradient on Flat-Plate Boundary-Layer Velocity Profiles and on Heat Transfer,'' ASME *Journal of Heat Transfer,* Vol. 89, pp. 169–176.

Kestin, J., Maeder, P. F., and Wang, H. E., 1961, ''Influence of Turbulence on the Transfer of Heat from Plates With and Without a Pressure Gradient,'' *Int. J. Heat Mass Transfer,* Vol. 3, pp. 133–154.

Kestin, J., 1966, ''The Effect of Free-Stream Turbulence on Heat-Transfer Rates,'' *Advances in Heat Transfer,* T. F. Irvine, Jr., and J. P. Hartnett, eds., Vol. 3, pp. 1–32.

Kestin, J., and Wood, R. T., 1971, ''The Influence of Turbulence on Mass Transfer From Cylinders,'' ASME *Journal of Heat Transfer,* Vol. 93, pp. 321–327.

Lowery, G. W., and Vachon, R. L., 1975, ''The Effect of Turbulence on Heat Transfer from Heated Cylinders,'' *Int. J. Heat Mass Transfer,* Vol. 18, pp. 1229–1242.

Mayle, R. E., 1991, ''The Role of Laminar–Turbulent Transition in Gas Turbine Engines,'' ASME JOURNAL OF TURBOMACHINERY, Vol. 113, pp. 509–537.

Rüd, K., 1985, ''Transitionale Grenzschichten unter dem Einfluß hoher Freistromturbulenz, intensiver Wandkühlung und starken Druckgradienten in Heißgasströmungen,'' Ph.D. Thesis, Universität Karlsruhe, Karlsruhe, Germany.

Schlichting, H., 1979, *Boundary-Layer Theory,* McGraw-Hill, New York.

Schulz, A., 1986, ''Zum Einfluß hoher Freistromturbulenz, intensiver Kühlung und einer Nachlaufströmung auf den äußeren Wärmeübergang einer konvektiv gekülten Gasturbinenschaufel,'' Ph.D. Thesis, U. Karlsruhe, Karlsruhe, Germany.

Sikmanovic, S., Oka, S., and Koncar-Djurdjevic, S., 1974, ''Influence of the Structure of Turbulent Flow on Heat Transfer From a Single Cylinder in a Cross Flow,'' *Proc. 5th Int. Heat Transfer Conf.,* Vol. 2, Tokyo.

Smith, M. C., and Kuethe, A. M., 1966, ''Effects of Turbulence on Laminar Skin Friction and Heat Transfer,'' *Physics of Fluids,* Vol. 9, pp. 2337–2344.

Turner, A. B., 1971, ''Local Heat Transfer Measurements on a Gas Turbine Blade,'' *J. Mech. Engng. Science,* Vol. 13, pp. 1–12.

Van Dresar, N. T., 1987, ''The Effect of Incident Wake Flow on Blunt-Body Transfer Rates,'' Ph.D. Thesis, Rensselaer Polytechnic Institute, Troy, NY (also see Van Dresar, N. T., and Mayle, R. E., 1989, ''A Quasi-Steady Approach to Leading Edge Transfer Rates,'' ASME JOURNAL OF TURBOMACHINERY, Vol. 111, pp. 483–490).

Yardi, N. R., and Sukhatme, S. P., 1978, ''Effect of Turbulence Intensity and Integral Length Scale of a Turbulent Free Stream on Forced Convection Heat Transfer From a Circular Cylinder in Cross-flow,'' *Proceedings 6th International Heat Transfer Conference,* Toronto, Canada, Vol. 5, FC(b)-29, pp. 347–352.

Zapp, G., Jr., 1950, ''The Effect of Turbulence on Local Transfer Coefficients around a Cylinder Normal to an Air Stream,'' Master's Thesis, Oregon State College, Corvallis, OR.

Effects of Elevated Free-Stream Turbulence on Flow and Thermal Structures in Transitional Boundary Layers

D. Zhou

T. Wang

Department of Mechanical Engineering,
Clemson University,
Clemson, SC 29634-0921

The effects of elevated free-stream turbulence on flow and thermal structures in transitional boundary layers were investigated experimentally on a heated flat plate. Detailed boundary layer measurements using a three-wire probe and wall heat transfer were made with free-stream turbulence intensities of 0.5, 3.8, 5.5, and 6.4 percent, respectively. The onset of transition, transition length, and the turbulent spot formation rate were determined. The statistical results of the streamwise and cross-stream velocity fluctuations, temperature fluctuation, Reynolds stresses, and Reynolds heat fluxes were presented. The eddy viscosity, turbulent thermal diffusivity, and the turbulent Prandtl number were calculated and related physical mechanisms are discussed.

Introduction

One of the key factors in improving the prediction of the thermal load on gas turbine blades is to improve the understanding of the momentum and thermal transports during the laminar–turbulent transition process (Graham, 1979, 1984; Mayle, 1991). As much as 50–80 percent of the surface of a typical turbine blade is commonly covered by flow undergoing transition (Turner, 1971). Transition from laminar to turbulent boundary layer flow significantly increases the local wall shear stresses and the convective heat transfer rates. These increases must be appropriately factored into the design of gas turbine blades. Unsatisfactory prediction of the location and streamwise coverage of transition on gas turbine blades can result in either reduced longevity and reliability of the blade or engine performance below design objectives. In gas turbine environments, one of the most important factors controlling the transition process is elevated free-stream turbulence intensity (FSTI). Measurements of FSTI at the inlet of the turbine show values of 5 to 10 percent due to the disturbances from the upstream conditions. Turbulence in the wakes following the trailing edges of the vanes can be as high as 15 to 20 percent (Mayle, 1991). Very few experiments have been conducted to examine transition at such FSTI levels.

At low FSTI levels, boundary layer transition begins with a weak instability in the laminar boundary layer and proceeds, through various stages of amplified instability, to fully turbulent flow (Schubauer and Skramstad, 1948; Klebanoff et al., 1962). The critical Reynolds number, above which the selective amplification of the two-dimensional infinitesimal disturbances may occur, and the growth rates of the amplified disturbances, can be predicted by linear instability theory. At high free-stream turbulence, the amplification of linear instability waves is bypassed in such a manner that turbulent spots are directly produced within the boundary layer by the influence of the finite perturbations, which provide a nonlinear transition mechanism (Morkovin, 1969). Since linear instability theory is irrelevant in this case, this bypass transition is much more difficult to analyze and is poorly understood. Even the conventional view of a laminar boundary layer must be modified or redefined in such high FSTI levels. Dyban et al. (1980) investigated the structure of laminar boundary layers that developed under elevated FSTI of from 0.3 to 25.2 percent. They found a peak in the rms streamwise velocity fluctuation (u') in the late-laminar boundary layers. The entire u' profiles were elevated due to the penetration of the high FSTI. The maximum penetration occurred for the 4.5 percent FSTI case. They called the laminar boundary layers generated at very high FSTI "pseudo-laminar" to distinguish them from both the purely laminar layer and the fully turbulent layer that develops at low turbulence. Their results, though interesting, were limited to the distribution of disturbances within the laminar boundary layer. The onset and end of transition for a flat plate was investigated by Abu-Ghannam and Shaw (1980) in a low-speed wind tunnel with FSTI ranging from 0.3 to 5 percent. Their results showed that the higher values of FSTI result in an earlier transition and a shorter transition length. Suder et al. (1988) investigated the effects of FSTI ranging from 0.3 to 5 percent on boundary layer transition. They observed linear growth of the Tollmien–Schlichting (T–S) waves with an FSTI of 0.3 percent and the bypass transition mechanism for an FSTI of 0.65 percent and higher. Their results indicated that there

---

Contributed by the International Gas Turbine Institute and presented at the 38th International Gas Turbine and Aeroengine Congress and Exposition, Cincinnati, Ohio, May 24–27, 1993. Manuscript received at ASME Headquarters February 18, 1993. Paper No. 93-GT-66. Associate Technical Editor: H. Lukas.

exists a critical value of the peak rms of the velocity fluctuations within the boundary layer of approximately 3 to 3.5 percent of the free-stream velocity. Once the unsteadiness within the boundary layer reached this critical value, turbulent bursting was initiated, regardless of the transition mechanism. More information on transition, especially the bypass transition, can be found in the discussion of instability and transition predictability by Morkovin (1978). Many other reviews of boundary layer instability and transition can be found in the literature, e.g., Reshotko (1976), Tani (1981), and Narasimha (1985). Recently, Volino and Simon (1995) reviewed published experimental data related to the bypass transition in boundary layers including curvature and favorable pressure gradient effects. An extreme wealth of information on the role of laminar–turbulent transition in gas turbine engines can be found in Mayle (1991).

Studies of elevated free-stream turbulence effects on heat transfer in transitional boundary layer flows are limited and are much less numerous than those treating fluid mechanics. Blair (1982) conducted several tests with a uniformly heated flat wall in accelerated transitional boundary layers with FSTI ranging from approximately 0.7 to 5 percent. He concluded that the transition Reynolds number is relatively insensitive to acceleration at even moderate turbulence levels (around 4 percent). The results of Blair's tests showed the combined effects of FSTI and pressure gradients; however, the isolated effects of the elevated FSTI alone were not available. Wang et al. (1987) investigated the heat transfer and fluid mechanics in transitional boundary layers with 0.68 and 2.0 percent FSTI. They observed that average turbulent Prandtl number values in the early turbulent flow are 20 percent higher than 0.9, a value known to apply to fully turbulent flow. This average Prandtl number is reduced as FSTI increases. Temperature profiles in the late transitional and early turbulent flows have a thicker conduction layer than those in fully turbulent flow. This conduction thickness decreases as the FSTI level increases. They also pointed out that the effect of elevated FSTI penetrates to very near the wall in the profiles of Reynolds streamwise normal stress (u'). However, the effect of elevated FSTI on the Reynolds shear stress ($-\overline{uv}$) and the mean velocity profiles is seen, predominantly, in the outer portion of the boundary layer. Kim et al. (1989) performed fluid mechanics and heat transfer measurements in transitional boundary layers, which were conditionally sampled on intermittency for two different values of FSTI, 0.32 and 1.79 percent. The turbulent heat flux was measured by using a triple-wire probe. The results showed that a large increase in turbulent heat flux above the wall heat flux value occurs within the turbulent spot, and the turbulent Prandtl numbers in the turbulent core region of the transitional flow are smaller than unity. Contrary to the results of Kim et al., the most recent experimental results of Sohn and Reshotko (1991), Shome (1991), and Wang et al. (1992) showed that the cross-stream heat fluxes ($\overline{vt}$) are highly negative values in the middle transitional region. The layer of negative $\overline{vt}$ becomes thinner and moves toward the wall as the flow proceeds downstream. Also, Sohn and Reshotko reported that the velocity profiles were observed to lag the temperature profiles during the transitional process to turbulent flow, which is the opposite of the observations of Blair (1982), Wang et al. (1987), and Kim et al. (1989). The boundary layer spectra in Sohn and Reshhotko's report indicated selected amplification of T–S waves for 0.4 percent FSTI as predicted by linear instability. For 0.8 percent and 1.1 percent FSTI, T–S waves are localized very near the wall and do not play a dominant role in the transition process.

The present experimental study investigates boundary layer transition over a heated flat plate with a free-stream turbulence range of from 0.5 to 7 percent. A miniature three-wire probe was employed to measure both the instantaneous streamwise, cross-stream velocity components and the temperature simultaneously. The onset and end of transition were obtained both from the wall Stanton number measurements and from boundary layer flow and thermal structure measurements. The emphasis of this paper is on the study of the evolution of Reynolds shear stresses and heat fluxes,

Nomenclature

C_f = skin friction coefficient = $\tau_w/(\rho U_\infty^2/2)$
C_p = specific heat
$E_1(f)$ = one-dimensional spectrum of u'
f = frequency
FSTI = free-stream turbulence intensity $= \sqrt{(u^2 + v^2 + w^2)/3}/U_\infty$
n = turbulent spot production rate, No./s · m
$\hat{n}$ = dimensionless turbulent spot production rate $= n\nu^2/U_\infty^2$
Pr_t = turbulent Prandtl number $= \epsilon_M/\epsilon_H$
q'' = heat flux
Re_x, $\mathrm{Re}_{\delta*}$, Re_θ = Reynolds numbers based on x, δ^*, and θ, respectively
St = Stanton number $= q''_w/[\rho C_p U_\infty(T_w - T_\infty)]$
t = instantaneous temperature fluctuation
t' = rms value of t
T = mean temperature
T^+ = mean temperature in wall units $= (T_w - T)\rho C_p u^*/q''_w$
u, v = instantaneous streamwise and cross-stream velocity fluctuations
u', v' = rms values of u and v
$u^* = \sqrt{\tau_w/\rho}$ = friction velocity
U = mean streamwise velocity
U^+ = mean streamwise velocity in wall units $= U/u^*$
x = streamwise distance from leading edge
y = distance away from the wall
$Y^+ = yu^*/\nu$
α = thermal diffusivity
δ = boundary layer thickness at $0.995U_\infty$
δ^* = displacement boundary layer thickness
ϵ_H = turbulent thermal diffusivity $= -\overline{vt}/(\partial T/\partial y)$
ϵ_M = turbulent viscosity $= -\overline{uv}/(\partial U/\partial y)$
θ = momentum boundary layer thickness
Λ_f = integral length scale $= U\int_0^\infty \overline{u(t)u(t+\tau)}/\overline{u^2}d\tau$
ν = kinematic viscosity
ρ = density
σ = turbulent spot propagation parameter
τ = shear stress

Subscripts

e = at transition end
s = at transition start
w = at the wall
∞ = in the free stream

eddy viscosity, turbulent thermal diffusivity, and turbulent Prandtl number under the influences of elevated FSTI during the process of laminar–turbulent transition.

Experimental Program

Wind Tunnel. The present research employed a two-dimensional, open-circuit, blowing type wind tunnel. The detailed description of the design considerations and construction specifications was documented by Kuan (1987) and Kuan and Wang (1990). Air is drawn through a filter box, then forced through two grids, a honeycomb, a heat exchanger, a screen pack, and a contraction nozzle before entering the test section. The flow rate can be adjusted steplessly from 0.5 m/s to 35 m/s by a combination use of an inlet damper and a constant-torque, variable frequency motor controller. The steadiness of the free-stream velocity and temperature can be maintained within 1 percent and 0.5°C for a 24-hour period, and the uniformity is within 0.7 percent and 0.1°C, respectively.

Test Section. The rectangular test section is 0.15 m wide, 2.4 m long, and 0.92 m high with an aspect ratio of 6. The large aspect ratio reduces edge effects and ensures the two dimensionality of the boundary layer flow. One of the test section walls served as the test wall. The heat patch inside the test wall was constructed of a serpentine heater foil sandwiched between glass cloth and silicon rubber sheets. A 1.56 mm thick aluminum sheet was vulcanized to the front surface of the heater pad to ensure uniformity of the heat flux. A 1.56 mm polycarbonate sheet was placed on the aluminum surface to provide a smooth test surface on which the air flows and measurements were taken. The surface temperature was measured by 184 3 mil E-type thermocouples, which were embedded strategically inside the test wall to capture the spanwise variation of wall heat transfer in a transitional boundary layer. Fourteen measuring holes were drilled along the outer observation wall centerline in the test section and measurements were obtained by traversing the probe through these holes into the test section. Boundary layer suction was applied at the leading edge of the test section so that a near zero thickness boundary layer can be achieved at the leading edge. The detailed construction consideration and description of the heated test wall are contained in Wang et al. (1992) and Zhou (1993).

Turbulence Generating Grids. The background FSTI of this wind tunnel was about 0.5 percent. The higher turbulence levels required for this study were generated by inserting various turbulence generating grids into the wind tunnel. The turbulence generating grids consisted of biplane rectangular bar arrays with approximately a 69 percent open area (Fig 1). The grids were designed based on the recommendation of Baines and Peterson (1951) to produce test section turbulence levels ranging from approximately 3 to 7 percent. Grid-generated turbulence decays with distance from the grid. The decaying rate becomes smaller when the distance from the grid increases. In order to generate homogeneous and slowly decaying turbulence, the turbulence generating grids were inserted at the entrance to the main tunnel contraction instead of placing them at the inlet of the test section. The grids are referred to as grids 1, 2, and 3, corresponding to mesh widths, M, of 19.05, 24.13, and 33.02 cm, respectively. The test case with only background turbulence (no grid) served as the baseline case.

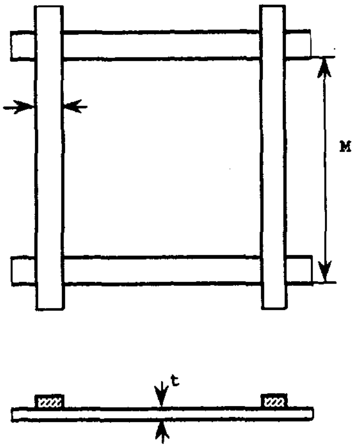

Grid Number	b (cm)	M (cm)	t (cm)	% Open Area
1	3.81	19.05	0.32	69
2	5.08	24.13	0.32	69
3	7.62	33.02	0.32	69

Fig. 1 Grid configuration

Instrumentation and Data Reduction. A three-wire sensor was specifically designed to measure the instantaneous longitudinal velocity, cross-stream velocity, and temperature simultaneously. The development and qualification of this three-wire sensor was described by Shome (1991) and Wang et al. (1992). Basically, an "X" array, consisting of gold-plated tungsten wires 1.0 mm long and 2.5 μm in diameter, is used for velocity measurement. The sensing length is 0.5 mm, and is etched in the center. The spacing between the "X" array is 0.35 mm. The temperature sensor is a 0.35 mm long (with a sensing length of 0.35 mm) and a 1.2 μm diameter unplated platinum wire placed in a plane parallel to the plane of the crossed wires and spaced 0.35 mm from the "X" array. To allow for near-wall measurement and to reduce probe interference, the probe support was bent at an angle of 10 deg from the wire axis. However, the x wires are still perpendicular to each other.

Two x wires were operated at an overheat ratio of about 1.2 (hot wires) in the constant temperature mode. The 1.2 μm platinum wire was operated at a very low current of 0.1 mA (cold wire) in the constant current mode. In order to have a sufficiently extended length of transition for detailed measurements on the test wall, extremely low speed flows were provided for elevated FSTI cases. The unsteadiness, which commonly occurs in low speed operations, was overcome by a combined use of the inlet fan damper and the frequency controller. The typical overheat ratio of 1.5 for a standard 4.5 μm tungsten wire was found to significantly contaminate the cold temperature wire. The temperature wire reading had an error of 10°C when the x wires were turned "on" compared with that when the x wires were turned "off" in the near-wall region in a boundary layer with the wall temperature 20°C above the free-stream temperature and at the free-stream velocity about 1 m/s. Therefore, relatively low overheat ratios for the x wires were required in order to minimize the "cross-talk" between the x wires and the temperature sensor. However, better velocity sensitivities for the x wires required higher overheat ratios. For compromise, an overheat ratio of about 1.2 was chosen. The method of Chua and Antonia (1990) was used for correcting temperature contamination of the hot wires. Based on this method, the hot-wire signals were corrected by using instantaneous temperatures instead of instantaneous temperature fluctuations. At low free-stream velocities, it was found that if the flow direction deviates a very small angle, from ±45 deg to the x wires, a significant change of the results of the Reynolds shear stress $(\overline{uv})$ and the cross-stream Reynolds heat flux $(\overline{vt})$ would occur. This small flow angle was found by assuming

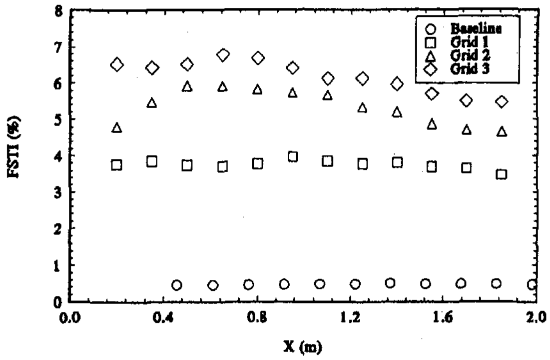

Fig. 2 FSTI distribution in the test section

that the mean cross-stream velocity (V) is zero in the free stream. A typical flow angle of 3 deg can result in a 50 percent error in the $\overline{uv}$ and $\overline{vt}$ measurements at free-stream velocity of 2 m/s. A TSI Model IFA 100 Intelligent Flow Analyzer system was used as a coolant temperature anemometer. The IFA 100 allows simultaneous operation of up to four channels. A DISA M20 temperature bridge was used for operating the cold wire in the constant current mode. Three TSI Model 157 signal conditioners were used in the external mode for low pass filtering of all anemometer signals including that from the DISA M20. An 80386 microprocessor based, 20 MHz personal computer was used as the data acquisition controller. A MetraByte DAS-20 multifunction high-speed A/D data acquisition board was internally installed in the PC. A high-speed data acquisition software routine, STREAMER, was used to stream digital input data from DAS-20 directly into the hard disk. The sampling rate was 2 kHz and the sampling duration was 20 seconds.

The wall temperature measurements were performed through a FLUKE Model 8842A 5 1/2 digital multimeter with a built-in A/D converter and a FLUKE 2205A 100-channel switch controller, which allowed scanning/acquisition of wall thermocouple emf at various switching rates up to 5 channels/second.

Wall Stanton number was calculated from the power supplied to the heated test wall and the wall temperature measurement. The heat flux was corrected for the radiation loss, back, and streamwise conduction loss. The wall temperature was corrected for front polycarbonate wall conduction effects, the radiation loss, back and streamwise conduction loss, compressibility, recover effect, and relative humidity.

The detailed instrumentation description is contained in Shome (1991) and Wang et al. (1992).

Results and Discussion

In this experiment, three different sizes of grid were used to produce different free-stream turbulence levels in the test section. The case with no grid served as the baseline case. The results of the baseline case were reported in a previous paper by Wang et al. (1992). The FSTI distributions along the streamwise direction in the test section, based on the three components of the velocity fluctuation, are shown in Fig. 2. For the baseline case and the grid 1 case, as shown in this figure, the FSTI remains almost constant through the test section. For the grid 2 and grid 3 cases, the FSTI increases at first, to station 4, and then starts to decay. The ratios of v'/u' and w'/u' in the freestream, as shown in Fig. 3, are not isotropic for the baseline and grid 2 cases, but they are near isotropic for the grid 1 and 3 cases. The three components of the velocity fluctuation and their length scales in the free stream were documented in detail by Zhou (1993).

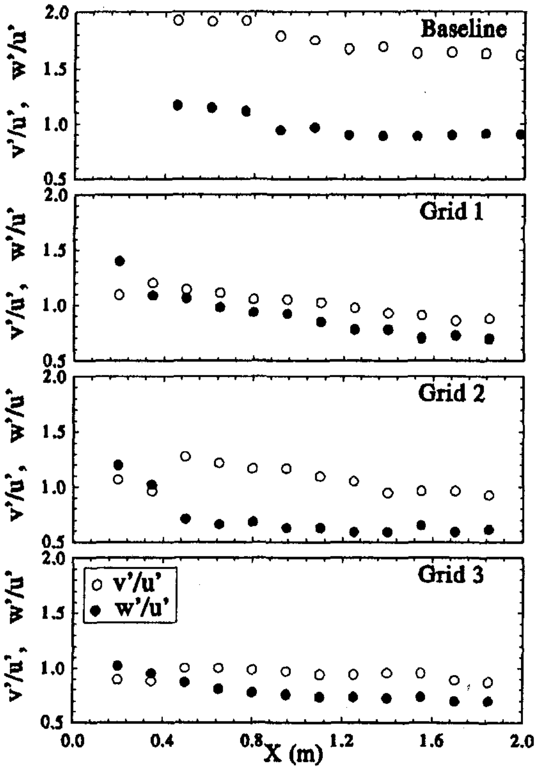

Fig. 3 v'/u', w'/u' in the free stream

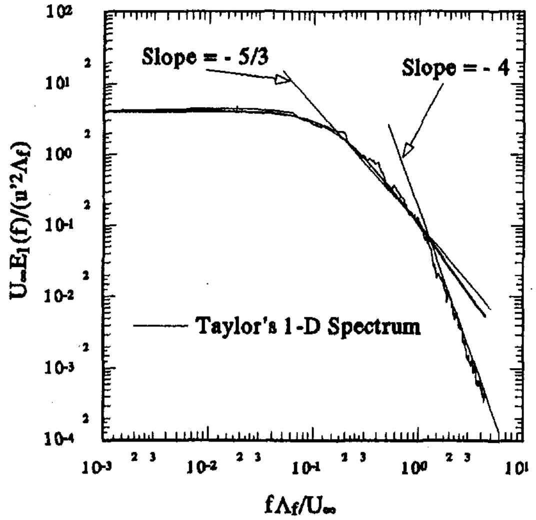

Fig. 4 Free-stream turbulence spectrum

The spectral distributions of u' in the free stream for all three elevated FSTI cases are similar. One representative case of grid 2 is shown in Fig. 4. The one-dimensional spectrum $E_1(f)$ is normalized by the u'^2, the integral length scale Λ_f, and the free-stream velocity U_∞. The frequency f is normalized by Λ_f and U_∞. Also shown in this figure is Taylor's one-dimensional energy spectrum (Hinze, 1975). The spectral distribution $E_1(f)$ follows Taylor's one-dimensional energy spectrum in the low-frequency range and deviates from it in the high-frequency range. In the high-frequency range, the spectrum $E_1(f)$ has a distinctive slope of -4. This is consistent with the typical spectrum of grid generated turbulence (Kistler and Vrebalorich, 1966).

Heat Transfer. Three sets of Stanton number data were taken for each case in each 22-hour run. The first set was obtained after a 12-hour stabilization period followed by two sets obtained at 17 hours and 22 hours, respectively. Between these measurements of wall temperatures, boundary layer measurements were conducted. The maximum variation in

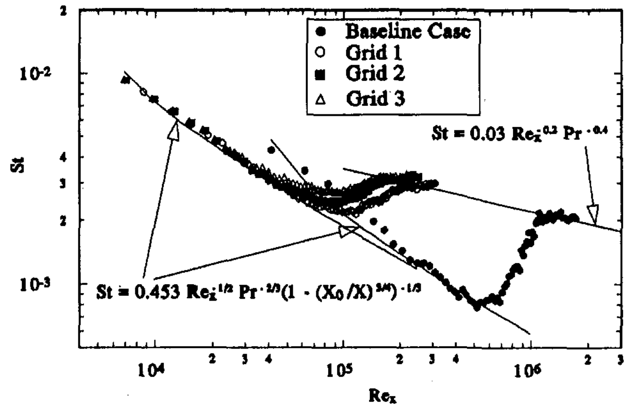

Fig. 5 Stanton number distribution

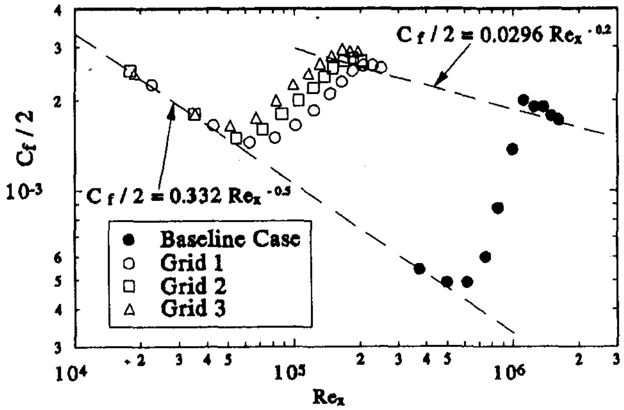

Fig. 6 Friction coefficient distribution

Table 1 Reynolds numbers at onset and end of transition

		Baseline	Grid 1	Grid 2	Grid 3
FSTI at Xs		0.5%	3.8%	5.5%	6.4%
U_∞ (m/s)		13.0	2.10	1.75	1.70
Onset of Transition	X(cm)	61	45	45	42
	Re_x	5.0×10^5	6.0×10^4	5.0×10^4	4.5×10^4
	Re_{δ^*}	1183	386	355	314
	Re_θ	434	161	148	131
End of Transition	X(cm)	136	150	144	139
	Re_x	1.1×10^6	2.0×10^5	1.6×10^5	1.5×10^5
	Re_{δ^*}	1947	735	659	608
	Re_θ	1327	480	404	375

Stanton numbers during a 10-hour period was approximately ±3 percent. An uncertainty analysis of the Stanton number measurement, following the procedure documented by Wang and Simon (1989), was conducted. The uncertainty was ±3 percent in the laminar and turbulent regions and ±5 percent in the transitional region. The centerline Stanton number distributions for the four cases are shown in Fig. 5. The unheated starting length effects for the laminar correlation has been included. It should be noted that the laminar correlation with unheated starting length appears different for different free-stream velocities when plotted in Fig. 5. To maintain clarity, it is plotted only for the baseline and the grid 2 cases. In the laminar portion, the Stanton number distributions follow the laminar correlation for the elevated FSTI cases. The onset of transition is defined as the location where the Stanton number reaches a minimum and starts to deviate from the laminar correlation, and the end of transition is defined as the location where the Stanton number merges with the turbulent correlation. As expected, higher FSTI leads to an earlier onset and an earlier end of transition. The effect of elevated FSTI on the heat transfer is negligible in the laminar region; however, in the turbulent region, the heat transfer is increased as can be seen from Fig. 5.

Skin Friction. The skin friction coefficients in the laminar region and transitional region were determined by extrapolating the linear correlation to the wall. The Clauser technique was employed for determining the skin friction coefficients in the turbulent region by best fitting the data points to the logarithmic law-of-the-wall profile. The development of the skin friction coefficients, shown in Fig. 6, is similar to that of the Stanton number (Fig. 5). The effect of the elevated FSTI on the skin friction in the laminar region is negligible. The effect in the turbulent region is not conclusive due to limited data points and the typical overshooting behavior of C_f in the early turbulent flow region.

Transition Start and Turbulent Spot Formation Rate. In the present study, the onset and end of transition were primarily judged by the Stanton number and cross checked with the skin friction distributions and the evolution of the mean velocity and temperature profiles. The corresponding values of x, Re_x, $\mathrm{Re}_{\delta*}$, and Re_θ at onset and at the end of transition for each case are listed in Table 1. The results indicate that elevated FSTI affects an early onset of transition and reduced extent of transition length based on Re_x, as well as on $\mathrm{Re}_{\delta*}$ and Re_θ.

The key characteristic in laminar–turbulent transition flow is the randomly intermittent laminar–turbulent behavior. The fraction of time the flow is turbulent is defined as the intermittency. Emmons (1951) presented a statistical theory for transition and provided an expression for the intermittency. Later, the theory was extended by Dhawan and Narasimha (1958) who showed, for time-averaged two-dimensional flows, that turbulent spots originate within a narrow region on the surface at some distance, x_t, from the leading edge, and that the turbulent spot production could be represented by a Dirac delta function. Based on this intermittency theory, once the location of the transition onset and the turbulent spot formation rate are known, the location of the end of transition and the intermittency distribution within the transition region can be predicted. The present calculation of the turbulent spot formation rate is based on the equation, $\hat{n}\sigma = 4.6/(\mathrm{Re}_{xe} - \mathrm{Re}_{xs})^2$ (Mayle, 1991), in which the effect of FSTI is implicitly embedded in the Re_{xe} and Re_{xs}.

The onset of transition, based on the momentum thickness Reynolds number, and the calculated turbulent spot formation rate, $\hat{n}\sigma$, are plotted in Fig. 7. Also shown are the empirical correlations, $\mathrm{Re}_{\theta s} = 400\ (\mathrm{FSTI})^{-5/8}$ and $\hat{n}\sigma = 1.5 \times 10^{-11}\ (\mathrm{FSTI})^{7/4}$, given by Mayle (1991), which were formulated based on flat-wall, nonaccelerated flow data. For the elevated FSTI cases, the present data agree with Mayle's correlation. For the baseline case, the onset of transition is earlier and the calculated $\hat{n}\sigma$ is larger than that predicted by Mayle's correlation. This indicates that some other factors, which were not incorporated into Mayle's correlations, influence the transition process in low FSTI environment. For a well-controlled experiment of a low-FSTI transitional flow study, typical factors that influence the onset of transition are related to inherent characteristics of the test facility and the uncontrollable disturbances in operating conditions. Some possible factors are the initial flow conditions at the leading edge, the free-stream integral length scale, floor vibration frequency, smoothness and flatness of the test surface, and precision of streamwise pressure gradient control.

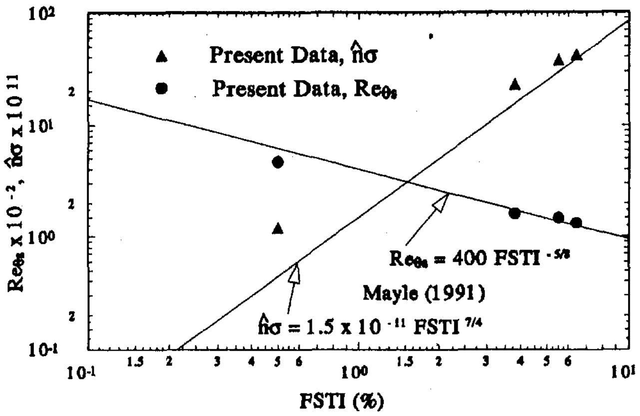

Fig. 7 Transition onset and turbulent spot formation rate

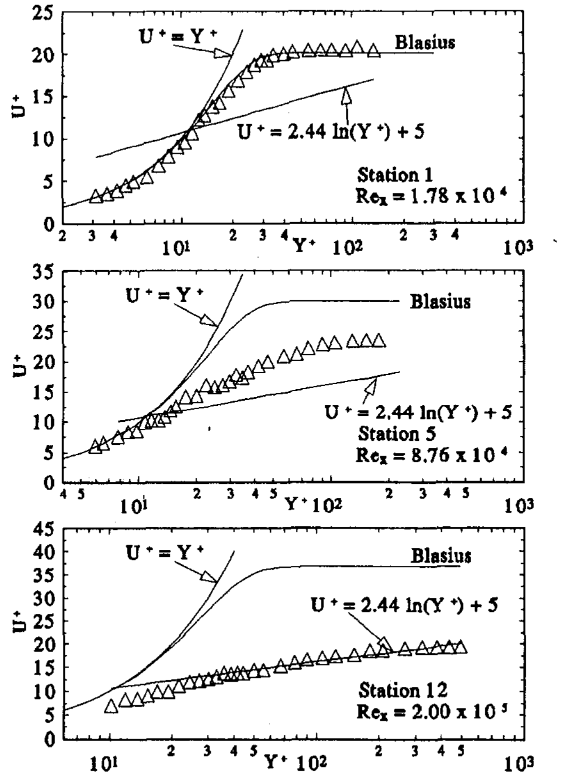

Fig. 8 Mean velocity profiles, U^+ versus Y^+

Mean Velocity and Temperature Profiles. Mean velocity and temperature profiles are plotted in wall units in Figs. 8 and 9, respectively. Since their overall evolution during the transition process is similar to that of the 2 percent FSTI case previously reported by Wang et al. (1987), only three profiles of each are shown as representative of the mean profile characteristics in the laminar, transitional, and turbulent flow region, respectively. In the laminar region, even at the elevated values of FSTI, the mean profiles are consistent with the laminar flow solution, as in the baseline case. In the turbulent region, both the mean velocity and temperature profiles preserve the logarithmic "law of the wall" characteristics over a sufficient range of Y^+ (from 30 ~ 300), but the wake regions are completely depressed beyond $Y^+ = 300$ due to the high FSTI, which is consistent with the previous results of Blair (1983a, b) and Wang et al. (1987). In the transition region, the mean profiles deviate from the typical laminar and turbulent profiles. No established method has been developed to compare them to those of the low-FSTI cases.

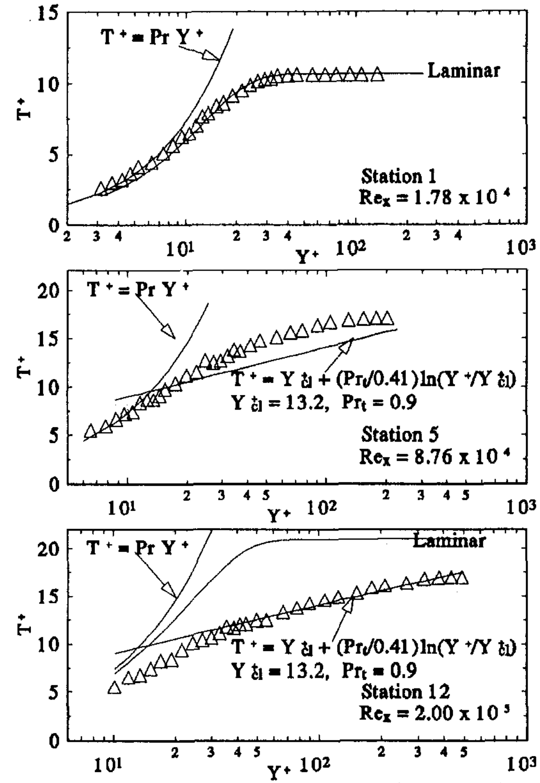

Fig. 9 Mean temperature profiles, T^+ versus Y^+

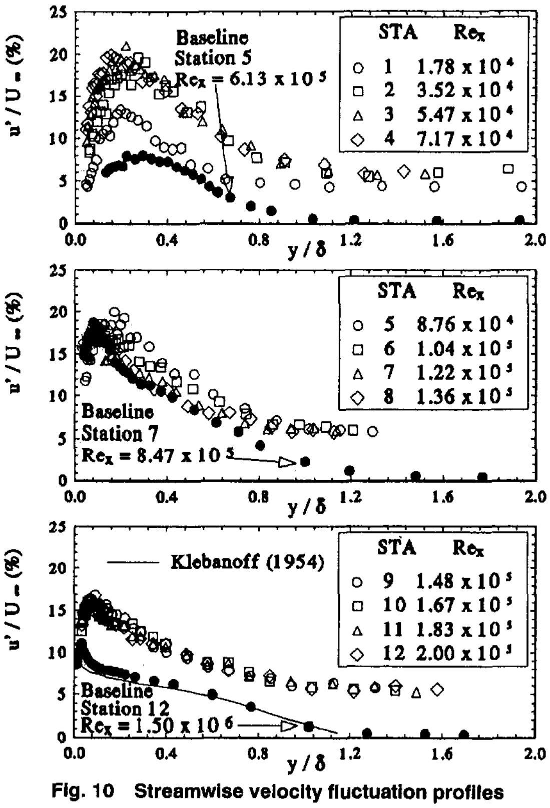

Fig. 10 Streamwise velocity fluctuation profiles

Streamwise Velocity Fluctuation (u'). The normalized streamwise evolution of velocity fluctuation, u'/U_∞, is shown in Fig. 10 for the grid 2 case. For comparison, three profiles of the baseline case, one near the onset of transition (station 5), one in the transition region with maximum u' (station 7), and one in the fully turbulent region (station 12), have also been incorporated into Fig. 10. The onset of transition for

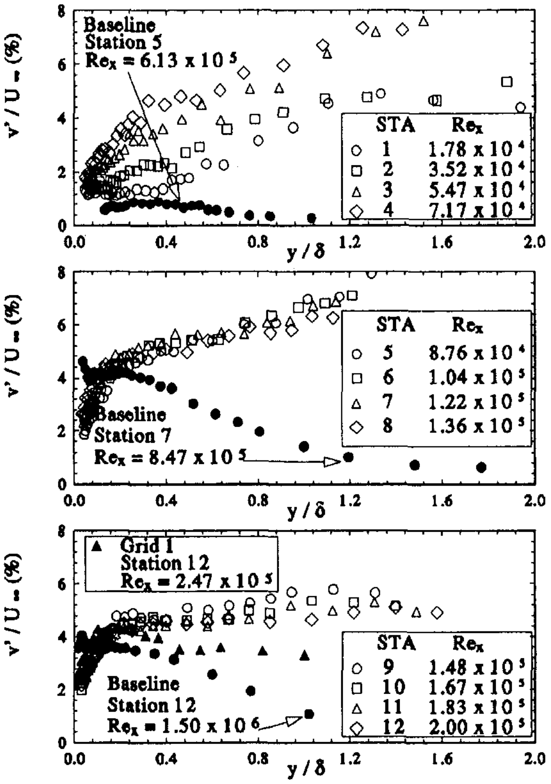

Fig. 11 Cross-stream velocity fluctuation profiles

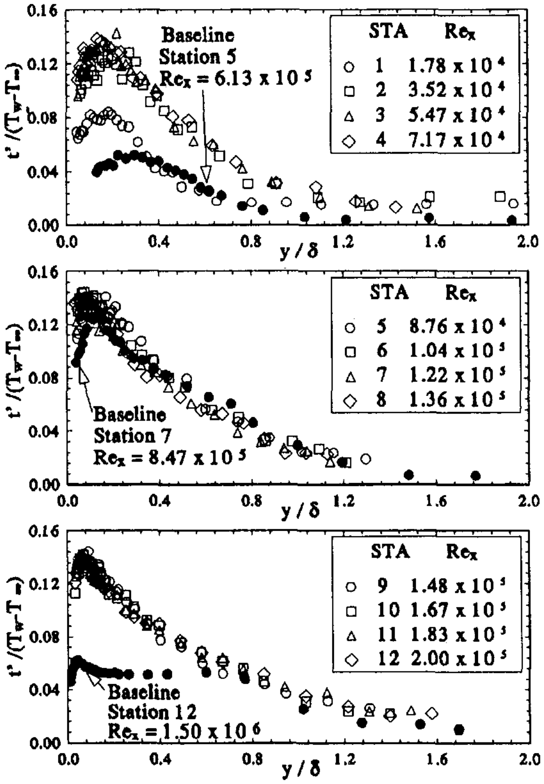

Fig. 12 rms temperature profiles

grid 2, based on Stanton number distribution, is at $\mathrm{Re}_x = 5 \times 10^4$. Therefore, stations 1 and 2 for the grid 2 case are in the laminar flow region. Comparison between the stations 1 and 2 for grid 2 case and station 5 for the baseline case indicates that the u' in the laminar flow was significantly elevated due to the higher FSTI. This is consistent with the results reported by Dyban et al. (1980). It is especially interesting to observe that the elevated u'/U_∞ distribution reaches 20 percent in the late laminar region (station 2) and remains at such high levels throughout the early half of the transition region until station 6. It is also to be noted that in the transitional flow, the maximum values of u'/U_∞ at stations 4 and 5 in the grid 2 case are only slightly higher than the maximum value at station 7 for the baseline case. This implies that even at elevated FSTI, the maximum Reynolds normal stresses due to the bursting activities are limited to around $u'/U_\infty = 20$ percent. This may also imply that the penetration of the turbulence energy from the free stream into the boundary layer results in a uniform redistribution of turbulence energy across the boundary layer rather than in providing more bursting energy. This second implication can be further verified by examining the u' distribution in the turbulent flow region as shown by the u'/U_∞ profiles of stations 10, 11, and 12 in Fig. 10. This deep penetration of elevated free-stream turbulence to near the wall is consistent with the results of Wang et al. (1987). This is inconsistent with the results reported by Sohn and Reshotko (1991).

Cross-Stream Velocity Fluctuation (v'). The evolution of v'/U_∞ for grid 2 case, as shown in Fig. 11, is very different from the baseline case in Wang et al. (1992) or other low FSTI cases in Kuan and Wang (1990) and Sohn et al. (1991). Three representative v'/U_∞ distribution curves, as mentioned in Fig. 10, are superimposed for comparison. It is obvious that the effect of elevated FSTI on v' is more predominant in the outer boundary layer than in the inner boundary layer. It appears that v', in the boundary layer, is affected by FSTI through an energy diffusion process rather than through a convective motion, or through a correlation with pressure fluctuations (return-to-isotropy). This speculation arises from by observing that the magnitude of v' in the free stream seems to control the v' distribution in the outer boundary layer since the data points for each curve, for all flow regions, indicate a smooth curve, which asymptotically approaches the free-stream value of v'. A typical near-wall peak of v', which appears in the transition region for the baseline case (e.g., at station 7), is not observed in the elevated FSTI cases. Apparently, the elevated turbulence in the free stream does not promote the cross-stream component of the near-wall turbulence energy production, which produces large magnitudes of energy in the streamwise component. The v'/U_∞ distribution in the turbulent flow region at station 12 for the grid 1 case, which has lower FSTI than the grid 2 case, is superimposed in Fig. 11. A peak in v' can be clearly seen near $y/\delta = 0.2$. The mechanism involved in producing this round peak can be very different from the near-wall sharp peak prevailing in the low-FSTI cases. However, it is not clear how the near-wall production of the v'-component turbulence energy is suppressed in the elevated FSTI cases and why the highest v' value occurs away from the wall. Also shown in this figure are the varying values of v'/U_∞ in the free stream along the streamwise direction in the test section. The value of v'_∞/U_∞, which can be read from values beyond $y/\delta = 1.6$ from Fig. 11, shows a variation from about 4.5 percent at stations 1 and 2 to 7 percent at stations 3 to 5 and back down to 4.5 percent at stations 10 to 12. This trend can also be seen from v'/u' in Fig. 3 since u' remains nearly constant along the streamwise direction.

rms Temperature Fluctuation (t'). The evolution of the rms temperature fluctuation for the grid 2 case, $t'/(T_w - T_\infty)$, as presented in Fig. 12, is very similar to u', with an elevated value across most of the boundary layer except in the outer boundary layer ($y/\delta > 0.8$), where the elevated FSTI does not enhance t' as would be expected in a nearly isothermal region.

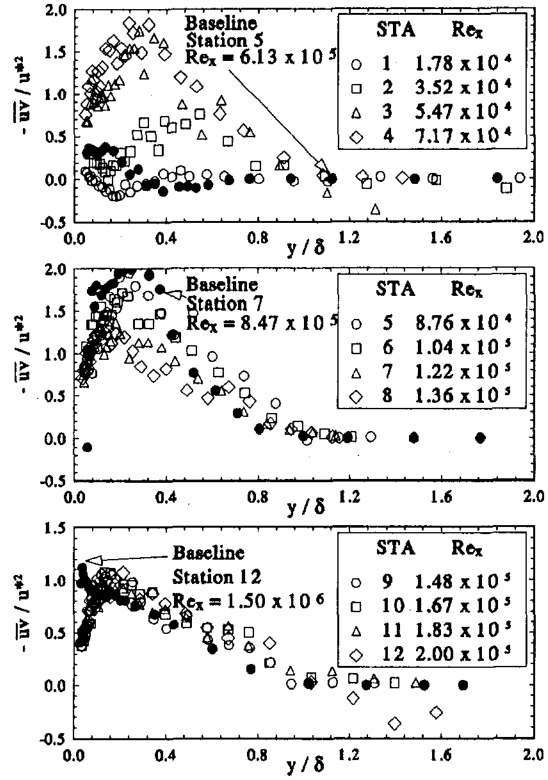

Fig. 13 Reynolds shear stress distribution

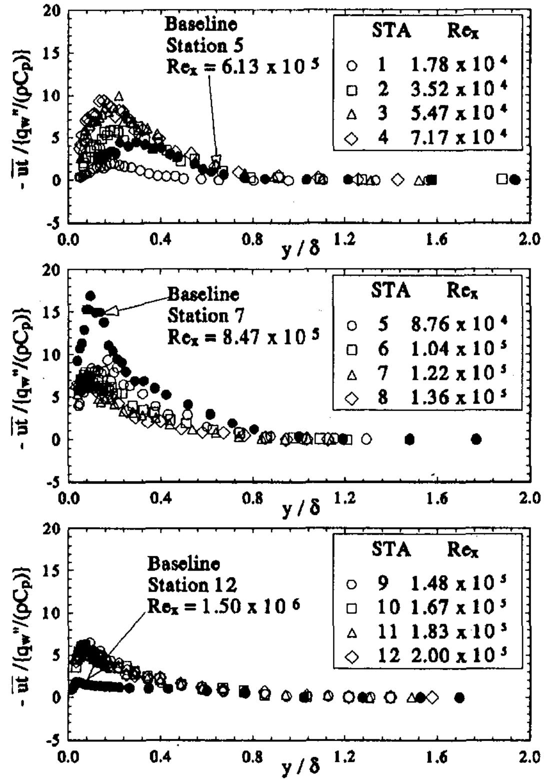

Fig. 14 Streamwise Reynolds heat flux distribution

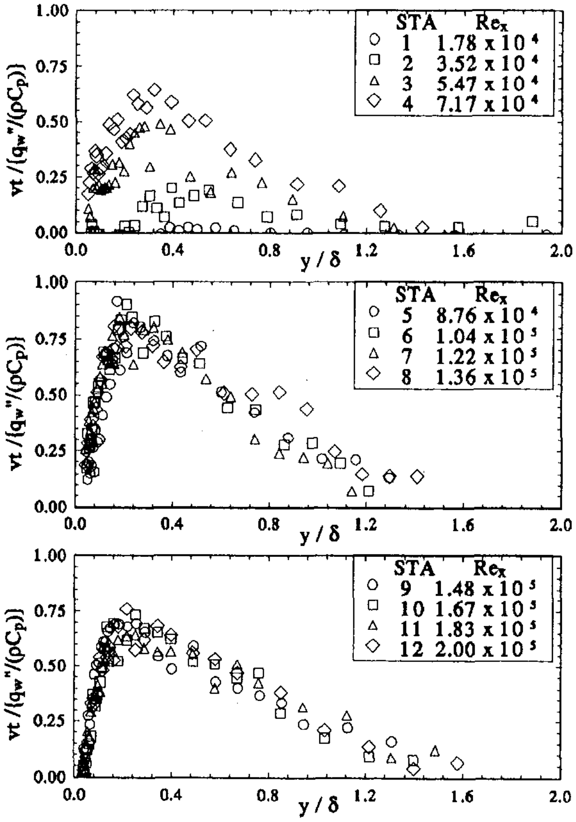

Fig. 15 Cross-stream Reynolds heat flux distribution

Reynolds Shear Stress ($\overline{uv}$). The evolution of the normalized Reynolds shear stress, $-\overline{uv}/u'^2$, for the grid 2 case, and also the comparison with the baseline case, are shown in Fig. 13. For the grid 2 case, the normalized Reynolds shear stress reaches a maximum value of about 1.9 at stations 4 and 5. The peak value in the boundary layer then decreases and the peak location moves closer to the wall. This evolution of $\overline{uv}$ indicates that the turbulent shear is not generated near the wall as is that for u', but is produced away from the wall, at about $y/\delta = 0.3$, and progresses toward the wall to eventually affect the wall shear. This progression is similar to that for the baseline case. The detailed description was provided by Wang et al. (1992). The peak location for the baseline case in the turbulent region at station 12 is closer to the wall than that for the grid 2 case. The effect of elevated FSTI on $\overline{uv}$ seems smaller than on u' and v'.

Reynolds Heat Fluxes ($\overline{ut}$ and $\overline{vt}$). The results of $-\overline{ut}$ and $\overline{vt}$, normalized by wall heat flux, for the grid 2 case are presented in Figs. 14 and 15. For the grid 2 case, $-\overline{ut}/\{q''_w/\rho C_p\}$ reaches its maximum value of almost 10 near stations 4 and 5. Then the peak value in the boundary layer decreases and the peak location moves closer to the wall. The peak value in the turbulent flow region is about 7. For the baseline case at station 12, the peak value is only about 2, much lower than that for the grid 2 case. The locations of these peaks closely correspond to those of the peaks for u' (Fig. 10) and t' (Fig. 12). As shown in Figs. 10 and 12, u' and t' are much higher in the laminar and turbulent regions for the grid 2 case than for the baseline case, but are about the same in the transition region as in the baseline case. The lower value of $-\overline{ut}/\{q''_w/\rho C_p\}$ in the transition region for the grid 2 case compared to that in the baseline case is unexpected. This is then identified as the low Reynolds number effect.

As shown in Fig. 15 for the grid 2 case, the normalized cross-stream Reynolds heat flux, $\overline{vt}/\{q''_w/\rho C_p\}$, reaches its maximum value of about 0.9 at stations 6 and 7 in the transition region. This is later than $\overline{ut}$, which reaches its maximum value at station 4. The peak value of $\overline{vt}/\{q''_w/\rho C_p\}$ then decreases with the peak value in the turbulent region to

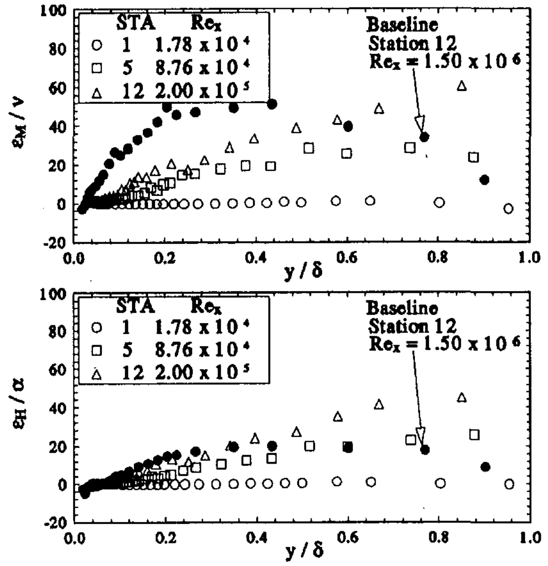

Fig. 16 Streamwise evolution of eddy viscosity and turbulent thermal diffusivity profiles

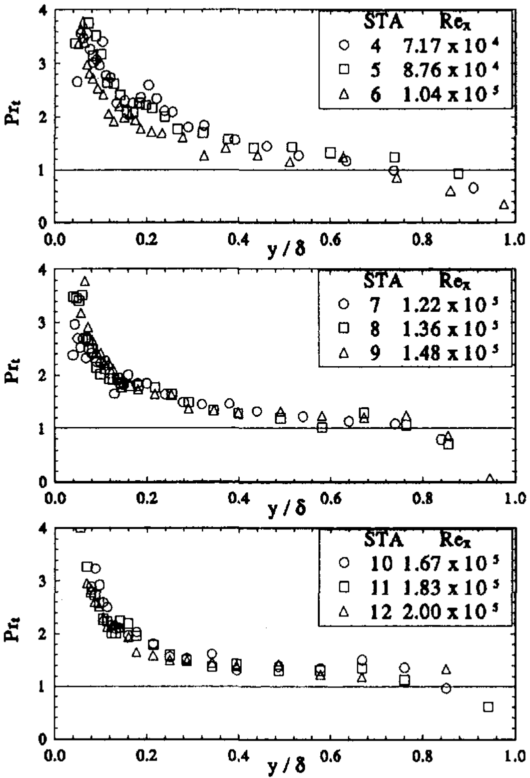

Fig. 17 Turbulent Prandtl number distribution

about 0.7. The baseline case at station 7 is also shown in Fig. 15 for comparison. Negative $\overline{vt}$ occurs in the inner boundary layer for the baseline case but no negative $\overline{vt}$ is observed in the elevated FSTI cases. The possible explanations of this negative value were discussed by Wang et al. (1992). The spatial resolution of the probe is of special concern near the wall because of the decreasing eddy size as the wall is approached and the thin boundary layer in the baseline case. For the higher FSTI cases, the free-stream velocity (~ 2 m/s) was much lower than that for the baseline case (~ 12 m/s), so that the boundary layer was much thicker. In the turbulent boundary layer the magnitude of $\overline{vt}$ is elevated across the entire boundary layer for the grid 2 case, as compared to the baseline case at station 12 in Fig. 15.

Eddy Diffusivities and Turbulent Prandtl Number. The eddy viscosity, ϵ_M, and the turbulent thermal diffusivity, ϵ_H, normalized by their molecular counterparts at three stations for the grid 2 case, are shown in Fig. 16. The results for the baseline case at station 12 are also shown for comparison. For the grid 2 case, at station 1, where the flow behaves as laminar, the turbulent transport is low compared with the molecular transport, as expected, whereas for transitional flow (station 5) and turbulent flow (station 12), the turbulent transport is much higher than the molecular transport except in the very near-wall region. For the baseline case, ϵ_M/ν shows a peak near $y/\delta = 0.3 \sim 0.4$ and gradually decreases in the outer boundary layer. ϵ_H/α shows a similar behavior except that the peak is not so obvious. For the grid 2 case, which is very different from the baseline case, a peak of ϵ_M/ν appears near $y/\delta = 0.7$ at station 5 in the transitional flow region and $y/\delta = 0.55$ at station 12 in the turbulent flow region. ϵ_H/α is similar to ϵ_M/ν in the turbulent flow region; however, in the transitional flow region, the maximum value of ϵ_H/α occurs in the outer boundary layer ($y/\delta \approx 0.85$).

The turbulent Prandtl number, Pr_t, the ratio of the eddy viscosity over the turbulent thermal diffusivity, is shown in Fig. 17 for the grid 2 case. The data points are scattered in the early transition region (stations 4 to 6) but stabilized in the turbulent region (stations 10 to 12). In the region between $y/\delta = 0.2$ to 0.8, the Pr_t values are close to 1.2 to 1.6, which are higher than 0.9, a value commonly applied to fully turbulent flow for low FSTI cases. In the near-wall region ($y/\delta < 0.2$), Pr_t values are larger than 2. The validity of these values needs further verification due to the limits in spatial resolution in the near-wall region. However, values of Pr_t in the region of $y/\delta \geq 0.2$ are believable. Based on these results, the higher turbulent Prandtl number (1.2 ~ 1.6) in the transitional and low-Reynolds-number turbulent flow should be considered in the modeling of transition.

The previous discussion is based on the comparison between the results of the baseline case and those of the grid 2 case. The comparisons among the grid 1, grid 2, and grid 3 cases are shown in Fig. 18. At maximum u' station in the transition region (Fig. 18*a*), the effects of the different grids on the u'/U_∞ and v'/U_∞ are confined in the outer region of the boundary layer ($y/\delta > 0.4$), which are influenced by the different FSTI levels. In the fully turbulent region, the peak value of u'/U_∞ is slightly elevated due to a higher FSTI level (e.g., higher grid number). A peak of v'/U_∞ in the boundary layer is evident for grid 1 case, but is not observed for grids 2 and 3 cases due to the higher FSTI levels. Since the streamwise evolutions of $\overline{uv}$, $\overline{ut}$, $\overline{vt}$, and Pr_t for these three grids are similar during the transition process, only the comparisons of the Pr_t distributions are presented. As shown in this figure, the Pr_t distributions for these three grids are very similar at maximum u' station and in the fully turbulent region.

Conclusion

Experiments were performed to investigate the effects of elevated FSTI (3 ~ 7 percent) on flow and thermal structures in heated transitional boundary layers. Wall heat transfer measurements indicated that elevated FSTI values result in an earlier onset of transition and reduced length of transition in terms of Re_x, $\mathrm{Re}_{\delta*}$, and Re_θ. The calculated turbulent spot formation rates at elevated FSTI cases agree with Mayle's correlation. In the turbulent region, the mean velocity and temperature profiles demonstrate the logarithmic "law of the wall" characteristics over a sufficient range of Y^+ (30 ~ 300). The wake regions are completely depressed.

The u' distribution is significantly elevated across the entire boundary layer in the laminar and turbulent regions

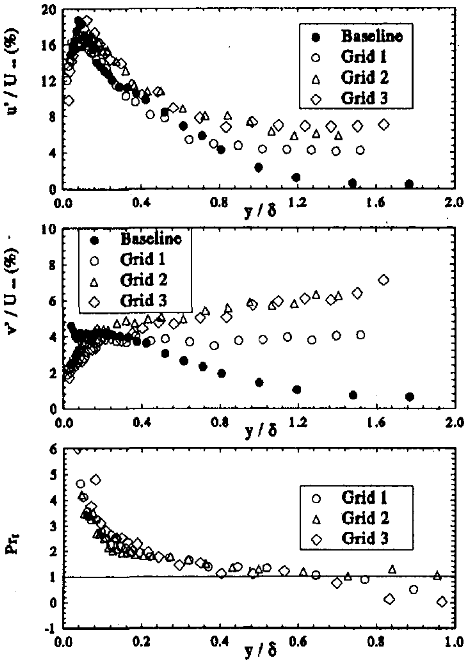

(a) at stations with maximum u'

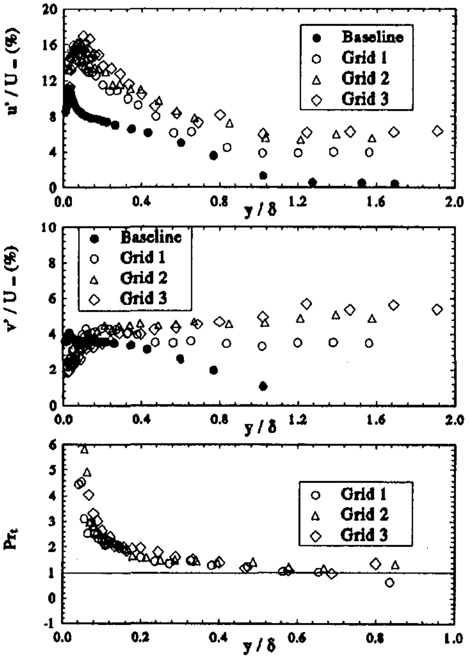

(b) at station 12

Fig. 18 Comparison among different grids

due to elevated FSTI. The u'/U_∞ distribution reaches 20 percent in the late laminar region and remains at such high levels throughout the early half of the transition region. In the transitional region, the maximum Reynolds normal stresses of bursting activities are only slightly higher than the baseline case but are limited to approximately $u'/U_\infty = 20$ percent. The evolution of the rms temperature fluctuation is very similar to u' with elevated values across 80 percent of the boundary layer.

The v' distribution in the outer boundary layer is controlled by the magnitude of v' in the free stream. The typical near-wall peak of v', which appears in the transition region at low FSTI, is not observed. In the turbulent region, the very near-wall peak of v' is suppressed and the maximum v' value occurs away from the wall in elevated FSTI cases.

The evolution of the $\overline{uv}$ distribution at elevated FSTI is similar to that at low FSTI. In the transition region, Reynolds shear stress is produced not in the near-wall region where the vigorous turbulence production of u' occurs but away from the wall, at about $y/\delta = 0.3$. This high turbulent shear progresses toward the wall and eventually affects the wall shear.

The $-\overline{ut}/\{q''_w/\rho C_p\}$ distributions are elevated in the laminar and turbulent regions but reduced in the transitional region at higher FSTI. This is caused by the low Reynolds effect.

The $\overline{vt}$ distributions reach maximum values in the transition region slower than the evolution of $\overline{ut}$. The regions of negative values of $\overline{vt}$, occurring in the transition region in the baseline case, are not observed in the elevated FSTI cases.

In the near-wall region ($y/\delta < 0.2$), the Pr_t values are very large (> 2); further verification of these high values is needed. In the region of $y/\delta = 0.2 \sim 0.8$, the Pr_t values are close to $1.2 \sim 1.6$. These higher Pr_t in the transitional and low-Reynolds-number turbulent flow should be considered in the numerical modeling of transitional boundary layers.

Acknowledgments

This program was sponsored by the Office of Naval Research (Grant No. N00014-89-J-3105) and the Air Force Office of Scientific Research (Grant No. AFOSR-89-0324). The program monitors are Dr. Gabriel Roy and Major Dan Fant, respectively. Part of the facility was constructed under a support from the National Science Foundation (Grant No. CBT-8708843).

References

Abu-Ghannam, J. B., and Shaw, R., 1980, "Natural Transition of Boundary Layers—the Effects of Turbulence, Pressure Gradient, and Flow History," *J. Mech. Eng. Sci.*, Vol. 22, pp. 213–228.

Baines, W. D., and Peterson, E. G., 1951, "An Investigation of Flow Through Screens," *Trans. ASME*, Vol. 73, pp. 467–480.

Blair, M. F., 1982, "Influence of Free-Stream Turbulence on Boundary Layer Transition in Favorable Pressure Gradients," ASME *Journal of Engineering for Power*, Vol. 104, pp. 743–750.

Blair, M. F., 1983a, "Influence of Free-Stream Turbulence on Turbulent Boundary Layer Heat Transfer and Mean Profile Development, Part I—Experimental Data," ASME *Journal of Heat Transfer*, Vol. 105, pp. 33–40.

Blair, M. F., 1983b, "Influence of Free-Stream Turbulence on Turbulent Boundary Layer Heat Transfer and Mean Profile Development, Part II—Analysis of Results," ASME *Journal of Heat Transfer*, Vol. 105, pp. 41–47.

Chua, L. P., and Antonia, R. A., 1990, "Turbulent Prandtl Number in a Circular Jet," *International Journal of Heat and Mass Transfer*, Vol. 33, No. 2, pp. 331–339.

Dhawan, S., and Narasimha, R., 1958, "Some Properties of Boundary Layer Flow During Transition From Laminar to Turbulent Motion," *J. Fluid Mech.*, Vol. 3, pp. 418–436.

Dyban, Y. P., Epik, E. Y., and Suprun, T. T., 1980, "Characteristics of the Laminar Boundary Layer in the Presence of Elevated Free-Stream Turbulence," *Fluid Mechanics—Soviet Research* [in English], Vol. 22, No. 5, pp. 213–228.

Emmons, H. W., 1951, "The Laminar-Turbulent Transition in a Boundary Layer—Part I," *J. Aero. Sci.*, Vol. 18, pp. 490–498.

Graham, R. W., 1979, "Fundamental Mechanisms That Influence the Estimate of Heat Transfer to Gas Turbine Blades," ASME Paper No. 79-HT-43.

Graham, R. W., ed., 1984, *Transition in Turbines*, NASA TM-79128.

Hinze, J. O., 1975, *Turbulence*, 2nd ed., McGraw-Hill, New York.

Kim, J., Simon, T. W., and Kestoras, M., 1989, "Fluid Mechanics and Heat Transfer Measurements in Transitional Boundary Layers Conditionally Sampled on Intermittency," presented at the 1989 ASME National Heat Transfer Conference, ASME HTD-Vol. 107, pp. 69–81.

Kistler, A. L., and Vrebalovich, T., 1966, "Grid Turbulence at Large Reynolds Numbers," *J. Fluid Mech.*, Vol. 26, pp. 37–44.

Klebanoff, P. S., Tidstrom, K. D., and Sargent, L. M., 1962, "The Three-Dimensional Nature of Boundary-Layer Instability," *J. Fluid Mech.*, Vol. 12, pp. 1–34.

Kuan, C. L., 1987, "An Experimental Investigation of Intermittent Behavior in the Transitional Boundary Layer," M.S. Thesis, Clemson University, Clemson, SC.

Kuan, C. L., and Wang, T., 1990, "Investigation of Intermittent Behavior of Transitional Boundary Layer Using a Conditional Averaging Technique," *Experimental Thermal and Fluid Science*, Vol. 3, pp. 157–170; also presented in 1989 at AIAA 20th Fluid Dynamics Plasma Dynamics and Lasers Conference, AIAA 89-1890.

Mayle, R. E., 1991, "The Role of Laminar-Turbulent Transition in Gas Transition Engines," ASME JOURNAL OF TURBOMACHINERY, Vol. 113, pp. 509–537.

Morkovin, M. V., 1969, "On the Many Faces of Transition," *Viscous Drag Reduction*, C. S. Wells, ed., Plenum Press, New York, pp. 1–31.

Morkovin, M. V., 1978, "Instability, Transition to Turbulence and Predictability," AGARDograph 236.

Narasimha, R., 1985, "The Laminar-Turbulent Transition Zone in the Boundary Layer," *Prog. Aerospace Sci.*, Vol. 22, pp. 29–80.

Reshotko, E., 1976, "Boundary Layer Stability and Transition," *Ann. Rev. Fl. Mech.*, Vol. 8, p. 311–350.

Schubauer, G. B., and Skramstad, H. K., 1948, "Laminar Boundary-Layer Oscillations and Transition on a Flat Plate," NACA Report 909.

Shome, B., 1991, "Development of a Three-Wire Probe for the Measurement of Reynolds Stresses and Heat Fluxes in Transitional Boundary Layers," MS Thesis, Dept. of Mech. Engr., Clemson University, Clemson, SC.

Sohn, K. H., and Reshotko, E., 1991, "Experimental Study of Boundary Layer Transition With Elevated Freestream Turbulence on a Heated Flat Plate," NASA CR-187068.

Sohn, K. H., Reshotko, E., and Zaman, K. B. M. Q., 1991, "Experimental Study of Boundary Layer Transition on a Heated Flat Plate," ASME FED-Vol. 114, pp. 163–171.

Suder, K. L., O'Brien, J. E., and Reshotko, E., 1988, "Experimental Study of Bypass Transition in a Boundary Layer," NASA TM-100913.

Tani, I., 1981, "Three-Dimensional Aspects of Boundary Layer Transition," *Proc. Indian Acad. Sci.*, Vol. 4, Part 2, pp. 219–238.

Turner, A. B., 1971, "Local Heat Transfer Measurements on a Gas Turbine Blade," *J. Mech. Eng. Sci.*, Vol. 13, pp. 1–12.

Volino, R. J., and Simon, T. W., 1995, "Bypass Transition in Boundary Layers Including Curvature and Favorable Pressure Gradient Effects," ASME JOURNAL OF TURBOMACHINERY, Vol. 117, No. 1, pp. 166–174.

Wang, T., and Simon, T. W., 1989, "Development of a Special-Purpose Test Surface Guided by Uncertainty Analysis," *Journal of Thermophysics*, Vol. 3, No. 1, pp. 19–26.

Wang, T., Simon, T. W., and Buddhavarapu, J., 1987, "Heat Transfer and Fluid Mechanics Measurements in Transitional Boundary Layer Flows," ASME JOURNAL OF TURBOMACHINERY, Vol. 109, No. 3, pp. 443–450.

Wang, T., Keller, F. J., and Zhou, D., 1992, "Experimental Investigation of Reynolds Shear Stresses and Heat Fluxes in a Transitional Boundary Layer," *Fundamental and Applied Heat Transfer Research for Gas Turbine Engines*, ASME HTD-Vol. 226, pp. 61–70.

Zhou, D., 1993, "Effects of Elevated Free-Stream Turbulence and Favorable Pressure Gradient on Flow and Thermal Structures in Transitional Boundary Layers," Ph.D. Dissertation, Dept. of Mech. Engr., Clemson University, Clemson, SC.

Enhanced Heat Transfer and Shear Stress Due to High Free-Stream Turbulence

K. A. Thole
Lehrstuhl and Institut für
Thermische Strömungsmaschinen,
Universität Karlsruhe,
Karlsruhe, Federal Republic of Germany

D. G. Bogard
Department of Mechanical Engineering,
University of Texas, Austin,
Austin, TX 78712

Surface heat transfer and skin friction enhancements, as a result of free-stream turbulence levels between 10 percent < Tu < 20 percent, have been measured and compared in terms of correlations given throughout the literature. The results indicate that for this range of turbulence levels, the skin friction and heat transfer enhancements scale best using parameters that are a function of turbulence level and dissipation length scale. However, as turbulence levels approach Tu = 20 percent, the St' parameter becomes more applicable and simpler to apply. As indicated by the measured rms velocity profiles, the maximum streamwise rms value in the near-wall region, which is needed for St', is the same as that measured in the free stream at Tu = 20 percent. Analogous to St', a new parameter, Cf', was found to scale the skin friction data. Independent of all the correlations evaluated, the available data show that the heat transfer enhancement is greater than the enhancement of skin friction with increasing turbulence levels. At turbulence levels above Tu = 10 percent, the free-stream turbulence starts to penetrate the boundary layer and inactive motions begin replacing shear-stress producing motions that are associated with the fluid/wall interaction. Although inactive motions do not contribute to the shear stress, these motions are still active in removing heat.

Introduction

Quantifying high free-stream turbulence effects on surface heat transfer and shear stress is important for improving predictions of the thermal loading and the aerodynamic losses on gas turbine blades, vanes, and endwalls. Although the typical free-stream turbulence levels that occur in gas turbines are greater than 20 percent (Kuotmos and McGuirk, 1989), most of the shear stress and heat transfer studies have focused on turbulence levels less than 7 percent. The emphasis of this paper is twofold. First, a comparison will be made between parameters that correlate the surface heat transfer and surface shear stress enhancements due to a turbulent free stream with levels between 10 percent < Tu < 20 percent. Second, a comparison will be made between the enhancements of skin friction relative to heat transfer.

Although free-stream turbulence studies date back to Kestin (1961), most of these studies have used free-stream turbulence levels generated with grids that are limited to 7 percent or less. There are several correlations that have been developed as a result of these lower (relative to the present study) free-stream turbulence studies. The most widely used correlation was developed by Hancock and Bradshaw (1983) based on the enhancement of skin friction due to grid-generated turbulence. Hancock and Bradshaw's correlating parameter, β, is both a function of turbulence level and ratio of dissipation length scale to boundary layer thickness and is of the form:

$$\beta = \frac{Tu\ (\text{percent})}{\left(\dfrac{L_u^\epsilon}{\delta} + 2\right)} \tag{1}$$

Blair (1983) applied the β parameter not only to his measured skin friction enhancement, but also to his heat transfer enhancement data. Blair reported two significant findings with regards to the Hancock and Bradshaw β parameter. First, Blair identified a low Reynolds number effect that attenuated the enhancement. Later, however, Castro (1984) found that this effect became increasingly less significant at higher free-stream turbulence levels. Second, Blair found that there were larger increases in the enhancement of heat transfer relative to skin friction as the free-stream turbulence levels increased.

Just recently, there have been studies done at free-stream turbulence levels above 7 percent, which have extended the range of the β parameter and have suggested other correlating parameters. This work includes that done by MacMullin et al. (1989) and researchers from the heat transfer group at Stanford University including Maciejewski and Moffat (1989, 1992a, b), Ames and Moffat (1990), and Sahm and Moffat (1992).

MacMullin et al. (1989) used a wall jet with turbulence levels ranging as high as 20 percent, but with a characteristically different velocity field than that of a boundary layer with a uniform mean field. When plotted in terms of the Hancock and Bradshaw β parameter, they found a large scatter in their data. For example at $\beta = 3.25$, $\mathrm{St}/\mathrm{St}_0|\mathrm{Re}_\theta$ ranged from 1.48 to 1.8. Maciejewski and Moffat (1989) also did an unconventional boundary layer study in which they used a free jet and were able to generate turbulence levels up to 60 percent. They were able to achieve up to $\beta \approx 28$ and found that there was a continual increase in the surface heat transfer. In contrast to Maciejewski and Moffat's results of continued increases in heat transfer, Johnson and Johnston's (1989) grid turbulence results showed that the shear stress enhancement peaked at $\beta \approx 2.8$.

Maciejewski and Moffat (1989) also proposed a new simpler parameter, St', which uses the maximum rms velocity found in the near-wall region. Their results in combination with other investigations indicated that, independent of flow geometry, St' was a function of turbulence level alone.

Ames and Moffat (1990) studied both skin friction and heat transfer enhancement, using a combustor simulator that generated turbulence levels as high as 20 percent. They proposed a TLR correlating parameter of the form:

$$\mathrm{TLR} = Tu\left(\frac{\Delta}{L_u^\epsilon}\right)^{0.33}\left(\frac{\mathrm{Re}_\Delta}{1000}\right)^{0.25} \tag{2}$$

Contributed by the International Gas Turbine Institue and presented at the 39th International Gas Turbine and Aeroengine Congress and Exposition, The Hague, The Netherlands, June 13–16, 1994. Manuscript received by the International Gas Turbine Institute March 19, 1994. Paper No. 94-GT-296. Associate Technical Editor: E. M. Greitzer.

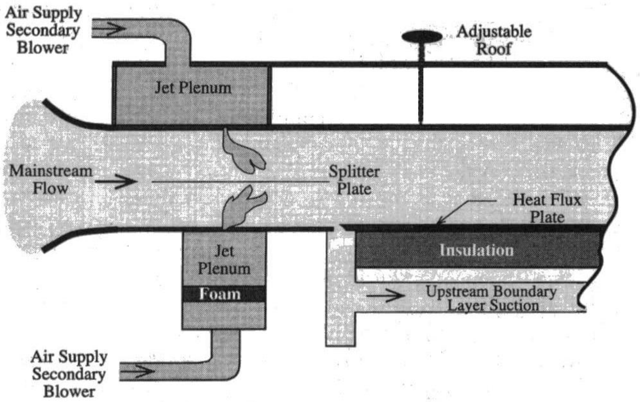

Fig. 1 Schematic of the wind tunnel test section including the turbulence generator

The TLR parameter uses integral quantities, where $\Delta = \theta$ for shear stress enhancement and $\Delta = \Delta 2$ for heat transfer enhancement, rather than boundary layer thicknesses. As pointed out by Ames and Moffat, defining the edge of a boundary layer with high free-stream turbulence levels is quite difficult.

Later, Sahm and Moffat (1992) used combinations of jets and grids to study the effects of free-stream turbulence levels as high as 30 percent on heat transfer and skin friction enhancements. Sahm found that both the β parameter and the TLR parameter were equal in correlating the skin friction and heat transfer enhancement. However, Sahm and Moffat point out that for their study there was a constant relation between the β parameter and the TLR parameter.

The following sections of this paper discuss the experimental facilities used for this study, the experimental flowfield investigated, and a comparison of the correlations given in the literature. There is also a comparison between the shear stress enhancement and heat transfer enhancement due to high free-stream turbulence.

Facility and Instrumentation

Experiments were conducted in a boundary layer wind tunnel located in the Turbulence and Turbine Cooling Research Laboratory at the University of Texas at Austin. The closed-loop tunnel was driven by a 5-hp fan. Located downstream of the fan were heat exchangers, which maintained a constant mainstream temperature, and a series of fine mesh screens, which conditioned the flow. Downstream of the screens and 9:1 tunnel contraction was the test section, which was 244 cm long, 61 cm wide, and 15.2 cm high. The test section, shown schematically in Fig. 1, contained the turbulence generator, a suction slot that removed any upstream boundary layer, an unheated leading edge plate, and the constant heat flux test plate.

The initial 60 cm of the test section was occupied by a turbulence generator specifically developed for this study (Thole et al., 1994). High free-stream turbulence levels were produced by high-velocity, normal jets injected into the mainstream cross-flow. On both the floor and roof of the wind tunnel were a row of opposing jets. Flow for the normal jets was driven by a 7.5-hp fan in a secondary flow loop. The flow was provided by diverting 20 percent of the flow from upstream of the main wind tunnel fan.

Downstream of the turbulence generator was the constant heat flux test plate. The plate consisted of a serpentine, monel heating element sandwiched between two thin Kapton films. The length and width of the test plate were 136 cm and 61 cm. The heater plate was bonded to a 12.7-mm-thick fiberglass composite (G-10). Below the plate were several layers of insulation, which minimized the conduction losses to less than 1 percent. The heat transfer data were corrected for radiation losses, which were between 15–20 percent of the total input power.

The measurements made for this study included surface temperatures, mean and rms velocity profiles, and turbulent integral length scales. Surface temperatures were measured using thermocouple strips previously used and reported by Sinha et al. (1990). The junction for these thin, Type E, thermocouples was 76 μm thick, or less than $y^+ = 2$. The uncertainty in Stanton numbers for the highly turbulent flow field was calculated to be ±5.5 percent at the start of the heat flux plate and ±4.1 percent at the end of the heat flux plate. A maximum deviation of 2.6 percent occurred between computed Stanton numbers using the boundary layer code TEXSTAN and measured Stanton numbers for the benchmark case.

The mean and rms velocities were measured using a Thermal Systems Inc., two-component laser-Doppler velocimeter (LDV) system with counterprocessors. The measured velocities were corrected for velocity bias errors using residence time weighting. The total uncertainty, including both precision and bias, for the mean velocity measurements in the case of the highly turbulent flow field was ±2.3 percent in the free stream and ±3.5 percent in the near-wall region. The total uncertainty for the fluctuating velocities in the case of the highly turbulent flow field was found to be ±2.5 percent in the free stream and ±3.7 percent near the wall. The uncertainty for the skin friction coefficient, which was due to the uncertainty in calculating the friction velocity, was ±3.6 percent. A maximum deviation of 3.6 percent occurred between calculated skin friction coefficients using correlations given by Kays and Crawford (1980) and coefficients obtained using a Clauser fit.

A hot-wire anemometer system measured the velocity fluctuations used to obtain integral time scales. The integral length

Nomenclature

Cf = friction coefficient
Cf' = friction coefficient based on $u'_{\max}$
Cf_0 = friction coefficient for a boundary layer with no free-stream turbulence
D = turbulence generator jet hole diameter
L_u^ϵ = dissipation length scale $[(\overline{u'^2})^{3/2}/U_\infty(d\overline{u'^2}/dx)$
$\mathrm{Re}_{\Delta 2}$ = enthalpy thickness Reynolds number
Re_θ = momentum thickness Reynolds number
St = Stanton number
St_0 = Stanton number for a boundary layer with no free-stream turbulence
St′ = Stanton number based on u'_{max}
TLR = turbulence scaling parameter (see Eq. (2))
Tu = streamwise turbulence intensity $= u'/U_\infty$
u' = rms velocity in streamwise direction
u_τ = wall friction velocity
U = mean local velocity in streamwise direction
U_∞ = free-stream velocity in streamwise direction
x = streamwise distance measured from the turbulence generator jets
y^+ = nondimensional vertical distance $= y\, u_\tau/\nu$
α = low-Re_θ function
β = turbulence scaling parameter (see Eq. (1))
Δ = boundary layer integral thickness
$\Delta 2$ = enthalpy thickness
δ = velocity boundary layer thickness
δ_{th} = thermal boundary layer thickness
Λ_x = integral turbulent length scale
θ = momentum thickness
τ_{total} = total wall shear stress

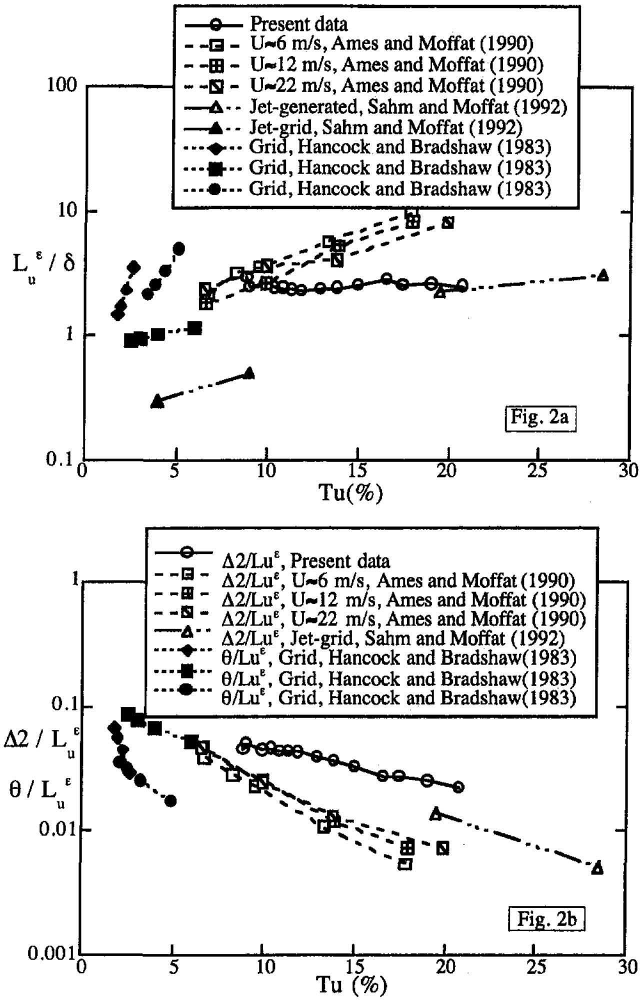

Fig. 2 Comparison of flow field characteristics for several studies in terms of the dissipation length scale and (*a*) boundary layer thickness ratios and (*b*) integral thickness ratios

scales were calculated using the measured time scales deduced from the autocorrelation, the local mean velocity, and invoking Taylor's hypothesis.

Turbulent Flow Field

The operating condition for the normal jet turbulence generator required a jet-to-mainstream velocity ratio of 17 at a mainstream velocity of nominally 8 m/s. The region of interest for this study was located 130 jet diameters downstream from the jet holes ($D = 5.08$ mm). This streamwise location corresponds to 25 cm downstream of the start of the heat flux plate, which was where the unheated starting length effects were negligible. At this location the turbulence level was $Tu = 20$ percent, which then decayed to a level of $Tu = 9$ percent at 300 jet diameters downstream from the jet holes. For the specific measurements of the streamwise turbulence decay, integral length scales (Λ_x), and the dissipation length scales (L_u^ϵ) for this study, refer to Thole and Bogard (1994). The mean and rms velocities were relatively uniform in the spanwise direction at ±4 and ±9 percent, respectively.

Figures 2(*a*) and 2(*b*) compare the flow field in this study to that used by other studies in terms of the turbulence level and normalized dissipation length scale. In comparison to the Hancock and Bradshaw grid-generated studies, the other studies shown in Figs. 2(*a*) and 2(*b*) have much higher turbulence levels. Taking into account all the data, the length scale ratios span two orders of magnitude.

In this study, the velocity and thermal boundary layer thicknesses were nominally the same thickness. The boundary layer growth with the decaying free-stream turbulence was severely attenuated and the boundary layer had essentially a constant thickness of nominally $\delta_{99} = 20$ mm along a streamwise distance of 60 cm. Attenuation of the boundary layer growth was also observed by Ames and Moffat (1990) and Sahm and Moffat (1992). Note that as the turbulence decays there is a loss of streamwise momentum flux, which causes an increase in pressure in the free stream, which may cause the growth attenuation.

In two independent grid-generated free-stream turbulence studies, both Blair (1983) and Simonich and Bradshaw (1978) indicated that there was a fixed value for the ratio of dissipation to integral length scales. However, they reported two different values with Blair having a ratio of $L_u^\epsilon/\Lambda_x = 1.5$, and Simonich and Bradshaw having a ratio of $L_u^\epsilon/\Lambda_x = 1.1$. For the study described here, the dissipation and integral length scales were also very similar, having a dissipation to integral length scale ratio ranging between $1.1 < L_u^\epsilon/\Lambda_x < 1.4$ over the region of interest. Data given by Ames and Moffat (1990), however, showed that this ratio varied from $1.6 < L_u^\epsilon/\Lambda_x < 2.6$, while data given by Sahm and Moffat (1992) varied from $1.8 < L_u^\epsilon/\Lambda_x < 3.6$. Assumptions that this ratio is a constant value cannot be made, in particular when devices other than grids are used.

Heat Transfer Enhancement

As described in the introduction, there are three correlations available to quantify high free-stream turbulence effects on surface heat transfer. These correlations include the Hancock and Bradshaw (1983) β parameter correlation, the Ames and Moffat (1990) TLR parameter correlation, and the Maciejewski and Moffat (1992a, b) St′ correlation.

Figure 3 shows β as a correlating parameter for the Stanton number enhancement due to high free-stream turbulence levels. The Hancock and Bradshaw β parameter does an adequate job in scaling the present data with those of Ames and Moffat (1990), but not the data of Sahm and Moffat (1992). Sahm and Moffat studied heat transfer in the presence of flat and convex walls, but only a limited set of data for the flat wall is discussed in this paper. Also shown in Fig. 3 is Blair's (1983) modification to the Hancock and Bradshaw correlation, which accounted for his larger measured heat transfer enhancements relative to skin friction enhancements.

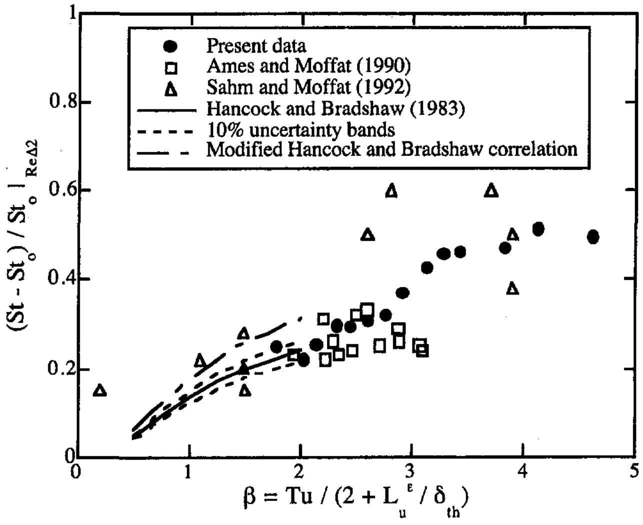

Fig. 3 Comparison of present data in terms of the Hancock and Bradshaw correlation (1983)

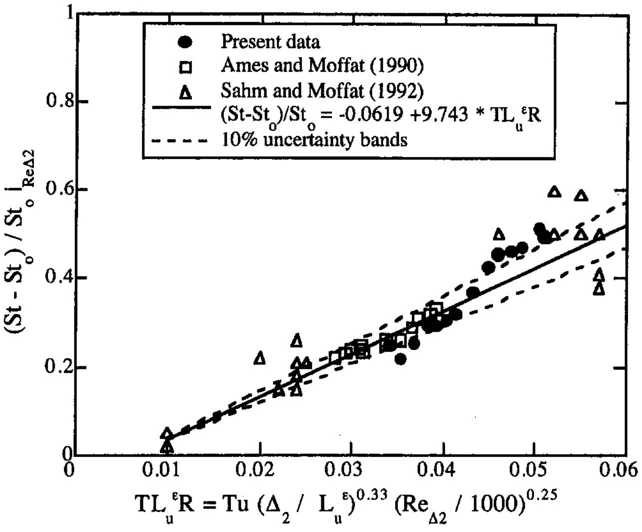

Fig. 4 Comparison of present data in terms of the Ames and Moffat (1990) correlation

Figure 4 compares the data in terms of the Ames and Moffat (1990) TLR parameter. The TLR parameter does a better job in scaling all three data sets. As was pointed out earlier, the boundary layer thickness is difficult to quantify in high free-stream turbulence studies and, hence, a better collapse using the TLR parameter may be due to using integral quantities.

The data plotted in terms of the Maciejewski and Moffat (1992b) St′ parameter are shown in Fig. 5. Included in Fig. 5 are data from Sahm and Moffat (1992) analyzed using two different $u'_{\max}$ values. The Stanford University data given in Fig. 5 were obtained from the appendices of the corresponding reports. However, the $u'_{\max}/u_\tau$ values given in the Sahm and Moffat appendix were somewhat lower than those peak values typically found in the near-wall region. Hence, the Sahm and Moffat St′ values for $Tu < 20$ percent were scaled, using $u'_{\max}/u_\tau = 2.8$. Again, the data represented in Fig. 5 do not include all of the Sahm and Moffat data, some of which show St′ values below the correlation. The Sahm and Moffat data that are represented here may include some unheated starting length effects. Sahm and Moffat have extensive data in both the pre- and post-curved regions, but a full discussion of this data is beyond the scope of this paper. Although there is some scatter in Fig. 5, the collapse is relatively good. However, the data do not indicate the 46 percent increase in St′ at a turbulence level of $Tu = 11$ percent as given by the correlation.

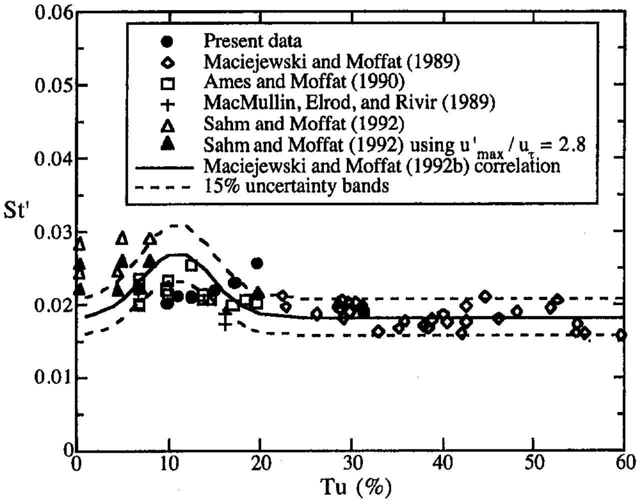

Fig. 5 Comparison of present data in terms of the Maciejewski and Moffat (1992b) correlation

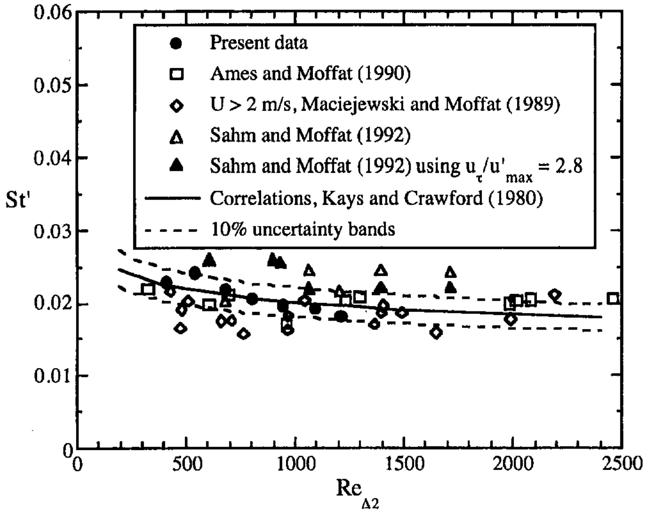

Fig. 6 Reynolds number effect on St′ compared with correlations

Figure 6 shows the dependence of St′ on the enthalpy thickness Reynolds number. The calculated St′ distribution with $Re_{\Delta 2}$ was based on turbulent boundary layer correlations given by Kays and Crawford (1980) and $u'_{\max}/u_\tau = 2.8$. The calculated St′ curve involved several steps with each step involving a turbulent boundary layer correlation. First, shear stresses were calculated based on Re_θ. Second, Re_θ was converted to Re_x. Third, Stanton numbers were calculated based on Re_x. Finally, using these Stanton numbers and an additional correlation, $Re_{\Delta 2}$ was calculated.

All of our data as well as most of Ames and Moffat's (1990) fall within the uncertainty of the values calculated from the correlations, indicating a slight Reynolds number dependence. The Sahm and Moffat (1992) data are slightly higher while Maciejewski and Moffat's (1989) data are slightly lower than those predicted by the correlation. For the Maciejewski and Moffat data, the turbulence levels were quite high ($Tu > 30$ percent) and, hence, may have a stronger effect than the Reynolds number.

One of the difficulties in applying the St′ correlation is that in order to determine the heat transfer coefficient, one must know beforehand what the $u'_{\max}$ value is. The $u'_{\max}$ used in this correlation is the value found in the near-wall region ($y^+ < 30$). However, if the turbulence levels are high enough, $u'_{\max}$ occurring in the near-wall region is the same rms velocity that occurs in the free stream. In this study, turbulence levels were measured throughout the boundary layer for free-stream turbulence levels ranging between 1 percent $< Tu <$ 20 percent. Figures 7(*a*) and 7(*b*) show the streamwise and vertical rms distributions for this range of turbulence levels. The data of Johnson and Johnston's (1989) grid turbulence study is also shown in Figs. 7(*a*) and 7(*b*). As seen in Fig. 7(*a*), the streamwise rms velocity distributions for free-stream turbulence levels below $Tu = 15$ percent show that the free-stream rms velocity is smaller than the $u'_{\max}$ that occurs inside the boundary layer. However, for the $Tu = 20$ percent case, the free-stream turbulence has penetrated very close to the wall such that the maximum streamwise rms value is the same as that of the free-stream level.

The vertical rms velocity distribution shown in Fig. 7(*b*) is significantly different from the streamwise rms velocity distribution. The velocity distributions indicate that while the streamwise fluctuations have a relatively flat profile throughout the boundary layer, the vertical fluctuations become attenuated to-

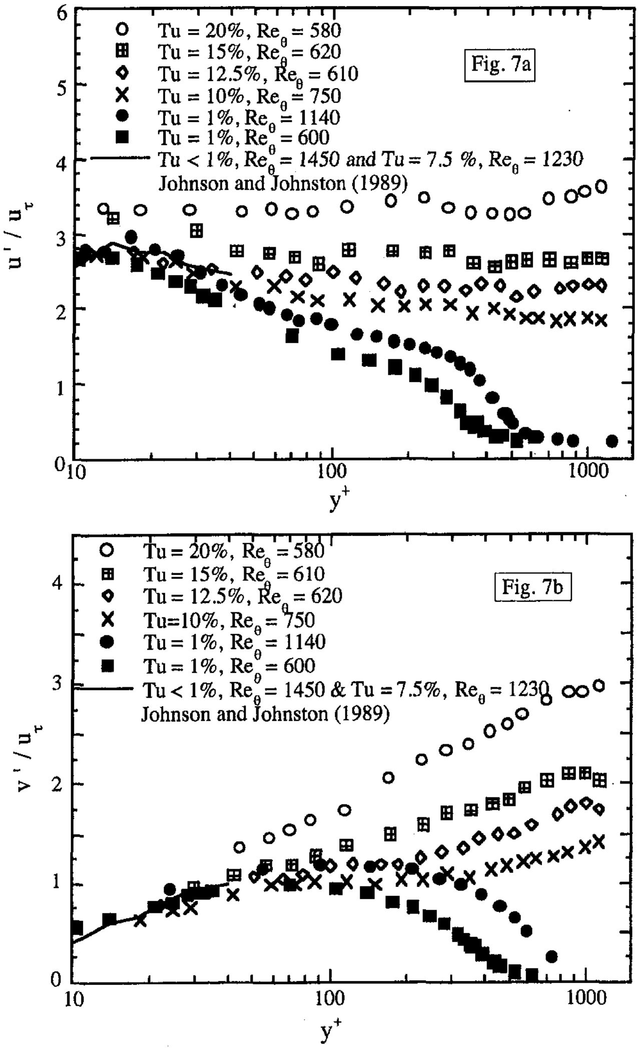

Fig. 7 Streamwise and vertical rms velocity profiles for several free-stream turbulence levels plotted in terms of inner variables

ward the wall. Large-scale eddies from the turbulent free stream have penetrated into the boundary layer, but only the vertical fluctuations of the large-scale eddies are restricted by the wall, which causes the attenuation through the boundary layer.

Skin Friction Enhancement

Similar to the heat transfer enhancement, the same correlations can be applied to scale the skin friction enhancement. The skin friction coefficient for the highly turbulent flow field was obtained using a Clauser fit to the log-law, similar to previous studies. These previous studies, including both grid-generated turbulence studies and the higher free-stream turbulence studies, have shown that increased free-stream turbulence levels cause fuller mean velocity profiles with sharply decreased wake strengths (Blair, 1983; Ames and Moffat, 1990; Thole, 1992; Sahm and Moffat, 1992).

In doing a Clauser fit, the data are forced to fall onto the log-law. To evaluate the accuracy of the wall shear stress using the Clauser fit, comparisons were made between the Clauser fit values for $\tau_{w,\mathrm{loglaw}}$ and measurements of the total stress, viscous plus Reynolds shear stress, near the wall. The total shear stress data were normalized using the shear velocity, $\tau_{w,\mathrm{loglaw}}$, determined from a Clauser fit to the log-law, and are shown in Fig. 8. The Clauser fit was done in the log-law region of the mean velocity profile between $y^+ = 30$ and $y/\delta_{99} = 0.2$. The von Kármán constant of $\kappa = 0.41$ and $C = 5.0$ were used in the log-law equation. Results from these measurements indicate a normalized total stress of nominally $\tau_{\mathrm{total}}/\tau_{w,\mathrm{loglaw}} = 1$ for all free-stream turbulence levels, confirming the accuracy of the log-law fit in determining the wall shear stress. The pressure gradient, expected due to the decaying free-stream turbulence, was estimated to have less than a 1 percent effect on the total stress in the near wall region.

Figures 9(a) and 9(b) show the skin friction enhancement in terms of the Hancock and Bradshaw (1983) β parameter. Figure 9(b) shows the data with the low Reynolds number correction given by Blair (1983). Although the data fall closer to the correlation with the low Reynolds number correction, there is more scatter in the data when the low Reynolds number correction is made.

The Hancock and Bradshaw correlation (1983) was obtained from their grid-generated study and has been found by other investigators, such as Blair (1983), to be in agreement with their own data. Except for the Johnson and Johnston (1989) and Rüd (1985) data, all the other data shown in Figs. 9(a) and 9(b) were obtained from very high free-stream turbulence tests (using devices other than grids). A large portion of these data falls below the Hancock and Bradshaw correlation even with the low Reynolds number correction (Fig. 9b). The data in Figs. 9(a) and 9(b) indicate that there is a leveling off of the skin friction enhancement. This is contrary to the heat transfer enhancement, which was shown in Fig. 3.

Figure 10 shows the skin friction enhancement in terms of Ames and Moffat's TLR parameter. Again it is evident that the shear stress enhancement for the higher turbulent studies falls below that of Hancock and Bradshaw's grid-generated turbulence study. In using the TLR parameter for the skin friction enhancement, there is a larger scatter as compared with the β parameter.

Analogous to St′, which was used to scale the heat transfer coefficient, a new parameter, Cf', was found to scale the wall shear stress. Similarly, Cf' uses the maximum rms streamwise velocity as the velocity scale and, hence, results in $Cf' = 2\,(u_\tau/u'_{\mathrm{max}})^2$. As was shown in Fig. 7(a), the peak rms levels start to increase for free-stream turbulence levels greater than 12.5 percent, which accordingly results in a decrease of Cf'. Figure 11 shows Cf' as a function of turbulence level for both the present data set as well as that of other investigators provided that the profiles were measured close enough to the wall to obtain the peak values. No length scale or Reynolds number effects on Cf' were detected. Unlike St′, which remains con-

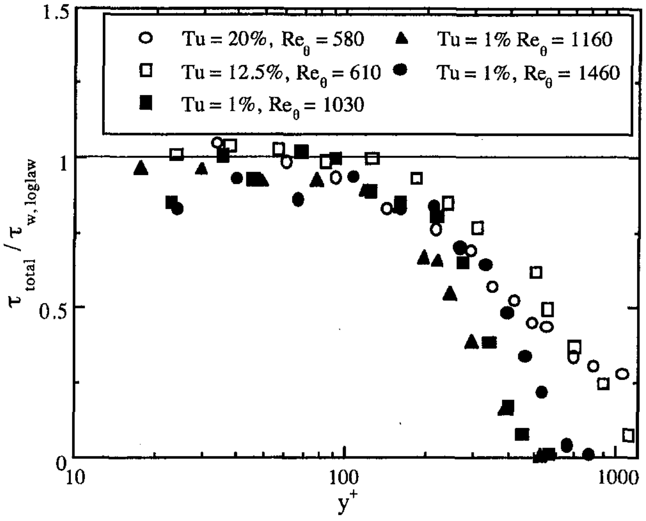

Fig. 8 Total shear stress normalized by log-law shear stress

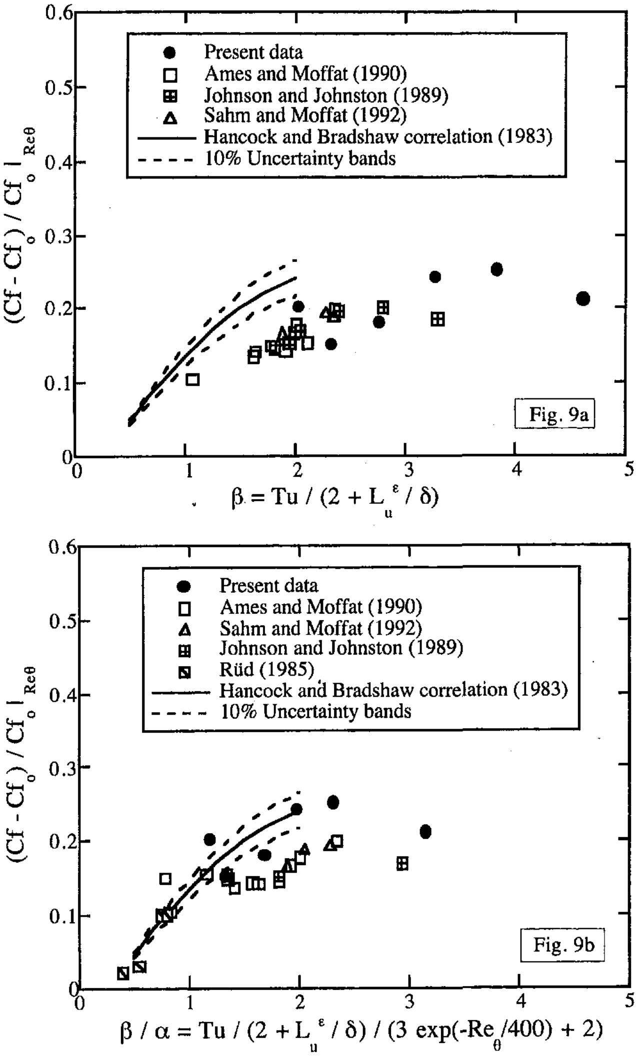

Fig. 9 Comparison of present data using the Hancock and Bradshaw correlation (*a*) without and (*b*) with low Reynolds number correlation

stant at all turbulence levels, Cf' starts to decrease above $Tu = 12.5$ percent.

Comparison of Heat Transfer and Skin Friction Enhancement

Enhancements of skin friction and surface heat transfer due to high free-stream turbulence have been presented in the last two sections. Figure 12 shows a comparison of the skin friction and heat transfer enhancements in terms of the β parameter. A consistent result for all the data is a similar enhancement for skin friction and surface heat transfer at smaller β values, but a significantly larger heat transfer enhancement at larger β values. The disparity between enhancement of skin friction and heat transfer occurs because the enhancement of heat transfer increases steadily with increasing β, but the skin friction enhancement peaks at $\beta \approx 3$ and decreases at larger β values.

At free-stream turbulence levels below 10 percent, there is an enhancement of skin friction due to the increase in boundary layer entrainment. At free-stream turbulence levels above 10 percent, the outer turbulence penetrates into the boundary layer, replacing shear-producing motions associated with the fluid/wall interaction with turbulent free-stream motions. These non-shear-stress-producing motions are called inactive motions.

The theory on inactive motions was first hypothesized by Townsend (1961) and later investigated by Bradshaw (1967).

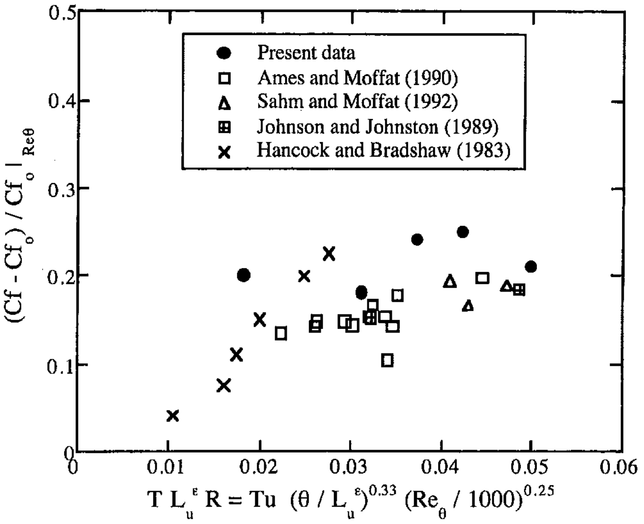

Fig. 10 Comparison of present data with the Ames and Moffat (1990) correlation

Inactive motions are large-scale eddies, typically in the outer part of the boundary layer. Active motions are responsible for the shear stress production and are smaller in scale.

The rms velocity profiles shown in Figs. 7(*a*) and 7(*b*) indicate the penetration of these large-scale motions from the free stream into the boundary layer. These inactive motions from the free stream carry a large streamwise fluctuating component while the vertical fluctuating component is attenuated due to the wall. Velocity spectra and length scales, reported for this same study by Thole and Bogard (1995), have also indicated the presence of these large-scale motions throughout the boundary layer with high free-stream turbulence levels.

In evaluating the correlations for heat transfer enhancement, St′ is particularly good at very high free-stream turbulence levels. A question arises as to why, at the higher turbulence levels, St′ shows no effect of length scale or Reynolds number. The reason that these effects are not apparent is because at these high turbulence levels ($Tu > 20$ percent), the large-scale motions from the free stream penetrate into the boundary layer with large streamwise fluctuating components. Although these motions are not active in producing shear stress (as shown by the decrease in Cf' with increasing turbulence levels), these motions are still thermally active.

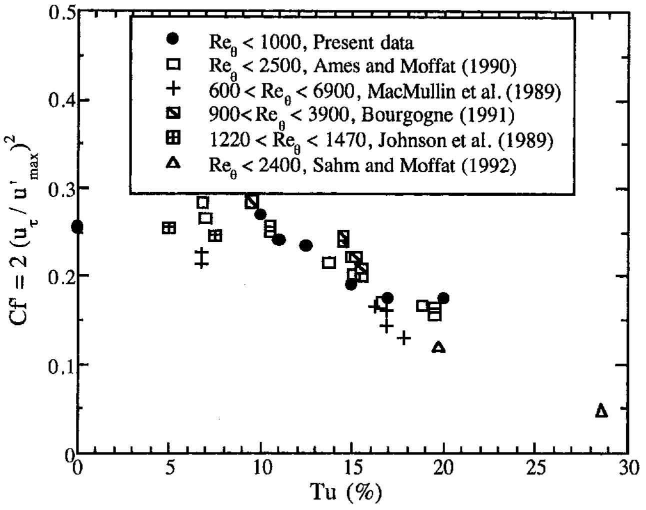

Fig. 11 Correlation of surface shear stress using Cf'

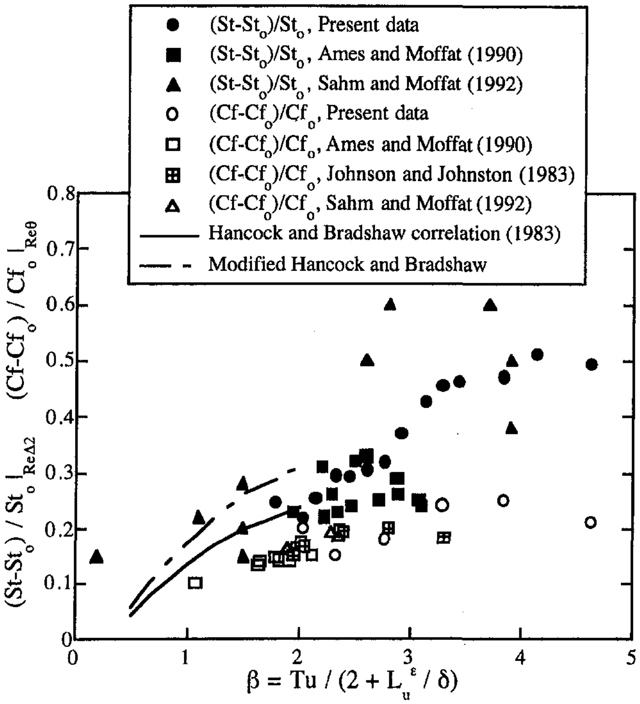

Fig. 12 Comparison of heat transfer and skin friction enhancement

Conclusions

The previous sections have compared the β, TLR, St$'$, and Cf' correlations for a wide range of turbulent flow field characteristics from several independent studies. Free-stream turbulence levels ranged from 1 percent $< Tu <$ 28 percent, while the dissipation length scale to boundary layer thickness ratio ranged over two orders of magnitude. The results of this study show that the TLR parameter is slightly more successful in scaling the heat transfer enhancement and the β parameter is slightly more successful at scaling the skin friction enhancement.

The simpler St$'$ correlation is particularly good at very high free-stream turbulence levels ($Tu >$ 20 percent) for two reasons. First, at $Tu =$ 20 percent the peak streamwise rms velocity in the near-wall region is the same as the free-stream rms velocity, which makes the correlation relatively easy to apply. Second, at high turbulence levels there do not appear to be any Reynolds number or length scale effects. At $Tu <$ 20 percent, there is more scatter in the St$'$ data, which is in part due to a Reynolds number effect.

A new parameter, Cf', was introduced to scale the skin friction. Cf' is inversely proportional to the square of $u'_{\max}/u_\tau$. Cf' remains constant until $Tu \approx$ 12 percent and then begins to decrease as free-stream turbulence levels increase.

All the data presented here indicate higher heat transfer enhancements relative to skin friction enhancements independent of the correlation used. The skin friction enhancement does not continue to increase at high turbulence levels because large-scale turbulent eddies from the free stream penetrate into the boundary layer. These large eddies, which are non-stress-producing and are also known as inactive motions, replace what would typically be smaller-scale stress-producing motions. These same large-scale eddies are, however, effective in removing heat and, hence, thermally active. This is particularly evident in comparing St$'$ and Cf'. St$'$ remains constant as free-stream turbulence levels continue to increase because the large-scale motions present from the free stream are continuing to remove heat. Hence, at high turbulence levels the heat transfer coefficient scales with the maximum streamwise rms level. Alternatively, Cf' decreases as free-stream turbulence levels increase because inactive motions penetrate into the boundary layer from the free stream and do not contribute to the wall shear stress.

Acknowledgments

We gratefully acknowledge the support of the Wright Laboratory and Allied-Signal Aerospace Corporation. We would like to thank Professor Michael Crawford for his helpful discussions. The first author would also like to thank Professor Sigmar Wittig and the Institut für Thermische Strömungsmaschinen for support while writing this paper.

References

Ames, F. E., and Moffat, R. J., 1990, "Heat Transfer With High Intensity, Large Scale Turbulence: The Flat Plate Turbulent Boundary Layer and the Cylindrical Stagnation Point," Stanford University Report No. HMT-44.

Blair, M. F., 1983, "Influence of Free-Stream Turbulence on Turbulent Boundary Layer Heat Transfer and Mean Profile Development, Part II—Analysis of Results," ASME *Journal of Heat Transfer*, Vol. 105, pp. 41–47.

Bourgogne, H. A., 1991, "The Development of a Turbulent Boundary Layer Beneath a Two-Stream Mixing Layer," M. S. Thesis, University of Houston.

Bradshaw, P., 1967, "Inactive Motion and Pressure Fluctuations in Turbulent Boundary Layers," *J. Fluid Mechanics*, Vol. 30, pp. 241–258.

Castro, I. P., 1984, "Effects of Freestream Turbulence on Low Reynolds Number Boundary Layer Flows," ASME *Journal of Fluids Engineering*, Vol. 106, pp. 298–106.

Comte-Bellot, G., and Corrsin, S., 1966, "The Use of a Contraction to Improve the Isotropy of Grid-Generated Turbulence," *J. Fluid Mechanics*, Vol. 25, pp. 657–682.

Hancock, P. E., and Bradshaw, P., 1983, "The Effect of Free-Stream Turbulent Boundary Layers," ASME *Journal of Fluids Engineering*, Vol. 105, pp. 284–289.

Hinze, J. O., 1975, *Turbulence*, 2nd ed., McGraw-Hill, New York.

Johnson, P. L., and Johnston, J. P., 1989, "Active and Inactive Motions in a Turbulent Boundary Layer—Interactions With Free-Stream Turbulence," presented at the Seventh Symposium on Turbulent Shear Flows, Stanford University.

Kays, W. M., and Crawford M. E., 1980, *Convective Heat and Mass Transfer*, 2nd ed., McGraw-Hill, New York.

Kestin, J., Maeder, P. F., and Wang, H. E., 1961, "Influence of Turbulence on the Heat Transfer From Plates With and Without a Pressure Gradient," *Int. J. Heat Mass Transfer*, Vol. 3, p. 133.

Koutmos, P., and McGuirk, J. J., 1989, "Isothermal Flow in a Gas Turbine Combustor—a Benchmark Experimental Study," *Experiments in Fluids*, Vol. 7, p. 344.

Maciejewski, P. K., and Moffat, R. J., 1989, "Heat Transfer With Very High Free Stream Turbulence," Stanford University, Report HMT-42.

Maciejewski, P. K., and Moffat, R. J., 1992a, "Heat Transfer With Very High Free-Stream Turbulence: Part I—Experimental Data," ASME *Journal of Heat Transfer*, Vol. 114, pp. 827–833.

Maciejewski, P. K., and Moffat, R. J., 1992b, "Heat Transfer With Very High Free-Stream Turbulence: Part II—Analysis of Results," ASME *Journal of Heat Transfer*, Vol. 114, pp. 834–839.

MacMullin, R., Elrod, W., and Rivir, R., 1989, "Free-Stream Turbulence From a Circular Wall Jet on a Flat Plate Heat Transfer and Boundary Layer Flow," ASME JOURNAL OF TURBOMACHINERY, Vol. 111, pp. 78–86.

Rüd, K., 1985, "Transitionale Grenzschichten unter dem Einfluß hoher Freistromturbulenz, intensiver Wandkühlung und starken Druckgradienten in Heißgasströmungen," Ph.D. Dissertation, Universität Karlsruhe, Karlsruhe, Germany.

Sahm, M. K., and Moffat, R. J., 1992, "Turbulent Boundary Layers With High Turbulence: Experimental Heat Transfer and Structure on Flat and Convex Walls," Stanford University, Report HMT-45.

Simonich, J. C., and Bradshaw, R., 1978, "Effect of Free Stream Turbulence on Heat Transfer Through a Turbulent Boundary Layer," ASME *Journal of Heat Transfer*, Vol. 100, pp. 671–677.

Sinha, A. K., Bogard, D. G., and Crawford, M. E., 1991, "Film Cooling Effectiveness Downstream of a Single Row of Holes With Variable Density Ratio," ASME JOURNAL OF TURBOMACHINERY, Vol. 113, No. 3.

Thole, K. A., 1992, "High Freestream Turbulence Effects on the Transport of Heat and Momentum," Ph.D. Dissertation, University of Texas at Austin, Turbulence and Turbine Cooling Research Laboratory.

Thole, K. A., and Bogard, D. G., 1995, "High Freestream Turbulence Effects on Turbulent Boundary Layers," under review for the ASME *Journal of Fluids Engineering*.

Thole, K. A., Bogard, D. G., and Whan-Tong, J. L., 1994, "Generating High Freestream Turbulence Levels," *Experiments in Fluids*, Vol. 17, pp. 375–380.

Townsend, A. A., 1961, "Equilibrium Layers and Wall Turbulence," *J. Fluid Mechanics*, Vol. 11, pp. 97–120.

Heat Transfer Measurements in an Annular Cascade of Transonic Gas Turbine Blades Using the Transient Liquid Crystal Technique

R. F. Martinez-Botas[1]

G. D. Lock

T. V. Jones

Department of Engineering Science,
Oxford University,
Oxford, United Kingdom

Heat transfer measurements have been made in the Oxford University Cold Heat Transfer Tunnel employing the transient liquid crystal technique. Complete contours of the heat transfer coefficient have been obtained on the aerofoil surfaces of a large annular cascade of high-pressure nozzle guide vanes (mean blade diameter of 1.11 m and axial chord of 0.0664 m). The measurements are made at engine representative Mach and Reynolds numbers (exit Mach number 0.96 and Reynolds number 2.0×10^6). A novel mechanism is used to isolate five preheated blades in the annulus before an unheated flow of air passes over the vanes, creating a step change in heat transfer. The surfaces of interest are coated with narrow-band thermochromic liquid crystals and the color crystal change is recorded during the run with a miniature CCD video camera. The heat transfer coefficient is obtained by solving the one-dimensional heat transfer equation for all the points of interest. This paper will describe the experimental technique and present results of heat transfer and flow visualization.

1 Introduction

The Oxford University Engineering Laboratory Blowdown Tunnel [1] has been successfully researching large-chord linear cascades at engine representative Mach and Reynolds numbers since 1978 [2]. The tunnel is a transient facility, enabling testing to be undertaken at low cost compared to the equivalent continuous running installations [3].

The Blowdown Tunnel has been substantially modified to test a large annular cascade of high-pressure nozzle guide vanes (NGVs) with a mean blade diameter of 1.11 m and an axial chord of 0.0664 m [4]. The annular geometry models the three-dimensional aspects of the flow through aeroengine blade rows. The vane geometry (1.4 times larger than engine scale) is given in Table 1. The correct radial pressure gradient is established and secondary flows can be studied in detail. The size of the facility is only matched by low-speed or short-duration tunnels and the test duration of the facility (about 7 seconds for engine design conditions) enables transient measurement techniques to be employed. The tunnel allows an independent variation of Reynolds number and Mach number, or equivalently the upstream and downstream pressures can be independently and continuously varied.

One of the main penalties in carrying out heat transfer tests within turbine passages is the requirement to heat the working fluid. In the facility used here this is avoided by preheating or precooling the surfaces under investigation. Once the required surface temperature is achieved, an unheated stream of air is passed over the NGVs and the heat transfer coefficient is measured by recording the changing blade surface temperature. This technique gives the name to the tunnel and represents a principal feature in the new facility.

The concept of a *cold heat transfer tunnel* (CHTT) was first suggested by Jones [5], and subsequent testing was performed on a small linear cascade [6]. This test showed the power of this technique to examine the detailed heat transfer distribution with particular application to turbine research.

Although the work described in this paper involves only solid blades, the primary aim of the CHTT is to test heavily film cooled blading under engine representative conditions. The research performed on solid blades is aimed at obtaining heat transfer and aerodynamic data for comparison with computational predictions. The aerodynamic studies are being performed in parallel with the heat transfer work described in this paper [7].

2 Experimental Technique

In the work reported here the heat transfer levels are obtained by employing the transient liquid crystal technique [8–10], which has been well established at Oxford. For completeness, the outline of the method and the conditions necessary for the analysis are outlined briefly below. The NGV surface tempera-

Table 1 NGV details

Mid-span axial chord (c_{ax})	0.0664 m
Mean pitch at exit	0.09718 m
Span at exit	0.08076 m
Turning angle	73°
Throat area	0.08056 m^2
Mean blade diameter	1.113 m

---

[1] Present address: Lecturer in Turbomachinery, Department of Mechanical Engineering, Imperial College of Science, Technology, and Medicine, London SW7 2BX United Kingdom.

Contributed by the International Gas Turbine Institute and presented at the 39th International Gas Turbine and Aeroengine Congress and Exposition, The Hague, The Netherlands, June 13–16, 1994. Manuscript received by the International Gas Turbine Institute February 19, 1994. Paper No. 94-GT-172. Associate Technical Editor: E. M. Greitzer.

ture is measured as it is subjected to a step change in convective heating. The NGV is made of a good thermal insulator, is initially at a uniform temperature, and the surface temperature is monitored using thermochromic liquid crystals. The surface temperature history is then governed by the one-dimensional transient conduction equation,

$$\frac{\partial^2 T}{\partial n^2} = \frac{1}{\alpha}\frac{\partial T}{\partial t}.$$

This is solved with the following boundary conditions:

$$-k\frac{\partial T}{\partial n_{n=0}} = h(T_{\text{gas}} - T_{n=0}),$$

$$-k\frac{\partial T}{\partial n_{n=\infty}} = 0,$$

and

$$T(n, 0) = T_{\text{initial}}.$$

In these equations T is the temperature, t is time, h is the heat transfer coefficient, k is the perspex conductivity, and n is a length normal to the surface. The solution to these equations for a constant heat transfer coefficient and gas temperature can be written as

$$\frac{T_{\text{crystal}} - T_{\text{initial}}}{T_{\text{gas}} - T_{\text{initial}}} = 1 - \exp\left(\frac{h^2 t}{\rho c k}\right)\operatorname{erfc}\left(\frac{h\sqrt{t}}{\sqrt{\rho c k}}\right).$$

Here ρ and c are the perspex density and heat capacity. This technique will be used in a transonic situation. It is therefore necessary to use the recovery or adiabatic wall temperature as T_{gas} in the equations above. This choice of gas temperature will take into account viscous heating through the boundary layer and ensure the constancy of the heat transfer coefficient [11]. This temperature was obtained assuming a recovery factor (r) equal to 0.87 (taken as the Prandtl number raised to the $\frac{1}{3}$ power), and using the relationship between the local Mach number and the adiabatic temperature, viz.

$$T_{\text{gas}} = T_\infty\left[1 + r\frac{\gamma - 1}{2}\text{M}_\infty^2\right]. \tag{1}$$

In this equation T_∞ and M_∞ are the local temperature and Mach number.

Hence the heat transfer coefficient is defined using $T_{\text{gas}} - T_{n=0}$ as the driving temperature [11]. From a knowledge of the color change time, the substrate material properties (conductivity, density, and heat capacity) and the temperature boundary conditions, the heat transfer coefficient can be found from these equations at every point on the NGV surface.

3 Experimental Apparatus

A schematic diagram of the CHTT [4] is shown in Fig. 1. The operation of the tunnel is controlled by pneumatically activated ball valves. Air flows from the high-pressure reservoir (31 m^3 at 3 MPa) into a regulator system from which part of the flow enters an ejector [12]. The remainder passes into the annular test section containing the NGVs, subsequently exhausting to atmosphere. An assembly drawing and photograph of the CHTT test section are shown in Figs. 2 and 3. Large levels of turbulence are created using a resistance plate using 20 mm holes and with an open area of 9 percent. The holes are approximately 40 hole diameters upstream of the NGV leading edge plane. Turbulence spectra, measured using a hot-wire anemometer, are presented in [4].

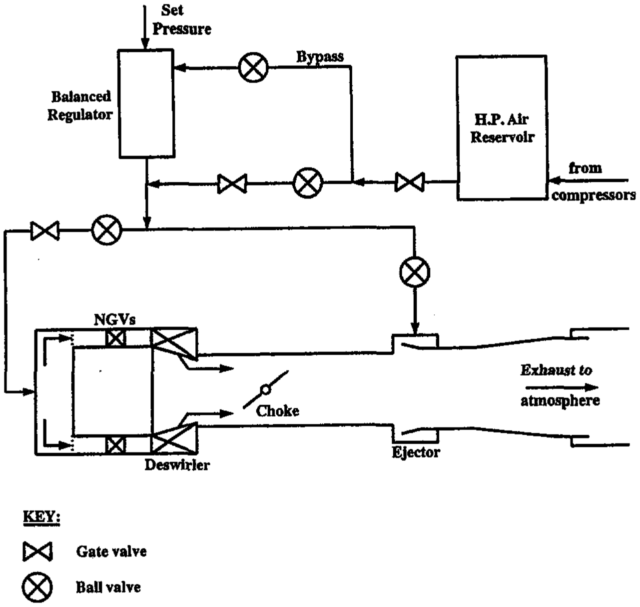

Fig. 1 Schematic diagram of the CHTT

In order to perform transient heat transfer tests, a step change in heat transfer is required. In the present study the NGVs are preheated before the run by isolating four passages of the annulus with a purposely designed shutter mechanism. This shutter is removed during the run when steady flow conditions have been achieved in the tunnel after the initial startup transient (~1.5 s) has ended.

Figures 4 and 5 show a schematic drawing and photograph of the shutter system. Two independently driven shutters are used to isolate five blades in the annulus. The upstream shutter seals against the leading edge of the two outside blades and along the inlet contraction to the NGVs on the inner casing. The downstream shutter seals by registering along the inner casing behind the blades and touching the trailing edges of the two outer blades. These shutters create a sealed volume containing the blades of interest. There is a difference between the inner and outer casing radii and a spring-loaded step has been designed so that the shutter plates are able to preserve the curvature of the outer casing when retrieved and seal against the inner casing when deployed. The three springs driving the upstream and downstream steps are of sufficient stiffness to ensure the step restores the inner casing curvature before the shutters arrive at the outer casing.

The shutters are driven by two pistons. The heat transfer cassette is placed in the side of the CHTT (see Fig. 3) so that the motion of the shutters is horizontal. In order to absorb the momentum of the shutters efficiently and without mechanical damage, heavy-load oil dampers are coupled with the double-ended pistons as shown in Fig. 5. The shutter plates move on two heavy-duty bearing-rail assemblies capable of withstanding

Nomenclature

c = specific heat
c_{ax} = axial chord
h = heat transfer coefficient
k = conductivity
M = Mach number
Nu = Nusselt number
n = normal length
r = recovery factor
Re = Reynolds number
t = time
T = temperature
ρ = density

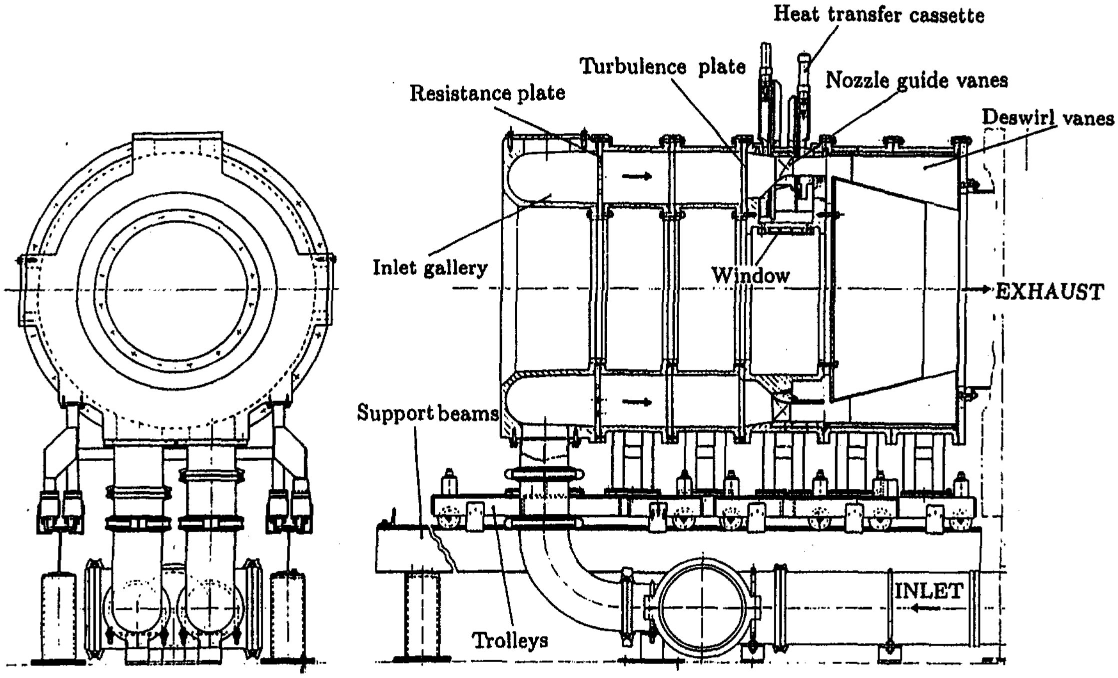

Fig. 2 A schematic diagram of the CHTT test section

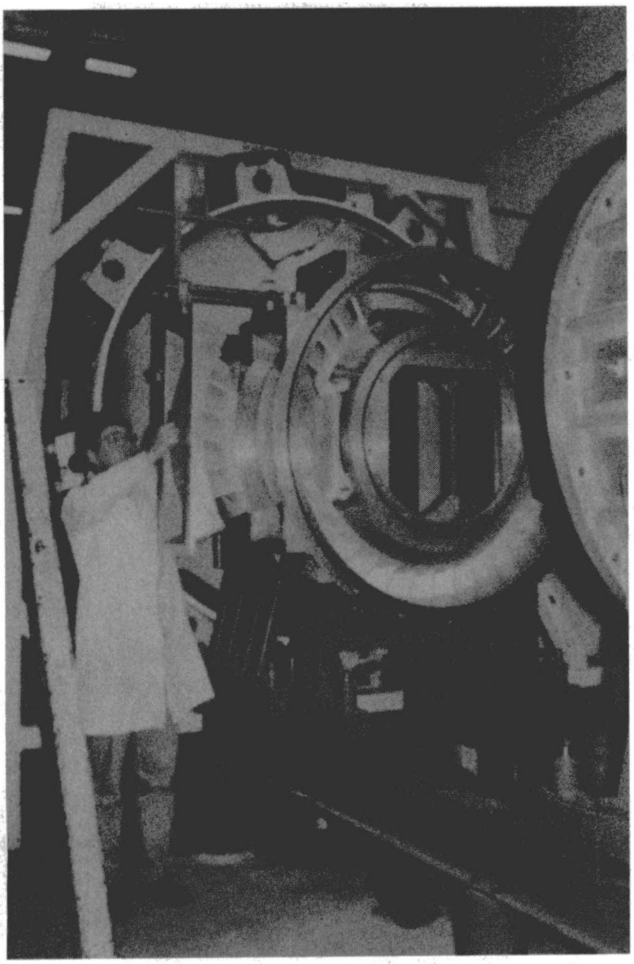

Fig. 3 Photograph of the CHTT test section

the large forces the plates experience during normal operation. The shutters experience these large forces when they open during the run where the pressure difference across them is 1.3 bars at design engine conditions. To create the necessary step change in heat transfer, the piston and shutter assembly was designed with the intention of opening in 100 ms. During actual operation, with flow through the cascade, a traveling time of 120 ms was achieved.

The blades in the cassette have been machined out of perspex. This material has good insulating properties that makes it suitable for use with the liquid crystal technique. It also keeps heat losses to a minimum and allows good visual access as it is transparent when polished.

As mentioned above the enclosure is preheated. A system that recirculates hot air has been constructed. A high head centrifugal fan is used to supply the air, heated by a 3 kW heater, which raises the temperature in the enclosure to the required level. There are four inlets to the cassette through which the air

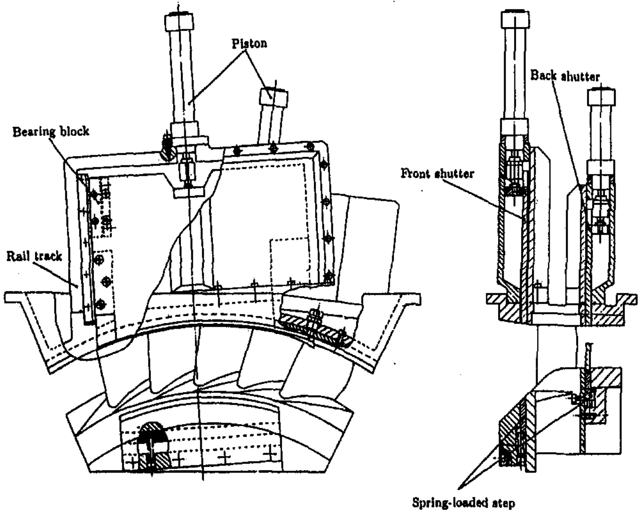

Fig. 4 Assembly drawing of the heat transfer cassette

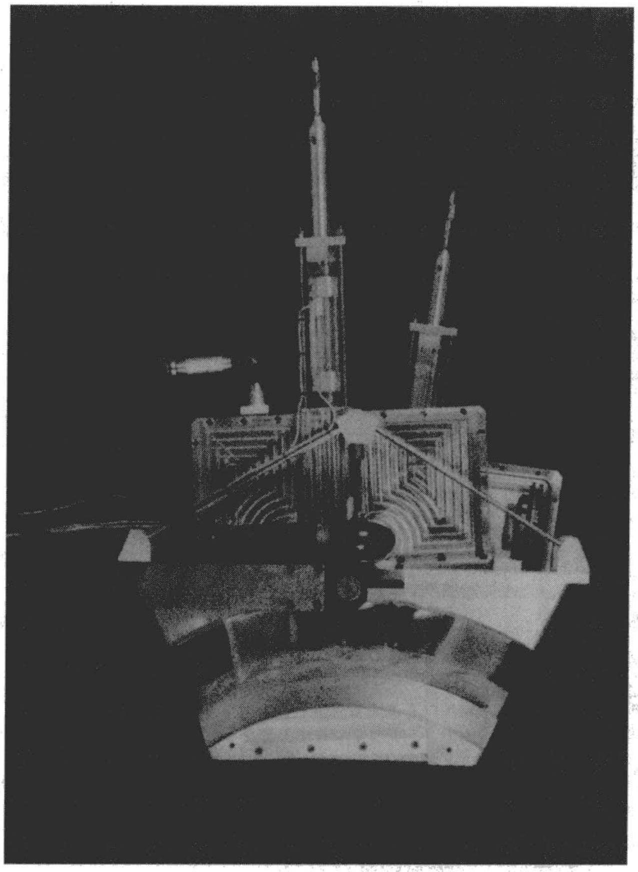

Fig. 5 Photograph of the heat transfer cassette

passes into twelve passages inside the shutter plate. By introducing the hot air into the enclosure in this manner, the shutter plates themselves are heated, and this eliminates the possibility of disturbing the temperature uniformity of the surfaces by the proximity of a cold surface.

4 Instrumentation

The positions of the moving shutters are recorded using four miniature proximity switches. These yield measurements of the times when the two shutters leave the inner casing and arrive at the outer casing. Thus the traveling times of the shutters are obtained and time markers are available to assess any disturbances of the flow caused by their motion.

In order to investigate the initial surface temperature uniformity of the blades, twelve thermocouples have been attached to the central test blade. Prior to the run the temperature readings from these thermocouples are equal within 1°C, indicating a uniform initial blade temperature. The initial temperature was typically 60°C. The error in the heat transfer coefficient h produced by this uncertainty was $\sim$2 percent. The overall error in h was 7 percent on average. The major contribution to the error resulted from the uncertainty in the start time and in tests subsequent to those reported here the shutter opening time has been reduced considerably.

Table 2 CHTT/engine comparison

Parameter	Engine	CHTT
Inlet total pres	32 bar	2 bar
Turbine inlet temp	1750-1800 K	290 K
Blade/gas$_{max}$ temp	0.58	0.8–1.15
Exit Re No (c_{ax})	2×10^6	2×10^6
Exit Mach No	0.96	0.96
Peak Nu No	3500	3500
Peak h	8400 Wm^{-2}K^{-1}	1300 Wm^{-2}K^{-1}
Mass flow rate	120 kg/s	38 kg/s

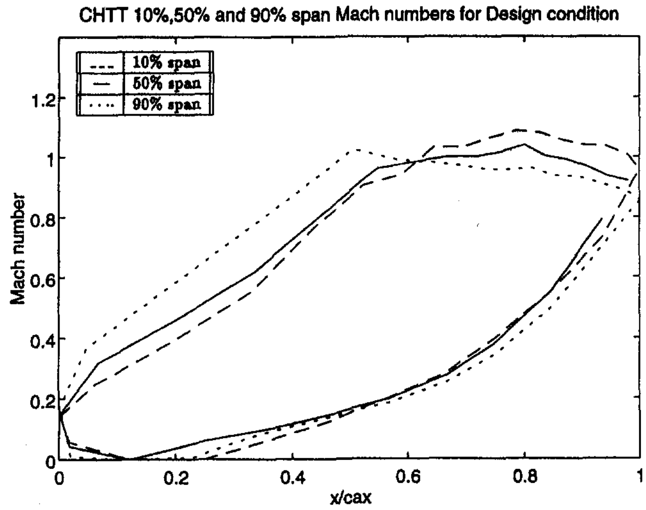

Fig. 6 Isentropic Mach number distribution

In the tests described in this paper the pressure and suction surfaces of the central perspex blade in the cassette were coated with two thermochromic liquid crystals. The crystal temperatures chosen for the pressure surface were 30°C and 25°C, while 25°C and 20°C were used on the suction surface. To view the color changes during the run a miniature CCD video camera was placed inside the rig. The head diameter of the camera is 17.4 mm and the body is 60 mm long. The camera is rigidly attached to the outer annulus upstream of the heat transfer cassette. It has been staggered considerably to avoid shedding a wake into the passage under study. The lighting for the enclosure came from the outside of the cascade, through the perspex portion of the outer end wall. A 500 W halogen light was used for this purpose.

It should be noted that different parts of the model subtended a range of angles at the camera during the test. The effect of angle on perceived color is relatively small for encapsulated

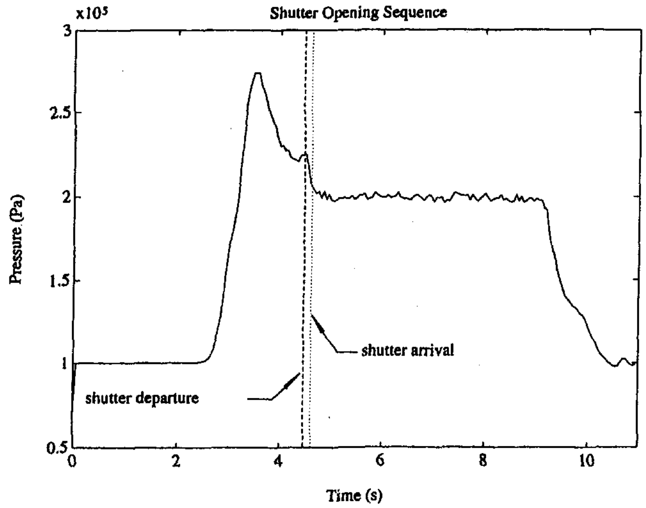

Fig. 7 Upstream pressure response during the shutter opening sequence

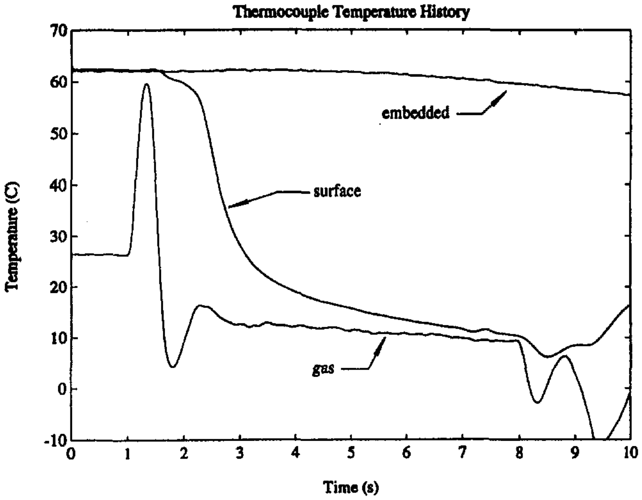

Fig. 8 Temperature histories from thermocouples

narrow-band liquid crystals. This was checked during the calibration of the liquid crystals for these tests.

5 Results and Discussion

The results described in this section correspond to the NGV design condition. A comparison between conditions in a typical modern aeroengine and the CHTT is summarized in Table 2. For the tests in the CHTT a turbulence intensity of 13 ± 3 percent and an integral length scale of 24 ± 5 mm was measured using a hot-wire anemometer in the leading edge plane [4, 13].

The CHTT does not model the engine blade to gas temperature ratio. The influence of this temperature ratio on heat transfer mainly enters through gas property variations through the boundary layer. This influence is well documented for both laminar and turbulent boundary layers. A secondary influence is through the stability of the laminar boundary layer and hence the transition point. However, above free-stream turbulence levels of 1–2 percent the transition is via a bypass mechanism and hence at the large levels of turbulence in the tests reported here the gas-to-blade temperature ratio would have no influence. The tests therefore represent engine conditions well in that transition is not influenced and property effects may be taken into account.

A comparison between the isentropic Mach distributions at 10, 50, and 90 percent span on both the suction and pressure aerofoil surfaces of the NGV is shown in Fig. 6. It is clear that the data show the inward (tip to hub) radial pressure gradient near the back of the blade.

Figure 7 shows the static pressure upstream of the working section with the shutter in operation. The shutter arrival and departure times are also shown. As can be seen the flow adjustment time is minimal. The variation of the perspex temperature on and below the surface, as well as the upstream gas temperature during the run, are shown in Fig. 8. These measurements are made using thermocouples located, respectively, on the aerofoil surface, 2 mm below the surface, and upstream of the test section. As the tunnel starts, cold air leaks into the enclosed volume, causing a drop in the initial temperature before the shutter opens. The thermocouple embedded in the blade indicates a very small change in the perspex temperature below the surface. The free-stream temperature is shown to vary between 12.5 and 10°C during the regulated region of the run. The initial peak is due to the compression heating of the gas in the upstream section.

Figures 9–12 are views of the suction surface and show the liquid crystal color changes at different times during the run. It should be noted that due to the transparency of polished perspex, the camera can view regions close to the trailing edge of the blade through the adjacent blade. The small region of the surface that cannot be viewed from this angle can be seen by moving the camera to another position in the annulus and repeating the test. This view is shown in Fig. 13. The white dots on the blade surface were used as a grid and are along locations of 10, 30, 50, 70, and 90 percent span. In these particular photographs the suction surface has been viewed through the pressure side of the blade with liquid crystals under a thin coat of black paint.

Figure 9 shows a region of high heat transfer in the fore part of the blade near the tip where the crystal has changed color first. As the run proceeds the crystal starts to change near the second or third spanwise dot. After 1.75 seconds the crystal has changed color on most of the blade except near the leading and trailing edges. Figure 12 clearly shows a region of low heat transfer near the tip of the blade. This corresponds to a region influenced by secondary flows. This region of separated flow on the suction surface has been identified using flow visualization with colored oil as shown in Fig. 14.

The video image has been imaged processed [14] to obtain light intensity plots for all the points of interest. A typical intensity history, near the surface thermocouple location, is shown in Fig. 15. Note that the reheating of the surface from the core of the blade after the run has finished is also shown. From these plots the times at which each crystal changed color at every position on the blade surface can be accurately measured.

Figure 16 shows the experimentally deduced Nusselt number (based on axial chord) variation at midspan. The data show that the highest levels of heat transfer occur near the trailing edge of the blade on the pressure surface. The heat transfer levels are at a minimum near the stagnation region and increase toward the rear of the blade. On the suction surface, a peak of heat transfer is observed near 8 percent surface distance. Beyond 20 percent surface distance the heat transfer level is fairly constant. The uncertainty limits on the measurements are also shown. The sources of uncertainty are the following: errors on the temperature measurements (0.2°C), errors resulting from the initial temperature variation of 1°C, flow initiation time errors (0.113 seconds), and present uncertainty in the knowledge of the thermal product ($\sqrt{\rho c k} = 569 \pm 29$ W m^{-2} K^{-1} $s^{0.5}$ [15]).

A two-dimensional boundary layer heat transfer prediction has been supplied by Rolls-Royce [16]. This code was run at the tunnel conditions and is also shown in Fig. 16 for comparison. The agreement is good except in the stagnation region and a general slight underprediction on the pressure surface. In the experiment, transition occurs at about 8 percent surface distance. The code predicts transition at about 15 percent and this difference is probably due to the large turbulence levels in the tunnel. The vane leading edge has a large radius of curvature and in such cases identification of the stagnation point can be difficult if point measurements (i.e., heat transfer gages) of heat transfer are made. In the liquid crystal measurements reported here the heat transfer rate was continuously measured hence there was no uncertainty in identifying the stagnation point.

Figures 17 and 18 show contours of the experimentally deduced heat transfer coefficient for the pressure and suction surfaces. These figures are projections of the curved aerofoil surfaces onto a two-dimensional plane. The pressure surface contours show a small variation in heat transfer coefficient with span position, as expected from the Mach number distribution and flow visualization carried out in the tunnel. The suction surface shows the interesting features discussed above. These are the region of high heat transfer in the forward part of the blade near the tip and the region of low heat transfer corresponding to the separation region shown in the flow visualization. Referring to the separation lines in Fig. 14, the passage vortex (*a*) and the horseshoe vortex (*b*) sweep onto the suction surfaces at different positions. The passage vortex creates the region of low heat transfer associated with the thicker thermal boundary layer, whereas the region of high heat transfer is apparent where the

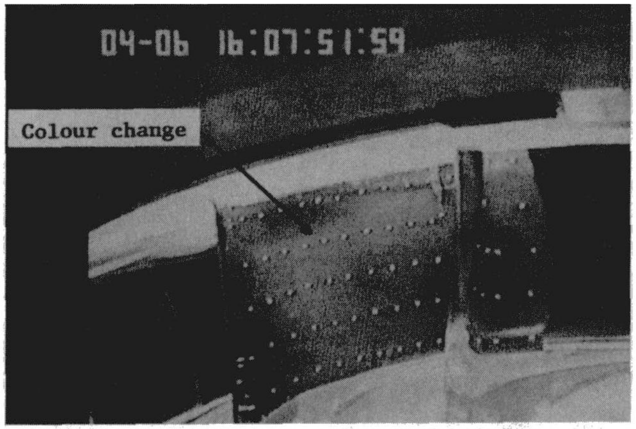

Fig. 9 View of the liquid crystals on the suction surface 1.4 s after the shutter opens

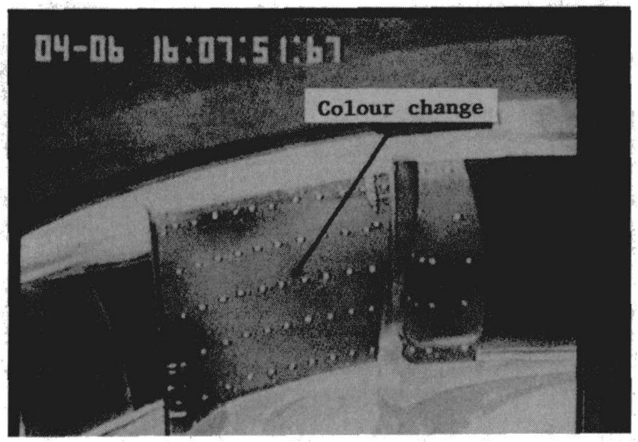

Fig. 10 View of the liquid crystals on the suction surface 1.48 s after the shutter opens

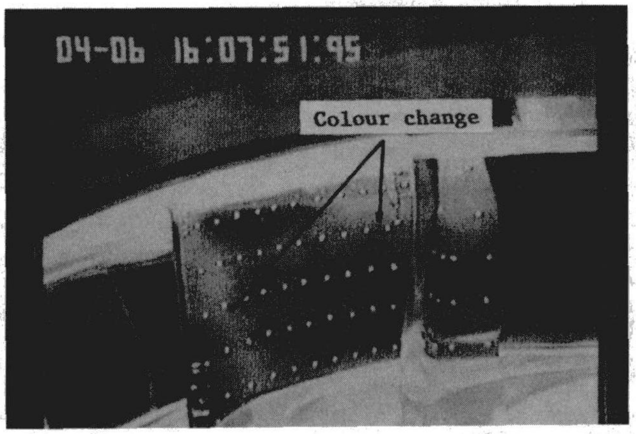

Fig. 11 View of the liquid crystals on the suction surface 1.76 s after the shutter opens

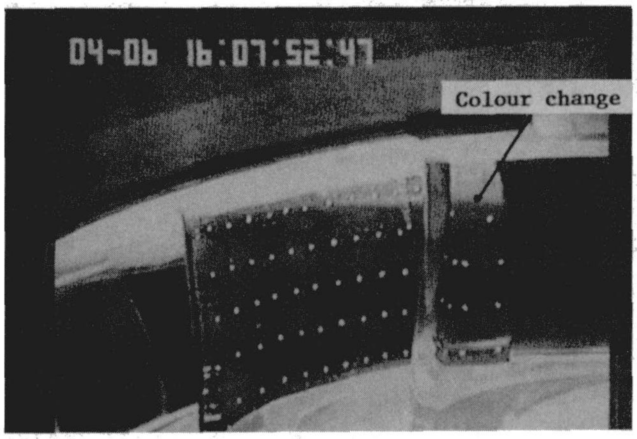

Fig. 12 View of the liquid crystals on the suction surface 2.28 s after the shutter opens

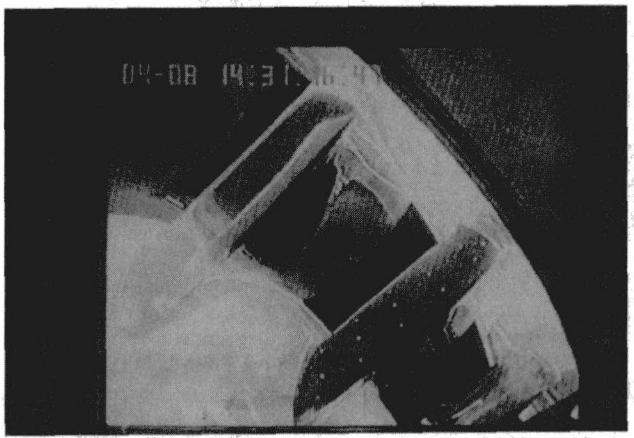

Fig. 13 View of the liquid crystals on the forward part of the suction surface

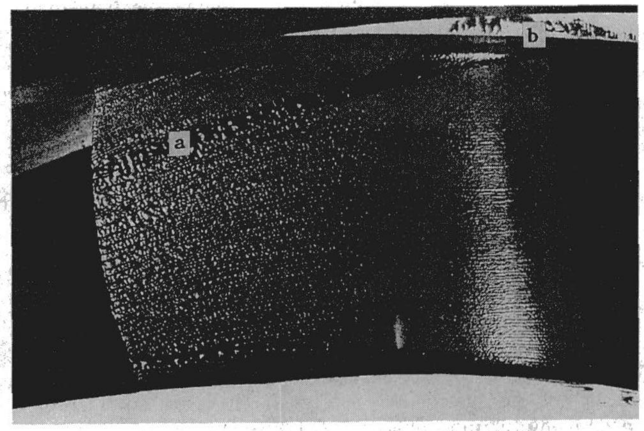

Fig. 14 Flow visualization on the suction surface

horseshoe vortex passes onto the suction surface. The central part of the vane shows a fairly uniform heat transfer level (about 850 W/m^2 K) and this level is well predicted by the two-dimensional heat transfer code.

6 Conclusions

The transient liquid crystal technique has been successfully used for the first time in an annular cascade of nozzle guide vanes at engine representative Reynolds and Mach numbers and free-stream turbulence intensity. Global measurements of the heat transfer coefficient have been obtained on both the pressure and suction surfaces. The principal features of the heat transfer on the aerofoil suction surface have been explained using flow visualization. The average uncertainty in the measurements of the heat transfer coefficient was 7 percent. These measurements have been compared favorably with a two-dimensional boundary-layer code at midspan.

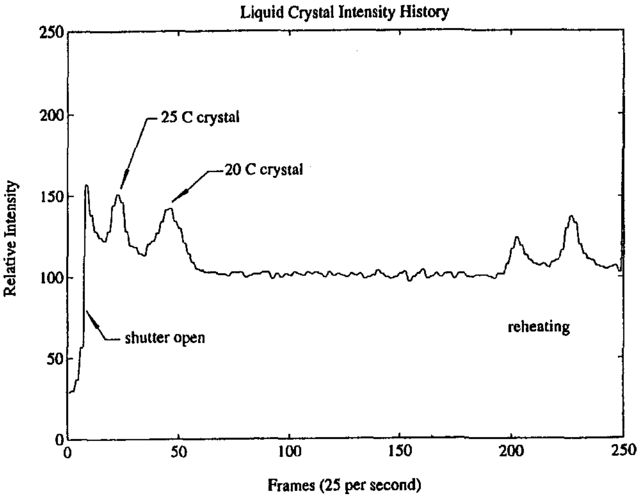

Fig. 15 Liquid crystal intensity history

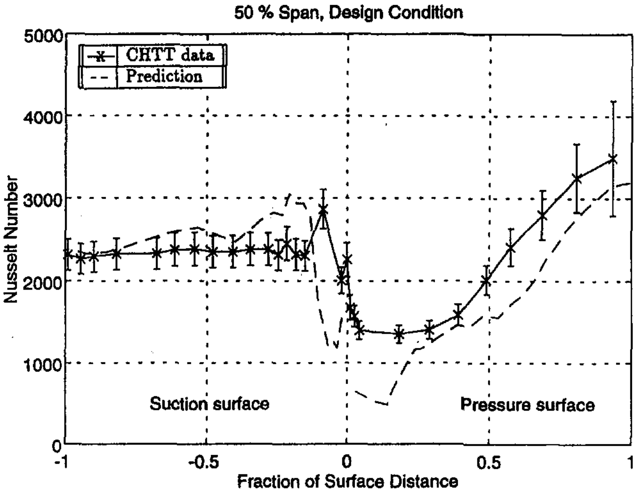

Fig. 16 Midspan heat transfer results at engine design condition

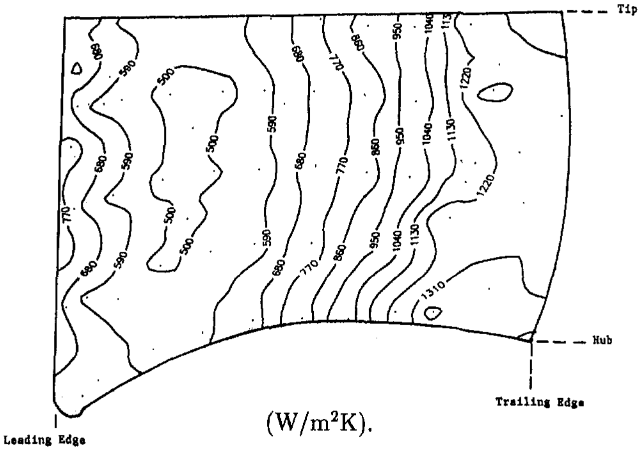

Fig. 17 Pressure surface heat transfer coefficient contours

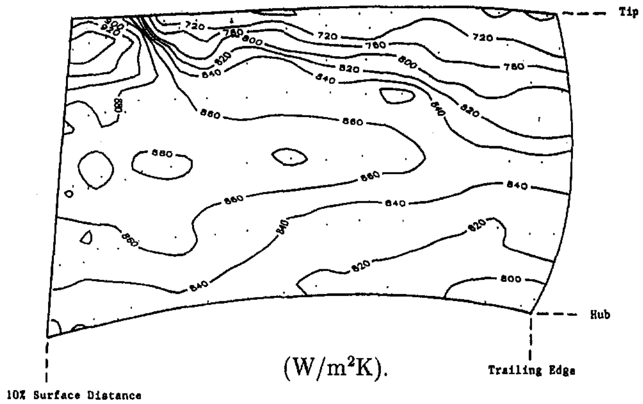

Fig. 18 Suction surface heat transfer coefficient contours

Acknowledgments

The authors would like to thank Rolls-Royce plc for funding this work, granting permission for publication, and supplying the heat transfer computational predictions. The authors are grateful for the assistance of Messrs. A. J. Main, M. C. Spencer, and Z. Wang.

References

1 Baines, N. C., Oldfield, M. L. G., Jones, T. V., Shultz, D. L., King, P. I., and Daniels, L. C., "A Short-Duration Blowdown Tunnel for Aerodynamic Studies on Gas Turbine Blading," ASME paper No. 82-GT-312, 1982.

2 Jones, T. V., "Gas Turbine Studies at Oxford, 1969–1987," ASME Paper No. 88-GT-112, 1988.

3 Jones, T. V., Oldfield, M. L. G., Ainsworth, R. W., and Arts, T., "Transient-Cascade Testing in Advanced Methods of Cascade Testing," AGARDograph AG 328, 1993.

4 Martinez-Botas, R. F., Main, A. J., Lock, G. D., and Jones, T. V., "A Cold Heat Transfer Tunnel for Gas Turbine Research on an Annular Cascade," ASME Paper No. 93-GT-248.

5 Jones, T. V., "A Cold Heat Transfer Tunnel," OUEL Internal Report No. 1274/78, 1978.

6 Ireland, P. T., Wang, Z., Jones, T. V., and Byerley, A. R., "A Cold Heat Transfer Tunnel Employing Liquid Crystals for Measuring Full Surface Heat Transfer Coefficients Over Turbine Blade Passages," presented at the 9th Symposium of Measuring Techniques for Transonic and Supersonic Flow in Cascades and Turbomachines, Oxford, 1988.

7 Main, A. J., "Experimental and Theoretical Cascade Areodynamics," First Year Report, Oxford University, 1991.

8 Harvey, N. W., Wang, Z., Ireland, P. T., and Jones, T. V., "Measurements in Nozzle Guide Vane Passages in Linear and Annular Cascades in the Presence of Secondary Flows," AGARD-CP-469, Paper 24, 1989.

9 Ireland, P. T., and Jones, T. V., "The Measurement of Local Heat Transfer Coefficients in Blade Cooling Geometries," AGARD-CP-390, Paper No. 28, 1986.

10 Ireland, P. T., and Jones, T. V., "Detailed Measurements of Heat Transfer on and Around a Pedestal in Fully-Developed Channel Flow," *Proc. 8th Int. Heat Transfer Conf.*, San Francisco, CA, 1986.

11 Jones, T. V., "Definition of Heat Transfer Coefficient in the Turbine Situation," Turbomachinery Conference, IMechE Paper No. C423/046, 1991.

12 Baines, N. C., King, P. I., Oldfield, M. L. G., and Daniels, L. C., "The Use of Tandem Ejector Pumps in an Intermittent Blowdown Tunnel," ASME Paper No. 84-GT-226.

13 Martinez-Botas, R. F., Spencer, M. C., Lock, G. D., and Jones, T. V., "The Measurement of Full Surface Heat Transfer Coefficients Over Turbine Blade Passages Using a Cold Heat Transfer Tunnel," *Proceedings of IMechE CCGT-3 Turbomachinery Seminar*, London, Oct. 1993.

14 Wang, Z., "The Application of Thermochromic Liquid Crystals to Detailed Turbine Blade Cooling Measurements," DPhil Thesis, Oxford University, 1991.

15 Baugh, J. W., Ireland, P. T., Jones, T. V., and Saniei, N., "A Comparison of the Transient and Heated-Coating Methods for the Measurement of Local Heat Transfer Coefficients in a Pin Fin," ASME *Journal of Heat Transfer*, Vol. 111, 1989, pp. 877–881.

16 Forest, A. E., "Engineering Predictions of Transitional Boundary Layers," AGARD-CP-224, 1977.

Heat Transfer Measurements on Turbine Airfoils Using the Naphthalene Sublimation Technique

M. Häring

A. Bölcs

Swiss Federal Institute of Technology,
EPFL,
Lausanne, Switzerland

S. P. Harasgama

ABB Power Generation Ltd.,
Gas Turbines,
Baden, Switzerland

J. Richter

Department of Flight Propulsion,
Technical University Darmstadt,
Darmstadt, Federal Republic of Germany

Results of heat transfer measurements on a typical turbine blade and a vane in a linear cascade have been obtained using the naphthalene sublimation technique. The tests on the vane were performed at the nominal flow angle, whereas for the turbine blade an off-design angle was chosen to study the influence of a separation bubble on the heat transfer. The exit Mach number was varied from $M_2 = 0.2$ to 0.4 and the exit Reynolds number ranged from $Re_2 = 300{,}000$ to 700,000. Comparisons with numerical codes have been conducted. The measurements were performed in a linear test facility containing five airfoils. Two tailboards and two bypass vanes allowed us to achieve a good periodicity of the flow. The aerodynamic flow conditions were measured using pressure taps and Laser-Two-Focus (L2F) anemometry. About 40 static pressure taps gave a precise Mach number distribution over the suction and the pressure side of the airfoil. L2F measurements were used to determine the downstream flow angles. The heat transfer coefficient was measured using the naphthalene sublimation technique. This method is based on the heat and mass transfer analogy for incompressible flow. A 0.5 mm thin naphthalene layer was applied to the middle airfoil and exposed to the flow for about 45 minutes. The sublimation was then measured in over 500 points on the airfoil, which allowed a high resolution of the heat transfer coefficient. Due to its high resolution, the sublimation technique shows the presence of and the precise location of the laminar-to-turbulent transition point and the separation bubble. The measurements on the vane were compared with two separate two-dimensional boundary layer programs, which were TEXSTAN (Texas University) and TEN (Sussex University). The programs incorporate the k–epsilon turbulence model with several different formulations. The laminar–turbulent transition was predicted quite well with TEN, which slightly damps out the production of turbulent kinetic energy in order to ensure a smooth transition zone. In the case of the blade, the naphthalene sublimation technique was able to predict the size and the location of the separation bubble as well as the reattachment with a very high precision.

Introduction

In modern gas turbines, the turbine inlet temperature has steadily been increased to improve the efficiency and the power output. High temperatures and transient temperature responses of engine components can, however, produce large thermal stresses. The lifetime of highly stressed components decreases significantly with increasing metal temperature. Hence, knowledge of the detailed heat transfer characteristics is required for the design of airfoils that have to operate for a certain guaranteed number of hours without failure. The main parameters that influence the heat transfer coefficient along the turbine airfoil are the Reynolds number, the free-stream turbulence, the surface curvature, the inlet Mach number, and the inlet flow angle. Further studies on the influence of the combined effects of these parameters are still needed to validate or to improve numerical predictions. In the present work, the naphthalene sublimation technique was used to measure the local heat transfer coefficient on two different turbine airfoils. This method was well established by Eckert and Goldstein (1976) and applied by Presser (1968), Chen and Goldstein (1992), and Berg et al. (1991). Chen and Goldstein used this technique to study the influence of secondary flow near the endwall on the local heat transfer coefficient on the suction side of a turbine airfoil, whereas Berg et al. applied the method to investigate the effect of rotation on the local coolant flow and heat transfer in turbine airfoils. The purpose of the present study is to give detailed heat transfer characteristics for turbine airfoils to validate and improve confidence in the accuracy of existing computational codes. Measurements were also conducted to study the influence of a separation bubble on the local heat transfer coefficient.

Test Facility and Measuring Equipment

Wind Tunnel. The experiments were performed in a large linear wind tunnel facility with a test section of 100 × 340 mm as shown in Fig. 1. This test facility is supplied from a continuously running air source, which delivers a mass flow of 10 kg/s with a maximum pressure ratio of 3.5. The experimental setup for the present study in the linear test facility consists of five airfoils, which are mounted on a disk. The inlet flow angle β_1 can then be adjusted by rotating the disk. Both the isentropic exit Mach number (M_{2s}) and the downstream flow periodicity are regulated by two tailboards. A further regulation of the flow periodicity can be achieved with the two bypass vanes. Although only five profiles are present in the cascade, a good flow

---

Contributed by the International Gas Turbine Institute and presented at the 39th International Gas Turbine and Aeroengine Congress and Exposition, The Hague, The Netherlands, June 13–16, 1994. Manuscript received by the International Gas Turbine Institute February 15, 1994. Paper No. 94-GT-171. Associate Technical Editor: E. M. Greitzer.

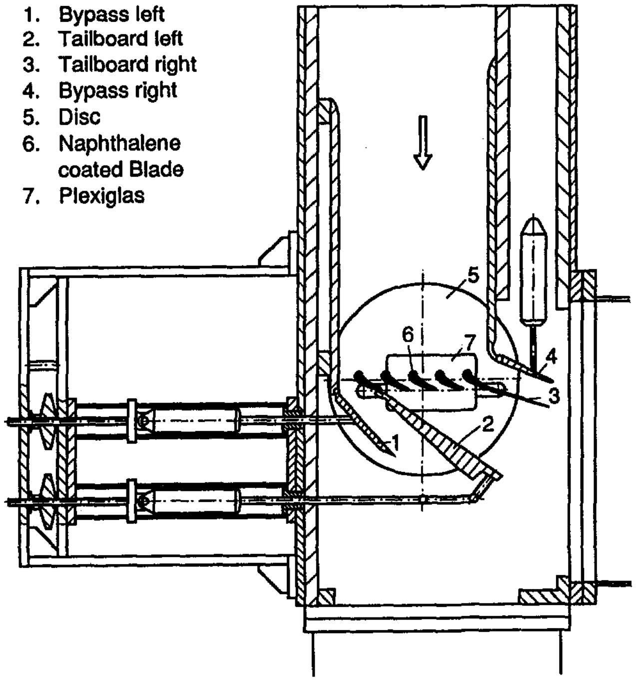

Fig. 1 Schematic view of the linear test facility

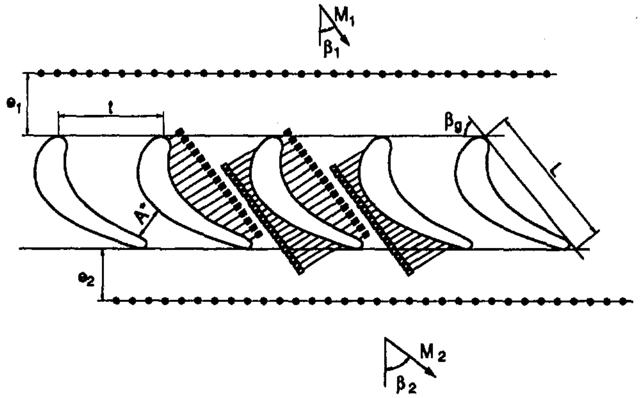

Fig. 2 Pressure taps in the linear test facility

periodicity is obtained (Bölcs and Sari, 1988). Total pressure and total temperature are measured in the settling chamber.

The inlet and outlet flow conditions are verified by blade endwall pressures up- (30 pressure taps) and downstream (30 pressure taps) of the cascade (Fig. 2). The airfoil surface pressures were measured at the midspan of the airfoil surfaces (both suction and pressure sides) forming the two center flow passages of the cascade. To determine the outlet flow angle a Laser Two-Focus anemometer was used. The turbulence intensity was obtained with a hot-wire probe of 5 μm diameter in conjunction with a DANTEC 55M10 anemometer system. The probe was located 75 mm in front of the airfoils. Only the turbulence intensity in the mean flow direction was measured.

Cascade Geometry. In the present study two different profiles, Cascade V and Cascade B, were measured. Their characteristics are summarized in the Table 1.

Test Airfoil. From the five airfoils, only the center airfoil was modified for mass transfer measurements. This airfoil consists of three parts: two smooth side pieces and a sand-blazed piece in the middle (Fig. 4). One side piece contains four thermocouples being located over the airfoil as well as the pressure taps described above. A special mechanism was constructed to have fast access to the center airfoil, which has to be exchanged rapidly.

Equivalent nondimensional parameters

Heat transfer	Mass transfer
Nusselt number	Sherwood number
$\mathrm{Nu} = \dfrac{\alpha L}{\lambda}$	$\mathrm{Sh} = \dfrac{b \cdot L}{D}$
Prandtl number	Schmidt number
$\mathrm{Pr} = \dfrac{c_p \mu}{\lambda}$	$\mathrm{Sc} = \dfrac{\nu}{D}$
Stanton number	Stanton number
$\mathrm{St} = \dfrac{\mathrm{Nu}}{\mathrm{Re\,Pr}}$	$\mathrm{St}' = \dfrac{\mathrm{Sh}}{\mathrm{Re\,Sc}}$

Nomenclature

b = mass transfer coefficient
c_N = concentration of naphthalene
c_p = specific heat capacity
C = empirical constant
d = thickness of the naphthalene layer
D = diffusion coefficient
e = distance (see Fig. 2)
L = chord length
M = Mach number
$\dot{m}$ = mass flow of naphthalene
m = empirical constant
n = empirical constant
p = pressure
p_D = pressure of naphthalene vapor
R = gas constant
s = curviline distance from leading edge
T = temperature
t = pitch
α = heat transfer coefficient
β = flow angle
β_g = stagger angle (see Fig. 3)
δ = boundary layer thickness
δ_T = temperature boundary layer thickness
Δd = sublimation losses
$\Delta\tau$ = exposure time
κ = isentropic exponent
λ = heat conduction coefficient
μ = dynamic viscosity
ν = kinetic viscosity
ρ = density
$\rho_{\dot{m},N}$ = free-stream partial density of naphthalene
$\rho_{s,N}$ = wall partial density of naphthalene

Subscripts

∞ = free stream
L = with respect to the chord length
N = naphthalene
s = surface
x = with respect to x
1 = inlet
2 = outlet

Table 1 Specification of the test cascades

Cascade	V	B
L [mm]	74.5	77.8
t/L [-]	0.86	0.82
β_g	51.85°	51°
e_1/L [-]	0.67	0.64
e_2/L [-]	0.36	0.35
# Pressure taps on the airfoil suction surface	19	21
# Pressure taps on the airfoil pressure surface	12	17
Nominal inlet flow angle	0°	46°
Nominal outlet flow angle	70°	64°

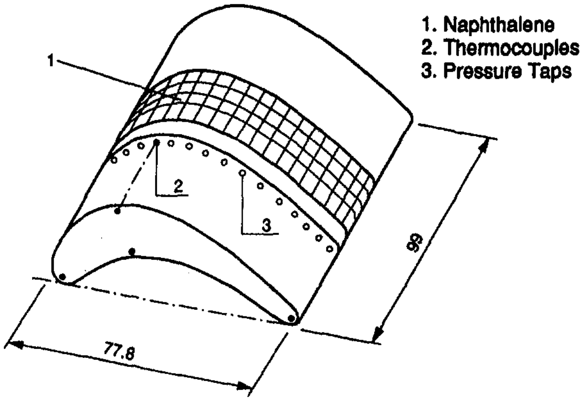

Fig. 4 Test airfoil

Coating of the Model. The airfoil consists of three parts (Fig. 4). The part in the middle is 0.5 mm smaller in contour to carry the naphthalene layer. This part was dipped several times into liquid naphthalene in order to get a coating thickness of more than 500 μm. It was subsequently retouched by a profile milling machine to obtain the same contour as the adjacent parts of the airfoil with satisfactory surface quality.

Measuring of the Naphthalene Layer Thickness. The local mass transfer coefficient β was determined by measuring the local sublimation mass flux $\dot{m}(x, z)$. Before and after the test run the naphthalene layer thickness was measured at discrete points by a conventional eddy-current probe (device: Permascope E 111; Helmut Fischer GmbH Sindelfingen) employing the principle that an electrically nonconductive layer thickness (naphthalene) can be determined by inducing eddy currents in the conductive substrate (aluminum) (Berg, 1991). On plane surfaces the accuracy for measuring the thickness in the range from 0 to 500 μm is within 1 μm. Due to the varying curvature of the airfoil surface, especially in the region of the leading edge, an influence on the linearity of the output signal can be observed. By means of a micrometer screw, the eddy-current probe was calibrated at different locations on the airfoil contour (without coating) within the thickness range mentioned above. The calibration data were used to correct the probe's output at strong curvatures. Thus, the accuracy of measuring the naphthalene sublimation (usually 100–200 μm) is within 1–2 percent. The measurement itself was carried out by a computer-controlled four-axis traversing mechanism (Fig. 5).

Therefore, the precise airfoil coordinates with respect to the center of rotation of the traversing axis were needed to touch the coating perpendicular. This data set was obtained by a three-axis coordinate measuring device (Leitz) and supported the probe traversing. The spatial resolution was 7 × 95 points with a meander-shaped traversing, which is seen in Fig. 5, to save measuring time.

Coating and measuring of naphthalene layer thickness were performed at the Dept. of Flight Propulsion, Technical University Darmstadt. Each coated airfoil was carried by airmail to the test rig of EPFL. The transport container itself was minimized in volume to keep the sublimation losses before and after the test runs small. Moreover, the inside surface was coated with naphthalene to generate a saturated atmosphere. In addition, a coated reference body accompanied the airfoil during mailing, measuring, mounting, and dismounting to determine the sublimation loss. It was found to total about 8 μm, which was considered in data reduction.

Heat and Mass Transfer Measurement. To measure the local heat transfer coefficient on the airfoil, the naphthalene sublimation technique was used. This method is based on the analogy between the energy equation for heat transfer and the diffusion equation for mass transfer and is valid only for incompressible flow.

After the test airfoil has been coated with a thin layer of naphthalene, the thickness of the layer is measured at designated locations before the test airfoil is installed in the wind tunnel and exposed to the air stream for a period of 30–45 minutes,

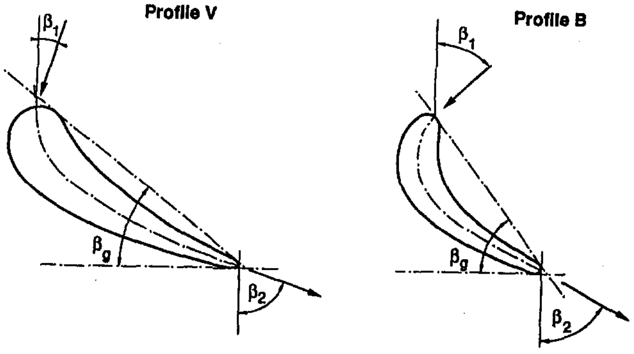

Fig. 3 Profiles V and B

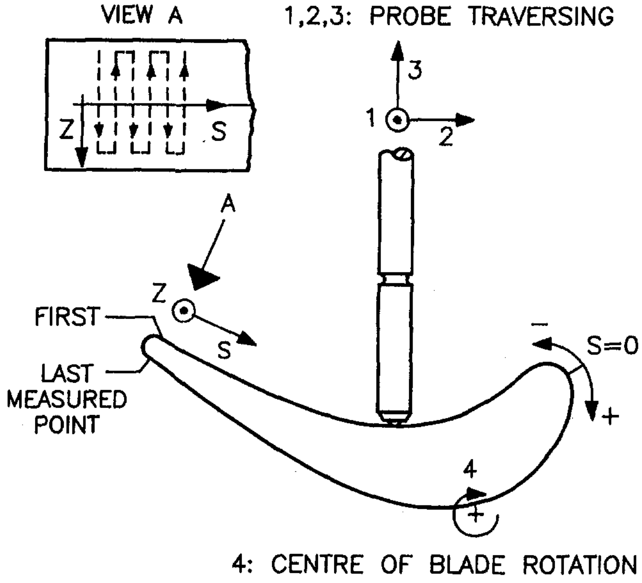

Fig. 5 Probe traversing airfoil surface

Table 2 Measurements on cascade V (NB: the Mach numbers and the Reynolds numbers are based on exit conditions)

Test	Re [-]	M [-]	Tu [%]	β_2 [°]
1	100000	0.06	4	67
2	340000	0.2	3.5	71
3	410000	0.25	3.5	71
4	490000	0.3	3.5	71
5	700000	0.4	3.5	71

depending on the test conditions. Meanwhile, the readings of the thermocouples and the pressure taps of the test cascade on the airfoils and at the inlet and outlet are recorded. Finally, the test airfoil is removed from the wind tunnel and installed back in the positioning mechanism. The thickness of the naphthalene layer is obtained at the same locations as for the first measurement. The local mass transfer can now be evaluated from the change in naphthalene thickness Δd during the exposure time $\Delta\tau$.

$$\dot{m} = \frac{\rho_N \Delta d}{\Delta\tau} \quad (\mathrm{kg/m^2 s}). \tag{1}$$

which is used to derive the local mass transfer coefficient b

$$b = \frac{\dot{m}}{\rho_{s,N} - \rho_{m,N}} \tag{2}$$

where $\rho_{m,N}$ represents the naphthalene concentration in the free stream ($\rho_{m,N} = 0$) and $\rho_{s,N}$ the concentration at the airfoil surface:

$$\rho_{s,N} = \frac{p_D}{R_N\, T_s} \quad (\mathrm{kg/m^3}) \tag{3}$$

The partial pressure p_D of naphthalene at saturation is a function of the surface temperature T_s (Berg, 1991)

$$\log_{10} p_D = 13.57 - \frac{3734}{T_s} \tag{4}$$

The mass transfer coefficient can be nondimensionalized using the Sherwood number

$$\mathrm{Sh} = \frac{b \cdot L}{D} \tag{5}$$

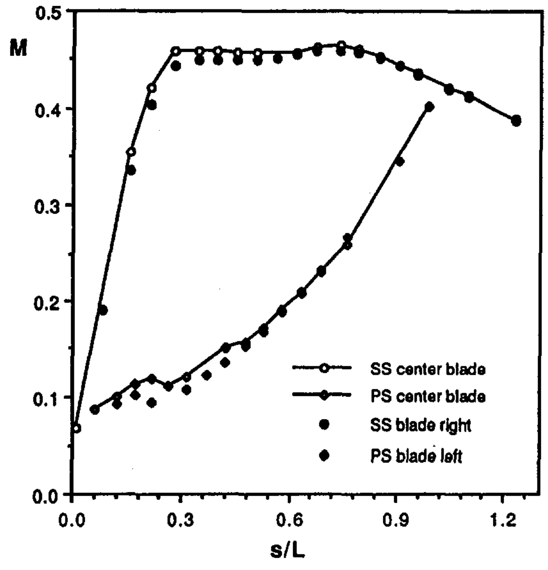

Fig. 6 Mach number distribution for test 5

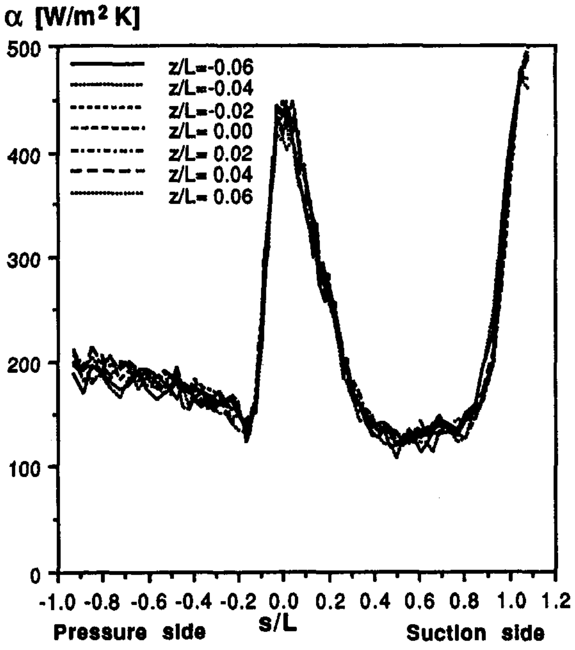

Fig. 7 Heat transfer distribution for test 3

where D is the diffusion coefficient of naphthalene in air (Keumnam et al., 1992). At the same flow conditions, the sublimation mass transfer system is equivalent to a heat transfer system with a constant wall temperature boundary condition. Empirical correlations are commonly applied to correlate the heat and mass transfer coefficients when the Schmidt number Sc and the Prandtl number Pr are not equal. Often the power law relation is used,

$$\mathrm{Nu} = C\,\mathrm{Re}^m \mathrm{Pr}^n \tag{6}$$

and

$$\mathrm{Sh} = C\,\mathrm{Re}^m \mathrm{Sc}^n \tag{7}$$

For the same Reynolds number the analogy function becomes

$$\mathrm{Nu} = \mathrm{Sh}\left(\frac{\mathrm{Pr}}{\mathrm{Sc}}\right)^n \tag{8}$$

For air the Prandtl number is approximately 0.7 and the value

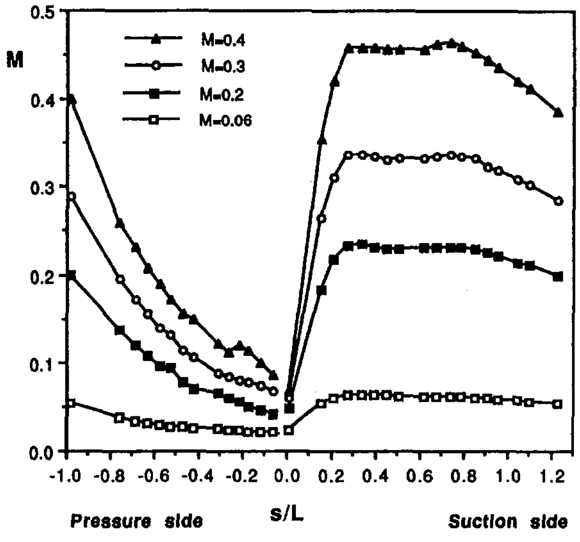

Fig. 8 Mach number distribution on the airfoil

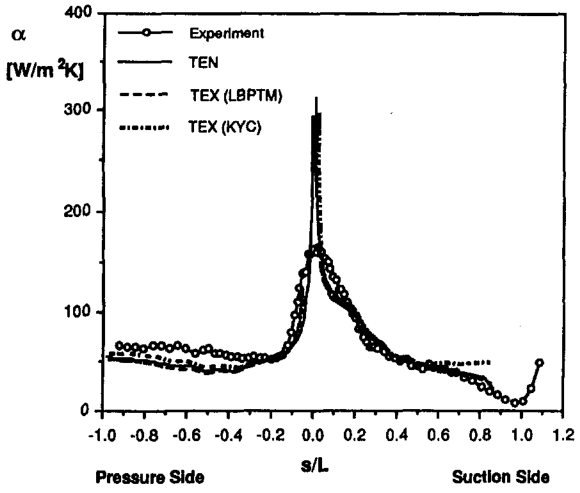

Fig. 9 Test 1, M = 0.06, Re = 100,000

of the Schmidt number for naphthalene in air is around 2.5, depending on the flow conditions and the temperature at the naphthalene surface. In eq. (8), n is an empirical constant. Chen and Goldstein (1992) apply a numerical value of $\frac{1}{3}$, the same accounts for Berg (1991), whereas Presser (1968) gives values of $n = 0.33$ for laminar and $n = 0.44$ for turbulent flow conditions. In the present study Presser's values were used.

Computer Codes

TEXSTAN. The TEXSTAN code has been derived from the well-known STAN5 (Crawford and Kays, 1976) formulation, which has been extended by Crawford (1986). The present version of TEXSTAN also incorporates various formulations of the $k-\epsilon$ model, these being (1) the Lam and Bremhorst (1981) [LB] low Reynolds number modifications, (2) the K.-Y. Chien (1982) [KYC] $k-\epsilon$ model, and (3) the modified Lam and Bremhorst Pressure Term Modification [LBPTM] as suggested by Schmidt and Patankar (1991).

TEN. The code is derived from the Cebeci–Smith formulation with the Keller Box solution algorithm. The variables are solved in nondimensional form and the KYC model is applied with some modifications to give a better transitional behavior by increasing the near-wall production of ϵ (Tarada, 1990).

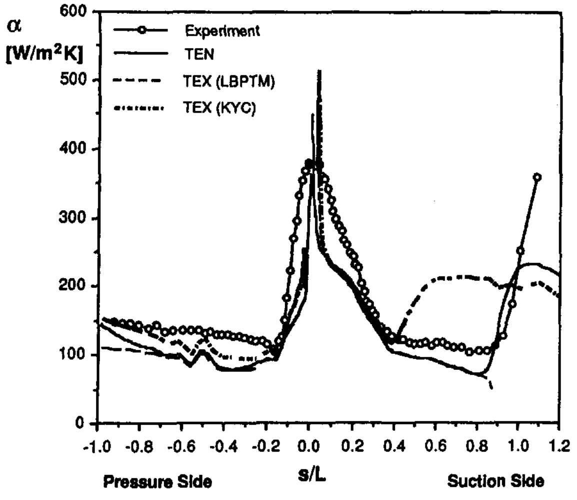

Fig. 10 Test 2, M = 0.2, Re = 340,000

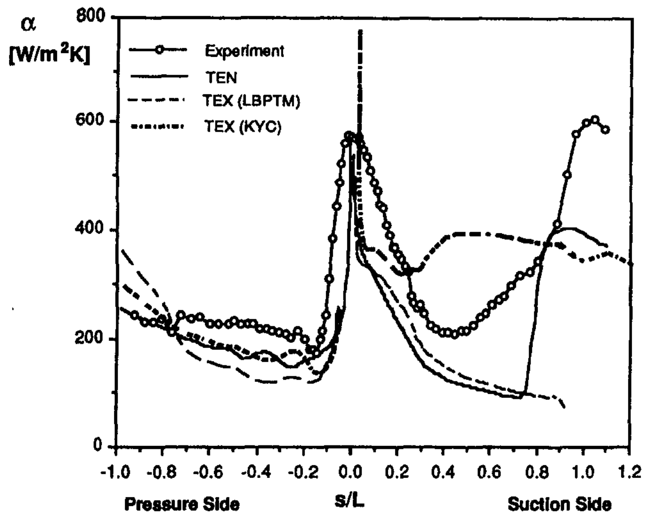

Fig. 11 Test 5, M = 0.4, Re = 700,000

Results and Discussion

Measurements on Cascade V. The measurements on the cascade V had the following objectives:

- evaluation of the local mass and heat transfer coefficients on the airfoil
- comparison with numerical computation.

Table 2 summarizes the tests that were conducted on this cascade.

In all cases the inlet flow angle was chosen $\beta_1 = 0$ deg whereas the outlet flow angle was measured with a Laser Two Focus anemometer (Table 2). As an example the Mach number distribution of test 5 is shown in Fig. 6.

On the suction side the velocity rapidly increases up to approximately 1.1 times the outlet velocity at $s/L = 0.3$. After the strong acceleration, the velocity is almost uniform along the whole suction surface, with a slight decrease toward the trailing edge. On the pressure side the acceleration is almost uniform. The Mach numbers, which are calculated from the pressure taps of the center airfoil and the two neighbor airfoils as indicated in Fig. 2, are located on the same curve showing a good periodicity of the flow. The sublimation losses were measured in 595 points (85 on the perimeter, 7 heights). The results of test 3 ($Re_2 = 410{,}000$) are presented in Fig. 7 and show the two-dimensional character of the flow. For this reason, only a mass transfer coefficient averaged spanwise is presented in the following figures.

On the suction side a laminar boundary layer grows from the stagnation point. Close to the trailing edge, the laminar boundary layer proceeds through transition, whereafter the flow becomes fully turbulent near the trailing edge. On the pressure surface a laminar boundary layer develops from the stagnation point and a small separation bubble forms near the leading edge. In the separation bubble, transition occurs and develops into a fully turbulent boundary layer. The turbulent boundary layer flow, subjected to a strong acceleration might relaminarize (Chen and Goldstein, 1992; Hodson and Dominy, 1987).

Comparison With Numerical Calculations. The experimental data was compared with the numerical results obtained from the computer codes TEN and TEXSTAN, described above. The calculations for the heat transfer were based on the measured isentropic. Mach number distributions on the airfoil shown in Fig. 8. Figures 9 to 11 present the calculated heat transfer coefficients along with the experimental data. For the test at low Mach and Reynolds numbers (Fig. 9) the flow stays

Table 3 Measurements on cascade B (NB: the Mach numbers and the Reynolds numbers are based on exit conditions)

Test	Re [-]	M [-]	Tu [%]	β1 [°]
1	580000	0.3	3.5	0
2	360000	0.2	3.5	22
3	580000	0.3	3.5	22
4	790000	0.4	3.5	22
5	1190000	0.5	3.0	22
6	1620000	0.6	3.0	22

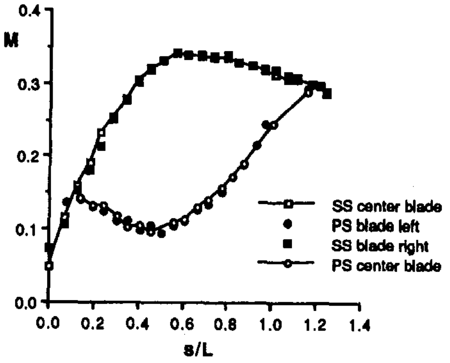

Fig. 12 Mach number distribution on the airfoil (test 1)

laminar and both codes are able to predict the heat transfer quite well, except for the stagnation region where the prediction of the heat transfer is quite poor.

For an outlet Mach number of $M_2 = 0.2$ ($Re_2 = 340{,}000$ transition occurs on the suction side a short distance before the trailing edge (Fig. 10). This transition is quite well predicted by TEN, whereas TEXSTAN/LBPTM stops the calculation shortly after transition. This may be due to the reduction of k to ensure a smooth transitional zone in the modified Lam and Bremhorst $k-\epsilon$ model. The K.-Y. Chien model predicts in both cases an early transition. On the pressure side, values calculated by both codes are below the measured heat transfer coefficients.

Figure 11 shows the numerical data along with the experimental values for an outlet Mach number of $M_2 = 0.4$ ($Re_2 = 700{,}000$). It should be mentioned again that the analogy between heat and mass transfer is only fully valid in the incompressible flow region. For higher Mach numbers the dissipation term in the energy equation, which does not exist in the mass transfer equation, becomes important and has to be taken into account. Further investigations will be needed to rely on the experimental data at Mach numbers in the compressible flow region.

Measurements on Cascade B. For the designer of turbine airfoils one region of concern is the leading edge, which needs to have a moderately small radius blending smoothly into the rest of the airfoil for good aerodynamic performance. On the other hand, present cooling schemes usually require a large leading edge radius (which cannot be blended smoothly) resulting in a rapid change in surface curvature immediately downstream of the leading edge. The curvature actually becomes negative on the pressure side of an airfoil, which can produce a localized overspeed region followed by an adverse pressure gradient. For operation at off-design conditions, an overspeed will occur on the pressure surface if incidence is toward the suction surface.

Due to its high resolution, the naphthalene sublimation technique is able to give precise information about the position and size of a separation bubble. The present investigation was conducted to examine the variation of the heat transfer coefficient in separated and reattached leading edge flows at different exit Mach and Reynolds numbers. Table 3 lists the measurements that were conducted.

As already described for cascade V, pressure measurements were conducted at the inlet and outlet and on the suction and pressure side of the three center airfoils. In Fig. 12, the Mach number distribution on the suction (SS) and pressure (PS) sides is presented and shows that the flow is periodic. Unfortunately, there is only a limited number of pressure taps mounted close to the leading edge, so that the separation bubble is not clearly visible on the pressure side.

For the same test the heat transfer distribution is presented in Fig. 13. On this profile the sublimation losses were measured in 665 points (95 points per perimeter, 7 heights). On the suction side, the flow is laminar and reaches transition only close to the trailing edge. On the pressure side the flow separates shortly after the leading edge. In the separation bubble the heat transfer coefficient tends to fall sharply. The reattachment of the bubble leads to a sudden rise of the heat transfer coefficient. This phenomenon was also observed by Bellows and Mayle (1986) who studied the heat transfer downstream of a leading edge separation bubble. They found that through the separation region, the surface heat transfer changed by almost an order of magnitude and was about 50 percent higher near reattachment than that predicted by the turbulent flat plate correlation.

Figure 14 shows the distribution of the heat transfer coefficient for two different inlet flow angles at the same inlet and outlet Reynolds numbers. On the suction side the heat transfer distribution is comparatively insensitive to incidence changes, which may be explained by the relatively big radius at the leading edge. On the pressure side the inlet flow angle influences the position and size of the separation bubble only slightly.

The linear test facility at the EPFL does not provide the possibility to study the influence of the Reynolds and the Mach number separately. Figure 15 presents the local heat transfer coefficient for outlet Mach numbers from $M_2 = 0.2-0.6$.

In Fig. 15 it can be seen that the position of the separation bubble is not influenced by the Reynolds number. With higher Mach number the bubble becomes smaller and the reattachment seems to move upstream, which results in a local heat transfer

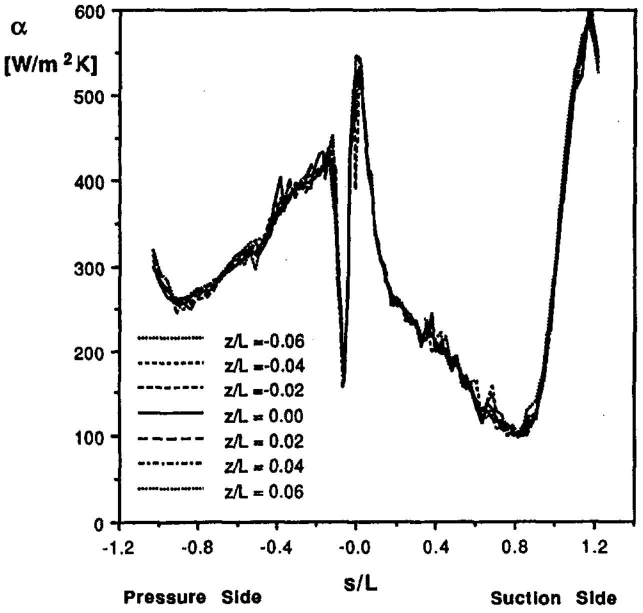

Fig. 13 Heat transfer coefficient on 665 points for profile B (test 2)

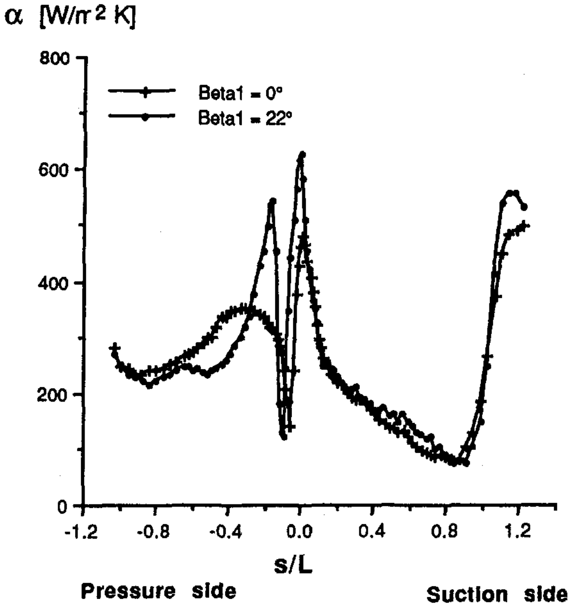

Fig. 14 Heat transfer distribution for two different inlet flow angles

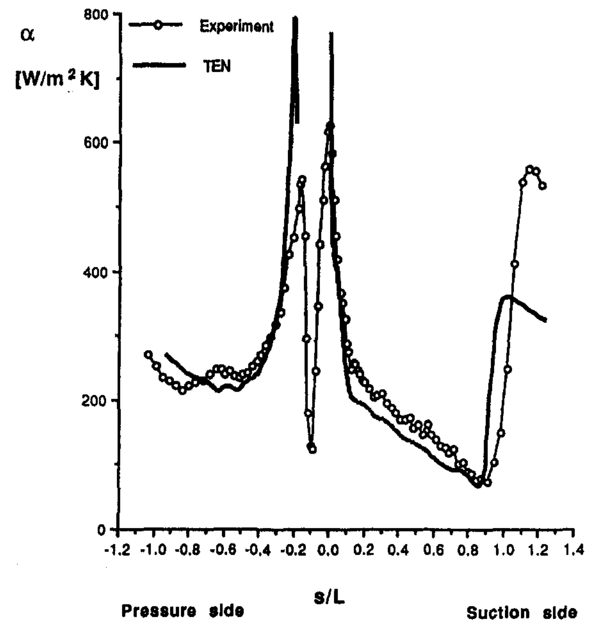

Fig. 16 Numerical comparison for test 3

after the reattachment, being possibly higher than at the stagnation line.

Figure 16 shows the predicted and the measured heat transfer coefficients for an exit Reynolds number of Re = 580,000. On the pressure side, after reattachment the flow tends to behave like a turbulent boundary layer with the starting point at reattachment.

Conclusions

- The naphthalene sublimation technique was applied to measure the heat transfer coefficient on turbine airfoils in a linear test facility at exit Mach numbers up to $M_2 = 0.4$ and Reynolds numbers up to $Re_2 = 700{,}000$.
- Due to its high resolution, the influence of separation, a separation bubble, or the laminar–turbulent transition on the heat transfer can be clearly shown by this method even for small-scale models.

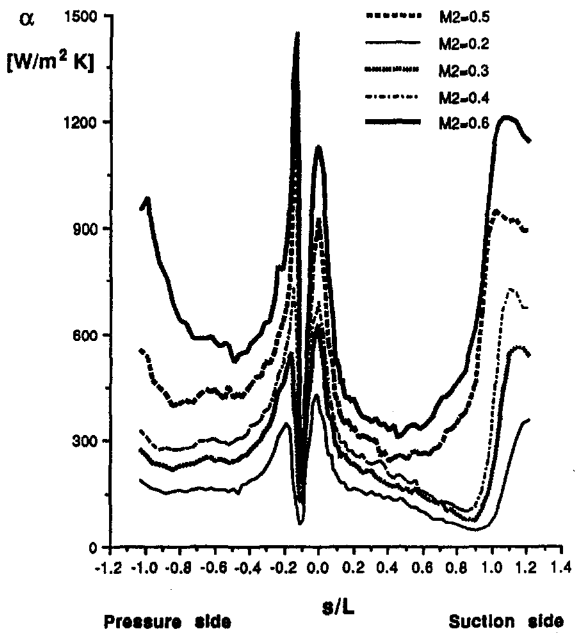

Fig. 15 Heat transfer distribution for different outlet Mach and Reynolds numbers (inlet flow angle β_1 = 22 deg)

- The analogy between heat and mass transfer is only fully valid in the incompressible flow region. At higher Mach number further investigations will be needed to apply the naphthalene sublimation technique.
- The experimental results were compared with numerical data from two boundary layer codes TEN and TEXSTAN. The best predictions of the local heat transfer coefficients were given by TEN, using a KYC turbulence model with some modifications to give a better transitional behavior by increasing the near wall production of epsilon.
- The codes, as used, do not predict transition location (TEXSTAN) and extent (TEN and TEXSTAN) well. Also the stagnation region is quite poorly predicted.
- A separation bubble occurred shortly after the leading edge on the pressure side for the tests with an off-design inlet flow angle. The reattachment of the separation bubble leads to a sharp increase in heat transfer, and values above the stagnation heat transfer were measured. The shape and size of the separation bubble were not influenced by the exit Mach number.

Acknowledgments

The present investigations were carried out in collaboration with the Technical University Darmstadt, Dept. of Flight Propulsion, Darmstadt, Germany, where the coating of the airfoils and the thickness measurements were conducted. This research project was subsidized by ABB, Baden, Switzerland and the "Commission pour l'encouragement de la recherche scientifique" (CERS-KWF), Switzerland.

References

Bellows, W. J., and Mayle, R. E., 1986, "Heat Transfer Downstream of a Leading Edge Separation Bubble," ASME JOURNAL OF TURBOMACHINERY, Vol. 108, pp. 131–136.

Berg, H. P., Hennecke, D. K., Elfert, M., and Hein, O., 1991, "The Effect of Rotation on Local Coolant Side Flow and Heat Transfer in Turbine Blades," *Proceedings 10th ISABE,* Nottingham, United Kingdom, Sept. 1–6.

Berg, H. P., 1991, "Experimentelle Bestimmung des örtlichen inneren Wärmeübergangs von Turbinenleit- und Laufschaufeln mit Hilfe der Analogie zwischen Wärme- und Stoffübergang," Dissertation No. 17, T. H. Darmstadt, Institut für Flugantriebe, Germany.

Bölcs, A., and Sari, O., 1988, "Influence of Deposit on the Flow in a Turbine Cascade," ASME JOURNAL OF TURBOMACHINERY, Vol. 110, pp. 512–519.

Chen, P. H., and Goldstein, R. J., 1992, "Convective Transport Phenomena on the Suction Surface of a Turbine Blade Including the Influence of Secondary Flows Near the Endwall," ASME JOURNAL OF TURBOMACHINERY, Vol. 114, pp. 776–787.

Chien, K. Y., 1982, "Predictions of Channel and Boundary Layer Flows With a Low Reynolds Number Turbulence Model, *AIAA J.,* Vol. 20, pp. 33–38.

Crawford, M. E., and Kays, W. M., 1976, "STAN5, a Program for Numerical Computation of Two Dimensional Internal and External Boundary Layer Flow," NASA CR-2742.

Crawford, M. E., 1986, "Simulation Codes for Calculation of the Heat Transfer to Convectively Cooled Turbine Blades," *Convective Heat Transfer & Film Cooling in Turbomachinery,* VKI—LS—1986-06.

Eckert, E. R. G., and Goldstein, R. J., 1976, *Measurement in Heat Transfer,* ISBN 0-07-018926-9.

Harasgama, S. P., Tarada, F. H., Baumann, R., Crawford, M. E., and Neelakantan, X. X., 1993, "Calculation of Heat Transfer to Turbine Blading Using Two-Dimensional Boundary Layer Methods," ASME Paper No. 93-GT-79.

Hodson, H. P., and Dominy, R. G., 1987, "Three-Dimensional Flow in a Low-Pressure Turbine Cascade at Its Design Condition," ASME JOURNAL OF TURBOMACHINERY, Vol. 109, pp. 201–209.

Keumnam, C., Thomas, F., Irvine, Jr., and Jacob, K., 1992, "Measurement of the Diffusion Coefficient of Naphthalene Into Air," *Int. J. Heat Mass Transfer,* Vol. 35 No. 4, pp. 957–966.

Lam, C. K. G., and Bremhorst K., 1981, "A Modified Form of the k–Epsilion Model for Predicting Wall Turbulence," *J. Heat Fluid Flow,* No. 4, pp. 331–345.

Presser, J., 1968, "Experimentelle Prüfung der Analogie zwischen konvektiver Wärme- und Stoffübertragung bei nicht abgelöster Strömung," *Wärme- und Stoffübertragung,* Vol. 1, pp. 225–236.

Schmidt, R., and Patankar, S. V., 1991, "Simulating Boundary Layer Transition With Low Reynolds Number k–Epsilion Models: Part 2 An Approach to Improve the Predictions," ASME JOURNAL OF TURBOMACHINERY, Vol. 113, pp. 18–26.

Tarada, F., 1990, "Prediction of Rough-Wall Boundary Layers Using a Low Reynolds Number $k-\epsilon$ Model," *Int. J. Heat Fluid Flow,* Vol. 11, No. 4, Dec.

Heat (Mass) Transfer and Film Cooling Effectiveness With Injection Through Discrete Holes: Part I—Within Holes and on the Back Surface

H. H. Cho
Department of Mechanical Engineering,
Yonsei University,
Seoul, Korea 120-749

R. J. Goldstein
Department of Mechanical Engineering,
University of Minnesota,
Minneapolis, MN 55455

A jet stream entering a crossflow is investigated for injection through a single hole and an array of holes for blowing rates of 0.2 to 2.2. The naphthalene sublimation technique has been employed to study the local mass (heat) transfer in the injection hole and in the vicinity of the hole entrance. The Sherwood number is fairly uniform along the circumference of the inside hole surface even at the low blowing rate considered. This is quite different from the case without injection (zero blowing rate), when the Sherwood number is highly nonuniform. The transfer rate in the hole is weakly influenced by the crossflow and the zone, which is directly affected, is confined close to the hole exit (about 0.15 hole diameter in depth). The average Sherwood number is similar to that in the absence of crossflow except at low blowing rates. The Sherwood numbers on the hole entrance surface (backside) are the same as when there is no crossflow. Thus, the Sherwood numbers inside the hole and on the back surface can be closely approximated from experiments without crossflow.

Introduction

Film cooling is used to protect a solid wall exposed to a high-temperature fluid flow. A secondary coolant flow is injected through arrays of holes or slits in the wall into the boundary layer of the fluid flowing over the surface. Near the injection, the secondary coolant may form a film along the surface, which isolates it from the hot fluid flow. Downstream of the injection, the secondary coolant can act as a heat sink, which reduces the average temperature in the boundary layer due to mixing of the secondary coolant and the hot mainstream. The efficiency of film cooling depends on the distribution of the secondary coolant over the surface. The situation is complex due to the interaction between the injected secondary flow and the mainstream. The major factors are hole geometry, spacing, injection angle, blowing rate, and density ratio between the main and secondary flows.

Porous materials or perforated plates (full coverage cooling) have characteristics of near-uniform heat/mass transfer rates on their surface for uniform flow. These characteristics are desirable to protect the surface from hot gases in components of high performance gas turbine engines. High engine operating temperatures are required to increase thrust output and efficiency. The operational temperature is limited by potential to structural failure of the engine components. A full-coverage cooling scheme has been developed for rocket nozzles and some components of gas turbines, notably the combustion chamber. This cooling scheme helps to prevent thermal stresses, increase efficiency, and reduce emission gases (less cooling flow).

The most common arrangement for film coolant injection on gas turbine blades is with single or double rows of injection holes, in which the cooling air is injected to protect the region at and downstream of the holes. The film cooling effectiveness (i.e., adiabatic wall temperature) in the downstream region, rather than near the holes, has been obtained from measurements by many investigators. The heat transfer coefficient in this region is determined from experiments or simulated from the flat plate flow because the heat transfer coefficient downstream is not far from that value without injection. However, the region near the injection holes is important for the full-coverage cooling scheme. The heat transfer in the injection holes and on the back surface as well as on the exposed surface near the holes should be studied; here the transfer rates are very different from those without injection.

In heat transfer experiments, it is difficult to measure the local heat transfer rate near the hole and inside the hole surface. Such measurement involves a large conduction error resulting from large spatial variation in the heat transfer rate and resulting sharp temperature gradients around the hole entrance. Thus, there is available primarily row-averaged heat transfer coefficient (Choe et al., 1976). A mass transfer technique can be used to measure local transfer rates on the inside hole surface and on the plate around the hole entrance and the hole exit. The mass transfer results can be easily converted to the heat transfer results using the heat/mass transfer analogy.

With full-coverage film cooling, the analysis of overall heat transfer requires the heat transfer coefficient distributions on exposed surfaces, at the internal walls, and inside hole surfaces as well as adiabatic wall temperature (film cooling effectiveness) on exposed surfaces (Fig. 1). Note that the film cooling effectiveness is nearly one on the inside hole surface. The primary objective of the present experiments is to determine the heat transfer coefficient distribution on inside hole surfaces and internal walls (Part I), as well as the effectiveness and the external heat transfer coefficient (Part II). These results will provide the information required to analyze overall heat fluxes around holes.

The local heat/mass transfer rates are obtained from the test plate cast with naphthalene around the hole and inside the hole. The naphthalene sublimation method is a well-known mass transfer technique. If the test surface is kept at a uniform temperature and pressure, the naphthalene vapor pressure and concen-

---

Contributed by the Heat Transfer Committee and presented at the ASME Winter Annual Meeting, New Orleans, Louisiana, November 28–December 3, 1993. Manuscript received at ASME Headquarters June 1994. Associate Technical Editor: M. G. Dunn.

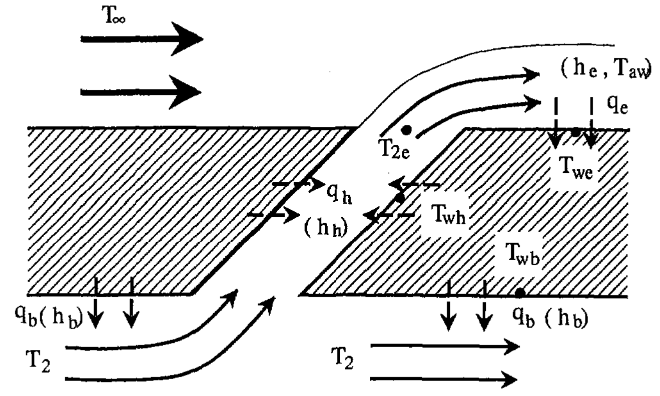

Fig. 1 Schematic diagram for heat transfer mode

tration at the surface will be uniform. This surface boundary condition corresponds to an isothermal surface in a corresponding heat transfer problem. Mass loss (sublimation of naphthalene) on the surface occurs continuously, due to diffusion and advection. Concentration gradients and the mass flux are analogous to temperature gradients and the heat flux. The time-averaged local mass transfer rates are obtained by measurement of the sublimation depths. The heat/mass transfer coefficient obtained with an isothermal condition can be applied to other boundary conditions in turbulent flows when the wall temperature variation is small.

The present work relates closely to full-coverage cooling in a combustor. Single-hole injection into crossflow is also examined in order to compare it with injection from an array of holes. Velocity measurements in an injection hole with a crossflow are shown in the literature (e.g., Bergeles et al., 1975; Andreopoulos, 1982) and temperature fields were obtained by Andreopoulos (1983). There are no available local heat transfer results for flow through a hole of short length.

In the present study, two sets of experiments are conducted to determine both the heat transfer coefficient and film cooling effectiveness. First, pure air is injected as a secondary flow that is equivalent to $T_2 = T_\infty$ ($\theta' = 0$) in the heat transfer case. Secondly, saturated naphthalene vapor in air is injected as secondary flow that is equivalent to $T_2 = T_w$ ($\theta' = 1$) (see below) in the heat transfer case.

Film Cooling Effectiveness and Heat Transfer Coefficient. Two different methods have been presented to predict film cooling effects in the literature. In most studies, constant fluid properties (which includes mainstream and coolant) are assumed in a control volume, while it is at a low velocity with a small temperature difference. Thus, the energy equation is linear and temperature fields can be superimposed on each other (Eckert, 1984). One method is based on an adiabatic wall temperature (effectiveness). The other method defines variable heat transfer coefficients at a given wall temperature.

The first method defines the heat transfer coefficient, h, with an adiabatic wall temperature. This method has been widely used in film cooling study and is reviewed by Goldstein (1971) and Eckert (1984). The heat flux at the wall is expressed as:

$$q_w = h(T_w - T_{aw}) \qquad (1)$$

For constant-property flow, the heat transfer coefficient, h, is invariant with this temperature difference. It is only a function

Nomenclature

C_2 = dimensionless mass fraction of naphthalene vapor in the secondary flow; $C_2 = 0$ for pure air injection and $C_2 = 1$ for naphthalene-saturated vapor injection
D_h = hole diameter
D_{naph} = mass diffusion coefficient for naphthalene vapor in air (Eq. (19))
H = shape factor = δ^*/δ_2
h = heat transfer coefficient (Eq. (1))
h' = heat transfer coefficient defined in Eq. (4)
h_m = mass transfer coefficient defined in Eq. (11)
h'_m = mass transfer coefficient defined in Eq. (12)
h'_{m0} = mass transfer coefficient for $\rho_{v,2} = \rho_{v,\infty}$ (Eq. (14)); $h'_{m0} = h_m$
h'_0 = heat transfer coefficient for $T_2 = T_\infty$ (Eqs. (6) and (8))
h'_1 = heat transfer coefficient for $T_2 = T_w$ (Eq. (7))
M = blowing rate = $\rho_2 U_2/\rho_\infty U_\infty$
$\dot{m}$ = naphthalene mass transfer rate per unit area (Eq. (18))
$\dot{m}_0$ = naphthalene mass transfer rate for $\rho_{v,2} = \rho_{v,\infty}$ (Eq. (14))
$\dot{m}_1$ = naphthalene mass transfer rate for $\rho_{v,2} = \rho_{v,w}$ (Eq. (14))
P = pitch of an array of holes = $3D_h$
q_w = heat flux

Re_h = Reynolds number based on the hole diameter and an average velocity in hole = $\bar{U}D_h/\nu$
Sc = Schmidt number for naphthalene in air = $\nu/D_{\text{naph}} \cong 2.28$ at 298 K and 0.1 MPa
$\text{Sh}(L)$ = Sherwood number based on characteristic length L; $\text{Sh}(L) = h_m L/D_{\text{naph}}$
Sh_h = Sherwood number based on hole diameter = $h_m D_h/D_{\text{naph}}$
Sh'_0 = Sherwood number for $\rho_{v,2} = \rho_{v,\infty}$ (Eq. (17)); $\text{Sh}'_0 = \text{Sh}$
Sh'_1 = Sherwood number for $\rho_{v,2} = \rho_{v,w}$ (Eq. (17))
Sh_{peak} = peak Sh on the reattachment point
$\overline{\text{Sh}}_h$ = average Sherwood number (integrated over θ direction)
$\overline{\overline{\text{Sh}}}_h$ = overall average Sh number (integrated over θ and Y directions)
T_2 = temperature of the secondary flow
T_{aw} = adiabatic wall temperature
T_r = recovery temperature
T_w = local wall temperature
T_∞ = free-stream temperature
$\bar{U}$ = average velocity in hole
U_∞ = approaching velocity (free-stream velocity)
X = streamwise (crossflow) distance from a trip wire

X_c = streamwise (crossflow) distance from center of injection holes
Y = axial distance from inlet of injection holes
Y_{peak} = peak Sh location inside the hole (reattachment point)
Z = lateral distance across span measured from center of injection holes
δ = boundary layer thickness (based on 99 percent of free-stream velocity)
δ^* = displacement boundary layer thickness = $\int (1 - u/U_\infty)dy$
δ_2 = momentum boundary layer thickness = $\int u/U_\infty(1 - u/U_\infty)dy$
$\delta\tau$ = run time (Eq. (18))
δz = local sublimation depth of naphthalene
η_{aw} = adiabatic wall cooling effectiveness (Eq. (2))
η_{iw} = impermeable wall effectiveness (Eq. (16))
K = constant defined in Eq. (7) = $(h'_1 - h'_0)/h'_0$
ν = kinematic viscosity = μ/ρ
θ = angle around injection hole = 0 deg at the leading edge
θ' = dimensionless temperature (Eq. (5))

of the flow field and the fluid properties for a given boundary condition. A film cooling effectiveness, η_{aw}, which is a nondimensional form of the adiabatic wall temperature with the secondary flow temperature, is defined as:

$$\eta_{aw} = \frac{T_{aw} - T_r}{T_2 - T_r} \tag{2}$$

where T_r is a recovery temperature. T_r is equal to the free-stream temperature for low-speed constant-property flows. Then, η_{aw} becomes:

$$\eta_{aw} = \frac{T_{aw} - T_\infty}{T_2 - T_\infty} \tag{3}$$

The heat transfer coefficient and the film cooling effectiveness are determined separately in this method. The wall temperature distribution can be obtained from Eq. (1) for any given situation, such as mainstream and secondary coolant temperatures and a prescribed wall heat flux.

The second method defines the heat transfer coefficient in the following equation (e.g., Metzger et al., 1968; Choe et al., 1976; Kumada et al., 1981):

$$q_w = h'(T_w - T_\infty) \tag{4}$$

The heat transfer coefficient denoted with a prime, h', now varies with temperature difference between mainstream and injection flow. With this approach one can determine the heat transfer coefficient for film cooling on an isothermal surface, which is approximated in full coverage film cooling. For constant-property flow, the heat transfer coefficient, h', varies linearly with the dimensionless temperature (Metzger et al., 1968; Choe et al., 1976; Kumada et al., 1981):

$$\theta' = \frac{T_2 - T_\infty}{T_w - T_\infty} \tag{5}$$

The heat transfer coefficient, h', can be determined from a function of θ' (i.e., an arbitrary secondary flow temperature, T_2) and a reference heat transfer coefficient, h_0', for the situation that $\theta' = 0$ ($T_2 = T_\infty$). The relation is obtained by superposition of temperature fields and expressed as:

$$\frac{h'}{h_0'} = 1 + K\theta' \tag{6}$$

The constant K is:

$$K = \frac{h_1' - h_0'}{h_0'} \tag{7}$$

where h_1' is the heat transfer coefficient when the secondary coolant temperature, T_2, is equal to the wall temperature, T_w ($\theta' = 1$).

Eckert (1984) showed the values of the heat transfer coefficients, h_0' and h_1', which are obtained on an isothermal surface, can be used as an approximation on a surface where temperature variations are expected to be small. In that condition, the parameters from the two approaches can be converted into each other. The heat transfer coefficient, h, defined by Eq. (1) is then identical to h_0' in case of $\theta' = 0$ ($T_2 = T_\infty$) in Eq. (4):

$$h_0' = h \tag{8}$$

From Eqs. (1) and (4), the film cooling effectiveness, η_{aw}, is related to the constant, K, given by Eq. (7):

$$\eta_{aw} = \frac{T_{aw} - T_\infty}{T_2 - T_\infty} = -K \left(= \frac{h_0' - h_1'}{h_0'} \right) \tag{9}$$

and the relation between h and h' is given by:

$$\frac{h'}{h} = 1 - \eta_{aw}\theta' \tag{10}$$

The h and η_{aw} in Eq. (1) are connected with the h' and K of the second method by Eqs. (9) and (10). Therefore, these parameters can be converted into each other. It is also noted that $\theta' = 1/\eta_{aw}$ (or $T_w = T_{aw}$) from Eq. (10) when $h' = 0$ (or $q_w = 0$; adiabatic wall condition).

In the present study of mass transfer, the parameters will be presented in both forms, although the condition is more similar to the second case. Two sets of experiments are conducted to determine the parameters: (*a*) pure air is injected as the secondary flow ($\rho_{v,2} = \rho_{v,\infty}$; $C_2 = 0$), that is equivalent to $T_2 = T_\infty$ ($\theta' = 0$) in the heat transfer case, and (*b*) the saturated vapor of naphthalene in air is injected as the secondary flow ($\rho_{v,2} = \rho_{v,w}$; $C_2 = 1$), that is equivalent to $T_2 = T_w$ ($\theta' = 1$) in the heat transfer case. For constant property flow, which is nearly achieved in the naphthalene sublimation technique because of the low vapor pressure for saturation in air, the mass transfer governing equation is linear. Thus, it is possible to superimpose the concentration fields.

The film cooling effectiveness is determined directly from the mass flux rather than the relations above between the first and the second methods. The mass flux at the wall can be expressed as:

$$\dot{m} = h_m(\rho_{v,w} - \rho_{v,iw}) \tag{11}$$

or

$$\begin{aligned} \dot{m} &= h_m'(\rho_{v,w} - \rho_{v,\infty}) \qquad (12) \\ &= h_m(1 - \eta_{iw}\theta')(\rho_{v,w} - \rho_{v,\infty}) \text{ (from Eq. (10))} \end{aligned}$$

where $\rho_{v,iw}$ is the vapor density (concentration) at an impermeable wall. This is equivalent to the adiabatic wall temperature in the heat transfer case. Note that h_m'/h_m is analogous to h'/h in Eq. (10).

In the case of (*a*) ($\rho_{v,2} = \rho_{v,\infty}$; $C_2 = 0$, $\theta' = 0$), the mass transfer coefficient, h_m, in Eq. (11) is equal to h_m' (or denoted as h_{m0}') in Eq. (12). Hence, the mass transfer coefficient is determined from:

$$h_m = \frac{\dot{m}}{\rho_{v,w} - \rho_{v,\infty}} \tag{13}$$

The ratio of the mass fluxes of (*a*) ($\dot{m}_0$, $\theta' = 0$) and (*b*) ($\dot{m}_1$, $\theta' = 1$) can be written as:

Nomenclature (cont.)

ρ_s = density of solid naphthalene (Eq. (18))
$\rho_{v,2}$ = naphthalene vapor density in the secondary flow
$\rho_{v,iw}$ = vapor density on the impermeable wall
$\rho_{v,w}$ = naphthalene vapor density on the surface
$\rho_{v,\infty}$ = naphthalene vapor density of approaching flow
σ = standard deviation

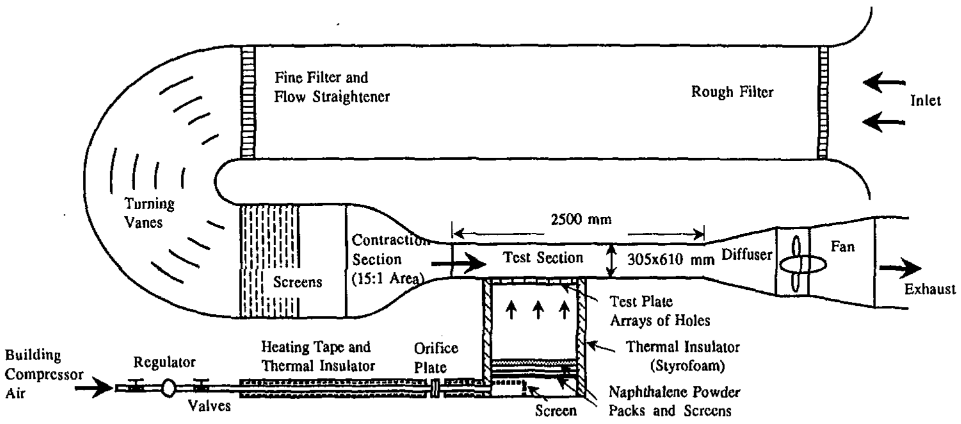

Fig. 2 Wind tunnel and secondary flow system (flow injected into cross stream)

$$\frac{\dot{m}_1}{\dot{m}_0} = \frac{h_m(1 - \eta_{iw})(\rho_{v,w} - \rho_{v,\infty})}{h_m(\rho_{v,w} - \rho_{v,\infty})} \tag{14}$$

$$= 1 - \eta_{iw} \tag{15}$$

where $\theta' = 1$ in the case of (b).

The film cooling effectiveness, η_{iw}, can be determined by:

$$\eta_{iw} = 1 - \frac{(\delta z/\delta \tau)_1}{(\delta z/\delta \tau)_0} \tag{16}$$

$$= 1 - \frac{\mathrm{Sh}_1'}{\mathrm{Sh}_0'} \tag{17}$$

Thus at a given temperature, the film cooling effectiveness is determined by the ratio of the unit sublimation depths of naphthalene surface between the cases of (a) and (b). In general, the effectiveness can also be determined from the ratio of resulting Sherwood numbers (mass transfer coefficients). Equation (17) is analogous to Eq. (10) for $\theta' = 1$. Hay et al. (1986) also employed a similar approach to determine effectiveness values using a swollen polymer technique (mass transfer) with laser holographic interferometry.

Experimental Apparatus and Procedure

1 Wind Tunnel and Secondary Flow System. Two different secondary (injected) fluids are tested; one is pure air (naphthalene free, $\theta' = 0$) and the other is naphthalene-saturated air ($\theta' = 1$). The secondary air supplied from the department building compressor passes through a pressure regulator, a needle valve, a thin plate orifice flowmeter, plenum chamber, and the test plate, and is then ejected into the crossflow. The pressure drop across the orifice plate is maintained to within ±1 percent of the desired pressure difference during a run. The crossflow is supplied from the room air through a large open-cycle, suction-type wind tunnel in the Heat Transfer Laboratory at the University of Minnesota.

The wind tunnel and the secondary flow system are shown schematically in Fig. 2. The test section following a contraction section (15:1 area ratio) is 610 mm across by 305 mm high by 2500 mm long. To obtain a fully developed turbulent velocity profile with a thick boundary layer, a trip wire, 1.6 mm ($\frac{1}{16}$ in.) in diameter, is placed at the junction of the contraction and test section. The first row of holes, seven holes placed across the section, is placed 721 mm downstream from the exit of the contraction (the trip wire) while the center hole of the fourth row, coated with naphthalene, is positioned 950 mm downstream. The tunnel fan is downstream of the test section. The nominal crossflow velocity is 8.8 m/s. The turbulence intensity of the free stream is 0.52 percent, which is measured without injection. The turbulence intensity and the velocity are measured by a hot-wire anemometer, a total tube, and a pilot tube. The tunnel air is discharged outside the building. A detailed description of the construction of the wind tunnel can be found in Raithby (1972).

The free-stream (crossflow) temperature is usually slightly higher than the temperature of the building compressor air, which comes from an outside room. The temperature of the secondary air is controlled using a heating tape, which is wrapped around the outside of the pipe line. The secondary air is heated to the level of the crossflow temperature and the temperature difference is maintained within 0.3°C.

To supply naphthalene-saturated secondary air, two naphthalene powder layers of about 25 mm thickness are placed between the screens and/or meshes inside the plenum chamber. The inside hole measurement, which should give a zero sublimation rate, is tested to check whether the secondary air is saturated or not. The naphthalene saturation vapor pressure is approximately 0.01 percent of atmospheric pressure, so that a small amount of naphthalene powder can supply a large amount of saturated naphthalene mixture. However, the vapor pressure changes about 10 percent with 1°C difference in the room temperature range. If the temperature of the secondary air is lower than that of the test plate and the crossflow, the secondary mixture flow has an undersaturated condition near the test plate even though it may be saturated in the plenum (naphthalene powder layers). Undersaturation is detected by sublimation on the inside hole surface. Conversely, the secondary mixture flow is oversaturated near the test plate when the mixture has a higher temperature than the plate. In this case, naphthalene deposits are detected on the inside hole surface. Thus, it is essential that the temperature difference between secondary air and the test plate be minimized by adjusting the heater power transformer for each run.

2 Test Plate. The objective of the experimental facility is to enable determination of the local naphthalene sublimation rate on the inside hole surface and on the surfaces near the hole. The test surface, which models short-hole flow, is fabricated by perforating the flat plates. Surface area designated as mass transfer active is coated with a naphthalene layer for sublimation prior to being exposed to the air stream.

The surface consists of a 7 by 7 square array of holes (in-line array) as shown in Fig. 3(a). Hole to hole spacing is $3D_h$ in each direction with a hole diameter of 25.4 mm. The center hole of the array is cast with naphthalene and is located 950 mm downstream of the trip wire. The square cast areas ($4D_h \times 4D_h$) on the top and bottom are one half diameter bigger on each edge than the one square symmetry region ($3D_h \times 3D_h$).

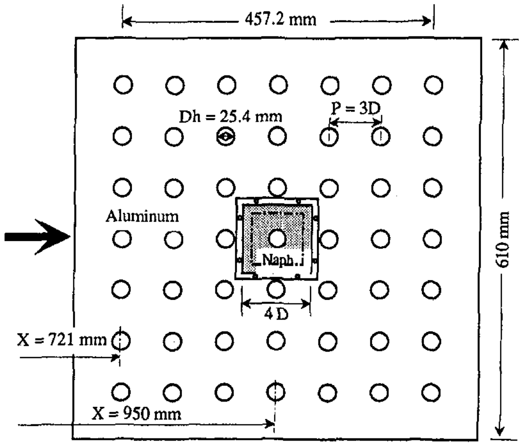

Fig. 3 (*a*) Test plate of an array of holes

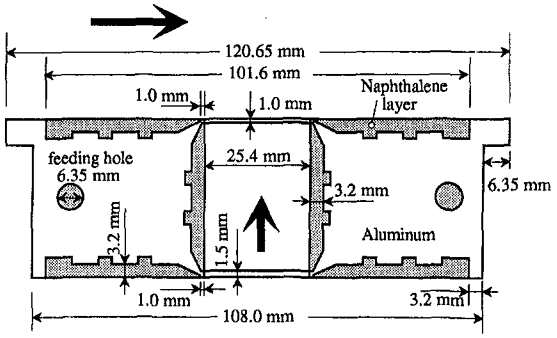

Fig. 3 (*b*) Naphthalene cast test plate (cross section)

When testing the single-hole flow, all of the holes in the array, except the center cast hole, are blocked.

A cross-sectional view of the test plate is shown in Fig. 3(*b*). The plate is an aluminum block pierced at its center by a hole of 25.4 mm (1 in.) diameter. In addition, the test plate contains a recess into which naphthalene is cast. Square cavities 101.6 mm ($4D_h$) by 101.6 mm ($4D_h$) are machined in the center of the test plate on both the top and bottom surfaces. These become the naphthalene surface after casting. The rims around the square cavities provide a surface on which reference points are placed. The center hole (25.4-mm-dia) is recessed about 3.2 mm deep. After casting, this recess is filled with naphthalene and the 25.4-mm-dia circular hole is formed. The center hole has a metal annular rim with thicknesses of 1.0 mm at the top and 1.5 mm at the bottom, which are exposed to the airflow. The rim at the bottom entrance is slightly thicker because it has a small indentation as an original point. The rims, which are nonsubliming surfaces, are used for inside hole measurements as reference points. Additional grooves, which roughen the recess area, provide stronger adhesion of naphthalene to the plate. The inserted thermocouple wires are glued in the groove of the surface.

3 Naphthalene Casting Procedure. The naphthalene surface employed in the experiments is made by a casting process. This is achieved by pouring molten naphthalene into a mold, allowing the naphthalene to solidify, and separating the mold from the test plate. The mold consists of the test plate, highly polished aluminum flat plates, and a circular cylinder. The smoothness of the exposed naphthalene surface is comparable to that of the polished aluminum adjacent to it.

4 Data Acquisition System. An automated surface measurement system is used to scan the profile of the naphthalene surface. This system satisfies several requirements to obtain useful local sublimation depths of a naphthalene surface, such as precise positioning of the plates, accurate depth measuring, and rapid data acquisition to minimize the natural convection losses. Two different computer-controlled measurement systems, an *XY*-Table and a Four-Axis Table, are used for the flat plate measurement and the inside hole measurement, respectively.

The measurement systems consist of a depth gage, a linear signal conditioner, a digital multimeter, stepper-motor driven positioners, a motor controller, and a microcomputer (detailed by Goldstein et al. (1985) for the flat plate measurement and Cho (1992) for the inside hole measurement). This automated system typically obtains about 2000 data points in one hour.

The depth gage (a linear variation differential transformer; LVDT) has 0.5 mm linear range and 25.4 nm (1.0 μin.) resolution. The nominal sublimation depth in a test is around 50 μm, about three orders of magnitude larger than the resolution. The linearity of the LVDT is within 0.1 percent of the measuring range (depth (mil) = 1.001 * voltage output (mV), within ±10 mil). The measurement errors of the LVDT are about 0.15 μm (6 μin.; 2σ) for the flat plate measurement and about 0.45 μm (18 μin.) for the inside hole measurement with a stylus of 50.8 mm length at a 95 percent confidence level.

5 Measurements. To measure inside hole mass transfer rates, an extended stylus is used to reach deep inside the hole. The profile of the naphthalene surface elevation is measured on the measurements tables (i.e., *XY*-Table and Four-Axis Table) before and after each data run. The difference between the two sets of surface elevations (with respect to a reference level on the nonsubliming metal surface) is a measure of the sublimation depth. The duration of the run is determined by the sublimation depth. The depth must be sufficient to make measurement errors small and yet the depth must not be large enough to influence the flow pattern. Each run time is selected so that the average sublimation depth of the naphthalene surface will be about 0.05 mm (0.002 inch). The sublimation depth is two or three orders of magnitude higher than the measuring error. The maximum sublimation depth, about 0.2 mm, is about 0.8 percent of the nominal hole diameter of 25.4 mm. At a typical room temperature (24°C), the run time ranged from 30 to 120 minutes depending on the Reynolds numbers. Because the vapor pressure of naphthalene is quite sensitive to temperature (about 10 percent change per °C), the naphthalene surface temperature is measured precisely using *T*-type (copper-constantan) thermocouples installed within the naphthalene, as close as possible to the surface. During the run, the temperature variation of the naphthalene surface is within about 0.2°C.

The local mass transfer coefficient is defined as:

$$h_m = \frac{\dot{m}}{\rho_{v,w} - \rho_{v,\infty}} = \frac{\rho_s(\delta z/\delta\tau)}{\rho_{v,w}} \tag{18}$$

where $\rho_\infty = 0$ in the free stream. The Sherwood number can be expressed as:

$$\mathrm{Sh}_h = \frac{h_m D_h}{D_{\mathrm{naph}}} \tag{19}$$

The naphthalene vapor pressure is obtained from a correlation (vapor pressure–temperature relation) of Ambrose et al. (1975). Then, the naphthalene vapor density, $\rho_{v,w}$, is calculated from the perfect gas law. D_{naph} is determined from average values of Cho (1989) and Chen and Wung (1990). A discussion of the values for naphthalene properties is given by Goldstein and Cho (1993). During the experiment, extraneous sublimation losses by natural convection cannot be neglected, as they can be as high as 10 percent of a measurement at 24°C, though normally they are less than 5 percent. The additional sublimation losses occur during the measurement on the table, during storage and during installation of the test plate. For data correction, an amount based on a natural convection rate and the

Table 1 Characteristics of boundary layer velocity profiles

X (mm)	freestream (m/s)	δ (mm)	δ^* (mm)	δ_2 (mm)	H (δ^*/δ_2)
721 (1st row)	8.88	21.3	3.68	2.64	1.39
950 (4th row)	8.85	26.1	4.28	3.06	1.40

Turbulence intensity, Tu ≅ 0.52%

Virtual origin of Turb. B.L., X = -253 mm
(upstream of the trip wire)

Injection hole diameter, D_h = 25.4 mm

Hole to hole spacing, P = $3D_h$

measuring times is subtracted from the total sublimation depth (Cho, 1992).

Uncertainty of the Sherwood numbers using Kline and McClintock's (1953) method for single-sample experiments, considering the measured temperature, depth, position and correlation equations, is within 7.1 percent in the entire operating range of the measurement based on a 95 percent confidence interval. This uncertainty is mainly attributed to the uncertainty of the properties of naphthalene, such as the naphthalene saturated vapor pressure (3.77 percent) and diffusion coefficient of naphthalene vapor in air (5.1 percent). In contrast, the error due to the depth measurement is only 0.9 percent. The other uncertainties are 0.1, 1.1, and 4.9 percent for T_w, ρ_s, and h_m, respectively.

6 Operating Conditions. The operating conditions for the free stream are specified in Table 1. In all experiments, the free-stream velocity, which is measured upstream of the injection holes, is within 2 percent of the nominal velocity of 8.8 m/s. The operational range of the secondary flow is at the blowing rate $M = 0.22$ to $M = 2.18$ (equivalent to the hole Reynolds number $\text{Re}_h = 3{,}000$ to $\text{Re}_h = 30{,}000$) for the single hole injection and $M = 0.22$ to $M = 0.6$ ($\text{Re}_h = 3000$ to $\text{Re}_h = 8300$) for the in-line array of holes.

Results and Discussion

1 Inside Hole Surface of Single-Hole Injection. The boundary layer thickness is 26.1 mm (thickness at 99 percent of free-stream velocity) at the center hole, which is about the same as the hole diameter, when the velocity is measured without injection. The inlet of the hole is located at $Y/D_h = 0$ and the exit at $Y/D_h = 1.48$ (Fig. 4). Each end of the injection hole

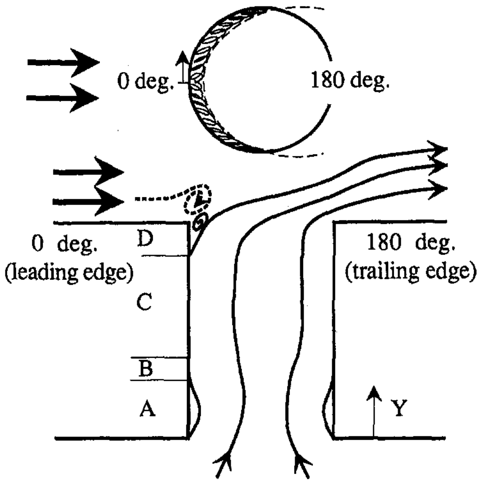

Fig. 4 Schematic flow pattern of inside hole with crossflow at low blowing rates

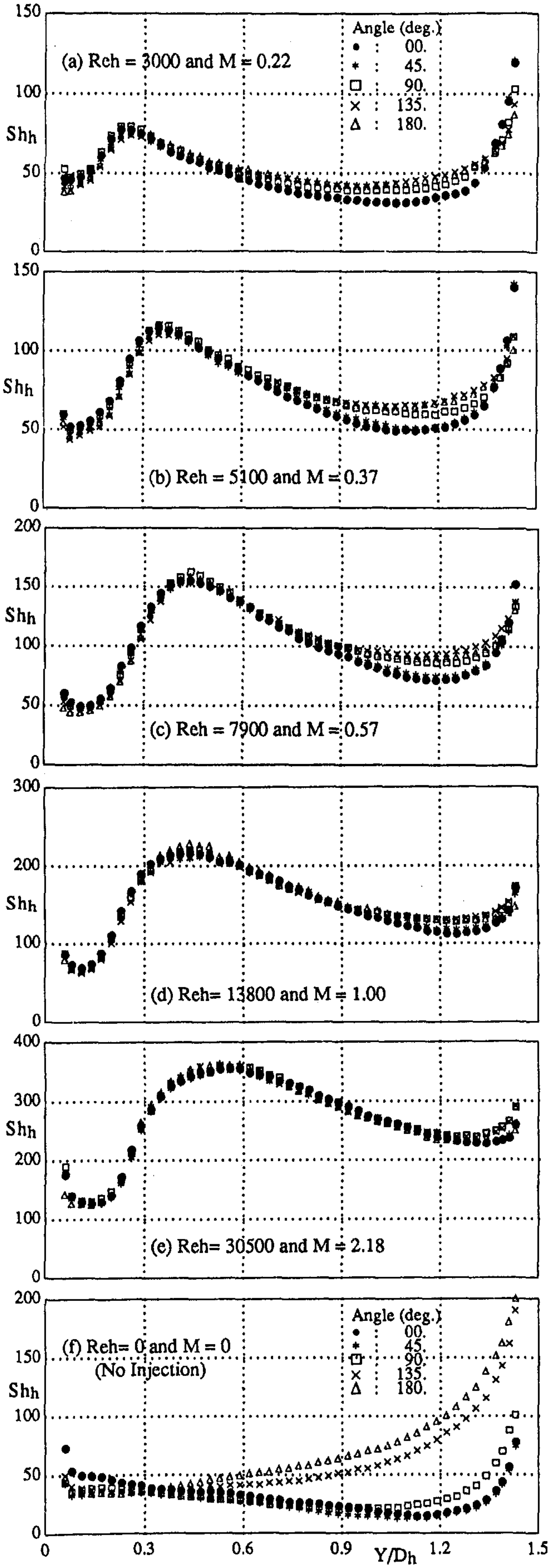

Fig. 5 Local Sh in hole with crossflow at exit for air injection ($C_2 = 0$)

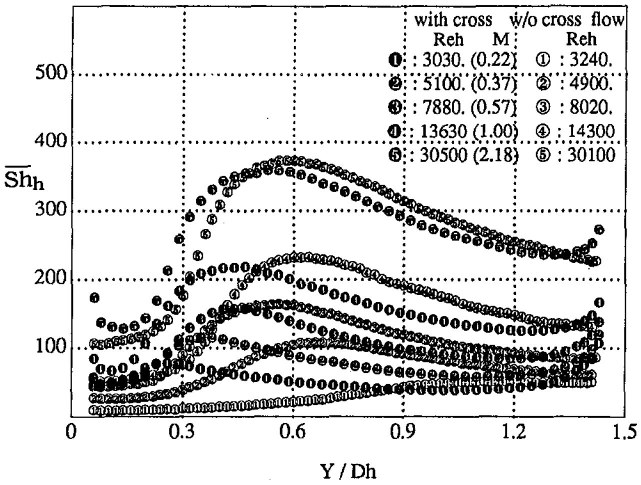

Fig. 6 Comparison of $\overline{Sh}_h$ with and without crossflow (single hole; C_2 = 0)

has a circular rim for measurement purposes. Thus there are no data points at each end including the near region of the rims. The angle (around the inside of the hole) is measured from the leading edge (0 deg) of the injection hole to the trailing edge (180 deg) with respect to the mainstream flow.

According to the flow pattern, which is based on the presentation with fog flow visualization (only exit area) by Foss (1980) and the mass transfer rate distribution, the inside of the hole can be divided into four different regions, shown in Fig. 4. They are:

(A) separation/recirculation region at the inlet of the hole due to separation
(B) reattachment region
(C) developing region
(D) region affected directly by crossflow at the exit of the hole including separation near $\theta = 0$ deg

(A) Separation/Recirculation Region. The flow may separate at the edge of inlet when the flow enters the hole, because the inlet is not a streamline shape but has a right-angled edge. The mass transfer rate in this region is usually low due to the recirculation of the flow, which produces a thermal pocket of low velocity fluid (Fig. 5). The Sherwood number distribution along the circumference is fairly uniform except at low blowing rates $M = 0.22$ and $M = 0.37$ (Figs. 5(a) and 5(b)). The peripheral variation of the Sherwood number at the low blowing rates is caused by the effect of the cross-stream flow, which can disturb the inside hole flow at low blowing rates. However, the variation is fairly small if it is compared with the case of no injection (Fig. 5(f)), even if the flow does not have a clear separation pocket. Bergeles et al. (1975) showed that the velocity distribution within a hole at 0.57 diameters from the exit and $M = 0.24$ is slightly different from that without crossflow. The size of the recirculation zone increases with the blowing rate because the jet at high blowing rates has more momentum and is less affected by the crossflow (it is a contrast to the longer laminar separation at low Re for no crossflow, Fig. 6). Thus, the recirculation zone at the high blowing rate, $M = 2.18$, reaches the same size as in the case without crossflow as shown in Fig. 6. A comparison of tests with and without crossflow shows that there is a big difference for $\mathrm{Re}_h \leq 5000$ (or $M \leq 0.37$). The Sherwood number in region A (recirculation zone) is higher than that without crossflow due to the small size of the separation bubble with crossflow.

Table 2 Comparison of the peak and average values and the peak locations of Sh with and without crossflow (single-hole injection)

		with cross-flow			without cross-flow		
Re_h	M	Sh_{peak}	$\overline{\overline{Sh}}_h$	Y_{peak}/D_h	Sh_{peak}	$\overline{\overline{Sh}}_h$	Y_{peak}/D_h
3100	0.22	77.1	52.9	0.26	39.2	30.1	1.15
5000	0.37	113.5	76.6	0.37	106.6	70.2	0.67
8000	0.57	155.6	103.5	0.44	155.8	107.2	0.56
14000	0.99	217.3	152.0	0.47	230.9	152.6	0.62
30000	2.18	358.1	268.7	0.54	372.0	266.6	0.58

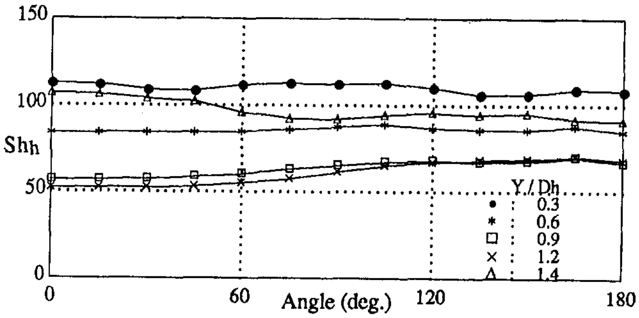

Fig. 7 Local Sh at Re_h = 5100 and M = 0.37 (C_2 = 0)

(B) Reattachment Region. The reattachment region has a high mass transfer rate because the flow essentially impinges on the wall (Fig. 5). Generally, the peak point of the mass transfer rate will be located just before the flow reattachment point. The reattachment point lies on a band rather than at one line due to the unsteadiness of the flow. Even though the location of the reattachment is very different as shown in Fig. 6, the level of the peak Sherwood number is about the same as without crossflow, except at $\mathrm{Re}_h = 3000$ ($M = 0.22$) where a laminar and weak reattachment is expected for no crossflow. This low Reynolds number flow generally has a long recirculation without crossflow. As explained, in region A the reattachment length increases with blowing rates (Re_h) and reaches the same length as in the case without crossflow. The reattachment

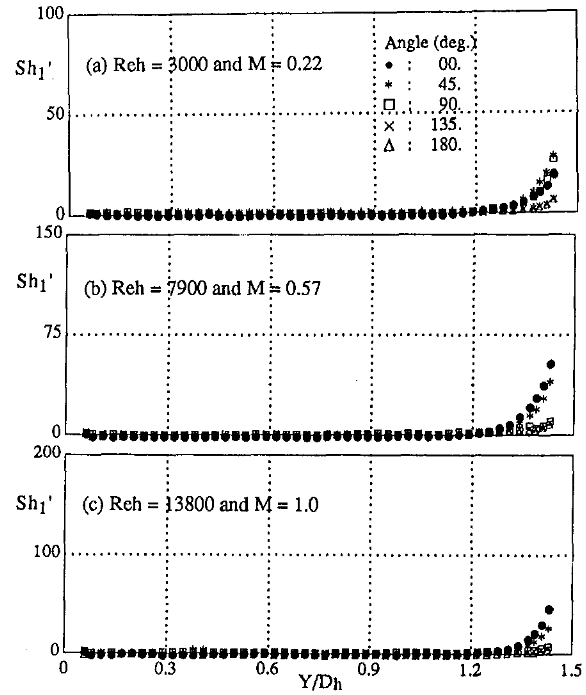

Fig. 8 Local Sh_l' in hole with crossflow at exit for saturated vapor injection (C_2 = 1)

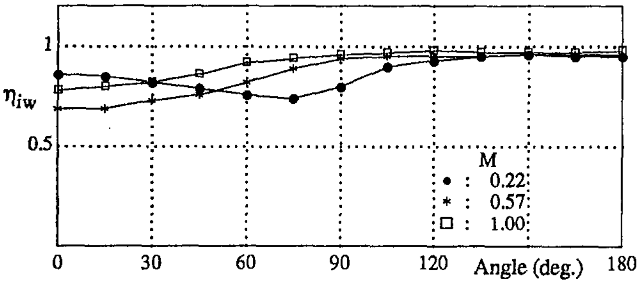

Fig. 9 Effectiveness (η_{iw}) in single hole at Y/D_h = 1.4 and U = 8.8 ms

length (the length from the inlet of the hole to the peak point of Sherwood number) is compared with the case without crossflow in Table 2, including the peak values. The Sherwood number at this region is fairly uniform in the circumferential direction.

(C) Developing Region. After reattachment, the boundary layers of flow and mass develop and the mass transfer rates decrease slowly at approximately the same rate as that without cross-flow (Figs. 5 and 6). In this region, the mass transfer rate is affected weakly by the crossflow at the exit. The affected area, which is indicated by nonuniform Sherwood number in circumferential direction, is reduced with the blowing rate and finally approaches zero at the blowing rate of M = 2.18 (Re_h = 30,500, Fig. 5(*e*)). As shown in the circumferential variation in Fig. 7, the Sherwood number increases with the angle from the minimum value at the leading edge (0 deg) to the maximum value at the trailing edge (180 deg). The boundary layer of flow is thinned at 180 deg due to pushing by the crossflow (shown by Bergeles et al. (1975) and Andreopoulos (1982)), which results in the higher mass transfer rates. The situation is reversed at 0 deg, however, even at the low blowing rate, the circumferential difference of the Sherwood number is relatively small (at most 30 percent) when it is compared with the axial variation of the Sherwood number.

(D) Region Near the Exit of the Hole. This region is directly affected by the crossflow. The crossflow pushes the jet toward the downstream edge of the hole. This detaches the jet from the leading edge (θ = 0 deg) of the hole at the hole exit as shown schematically in Fig. 4. The resulting vortex at the edge rolls along the periphery of the hole. The rolling vortex, which disturbs and interacts with the jet flow, helps to increase the mass transfer rates in this region (around θ = 0 deg, Fig. 5). The increased rate and affected area of Sherwood number decrease with an increase in the blowing rate. For high blowing rates this region is limited to a small area at the exit. In this region, the Sherwood number at the leading edge (θ = 0 deg) is higher than at the trailing edge (θ = 180 deg), shown in Fig. 7 at Y/D_h = 1.4, due to the vortex.

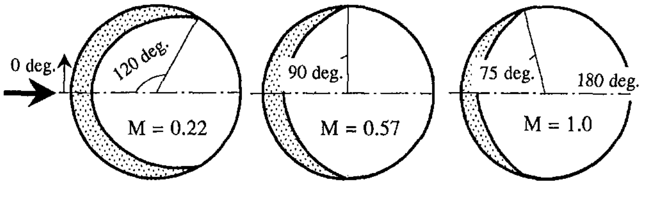

Fig. 10 Affected area of inside hole surface by crossflow (near exit of hole)

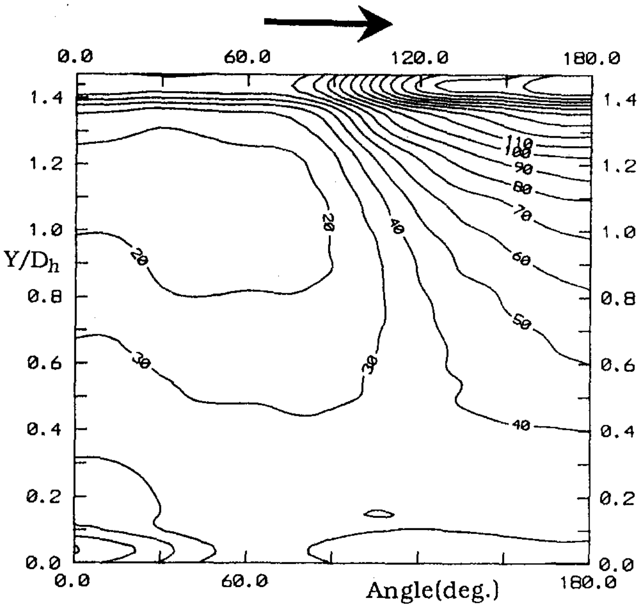

Fig. 11 Local Sh contours at Re_h = 0 and M = 0 (no injection)

For flows injected with saturated naphthalene vapor (Fig. 8), mass transfer is found only in the vortex-affected exit area ($Y/D_h \sim 1.34 - 1.48$), which indicates mixing of pure air from the crossflow. Figure 9 shows the effectiveness, η_{iw} (Eq. (17)), near the exit (Y/D_h = 1.4) and indicates that the vortex-affected area is reduced with an increase in blowing rate. Note η_{iw} = 1, meaning that coolant flows cover the surface perfectly. From results based on the local measurement and naphthalene visualization (obtained with a long time run until the sublimation area was distinguished by the naked eye), the affected zone and depth are plotted schematically in Fig. 10 (the dotted area represents the band on inside hole surface for which the effectiveness is less than 1.0). This small area can be compared with the case of no injection in Figs. 5(*f*) and 11, which shows that the entire hole area is affected. This implies that the inside of the hole will be damaged greatly by mainstream for no injection but can be protected from the mainstream with even a low blowing rate and the flow inside of a hole is not greatly affected by the mainstream except at low blowing rates.

The overall average values (integrated over θ and Y directions) of Sherwood number are compared with the case without crossflow in Table 2. This shows that the average values from the case without crossflow can apply to the case with crossflow except at the low blowing rate, M = 0.22. The average Sherwood numbers are plotted in Fig. 12 and are correlated well by

$$\overline{\overline{\mathrm{Sh}}}_h = 0.19\ \mathrm{Re}_h^{0.7024} \qquad (20)$$

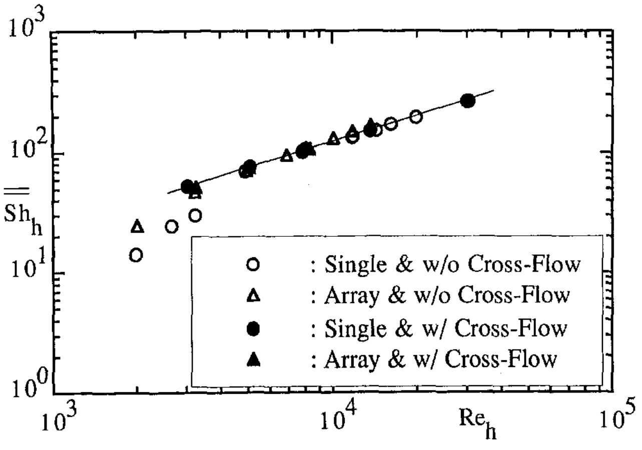

Fig. 12 Overall average Sh at inside holes

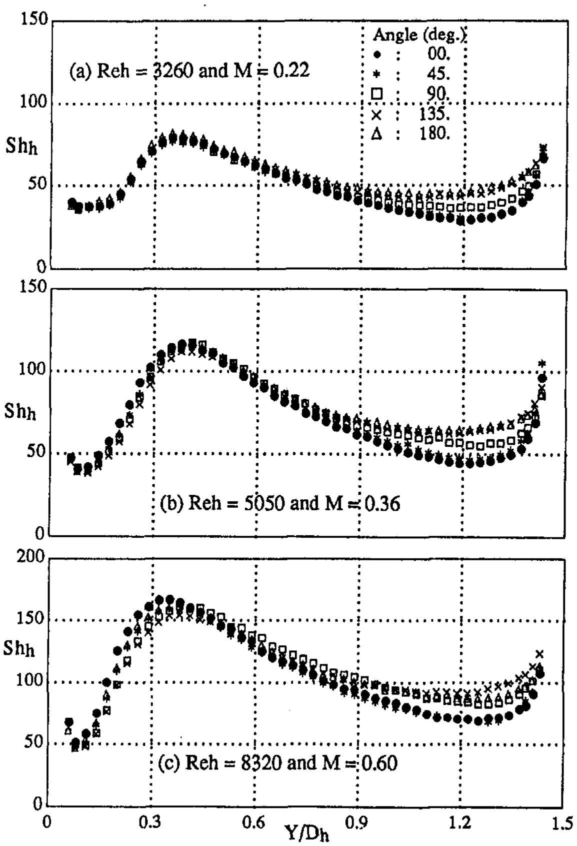

Fig. 13 Local Sh at the fourth row in an array of holes for air injection ($C_2 = 0$)

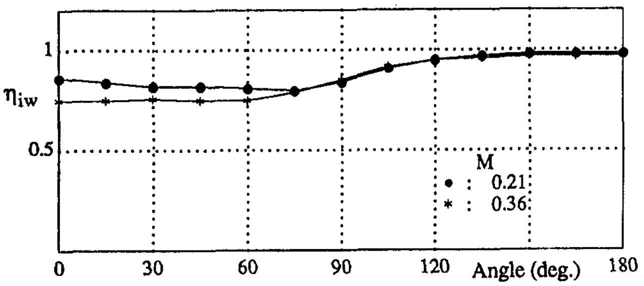

Fig. 15 Effectiveness (η_{iw}) in an array of holes (fourth row) at Y/D_h = 1.4 and U = 8.8 m/s

2 Inside Hole Surface of Arrays of Holes. The array in the present study is seven holes by seven holes, sometimes five holes by seven holes with each end hole blocked to obtain a high blowing rate. The center hole in the fourth row is coated with naphthalene. All data presented are determined from this center hole in the fourth row. It is not clear that this represents a fully developed condition at the fourth row; however, an ammonia and diazo paper surface visualization (presented in part II) shows a fairly developed pattern. Both the hole and row spacings are three diameters and the array of holes consists of an in-line pattern. The boundary layer thickness is 21.3 mm (slightly less than the hole diameter) at the center of the first row (X = 721 mm; see Table 1) when the velocity is measured without injection. Other conditions are the same as for the case of single-hole injection described in the previous section.

The overall pattern of Sherwood number distribution is similar to the case for single hole injection (Figs. 5 and 13). The mass transfer rate is affected slightly less by the crossflow than that of the single hole injection, due to upstream jet flows. Zone D (Fig. 4) is confined only by the exit, and the increasing rate of Sherwood number at the exit is much less than for the single-hole injection. The values of Sh_l' are lower, as expected, than those of single-hole injection, Figs. 14. This is caused by the thickened boundary layer and the decreased near wall velocity of crossflow due to injection from the previous rows. As shown in Fig. 15, the values of effectiveness (η_{iw}, Eq. (17)) and the affected zone (zone D) do not change much with blowing rate. The affected zone of the inside hole surface depends on not only the cross-stream velocity (blowing rate) but also on the disturbance from neighboring jets (turbulence level).

The reattachment point (exactly the peak points of Sh_h) at the blowing rate M = 0.22 shifts slightly downstream (Fig. 16) because the effective blowing rate will be higher due to the lower velocity of the crossflow at the surface of the fourth row. However, as shown in Fig. 16, the reattachment point is changed little with an increasing blowing rate for the array of holes. Note a separation zone is weakly changed with Reynolds numbers in turbulent flow. At about Re_h = 8000 (where turbulent reattachment is expected for both cases), the reattachment point is earlier than for the single hole. The reason is that the array case

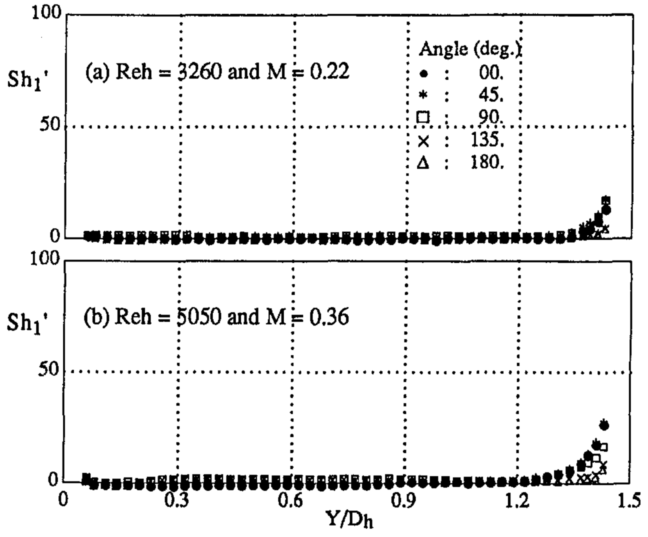

Fig. 14 Local Sh_l' at the fourth row in an array of holes for saturated vapor injection ($C_2 = 1$)

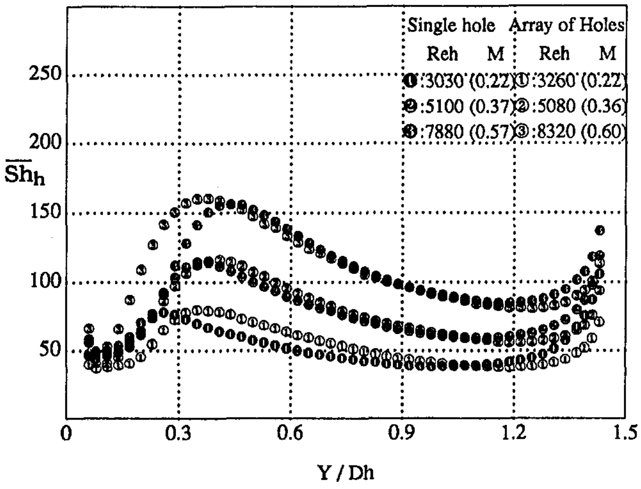

Fig. 16 Comparison of average Sh with crossflow for a single hole and an array of holes (fourth row)

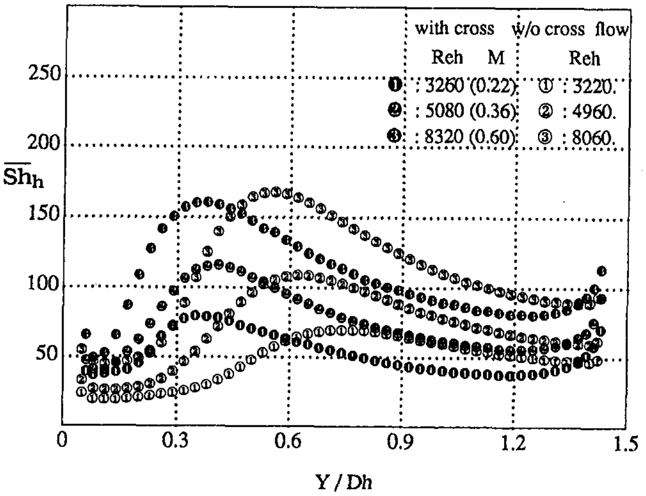

Fig. 17 Comparison of average Sh with and without crossflow (fourth row)

has less lateral momentum at the hole inlet due to the confined approaching flow.

The overall average values (integrated over θ and Y directions) and the peak point of Sherwood number are compared with the case without crossflow in Table 3. These values also can be compared with the single-hole injection in Table 2 and Fig. 12. The comparison suggests that the average values from the case of single-hole injection and without crossflow can apply to the case of an array of holes with crossflow except at the low blowing rate. However, the reattachment points are different. As presented in Fig. 17 and Table 3, the reattachment length is approximately 0.2 hole diameters shorter than the case without crossflow at the same Re_h.

3 Mass Transfer on the Hole Entrance Surface (Back or Windward Surface). Local values of the transfer coefficient on the hole entrance surface is shown in Fig. 18. There is little difference, as expected, between the results with and without crossflow. Thus, data from tests without crossflow can be used to determine the heat/mass transfer on the back surface when crossflow is present.

Conclusions

Single Hole Injection

(*i*) Sh_h is fairly uniform along the circumference of the inside hole surface even at a low blowing rate of $M = 0.22$. This is very different from the case without injection, $M = 0$, which is highly nonuniform.

(*ii*) The separation zone near the hole entrance is greatly shrunk by a crossflow at low blowing rates. However, at a high blowing rate, this zone increases to the same length as that for no crossflow. The Sh_h increases for a low blowing rate due to the short separation zone, but the Sh_h downstream of reattachment is similar to that in the absence of crossflow.

Table 3 Comparison of the overall average values and the peak locations of Sh in an array of holes with and without crossflow

		with cross-flow		without cross-flow	
$\mathrm{Re_h}$	M	$\overline{\overline{\mathrm{Sh}}}_\mathrm{h}$	$\mathrm{Y_{peak}/D_h}$	$\overline{\overline{\mathrm{Sh}}}_\mathrm{h}$	$\mathrm{Y_{peak}/D_h}$
3200	0.22	51.7	0.36	47.2	0.74
5000	0.36	74.4	0.41	70.4	0.62
8200	0.60	106.8	0.37	108.9	0.56

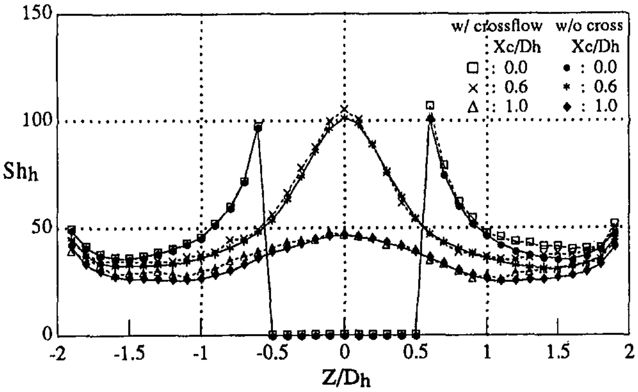

Fig. 18 Local Sh on the backside surface at Re_h = 30,500 and M = 2.19

(*iii*) The zone, inside the hole, affected directly by the cross stream is confined to the exit of the injection hole even at low blowing rates. The affected zone (effectiveness, η_{iw}, less than 1.0) is about $0.15D_h$ in depth and about ±120 deg for $M = 0.22$ (from the leading edge: i.e., not affected at 180 deg) to ±75 deg for $M = 1.0$. This is very different from the case without injection. This suggests that the inside hole surface can be protected from the main stream even with the injection at low blowing rate.

(*iv*) The averaged Sh_h is similar to that in the absence of crossflow except at low blowing rate. This implies that the averaged Sh_h without crossflow can often be used to predict that for flow into cross stream.

For an Array of Holes. Sh_h is slightly different from that for the single-hole case. Sh_h is less affected by the crossflow due to presence of the previous rows.

On the Back Surface. The Sh_h is essentially the same with and without crossflow. Thus, Sh_h on the back surface can be obtained directly by experiments without crossflow.

Acknowledgments

Support from the Air Force Office of Scientific Research and through the Engineering Research Program of the Department of Energy aided greatly in the conduct of this study.

References

Andreopoulos, J., 1982, "Measurements in a Jet-Pipe Flow Issuing Perpendicularly Into a Cross Stream," ASME *Journal of Fluids Engineering*, Vol. 104, pp. 493–499.

Andreopoulos, J., 1983, "Heat Transfer Measurements in a Heated Jet-Pipe Flow Issuing Into a Cold Cross Stream," *Phys. Fluids*, Vol. 26, pp. 3201–3210.

Bergeles, G., Gosman, A. D., and Launder, B. E., 1975, "The Near-Field Character of a Jet Discharged Through a Wall at 90 Deg to a Main Stream," ASME Paper 75-WA/HT-108.

Chen, P. H., and Wung, P. H., 1990, "Diffusion Coefficient of Naphthalene in Air at Room Temperature," *J. Chin. I. Ch. E.*, Vol. 21, pp. 161–166.

Cho, H. H., 1992, "Heat/Mass Transfer Flow through an Array of Holes and Slits," Ph.D. Thesis, Univ. of Minnesota.

Cho, K., 1989, "Measurement of the Diffusion Coefficient of Naphthalene Into Air," Ph.D. Thesis, State Univ. of New York at Stony Brook.

Choe, H., Kays, W. M., and Moffat, R. J., 1976, "Turbulent Boundary Layer on a Full-Coverage Film-Cooling Surface—An Experimental Heat Transfer Study With Normal Injection," NASA CR-2642.

Eckert, E. R. G., 1984, "Analysis of Film Cooling and Full-Coverage Film Cooling of Gas Turbine Blades," ASME *Journal of Engineering for Gas Turbines and Power*, Vol. 106, pp. 206–213.

Foss, J. F., 1980, "Interaction Region Phenomena for the Jet in a Cross-flow Problem," Rep. SFB 80/E/161, Univ. Karlsruhe.

Goldstein, R. J., 1971, "Film Cooling," *Advances in Heat Transfer,* Vol. 7, Academic Press, pp. 321–379.

Goldstein, R. J., and Cho, H. H., 1993, "A Review of Mass (Heat) Transfer Measurements Using Naphthalene Sublimation," 3rd World Conf. on Experimental Heat Transfer, Fluid Mechanics and Thermodynamics, Hawaii; *Experimental Thermal and Fluid Science,* Vol. 10, 1995, pp. 416–434.

Goldstein, R. J., Chyu, M. K., and Hain, R. C., 1985, "Measurement of Local Mass Transfer on a Surface in the Region of the Base of a Protruding Cylinder With a Computer Controlled Data Acquisition System," *Int. J. Heat Mass Transfer,* Vol. 28, pp. 977–985.

Hay, H., Lampard, D., Maali, R., and Burns, I., 1986, "Simultaneous Determination of Heat Transfer Coefficient and Adiabatic Wall Effectiveness on a Film Cooled Surface Using the Swollen Polymer Technique," *Proc. 8th Int. Heat Transfer Conf.,* U.S.A., pp. 489–494.

Kline, S. J., and McClintock, F. A., 1953, "Describing Uncertainty in Single-Sample Experiments," *Mechanical Engineering,* Vol. 75, Jan., pp. 3–8.

Kumada, M., Hirata, M., and Kasagi, N., 1981, "Studies of Full-Coverage Film Cooling Part 2: Measurement of Local Heat Transfer Coefficient," ASME Paper No. 81-GT-38.

Metzger, D. E., Carper, H. J., and Swank, L. R., 1968, "Heat Transfer With Film Cooling Near Nontangential Injection Slots," ASME *Journal of Engineering for Power,* Vol. 90, pp. 157–163.

Raithby, A. D., 1972, "The Effect of Turbulence Parameters and Support Position on the Heat Transfer From, and Flow Around, Spheres," Ph.D. Thesis, University of Minnesota.

Heat (Mass) Transfer and Film Cooling Effectiveness With Injection Through Discrete Holes: Part II—On the Exposed Surface

H. H. Cho
Department of Mechanical Engineering,
Yonsei University,
Seoul, Korea 120-749

R. J. Goldstein
Department of Mechanical Engineering,
University of Minnesota,
Minneapolis, MN 55455

The heat (mass) transfer coefficient and the film cooling effectiveness are obtained from separate tests using pure air and naphthalene-saturated vapor injected through circular holes into a crossflow of air. The experiments indicate that Sherwood numbers around the injection hole are up to four times those on a flat plate (without injection holes) due to the interaction of the jets and the mainstream. The mass transfer around the injection holes is dominated by formations of horseshoe, side, and kidney vortices, which are generated by the jet and crossflow interaction. For an in-line array of holes, the effectiveness is high and uniform in the streamwise direction but has a large variation in the lateral direction. The key parameters, including transfer coefficients on the back surface (Part I), inside the hole (Part I), and on the exposed surfaces, and the effectiveness on the exposed surface, are obtained so that the wall temperature distribution near the injection holes can be determined for a given heat flux condition. This detailed information will also aid the numerical modeling of flow and mass/heat transfer around film cooling holes.

Introduction

Film cooling has been studied by many investigators. The studies include injection through a single hole and multiple hole arrangements, as well as the effects of geometry (e.g., hole angles and spacing). Goldstein (1971) provided an early review of these film cooling studies. Film cooling effectiveness has seldom been measured near injection holes due to experimental difficulty and measurement errors; however, information in this region is essential in full coverage film cooling. Full-coverage film cooling is desirable in modern high-performance gas turbine engines, notably for a combustion chamber. In most full-coverage film cooling studies, average values are measured for both parameters (heat transfer coefficient and film cooling effectiveness) due to the error caused by heat conduction. As an example, Choe et al. (1976) measured the row average heat transfer coefficient (averaged each row) for a geometry similar to that used in the present study (normal injection). Table 1 presents a summary of work done in the full-coverage film cooling area. Recently, the local transfer coefficient near injection holes, which is difficult to measure with heat transfer methods, has been measured using naphthalene sublimation techniques [e.g., Kumada et al. (1981), Goldstein and Taylor (1982), and Karni and Goldstein (1989)].

In Part I of the paper, mass (heat) transfer coefficient distributions on inside hole surfaces and internal walls (back surface) have been presented for normal injection through a single hole and an array of holes into a crossflow. The objective of Part II is to determine both cooling effectiveness values and heat/mass transfer coefficients on the exposed surface near the injection holes. These results will provide the information required to analyze temperature distributions and/or overall heat fluxes around injection holes.

As explained in Part I, two sets of experiments are conducted to determine both parameters, which are the heat transfer coefficient and the adiabatic film cooling effectiveness. Pure air is used as the secondary (injected) flow ($C_2 = 0$). That is equivalent to $T_2 = T_\infty$ ($\theta' = 0$) in the heat transfer case. When air saturated with naphthalene vapor is injected as the secondary flow ($C_2 = 1$), the mass transfer system is equivalent to $T_2 = T_w$ ($\theta' = 1$) in the heat transfer case. Thus (as detailed in part I), the equivalent to film cooling effectiveness, the mass transfer impermeable wall effectiveness, η_{iw}, can be determined by:

$$\eta_{iw} = 1 - \frac{\dot{m}_1}{\dot{m}_0} \tag{1}$$

$$= 1 - \frac{\mathrm{Sh}'_1}{\mathrm{Sh}'_0} \tag{2}$$

Metzger et al. (1968) and Choe et al. (1976) presented their data in the form of h', which shows a linearity with θ'. Kumada et al. (1981) determined h' on a full-coverage film-cooled wall using a mass transfer method. The transfer coefficient, h', was obtained for different θ' using a mixture of air and naphthalene vapor (but not saturated) as a secondary gas. They also showed the linear relation between h' and θ' such that superposition of concentration fields is valid in the naphthalene sublimation method. The simultaneous determination of transfer coefficients and effectiveness values downstream of a tangential slot injection was presented by Hay et al. (1986). They employed a swollen polymer technique (mass transfer) with laser holographic interferometry to obtain these parameters using a saturated swelling agent vapor in secondary air injection.

In the present study, the parameters are presented in both forms (i.e., Sh and η_{iw} in the first method (refer to Part I) and Sh'_1 in the second method; note $\mathrm{Sh}'_0 = \mathrm{Sh}$). In addition, the effectiveness is compared with that obtained from an ammonia vapor and diazo paper visualization.

Contributed by the Heat Transfer Committee and presented at the ASME Winter Annual Meeting, New Orleans, Louisiana, November 28–December 3, 1993. Manuscript received at ASME Headquarters June 1994. Associate Technical Editor: M. G. Dunn.

Table 1 Full-coverage film cooling studies

Author	Hole Arrangement	Spacing (P/D)	Injection Angles	Blowing Rate (M)	Remarks
Papell (1960)	staggered	2	normal	0.5 - 21.8	effectiveness (only recovery area)
Metzger et al. (1973)	staggered & in-line	4.8	normal	0.1 - 0.2	heat transfer coef. & effectiveness
Metzger et al. (1976)	staggered & in-line	4.8	normal	0.1 - 0.5	heat transfer coef. & effectiveness
Mayle & Camarata (1975)	staggered	8 - 14	30° & 45°	0.5 - 2.0	heat transfer coef. & effectiveness
Choe et al. (1976)	staggered	5 & 10	normal	0.1 - 1.0	heat transfer coef.
Crawford et al. (1976)	staggered	5 & 10	30°	0.1 - 1.3	heat transfer coef.
Kim et al. (1979)	staggered	5 & 10	30° & 45°	0.0 - 1.5	heat transfer coef.
Le Grives et al. (1979)	staggered	8	normal	0.0 - 2.0	heat transfer coef.
Sasaki et al. (1979)	staggered	3 (5 & 10)	45°	0.15 - 0.5	effectiveness
Luckey & L'Ecuyer (1981)	staggered	5 & 10	90° & 25°	0.0 - 2.0	heat transfer coef. (circular cylinder: stagnation area)
Kasagi et al. (1981)	staggered	5 & 10	30°	0.3 - 0.7	effectiveness
Kumada et al. (1981)	staggered	5	30°	0.3 - 0.7	heat (mass) transfer coef.
Furuhama & Moffat (1983)	staggered	5	30°	0.4	heat transfer coef. (convex wall)
Kasagi et al. (1988)	staggered	5	30°	0.3 - 0.7	effectiveness (concave, flat, & convex walls)
Yavuzkurt (1979, 1985)	staggered	5 & 10	30°	0.4 & 0.9	velocity & Turb. K.E. (exp. & numerical)
Miller & Crawford (1984)				up to 1.0	heat transfer coef. & effectiveness (numerical)

Experimental Apparatus and Operating Conditions

The experimental apparatus and the operating conditions are the same as in Part I of the paper. The surface consists of a 7 × 7 square array of holes. Hole to hole spacing is $3D_h$ in each direction. The first row of holes is located 721 mm downstream of a boundary layer trip wire. The center hole of the array is cast with naphthalene and is located 950 mm downstream of the trip wire (starting point of naphthalene surface is 899 mm downstream of the trip wire). When testing single hole injection, all of the holes in the array, except the center cast hole, are blocked.

The free-stream velocity is approximately 8.8 m/s for all of the tests. The average turbulence intensity of the free stream is measured as 0.52 percent. The boundary layer velocity profiles, measured in the absence of injection and with the holes blocked, have characteristics of a fully developed turbulent boundary layer. The free-stream Reynolds number based on the injection hole diameter is 1.4×10^4 (equivalent to 5.2×10^5 based on streamwise distance at the center hole). The boundary layer thickness (based on 99 percent of free-stream velocity) of crossflow at the center hole is 26.1 mm, which is close to the injection hole diameter of 25.4 mm. This condition is different from transpiration cooling, where the boundary layer is much thicker than the pore size. The virtual origin of the turbulent boundary layer is 253 mm upstream of the trip wire. This leads to a virtual starting length of 1152 mm (i.e., 45.4 D_h) for the velocity boundary layer before it encounters the naphthalene surface.

Ammonia Vapor and Diazo Paper Surface Visualization

The general method of ammonia vapor and diazo paper used for the mass transfer analogy is presented by Eckert (1976). Johnston (1964) and Dring et al. (1980) used an ammonia and diazo paper method to visualize the effects of film cooling jets on the endwall and/or of the flow around a rotating blade. This method is adopted to visualize the effectiveness patterns downstream of the injection holes. Anhydrous ammonia and diazo paper are used for this surface visualization study. When the ammonia vapor, mixed with the secondary air prior to injection, makes contact with the diazo paper, the yellow color of the diazo paper changes to blue. The blue shade shows the traces of the jet streams and thus where the surface is protected from the mainstream, which is free of ammonia. Therefore, the darker shade can be analyzed as relatively higher film cooling effectiveness. However, the diazo paper is not an impermeable surface and the paper may absorb some of the ammonia vapor. The blue shadings represent a combination of the effectiveness and the mass transfer rate. However, the visualizations provide good qualitative data for the local effectiveness.

Using a video image processor, the subtle shadings of the resulting visualizations are analyzed. The various gray shadings are transferred to their corresponding numerical values on each

Nomenclature

C_2 = dimensionless mass fraction of naphthalene vapor in the secondary flow; $C_2 = 0$ for pure air injection and $C_2 = 1$ for naphthalene saturated vapor injection
D_h = hole diameter = 25.4 mm in present study
D_{naph} = mass diffusion coefficient for naphthalene vapor in air
H = height of protruding cylinder
h = heat transfer coefficient
h' = heat transfer coefficient defined by Eqs. (4) and (10) in Part I
h_m = mass transfer coefficient
h'_m = mass transfer coefficient (Eq. (12) in Part I)
h'_0 = heat transfer coefficient for $T_2 = T_\infty$, $h'_0 = h$
M = blowing rate = $\rho_2 U_2 / \rho_\infty U_\infty$
$\dot{m}$ = naphthalene mass transfer rate per unit area
$\dot{m}_0$ = naphthalene mass transfer rate for $\rho_{v,2} = \rho_{v,\infty}$ (Eq. (1))
$\dot{m}_1$ = naphthalene mass transfer rate for $\rho_{v,2} = \rho_{v,w}$ (Eq. (1))
n = an exponent in the analogy: Nu/Sh = $(\text{Pr}/\text{Sc})^n$
P = pitch of an array of holes (i.e., hole-to-hole spacing; $3D_h$)
Pr = Prandtl number = $\mu\, C_p / k$
q_w = heat flux
Re_h = Reynolds number based on the hole diameter and an average velocity in hole = $\bar{U} D_h / \nu$
Sc = Schmidt number for naphthalene in air = $\nu / D_{\text{naph}} \cong 2.28$ at 298 K and 0.1 MPa
Sh = Sherwood number based on the hole diamter D_h; Sh = $h_m D_h / D_{\text{naph}}$
Sh_s = Sherwood number for flow over a solid flat plate
Sh′ = Sherwood number based on h'_m, $h'_m D_h / D_{\text{naph}}$
Sh'_0 = Sherwood number for $\rho_{v,2} = \rho_{v,\infty}$ (Eq. (2)); Sh'_0 = Sh
Sh'_1 = Sherwood number for $\rho_{v,2} = \rho_{v,w}$ (Eq. (2))
$\overline{\text{Sh}}$ = lateral average Sherwood number (over $-1.5 \leq Z/D_h \leq 1.5$)
T_2 = temperature of the secondary flow
T_{aw} = adiabatic wall temperature
T_w = local wall temperature
T_∞ = free-stream temperature
$\bar{U}$ = average velocity in hole
U_∞ = approaching velocity (free-stream velocity); about 8.8 m/s in present study
X = streamwise (crossflow) distance from center of injection holes
Z = lateral distance across span measured from center of injection holes
δ = boundary layer thickness (based on 99 percent of free-stream velocity)
η_{aw} = adiabatic wall cooling effectiveness
η_{iw} = impermeable wall effectiveness
K = constant defined in Eq. (7) = $(h'_1 - h'_0)/h'_0$
ν = kinematic viscosity = μ/ρ
θ = angle around injection hole = 0 deg at the leading edge
θ' = dimensionless temperature = $(T_2 - T_\infty)/(T_w - T_\infty)$

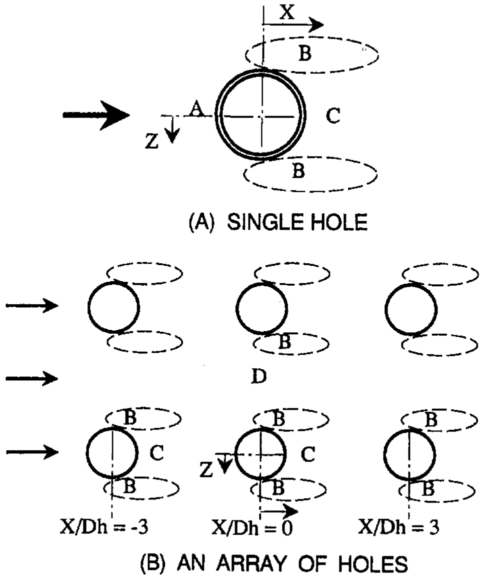

Fig. 1 Divided regions with jet injected into crossflow (cf. Goldstein and Taylor, 1982)

pixel. The numerical values of the image are not correlated linearly with the effectiveness values, however the numerical values (i.e., relative values, but not absolute values) match fairly well with the local effectiveness.

Results and Discussion

First, the flat plate mass transfer coefficient is measured from the naphthalene test plate (the center hole is plugged by naphthalene) with all of the injection holes blocked. The resulting coefficients are compared with the heat transfer correlations using the heat/mass transfer analogy and with a correction factor of inactive/equivalent of unheated starting length. The measured mass Stanton numbers fall within 4 percent from the results of von Karman's formulation (1939). This indicates the validity of the analogy with which the present results can apply for heat transfer. The discrepancy is within the estimated uncertainty of 7.1 percent with a 95 percent confidence level.

The measured local mass transfer rates are presented in a normalized form with the ratio of the mass transfer rate with injection to the mass transfer rate from a solid flat plate. Presenting the results in the normalized form may eliminate bias errors existing in the experimental system or in the properties of naphthalene. Also, the normalized value can be converted easily to a heat transfer value without determining the unknown exponent in the analogy $\mathrm{Nu/Sh} = (\mathrm{Pr/Sc})^n$.

1 Injection Through Single Hole

1.1 Local Heat/Mass Transfer Coefficient. The mass transfer rate around a normal jet injected into a crossflow can be divided into three different regions as shown schematically in Fig. 1(*a*). They are:

(A) Upstream region of the injection hole
(B) Adjacent side regions of the injection hole
(C) Region downstream of the injection hole

(A) Upstream region of the injection hole. This area shows little change due to the jet injection at low blowing rates, but the Sherwood number in this area increases quickly as the blowing rate is increased. The flow pattern around the injected jet can be divided into two different forms with respect to the blowing. The expected flow patterns are drawn in Fig. 2 for both cases. The injected jet stream will be suppressed by the crossflow and spreads on the surface at low blowing rates. Thus, mass transfer rates at the upstream region (region A) are slightly different from those of flow over a solid flat plate (Figs. 3(*a*) and 3(*c*)). At high blowing rates, the jet will penetrate into the crossflow, and the vortex shedding of the jet takes the form of ring vortices, Fig. 2. This results in a crossflow that is highly disturbed by the jet injection, even upstream of the jet. At the high blowing rate $M = 2.19$, a peak Sherwood number, at $X/D_h = -0.5$ and $Z/D_h = \pm 0.3$, is approximately three times that of flow over a solid flat plate (Fig. 3(*g*)). A high Sherwood number is obtained in all regions around the periphery of the injection hole (cf. the contour plot in Fig. 4(*e*)). Note that the area between the two circles in the contour plots represents the (0.04 D_h wide) rim of the nonsubliming metal, which is used for reference points, where the smaller circle represents the injection hole. This high value will be caused by interaction between the jet and the crossflow, which results in the vortex shedding of the jet and the horseshoe vortex formed by the crossflow. The surface trace of the horseshoe vortex, formed around a solid bar in crossflow, is clearly shown in Figs. 3(*i*), 3(*j*), and 4(*f*). These results are obtained by the measurements with circular solid bars, which are placed at the hole site with ratios of height to diameter $H/D_h = 1$. When the Sherwood number of the jet flow is compared with the flow around the solid bar, the magnitude and the affected area associated with the jet are less than with flow around the solid bar. The horseshoe vortex system around the jet (at high M) may be formed by crossflow as the geometric similarity. However, Andreopoulos (1985) has shown that the horseshoe-vortex around the jet is weak and may be collapsed by the jet vortex shedding. When the jet is injected into the crossflow at 35 deg from the surface, the high Sherwood number upstream of the jet does not occur (Goldstein and Taylor, 1982).

(B) Adjacent side regions of the injection hole. This region is formed beside the injection hole due to the interaction of the crossflow and the injected jet. A high mass transfer rate generally occurs in this region due to the high shear from the interaction. This region is confined between $Z/D_h = 0.5$ and 1.0 with the region, $Z/D_h > 1.0$, not affected by the jet injection (Figs. 3 and 4). The peak point of the Sherwood number moves upstream with an increased blowing rate. This peak occurs at $X/D_h = 0.2$ for $M = 0.22$ and at $X/D_h = 0.0$ for $M = 2.19$. The peak value increases from $\mathrm{Sh/Sh}_s = 2.5$ at $M = 0.22$ to $\mathrm{Sh/Sh}_s = 3.6$ at $M = 0.57$, and then decreases gradually to $\mathrm{Sh/Sh}_s = 3.4$ at $M = 0.99$ and $\mathrm{Sh/Sh}_s = 3.0$ at $M = 2.19$ (Fig. 3). The side vortex, created by the shearing action, is formed near the surface at low blowing rates where the injected jet stream

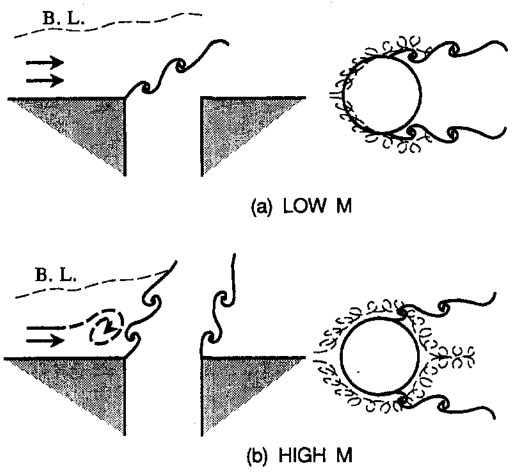

Fig. 2 Expected vortex patterns with jet injected into crossflow

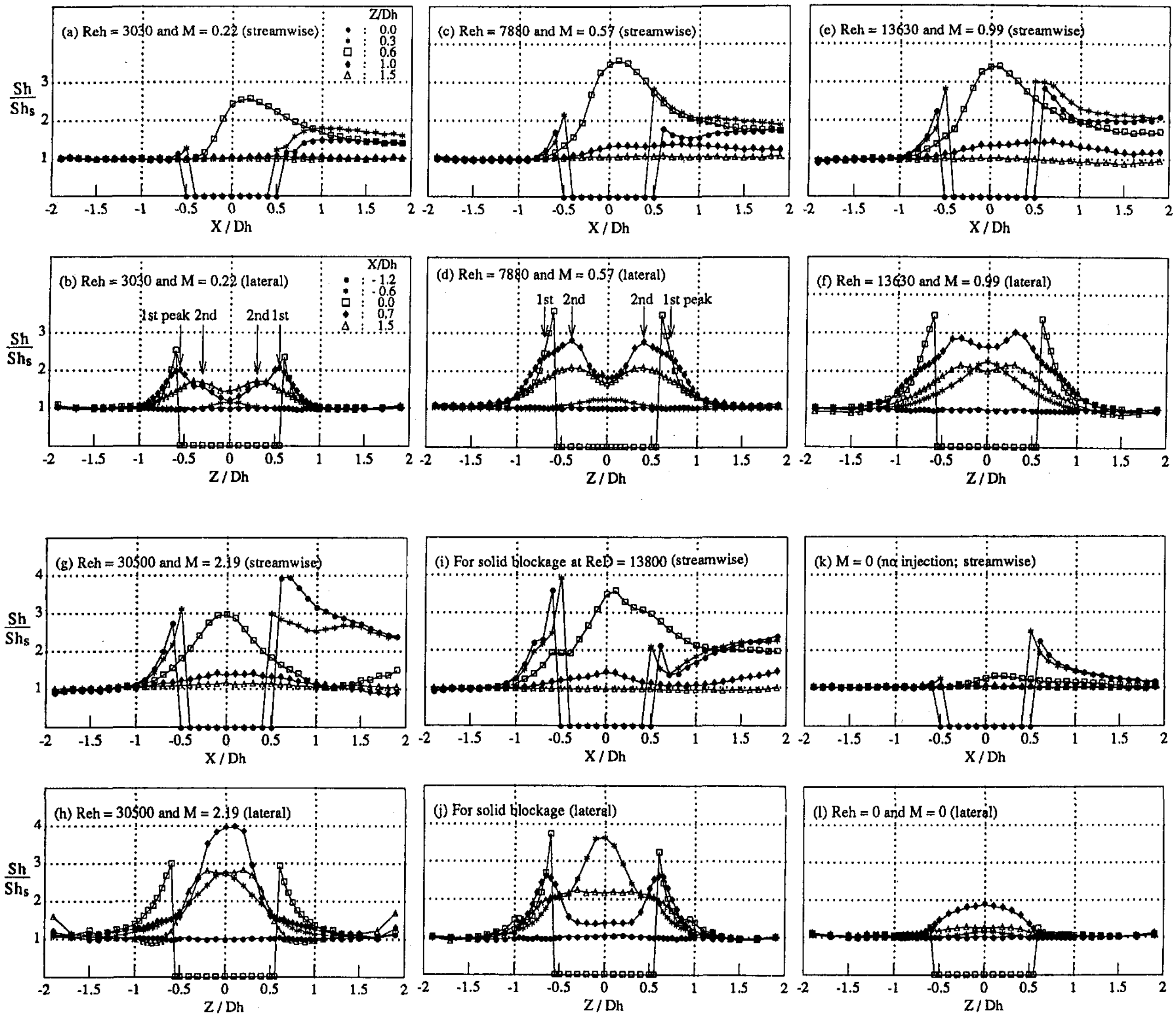

Fig. 3 Normalized Sh for single-hole injections

spreads on the surface by the crossflow. This side vortex is responsible for the high transfer coefficient. However, the side vortex will form farther from the surface at higher blowing rates; likewise, the jet will penetrate farther into the crossflow and will be confined within the horseshoe vortex formed upstream of the injection hole. The Sherwood number contours (Fig. 4), which are obtained on the surface, show that the side vortex shrinks with increasing blowing rate and is formed like a corner vortex surrounded by a horseshoe vortex around a solid bar within a crossflow. The contour pattern indicates that the vortices formed around the jet stream are weaker than the vortices around the solid bar.

(C) Region downstream of the injection hole. In this region, the pattern of Sherwood number distribution can be divided into two groups based on whether the injected jet lifts up or not. Close examination of the contour plots shows that the low transfer region just downstream of the hole is bounded by two high transfer zones due to the side vortices (Figs. 4(*a*) and 4(*b*)). This area decreases in width with increased blowing rate in the low blowing rate range. This contour pattern is quite different from that with angled injection (35 deg and a row of injection holes; Goldstein and Taylor, 1982). By increasing the blowing rate to $M = 0.57$ (Fig. 4(*c*)), the low transfer region is narrowed and detached from the periphery of the injection hole. The isolated low transfer region moves downstream as the blowing rate is increased (Fig. 4(*d*)); at $M = 2.19$ this low region has moved off the measurement domain (Fig. 4(*e*)). This region is related to the area of high film cooling effectiveness, which will be discussed later. This region is created because the injected jet blocks the crossflow and is somewhat similar to the separation region created by flow around a solid bar. Note the low transfer coefficient on the endwall appears in the wake zone behind the solid cylinder.

The Sherwood number variation in the axial direction (along $Z/D_h = 0$) has three patterns (Figs. 3 for $X/D_h \geq 0.5$). At low blowing rates $M \leq 0.35$, the Sherwood numbers, following a minimum just downstream of the injection hole, increase up to $X/D_h = 1.1$ at $M = 0.22$ (Fig. 3(*a*)). The Sherwood numbers gradually decrease downstream of the peak points. At a moderate blowing rate ($M = 0.57$), the Sherwood number has a maximum at the trailing edge of the hole, reaches a minimum downstream, and then increases slowly as shown in Fig. 3(*c*). At the higher blowing rates $M \geq 1.0$, the Sherwood number shows a maximum at the trailing edge of the hole and decreases downstream (Figs. 3(*e*) and 3(*g*)). With a crossflow around a solid bar, the location of the minimum is at $X/D_h = 0.7$ and 1.5 for the heights $H/D_h = 1$ and 6 (Figs. 3(*i*) and 5(*c*)), respectively. When there is no injection through the hole (cavity flow on a flat plate), the affected area is closely confined downstream from the hole, although there is a big effect on the inside

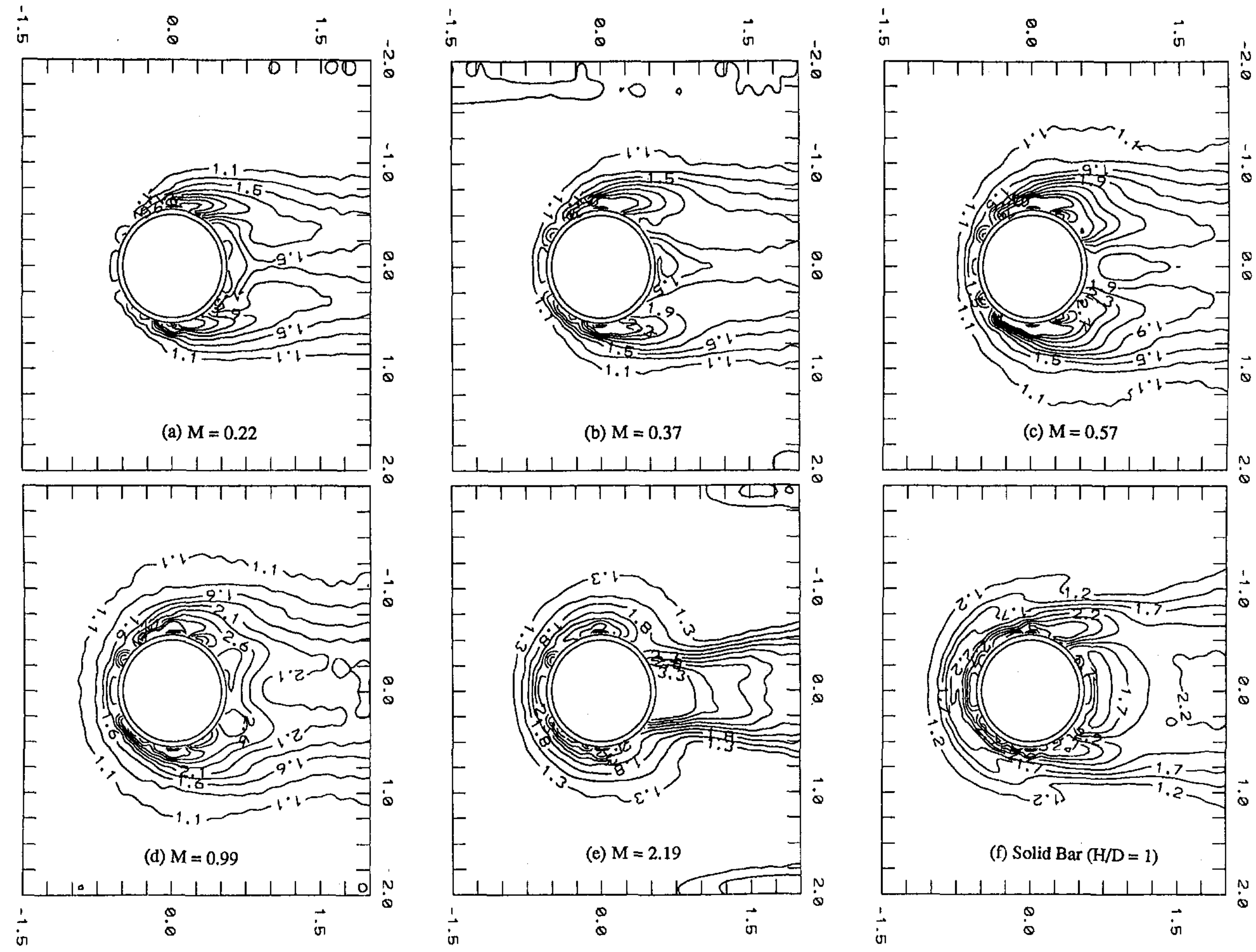
(a) M = 0.22
(b) M = 0.37
(c) M = 0.57
(d) M = 0.99
(e) M = 2.19
(f) Solid Bar (H/D = 1)

Fig. 4 Sh/Sh_0 contours for single-hole injections

surface of the hole (Part I). The Sherwood numbers achieve a maximum at the trailing edge of the hole and then decrease quickly downstream, Fig. 3(*k*). This cavity flow behavior is completely different from that involving blowing from the hole in which the jet blocks and deflects the crossflow, even for the low blowing rate case.

A kidney-type vortex is formed downstream of a jet as shown by Goldstein et al. (1968). In the lateral view, the minimum (valley) of the Sherwood number is between two peaks as indicated in Fig. 3. The two peak points correspond to the high shear regions that are swept by the side and the kidney-type vortices. At blowing rate $M = 0.22$ as shown in Fig. 3(*b*), the first peaks for $X/D_h = 0.7$ are placed at $Z/D_h = \pm 0.55$, while the second "peak" barely exists at $Z/D_h = \pm 0.3$. The first peaks, which are caused by the upstream side vortex, are diminished at $X/D_h = 1.5$. The second peaks, which result from the kidney vortex, are developed as the jet moves downstream and are shown clearly at $X/D_h = 1.5$. At the blowing rate $M = 0.57$ (Fig. 3(*d*)), the first "peak" is indicated at $Z/D_h = \pm 0.7$ as a break in the slope of Sh and the second (true) peaks at $Z/D_h = \pm 0.4$ have a higher value. The Sherwood numbers at the peaks (the second peaks) and the valley at the center between the peaks increase quickly with the blowing rate and reach a higher value than at the sides of the hole. At the blowing rate $M = 2.19$ (Fig. 3(*h*)), there is only one high peak (no valley point), which is four times higher than Sh for flat plate flow, located at the center for $X/D_h = 0.7$; two peaks also exist downstream at $X/D_h = 1.5$. When the pattern of Sherwood number distribution is compared with the crossflow around a solid bar, there are differences. Even the distributions of Sherwood numbers for the different ratios of height to the diameter of solid cylinders, $H/D = 1$ and 6, show a big difference in the downstream region (Cho, 1992).

1.2 Average Mass Transfer Rates. The nondimensional Sherwood numbers, averaged over $-1.5 \leq Z/D_h \leq 1.5$, excluding the injection hole area, are presented in Fig. 5. The selected averages increase with blowing rates in region A ($X/D_h \leq -0.1$) where they show a small peak at $X/D_h = -0.6$. At the middle part (region B around $X/D_h = 0.5$), the averaged Sherwood numbers divide to two groups. One group at low blowing rates ($M \leq 0.37$) shows that the average Sherwood numbers, even low values, increase gradually and then decrease slowly after $X/D_h = 0.4$ (Fig. 5(*a*)). The other group with the higher blowing rates ($M \geq 0.57$) indicate that the average values reach a peak at $X/D_h = 0.6$ and then drop to a value of 1.5 or 1.6, which is almost invariant with blowing rate (Fig. 5(*b*)). The pattern of the average values around the solid bars, as shown in Fig. 5(*c*), is somewhat different from the jet injection.

Figures 5(*a*) and 5(*b*) present a comparison with angled injection (35 deg) results for a row of injection holes from Goldstein and Taylor (1982) at various blowing rates. The average values for normal injection are approximately 30 percent higher than the 35 deg injection (cf. the normal jet covers less exposed surface area). At low blowing rates (Fig. 5(*a*)), the angled injection has two clear peaks. At $M \cong 2.0$ (Fig. 5(*b*)), the normalized average Sherwood numbers have a similar trend (but with different magnitudes) in both cases for $X/D_h * \sin * \theta) \geq -0.3$. However, the 35 deg injection has a low value at the upstream part (about $X/D_h * \sin(35 \text{ deg}) \leq -0.3$; the leading

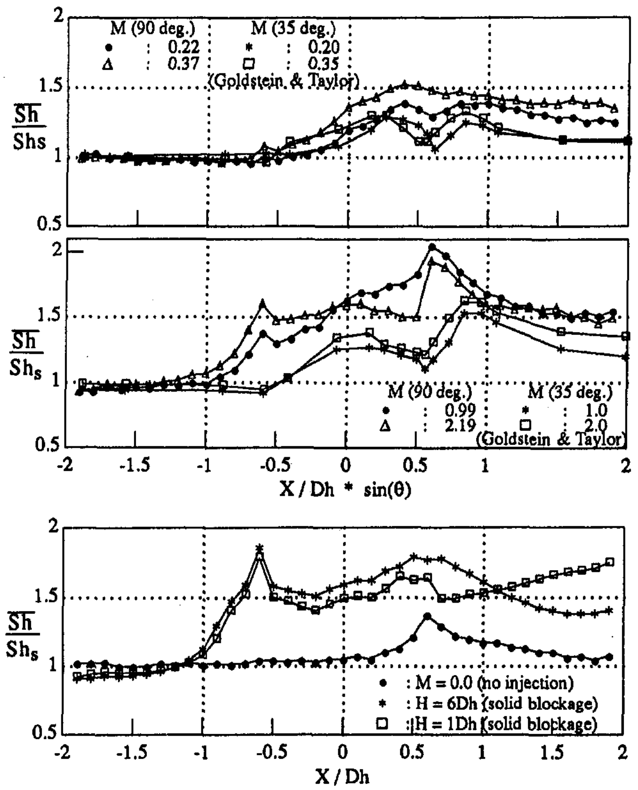

Fig. 5 Normalized average Sh for single-hole injections ($-1.5 \le Z/D_h \le 1.5$) (compared to a row of 35 deg injections, Goldstein and Taylor, 1982)

edge of the hole) due probably to absence of the horseshoe vortex.

Heat/mass transfer coefficient around the injection hole is about four times higher in local value than flow over a solid flat plate and twice as large on the lateral average. However, the area taken for the average is arbitrarily chosen, $-1.5 < Z/D_h < 1.5$. Therefore, heat/mass flux around the injection hole must be determined by the local coefficient rather than an average value or that of flow over a solid plate.

1.3 Film Cooling Effectiveness. The pattern of film cooling effectiveness is shown with local values and in contour plots. In region A (Fig. 1(*a*)), the effectiveness has a nonzero value, although very small, at blowing rates of $M \ge 0.57$ (Fig. 6(*c*)). This can be explained by the mixing of the jet stream and the crossflow that forms the down-washing (horseshoe) vortex and/or the vortex shedding of the jet stream (Fig. 2(*b*)). High effectiveness values are obtained near the hole at the lower blowing rate $M = 0.22$ because the injected jet spreads over the downstream surface. However, the effectiveness decreases quickly downstream because there is less mass flux for a low blowing rate of injection jets. The effectiveness decreases with an increasing blowing rate due to the jet penetrating into the crossflow. The film cooling effectiveness reaches the maximum near the downstream edge of the injection hole and decreases downstream from it at $M \le 0.57$ (Figs. 6(*a*) and 6(*c*)). However at higher blowing rate $M = 1.0$ (Fig. 6(*e*)), the maximum point of effectiveness (along $Z/D_h = 0$) is placed at $X/D_h = 0.8$, at which the low transfer rate occurred. Generally, the low transfer region downstream of the injection hole corresponds with the highest film cooling effectiveness. However, the high effectiveness also is found at the high heat transfer region, which is caused by the jet stream rather than the crossflow, such as the zone swept by the kidney vortex. As shown in Figs. 6(*b*), 6(*d*), and 6(*f*), the uniform high effectiveness zone for $X/D_h = 0.7$ is within the two peaks of the Sherwood number, which will be related to the location swept by the kidney vortex and was explained as the "second peak" in the previous section. The kidney vortex region having a relatively high value of effectiveness is in the same region of high transfer rates ($Sh/Sh_s > 1.0$; the flow field affected by the jet injection). This phenomenon is found for low blowing rates $M \le 0.57$. A jet stream touching the surface can produce high effectiveness and mass transfer but the main flow can only produce high mass transfer. The region with nonzero effectiveness is smaller than the high mass transfer region caused by the injected jet for blowing rate $M = 1.0$ (Figs. 3(*f*) and 6(*f*)). The area common to the two regions (zero effectiveness but high transfer rate) will have higher surface temperature because of the increasing transfer rate. Figure 7 shows values of average effectiveness over $-1.5 \le Z/D_h \le 1.5$.

The surface visualizations, Fig. 9, obtained with ammonia and diazo paper, agree fairly well with the contour plots in Fig. 8. The magnitude of the contour plots, Figs. 9(*b*) and 9(*d*), obtained from the gray shadings of the visualization (Figs. 9(*a*) and (*c*)), is somewhat arbitrary. The darkest point (maximum effectiveness point) is assigned a value of 100 and a light region (zero effectiveness) is assigned a value of 0.

The surface temperature distribution around the injection hole can be derived from the heat transfer coefficient, the film cooling effectiveness, and a presumed heat flux.

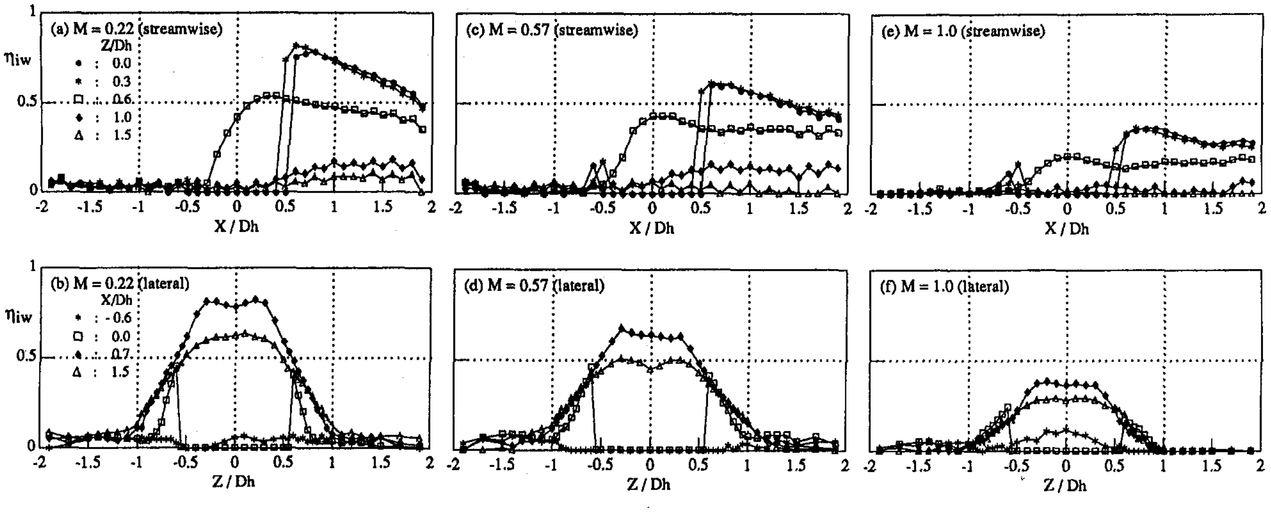

Fig. 6 Effectiveness values for single-hole injection ($U_\infty = 8.8$ m/s)

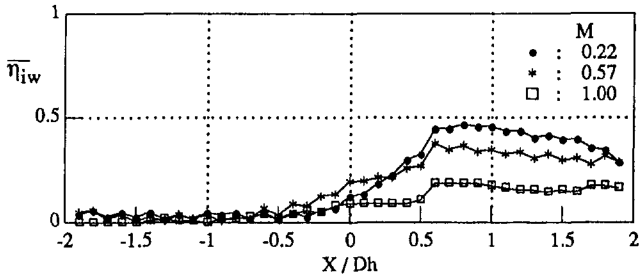

Fig. 7 Lateral average effectiveness values for single-hole injection ($-1.5 \le Z/D_h \le 1.5$)

1.4 Sherwood number, Sh'_1, With Saturated Vapor Injection. Local values of the Sherwood number, Sh'_1, obtained from the saturated vapor injection, are plotted in Fig. 10. In region A (Fig. 1(*a*)), Sh'_1 is slightly different from Sh. That can be explained by small mixing of the jet stream with the down-washing vortex (horseshoe vortex) of the crossflow. In region B, the side vortex (interaction) mixes well with the jet stream and the crossflow, and results in a high vapor concentration and less mass transfer on the surface. This effect is greater at lower blowing rates since the vortex remains on the surface. At high blowing rates, the vortex lifts up and has less effect on the surface.

In region C, the injected jet stream, which consists of saturated naphthalene vapor in air, covers the downstream surface. This results in smaller mass transfer, less than that of flow over a solid flat plate, and high film cooling effectiveness. At $M = 0.22$ (Fig. 10(*a*)), Sh'_1 has a minimum just downstream of the injection hole, and increases downstream from this. However, at higher blowing rates $M \ge 0.57$ (Figs. 10(*c*) and 10(*e*)), Sh'_1 has a maximum near the trailing edge of the injection hole, reaches a minimum downstream and then increases slowly beyond the minimum location. The locations of the minimum (along $Z/D_h = 0$) are at $X/D_h = 0.8$ and 1.0 at blowing rates $M = 0.57$ and 1.0, respectively. Sh'_1 is higher than for the lower blowing rate, even though it has a higher mass flux of naphthalene, because the jet penetrates into the crossflow for high blowing rates.

A second effect is caused by the movement of the mixed side vortex. For $X/D_h = 0.7$ in Fig. 10(*d*), the "first peak" of Sh'_1, which is caused by the side vortex, has a lower value at $Z/D_h = \pm 0.7$, and the "second peak", shown in pure air used as the injected flow (Fig. 3(*d*)), disappears due to sweeping of the kidney vortex with saturated vapor. At $M = 1.0$ (Fig. 10(*f*)), Sh'_1 at $X/D_h = 1.5$ is lower than at $X/D_h = 0.7$. This is caused by touchdown of the jet stream after lifting up. Figure 11 shows the average values of Sh'_1.

2 Injection Through an Array of Holes

2.1 Heat/Mass Transfer Coefficient. The injection holes for the seven by seven in-line array have a spacing of three hole diameters in both directions. The center hole area of the fourth row is cast with naphthalene (active area) rather than the entire array of holes; thus this closely, but not perfectly simulates an active area for the entire array. However, Kumada et al. (1981) show that the coefficient remains almost constant, depending on the blowing rate, from row to row. Thus in the present results (Fig. 12), the heat/mass transfer coefficient is a local value for an active region surrounding one hole in the array, but it is close to the local values on an active array surface. In the upstream region ($-2.0 < X/D_h < -1.0$), the values of Sherwood number presented will be different from an active array value as discussed, but these can be replaced by the values in the region $1.0 < X/D_h < 2.0$, assuming periodicity. However, film cooling effectiveness, which is determined in

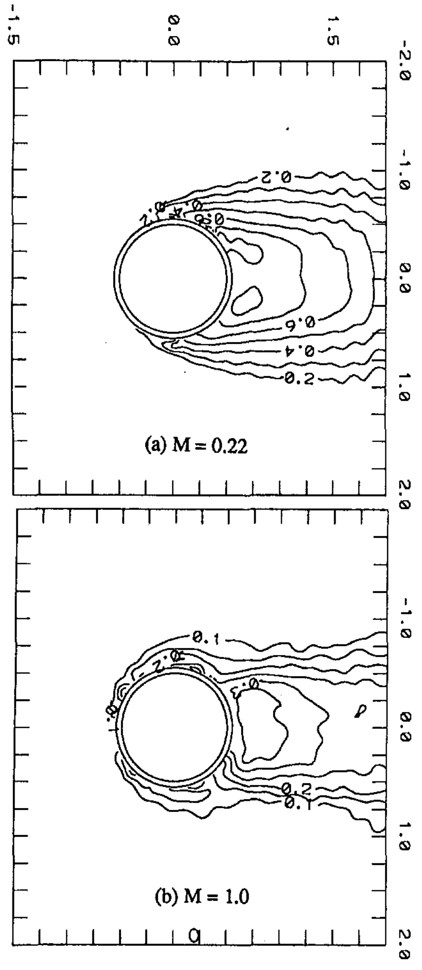

Fig. 8 Contours of η_{iw} for single-hole injections

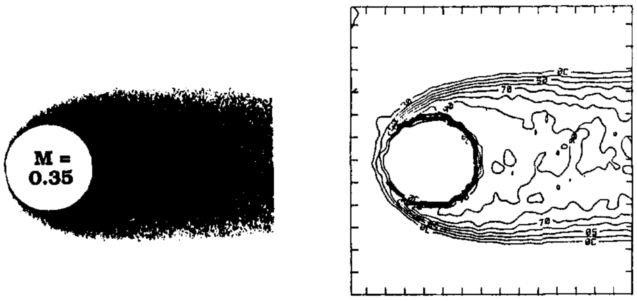

VISUALIZATION AT M = 0.35

CONTOURS OF IMAGE AT M = 0.35

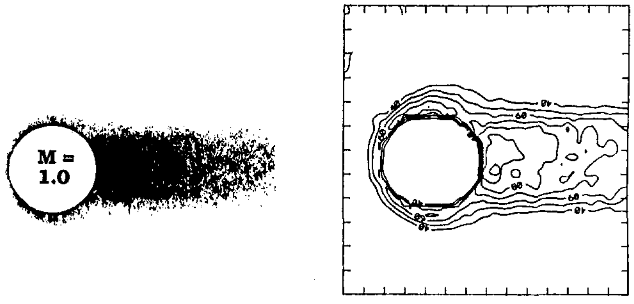

VISUALIZATION AT M = 1.0

(d) CONTOURS OF IMAGE AT M = 1.0

Fig. 9 Ammonia-diazo surface visualization for single-hole injection

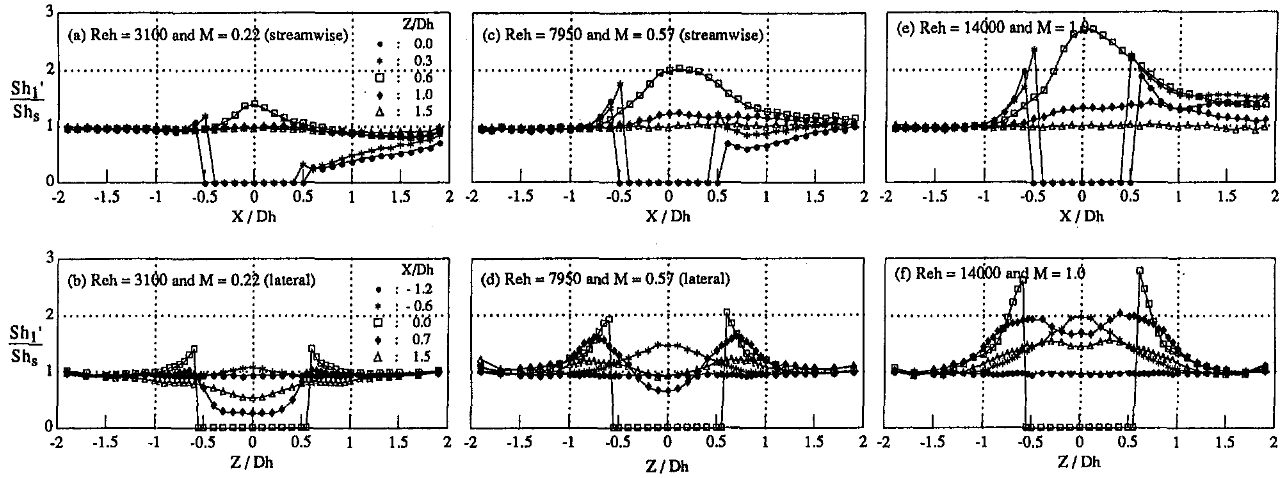

Fig. 10 Normalized Sh_l' (using saturated naphthalene vapor) for single-hole injection

Eq. (1) or (2), represents the same value as would be found with an active array because the effectiveness correlates with both pure air and saturated vapor injections. At the fourth row, the change in the flow pattern in subsequent rows is small as shown in surface visualizations and local measurements. To show the difference from the first row to the fourth row, extra measurements were conducted with the first three, two, or one rows blocked. It follows that the heat/mass transfer coefficients are determined at each row, from the first to the fourth. The values change slightly from the third row to the fourth row shown by Cho (1992).

In arrays of normal injection holes, the mass transfer rate on the exposed surface can be divided into three different zones as shown schematically in Fig. 1(*b*). Region A in the single-hole injection is replaced by region C due to the periodic pattern. The regions are:

(B) adjacent side regions of the injection holes
(C) regions downstream (or upstream) of the injection holes
(D) middle regions between the injection holes

The boundary layer thickness, 99 percent of free-stream velocity, of the crossflow at the first row is 21.3 mm. Region B has a reduced area with respect to the single-hole injection, and it is shifted slightly to the downstream side. In this region, the peak value around $X/D_h = 0.1$ for $Z/D_h = 0.6$ is reduced approximately 20 percent from that with single-hole injection (Figs. 3 and 12). This is a result of the neighboring holes, which restrict the flow. In region C, two differences are indicated. The first is that the pattern of Sherwood numbers is similar to a slightly higher blowing rate with a single-hole injection. This can be attributed to a more developed boundary layer and a lower near-wall velocity of the crossflow due to the interference with the preceding rows. The other difference is that the two peaks for $X/D_h = 0.7$ shift to the center and the values for $X/D_h = 1.5$ are flat. This is because the flow is restricted by the neighboring holes and the kidney vortex cannot develop or may lift up from the surface due to injection from the next rows. In region D, the values are affected slightly because the holes lie in an in-line array.

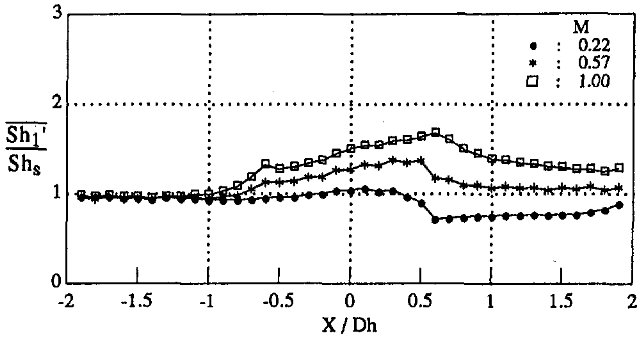

Fig. 11 Normalized average Sh_l' for single-hole injections ($-1.5 \le Z/D_h \le 1.5$)

The variation of the local values is milder than at the single-hole injection. The flow is disturbed and mixed in the whole flow field, and this reduces the strength of the individual vortices. If the average values are compared with the single-hole injection, the average values are approximately the same at the blowing rates $M = 0.22$ and 0.36, but the average value at $M = 0.6$ is lower for the array.

2.2 Film Cooling Effectiveness. The local values of film cooling effectiveness at the fourth row in an array with normal injections are presented in Fig. 13. The center lines between rows of holes are placed at $X/D_h = \pm 1.5$. The values at $X/D_h = \pm 1.5$ match each other well, except along $Z/D_h = 1.0$ and 1.5 lines, which are in region D (Fig. 3(*b*)). This may be due to the gradual accumulation and spread of injectant along hole columns. In regions B and C (adjacent side and behind hole), the film cooling effectiveness values are about the same as for the single hole injection. However, the values are compared only at a low blowing rate (at which the injected jet spreads on the surface) and near the injection hole with a small spacing. If a high blowing rate were used, the results might be somewhat different. The effectiveness values increase gradually in region D because injectant accumulates from the front rows. Figure 14 shows the laterally averaged values.

Sh_l' is presented in Fig. 15 at a blowing rate $M = 0.22$. The overall pattern of the values is similar to the single-hole injection, except for the region some distance upstream of the hole.

Conclusions

With injection through a single hole the peak heat/mass transfer is up to four times that for a similar mainstream flow over a solid plate. The corresponding ratio of the average value of Sh is about 2.4 for blowing rate from 0.22 to 2.19. The peak value of the film cooling effectiveness is approximately 1.7 times the laterally averaged value. With injection through the in-line array of holes, the peak mass transfer coefficient, Sh, is approximately two times the laterally averaged value even in the low blowing rate range $M = 0.22$ to 0.6. As a result of the extreme differences between peaks and the average, it is difficult

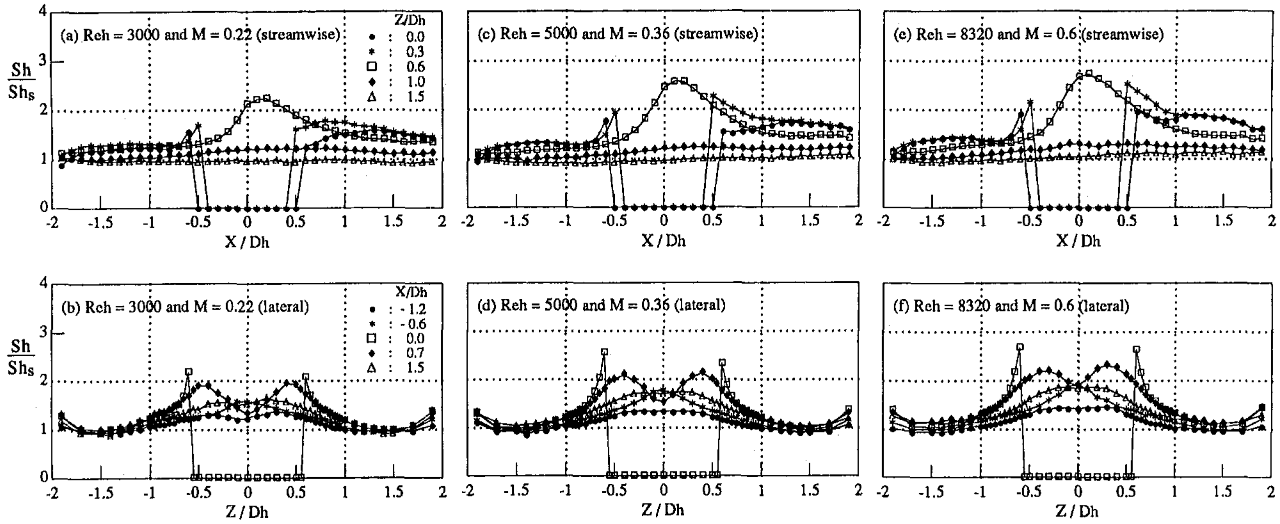

Fig. 12 Normalized Sh for an array of hole injections (at fourth row)

to predict the heat transfer coefficient and the film cooling effectiveness from a local averaged measurement in the near hole region.

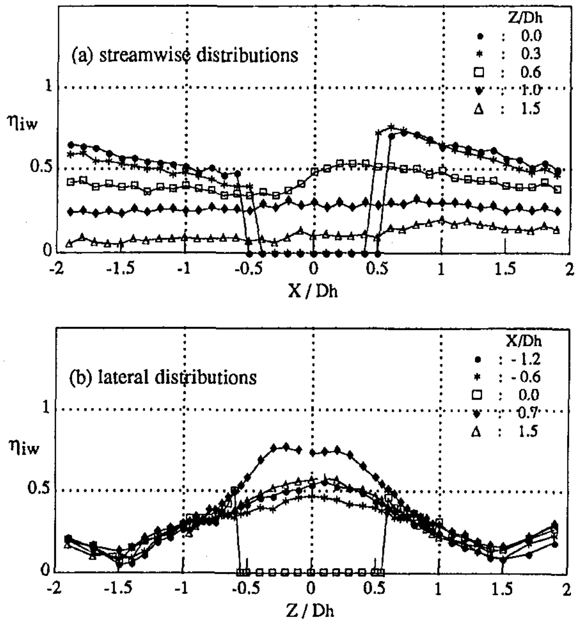

Fig. 13 Effectiveness for an array of holes at M = 0.21, U = 8.8 m/s, and fourth row

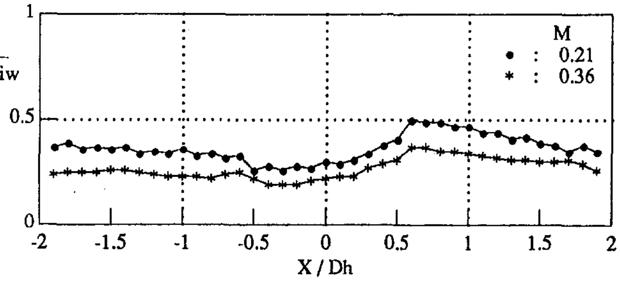

Fig. 14 Lateral average effectiveness for an array of holes at U_∞ = 8.8 m/s and fourth row ($-1.5 \leq Z/D_h \leq 1.5$)

Injection Through a Single Hole

(*i*) For $M < 1.0$, the Sh is high on the side region of the injection hole due to an interaction of the jet and the main stream. The Sh is approximately three to four times that of flow over a solid flat plate. For $M \gtrsim 1.0$, Sh is high on the downstream surface of the injection hole and the value is about three to four times higher than with a solid flat plate.

(*ii*) The mass transfer around the injection holes is dominated by formations of horseshoe, side, and kidney-type vortices, which are generated by the jet stream and crossflow interaction. However, the Sh pattern is different from flow around a solid bar, which is dominated by the horseshoe and corner vortices.

(*iii*) For a case without injection, but open holes, the Sh is slightly different from that with a solid flat plate. The affected area on the exposed surface is confined only to the downstream region. However, the inside hole surface is largely affected by the crossflow (Part I).

(*iv*) The local film cooling effectiveness near the injection

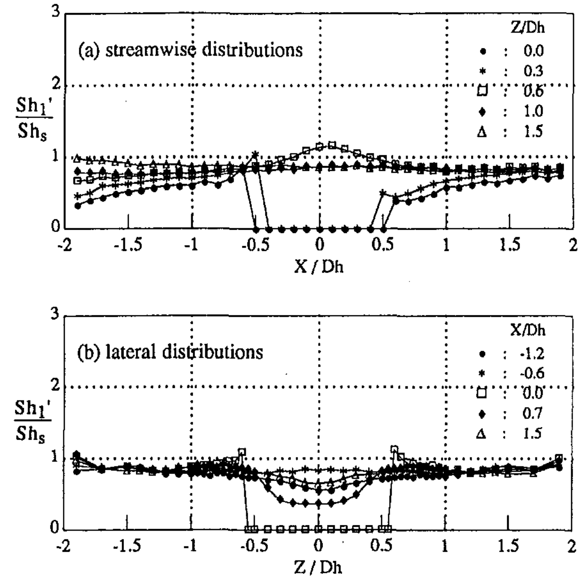

Fig. 15 Normalized Sh_l' for an array of holes at M = 0.22 and fourth row

hole is obtained by pure air and naphthalene-saturated vapor injections. The results compare favorably with the ammonia and diazo paper surface visualization.

Injection Through an Array of Holes

(*i*) The overall pattern of Sh is similar to that for the single hole injection, except at the upstream region, which is, however, the downstream region of the previous hole (cf. periodic for an array). The variation is milder than for the single-hole injection due to mixing of the flows.

(*ii*) On the side region of the holes, Sh is reduced slightly from that with single-hole injection because the crossflow is restricted by the neighboring holes. The overall Sh is comparable to that of a slightly higher M with single-hole injection because the near-wall velocity of cross stream is lower near the surface due to jet interference.

(*iii*) The effectiveness is high and uniform in the streamwise direction but not in the lateral direction (across the holes) in the in-line array of holes.

Acknowledgments

Support from the Air Force Office of Scientific Research and through the Engineering Research Program of the Department of Energy aided greatly in the conduct of this study.

References

Andreopoulos, J., 1985, "On the Structure of Jets in a Crossflow," *J. Fluid Mech.*, Vol. 157, pp. 163–197.

Cho, H. H., 1992, "Heat/Mass Transfer Flow Through an Array of Holes and Slits," Ph.D. Thesis, Univ. of Minnesota.

Choe, H., Kays, W. M., and Moffat, R. J., 1976, "Turbulent Boundary Layer on a Full-Coverage Film-Cooling Surface—An Experimental Heat Transfer Study With Normal Injection," NASA CR-2642.

Crawford, M. E., Kays, W. M., and Moffat, R. J., 1976, "Heat Transfer to a Full-Coverage Film-Cooling Surface With 30° Slant-Hole Injection," NASA CR-2786.

Dring, R. P., Blair, M. F., and Joslyn, H. D., 1980, "An Experimental Investigation of Film Cooling on a Turbine Rotor Blade," ASME *Journal of Engineering for Power*, Vol. 102, pp. 81–87.

Eckert, E. R. G., 1976, "Analogies to Heat Transfer Processes," *Measurement in Heat Transfer*, E. R. G. Eckert and R. J. Goldstein, eds., Hemisphere Publishing Corp., New York, pp. 397–423.

Eckert, E. R. G., 1984, "Analysis of Film Cooling and Full-Coverage Film Cooling of Gas Turbine Blades," ASME *Journal of Engineering for Gas Turbines and Power*, Vol. 106, pp. 206–213.

Furuhama, K., and Moffat, R. J., 1983, "Turbulent Boundary Layer Heat Transfer on a Convex Wall With Discrete Hole Injection," presented at the Joint ASME/JSME Gas Turbine Conference, Tokyo, Japan.

Goldstein, R. J., Eckert, E. R. G., and Ramsey, J. W., 1968, "Film Cooling With Injection Through Holes: Adiabatic Wall Temperature Downstream of a Circular Holes," ASME *Journal of Engineering for Power*, Vol. 100, pp. 384–395.

Goldstein, R. J., 1971, "Film Cooling," *Advances in Heat Transfer*, Vol. 7, Academic Press, pp. 321–379.

Goldstein, R. J., and Taylor, J. R., 1982, "Mass Transfer in the Neighborhood of Jets Entering a Crossflow," ASME *Journal of Heat Transfer*, Vol. 104, pp. 715–721.

Goldstein, R. J., and Karni, J., 1984, "The Effect of a Wall Boundary Layer on Local Mass Transfer From a Cylinder in Crossflow," ASME *Journal of Heat Transfer*, Vol. 106, pp. 260–267.

Hay, H., Lampard, D., Maali, R., and Burns, I., 1986, "Simultaneous Determination of Heat Transfer Coefficient and Adiabatic Wall Effectiveness on a Film Cooled Surface Using the Swollen Polymer Technique," *Proc. 8th Int. H. T. Conf.*, U.S.A., Vol. 2, pp. 489–494.

Johnston, J. P., 1964, "A Wall-Trace, Flow Visualization Technique for Rotating Surfaces in Air," ASME *Journal of Basic Engineering*, Vol. 86, pp. 907–908.

Karni, J., and Goldstein, R. J., 1990, "Surface Injection Effect on Mass Transfer From a Cylinder in Crossflow: A Simulation of Film Cooling in the Leading Edge Region of a Turbine Blade," ASME *Journal of Turbomachinery*, Vol. 112, pp. 418–427.

Kasagi, N., Hirata, M., and Kumada, M., 1981, "Studies of Full-Coverage Film Cooling. Part 1: Cooling Effectiveness of Thermal Conductive Wall," ASME Paper No. 81-GT-37.

Kasagi, N., Hirata, M., Ikeyama, M., Makino, M., and Kumada, M., 1988, "Full-Coverage Film Cooling on Curved Walls, Part 3, Cooling Effectiveness on Concave and Convex Walls," *Trans. JSME*, Ser. B, Vol. 54 No. 497, pp. 217–223.

Kim, H. K., Moffat, R. J., and Kays, W. M., 1979, "Heat Transfer to a Full-Coverage Film-Cooling Surface With Compound Angle (30° and 45°) Hole Injection," NASA CR-3103.

Kumada, M., Hirata, M., and Kasagi, N., 1981, "Studies of Full-Coverage Film Cooling Part 2: Measurement of Local Heat Transfer Coefficient," ASME Paper No. 81-GT-38.

Le Grives, E., Nicolas, J.-J., Genot, J., 1979, "Internal Aerodynamics and Heat Transfer Problems Associated to Film Cooling of Gas Turbines," ASME Paper No. 79-GT-57.

Luckey, D. W., and L'Ecuyer, R., 1981, "Stagnation Region Gas Film Cooling—Spanwise Angled Injection from Multiple Rows of Holes," NASA CR-165333.

Mayle, R. E., and Camarata, F. J., 1975, "Multihole Cooling Film Effectiveness and Heat Transfer," ASME *Journal of Heat Transfer*, Vol. 97, pp. 534–538.

Metzger, D. E., Carper, H. J., and Swank, L. R., 1968, "Heat Transfer With Film Cooling Near Nontangential Injection Slots," ASME *Journal of Engineering for Power*, Vol. 90, pp. 157–163.

Metzger, D. E., Takeuchi, D. I., and Kuenstler, P. A., 1973, "Effectiveness and Heat Transfer With Full-Coverage Film Cooling," ASME *Journal of Engineering for Power*, Vol. 95, pp. 180–184.

Metzger, D. E., Kuenstler, P. A., and Takeuchi, D. I., 1976, "Heat Transfer With Film Cooling Within and Downstream of One to Four Rows of Normal Injection Holes," ASME Paper No. 76-GT-83.

Miller, K. L., and Crawford, M. E., 1984, "Numerical Simulation of Single, Double, and Multiple Row Film Cooling Effectiveness and Heat Transfer," ASME Paper No. 84-GT-112.

Papell, S. S., 1960, "Effect on Gaseous Film Cooling of Coolant Injection Through Angled Slots and Normal Holes," NASA TND-299.

Sasaki, M., Takahara, K., Kumagai, T., and Hamano, M., 1979, "Film Cooling Effectiveness for Injection From Multirow Holes," ASME *Journal of Engineering for Power*, Vol. 101, pp. 101–108.

von Karman, T. H., 1939, "The Analogy Between Fluid Friction and Heat Transfer," *Trans. ASME*, Vol. 61, pp. 705–710.

Yavuzkurt, S., Moffat, R. J., and Kays, W. M., 1979, "Full-Coverage Film-Cooling: 3-Dimensional Measurements of Turbulence Structure and Prediction of Recovery Region Hydrodynamics," NASA CR-3104.

Yavuzkurt, S., 1985, "Full-Coverage Film-Cooling: A One-Equation Model of Turbulence for the Calculation of the Full-Coverage and the Recovery-Region Hydrodynamics," ASME Paper No. 85-GT-119.

Buoyancy-Affected Flow and Heat Transfer in Asymmetrically Heated Rotating Cavities

C. A. Long

A. P. Morse

N. Zafiropoulos

Thermo-Fluid Mechanics Research Center,
School of Engineering,
University of Sussex,
Brighton, Sussex, United Kingdom

Finite-volume predictions are presented for the convective heat transfer rates in a rotating cavity, formed by two corotating plane disks and a peripheral shroud, and subjected to a radial outflow of cooling air. The heating of the disks is asymmetric, the air entering the cavity through a central hole in the cooler (upstream) disk. The predicted Nusselt number distributions for each disk are compared with unpublished data from the University of Sussex for dimensionless mass-flow rates in the range $2800 \leq C_w \leq 14{,}000$ *and rotational Reynolds numbers,* Re_θ*, up to* 5.2×10^6*. A single-grid elliptic procedure was used with turbulent transport represented via a low-Reynolds-number* $k-\epsilon$ *model and the turbulence Prandtl number concept. In comparing the predicted and measured convective heat fluxes, it is important to consider the radiative heat exchange between the disks. This is estimated using a conventional view-factor approach based on black-body emission. Under conditions of asymmetric heating, rotationally induced buoyancy forces can exert significant effect on the flow structure, the induced motion tending to oppose that imposed by the radial outflow. Indeed, flow visualization studies have revealed that, as the rotational Reynolds number is increased (for a fixed value of* C_w*), the flow in the source region initially becomes oscillatory in nature, leading eventually to the onset of chaotic flow in which the usual Ekman layer structure does not persist in all angular planes. The extent to which the effects of such flow behavior can be captured by the steady, axisymmetric calculation approach used here is questionable, but it is found that the turbulence model (used previously for the prediction of heat transfer in symmetrically heated cavities) still leads to good (±10 percent) predictive accuracy for the heated (downstream) disk. However, the predicted Nusselt numbers for the cooler (upstream) disk generally show little accord with experimental data, often signifying heat flow into the disk instead of vice versa. It is concluded that the modeling of the turbulent heat transport across the core region of the flow is erroneous, especially at high rotational Reynolds numbers: This is attributed to overestimated turbulence energy production in that region due to the action of the radial-circumferential component of shear stress* ($\overline{vw}$)*. Adoption of an algebraic-stress model for this shear stress is partly successful in removing the discrepancies between prediction and experiment.*

1 Introduction

The continual improvements in gas-turbine engine performance brought about by increased operating temperatures are largely due to advances in materials technology and the extensive use of internal cooling systems. Internal cooling is obtained by extracting air from the compressor in order to maintain the temperatures of the turbine blades and disks within safe working limits. Knowledge of the flow around such rotating components and the associated heat transfer processes that occur is essential to the design process, where the material stresses and likely fatigue behavior have to be estimated. Such knowledge can be obtained either directly from experiment or, as is becoming increasingly common, by the use of computational fluid dynamics. In the latter context, idealized geometries are envisaged as being able to provide information of relevance to the more complex geometries of real engine configurations. One such example is the annular rotating cavity formed by two parallel plane disks and subjected to a radial outflow of cooling air. This configuration models the wheelspace between adjacent corotating turbine disks, where the disks are heated by windage and, more significantly, by conduction from the hot turbine blades. The ultimate objective of the exercise can be seen as optimization of the amount of cooling air required for safe operation.

The isothermal flow structure in rotating-cavity geometries has been extensively studied by Owen et al. (1985) using flow visualization techniques and laser-Doppler anemometry. Influential parameters are the rotational Reynolds number, Re_θ ($=\omega b^2/\nu$), the dimensionless mass-flow rate, C_w ($=\dot{m}/\mu b$), and, to a lesser extent, the disk gap ratio, G ($=s/b$). The flow structure for an axial inlet generally comprises four distinct regions: (*i*) a source region where entrainment into the disk boundary layers occurs, and which is characterized by streamline divergence as the jet is deflected by the downstream disk, creating a recirculating toroidal vortex adjacent to the upstream disk, (*ii*) thin boundary layers on the disks, which become nonentraining (Ekman) layers beyond the source region, (*iii*) an inviscid interior core of rotating fluid between the Ekman layers, and (*iv*) a sink layer on the rotating peripheral shroud, through which fluid leaves the cavity. The relative sizes of the individual flow regions vary in a systematic way with both Re_θ and C_w. In particular, the Ekman layer thickness and the radial extent of the source region increase with increasing C_w and decrease with increasing Re_θ. The observed behavior appears to have been reproduced with good quantitative accuracy by CFD predictions (e.g., Chew, 1985; Iacovides and Theofanopoulos, 1991; Morse, 1991a). The flow structure for symmetri-

---

Contributed by the International Gas Turbine Institute and presented at the 38th International Gas Turbine and Aeroengine Congress and Exposition, Cincinnati, Ohio, May 24–27, 1993. Manuscript received at ASME Headquarters February 19, 1993. Paper No. 93-GT-88. Associate Technical Editor: H. Lukas.

cally heated cavities and indeed for the case of asymmetric heating, under conditions for which rotationally induced buoyancy forces are unimportant, is similar to that for isothermal flow at the same values of Re_θ and C_w, although slight variation in the relative sizes of the four flow regions can be expected.

Extensive experimental data for convective heat transfer in symmetrically heated rotating cavities were published by Northrop and Owen (1988b) for dimensionless flow rates in the (nominal) range $1400 \le C_w \le 14{,}000$ and rotational Reynolds numbers up to 3.7×10^6. The temperature distributions on the disks were closely similar, be they sensibly constant (as for steady-state operation of a turbine), or radially increasing (as during the acceleration of aircraft takeoff) or radially decreasing (as for the deceleration of landing). The heat transfer data were presented in terms of Nusselt numbers based on the local disk-to-inlet air temperature difference, the surface heat transfer rates being obtained from thermopile heat fluxmeters installed at four radial locations, supported by a solution of Laplace's conduction equation within the disks. For the case of symmetric heating, rotationally induced buoyancy forces exert negligible effect on the flow structure, consideration of heat transport in the core region of the flow is unimportant, and radiative heat interchange between the disks is also of little consequence in comparison to the convective heat fluxes.

The predictions of Northrop and Owen's data formed an object study by Morse and Ong (1992) in which a low-Reynolds-number k–ϵ model was used to estimate turbulent momentum fluxes and the turbulence Prandtl number concept to obtain the corresponding heat fluxes. Morse and Ong validated the model for the heat transfer from a free disk and examined its performance for the rotating cavity over the whole parameter range for which data were available. The predictive accuracy was generally better for the downstream disk, which has the more well-defined flow structure, and tended to improve with increasing Re_θ. Global accuracy for the local Nusselt numbers for both disks was estimated to be ± 10 percent, although there were wider excursions (*i*) at low C_w and above a critical value of Re_θ, where accuracy deteriorated abruptly, possibly as a result of fluid ingress through the shroud and/or flow instability in the experiments, and (*ii*) at high C_w and low values of Re_θ, where the pronounced wall-jet behavior on the downstream disk and its effect on the size of the vortex in the source region did not seem to be fully accounted for in the turbulence model. At intermediate conditions, roughly 50 percent of the predicted Nusselt numbers were, remarkably, within ± 2 percent of the experimental values.

The flow and heat transfer in asymmetrically heated cavities with radial outflow were investigated by Owen and Onur (1983) and Long and Owen (1986). There are further data available in Long (1984), Northrop (1984), and unpublished work by Firouzian at the University of Sussex. Corroborating evidence on the flow structure, obtained from flow visualization studies, is contained in Pincombe (1983). In these experiments, the downstream disk was heated to a temperature typically 80°C above ambient, giving a value of the buoyancy parameter $\beta\Delta T$ (where ΔT is the disk-to-fluid inlet temperature difference and β the volumetric expansion coefficient) of approximately 0.27. Cooling air entered the cavity through a central hole in the upstream disk. Although not heated directly, this disk received heat by radiation and by conduction across the outer shroud.

Owen and Onur identified four regimes for the heat transfer processes: (*i*) At low values of Re_θ and high values of C_w, the mean Nusselt number for the heated disk was found to be governed by the wall jet mechanism and largely independent of the rotational speed; (*ii*) at higher values of Re_θ, corresponding to the occurrence of Ekman layer flow on the disks, the Nusselt

Nomenclature

a, b = inner and outer radius of cavity
A^+ = coefficient in near-wall damping function
Cp = constant-pressure specific heat
$C_w = \dot{m}/\mu\, b$ = nondimensional flow rate
C_μ = turbulent viscosity coefficient
c = fractional rotational speed of coordinate system
$c_{\epsilon 1}, c_{\epsilon 2}$ = coefficients of source terms in ϵ equation
c_1 = pressure-scrambling coefficient (return to isotropy)
c_2 = pressure-scrambling coefficient ("rapid part")
$E(\;)$ = error in
$F_{j,k}$ = view factor (from surface j to surface k)
f_μ = near-wall damping function
$G = s/b$ = cavity gap ratio
$\mathrm{Gr} = \beta\Delta T \mathrm{Re}_\theta^2$ = rotational Grashof number
$\tilde{h}$ = stagnation enthalpy = $\int CpdT + \frac{1}{2}(U^2 + V^2 + W^2) + k$
k = turbulent kinetic energy; thermal conductivity
$\dot{m}$ = coolant mass flow rate
N = number of sectors in radiative heat flow calculation
Nu = local Nusselt number
$\overline{\mathrm{Nu}}$ = mean Nusselt number for whole disk
P = production rate of turbulent kinetic energy
p = static pressure
q = heat flux
r = radial coordinate
r_i = inner disk radius
$R_T = k^2/\epsilon\nu$ = turbulence Reynolds number
$R_y = yk^{1/2}/\nu$ = wall-distance Reynolds number
$\mathrm{Re}_\theta = \omega b^2/\nu$ = rotational Reynolds number
s = axial gap between the disks
T = static temperature
U, V, W = time-averaged axial, radial, and tangential velocity components
$U_\tau = (\tau_s/\rho)^{1/2}$ = friction velocity
$\overline{u_i u_j}$ = Reynolds stress tensor
$x = r/b$ = nondimensional radial coordinate
y = generalized wall distance
$y^+ = yU_\tau/\nu$ = wall-distance Reynolds number
z = axial coordinate
$\beta = 1/T$ = volumetric expansion coefficient
Γ = diffusivity
ΔT = temperature difference
δ_{ij} = Kronecker delta
ϵ = dissipation rate
$\epsilon_z = U/\omega a$ = axial Rossby number
ξ = coefficient in pressure scrambling model
μ = dynamic viscosity
ν = kinematic viscosity
ρ = density
$\sigma = \mu C_p/k$ = Prandtl number
σ = Stefan–Boltzmann constant = 56.7×10^{-12} kW/m^2 K^4
σ_h = turbulent transport coefficient for enthalpy
σ_{ij} = stress tensor for laminar flow
σ_k = turbulent transport coefficient for k
$\sigma_{\overline{vw}}$ = turbulent transport coefficient for $\overline{vw}$
σ_ϵ = turbulent transport coefficient for ϵ
τ = total shear stress

number was dependent on both Re_θ and C_w; (*iii*) the onset of oscillatory flow, with a frequency of approximately 70 percent of the cavity rotation, in the source region at a certain critical speed; and (*iv*) the subsequent breakdown of the flow into a chaotic structure, when, it was believed, free convection effects due to rotationally induced buoyancy dominated the flow and heat transfer processes. In this chaotic regimen, it appeared that the flow structure broke down into cells where alternate Ekman layer and non-Ekman layer flow prevailed.

Both Owen and Onur and also Pincombe presented evidence suggesting that the onset of the oscillatory and chaotic modes of behavior depends on the temperature difference between the heated disk and the inlet air. The former correlated their results in terms of the parameter $\mathrm{Gr}^{1/2}/C_w$, a value of about 180 signaling the beginning of oscillatory flow and 330 the beginning of chaotic flow (Gr denotes the rotational Grashof number, which may be written as $\beta\Delta T\mathrm{Re}_\theta^2$, where ΔT was taken as the maximum temperature difference between the heated disk and inlet air). Pincombe's visualization studies indicated a strong dependence of the two modes of unsteady flow behavior on the size of the discrete holes in the shroud. The associated phenomenon of fluid ingress was also observed, where at sufficiently high rotational speeds, the pressure in the cavity became subatmospheric and fluid was drawn into the cavity through the holes in the shroud. This occurred despite the fact that the net flow remained radially outward. Pincombe concluded that his results "support the belief that the chaotic regime results from a combination of destabilisation of the Ekman layer flow structure by buoyancy effects and by ingress through the shroud, which is affected by the size of the holes in the shroud."

Figure 1 shows computed streamlines for three test cases examined in the present work where the heating of the disks is asymmetric with $\beta\Delta T \approx 0.27$. These results were obtained for values of the mass-flow rate parameter, $C_w = 2800$, using the modified version of the $k-\epsilon$ model as detailed in Section 2.2. At low values of Re_θ (Fig. 1*a*), the inlet flow impinges directly onto the downstream disk, forming a wall jet, which flows radially outward to such an extent that Ekman layer flow, if it truly occurs, is confined to the outer part of the cavity. In the figure, the stream function, ψ, has been normalized with the total flow rate to give values of 0 on the upstream disk and 100 on the downstream disk and at the axis of symmetry. The large toroidal vortex in the source region is predicted to recirculate almost half of the superimposed flow. For the conditions of Fig. 1(*a*), $\mathrm{Gr}^{1/2}/C_w \approx 23$, and the influence of buoyancy is minimal. Consequently, the flow structure is essentially the same as for isothermal or for symmetric-heating conditions. A tenfold increase in the rotational Reynolds number (Fig. 1*b*) brings about a dramatic reduction in the size and strength of the source vortex with a corresponding increase in the rate of entrainment of fluid into the boundary layer on the upstream disk. The predicted flow structure now exhibits a definite effect of rotationally induced buoyancy forces, seen here as the formation of a weak "axial wind." This transfers fluid from the hotter (downstream) disk to the cooler (upstream) disk, across the core region of the flow. Note that at large radii, the streamline representing 57.5 percent of the total mass flow rate is associated with the upstream side of the cavity. For $\mathrm{Re}_\theta = 3.68 \times 10^6$ (Fig. 1*c*), where $\mathrm{Gr}^{1/2}/C_w \approx 680$, most of the axial flow does not impinge on the downstream disk, but is entrained directly into the boundary layer on the upstream disk and nonentraining Ekman layers form at a lower radius than the previous two figures. At high radii, as much as 65 percent of the flow is predicted to leave the cavity from the upstream-disk side. Comparison with the streamline patterns obtained by Morse and Ong (1992), for conditions of symmetric heating, shows that it is only beyond the source region that the effects of rotationally induced buoyancy forces become apparent. This point can be more readily appreciated by reference to the sealed cavity predictions, which will be discussed in Section 3.1.

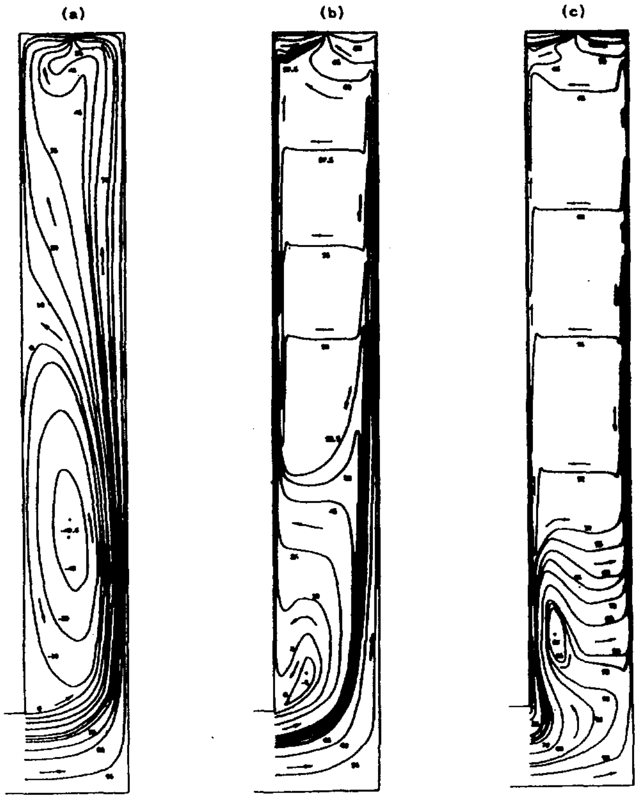

Fig. 1 **Predicted streamlines for asymmetrically heated flow in rotating cavities: $C_w = 2800$, Re_θ = (*a*) 1.25×10^5, (*b*) 1.30×10^6, (*c*) 3.68×10^6 ($\beta\Delta T \sim 0.27$ and heated disk is on the right)**

The three-dimensional and unsteady nature of the flow likely to prevail under real engine conditions (where $\mathrm{Gr}^{1/2}/C_w$ is large) obviously presents limitations on the predictive accuracy of the two-dimensional, steady-flow approach used here. However, there are clearly distinct advantages in the computational economy of this approach should it produce values of disk heat fluxes that are acceptable for engineering design purposes. The predictions also provide a standard against which the degree of improvement obtained by more sophisticated procedures can be assessed.

2 Numerical and Turbulence Modeling

The computational procedure is based on a single-grid elliptic solver with the assumption that the flow is steady and axisym-

Nomenclature (cont.)

ϕ = generalized transport variable
ψ = stream function
ω = rotational speed of the disks

Subscripts

avg = radially weighted average
b = bulk or reference value
c = pertaining to the cold disk
eff = effective (=laminar + turbulent)
ent = entrained
h = pertaining to the hot disk
I = inlet value
R = radiative component
s = value at disk surface
T = turbulent

metric. Natural convection due to gravitational buoyancy and the role of density fluctuations in the turbulence equations are ignored since the work of Morse and Ong (1992) for symmetrically heated cavities confirmed the belief that these effects are of minor importance. Orthogonal meshes of 65 × 78 and 75 × 92 (axial–radial) nodes were employed, the latter being more appropriate for flows at high rotational Reynolds numbers where the disk and shroud boundary layers can become exceedingly thin. The axial node distribution was based on a geometric expansion with the nodes a mirror image of each other about the midaxial plane. The radial grid was generally adaptable to suit the flow conditions being studied. For all the test cases considered, the closest off-wall node spacing for both the disks and the shroud was maintained at $y^+ < 0.5$ ($y^+ = yU_\tau/\nu$, where y denotes the normal distance from the wall and U_τ is the "friction velocity" corresponding to the resultant wall shear stress). The wall fluxes were calculated using a second-order accurate forward or backward gradient as appropriate.

2.1 Transport Equations and Discretization Schemes. Coupled transport equations are solved for the three components of momentum, the stagnation enthalpy, and the turbulence quantities k and ϵ (respectively the kinetic energy and kinematic dissipation rate).

By analogy with the stress–strain relationship for laminar flow, viz.,

$$\sigma_{ij} = -p\delta_{ij} + \mu(\partial U_i/\partial x_j + \partial U_j/\partial x_i - 2/3\delta_{ij}\nabla\cdot\mathbf{V}), \quad (1)$$

the constitutive relationship for the turbulent Reynolds stresses appearing in the time-averaged momentum equations is written as

$$-\rho\overline{u_i u_j} = -2/3\delta_{ij}\rho k + \mu_T(\partial U_i/\partial x_j + \partial U_j/\partial x_i - 2/3\delta_{ij}\nabla\cdot\mathbf{V}), \quad (2)$$

where μ_T is a "turbulent viscosity" and $\nabla\cdot\mathbf{V}$ denotes the divergence of the velocity vector. Similarly, turbulent heat fluxes are assumed to be proportional to the local enthalpy gradient, the turbulent diffusivity of heat being obtained from μ_T via the "turbulence Prandtl number" concept. These assumptions enable the equations for the axial and radial momentum and stagnation enthalpy, together with the modeled forms of the k and ϵ equations to be written in the common form

$$\partial/\partial z(\rho U\phi - \Gamma_{\phi,z}\partial\phi/\partial z) + 1/r\partial/\partial r[r(\rho V\phi - \Gamma_{\phi,r}\partial\phi/\partial r)] = S_\phi, \quad (3a)$$

where ϕ denotes the generalized transport variable, $\Gamma_{\phi,z}$ and $\Gamma_{\phi,r}$ are the effective (=laminar + turbulent) diffusivities for the axial and radial directions respectively, and S_ϕ indicates the net source term for each variable. The full set of transport equations within this format is listed in Table 1. Note that the axial and radial momentum equations are solved in a form using gradients of a reduced pressure based on solid-body rotation of the fluid at a fraction, c, of the rotational speed of the cavity and a reference density ρ_b. In the radial momentum equation, W' ($=w - \omega r$) represents the tangential velocity of the fluid relative to that of the disks at the same radius. This treatment (with $c = 1$) results in much reduced values of the radial pressure gradient and the "centrifugal force" terms when the fluid is in a state close to solid-body rotation (as for the case of a sealed cavity). Otherwise, the small imbalance between these two (large) terms results in slow and unsteady convergence of the iterative procedure.

Table 1 Forms of transport equations

ϕ	$\Gamma_{\phi,z}$	$\Gamma_{\phi,r}$	S_ϕ
U	$2\mu_{eff}$	μ_{eff}	$-\partial/\partial z(p'+2/3\rho k) + 1/r\partial/\partial r(r\mu_{eff}\partial V/\partial z) - 2/3\partial/\partial z\,(\mu_{eff}\nabla.\underline{V})$
V	μ_{eff}	$2\mu_{eff}$	$-\partial/\partial r(p'+2/3\rho k) + \rho W'^2/r + 2\rho W'c\omega$ $+ (\rho - \rho_b)rc^2\omega^2 - 2\mu_{eff}V/r^2 + \partial/\partial z(\mu_{eff}\partial U/\partial r)$ $- 2/3\partial/\partial r\,(\mu_{eff}\nabla.\underline{V})$ where $W' = W - rc\omega,\ p' = p - 1/2\rho_b r^2 c^2\omega^2$
$\tilde{h}$	$\mu/\sigma + \mu_T/\sigma_h$		$\partial/\partial z\,[\mu_{eff}(1 - 1/\sigma_{eff,h})\partial/\partial z\{(U^2 + V^2 + W^2)/2\}]$ $+ 1/r\partial/\partial r\,[r\mu_{eff}(1 - 1/\sigma_{eff,h})\partial/\partial r\{(U^2 + V^2 + W^2)/2\}]$
k	$\mu + \mu_T/\sigma_k$		$P - \rho\varepsilon - D$ where $P = \mu_T\{2[(\partial U/\partial z)^2 + (\partial V/\partial r)^2 + (V/r)^2]$ $+ (\partial U/\partial r + \partial V/\partial z)^2 + (\partial W/\partial z)^2$ $+ 1/\sigma_{\overline{vw}}[r\partial/\partial r(W/r)]^2\}$ $D = 2\mu[(\partial\sqrt{k}/\partial z)^2 + (\partial\sqrt{k}/\partial r)^2]$
ε	$\mu + \mu_T/\sigma_\varepsilon$		$c_{\varepsilon 1}\varepsilon P/k - c_{\varepsilon 2}\rho\varepsilon^2/k + E - F$ where $E = 2\mu\mu_T/\rho\{(\partial^2 V/\partial z^2)^2 + (\partial^2 W/\partial z^2)^2$ $+ (\partial^2 U/\partial r^2)^2 + (\partial^2 W/\partial r^2)^2\}$ $F = 2\mu[(\partial\sqrt{\varepsilon}/\partial z)^2 + (\partial\sqrt{\varepsilon}/\partial r)^2]$

Table 2 Constants and functions in transport equations

Coefficient		Value/Function
C_μ		0.09
A^+		24.5
$c_{\varepsilon 1}$		1.44
$c_{\varepsilon 2}$		$1.92 - \{0.43\exp(-R_T^2/36)\}$
σ_k		1.0
σ_ε		1.3
σ_h		0.9
$\sigma_{\overline{vw}}$	model 1:	1.0
	model 2:	Equation (8) with
c_1		3.0
c_2		0.3
ξ		0.0

The tangential momentum equation used is formally an equation for the angular (moment of) momentum, rW, so chosen because of the absence of any source term, a formulation that allows better satisfaction of the torque-angular momentum relationship on a global basis. However, in order to avoid complications near a symmetry axis, the equation is best solved as one for the angular velocity, W/r. This then takes the nonstandard form

$$\partial/\partial z(\rho U\phi - \mu_{\text{eff}}\partial\phi/\partial z) + 1/r^3\partial/\partial r[r^3(\rho V\phi - (\mu_{\text{eff}}/\sigma_{\overline{vw}})\partial\phi/\partial r)] = S_\phi. \quad (3b)$$

In order to be compatible with the discretization algorithm employed for the other transport equations, this procedure necessitates multiplication of the convection and diffusion coefficients by an appropriate radius squared, and also the inclusion of a source term to satisfy mass continuity. The turbulent transport coefficient for radial diffusion, $\sigma_{\overline{vw}}$, is assigned values according to the form of the turbulence model used (see Section 2.2 and Table 2).

As alternatives to the rather arbitrary hybrid differencing scheme of Patankar (1980), the QUICK scheme of Leonard

(1979) and the linear upwind-differencing scheme advocated by Castro and Jones (1987) were employed for discretization of the convection terms. Both schemes have a higher formal order of accuracy than hybrid differencing and were coded so as to take fully into account the nonuniformity of the grid-node spacing. Linear upwind-differencing proved, if anything, to be more stable than the hybrid scheme although the Cpu time requirement per iteration is approximately 20 percent greater. The QUICK scheme gave some convergence problems in the equations for the turbulence quantities, for transitional flows, where the values of k and ϵ can change by an order of magnitude between adjacent grid nodes. These difficulties were circumvented by using linear upwind differencing for the turbulence equations. At high values of Re_θ and C_w, the solution algorithm proved to be sufficiently robust for converged solutions to be obtained using QUICK (albeit with the necessity to begin the iterative process with one of the simpler schemes and an increased Cpu time requirement, relative to upwind-differencing, of the order of 40 percent). On the fine meshes employed, differences in local Nusselt numbers using QUICK and linear upwind-differencing were seldom greater than ±1 percent. Using the hybrid scheme with these meshes typically resulted in the peak values (which occur close to the edge of the source region) being about 5 percent lower.

2.2 Turbulence Modeling. A low-Reynolds-number k–ϵ model represents the turbulent viscosity in Eq. (2) by the expression

$$\mu_T = C_\mu f_\mu \rho k^2/\epsilon, \tag{4}$$

where f_μ is a function that essentially accounts for the preferential damping of the normal velocity fluctuations close to the wall. A correlation of f_μ in terms of y^+ has been found previously to give better predictive performance for flows in rotating disk geometries than correlations using the alternative Reynolds numbers R_y $(=yk^{1/2}/\nu)$ and R_T $(=k^2/\epsilon\nu)$. These latter, it can be noted, often result in a tendency of the flow to laminarize under conditions that are known from experiment to produce turbulent flow. Here, as in the work of Morse and Ong (1992), f_μ is expressed as

$$f_\mu = [1 - \exp(-y^+/A^+)]^2, \tag{5}$$

where A^+ is assigned a value of 24.5 on the basis of computer optimization for equilibrium flows such as pipe flow and the flat-plate boundary layer. For flows in strongly favorable or adverse pressure gradients, the present form of the model appears to fare no better, though certainly no worse, than other proposed forms of low-Reynolds-number k–ϵ models (see, e.g., Rodi, 1991). Values of the model constants employed in this work are identical to those used by Morse and Ong (1992) and are listed in Table 2.

It is well known that Eq. (2) provides a completely inadequate prescription for the normal stresses $(i = j)$ in many flow situations, particularly fully developed pipe flow, where the normal stresses are predicted to be equal (to $2/3k$), in contrast to the marked anisotropy indicated by experiment. However, what is not so widely recognized is that, for swirling flows in general, the formulation does not hold at all well for the shear stress governing turbulent transport of angular momentum in the streamwise direction (Morse, 1980). Examination of the full Reynolds stress transport equations suggests that, for the present class of flows, use of an isotropic viscosity hypothesis leads to an underestimate (of at least an order of magnitude) for the stress $\overline{vw}$ near the disks. A similar error occurs for the shear stress $\overline{uw}$ in the sink layer on the shroud. The resultant ill effects are, however, likely to be small, since it is the action of $\overline{uw}$ that dominates (both in the tangential momentum equation and its rate of production of turbulence energy) near the disks, and $\overline{vw}$, for the same reasons, near the shroud. Although Eq. (2) probably represents the shear stress $\overline{uv}$ fairly well in both the disk and shroud boundary layers, it appears fortuitous that individual components of the Reynolds stress tensor are badly predicted only in regions of flow where they are unimportant!

The present predictions for asymmetrically heated rotating cavities soon revealed that the turbulence model seriously overestimated the turbulent transport of heat across the core region of the flow between the Ekman layers. In this region, the only significant component of velocity is in the tangential direction and the only significant velocity gradients are the radial derivatives W/r and $\partial W/\partial r$. This led to questioning of the veracity of the isotropic viscosity formulation for the shear stress $\overline{vw}$, as this produces turbulent kinetic energy by its action against these gradients. Using the algebraic-stress modeling approach of Rodi (1972) to reduce the formal transport equation for $\overline{vw}$ in the core region results in

$$\begin{aligned} -\rho\overline{vw} = {} & [(1 - c_2)/(P/\epsilon - 1 + c_1)] \\ & \times (\rho\overline{v^2}k/\epsilon) r\partial/\partial r(W/r) - [(2 - (\xi + 1)c_2)/ \\ & (P/\epsilon - 1 + c_1)]\rho(\overline{w^2} - \overline{v^2})kW/\epsilon r, \end{aligned} \tag{6}$$

where P/ϵ denotes the local production/dissipation ratio and c_1 and c_2 are pressure-scrambling constants associated with the return to isotropy of the Reynolds stress tensor and its production term (the "rapid part"), respectively. The coefficient ξ is dependent on whether production-like terms, which appear in the transformation of the convection terms from Cartesian to cylindrical-polar coordinates, are included $(\xi = 1)$ or are not included $(\xi = 0)$ in the modeling of the rapid part of the redistribution term. Interpreting the first term on the right-hand side of Eq. (6) as the conventional "turbulent viscosity" formulation, the magnitudes of $\overline{vw}$ in the core flow can be seen to be affected by the second term, which is proportional to the difference between the normal stresses $\overline{v^2}$ and $\overline{w^2}$. When similar algebraic-stress modeling is applied to the transport equations for these stresses, the final result becomes expressible as

$$-\rho\overline{vw} = \frac{\mu_T r\partial/\partial r(W/r)}{\sigma_{\overline{vw}}} \tag{7}$$

where

$$\sigma_{\overline{vw}} = 1 + \frac{2[(2 - (\xi + 1)c_2)][(1 - c_2)\partial W/\partial r + \{(1 - c_2) + 2(1 - \xi c_2)\}W/r](k/\epsilon)^2 W/r}{(P/\epsilon - 1 + c_1)^2}. \tag{8}$$

In Eq. (8), $\sigma_{\overline{vw}}$ adopts the role of a turbulent transport coefficient for $\overline{vw}$, which acts to reduce the values of this shear stress in the core region of the flow. It should be noted that the modification is based on high turbulence Reynolds number modeling of the transport equation, but can still be used throughout the flow field as its effects in the disk and shroud boundary layers are indeed minimal.

Zafiropoulos (1992) has presented predictions based on the Reynolds stress closure of Launder et al. (1975), where $c_1 = 1.5$ and $c_2 = 0.6$ (in this case, it is necessary to take $\xi = 1$ in order to obtain the correct shear stress levels in swirling flows). In the work presented here, the approach of Gibson and Younis (1986) is adopted, with $c_1 = 3.0$, $c_2 = 0.3$, and $\xi = 0$. There appears to be little loss of generality from taking $P/\epsilon = 1$ in the core flow, when the two formulations reduce to

$$\sigma_{\overline{vw}} = 1 + (k/\epsilon)^2[0.284\partial W/\partial r + 0.569W/r]W/r \tag{9a}$$

and

$$\sigma_{\overline{vw}} = 1 + (k/\epsilon)^2[0.264\partial W/\partial r + 1.02W/r]W/r \tag{9b}$$

respectively. Equation (9b), based on the model constants of

Gibson and Younis, gives the larger modification and performs better for high rotational Reynolds numbers. Equation (9*a*) gives slightly better results for low values of Re_θ.

2.3 Computational Procedure. The staggered-grid approach of Patankar (1980) was used, the pressure corrections required to satisfy mass continuity and to update the pressure field being obtained from the SIMPLEC algorithm of Van Doormal and Raithby (1984) in conjunction with a block-correction procedure. Use of the latter is particularly effective in preventing instability in the early stages of the computation. The solution takes fully into account the effects of compressibility, buoyancy, fluid property variation, and frictional heating. Values for the fluid enthalpy ($=\int CpdT$), constant-pressure specific heat, thermal conductivity, and viscosity were obtained from curve-fitted functions, which are accurate to within ±0.5 percent for temperatures up to 1000°C. The density was determined from the ideal gas law.

The attainment of convergence was assessed by the two usual criteria based on the aggregate residuals and rms changes for each of the dependent variables, where the respective tolerances were set at 10^{-6} and 10^{-5}. Additionally, and overriding these criteria, was the requirement that the solutions provided global satisfaction of the torque-angular momentum relationship (that the net torque exerted on the fluid at the boundaries equals the change in angular-momentum flow rate through the cavity) and the first law of thermodynamics (that the difference between the boundary heat and work transfer rates, the usual thermodynamic sign convention applying, equals the corresponding change in the flux of stagnation enthalpy). The tolerance here was set at 10^{-3} of the largest term in each balance. This proved a strict criterion, considered necessary on account of the importance of the wall fluxes as the objective of the exercise.

Although the boundary conditions of the flow at entry to the cavity are not well documented for engineering calculation purposes, the predicted quantities of interest are largely insensitive to the precise conditions imposed, with the possible exception of the inlet swirl fraction. A $\frac{1}{7}$th power-law axial velocity profile was chosen, together with a turbulence intensity of 1 percent and a value of $R_T = 150$ to determine the dissipation rate. Although some streamline divergence might be expected before the inlet plane, no material difference resulted from equating the inlet radial velocity component to zero. As in Morse and Ong (1992), an inlet swirl fraction that varied linearly from zero at the symmetry axis to unity at the pipe radius was employed. Radial temperature profiles on the disks were obtained from smoothed variations of the raw experimental data. As the first measurement location was at $x = 0.323$, the disk temperatures at the lower radii were assumed to vary linearly between this value and the inlet air temperature at $r = a$ on the upstream disk and $r = 0$ on the downstream disk. The outer shroud was assumed adiabatic and the series of discrete holes, through which the flow left the cavity, was modeled as a uniform gap of equivalent area.

Cpu times for converged solutions were typically 2 to 4 h (500 to 1000 iterations) on a Solbourne S4000 workstation. The use of scaling laws, to transfer a starting solution from one flow condition to another, was helpful in promoting faster convergence than would have been obtained if starting the second solution afresh.

2.4 Radiation Estimation. The radiative heat interchange between the disks was estimated by considering the cavity to be an enclosure comprising 15 annular segments on each disk and one cylindrical segment on the shroud. Each of these segments was considered to be of constant surface temperature, T_s. The materials of the inner surfaces of the disks and shroud have emissivities sufficiently close to unity that black body radiation may be assumed. For a total of N surfaces (i.e., $N - 1$ annular surfaces on the two disks and one for the shroud), the radiative heat flux at surface j, $q_{R,j}$, was obtained by considering that from the other ($k = 1, 2, \ldots, N$) surfaces:

$$q_{R,j} = \sigma \sum_{k=1}^{N} F_{j,k}(T_{s,j}^4 - T_{s,k}^4), \tag{10}$$

where σ is the Stefan–Boltzmann constant and $F_{j,k}$ is the view factor (the fraction of thermal radiation emitted from surface j that falls on surface k). The tabulated correlations of Howell (1982) for concentric annuli were used to obtain values of $F_{j,k}$. The view factors for the shroud can be obtained through the summation rule: The sum of all the disk segment view factors is subtracted from unity. For $r > a$ (the cavity inlet radius), T_s was taken as the time-smoothed disk surface temperature and, for $r < a$, the air inlet temperature was used. The surface temperature of the shroud was not measured and so was assumed to be the temperature of the air at exit from the cavity (this quantity was estimated from an energy balance using disk heat fluxes from the conduction solution). With hindsight, the temperature variation across the shroud could have been better estimated using the converged results from the computational procedure, which assumed the shroud to be adiabatic. Radiative heat fluxes were subtracted from the measured values to obtain the fluxes due to convection.

3 Numerical Results

Comparison is drawn with unpublished data obtained from the Mark 2 rotating-cavity rig at the University of Sussex. The outer radius of the cavity is 428 mm, the disk spacing 59 mm (giving a gap ratio, G, of 0.138) and the inner-to-outer radius ratio (a/b), 0.104. The series of 32 holes of 9 mm diameter in the center of the peripheral shroud corresponds to a uniform gap of width 0.75 mm.

The local Nusselt numbers for the rotating cavity with superimposed radial outflow are defined as

$$\text{Nu} = q_s r/k_I(T_s - T_I), \tag{11}$$

where the subscript s refers to the disk surface and subscript I to the fluid inlet. A positive Nusselt number indicates heat flow from the disk to the surrounding fluid and vice versa. Experimental values were obtained from thermopile heat fluxmeters located at $x = 0.417$, 0.606, 0.751, and 0.978 on the upstream disk and 0.419, 0.611, 0.756, and 0.983 on the downstream disk. Unfortunately, in some of the tests, the outermost fluxmeter on both disks was nonoperational. The mean Nusselt number for each disk is determined from the expression

$$\overline{\text{Nu}} = 2b \int_{r_i}^{b} rq_s dr/(b^2 - r_i^2)k_I \Delta T_{\text{avg}} \tag{12}$$

where r_i denotes the inner radius of the disks and ΔT_{avg} is a radially weighted temperature difference between the disk surface and the inlet air. For the idealized sealed-cavity predictions of Section 3.1, where uniform disk temperatures are assumed, the corresponding definitions become

$$\text{Nu} = \pm q_s r/k_c|T_h - T_c|, \tag{13}$$

and

$$\overline{\text{Nu}} = \pm 2 \int_0^b rq_s dr/bk_c|T_h - T_c|, \tag{14}$$

where the subscripts h and c refer to the hot and cold disks, respectively.

3.1 Buoyancy-Driven Flow in a Sealed Cavity. A basic understanding of rotationally induced buoyancy effects can be gained from the flow behavior in an asymmetrically heated sealed cavity. Figures 2(*a*) and 2(*b*) show computed streamlines for a cavity with a gap ratio of 0.138 in which the right-hand disk is heated to a uniform temperature of 100°C: The

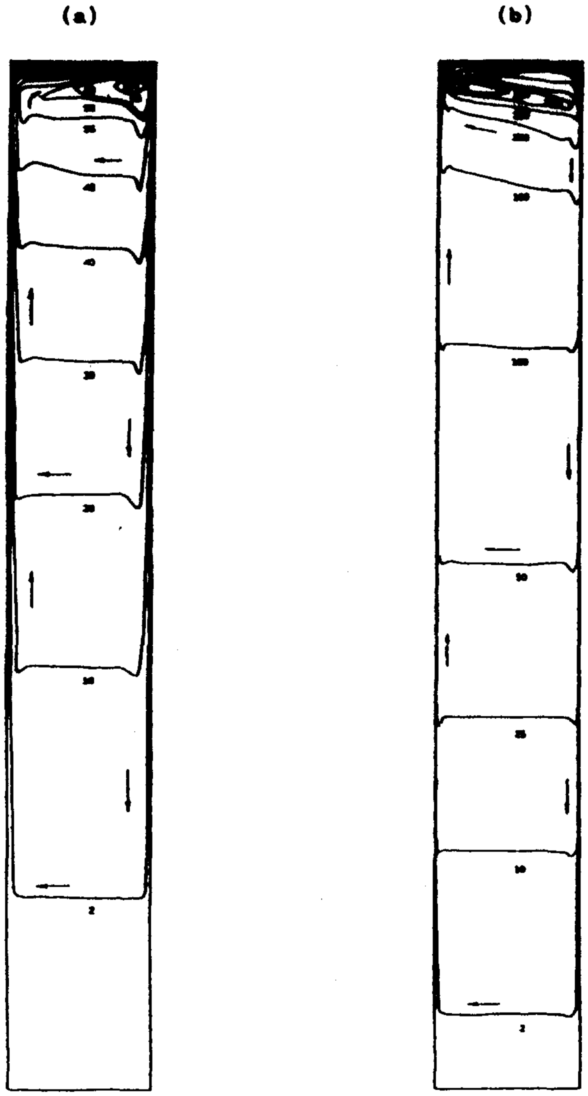

Fig. 2 Predicted streamlines for buoyancy-driven flow in a sealed cavity: Re_θ = (*a*) 10^5, (*b*) 10^6 ($\beta\Delta T \sim 0.27$ and heated disk is on the right)

left-hand disk is maintained at 20°C, giving a value of $\beta\Delta T$, based on the cold disk temperature, of 0.273. The radial pressure gradient is insufficiently large to provide the centripetal acceleration necessary to maintain the denser fluid near the cold disk in solid-body rotation; hence, this fluid spirals outward. Similarly, the less dense fluid near the hot disk spirals inward, so that a recirculating toroidal vortex is established. The angular velocity of the fluid (relative to the cavity) is sheared from a positive value adjacent to the hot disk to a negative value near the cold disk. The hot disk thus experiences a forwarding frictional torque, which is balanced by the retarding torques on the cold disk and the shroud.

Figure 2(*a*) shows the streamlines in the $r-z$ plane for a rotational Reynolds number (based on fluid properties evaluated at the cold-disk temperature) of 10^5, where the flow is predicted to be laminar throughout the cavity. The center of rotation of the vortex system is then close to the corner between the heated disk and the peripheral shroud. Figure 2(*b*) shows corresponding predictions for $\mathrm{Re}_\theta = 10^6$, where the flow is apparently turbulent (at least at high radii). Note the significant reduction in the thickness of the disk boundary layers and the predicted shift of the center of rotation of the vortex to a position close to the surface of the cold disk. The stream-function values indicated denote mass flow rates nondimensionalized with the product μb (where μ is the viscosity evaluated at the cold-disk temperature). It can be seen that the induced flow is largely confined to the outer parts of the cavity. Predictions were also obtained with $T_h = 260°\mathrm{C}$, $T_c = 20°\mathrm{C}$ ($\beta\Delta T = 0.819$) for rotational Reynolds numbers up to 6×10^6 ($\mathrm{Gr} = 2.95 \times 10^{13}$). For $\mathrm{Gr} \geq 3 \times 10^{11}$, which appears to indicate fully turbulent flow, the magnitude of the induced mass flow was found to be correlated, to within ±2 percent, by

$$C_{w,\mathrm{ent}} = 0.0225\ \mathrm{Gr}^{1/3}(T_h/T_c)^{1.75}. \qquad (15)$$

In a sealed cavity, frictional windage is negligible. The assumption that the shroud is adiabatic therefore brings about equality of the mean Nusselt numbers for the two disks (though these are, of course, of opposite sign). The correlations obtained for laminar flow ($\mathrm{Gr} \leq 10^{10}$) and for turbulent flow ($\mathrm{Gr} \geq 3 \times 10^{11}$) were, respectively,

$$\overline{\mathrm{Nu}} = \pm 0.072\ \mathrm{Gr}^{1/4}(T_h/T_c)^{2/3}, \qquad (16a)$$

$$\overline{\mathrm{Nu}} = \pm 0.00866\ \mathrm{Gr}^{1/3}(T_h/T_c)^{2/3}, \qquad (16b)$$

each being satisfied to within ±0.5 percent. The exponents of the Grashof number are identical to those used in conventional engineering correlations for natural convection from heated flat plates. Over the transitional range ($10^{10} \leq \mathrm{Gr} \leq 3 \times 10^{11}$), the exponent increases gradually from $\frac{1}{4}$ to $\frac{1}{3}$. The term involving the disk temperature ratio in Eqs. (15) and (16) accounts for fluid property variation since Gr is evaluated at the cold-disk temperature.

The imposition of a radial outflow will be opposed by the radially inward buoyancy-induced flow on the heated disk, giving rise to a potential source of flow instability at high values of the ratio $\mathrm{Gr}^{1/2}/C_w$. Indeed, Pincombe (1983) provides some evidence that radial inflow occurs on the heated disk during the so-called chaotic flow regime. However, given the extent of the induced flow rates for the sealed cavity (see Eq. (15)), only a low value of C_w is required to cancel out this effect and promote radial outflow over the whole of the heated disk. On the basis of a limited number of exploratory tests, it would seem that the (predicted) critical value of $\mathrm{Gr}^{1/2}/C_w$ at which radial inflow is suppressed is approximately 1500, although some convergence difficulties have been experienced with the computational procedure for conditions where simultaneous outflow and inflow occur. (This might suggest that, in practice, the flow would become three-dimensional and/or unsteady.) For $\mathrm{Gr}^{1/2}/C_w < 1500$, radial inflow does not occur immediately adjacent to the heated disk, but, as illustrated in Figs. 1(*b*) and 1(*c*), the flow in the outer part of the boundary layer is reversed to form an "axial wind," which transports fluid across the core of the flow to the boundary layer on the cooler (upstream) disk.

3.2 Asymmetrically Heated Cavity With Radial Outflow. Predictions are presented for nominal values of the mass-flow rate parameter, C_w, of 2800, 7000, and 14000. These have utilized the basic form of the $k-\epsilon$ model (Model 1) and the modified version (Model 2). This latter model uses Eq. (9*b*) to reduce turbulent heat transport across the core region of the flow. Predicted Nusselt number distributions for the disks are labeled u1 (upstream disk, Model 1), d2 (downstream disk, Model 2), etc.

The relative importance of convection and radiation for varying flow conditions is illustrated in Fig. 3. It can be seen that radiation is much more significant in the case of the upstream disk. At low values of C_w (Fig. 3*a*), the net heat flux is close to zero, so that convection and radiation are approximately in balance. For large values of C_w (Fig. 3*b*), convection outweighs radiation, but the corresponding Nusselt numbers are both numerically large in comparison to that based on the net (convective + radiative) heat flux. For the downstream disk, convection and radiation are of the same sign (indicating heat transfer from

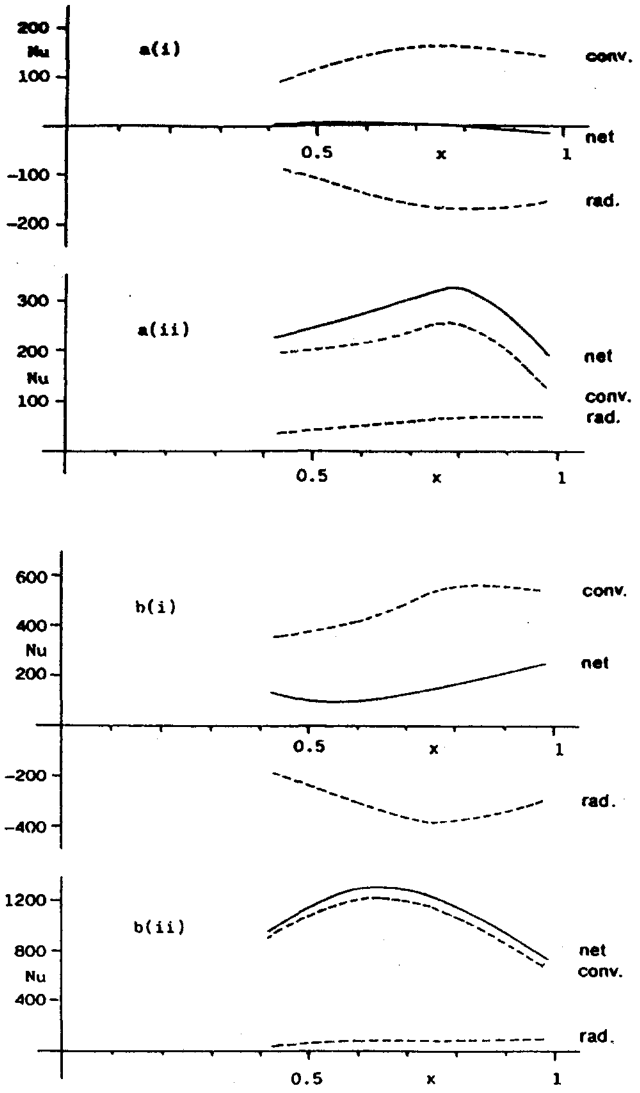

Fig. 3 Comparison of local convective and radiative Nusselt numbers: (*a*) $\mathrm{Re}_\theta = 3.28 \times 10^5$, $C_w = 2800$, (*b*) $\mathrm{Re}_\theta = 3.15 \times 10^6$, $C_w = 14000$; (*i*) upstream disk, (*ii*) downstream disk.

the disk), the contribution of radiation to the total heat flux varying from approximately 21 percent for the conditions of Fig. 3(*a*) to 6 percent for those of Fig. 3(*b*).

Figure 4 shows the predicted Nusselt number distributions for $C_w = 2800$ and $1.25 \times 10^5 \le \mathrm{Re}_\theta \le 3.68 \times 10^6$. As can be seen from Figs. 4(*a*) and 4(*b*), the modification to the model makes very little difference for either disk at low rotational Reynolds numbers, where the wall-jet effect on the downstream disk is dominant and the source region fills the entire cavity (see also Fig. 1*a*). Under these conditions, Ekman layers do not form on the disks and there is no interior core. Agreement with measurement is here good for the upstream disk, but the Nusselt numbers for the downstream disk are slightly underpredicted. As Re_θ is increased (Figs. 4*c*, 4*d*, and 4*e*), the radial extent of the source region is reduced, leading to the formation of Ekman layers and the interior core. Model 2 now gives a marked improvement for the upstream disk, where the predicted Nusselt numbers begin to fall away sharply in the absence of the modification, becoming negative in the outer part of the cavity at $\mathrm{Re}_\theta = 1.30 \times 10^6$. Negative values of the Nusselt number indicate clearly that there is excessive turbulent heat transport across the core flow, since frictional heating is not significant at this rotational speed. The improvement in the predictions for the upstream disk brought about by using Model 2 is reflected in a similar improvement for the downstream disk, where the Nusselt numbers are otherwise overpredicted. Note that the corresponding changes resulting from the modification are approximately four times greater for the upstream disk due to the lower temperature difference ΔT (disk-to-inlet) used in the definition of Nu (Eq. (11)). The effect of Model 2 is to bring the Nusselt numbers for the two disks closer together, in good quantitative agreement with the experimental data.

At $\mathrm{Re}_\theta = 2.55 \times 10^6$ (Fig. 4*f*), there is a loss of predictive accuracy for the downstream disk, Model 1 giving an overprediction of the Nusselt numbers in the outer part of the cavity and Model 2 an underprediction. The disagreement between prediction and experiment is even more apparent at $\mathrm{Re}_\theta = 3.13 \times 10^6$ (Fig. 4*g*), although there is a slight improvement at $\mathrm{Re}_\theta = 3.68 \times 10^6$ (Fig. 4*h*). It can be remarked that an abrupt departure from accurate prediction also occurred for *symmetric* heating at $\mathrm{Re}_\theta = 3.13 \times 10^6$ (Morse and Ong, 1992), although there was then a similar loss of accuracy for the upstream disk. The current predictions do not show this and are in fact in good accord with the experimental data up to the highest rotational Reynolds number (at least at the last three fluxmeter locations). At the first location, there is a significant overestimate of Nu, which first becomes apparent at $\mathrm{Re}_\theta = 1.30 \times 10^6$. The extent of the overprediction increases from 48 percent at $\mathrm{Re}_\theta = 1.30 \times 10^6$ to 70 percent at $\mathrm{Re}_\theta = 3.13 \times 10^6$, before falling to 35 percent at $\mathrm{Re}_\theta = 3.68 \times 10^6$. At this first fluxmeter location, Model 1 generally gives the better prediction for the upstream disk, but Model 2 fares better for the downstream disk. Note that, with the increasing importance of frictional heating at high rotational speeds, both the experimental data and the predictions from Model 2 indicate negative values of the Nusselt number for the upstream disk for $\mathrm{Re}_\theta \ge 1.86 \times 10^6$. For the downstream disk, a small region of heat inflow to the disk is predicted to occur near the shroud for $\mathrm{Re}_\theta \ge 2.55 \times 10^6$.

Corresponding results for $C_w = 14{,}000$ and $1.20 \times 10^5 \le \mathrm{Re}_\theta \le 4.52 \times 10^6$ are shown in Fig. 5. These follow the same trends as for those at the lower flow rate, but since the source region is now larger, the relative effects become apparent at higher values of Re_θ. There is little difference between the predictions for Models 1 and 2 for $\mathrm{Re}_\theta \le 1.24 \times 10^6$ (Figs. 5*a*, 5*b*, 5*c*), where accuracy is good for the downstream disk but the predicted Nusselt numbers for the upstream disk bear no resemblance to the experimental values. There is the possibility of significant experimental errors here, associated with the low level of heat transfer (the temperature of the upstream disk, at the four fluxmeter locations, varies from only 2°C to 10°C above ambient for $\mathrm{Re}_\theta = 5.99 \times 10^5$). However, the convective fluxes have to be significant in order to balance the radiative fluxes. The predictions for the upstream disk fall more closely into line with the experimental data at $\mathrm{Re}_\theta = 1.88 \times 10^6$, 2.45×10^6 and 2.50×10^6 (Figs. 5*d*, 5*e*, and 5*f*, respectively). Beginning at $\mathrm{Re}_\theta = 2.50 \times 10^6$, Model 2 gives an improvement in the predictions for the upstream disk at fluxmeter locations 3 and 4, but generally a slight overestimate of the experimental values at locations 1 and 2. In contrast, the values are overpredicted at $\mathrm{Re}_\theta = 4.52 \times 10^6$ (Fig. 5*i*), but this still represents an improvement over the results obtained using Model 1 (where heat is predicted to flow into the disk for $x > 0.66$). Predictive accuracy for the downstream disk is generally good, although at the higher values of Re_θ (Figs. 5*g*, 5*h*, 5*i*), there is some overestimate of the experimental data at fluxmeter locations 2 and 3 with both variants of the model.

Table 3 summarizes the errors in the aggregate heat fluxes predicted at the four fluxmeter locations. In calculating the errors, a subjective, but unbiased approach has been used in that the fluxmeters at location 4 were given only half weighting in the summation. This policy was adopted since these fluxmeters were nonoperational for some of the tests, the heat fluxes so close to the shroud are not really representative of those from

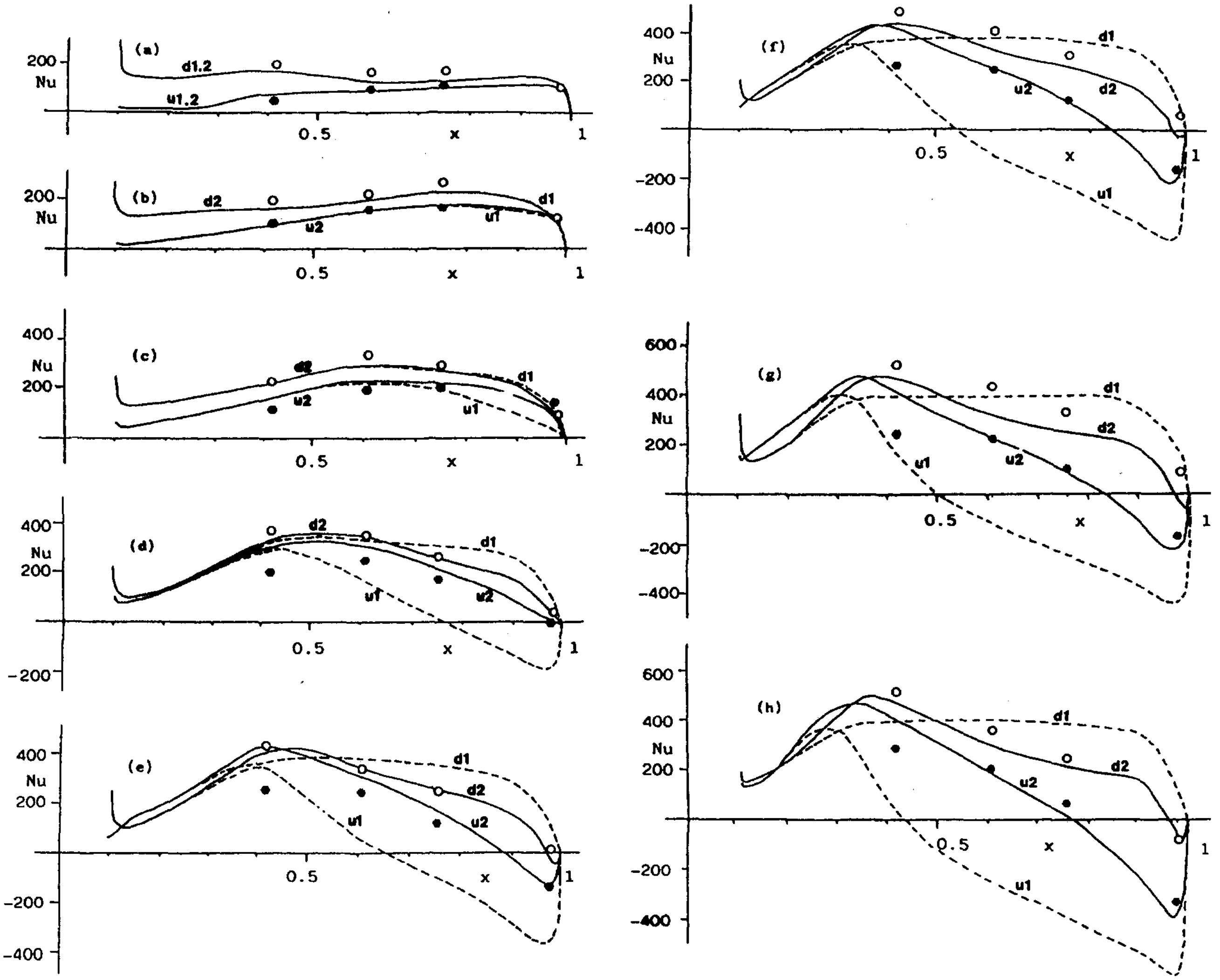

Fig. 4 Predicted local Nusselt numbers for $C_w = 2800$: (*a*) $Re_\theta = 1.25 \times 10^5$ ($\epsilon_z = 6.43$), (*b*) $Re_\theta = 3.28 \times 10^5$ ($\epsilon_z = 2.45$), (*c*) $Re_\theta = 6.51 \times 10^5$ ($\epsilon_z = 1.23$), (*d*) $Re_\theta = 1.30 \times 10^6$ ($\epsilon_z = 0.618$), (*e*) $Re_\theta = 1.90 \times 10^6$ ($\epsilon_z = 0.423$), (*f*) $Re_\theta = 2.55 \times 10^6$ ($\epsilon_z = 0.315$), (*g*) $Re_\theta = 3.13 \times 10^6$ ($\epsilon_z = 0.257$), (*h*) $Re_\theta = 3.68 \times 10^6$ ($\epsilon_z = 0.218$); ● upstream disk, ○ downstream disk

the disks as a whole, and yet differences between the Model 1 and Model 2 predictions are most apparent at large radii. Values of the mean Nusselt number $\overline{Nu}$, as defined by Eq. (12), are also given for both disks using the results from Model 2.

For $C_w = 2800$, there is clearly some improvement obtained for the upstream disk. Although significant errors remain with Model 2, these are mostly due to the overestimation of the Nusselt number at fluxmeter location 1. The degree of improvement for the downstream disk appears debatable from these results, there being some evidence of the overestimate with Model 1 becoming an underestimate with Model 2. However, the figures can be deceptive, especially the result for Model 1 at $Re_\theta = 3.13 \times 10^6$, which disguises a large standard deviation between predicted and measured values (see Fig. 4*g*). For $C_w = 14{,}000$, differences between the two models are less pronounced, but there is an improvement for the upstream disk at high rotational Reynolds numbers, and a slight, but definite improvement for the downstream disk throughout the rotational Reynolds number range. (Starred entries in the table indicate test cases for which the outermost fluxmeter was nonoperational.)

Finally, predictions are shown in Fig. 6 for an intermediate flow rate of $C_w = 7000$ ($1.24 \times 10^5 \leq Re_\theta \leq 5.20 \times 10^6$). These results were obtained using Model 2 only. Again, accuracy is better for the downstream disk, as reflected in both the diagrams and the errors in aggregate heat flux listed in Table 3. Also, the value of the Nusselt number at the first fluxmeter location on the upstream disk is seriously overestimated for $Re_\theta \geq 1.29 \times 10^6$, the error increasing with rotational Reynolds number. In contrast to the situation for $C_w = 2800$ (see Fig. 4), this overestimate also spreads to the second fluxmeter location, although there is some recovery in accuracy at the two highest values of Re_θ (Figs. 6*i* and 6*j*). Predictive accuracy for the downstream disk is clearly good for the entire range of rotational Reynolds numbers at this flow rate, the peak values of local Nusselt number generally being about 5 percent lower than the measurements.

4 Discussion

Prediction of the convective heat transfer in asymmetrically heated rotating cavities has highlighted a defect in the $k-\epsilon$ turbulence model, which was not evident in the previous work on symmetric heating (Morse and Ong, 1992). The two situations differ because asymmetric heating imposes an axial temperature gradient across the core region of the flow. This requires accurate modeling of the high Reynolds number turbulence in the core in order to obtain the correct level of heat transfer from the hotter to the cooler disk. The defect in the model was traced to the radial-circumferential shear stress,

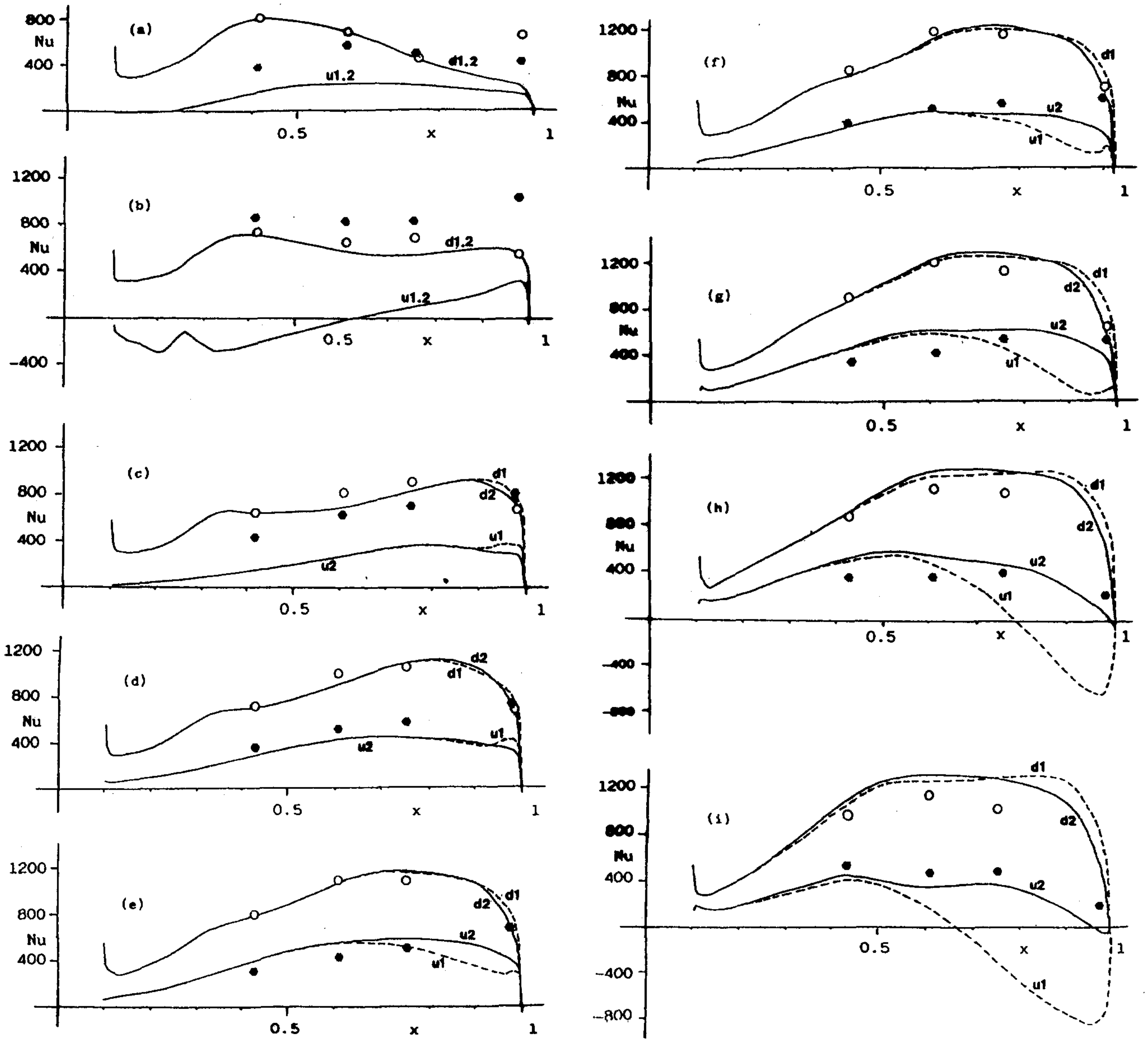

Fig. 5 Predicted local Nusselt numbers for $C_w = 14{,}000$: (*a*) $Re_\theta = 1.20 \times 10^5$ ($\epsilon_z = 33.5$), (*b*) $Re_\theta = 5.99 \times 10^5$ ($\epsilon_z = 6.71$), (*c*) $Re_\theta = 1.24 \times 10^6$ ($\epsilon_z = 3.24$), (*d*) $Re_\theta = 1.88 \times 10^6$ ($\epsilon_z = 2.14$), (*e*) $Re_\theta = 2.45 \times 10^6$ ($\epsilon_z = 1.64$), (*f*) $Re_\theta = 2.50 \times 10^6$ ($\epsilon_z = 1.61$), (*g*) $Re_\theta = 3.15 \times 10^6$ ($\epsilon_z = 1.28$), (*h*) $Re_\theta = 3.86 \times 10^6$ ($\epsilon_z = 1.04$); (*i*) $Re_\theta = 4.52 \times 10^6$ ($\epsilon_z = 0.889$). ● upstream disk, ○ downstream disk

$\overline{vw}$, which does not conform well to the simple constitutive relationship of Eq. (2) in the core flow, leading to excessive turbulence generation. The discrepancies between prediction and experiment can be largely offset by the use of Eq. (8), which was derived from algebraic-stress modeling with the retention of only the most significant production terms in the formal transport equations for $\overline{vw}$, $\overline{v^2}$, and $\overline{w^2}$. The efficacy of this approach depends closely on the pressure-scrambling model employed and also on the values of the associated numerical constants (about which there is considerable diversity of opinion). The significant improvement in accuracy obtained by the modification certainly justifies the modest (approximately 4 percent) increase in Cpu time required for its implementation. Similar algebraic-stress modeling is not considered necessary for the other five components of the Reynolds-stress tensor, at least not for the present class of flow, but this is unlikely to remain the case for flows of greater complexity.

There appear to be three complicating physical factors that limit the ability of the computational procedure to portray the flow accurately, viz., fluid ingress through the shroud, vortex breakdown of the inlet jet, and buoyancy-induced instability. All three of these phenomena attain extra significance at high rotational Reynolds numbers, and may be interrelated.

As regards buoyancy-induced instability, Pincombe (1983) correlated his flow visualization data for the onset of oscillatory flow (for $1.5 \times 10^5 \leq Re_\theta \leq 2.6 \times 10^6$, $350 \leq C_w \leq 1750$) in terms of the axial Rossby number ϵ_z. For a downstream disk heated to give $\beta\Delta T \approx 0.27$ and a shroud with thirty 28.6-mm-dia holes, oscillatory flow occurred at $\epsilon_z = 0.9$ and chaotic flow at $\epsilon_z = 0.5$. For $\beta\Delta T \approx 0.14$, oscillatory flow began at a lower value ($\epsilon_z = 0.7$), while the onset of chaotic flow remained unchanged. For $\beta\Delta T \approx 0.1$, there was no sign of either flow regime within the rotational speed limits of the experimental rig. With a peripheral shroud with thirty 6.4-mm-dia holes, the onset of oscillatory flow was unaffected, although the amplitude of the oscillations was attenuated: Chaotic flow was not observed. These results suggest a dependence on the rotational Grashof number, an average value of $Gr^{1/2}/C_w$ of 155 being

Table 3 Asymmetrically heated rotating cavities with radial outflow: summary of predictions

C_w (nominal)	Re_θ	UPSTREAM DISC E(aggregate heat flux) model 1/ model 2	UPSTREAM DISC $\overline{Nu}$ (model 2)	DOWNSTREAM DISC E(aggregate heat flux) model 1/ model 2	DOWNSTREAM DISC $\overline{Nu}$ (model.2)
2800	1.25×10^{5}	-1.6%/ -1.3% *	134.2	-13.7%/-13.6%	227.3
	3.28	+5.8%/ +9.0% *	204.5	-7.0%/ -6.8%	297.5
	6.51	-2.8%/+14.0%	256.5	-5.2%/ -7.2%	345.6
	1.30×10^{6}	-61.5%/+31.7%	300.1	+3.5%/-10.0%	365.6
	1.90	-120%/+54.1%	268.3	+22.4%/ -1.8%	369.5
	2.55	-215%/+15.8%	211.3	+10.2%/-15.4%	382.4
	3.13	-251%/+17.3%	194.7	-0.2%/-27.7%	379.8
	3.68	-573%/-25.3%	89.3	-13.5%/-12.4% *	366.9
7000	1.24×10^{5}	/-34.9%	206.0	/-14.9%	411.0
	3.25	/-17.8%	263.4	/ -6.9%	494.7
	6.43	/ -0.1%	352.0	/ +3.4%	621.6
	1.29×10^{6}	/+14.5%	477.2	/ -4.7%	757.5
	1.92	/+15.6%	575.3	/ -6.2%	825.9
	2.55	/+20.3%	573.4	/ -8.7%	853.9
	3.18	/+19.1%	593.8	/-13.2%	862.9
	3.93	/ -5.0%	382.2	/ -7.9% *	862.9
	4.53	/+30.0%	445.8	/ +5.0% *	877.1
	5.20	/-16.8% *	243.1	/ -2.5% *	808.1
14000	1.20×10^{5}	-60.8%/-62.7%	240.7	-14.8%/-14.7%	719.4
	5.99	-89.4%/-86.5%	161.5	-9.4%/ -9.0%	894.8
	1.24×10^{6}	-51.3%/-53.6%	419.8	+1.6%/ +0.8%	1144
	1.88	-25.4%/-29.2%	528.3	+6.7%/ +4.1%	1318
	2.45	-4.6%/ +3.5%	708.9	+9.4%/ +6.2%	1429
	2.50	-33.0%/-23.0%	577.6	+1.7%/ -0.6%	1442
	3.15	-16.9%/+10.9%	744.4	+10.7%/ +7.4%	1510
	3.86	-67.3%/ +8.1%	567.5	+9.2%/+11.1% *	1552
	4.52	-143%/-35.3%	370.3	+12.3%/+12.6% *	1550

appropriate for the onset of oscillatory flow and 250 for chaotic flow. Note that these findings accord fairly well with those of Owen and Onur (1983), where corresponding values of 180 and 330 were quoted. A liberal interpretation of the combined results suggests that oscillatory flow might be expected to occur in the present test cases for $Re_\theta = 1.30 \times 10^6$ ($C_w = 2800$) and $Re_\theta = 2.55 \times 10^6$ and 3.18×10^6 ($C_w = 7000$), with chaotic flow for $Re_\theta \geq 1.90 \times 10^6$ and $Re_\theta \geq 3.93 \times 10^6$, respectively. Neither regime would occur for $C_w = 14{,}000$ over the test range of rotational Reynolds number.

The extent to which buoyancy-induced instability can be divorced from the phenomena of fluid ingress and vortex breakdown is unclear. The size of the exit holes in the shroud does have some effect on the critical values of ϵ_z for unsteady flow, and, as shown in Pincombe's studies, is also clearly linked to ingress. It is believed that ingress occurs at rotational Reynolds numbers considerably lower than those that cause buoyancy-induced instability. Ingress is characterized by air being drawn into the cavity through holes in the shroud and penetrating to the source region via the reverse-flow regions of the Ekman layers. However, this (ingressive) air is just as likely to be heated fluid previously expelled from the cavity as it is to be cooler ambient fluid. It therefore seems improbable that ingress, in isolation, has a significant effect.

Pincombe also investigated the phenomenon of vortex breakdown in the central inlet jet (albeit for $C_w = 314$ and isothermal flow) and found that spiral vortex breakdown (an axisymmetric precession of the jet about its rotational axis) occurred for $\epsilon_z \leq 1.0$. When ingress and spiral vortex breakdown occurred simultaneously, the flow became chaotic with the Ekman layer structure partly destroyed. Smoke injected outside the cavity then appeared to penetrate "almost instantaneously" to the source region. This behavior is very similar to that attributed to buoyancy-induced instability as described above. The inlet jet appeared to regain its axisymmetry at lower values of the axial Rossby number ($\epsilon_z \leq 0.3$), resulting in axisymmetric vortex breakdown with intermittent stagnation on the axis of rotation. The chaotic flow associated with spiral vortex breakdown is likely to have a greater effect in limiting the predictive ability of the present approach than the more orderly axisymmetric mode of vortex breakdown. In both the current work and the symmetric-heating study of Morse and Ong (1992), the predictions for $C_w = 2800$ suffer an abrupt loss of accuracy at a critical value of ϵ_z in the range 0.25–0.30, with a partial recovery for $\epsilon_z \leq 0.2$. These values are lower than found in Pincombe's study (where the flow is essentially laminar), but the occurrence of vortex breakdown and the interchange of mechanisms provides a plausible, if speculative, explanation for the discrepancies between prediction and experiment (axial Rossby numbers of 0.3 are beyond the experimental range for $C_w = 7000$ and 14,000). That the effect occurs for conditions of symmetric heating appears to signify that vortex breakdown and ingress are mechanisms at least as important as buoyancy-induced instability.

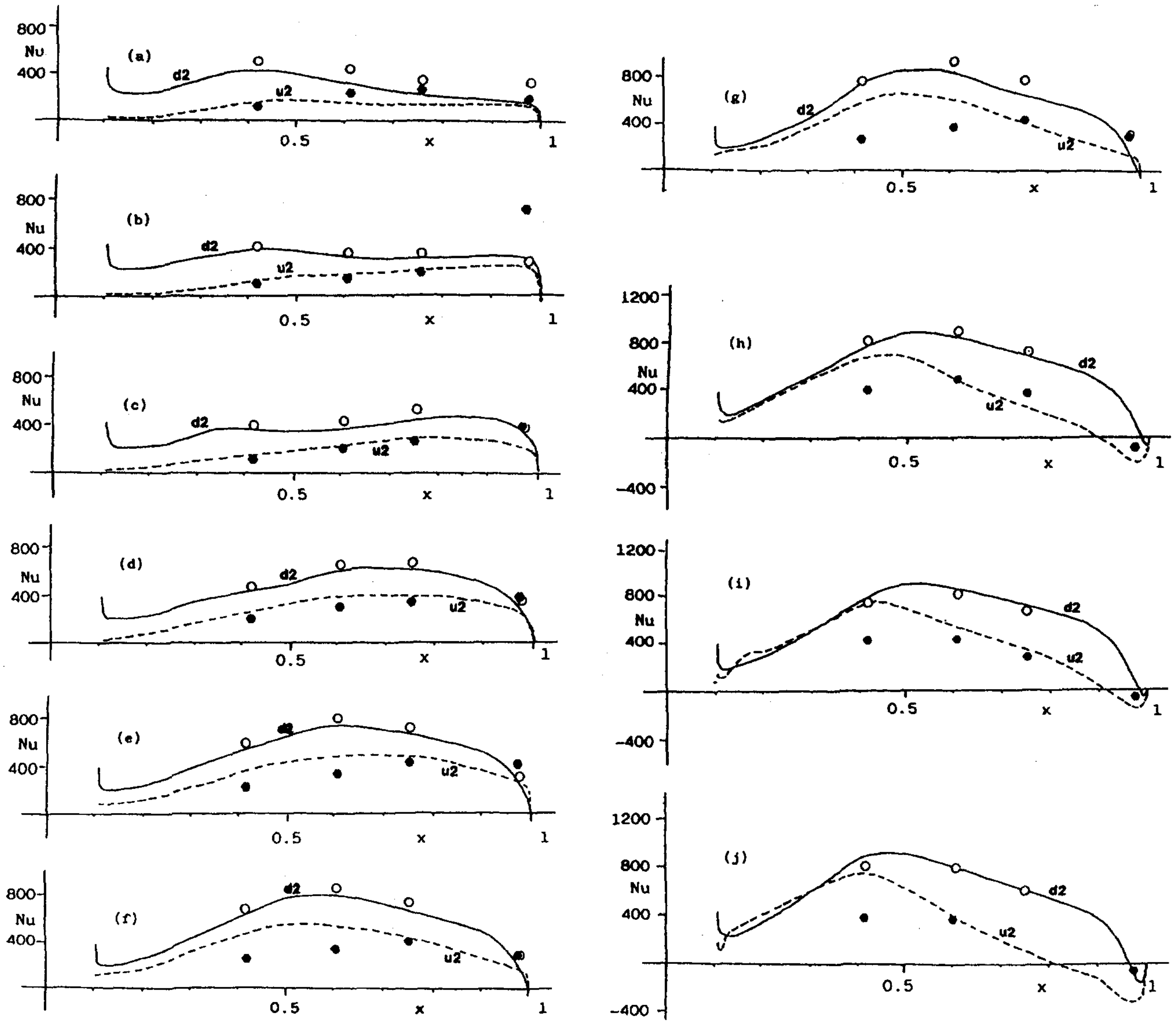

Fig. 6 Predicted local Nusselt numbers for $C_w = 7000$: (*a*) $Re_\theta = 1.24 \times 10^5$ ($\epsilon_z = 16.2$), (*b*) $Re_\theta = 3.25 \times 10^5$ ($\epsilon_z = 6.19$), (*c*) $Re_\theta = 6.43 \times 10^5$ ($\epsilon_z = 3.12$), (*d*) $Re_\theta = 1.29 \times 10^6$ ($\epsilon_z = 1.56$), (*e*) $Re_\theta = 1.92 \times 10^6$ ($\epsilon_z = 1.05$), (*f*) $Re_\theta = 2.55 \times 10^6$ ($\epsilon_z = 0.788$), (*g*) $Re_\theta = 3.18 \times 10^6$ ($\epsilon_z = 0.632$), (*h*) $Re_\theta = 3.93 \times 10^6$ ($\epsilon_z = 0.511$); (*i*) $Re_\theta = 4.29 \times 10^6$ ($\epsilon_z = 0.468$). (*j*) $Re_\theta = 5.20 \times 10^6$ ($\epsilon_z = 0.386$); ● upstream disk, ○ downstream disk

The poor predictive accuracy for the upstream disk at the opposite extreme of flow conditions (i.e., low values of Re_θ and high values of C_w) is puzzling, especially as the predicted values for the downstream disk are in good accord with experimental data. From previous studies of isothermal and symmetrically heated flow, it is known that the turbulence model is less accurate under conditions for which the source region is large in extent, than under those for which Ekman layer flow occurs. Even so, for $C_w = 14{,}000$ and values of Re_θ similar to those of Figs. 5(*a*) and 5(*b*), the predicted Nusselt numbers of Morse and Ong for the upstream disk in a symmetrically heated cavity are lower than the measured values by only 20 percent. In this context, the predicted size of the vortex in the source region and its implications for the degree of flow entrainment into the boundary layer on the upstream disk can be seen to be of paramount importance, but the authors cannot as yet offer any firm explanation for the wholesale lack of agreement between the predicted and measured values of the Nusselt numbers for the upstream disk.

For intermediate values of C_w and Re_θ, errors are also apparent, with both variations of the model, in the overestimated values of Nusselt number for the upstream disk at low radii. Similar errors did not occur in the studies of a symmetrically heated cavity, so this suggests that the fault lies in the high turbulence Reynolds number form of the model, and not in the near-wall modeling. It can also be noted that typically one-third of the overshoot at the first fluxmeter location can be removed by imposing zero swirl at the cavity inlet, which may be a closer approximation to reality than the condition of a linearly varying angular velocity as used here. (Reduction of the initial degree of swirl leads to less rapid entrainment of the flow into the boundary layer on the upstream disk and consequently lower local Nusselt numbers for this disk in the source region.) Finally, the wisdom behind the use of the "turbulence Prandtl number" concept as a simple interlinkage between the turbulent transport of heat and momentum is open to question in view of the anisotropic turbulent viscosity approach found necessary for the present flows.

5 Conclusions

A low-Reynolds-number $k-\epsilon$ model has been used to predict convective heat transfer in an asymmetrically heated rotating cavity, for which the extent of turbulent heat transport across the core region is an important consideration. The form of the model used previously for symmetric heating overestimates turbulence levels in the core flow, leading to excessive heat transport, with the result, particularly at high rotational Reynolds numbers, that there is convective heat transfer to the upstream disk from the adjacent fluid—in direct contrast to experimental measurement. The error is traceable to the action of the radial-circumferential shear stress $\overline{vw}$, which produces unrealistically high rates of turbulence generation in the core. A modified version of the model, based on algebraic-stress modeling, generally leads to improved accuracy. Systematic errors remain, particularly for the upstream disk. The observed loss of accuracy for high rotational Reynolds numbers and low values of C_w seems likely to be a consequence of the three-dimensional and unsteady nature of the flow, which prevails in practice. The exact mechanisms that cause this are at present unknown. At the opposite extreme of flow conditions, no explanation can be offered for the large discrepancy between prediction and experiment for the upstream disk.

The predicted Nusselt numbers for the downstream disk have a global accuracy of ±10 percent, notwithstanding larger errors at high rotational speeds. It is considered that this is probably sufficiently accurate for normal engineering design purposes. In an engine, the necessity to know the heat transfer for the cooler (in this case the upstream) disk would require some improvement in the predictive accuracy of the model. However, the present computations do serve as a standard against which further improvements in turbulence modeling and the use of more sophisticated computer codes can be assessed.

References

Castro, I. P., and Jones, J. M., 1987, "Studies in Numerical Computations of Recirculating Flows," *Int. J. Num. Methods in Fluids,* Vol. 7, p. 793.

Chew, J. W., 1985, "Prediction of Flow in a Rotating Cavity With Radial Outflow Using a Mixing Length Turbulence Model," *Proc. 4th International Conference on Numerical Methods in Laminar and Turbulent Flow,* Swansea, Pineridge Press, United Kingdom.

Gibson, M. M., and Younis, B. A., 1986, "Calculation of Swirling Jets With a Reynolds Stress Closure," *Phys. Fluids,* Vol. 29(1), p. 38.

Howell, J. R., 1982, *A Catalog of Radiation Configuration Factors,* McGraw-Hill, New York.

Iacovides, H., and Theofanopoulos, I. P., 1991, "Turbulence Modelling of Axisymmetric Flow Inside Rotating Cavities," *Int. J. Heat Fluid Flow,* Vol. 12, p. 2.

Launder, B. E., Reece, G. J., and Rodi, W., 1975, "Progress in the Development of a Reynolds Stress Turbulence Closure," *J. Fluid Mech.,* Vol. 68, p. 537.

Leonard, B. P., 1979, "A Stable and Accurate Convective Modelling Procedure Based on Quadratic Upstream Interpolation," *Computer Methods in Appl. Mech. Eng.,* Vol. 19, p. 59.

Long, C. A., 1984, "Transient Heat Transfer in a Rotating Cylindrical Cavity," D.Phil. Thesis, University of Sussex.

Long, C. A., and Owen, J. M., 1986, "The Effect of Inlet Conditions on Heat Transfer in a Rotating Cavity With a Radial Outflow of Fluid," ASME JOURNAL OF TURBOMACHINERY, Vol. 108, p. 145.

Morse, A. P., 1980, "Axisymmetric Free Shear Flows, With and Without Swirl," Ph.D. Thesis, University of London.

Morse, A. P., 1991a, "Application of a Low Reynolds Number $k-\epsilon$ Turbulence Model to High-Speed Rotating Cavity Flows," ASME JOURNAL OF TURBOMACHINERY, Vol. 113, p. 98.

Morse, A. P., 1991b, "Assessment of Laminar-Turbulent Transition in Closed Disk Geometries," ASME JOURNAL OF TURBOMACHINERY, Vol. 113, p. 131.

Morse, A. P., and Ong, C. L., 1992, "Computation of Heat Transfer in Rotating Cavities Using a Two-Equation Model of Turbulence," ASME JOURNAL OF TURBOMACHINERY, Vol. 114, p. 247.

Northrop, A. N., 1984, "Heat Transfer in a Cylindrical Rotating Cavity," D. Phil. Thesis, University of Sussex.

Northrop, A. N., and Owen, J. M., 1988a, "Heat Transfer Measurements in Rotating Disc-Systems. Part 1: The Free Disc," *Int. J. Heat Fluid Flow,* Vol. 9, p. 19.

Northrop, A. N., and Owen, J. M., 1988b, "Heat Transfer Measurements in Rotating Disc-Systems. Part 2: The Rotating Cavity With a Radial Outflow of Cooling Air," *Int. J. Heat Fluid Flow,* Vol. 9, p. 27.

Owen, J. M., and Pincombe, J. R., 1980, "Velocity Measurements Inside a Rotating Cylindrical Cavity With a Radial Outflow of Fluid," *J. Fluid Mech.,* Vol. 99, p. 111.

Owen, J. M., and Onur, H. S., 1983, "Convective Heat Transfer in a Rotating Cylindrical Cavity," ASME *Journal of Engineering for Power,* Vol. 105, p. 265.

Owen, J. M., Pincombe, J. R., and Rogers, R. H., 1985, "Source-Sink Flow Inside a Rotating Cylindrical Cavity," *J. Fluid Mech.,* Vol. 155, p. 233.

Patankar, S. V., 1980, *Numerical Heat Transfer and Fluid Flow,* Hemisphere Books, Washington, DC.

Pincombe, J. R., 1983, "Optical Measurements of the Flow Inside a Rotating Cylinder," D.Phil. Thesis, University of Sussex.

Rodi, W., 1972, "The Prediction of Free Turbulent Boundary Layers by Use of a Two-Equation Model of Turbulence," Ph.D. Thesis, University of London.

Rodi, W., 1991, "Some Current Approaches in Turbulence Modelling," AGARD-AR-291.

Van Doormal, J. P., and Raithby, G. D., 1984, "Enhancements of the SIMPLE Method for Predicting Incompressible Fluid Flows," *J. Num. Heat Trans.,* Vol. 7, p. 147.

Zafiropoulos, N., 1992, "Numerical Fluid Flow and Heat Transfer in Asymmetrically-Heated Rotating Cavities," M.Sc. Thesis, University of Sussex.

Developing Buoyancy-Modified Turbulent Flow in Ducts Rotating in Orthogonal Mode

T. Bo

H. Iacovides

B. E. Launder

Department of Mechanical Engineering,
UMIST,
Manchester, M60 1QD, United Kingdom

A numerical study of developing flow through a heated duct of square cross section rotating in orthogonal mode is reported. The two main aims are to explore the effects of rotational buoyancy on the flow development and to assess the ability of available turbulence models to predict such flows. Two test cases have been computed corresponding to values of the rotation number, Ro, of 0.12 and 0.24, which are typical of operating conditions in internal cooling passages of gas turbine blades. Computations from three turbulence models are presented: a $k-\epsilon$ eddy viscosity (EVM) model matched to a low-Reynolds-number one-equation EVM in the near-wall region; a low-Re $k-\epsilon$ EVM; and a low-Re algebraic stress model (ASM). Additional computations in which the fluid density is assumed to remain constant allow the distinct contributions from buoyancy and Coriolis forces to be separated. It is thus shown that rotational buoyancy can have a substantial influence on the flow development and that, in the case of outward flow, it leads to a considerable increase of the side-averaged heat transfer coefficient. The Coriolis-induced secondary motion leads to an augmentation of the mean heat transfer coefficient on the pressure surface and a reduction on the suction side. The $k-\epsilon$/one-equation EVM produces a mostly reasonable set of heat transfer predictions, but some deficiencies do emerge at the higher rotation number. In contrast, predictions with the low-Re $k-\epsilon$ EVM return a spectacularly unrealistic behavior while the low-Re ASM thermal predictions are in encouragingly close agreement with available measurements.

1 Introduction

The distribution of the coefficient of convective heat transfer for a duct rotating in orthogonal mode (Fig. 1) is of particular interest to the designers of internal cooling passages of gas turbine blades. The thermal behavior within such passages is, of course, influenced by several factors, such as the presence of sharp 180 deg bends and also the use of heat transfer-enhancing ribs. The effects of rotation are nevertheless of primary importance. The ability to predict how wall heat transfer coefficients are affected by rotation, even in ducts of simple geometry, is thus of considerable value to the engine designer. In the case of flow through heated rotating ducts, rotation induces two body forces: that due purely to rotation (the Coriolis force) and that associated with the varying centrifugal force over the duct's cross section due to significant variations in coolant density. These forces act both in the mean momentum equations and also directly on the turbulent velocity fluctuations. So far as the mean motion is concerned, the Coriolis force interacts with the slow-moving boundary layer fluid and generates a secondary mean motion, which promotes mixing and thus, overall, would be expected to enhance heat transfer rates. The direct action of the Coriolis force on the turbulent fluctuations will tend to suppress turbulent transport on the suction face and augment it on the pressure surface. In the case of heated rotating ducts, when the mean flow direction is away from the center of rotation, *outward flow,* the rotational buoyancy force tends to slow down the lighter near-wall fluid, producing thicker boundary layers. For inward flows, rotational buoyancy will have the opposite effect on the mean flow, leading to a more uniform streamwise velocity distribution. Reference to somewhat analogous data on mixed-convection flows through strongly heated vertical (stationary) tubes (Cotton and Jackson, 1987), indicates that rotational buoyancy might also be expected to enhance turbulent transport in outward flows.

The combined effect of the above-mentioned influences on the hydrodynamic and thermal behavior is difficult to foresee and even more difficult to quantify. Moreover, in experimental investigations of heat transfer in rotating ducts it is not easy to separate the Coriolis effects from the influence of rotational buoyancy, a fact that inhibits the development of general and reliable heat transfer correlations for rotating duct flows.

The problem of predicting flow in rotating ducts has attracted the attention of many researchers. Most of the earlier efforts have been directed toward the computation of *fully developed* flow through rotating ducts. Laminar flow studies by Speziale (1982) and by Kheshgi and Scriven (1985) showed that at high rotational speeds the conventional double vortex secondary motion structure bifurcated into a four-vortex mode. Hart's (1971) flow visualizations provide some support for the existence of this phenomenon. Subsequent work by two of the present authors, Iacovides and Launder (1987, 1991), suggested that a similar transition at high rotational speeds also takes place in fully developed turbulent flows in rotating ducts. The effects of rotation on heat transfer have been explored in a number of recent experimental investigations by Guidez (1989), Wagner et al. (1991), and Morris and Ghavami-Nasr (1991) among others, indicating that there is a strong circumferential variation in the local Nusselt number in developing flows through rotating ducts. The trailing (pressure) side heat transfer rates are found to be substantially higher than for the corresponding flow through a stationary duct whereas, over the leading (suction) side of the duct, wall heat transfer rates are observed to be severely suppressed by rotation. These studies also indicate that rotation affects the overall level of heat transfer, a fact confirmed by the measurements of Soong et al. (1991).

Our initial numerical explorations (Iacovides and Launder, 1987, 1991) were concerned with fully developed flow in rotating ducts. As in all our duct flow predictions, the need to resolve

---

Contributed by the International Gas Turbine Institute for publication in the JOURNAL OF TURBOMACHINERY. Manuscript received at ASME Headquarters March 1995. Associate Technical Editor: T. H. Okiishi.

the strong secondary motion within the near-wall regions had led us to eschew the usual wall-function approach and, instead, adopt a fine mesh across the near-wall sublayer, employing a low-Reynolds-number turbulence model to evaluate turbulent diffusivities there. A low-Re one-equation model (Wolfshtein, 1969) was interfaced with the usual $k-\epsilon$ EVM in the fully turbulent core (which extends over more than 90 percent of the cross section). The trends present in heat transfer measurements of developing flow through rotating ducts were well captured. More recently, in Bo et al. (1991), the same turbulence modeling practice was used to predict some of the heat transfer measurements of Wagner et al. (1991) for developing flows through a rotating duct of square cross section. By performing additional computations, in which the fluid density was assumed to remain constant, it was possible to separate the effects of rotational buoyancy and Coriolis forces. It was shown that, at a Reynolds number of 25,000, rotational buoyancy begins to have a significant impact on the flow development at rotational Rayleigh numbers (Ra) greater than 10^8. The measured strong augmentation of heat transfer rates along the pressure surface was reproduced with reasonable accuracy by these $k-\epsilon$/one-equation computations. Along the suction side, however, the severe reduction indicated by the heat transfer measurements in the development region was not fully captured. In another recent numerical study of flow and heat transfer through rotating ducts, Prakash and Zerkle (1992) employed the high-Reynolds-number version of the $k-\epsilon$ model with the wall function approximation providing wall boundary conditions. In common with Bo et al. (1991), Prakash and Zerkle also demonstrated that rotational buoyancy effects are significant at engine operating conditions. They also concluded that the high-Re $k-\epsilon$ EVM could not return quantitatively accurate heat transfer predictions and recommended that more refined turbulence models should be tested.

In this contribution, our aim is to address the shortcomings that earlier studies identified in the $k-\epsilon$/one-equation and $k-\epsilon$/wall-function computations by successively refining the turbulence model. By first introducing a low-Reynolds-number $k-\epsilon$ EVM, an attempt is made to account for the nonuniversalities in the near-wall length scale while retaining the effective viscosity framework. This model is subsequently replaced by a low-Re ASM closure we have recently developed and successfully applied to computations of flow in stationary curved ducts (Iacovides and Launder, 1992; Abou-Haidar et al., 1991). This second level of model refinement abandons the linear stress–strain relation, thus allowing for a more realistic representation of the effects of rotation on turbulence.

2 The Mathematical and Physical Model

2.1 The Mean Field Equations. The Reynolds and continuity equations describing the motion of turbulent flow in an arbitrarily rotating coordinate system may be written as follows:

$$\frac{\partial}{\partial x_j}(\rho U_j U_i) = \frac{\partial P}{\partial x_i} + \frac{\partial}{\partial x_j}\left(\mu\left[\frac{\partial U_i}{\partial x_j} + \frac{\partial U_j}{\partial x_i}\right] - \rho\overline{u_i u_j}\right)$$

$$- 2\rho\epsilon_{ipj}\Omega_p U_j - \rho(\Omega_j X_j \Omega_i - \Omega_j X_i \Omega_j) \quad (1)$$

$$\frac{\partial}{\partial x_i}(\rho U_i) = 0 \quad (2)$$

Here U_i is the mean velocity vector, Ω_i the coordinate rotation vector, and $\overline{u_i u_j}$ the unknown Reynolds-stress tensor. The local density ρ is related to the mean temperature Θ through

$$\rho = \frac{\rho_0 \Theta_0}{\Theta} \quad (3)$$

This approximation can be introduced because in the flows examined the density changes are mainly caused by temperature variations within the fluid, which is assumed to behave as an ideal gas.

The temperature Θ, is obtained from the energy equation:

Nomenclature

c_1, c_2, $c_{\epsilon 1}$, $c_{\epsilon 2}$, c_1', c_2', c_θ, c_μ, c_k, c_ϵ = turbulence modeling constants
D = duct hydraulic diameter
E = low-Re term in ϵ equation
f_2, f_μ, f_ϵ, f_ω, f_i, f_j = damping functions
H_{ij} = low-Re term in stress equations
H_z = streamwise distance from center of rotation
k = turbulent kinetic energy
l_e = equilibrium length scale
l = local turbulent length scale $\equiv k^{1.5}/\epsilon$
Nu = Nusselt number $\equiv q_w D/(\lambda(\Theta_w - \Theta_b))$
P = pressure
P_{ij} = generation rate of turbulent stress $= \overline{u_i u_j}$
P_k = generation rate of turbulence energy
Ro = inverse Rossby number $\equiv \Omega D/W_b$
Ra = Rayleigh number $= \Omega^2 H_z D^3(\Theta_w - \Theta_b)\sigma/(\nu^2\Theta_b)$
Re = Reynolds number $\equiv W_b D/\nu$
R_τ = turbulence Reynolds number $\equiv k^2/\nu\epsilon$
U_c = Cartesian mean velocity component
U = cross-duct velocity component
u_i = Cartesian fluctuating velocity component
u = cross-duct fluctuating velocity component
V = mean velocity component parallel to rotation axis
v = fluctuating velocity component parallel to the rotation axis
W = streamwise mean velocity component
w = streamwise fluctuating velocity component
W_b = bulk velocity
x = cross-duct direction
Y = near-wall distance
y = direction parallel to axis of rotation
y^+ = dimensionless wall distance $\equiv Y\sqrt{\tau_w/\rho}/\nu$
y^* = dimensionless wall distance $\equiv Y\sqrt{k}/\nu$
z = streamwise direction
γ = thermal diffusivity
δ_{ij} = Kronecker delta
ϵ = dissipation rate of turbulence energy k
ϵ_{ij} = dissipation rate of $\overline{u_i u_j}$
ϵ_{ipj} = third-order alternating tensor
Θ = mean temperature
θ = fluctuating temperature
Θ_b = bulk temperature
Θ_w = wall temperature
λ = thermal conductivity
μ = dynamic viscosity
μ_t = turbulent dynamic viscosity
ν = kinematic viscosity
ν_t = turbulent kinematic viscosity
ρ = density
ρ' = fluctuating density
σ = Prandtl number
σ_ϕ = turbulent Prandtl number
τ_w = local wall shear stress
ϕ_{ij} = redistribution term
Ω = angular velocity

$$\frac{\partial}{\partial x_j}(\rho U_j \Theta) = \frac{\partial}{\partial x_j}\left(\gamma \frac{\partial \Theta}{\partial x_j} - \rho \overline{u_j \theta}\right) \tag{4}$$

where γ is the dynamic thermal diffusivity μ/σ and $\overline{u_j\theta}$ is the kinematic turbulent heat flux.

2.2 Turbulence Models. As mentioned in the introduction, the turbulent stresses have been modeled in two different ways: through an eddy viscosity model (EVM) and through an algebraic second-moment (ASM) closure. The latter approach allows us to investigate the influence exerted by nonisotropic turbulence on mean flow and heat transfer. Both models extend across the viscosity-dominated near-wall sublayer. In both sets of turbulence equations, the effects of near-wall damping are modeled through the introduction of terms that depend on the local turbulence Reynolds numbers, $R_t \equiv k^2/\nu\epsilon$, and thus do not rely on the near-wall distance.

Low-Re $k-\epsilon$ Model. This is the version proposed by Launder and Sharma (1974). The turbulent stresses are obtained through the effective viscosity approximation

$$\overline{u_iu_j} = \frac{2}{3}k\delta_{ij} - \nu_t\left(\frac{\partial U_i}{\partial x_j} + \frac{\partial U_j}{\partial x_i}\right) \tag{5}$$

where $\nu_t = c_\mu f_\mu k^2/\epsilon$ and

$$f_\mu = \exp\left(\frac{-3.4}{(1 + 0.02R_t)^2}\right) \tag{6}$$

The effective viscosity approximation is also used for the turbulent heat fluxes:

$$\overline{u_i\theta} = -\frac{\nu_t}{\sigma_\theta}\frac{\partial \Theta}{\partial x_j} \tag{7}$$

The turbulent kinetic energy k and its dissipation rate ϵ are obtained through the solution of separate transport equations of the form

$$\frac{\partial}{\partial x_j}(\rho U_j k) = d_k + \rho P_k - \rho\epsilon \tag{8}$$

and

$$\frac{\partial}{\partial x_j}(\rho U_j \tilde{\epsilon}) = d_{\tilde{\epsilon}} + c_{\epsilon 1}\frac{\tilde{\epsilon}}{k}P_k - c_{\epsilon 2}f_2\rho\frac{\tilde{\epsilon}^2}{k} + \rho E \tag{9}$$

where

$$\tilde{\epsilon} \equiv \epsilon - 2\nu\left(\frac{\partial\sqrt{k}}{\partial x_j}\right)^2 \tag{10}$$

$$E = 2\nu\nu_t\left(\frac{\partial U_i}{\partial x_j \partial x_k}\right)^2 \tag{11}$$

$$f_2 = [1 - 0.3\exp(-R_t^2)] \tag{12}$$

The production rate term P_k contains mean shear and buoyant terms:

$$P_k = \overline{u_iu_j}\frac{\partial U_i}{\partial x_j} - \frac{\overline{\rho' u_i}}{\rho}(\Omega_j X_j \Omega_i - \Omega_j \Omega_j X_i) \tag{13}$$

while the averaged product of the velocity-density fluctuations in Eq. (13) is obtained from the turbulent heat fluxes according to:

$$\frac{\overline{\rho' u_i}}{\rho} = -\frac{\overline{u_i\theta}}{\Theta} \tag{14}$$

a relationship that applies for a perfect gas at low Mach numbers. We note there are no effects of Coriolis forces in the energy production term: While there are contributions from this source in the two normal stress directions orthogonal to the rotation axis, they are of opposite sign and thus cancel out in the turbulence energy equation. In the case of *two-dimensional* flow in a rotating channel—where secondary motions are absent—this neglect of Coriolis forces means that effects of rotation cannot be captured using an eddy viscosity model. In a rotating square duct, secondary motion (due to Coriolis terms in the *mean* momentum equation) is sufficiently strong that the direct contribution in the turbulence equations is arguably of small importance. That is the rationale for employing eddy viscosity models in such flows.

Finally, the diffusion rate of k and ϵ is obtained from the simple gradient-diffusion approximation

$$d_\phi = \frac{\partial}{\partial x_j}\left(\left[\mu + \frac{\mu_t}{\sigma_\phi}\right]\frac{\partial \phi}{\partial x_j}\right); \quad \phi = k, \epsilon \tag{15}$$

The empirical constants appearing in the equations above take the following standard values:

c_μ	$c_{\epsilon 1}$	$c_{\epsilon 2}$	σ_ϵ	σ_k	σ_θ
0.09	1.44	1.92	1.22	1.0	0.9

In some low-Re $k-\epsilon$ computations, the Yap (1987) correction term [YC] was also added to the ϵ transport Eq. (9). This term acts to reduce the departure of the near-wall turbulent length scale from its equilibrium level by raising the dissipation rate

$$YC \equiv \max\left(0.83\left(\frac{l}{l_\epsilon} - 1\right)\left(\frac{l}{l_\epsilon}\right)^2\frac{\epsilon^2}{k}, 0.00\right) \tag{16}$$

Here l is the local length scale $k^{3/2}/\epsilon$ and l_ϵ is the equilibrium level assumed to be $2.55Y$.

Low-Re ASM Closure. This is a near-wall extension of the high-Reynolds-number ASM scheme, widely used for the computation of fully turbulent flows, that has been recently proposed by Iacovides and Launder (1992) and applied to the computation of flow and heat transfer through a stationary 180 deg pipe bend. The turbulent stresses are obtained from:

$$\frac{\overline{u_iu_j}}{k}(P_k - \epsilon) = P_{ij} - \epsilon_{ij} + \phi_{ij} + f_w\phi_{ij}^w - \left[H_{ij} - \frac{1}{3}H_{kk}\delta_{ij}\right] + 0.06k\left(\frac{\partial U_i}{\partial x_j} + \frac{\partial U_j}{\partial x_i}\right)\exp\left(-\frac{R_t}{8}\right) \tag{17}$$

The production rate P_{ij} includes contributions from the Coriolis and the centrifugal force:

$$\begin{aligned} P_{ij} = &-\overline{u_iu_k}\frac{\partial U_j}{\partial x_k} - \overline{u_ju_k}\frac{\partial U_i}{\partial x_k} - 2\Omega_p(\epsilon_{ipq}\overline{u_qu_j} + \epsilon_{jpq}\overline{u_qu_i}) \\ &- \frac{\overline{u_i\rho'}}{\rho}(\Omega_k X_k \Omega_j - \Omega_j \Omega_k X_j) \\ &- \frac{\overline{u_j\rho'}}{\rho}(\Omega_k X_k \Omega_i - \Omega_k \Omega_k X_i) \end{aligned} \tag{18}$$

In contrast to the $k-\epsilon$ model, it is noted that Coriolis contribution to stress generation makes itself felt through the second group of terms in Eq. (18). Note that the term ϵ_{ipq} is the third-rank alternating tensor.

The dissipation rate ϵ_{ij} is obtained from

$$\epsilon_{ij} = \frac{2}{3}\left(1 - \exp\left(-\frac{R_t}{12}\right)\right)\epsilon\delta_{ij} + \overline{u_iu_j}\exp\left(-\frac{R_t}{12}\right)\frac{\epsilon}{k} \tag{19}$$

The redistribution term ϕ_{ij} adopts the form

$$\phi_{ij} = -c_1 \frac{\epsilon}{k} (\overline{u_i u_j} - \tfrac{2}{3}k\delta_{ij}) - c_2(P_{ij} - \tfrac{2}{3}P_k\delta_{ij}) \qquad (20)$$

The "wall-echo" part of the pressure strain correlation ϕ_{ij}^w is approximated by the proposal of Gibson and Launder (1978)

$$\phi_{ij}^w = f_w\left(c_1' \frac{\epsilon}{k} (\overline{u_q u_m} n_q n_m \delta_{ij} - \tfrac{3}{2}\overline{u_i u_q} n_q n_j - \tfrac{2}{3}\overline{u_j u_q} n_i n_q) \right.$$

$$\left. + c_2'(\phi'_{qm} n_q n_m \delta_{ij} - \tfrac{3}{2}\phi'_{qi} n_q n_j - \tfrac{3}{2}\phi'_{qj} n_i n_q) \right) f\left(\frac{l}{Y}\right) \qquad (21)$$

where

$$\phi'_{ij} = -c_2(P_{ij} - \tfrac{2}{3}P_k\delta_{ij}) \qquad (22)$$

n_q is the unit vector normal to the wall in question, Y the distance to the wall, and l is the local turbulent length scale, defined earlier. Although this form was originally devised for a single plane surface, as in all our earlier work on flows through rectangular ducts, we have simply superimposed the effects due to the two pairs of opposite walls. For the walls in the $y-z$ and $x-z$ planes, respectively, the wall influence functions just become:

$$f(l/n_x Y) = \frac{l}{x} + \frac{l}{D - x}$$

$$f(l/n_y Y) = \frac{l}{D/2 - y} + \frac{l}{D/2 + y} \qquad (23)$$

Within the viscous sublayer this wall reflection term is damped by multiplying it by the function f_w

$$f_w = \left[1 - \exp\left(-\frac{R_t}{20}\right)\right]\left[1 + \exp\left(-\frac{R_t}{100}\right)\right] \qquad (24)$$

The task of the pressure-strain process within the viscous sublayer is then performed by $(H_{ij} - \tfrac{1}{3}H_{kk}\delta_{ij})$, where

$$H_{ij} = (15.6 + 2.4R_t)$$

$$\left(\overline{u_i u_l}\frac{\partial\sqrt{k}}{\partial x_j}\frac{\partial\sqrt{k}}{\partial x_l} + \overline{u_l u_j}\frac{\partial\sqrt{k}}{\partial x_i}\frac{\partial\sqrt{k}}{\partial x_l}\right)\exp\left(-\frac{R_t}{20}\right) \qquad (25)$$

The contribution of this term is more extensively discussed in the appendix. In essence, adoption of this formation represented a fairly simple way of achieving approximately the correct distribution of the Reynolds stresses across the viscosity-affected sublayer.

The turbulent heat fluxes are now obtained from the generalized gradient diffusion hypothesis (GGDH)

$$\overline{u_i\theta} = -c_\theta \frac{k}{\epsilon}\overline{u_i u_j}\frac{\partial\Theta}{\partial x_j} \qquad (26)$$

The k and ϵ transport equations are essentially the same as those presented in Eqs. (8) and (9) for the $k-\epsilon$ model. For consistency with Eq. (23), however, the diffusion of k and ϵ is obtained from the GGDH:

$$d_\phi = \frac{\partial}{\partial x_j}\left(\left[\nu\delta_{ij} + c_\phi\frac{k}{\epsilon}\overline{u_i u_j}\right]\frac{\partial\phi}{\partial x_i}\right) \quad \phi \equiv k, \tilde{\epsilon} \qquad (27)$$

A further difference arises from the E term, defined in Eq. (11), that appears in the ϵ transport equation. The damping function f_μ appearing in ν_t is now obtained from:

$$f_\mu = \exp\left(-\frac{2.9}{(1 + 0.003R_t)(1 + 0.004R_t)}\right) \qquad (28)$$

The additional constants that appear in the ASM equations take the following standard values:

c_1	c_2	c_k	c_ϵ	c_θ	c_1'	c_2'
1.8	0.6	0.22	0.15	0.26	0.5	0.3

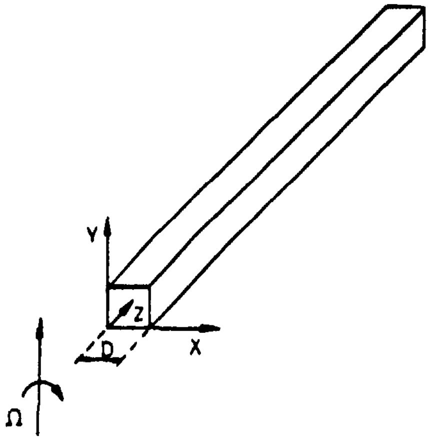

Fig. 1 Flow geometry

3 Numerical Aspects

The flow equations are solved for a Cartesian coordinate system rotating in orthogonal mode, as shown in Fig. 1. The solution domain covers a rectangular half-section of the square duct on one side of the duct symmetry plane. The existence of a predominant flow direction permits the use of a three-dimensional parabolic solution procedure. The parabolic solver facilitates the use of fine meshes, but would be unsuitable for rotational speeds higher than the ones examined in this study, because of the likelihood of flow separation should rotational buoyancy effects become appreciably stronger. The solver is of finite-volume type with staggered locations for the velocity and turbulent stress components relative to the pressure. For the discretization of the cross-stream convection of mean-field variables, the nondiffusive QUICK scheme is employed. The code has been adapted from a semi-elliptic solver originally applied to flow in curved ducts by Choi et al. (1989). A fuller description of the solver and program details is provided by Bo (1992).

The cross-stream mesh consisted of 45 by 87 nodes. Earlier work on stationary and rotating duct flows (Iacovides and Launder, 1987; Launder and Loizou, 1989) has shown that such a cross-stream mesh is sufficiently fine to reduce numerical errors to insignificant levels. Within each near wall region, 25 grid nodes were used to resolve the transition from the viscosity dominated sublayer to fully turbulent flow. The grid distribution was determined with reference to fully developed flow in a stationary pipe at the same Reynolds number. The y^+ value of the near-wall node was less than 1 and the first 25 near-wall nodes covered a region extending up to y^+ values of 40. In the streamwise direction, 10 planes per hydraulic diameter were employed.

At the entry to the solution domain, fully developed stationary duct flow conditions were imposed. So far as could be judged, these were the hydrodynamic entry conditions that most closely resembled those of the experimental study of Wagner et al. (1991). For the same reason a uniform gas temperature was assumed at entry. Constant wall temperature thermal boundary conditions were employed.

4 Presentation and Discussion of Computations

Computations have been made for two rotating flow conditions for which Wagner et al. (1991) have provided side-averaged Nusselt number measurements. These data were chosen for validation purposes because they covered the range of rotation and rotational buoyancy numbers that were relevant to blade cooling applications and also because in this experimental study, entry and thermal boundary conditions were well defined. The selected rotation numbers ($Ro \equiv \Omega D/W_b$) of 0.12 and 0.24

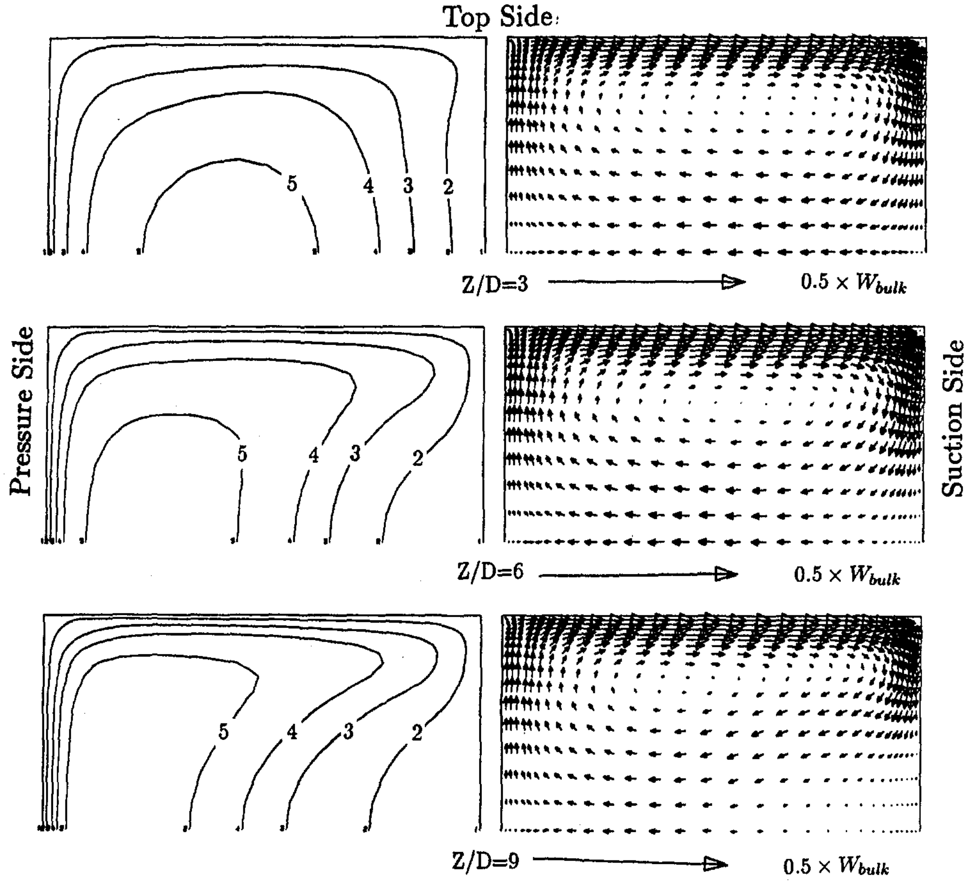

Fig. 2 Predicted mean flow development at Re = 25,000, *Ro* = 0.12, and Ra = 0.4 × 10^8, using the low-Re ASM

correspond to entry Rayleigh numbers of 0.4 × 10^7 and 1.6 × 10^8, respectively. The Rayleigh number defined as Ra ≡ $\rho^2\Omega^2 H_z D^3(\Theta_w - \Theta_b)\sigma/(\mu^2\Theta_b)$ characterizes the relative strength of rotational buoyancy. These combinations of parameters are broadly in line with those found in gas turbine practice. The flow Reynolds number is 25,000 for both cases. To distinguish, in the computations, the contribution made by Coriolis forces (as opposed to Coriolis and buoyant forces in combination), computations were also made with the fluid density held strictly constant, a practice that eliminated buoyant effects. In making heat transfer comparisons, in order to minimize the effects of any inconsistencies between the numerical and experimental entry conditions and also to highlight the effects of rotation on heat transfer, the values of the side-averaged Nusselt number were normalized by those of the corresponding stationary duct at the same stage of thermal development.

No experimental data of the velocity field are yet available but consideration of the computed flow field development helps to provide a clearer understanding of the effects of rotation. This development, over the first 9 hydraulic diameters for *Ro* = 0.12, is shown through the computed streamwise velocity contour plots and secondary velocity vector plots of Fig. 2. The computations are based on the low-Re ASM model. The plots reveal that at this rotational speed the Coriolis force generates the conventional two-vortex structure (one in each symmetric half). Due to the action of the substantial secondary motion, progress toward the fully developed state is more rapid than in developing flow through a stationary straight duct. The high-momentum fluid, originally in the central core, is convected to the pressure (trailing) side of the duct, causing a significant reduction in the thickness of the boundary layers along the pressure and top surfaces. Low-momentum fluid accumulates along the suction side, causing the boundary layer thickness there to increase. The corresponding constant density computation (not presented here) produced a mean flow field, which differed only in minor respects from that shown in Fig. 2. At these values of *Ro* and Ra rotational buoyancy does not appear to influence the flow development significantly.

Attention is now turned to the mean flow development at the higher rotational speed (*Ro* = 0.24). The corresponding low-Re ASM computations for the first 15 hydraulic diameters are presented in Fig. 3(*a*). While the Coriolis effects are now twice as strong as in the case presented in Fig. 2, the rotational buoyancy effects are four times greater (Ra = 1.6 × 10^8). The vector plots of Fig. 3 indicate that initially a two-vortex secondary motion is formed that is substantially stronger than that encountered at *Ro* = 0.12. After about six diameters of flow development an extra pair of counterrotating vortices is formed along the suction surface of the duct though, by the nine-diameter location, the two-vortex structure is again re-established. This transient entry phenomenon is only predicted by the ASM model. As seen in Fig. 3(*b*), predictions with the effective viscosity model for this case, obtained during our earlier (Bo et al., 1991) study, indicate a two-vortex structure throughout the entry region. Beyond the nine-diameter location the changes to the flow field are relatively small with the evolution of the streamwise velocity being similar to that observed at the lower rotational speed. Because of the stronger secondary flow the boundary layers along the pressure and the top sides are even thinner than at the lower rotational speed. The higher rotational speed also leads to a greater accumulation of low-momentum fluid on the suction side of the duct.

The flow field plots of the corresponding constant-density computations appear in Fig. 4. Comparison with the plots of Fig. 3 reveals that, over the first six diameters of flow development, the absence of the buoyancy force weakens the secondary

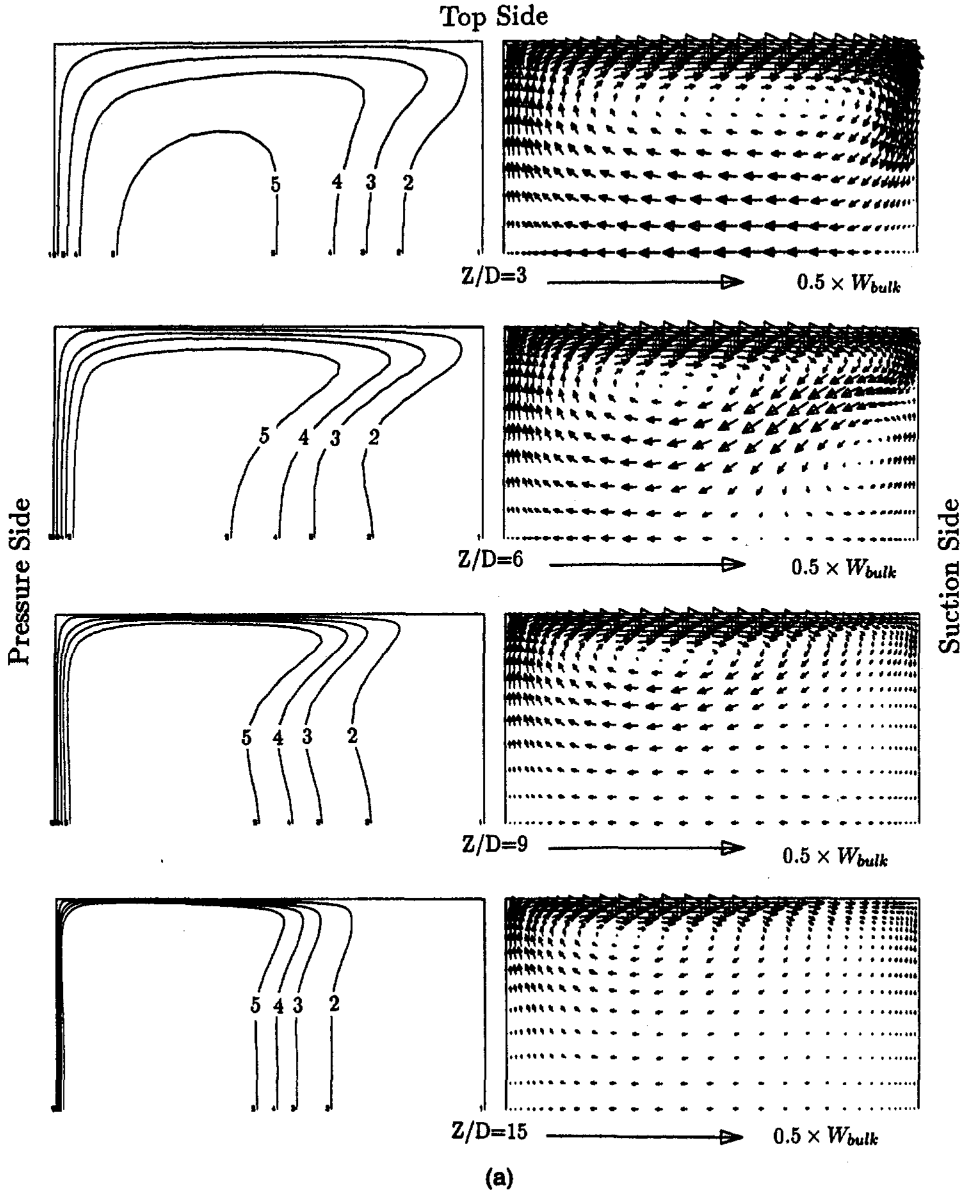

Fig. 3 Predicted mean flow development at Re = 25,000, *Ro* = 0.24, and Ra = 1.6 × 10^8: (*a*) low-Re ASM model

motion somewhat but does not alter its overall character. Farther downstream, the two-vortex pattern bifurcates to a four-vortex mode with the additional pair of vortices being formed near the symmetry plane close to the pressure surface. These extra vortices (which have been reported in our earlier study of fully developed flows (Iacovides and Launder, 1987)) grow in strength and progressively distort the streamwise flow pattern. While the present computations extend only to 18 diameters, our earlier study, based on an eddy viscosity model, suggest that the secondary vortex near the pressure surface continues to develop over the first 30 diameters of flow development. Thus, attaining the fully developed state requires a greater development length than when buoyancy forces are included. Evidently, therefore, at this higher rotation rate buoyant forces are appreciably affecting the mean-flow field.

The examination of the corresponding thermal behavior begins with the computed development of the local Nusselt number shown in Fig. 5. In this and all the subsequent plots, the predicted and measured Nusselt numbers at each plane are normalized with the corresponding average Nusselt number Nu_0 for a stationary duct at the same length of thermal development. This normalization practice highlights the effects of rotation on heat transfer and also minimizes the effects of possible discrepancies between experimental and computational entry conditions. As would be anticipated from the computed evolution of the mean flow, the Nusselt number levels along the pressure side increase with downstream distance while those along the suction side are reduced. At a given location these effects appear to be stronger at higher rotational speeds. For $Ro = 0.24$ important differences develop between the Nusselt number distributions returned by the constant- and variable-density flow predictions. Rotational buoyancy causes a marked enhancement in the heat transfer coefficients along the pressure and top sides. Some differences between the buoyant and nonbuoyant heat transfer levels are also evident along the suction side for $Ro =$ 0.24, but these are mainly confined to the entry region where the transient suction-side vortex appears in the buoyant flow computations.

At present the side-averaged Nusselt number measurements of Wagner et al. (1991) provide the only data against which the effectiveness of the turbulence models employed in this study can be assessed. We begin by reproducing the $k-\epsilon$/one-

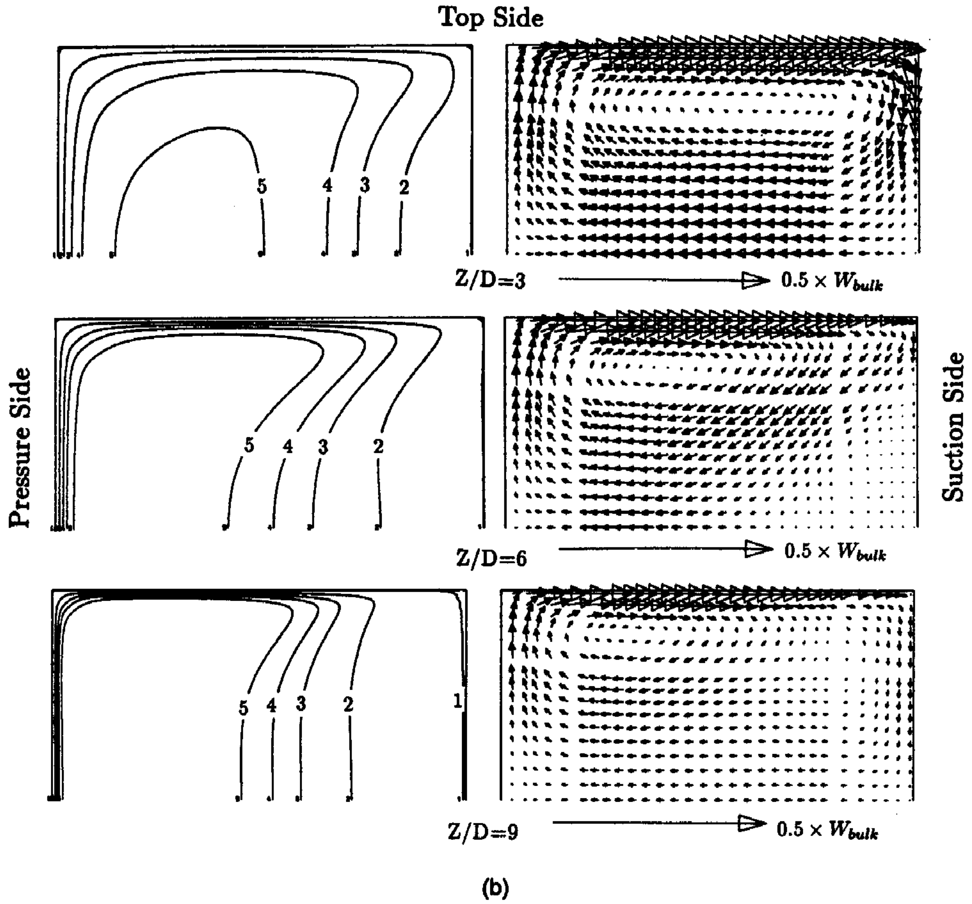

Fig. 3 (Continued) (b) k–ϵ/one-equation model

equation comparisons from our earlier investigation (Bo et al., 1991) in Fig. 6, together with a $k-\epsilon$/wall-function prediction of Prakash and Zerkle (1992). These comparisons confirm that, at the lower of the two rotational speeds examined, rotational buoyancy has only a minor influence on heat transfer. Furthermore, the augmentation of heat transfer coefficient along the pressure side of the duct and the corresponding reduction along the suction side are faithfully reproduced by the $k-\epsilon$/one-equation model for $Ro = 0.12$. At the higher rotational speed the previously noted influence of rotational buoyancy is clearly evident. The buoyant flow computations reproduce the strong augmentation on the pressure side Nusselt number (150 percent higher than the stationary levels) with an encouraging degree of accuracy. The severe reduction in the measured mean Nusselt number along the suction side, which falls to as low as 40 percent of the stationary values after eight diameters of development, is not fully captured by the simple $k-\epsilon$/one-equation turbulence model, which predicts a minimum of about 60 percent of that found for a nonrotating duct. The $k-\epsilon$/wall-function computations of the side-averaged Nusselt number also fail to predict the strong reduction of the heat transfer rate along the suction side. Moreover, this simpler near-wall treatment returns a more oscillatory development of Nusselt number along both walls. It was the hope of achieving a more faithful representation of the Nusselt-number distribution along the suction face that has motivated the present exploration with more refined turbulence models.

The thermal behaviour that results from replacing the near-wall one-equation model by the Launder–Sharma (1974) low-Re $k-\epsilon$ EVM, is summarized in Fig. 7. The constant-density computations return significantly lower heat transfer levels than those present in the measurements. The constant-density computations of the low-Re $k-\epsilon$ model thus appear to predict substantially lower near-wall turbulence levels than the corresponding buoyant flow predictions. The fact that the inclusion of the Yap correction term (Fig. 7(*b*)) does not alter the Nusselt number predictions of the low-Re $k-\epsilon$, in the absence of rotational buoyancy, confirms that for this case the above-mentioned model predicts near-wall turbulent length scales that are not higher than the equilibrium length scales. When buoyancy effects are taken into account, far from improving the prediction of Nu along the suction side, introduction of the low-Re $k-\epsilon$ model causes a dramatic and surprising deterioration in the quality of these predictions. Indeed, the predicted heat transfer coefficients along the suction side are now higher than those of the pressure side, a trend that is clearly erroneous. However, the computed mean flow field arising from this turbulence model (not reproduced here) does not show any similarly striking differences from the corresponding $k-\epsilon$/1-equation computations. It may thus be supposed that the poor-quality heat transfer predictions are caused by excessive near-wall levels of turbulence energy as will be discussed later. Figure 7(*b*) shows that inclusion of the Yap correction, Eq. (16), which limits the growth of the near-wall turbulent length scale, leads to a marked improvement in the predicted heat transfer levels of the suction side. Nevertheless, even with this term included, suction-side heat transfer coefficients are higher than those in the corresponding stationary duct flow. In heated flows through rotating ducts it therefore appears to be rather difficult to produce a reasonable representation of near-wall turbulent transport within the framework of the effective viscosity approximation. A similar conclusion was also reached in our recent investigation of flow and heat transfer through curved pipes (Iacovides and Launder, 1992).

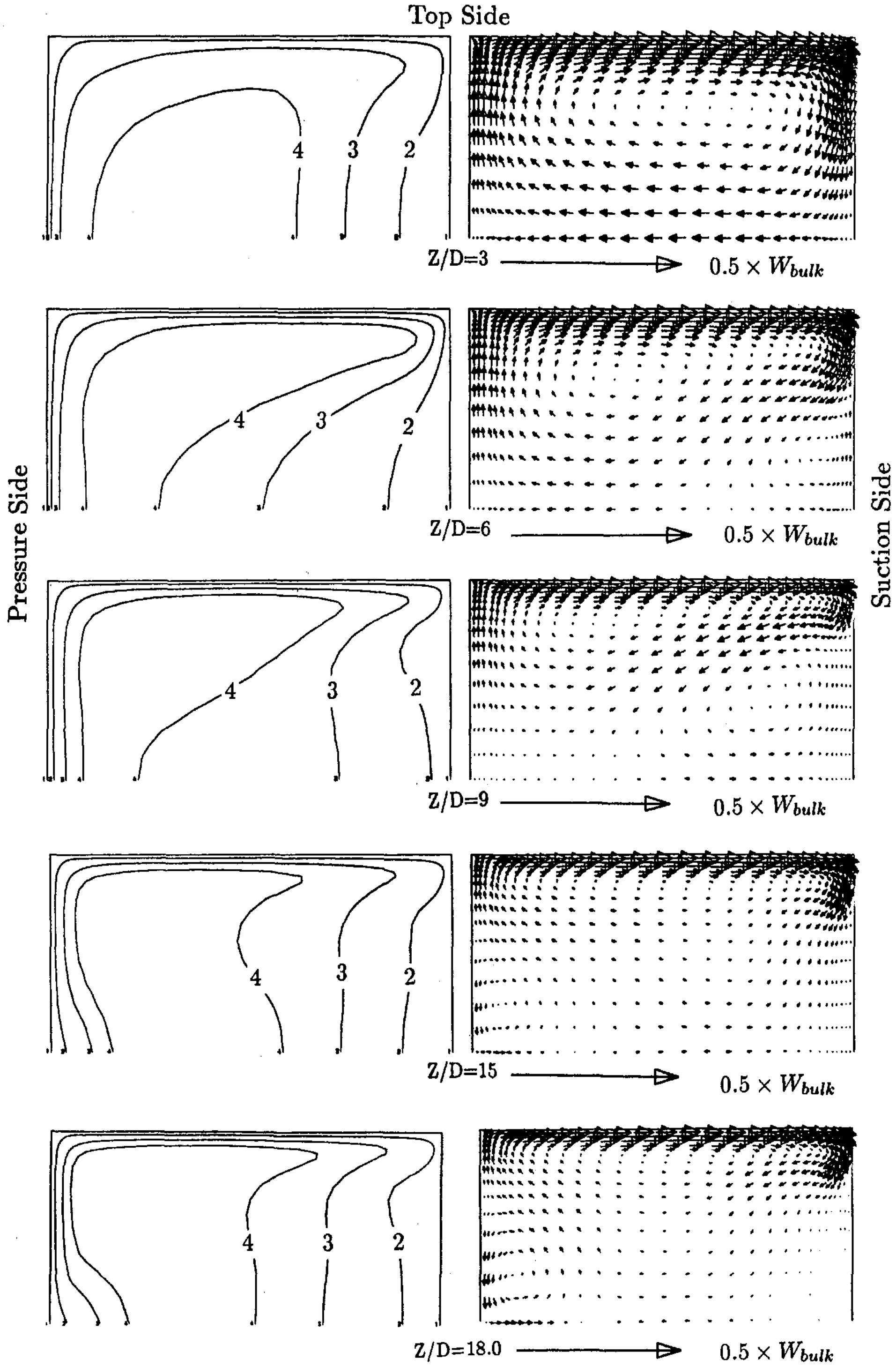

Fig. 4 Predicted mean flow development for nonbuoyant case at Re = 25,000 and *Ro* = 0.24 using the low-Re ASM

The final set of comparisons in Fig. 8 reveals that replacement of the low-Re $k-\epsilon$ model by the low-Re second-moment closure produces very marked improvements in the prediction of heat transfer in rotating ducts. At $Ro = 0.24$ the high heat transfer levels returned by the ASM model along the pressure side are in close agreement with the measurements. Moreover, the maximum reduction in the suction-side heat transfer coefficients after eight diameters of flow development is also now reproduced with reasonable accuracy. After the first four diameters of flow development, the predicted Nusselt number along the suction side begins to rise, reaching a maximum level at about 6.5 diameters, and then rapidly falling to levels similar to those of the measurements. This curious entry flow behavior is related to the formation, and subsequent disappearance over the same region, of the two counterrotating vortices along the suction side of the duct, which was noted in the mean flow predictions (Fig. 4). The available measurements have not been taken close enough together either to confirm or refute this prediction. (In any event, the initial entry flow development is likely to be highly sensitive to the entry conditions.) In support of the pre-

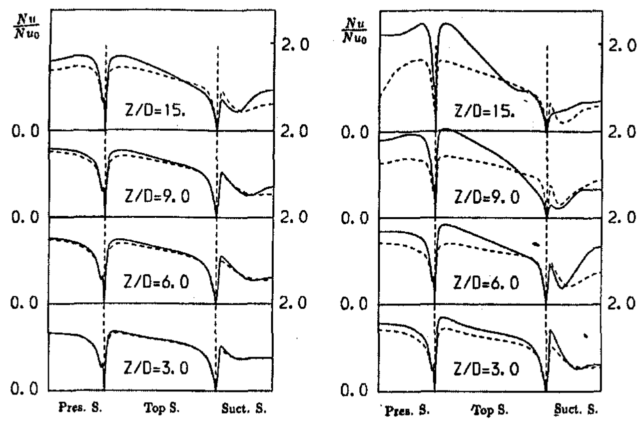

(a) $Ro = 0.12$ (b) $Ro = 0.24$

Fig. 5 Predicted local Nusselt number development using the low-Re ASM at Re = 25,000: —— buoyant flow prediction; - - - const density flow prediction

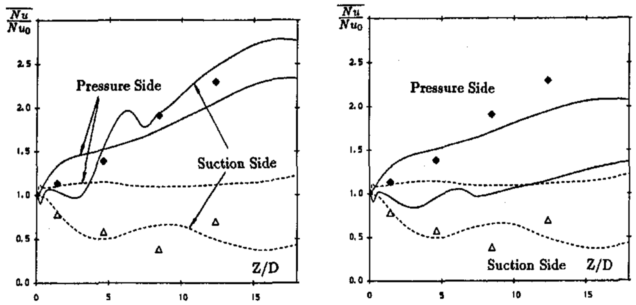

(a) Low-Re $k-\epsilon$ model (b) Low-Re $k-\epsilon$ model with Yap Term

Fig. 7 Comparisons of side-averaged Nusselt number development at Re = 25,000, Ro = 0.24, and Ra = 1.6×10^8, using the low-Re $k-\epsilon$ model: —— buoyant flow; - - - constant-density flow; ◇ △ experimental data (Wagner et al., 1991)

dictions, however, we note that the data indicate a rise in Nu beyond ten diameters. So far as the computations are concerned, the rise can be firmly attributed to the buoyant terms for it is seen that the uniform-density predictions indicated a marked decrease in Nu over the same range.

At the lower rotational speed, Fig. 8(*b*), the low-Re ASM computations display broadly satisfactory agreement with the relevant measurements though the Nusselt number levels along the pressure side are somewhat further from the measurements than those obtained with the $k-\epsilon/1$-equation model. The performance of the low-Re ASM model is, however, the more consistent over the range of operating conditions examined on this study. Near-wall turbulence models that rely on a prescribed turbulent length scale are unable to predict the strong reduction in suction side heat transfer rates associated with the strong secondary motion at high rotation rates. Moreover, eddy viscosity models are unreliable for rotating duct flows. It thus appears that in such situations, near-wall turbulent transport, so important for the correct prediction of the wall heat transfer coefficient, can only be realistically represented through the use of low-Reynolds-number second-moment closures. These conclusions are in accord with those of other recent investigations of three-dimensional duct flows both within the authors' group (Iacovides and Launder, 1992; Abou-Haidar et al., 1991) and elsewhere (Lai et al., 1991).

The differences in the predictive behavior of the turbulence models can be more clearly brought out by an examination of the predicted development of the turbulence field. Figure 9 presents profiles of the turbulent kinetic energy along the duct symmetry plane for $Ro = 0.24$. One feature common to the predictions of the three models is that, as one proceeds downstream, the buoyant flow computations begin to return higher k levels than the corresponding constant density results. This behavior is consistent with the generally lower heat transfer coefficients reported above for the uniform-density case. The $k-\epsilon$/one-equation computations of Fig. 9(*a*) suggest that the turbulent kinetic energy distribution is fairly uniform across the duct with the overall turbulence levels gradually rising as the flow progresses through the rotating duct. The low-Re $k-\epsilon$ computations in Fig. 9(*b*), show a largely similar behavior. Careful scrutiny does reveal, however, that here the turbulence levels are higher within the suction side boundary layer. This is more clearly demonstrated in Fig. 10, in which near-wall profiles of turbulence energy, predicted with the $k-\epsilon$/one-equation and the low-Re $k-\epsilon$ model are presented at selected locations. The behavior is consistent with the known response of the $k-\epsilon$ model in conditions giving rise to an appreciably lower shear stress at the wall than away from the surface. For example, Rodi and Scheuerer (1983) and others have reported that, for a turbulent boundary layer developing in an adverse pressure gradient, excessive turbulent length scales are generated leading to appreciably too-high skin-friction coefficients. In the present case, due to its lower density, the warm near-wall fluid also experiences a positive streamwise (radial) pressure gradient (additional to that associated with the duct rotation) and this produces an equivalent outcome. When the density is held constant over the cross section the effect is absent. The turbulence energy is then much lower, and there is no anomalous increase in the suction-side Nusselt number (Fig. 7).

The low-Re ASM closure returns a strikingly different turbulence field in which the distribution of turbulence energy across the duct is highly nonuniform. The location of minimum turbulent energy gradually moves from the duct center toward the

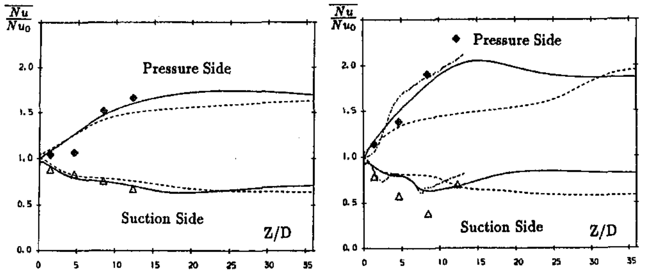

(a) $Ro = 0.12$ (b) $Ro = 0.24$

Fig. 6 Comparisons of the side-averaged Nusselt number development at Re = 25,000, using the $k-\epsilon$/one-equation model: —— buoyant flow $k-\epsilon$/one-equation; - - - constant-density flow $k-\epsilon$/one-equation; – – – buoyant flow $k-\epsilon$/wall-function (Prakash and Zerkle, 1992); ◇ △ experimental data (Wagner et al., 1991)

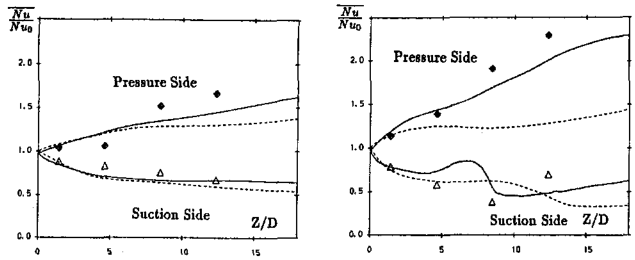

(a) $Ro = 0.12$ (b) $Ro = 0.24$

Fig. 8 Comparisons of side-averaged Nusselt number development at Re = 25,000 using the low-Re ASM model: —— buoyant flow prediction; - - - constant-density flow prediction; ◇ △ experimental data (Wagner et al., 1991)

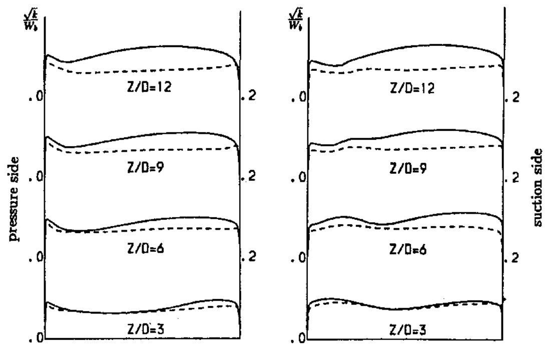

(a) $k-\epsilon$/1-Eqn (b) Low-Re $k-\epsilon$

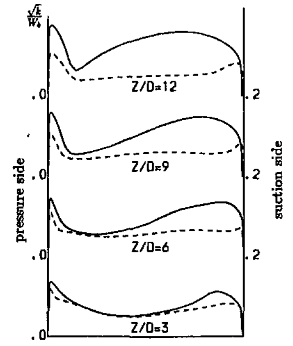

(c) Low-Re ASM

Fig. 9 Turbulent intensity profiles along the duct symmetry plane at Re = 25,000 and Ro = 0.24; —— buoyant flow prediction; --- constant-density prediction

duct pressure face. Within the immediate vicinity of the pressure surface, a steep rise in the turbulence levels is observed, which occurs from the early stages of flow development. A progressive rise in the suction side turbulence levels is also noted. Beyond the first nine diameters of flow development, by which point the suction side entry vortices have disappeared (Fig. 4), a thin layer of almost zero turbulence is formed along the suction-side wall.

Evidently, there are important differences between the turbulence field obtained with the low-Re ASM model and those returned by the two EVM models. The ability of second moment closures to provide a more accurate representation of the effects of rotation on turbulence is evidently the cause of these differences. The strongly inhomogeneous turbulence field of the ASM computations is responsible for the substantial (and largely correct) variations in the heat transfer coefficients given by the ASM computations.

5 Conclusions

The article has reported the application of several turbulence-model variants to the prediction of strongly heated, developing flow through a square duct rotating in orthogonal mode. Computations have considered outward flows for two levels of rotation and buoyancy representative of blade-cooling situations. The computations have shown that rotational buoyancy can have a significant influence on the hydrodynamic and thermal development of rotating duct flows. The standard $k-\epsilon$ eddy viscosity model, matched to a one-equation EVM across the wall sublayers, captures the combined effects of rotation and buoyancy fairly well but underestimates the suppression of heat transport on the suction surface of the rotating duct. The low-Re $k-\epsilon$ model returns excessively high near-wall turbulence levels along the suction side, which lead to the prediction of heat transfer coefficients on that surface that are not even in qualitative agreement with the measurements. The low-Re ASM model provides a more realistic response to the effects of rotation on turbulence, which consequently alter the predicted hydrodynamic and thermal development bringing the latter to better accord with the available data.

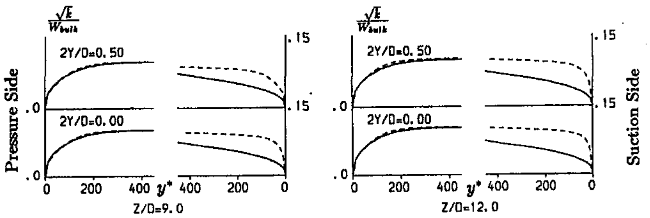

Fig. 10 Predicted near-wall distribution of turbulence intensity at Ro = 0.24 and Ra = 1.6 × 10^8: —— $k-\epsilon$/one-equation; --- low-Re $k-\epsilon$

The provision of consistently realistic predictions of the thermal development through rotating duct flows thus requires a careful accounting of near-wall turbulence transport. Because of the presence of rotation-induced body forces, it appears necessary to employ low-Re second-moment closures to capture the flow behavior satisfactorily.

6 Acknowledgments

The research has been jointly supported by Rolls-Royce and RAE Pystock under Research Brochure B1D2-125D and is published by permission. Mr. Michael Newman has prepared the manuscript for publication with appreciated care.

Authors' names are listed alphabetically.

References

Abou-Haidar, N. I., Iacovides, H., and Launder, B. E., 1991, "Computational Modelling of Turbulent Flow in S-Bends," AGARD Conf. Proc. 510, *77th Symposium of Propl and Energetics Panel on CFD Techniques for Propulsion Applications,* San Antonio, TX, May.

Bo, T., Iacovides, H., and Launder, B. E., 1991, "The Prediction of Convective Heat Transfer in Rotating Square Ducts," presented at the 8th Symposium of Turbulent Shear Flows, Munich, Germany.

Bo, T., 1992, "The Computation of Flow and Heat Transfer in Rotating Ducts and U-Bends," PhD Thesis, Faculty of Technology, University of Manchester, United Kingdom.

Choi, Y. D., Iacovides, H., and Launder, B. E., 1989, "Numerical Computation of Turbulent Flow in a Square-Sectioned 180° Bend," ASME *Journal of Fluids Engineering,* Vol. 111, pp. 59–68.

Cotton, M. A., and Jackson, J. D., 1987, "Calculation of Turbulent Mixed Convection in a Vertical Tube Using a Low-Reynolds-Number $k-\epsilon$ Turbulence Model," presented at the 6th Symposium on Turbulent Shear Flows, Toulouse, France.

Gibson, M. M., and Launder, B. E., 1978, "Ground Effects on Pressure Fluctuations in Atmospheric Boundary Layers," *J. Fluid Mechanics,* Vol. 85, p. 491.

Guidez, J., 1989, "Study of the Convective Heat Transfer in a Rotating Coolant Channel," ASME JOURNAL OF TURBOMACHINERY, Vol. 111, pp. 43–50.

Hart, J. E., 1971, "Instability and Secondary Motion in a Rotating Channel Flow," *J. Fluid Mech.,* Vol. 45, pp. 341–351.

Iacovides, H., and Launder, B. E., 1987, "Turbulent Momentum and Heat Transport in Square-Sectioned Duct Rotating in Orthogonal Mode," *Numerical Heat Transfer,* Vol. 12, pp. 475–491.

Iacovides, H., and Launder, B. E., 1991, "Parametric and Numerical Study of Fully Developed Flow and Heat Transfer in Rotating Rectangular Duct," ASME JOURNAL OF TURBOMACHINERY, Vol. 113, pp. 331–338.

Iacovides, H., and Launder, B. E., 1992, "The Computation of Convective Heat Transfer in a 180° Pipe Bend," presented at ICHMT, Int. Symp. on Heat Transfer in Turbomachinery, Athens, Greece, Aug.

Kheshgi, H. S., and Scriven, L. E., 1985, "Viscous Flow Through a Rotating Square Channel," *Phys. Fluids,* Vol. 28, pp. 2968–2979.

Lai, Y. G., So, R. M. C., Anwer, M., and Hwang, B. C., 1991, "Calculations of a Curved-Pipe Flow Using Reynolds Stress Closure," *Proc. Instn. Mech. Engineers,* Vol. 205, pp. 231–244.

Launder, B. E., and Sharma, B. I., 1974, "Application of the Energy-Dissipation Model of Turbulence to the Calculations of Flow Near a Spinning Disc," *Letters in Heat and Mass Transfer,* Vol. 1, pp. 131–136.

Launder, B. E., and Loizou, P. A., 1989, "Laminarization in 3-Dimensional Accelerating Flow Through Curved Rectangular Ducts," presented at the 7th Symposium on Turbulent Shear Flows, Stanford, CA.

Morris, W. D., and Ghavami-Nasr, G., 1991, "Heat Transfer Measurements in Rectangular Channels With Orthogonal Mode Rotation," ASME JOURNAL OF TURBOMACHINERY, Vol. 113, pp. 339–345.

Prakash, C., and Zerkle, R., 1992, "Prediction of Turbulent Flow and Heat Transfer in a Radially Rotating Square Duct," ASME JOURNAL OF TURBOMACHINERY, Vol. 114, pp. 835–846.

Rodi, W., and Scheurer, G., 1983, "Scrutinizing the $k-\epsilon$ Model Under Adverse Pressure Gradient Conditions," *Proc. 4th Symposium on Turbulent Shear Flows,* Karlsruhe, Germany.

Soong, C. Y., Lin, S. T., and Hwang, G. J., 1991, "An Experimental Study of Convective Heat Transfer in Radially Rotating Rectangular Ducts," ASME *Journal of Heat Transfer,* Vol. 113, pp. 604–611.

Speziale, C. G., 1982, "Numerical Study of Viscous Flow in Rotating Rectangular Ducts," *J. Fluid Mech.,* Vol. 122, pp. 251–271.

Wagner, J. H., Johnson, B. V., and Hajek, T. J., 1991, "Heat Transfer in Rotating Passages With Smooth Walls and Radial Outward Flow," ASME JOURNAL OF TURBOMACHINERY, Vol. 113, pp. 42–51.

Wolfshtein, M., 1969, "The Velocity and Temperature Distribution in One-Dimensional Flow With Turbulence Augmentation and Pressure Gradient," *Int. J. Heat Mass Transfer,* Vol. 12, p. 301.

Yap, C. R., 1987, "Turbulent Heat and Momentum Transfer in Recirculating and Impinging Flows," PhD Thesis, Faculty of Technology, University of Manchester, United Kingdom.

APPENDIX

Task Performed by H_{ij}

The redistributive nature of the H_{ij} term is best illustrated by considering a two-dimensional boundary layer flow in which x_1 is the streamwise direction and x_2 the direction normal to the wall. Derivatives of k along x_1 and x_3 may then assumed to be zero. Shear stress components $\overline{u_1u_3}$ and $\overline{u_2u_3}$ will also be zero.

The elements of $[H_{ij} - \frac{1}{3}H_{kk}\delta_{ij}]$ are then obtained through the following expressions:

$$-\left[H_{11} - \frac{1}{3}H_{kk}\delta_{11}\right] = +\frac{2}{3}\overline{u_2^2}\left(\frac{\partial\sqrt{k}}{\partial x_2^2}\right)^2 C_H \qquad (A1)$$

$$-\left[H_{22} - \frac{1}{3}H_{kk}\delta_{22}\right] = -\frac{4}{3}\overline{u_2^2}\left(\frac{\partial\sqrt{k}}{\partial x_2}\right)^2 C_H \qquad (A2)$$

$$-\left[H_{33} - \frac{1}{3}H_{kk}\delta_{33}\right] = +\frac{2}{3}\overline{u_2^2}\left(\frac{\partial\sqrt{k}}{\partial x_2}\right)^2 C_H \qquad (A3)$$

$$-\left[H_{12} - \frac{1}{3}H_{kk}\delta_{12}\right] = -\overline{u_1u_2}\left(\frac{\partial\sqrt{k}}{\partial x_2}\right)^2 C_H \qquad (A4)$$

where

$$C_H = (15.6 + 2.4R_t)\exp\left(-\frac{R_t}{20}\right)$$

Equations (A1) to (A3) show that the H_{ij} term removes kinetic energy from the fluctuating component normal to the wall and redistributes it equally to the two fluctuating components that are parallel to the wall surface. As far as the shear stress component is concerned Eq. (A4) indicates that H_{ij} provides additional near-wall damping for the shear stresses.

Equations (A2) and (A4) also reveal a highly desirable numerical property of the H_{ij} term. In the equations where the H_{ij} term makes a negative contribution to the level of a particular stress component, the stress component in question is also present in the resulting expressions. Consequently, the diagonal dominance of the coefficient matrix of the resulting discretized equations will be enhanced within the sublayer regions, leading to a more stable solution procedure for the turbulent stresses.

Journal of Turbomachinery

Technical Briefs

Retained Lift: Theoretical Difficulties With the Concept and an Alternative Explanation of Observations

R. J. Kind,[1,3] S. A. Sjolander,[1,3]
and M. I. Yaras[2,3]

Introduction

Tip-clearance effects are an important source of losses in axial compressor and turbine blade rows. This has motivated a considerable number of experimental investigations of tip-clearance flows and efforts to develop models for the prediction of tip-clearance losses (e.g., Lakshminarayana and Horlock, 1962; Lewis and Yeung, 1977; Inoue et al., 1986; Yaras and Sjolander, 1990; Heyes and Hodson, 1993). An important element of the flow field is the streamwise vorticity shed from the blades in the tip region. Most of the experiments indicate that the shed vorticity rolls up into a tip vortex. The circulation or strength of this vortex is employed as a key variable in many of the loss-prediction models. All of the studies indicate that the circulation of the tip vortex is significantly less than the bound circulation around the blade. Lakshminarayana and Horlock (1962) offered an explanation of this in terms of a concept of "retained lift." That is, they postulated that not all of the bound vorticity is shed and that some fraction of the bound vortex lines span the gap between the blade tip and the endwall. The lift "retained" increases with decreasing tip clearance.

The retained lift concept has become widely accepted in the tip-clearance research community. It received a notable impetus from the work of Lewis and Yeung (1977). They used an integral of the static pressure on the endwall around a contour corresponding to the blade profile as a measurement of the retained lift. Their results were in fair agreement with the retained lift values of Lakshminarayana and Horlock (1962) and they proposed a correlation for the retained-lift fraction as a function of the gap-to-chord ratio. Inoue et al. (1986) and Yaras and Sjolander (1990) did detailed measurements of the flow fields downstream of a rotating compressor blade row and a turbine cascade with tip clearance, respectively, and thus determined the streamwise circulation downstream of their blade rows. They discussed their results in terms of the retained-lift concept and compared their results with those of the aforementioned authors. In his book, Cumpsty (1989) also implicitly accepts the retained lift concept.

Despite its broad acceptance, the present authors have come to believe that there are serious theoretical difficulties with the retained-lift concept. These difficulties were outlined by Yaras et al. (1992), who also presented an alternative explanation for the experimental observations. The title of this paper, however, reflected its broader content and the relatively brief comments regarding retained lift understandably attracted little attention. The present note contains a more thorough discussion of the theoretical considerations, which indicate that the retained-lift concept is invalid. It also contains an alternative physical explanation of why measured streamwise circulation is less than the bound circulation for typical tip clearances.

Theoretical Difficulties

In the discussion a number of well-known theorems on fluid motion are invoked; derivations of these are widely available, for example in Kuethe and Chow (1965) or Moran (1984).

Although the present arguments are essentially valid even when the end-wall boundary layer is very thick and the upstream flow is rotational, they are probably most easily grasped if initially presented in the context of a relatively thin endwall boundary layer and irrotational upstream flow outside this boundary layer. These assumptions are therefore adopted to begin with.

Those assumed conditions prevailed in the cascade flow field measurements of Yaras et al. (1989). Their data, for gap-to-chord ratios of 0.02, 0.028, and 0.032, show that the flow in the tip region behaves essentially as originally proposed by Rains (1954) and as sketched in Figs. 1 and 2. That is, there is a strong jet flow through the gap, driven by the static pressure difference between the pressure and suction surfaces of the blade. The flow in this jet is approximately perpendicular to the blade chord and its total pressure is essentially equal to the inlet free-stream value. In other words, the jet flow through the gap is essentially inviscid and irrotational. Other cascade experiments (e.g., Storer and Cumpsty, 1991; Heyes and Hodson, 1993) also support the flow model sketched in Figs. 1 and 2, at least for blades that are not particularly thick.

In Fig. 1 circuit C consists of a marked collection of fluid particles, which will flow through the gap and, at a slightly later time, will assume the position denoted by circuit C′. The circuit C is simply chosen such that at C′ the marked particles are in the inviscid portion of the gap flow; at C′ the circuit lies in a plane roughly parallel to the endwall. During convection from C to C′ the circuit is in inviscid flow and application of Kelvin's theorem is valid. This theorem states that the circulation around C′ is equal to that around C: that is, zero. It follows from Stokes' theorem that there can be no net vorticity enclosed by C′. This means that there can be no vortex lines spanning the gap as would be required by the retained lift concept.

---

[1] Professor; Mem. ASME.

[2] Assistant Professor.

[3] Department of Mechanical and Aerospace Engineering, Carleton University, Ottawa, Ontario, Canada K1S 5B6.

Contributed by the International Gas Turbine Institute of THE AMERICAN SOCIETY OF MECHANICAL ENGINEERS. Manuscript received at ASME Headquarters July 1994. Associate Technical Editor: N. A. Cumpsty.

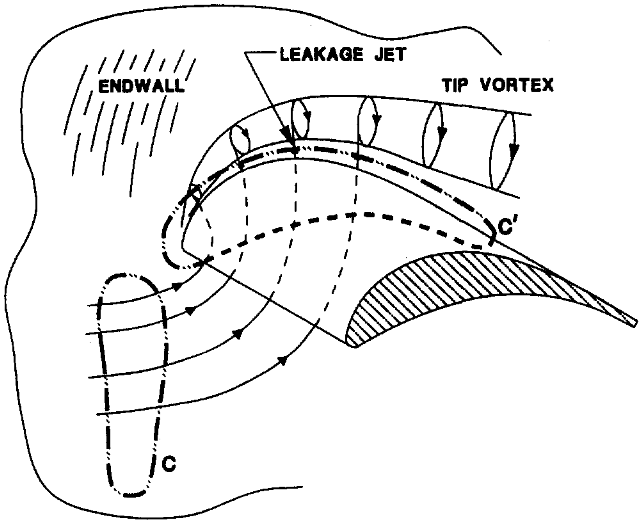

Fig. 1 Schematic of the tip-leakage flow

According to Helmholtz' vortex theorems, vorticity "adheres" to the fluid particles in inviscid flow. That is, it is a convective quantity. The experimental evidence (e.g., Lakshminarayana and Horlock, 1962; Yaras et al., 1989) convincingly shows that there is a strong leakage flow through the gap all along the blade chord. Any spanwise vorticity would be carried out of the gap by this flow and there is no plausible mechanism for replacement of such vorticity. The flow entering the gap region carries negligible spanwise vorticity and there is no solid surface in the gap region with orientation suitable to production of spanwise vorticity. Again the possibility of vorticity spanning the gap is ruled out. Another way of looking at this is that a force similar to the Kutta–Joukowski force, $\rho U\Gamma$, would be required to act on any spanwise vortex of strength Γ to retain it in the gap, if U is the velocity of the gap flow. There is, however, nothing that can provide this force. In the case of the bound vorticity the necessary force is provided by the force in the blade metal. The Kutta–Joukowski theorem is not quantitatively valid here because the extent of approximately two-dimensional flow is quite limited but there is still a requirement for a force to hold fluid having a cross-stream component of vorticity and a velocity, U, relative to the surrounding fluid.

Experiments (e.g., Lewis and Yeung, 1977; Yaras et al., 1989) show that the pressure field around the loaded blade is imposed onto the endwall with relatively little change. This is only to be expected because any strong pressure gradients in the spanwise direction from the blade to the wall would imply large spanwise accelerations and large flow velocity components; these are, however, largely prevented by the wall (the tip-leakage vortex that often forms is generally located somewhat away from the suction surface of the blade, outside the gap, and is thus immaterial to the argument). The loaded blade thus imposes onto the gap and endwall a static pressure difference roughly equal to that between its pressure and suction surfaces. It is important to realize that this pressure difference does not correspond to a retained lift force as assumed by Lewis and Yeung (1977). Rather, it produces an acceleration through the gap and is responsible for the strong flow through the gap, sketched in Figs. 1 and 2. In other words, this pressure difference is "reacted" by the inertia force associated with the acceleration through the gap, not by any "retained lift" force.

Kelvin's theorem and the Helmholtz vortex theorems only apply exactly if the flow is inviscid, that is, if vorticity cannot be transported by viscous or turbulent diffusion. This does not significantly undermine the arguments above because the leakage fluid passes through the gap region so quickly that very little diffusion could occur even if the molecular or eddy viscosity were substantial. Thus, retained lift is believed to be insignificant even where turbulent diffusion tends to be relatively large, as in rotating blade rows. The theorems are valid for rotational flow so the conclusions above should also be valid if the upstream flow is rotational.

The authors believe that retained lift can be significant only when tip clearances are extremely small, such that the gap constitutes a hydraulically long flow channel. This requires that $t/\tau \gg 1$, where τ is the clearance and t is the local blade thickness. Viscous shear forces on the blade tip and endwall would then be sufficiently large to react a significant fraction of the pressure difference between the blade pressure and suction surfaces. Using a typical friction factor value of 0.03 suggests that this effect would only become significant (more than 5 percent) for $\tau/t < 0.1$. Practical tip clearances are seldom this small. The lift retention mechanism in this case would not involve spanwise vorticity; rather, the pressure difference would be reacted directly by opposing shear stresses.

Alternative Explanation of Experimental Observations

As mentioned in the introduction, all of the experimental studies indicate that the circulation of the tip vortex, or the streamwise circulation measured downstream of the blade row, is less than the bound circulation unless the clearance is very large. If the retained lift concept is invalid, an alternative physical explanation is required for this experimental observation.

The required explanation rests on the flow pattern in the crossflow planes, sketched in Fig. 2. There are two sources of streamwise vorticity in this flow. One is at the pressure-surface corner of the blade tip (point A in Fig. 2) where the leakage flow separates, forming a vortex sheet whose associated circulation is in the same sense as the bound circulation; this is where the bound circulation is shed. The other source is on the endwall (region B–B in Fig. 2) where the leakage flow acquires a substantial transverse velocity by virtue of the acceleration through the gap; since the no-slip condition applies at the wall, vorticity must be created in the fluid close to the wall along B–B. This vorticity is of opposite sign to that created at A. Moreover, for the stationary wall case, the total strength, or circulation, of the vorticity created at B–B must be comparable in magnitude to that created at A since the experimental data (Yaras et al., 1989) show that the velocity of the leakage jet is approximately uniform in the cross-stream direction. After the leakage flow emerges from the gap it interacts with the passage flow. Flow visualization on the endwall (e.g., Sjolander and Amrud, 1987) has shown that this interaction results in separation of the endwall shear layer, as indicated in Fig. 2. It seems inevitable that much of this separated fluid will become part of the tip-leakage vortex. Since it has vorticity of the opposite sign to that of the vorticity shed at the blade tip, the resulting circulation in the tip-leakage vortex should be less than the bound circulation, as is observed. Of course not all of the end-

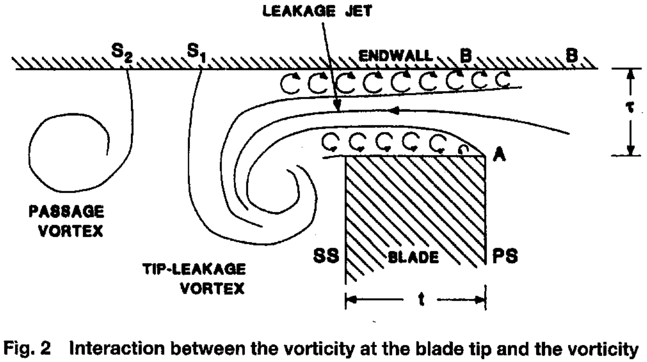

Fig. 2 Interaction between the vorticity at the blade tip and the vorticity layer on the endwall

wall fluid, and thus not all of the vorticity created at BB, is expected to be entrained into the tip-leakage vortex. As tip clearance increases, less entrainment and thus stronger tip-leakage vortices would be expected, again as observed experimentally.

When there is relative motion between the blades and the endwall the explanation above suggests that streamwise circulation observed downstream of the blade row will be less for turbines and greater for compressors. This is because the vorticity in the layer on the endwall is directly related to the velocity difference between the wall (as controlled by the no-slip condition) and the mainstream. In the case of turbines, the wall relative velocity is in the opposite direction to the leakage velocity. Thus, more vorticity of opposite sign is generated in the endwall layer, and after the mixing process the circulation observed downstream should be reduced. The data of Yaras et al. (1992) exhibit this trend. The data of Inoue et al. (1986) for a rotating compressor blade row show much greater downstream circulation, normalized by the bound circulation at midspan of the blades, than that measured by Yaras and Sjolander (1990) for a stationary cascade and corresponding gap-to-chord ratios. This again fits in with the expected trend.

It should be noted that no experiments have ever directly revealed any retained lift. Lakshminarayana and Horlock (1962) hypothesized its existence mainly on the basis of the high loadings observed at the tips of their blades. This observation is, however, also consistent with the shedding of all remaining bound circulation at the blade tip, point A in Fig. 2. In addition, Lakshminarayana and Horlock observed that smaller midspan gaps in their blades resulted in weaker trailing vortices; this can be explained in terms of mixing since fluid from opposite sides of the gap has vorticity of opposite sign. The experiments of Lewis and Yeung (1977) also should not be interpreted as indicating existence of retained lift, as explained earlier.

Conclusions

Theoretical difficulties with the retained lift concept have been pointed out. These indicate that the concept is invalid.

An alternative hypothesis is proposed to explain the experimental findings regarding streamwise circulation downstream of blade rows with tip clearance. The experimentally observed trends due to wall relative motion are consistent with this hypothesis.

Acknowledgments

The authors are grateful for support of this work under operating grants from the Natural Sciences and Engineering Research Council of Canada.

References

Cumpsty, N. A., 1989, *Compressor Aerodynamics*, Longman's Scientific & Technical, United Kingdom, p. 351.

Heyes, F. J. G., and Hodson, H. P., 1993, "Measurement and Prediction of Tip Clearance Flow in Linear Turbine Cascades," ASME JOURNAL OF TURBOMACHINERY, Vol. 115, pp. 376–382.

Inoue, M., Kuroumaru, M., and Fukuhara, M., 1986, "Behavior of Tip Leakage Flow Behind an Axial Compressor Rotor," ASME *Journal of Engineering for Gas Turbines and Power*, Vol. 108, pp. 7–14.

Kuethe, A. M., and Chow, C.-Y., 1965, *Foundations of Aerodynamics*, 3rd ed., Wiley, New York.

Lakshminarayana, B., and Horlock, J. H., 1962, "Tip-Clearance Flow and Losses for an Isolated Compressor Blade," Aeronautical Research Council of Great Britain, R & M 3316.

Lewis, R. I., and Yeung, E. H. C., 1977, "Vortex Shedding Mechanisms in Relation to Tip Clearance Flows and Losses in Axial Fans," Aeronautical Research Council R & M 3829, United Kingdom.

Moran, J., 1984, *An Introduction to Theoretical and Computational Aerodynamics*, Wiley, New York.

Rains, D. A., 1954, "Tip Clearance Flows in Axial Flow Compressors and Pumps," Rept. 5, Hydrodynamics and Mechanical Engineering Laboratories, California Institute of Technology.

Sjolander, S. A., and Amrud, K. K., 1987, "Effects of Tip Clearance on Blade Loading in a Planar Cascade of Turbine Blades," ASME JOURNAL OF TURBOMACHINERY, Vol. 109, pp. 237–245.

Storer, J. A., and Cumpsty, N. A., 1991, "Tip Leakage in Axial Compressors," ASME JOURNAL OF TURBOMACHINERY, Vol. 113, pp. 252–259.

Yaras, M. I., Zhu, Y., and Sjolander, S. A., 1989, "Flow Field in the Tip Gap of a Planar Cascade of Turbine Blades," ASME JOURNAL OF TURBOMACHINERY, Vol. 111, pp. 276–283.

Yaras, M. I., and Sjolander, S. A., 1990, "Development of the Tip-Leakage Flow Downstream of a Planar Cascade of Turbine Blades: Vorticity Field," ASME JOURNAL OF TURBOMACHINERY, Vol. 112, pp. 609–617.

Yaras, M. I., Sjolander, S. A., and Kind, R. J., 1992, "Effects of Simulated Rotation on Tip Leakage in a Planar Cascade of Turbine Blades: Part II, Downstream Flow Field and Blade Loading," ASME JOURNAL OF TURBOMACHINERY, Vol. 114, pp. 660–667.

Factors Affecting Measured Axial Compressor Tip Clearance Vortex Circulation

S. A. Khalid[1]

The relationship between turbomachinery blade circulation and tip clearance vortex circulation measured experimentally is examined using three-dimensional viscous flow computations. It is shown that the clearance vortex circulation one would measure is dependent on the placement of the fluid contour around which the circulation measurement is taken. Radial transport of vorticity results in the magnitude of the measured clearance vortex circulation generally being less than the blade circulation. For compressors, radial transport of vorticity shed from the blade tip in proximity to the endwall is the principal contributor to the discrepancy between the measured vortex circulation and blade circulation. Further, diffusion of vorticity shed at the blade tip toward the endwall makes it impossible in most practical cases to construct a fluid contour around the vortex that encloses all, and only, the vorticity shed from the blade tip. One should thus not expect agreement between measured tip clearance vortex circulation and circulation around the blade.

Nomenclature

c = chord length at blade tip
C_x = inlet area-averaged axial velocity
Γ = circulation
ω_y = vorticity component in stagger direction

Introduction

Several researchers have attempted to measure the circulation in the clearance vortex of a turbomachine blade passage. A common result is that the measured clearance vortex circulation is less than the circulation around the blade. Lakshminarayana and Horlock (1962) proposed that this observation is due to "retained lift." They suggested that only a fraction of the "bound" circulation is shed from the blade tip. However, Storer and Cumpsty (1991) showed that for typical clearances the leakage flow is essentially irrotational. If so, vortex lines from the blade cannot span the leakage jet and thus all of the circulation must be shed. Nevertheless, it will be shown below that

---

[1] Massachusetts Institute of Technology, Cambridge, MA 02139.

Contributed by the International Gas Turbine Institute of THE AMERICAN SOCIETY OF MECHANICAL ENGINEERS. Manuscript received at ASME Headquarters July 1994. Associate Technical Editor: N. A. Cumpsty.

wall fluid, and thus not all of the vorticity created at BB, is expected to be entrained into the tip-leakage vortex. As tip clearance increases, less entrainment and thus stronger tip-leakage vortices would be expected, again as observed experimentally.

When there is relative motion between the blades and the endwall the explanation above suggests that streamwise circulation observed downstream of the blade row will be less for turbines and greater for compressors. This is because the vorticity in the layer on the endwall is directly related to the velocity difference between the wall (as controlled by the no-slip condition) and the mainstream. In the case of turbines, the wall relative velocity is in the opposite direction to the leakage velocity. Thus, more vorticity of opposite sign is generated in the endwall layer, and after the mixing process the circulation observed downstream should be reduced. The data of Yaras et al. (1992) exhibit this trend. The data of Inoue et al. (1986) for a rotating compressor blade row show much greater downstream circulation, normalized by the bound circulation at midspan of the blades, than that measured by Yaras and Sjolander (1990) for a stationary cascade and corresponding gap-to-chord ratios. This again fits in with the expected trend.

It should be noted that no experiments have ever directly revealed any retained lift. Lakshminarayana and Horlock (1962) hypothesized its existence mainly on the basis of the high loadings observed at the tips of their blades. This observation is, however, also consistent with the shedding of all remaining bound circulation at the blade tip, point A in Fig. 2. In addition, Lakshminarayana and Horlock observed that smaller midspan gaps in their blades resulted in weaker trailing vortices; this can be explained in terms of mixing since fluid from opposite sides of the gap has vorticity of opposite sign. The experiments of Lewis and Yeung (1977) also should not be interpreted as indicating existence of retained lift, as explained earlier.

Conclusions

Theoretical difficulties with the retained lift concept have been pointed out. These indicate that the concept is invalid.

An alternative hypothesis is proposed to explain the experimental findings regarding streamwise circulation downstream of blade rows with tip clearance. The experimentally observed trends due to wall relative motion are consistent with this hypothesis.

Acknowledgments

The authors are grateful for support of this work under operating grants from the Natural Sciences and Engineering Research Council of Canada.

References

Cumpsty, N. A., 1989, *Compressor Aerodynamics*, Longman's Scientific & Technical, United Kingdom, p. 351.

Heyes, F. J. G., and Hodson, H. P., 1993, "Measurement and Prediction of Tip Clearance Flow in Linear Turbine Cascades," ASME JOURNAL OF TURBOMACHINERY, Vol. 115, pp. 376–382.

Inoue, M., Kuroumaru, M., and Fukuhara, M., 1986, "Behavior of Tip Leakage Flow Behind an Axial Compressor Rotor," ASME *Journal of Engineering for Gas Turbines and Power*, Vol. 108, pp. 7–14.

Kuethe, A. M., and Chow, C.-Y., 1965, *Foundations of Aerodynamics*, 3rd ed., Wiley, New York.

Lakshminarayana, B., and Horlock, J. H., 1962, "Tip-Clearance Flow and Losses for an Isolated Compressor Blade," Aeronautical Research Council of Great Britain, R & M 3316.

Lewis, R. I., and Yeung, E. H. C., 1977, "Vortex Shedding Mechanisms in Relation to Tip Clearance Flows and Losses in Axial Fans," Aeronautical Research Council R & M 3829, United Kingdom.

Moran, J., 1984, *An Introduction to Theoretical and Computational Aerodynamics*, Wiley, New York.

Rains, D. A., 1954, "Tip Clearance Flows in Axial Flow Compressors and Pumps," Rept. 5, Hydrodynamics and Mechanical Engineering Laboratories, California Institute of Technology.

Sjolander, S. A., and Amrud, K. K., 1987, "Effects of Tip Clearance on Blade Loading in a Planar Cascade of Turbine Blades," ASME JOURNAL OF TURBOMACHINERY, Vol. 109, pp. 237–245.

Storer, J. A., and Cumpsty, N. A., 1991, "Tip Leakage in Axial Compressors," ASME JOURNAL OF TURBOMACHINERY, Vol. 113, pp. 252–259.

Yaras, M. I., Zhu, Y., and Sjolander, S. A., 1989, "Flow Field in the Tip Gap of a Planar Cascade of Turbine Blades," ASME JOURNAL OF TURBOMACHINERY, Vol. 111, pp. 276–283.

Yaras, M. I., and Sjolander, S. A., 1990, "Development of the Tip-Leakage Flow Downstream of a Planar Cascade of Turbine Blades: Vorticity Field," ASME JOURNAL OF TURBOMACHINERY, Vol. 112, pp. 609–617.

Yaras, M. I., Sjolander, S. A., and Kind, R. J., 1992, "Effects of Simulated Rotation on Tip Leakage in a Planar Cascade of Turbine Blades: Part II, Downstream Flow Field and Blade Loading," ASME JOURNAL OF TURBOMACHINERY, Vol. 114, pp. 660–667.

Factors Affecting Measured Axial Compressor Tip Clearance Vortex Circulation

S. A. Khalid[1]

The relationship between turbomachinery blade circulation and tip clearance vortex circulation measured experimentally is examined using three-dimensional viscous flow computations. It is shown that the clearance vortex circulation one would measure is dependent on the placement of the fluid contour around which the circulation measurement is taken. Radial transport of vorticity results in the magnitude of the measured clearance vortex circulation generally being less than the blade circulation. For compressors, radial transport of vorticity shed from the blade tip in proximity to the endwall is the principal contributor to the discrepancy between the measured vortex circulation and blade circulation. Further, diffusion of vorticity shed at the blade tip toward the endwall makes it impossible in most practical cases to construct a fluid contour around the vortex that encloses all, and only, the vorticity shed from the blade tip. One should thus not expect agreement between measured tip clearance vortex circulation and circulation around the blade.

Nomenclature

c = chord length at blade tip
C_x = inlet area-averaged axial velocity
Γ = circulation
ω_y = vorticity component in stagger direction

Introduction

Several researchers have attempted to measure the circulation in the clearance vortex of a turbomachine blade passage. A common result is that the measured clearance vortex circulation is less than the circulation around the blade. Lakshminarayana and Horlock (1962) proposed that this observation is due to "retained lift." They suggested that only a fraction of the "bound" circulation is shed from the blade tip. However, Storer and Cumpsty (1991) showed that for typical clearances the leakage flow is essentially irrotational. If so, vortex lines from the blade cannot span the leakage jet and thus all of the circulation must be shed. Nevertheless, it will be shown below that

---

[1] Massachusetts Institute of Technology, Cambridge, MA 02139.

Contributed by the International Gas Turbine Institute of THE AMERICAN SOCIETY OF MECHANICAL ENGINEERS. Manuscript received at ASME Headquarters July 1994. Associate Technical Editor: N. A. Cumpsty.

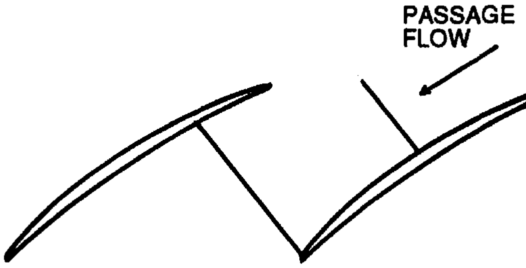

Fig. 1 Radial view of blade passage with midchord and trailing edge crossflow planes

there is no reason to expect the measured clearance vortex circulation to equal the circulation shed from the blade tip, or for that matter, the blade circulation.

The Tip Region Vorticity Field

To determine the factors that affect the circulation measured in a plane intersecting the trailing edge of a blade passage, we will consider the vorticity field near the blade tip. Figure 1 shows a radial view of an axial compressor blade passage with two crossflow planes oriented normal to the blade stagger. One crossflow plane intersects the suction surface at midchord. The other crossflow plane intersects the suction surface at the trailing edge. The midchord plane will be used to illustrate the vorticity distribution near the tip at a typical chordwise location along the blade. The trailing edge plane will be used for the calculation of the clearance vortex circulation since such a plane must be located downstream of all locations along the blade tip from which bound vorticity is shed. The contour around which the clearance vortex circulation will be calculated is located in the trailing edge plane. The blade boundary layers will not be enclosed by the contour.

The component of vorticity relevant for the measurement of circulation in a given plane is the component normal to that plane. Figure 2 shows a sketch of the distribution of the vorticity component along the stagger, ω_y, in the midchord crossflow plane. Greater ω_y strength is indicated by darker gray shading. A contour in the *trailing edge* crossflow plane around which one might calculate the clearance vortex circulation is superimposed. The segment of the contour, labeled A, which is nearest to the endwall would typically be placed at a radius between the blade tip and the endwall radii. The radius of segment A would be made greater than the tip radius in an attempt to enclose the vorticity shed from the tip, but less than the endwall radius to avoid measuring a circulation due to the motion of the endwall relative to the blade.

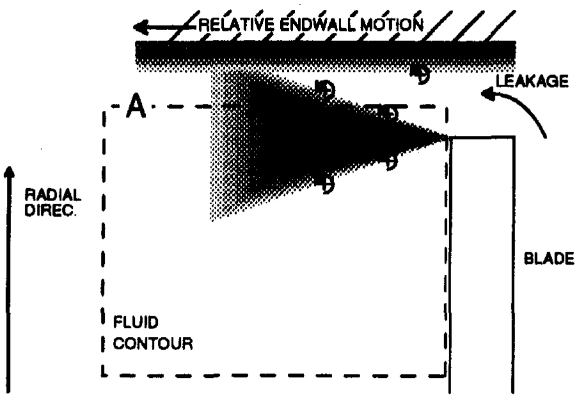

Fig. 2 Sketch of ω_y distribution near tip in midchord crossflow plane. Trailing edge contour for circulation measurement also shown.

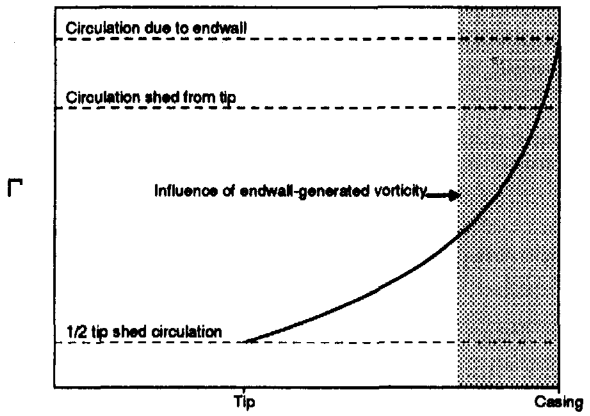

Fig. 3 Sketch of circulation as a function of radial placement of downstream contour used to measure clearance vortex circulation

The shear layer between the leakage and passage flow, which contains the vorticity shed from the blade tip, spreads due to turbulent diffusion. There may also be vorticity generated at the endwall, which diffuses into the passage flow. Since the spreading angle for a turbulent free shear layer is larger than that for a wall bounded layer, one should expect that the vorticity diffusion from the blade tip region penetrates the region between the blade tip and the endwall faster than the vorticity diffusing from the wall. Thus, regardless of the sign of the streamwise vorticity generated at the endwall, it is possible for vorticity shed from the blade tip to reach the trailing edge plane between segment A and the endwall (so some vorticity shed from the blade tip would not be enclosed by the contour). Since the radial velocities near the endwall are small, turbulent diffusion would be expected to be important in the vorticity transport near the endwall. Note that, for compressors, the vorticity generated at the endwall can contribute circulation of the same sign as circulation shed from the blade tip.

Consider the circulation calculated along the dashed contour shown in Fig. 2. The midchord plane ω_y distribution will be taken as representative of the vorticity field that reaches the downstream contour. The circulation obtained using the contour depends on the radial location of segment A. If segment A is positioned as shown in Fig. 2 such that some of the vorticity shed from the blade tip is not enclosed by the contour, circulation around the contour will be less than the circulation shed from the blade tip. If the radius of segment A is increased such that vorticity generated at the endwall is enclosed by the contour, the circulation value obtained cannot represent the circulation shed from the blade tip.

In Fig. 3, the range of circulation values that can be obtained with different trailing edge crossflow plane contours is indicated qualitatively as a function of radial placement of segment A of the downstream contour. If we assume that the spreading of the shear layer is equal in both radial directions, for segment A at the tip radius the circulation around the contour is half the circulation shed from the blade tip. As the radius of segment A is increased the measured circulation increases. As long as the contour does not enclose all the vorticity shed from the blade tip and excludes the vorticity generated at the endwall, the measured circulation will be less than circulation shed from the blade tip.

In the situation illustrated in Fig. 2, the vorticity field of the free shear layer merges with the vorticity field at the endwall. In this case the measured circulation cannot increase to the value shed from the blade tip until vorticity associated with the endwall is included within the contour. Even when segment A is positioned such that the circulation around the contour is the same as that shed at the blade tip, this circulation is not a measure of the shed circulation alone. The range of radii for

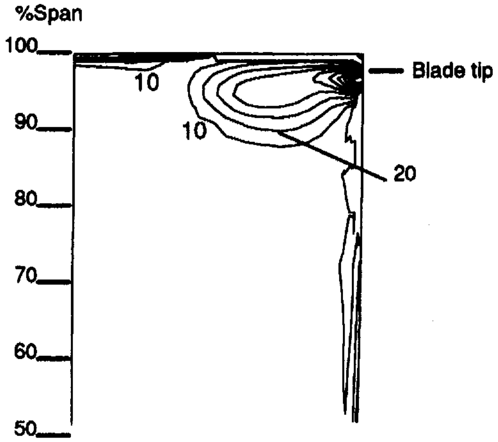

Fig. 4 $\omega_\gamma/(C_x/c)$ near tip in midchord crossflow plane for Navier–Stokes computation

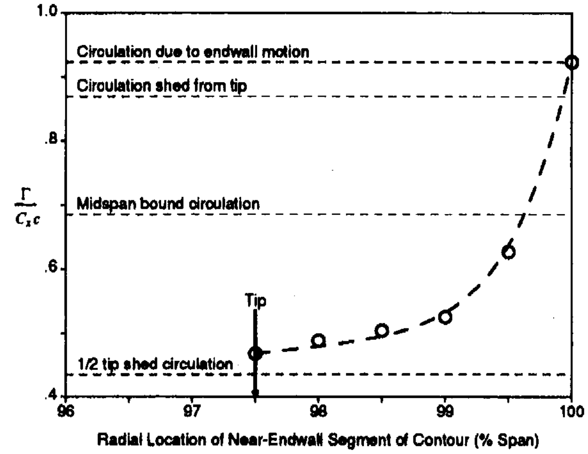

Fig. 5 $\Gamma/(C_x c)$ for computed flow field as a function of radial placement of downstream contour used to measure clearance vortex circulation

which vorticity generated at the endwall influences the circulation calculation is indicated by the shaded region in Fig. 3.

For compressors when the radius of segment *A* equals the endwall radius, the measured circulation exceeds the blade circulation. Neglecting any contribution along the contour except from segment *A*, the circulation equals the product of the relative wall speed resolved along segment *A* and the length of segment *A*.

A range of measured vortex circulation values can thus be obtained depending on the radial position of the contour around which the measurement is taken. If there were an irrotational region extending across the passage between the shear layer and the endwall, a contour could be chosen for which the measured circulation is equal to the circulation shed from the blade tip. However, as will be shown below, an unusually large tip clearance would be required for an irrotational region to separate the vorticity shed from the tip from the vorticity generated at the endwall. Reducing the clearance would tend to reduce the measured circulation for a given distance of segment *A* from the endwall since bringing the tip closer to the endwall would result in less of the shed circulation being enclosed by the contour.

For turbines or stationary cascades the same general considerations apply to the discrepancy between the blade bound and measured clearance vortex circulation. However, including the endwall in the contour used to obtain the vortex circulation would yield opposite sign circulation (compared to the sign of the shed circulation) for a turbine, and zero circulation for a stationary cascade.

Computational Results

Description of the Computations. The trends described above are illustrated below using a three-dimensional computation. A numerical simulation of a low-speed rotor passage was obtained using a three-dimensional Reynolds-averaged Navier–Stokes flow solver developed by Adamczyk et al. (1989). The Navier–Stokes solver uses a mixing length turbulence model appropriate for wall bounded flows. The geometry is the General Electric low speed E^3 Rotor B, described by Wisler (1977). The blade row has a clearance of 3 percent of chord and a flow coefficient of 0.42. The inlet conditions used are described by Wisler (1981) for the Rotor B/Stator B single-stage configuration near design conditions. The tip of the blade was located at 97.5 percent of span. The computations are described in more detail by Khalid (1995).

Vorticity Field and Circulation. Contours of $\omega_\gamma/(C_x/c)$ in the midchord crossflow plane indicated in Fig. 1 are shown in Fig. 4. The two sources of vorticity described in Section are evident in Fig. 4: (1) vorticity shed from the blade tip, which resides in the free shear layer, and (2) vorticity generated at the endwall. The ω_γ generated at the endwall is of the same sign as that shed from the blade tip, so the inclusion of endwall-generated vorticity in the clearance vortex circulation measurement increases the magnitude of the circulation obtained. The figure also indicates that there is more radial spreading of vorticity shed at the blade tip than of the vorticity generated at the endwall.

The circulation was calculated using a trailing edge crossflow plane contour similar to that shown in Fig. 2. The minimum radius segment of the contour was at roughly 50 percent span and the location of the maximum radius segment (segment *A* in Fig. 2) was varied between the blade tip and the endwall. Figure 5 shows $\Gamma/(C_x c)$ calculated around the contour as a function of radial placement of the maximum radius segment. The trend in measured circulation with maximum radius enclosed by the contour is like that sketched in Fig. 3.

The circulation shed from the blade tip can be obtained as the flux of vorticity for a surface defined such that it intersects all vortex lines, leaving the blade tip and only those vortex lines. This requirement was satisfied by choosing a surface 5 percent pitch from the suction surface and extending 96 to 98.5 percent span. The value of $\Gamma/(C_x c)$ obtained with this surface was 0.86. This value indicated as the circulation shed from the tip in Fig. 5 and is essentially the same as the circulation obtained by using a closed contour extending 11.5 percent pitch from the blade surfaces at the tip radius. The agreement between

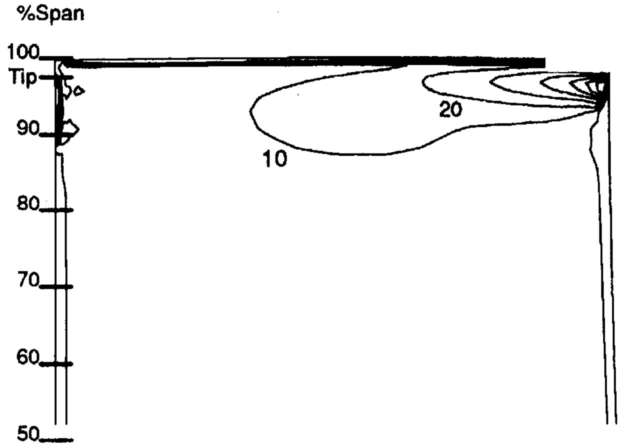

Fig. 6 $\omega_\gamma/(C_x/c)$ near tip in trailing edge crossflow plane for Navier–Stokes computation

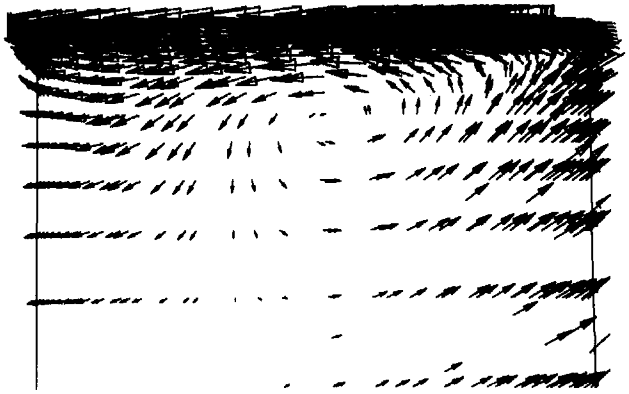

Fig. 7 Velocity vectors viewed along stagger in trailing edge crossflow plane for Navier–Stokes computation, 50–100 percent span

the shed circulation calculated 5 percent pitch from the suction surface and the blade circulation demonstrates the importance of entirely and exclusively enclosing the vorticity shed from the blade tip to obtain the blade circulation.

Because of the influence of the clearance vortex, the loading near the blade tip excedes the loading at midspan. Thus, as indicated in Fig. 5, the blade circulation at midspan is less than the circulation shed from the blade tip. However, for all the radial placements of the contour that excluded the endwall, the circulation calculated for the clearance vortex is less than the blade bound circulation at midspan. This is consistent with the experimental observation that the measured clearance vortex circulation is less than the blade "bound" circulation at midspan.

Estimate of Spread of Shear Layer. Diffusion also affects the measured clearance vortex circulation. We can estimate its importance by examining the growth of the shear layer. Although the shear layer formed by the tip leakage flow is not planar and does not have a unique velocity ratio, we can still get a rough idea of the vorticity layer thickness as a function of streamwise distance by using appropriate averages.

To obtain a velocity representative of the leakage side of the shear layer, the velocity resolved into the primary flow direction is area averaged over the clearance. The velocity on the freestream side of the shear layer was represented by the velocity magnitude area averaged over a surface two clearance heights from the endwall. Using these values in the expression for the growth of a shear layer (Dimotakis, 1989) we find that a distance of 50 percent chord would be required for the vorticity thickness to spread one clearance height (3 percent of chord). Thus, the shear layer is likely to be affected by the endwall *within* the blade passage even for this rather large clearance of 3 percent of chord.

Contours of $\omega_Y/(C_x/c)$ in the trailing edge crossflow plane are shown in Fig. 6 from the Navier–Stokes computation. The absence of an irrotational region between the two sources of vorticity (blade tip and endwall) means that the shear layer is affected by diffusion of vorticity from the endwall and one cannot construct a contour that encloses all and only the vorticity shed from at the tip.

Complexity of Tip Region Flow

Much of the past ambiguity concerning clearance vortex circulation appears to stem from oversimplifying the description of the flow in the tip region. Before summarizing the conclusions concerning the measured clearance vortex circulation, therefore, some common misconceptions will be addressed.

Figure 7 shows velocity vectors viewed normal to the trailing edge crossflow plane. Comparing Figs. 6 and 7 reveals that the vortex core is not the location of maximum ω_Y and that the highest vorticity component normal to the crossflow plane resides outside the vortex core. Thus, one cannot account for the circulation shed from the blade tip by calculating the circulation associated only with the vortex core.

Also, it is inappropriate to attempt to relate the circulation around the clearance space to a lift force there. The Kutta–Joukowsky theorem relates bound circulation to the force for a two-dimensional flow. The vorticity shed from the blade is not bound vorticity—it is convected with the flow and sustains no load. As shown in Fig. 2, this vorticity is present in the region between the tip and the endwall. The circulation around contours in a constant radius surface between the tip and the endwall (at the radius of segment A, say) will generally be nonzero.

Conclusions

For most practical cases, the circulation one measures for a turbomachine tip clearance vortex varies continuously with radial placement of the contour around which the measurement is taken. The primary factors contributing to the discrepancy between blade bound circulation and measured clearance vortex circulation are diffusion of vorticity shed from the blade tip and the proximity of the blade tip to the endwall. Diffusion causes shed vorticity to be transported toward the endwall. The proximity of the endwall prevents one from constructing a contour downstream of the blade that encloses all the vorticity shed from the blade tip and only that vorticity. Therefore, reducing the clearance tends to reduce the measured clearance vortex circulation.

In measuring the circulation associated with the clearance vortex rather than the circulation associated with the relative endwall motion, contours are commonly positioned so as to exclude the endwall. Therefore, measured clearance vortex circulation is typically less than the circulation shed from the blade tip. This suggests that vorticity generation at the endwall is not a primary factor affecting the measured circulation.

The clearance vortex should not be regarded as an isolated vortex in which all the vorticity is contained within its core. Also, there can be a net circulation in a contour lying in a radial plane between the blade tip and the endwall, even though there is no lift force there.

Acknowledgments

The author wishes to thank Allison Engine Company, Dr. R. A. Delaney technical monitor, for its support and funding of this research at the MIT Gas Turbine Laboratory on the effects of tip clearance in axial compressors. The author is also grateful for the assistance of Dr. J. J. Adamczyk, Dr. K. R. Kirtley, and Mr. M. L. Celestina in carrying out the computations. Also, the helpful advice from Professors E. M. Greitzer and I. A. Waitz at the Gas Turbine Laboratory regarding the presentation of these results is greatly appreciated.

References

Adamczyk, J. J., Celestina, M. L., Beach, T. A., and Barnett, M., 1989, "Simulation of Three-Dimensional Viscous Flow Within a Multistage Turbine," ASME JOURNAL OF TURBOMACHINERY, Vol. 112, pp. 370–376.

Dimotakis, P., 1989, "Turbulent Free Shear Layer Mixing," Paper No. AIAA-89-0262.

Khalid, S. A., 1995, "The Effects of Tip Clearance on Axial Compressor Pressure Rise," Ph.D. Thesis, Department of Mechanical Engineering, Massachusetts Institute of Technology, Cambridge, MA.

Lakshminarayana, B., and Horlock, J. H., 1962, "Tip-Clearance Flow and Losses for an Isolated Compressor Blade," Aeronautical Research Council of Great Britain, R & M 3316.

Storer, J. A., and Cumpsty, N. A., 1991, "Tip Leakage Flow in Axial Compressors," ASME JOURNAL OF TURBOMACHINERY, Vol. 113, pp. 252–259.

Wisler, D. C., 1977, "Core Compressor Exit Stage Study, Vol. I—Blading Design," NASA CR-135391.

Wisler, D. C., 1981, "Core Compressor Exit Stage Study, Vol. IV—Data and Performance Report for the Best Stage Configuration," NASA CR-165357.